JOURNAL OF CONDENSED MATTER NUCLEAR SCIENCE

Experiments and Methods in Cold Fusion

Proceedings of the ICCF18 Conference, July 21–27, 2013, University of Missouri, Columbia, Missouri, U.S.A.

VOLUME 15, March 2015

JOURNAL OF CONDENSED MATTER NUCLEAR SCIENCE

Experiments and Methods in Cold Fusion

JOURNAL OF CONDENSED MATTER NUCLEAR SCIENCE

Volume 15, March 2015

ISSN 2227-3123

Orders, claims, author inquiries and journal inquiries

Please contact the Editor in Chief, CMNSEditor@iscmns.org or webmaster@iscmns.org

J. Condensed Matter Nucl. Sci. 15 (2015) 1–327
©2015 ISCMNS. All rights reserved. ISSN 2227-3123

JOURNAL OF CONDENSED MATTER NUCLEAR SCIENCE

Volume 15 2015

CONTENTS

PREFACE

RESEARCH ARTICLES

Preface

My thanks to everyone who attended ICCF-18, which was held at the University of Missouri. We had a total of 215 registered participants, of whom 125 submitted original work that was presented within the scientific program. This was the first time in many years that ICCF has been held on the campus of a major research university, and we were delighted to have the opportunity to host this important conference.

Instead of summarizing the research highlights of the ICCF-18 meeting in this preamble, I prefer to speak to the evolving style of presentations that were made at this meeting, since I see this progression as being essentially important to the advancement of this exciting discipline of condensed matter nuclear science (CMNS) in the world's scientific agenda. The papers within this volume convey their scientific significance intrinsically, and all have made a contribution to this field, so I will not single out particular presentations in my comments below.

At ICCF-18 scientists presented their own original work and compared and contrasted their results to those of other authors. Far more 'data centric' talks were presented at this conference than 'futuristic opinion' talks, and personally I think that this is an excellent trend that should continue well into the future of the ICCF series. While there were a number of areas of agreement, there were also starkly different results reporting on the same phenomena, all presented by quite credible scientists from around the world. As in any scientific community, this often led to strong emotions and heated debate and exchanges. But it is exactly these tense discussions that are an essential ingredient in the advancement of science. It is essential that we all have confidence in the validity of our work, and that we openly and honestly provide a critical self-assessment of our results. When we independently arrive at differing results, then it is essential that we as a community keep an objective, open mind as we collectively work to resolve these different reports through more data and further study. Yes, eventually some results will be shown to be wrong, possibly do to an unknown experimental artifact at the time, and others will be borne out to be accurate based upon large-scale reproducibility across many different labs world-wide. This is the natural and healthy way that science is conducted. It is impossible to know initially if the positive result or the negative result is accurate, until many others attempt to reproduce the measurements with improved metrology. Hence, both results must be carefully considered and respected until much more data is obtained, hopefully from many other labs that utilize different experimental techniques. This initial ambiguity regarding the early reports on new phenomenology is both natural, and to be encouraged. There is nothing more dangerous to the progression of science than an inferred 'requirement' that our results must agree with each other. I think that we have all suffered severely in the past from journals, funding agencies, and professional societies that have thoughtlessly rejected interesting new work simply because it didn't agree with the prevailing trends and beliefs of the time. Let's be certain that we never make that same mistake within our own ICCF community. As exciting new results emerge from our efforts, the world will rapidly come to view our community as an example of how essential it is to keep an open mind when one encounters new empirical results that initially appear to be inconsistent with the preferred theoretical interpretation of the time.

So please join me in reading the proceedings of ICCF-18 with a critical, open mind. Thanks to everyone who presented their work here, and I look forward to more intense and vigorous scientific exchanges during our future meetings.

Sincerely,

Rob Duncan
(*ICCF-18 Conference Chair*)
March 2015

J. Condensed Matter Nucl. Sci. 15 (2015) 1–10

Research Article

Flux Effects in Metal Hydrogen Loading: Enhanced Mass Transfer

Michael C.H. McKubre* and Francis L. Tanzella

Energy Research Center, SRI International, CA, USA

Abstract

SRI has shown over hundreds of electrochemical experiments that the Fleischmann–Pons heat effect can be generated if high current, high loading and deuterium flux are present. Until the work of Dardik and the Energetics group, we were unable to generate the deuterium flux synthetically. Using Dardik's Superwave® method to generate deuterium flux, we have shown that excess heat is regularly seen in PdD*x* electrolysis cells, given the appropriate cathode metallurgy.

Keywords: Deuterium, Flux, Loading, Palladium

---

1. Introduction

On March 23rd 1989 Fleischmann, Pons and Hawkins [1] publicly reported results of an anomalous heat effect resulting from the intensive, electrochemical insertion of deuterium into palladium cathodes occurring over an extended period of time. This was already a well-studied system, and the SRI team, having worked on Pd/D_2O for more than a decade, was better positioned than most to judge this claim experimentally. If anomalous large heat production was indeed present in palladium cathodes loaded electrolytically with D, then the only possibility was that this occurred in the very high loading regime with the atomic loading ratio D/Pd greater than about 0.8 where the system had been infrequently and poorly studied. This intuition regarding the effect of the D/Pd loading ratio on the excess power production was supported experimentally when the groups at SRI [2] and IMRA-Japan [3] reported simultaneously and independently the effect of threshold loading of D/Pd ~ 0.85 on the Fleischmann Pons Heat Effect (FPHE) for bulk Pd wire cathodes at ICCF3 in Nagoya in October 1992.

Several mysteries relating to the FPHE remained to be revealed and resolved at that time. The appearance of heat in excess of electrical input appeared to exhibit a threshold effect on current density at levels significantly greater than the current density of maximum loading [4][a]. A significant time delay separated complete deuterium saturation and the onset of thermal activities that suggested the initiation or incubation time of an unknown process presumably of chemical

---

*E-mail: michael.mckubre@sri.com

[a] Threshold current densities of 100 mA cm^{-2} or larger were observed, well beyond the current density of maximum loading that is between is between 15 and 25 mA cm^{-2} for Pd cathodes in 0.1–1.0 M LiOD solutions typically used in these experiments [4].

or metallurgical origin. In 1995 it was discovered that there was another materials or electrochemical constraint on the demonstration of the FPHE [5]. Excess power was shown not to occur for equilibrium-loaded bulk-wire cathodes no matter how highly loaded, but did occur when a flux of deuterium was present. The excess power was roughly proportional to the flux of deuterium through the cathode interface[b] independent of direction.

We will use the space here to discuss the materials and electrochemical significance of these observations with regard to demonstrating and hopefully utilizing the FPHE. We adopt an empirical approach and do not attempt to understand or explain the fundamental physical processes behind the need for high loading, high current, long times and high flux. Of pragmatic interest is how one can tailor the metallurgical and electrochemical processes to achieve these four conditions simultaneously.

2. The Flux Condition

SRI experiment M4 was performed in a helium leak-tight calorimeter [6] and employed a Johnson Matthey low platinum group metal palladium cathode 0.1 cm dia., × 10 cm long formed into the shape of a "lasoo" [6]. The electrolyte was 1.0 M LiOD with 200 ppm Al added initially. The cell was evacuated and electrolyte added with the power supply delivering 2 V cathodic. The cell was then filled with D_2 gas containing 0.34 ppm ^{4}He to a pressure of 5 psig. Two slow current ramps were undertaken in an attempt to engender loading and exhibit an excess heat effect[c]. The first current ramp from 70 to 210 h yielded excess power and energy below the measurement uncertainty ($P_{\mathrm{XS,\,Max}} = 12 \pm 21$ mW and $E_{\mathrm{XS}} = 12 \pm 18$ kJ) and the second from 350 to 390 h showed a small effect at the limit of calorimetric accuracy ($P_{\mathrm{XS,\,Max}} = 53 \pm 25$ mW and $E_{\mathrm{XS}} = 17 \pm 8$ kJ).

At 472 h and prior to the third current ramp an important change was observed in the properties of the measured cathode axial resistance ratio and, consequently, in the inferred loading; the measured resistance appeared to become spontaneously noisy[d]. No change was made (intentionally or knowingly) to the electrical circuit at this time, other than repeating a previously performed current profile. A third current ramp was started at 504 h from 32 mA cm^{-2} to 985 mA cm^{-2}over a period of ~60 h. Figure 1 shows the effect of this ramp on the loading inferred from the 4-wire resistance measurement [7]. While not particularly well loaded, the cathode responded positively to increasing current up to a surprisingly high value of current density and a maximum loading of D/Pd = 0.88±.01 was obtained at a current density of ~376 mA cm^{-2}. What is of interest and was first seen in this data set, the loading appeared to fluctuate or oscillate with an amplitude that varied during the 240 h period of Fig. 1. The red line in Fig. 1 will be discussed below.

Figure 2 shows the effect of current, loading and loading oscillations on the measured excess power normalized to the cathode volume (0.079 cm^3). Also shown in Fig. 2 is a fitting function

$$P_{\mathrm{XS}} = M(x - x^{\circ})^2(i - i^{\circ})|i_{\mathrm{D}}|, \tag{1}$$

where P_{X} is the excess power density (W cm^{-3}), M is a proportionality constant (in this case 3×10^6), x = D/Pd, x°~0.833, i is the electrochemical current density for the cathode, i°=0.45 A cm^{-2}, and i_{D} is the absorption/desorption deuteron flux through the surface expressed as current density (A cm^{-2}) that is required to load and unload the cathode during the period of the spontaneous loading oscillations.

With two adjustable parameters[e] (x° and i°) the green function in Fig. 2 exhibits a cross correlation r = 0.853 with the measured excess power density indicating that ~73% of the excess power is reflected linearly in the terms

---

[b] Other fluxes may be important as well, notably axial fluxes of deuterons and electrons in the metal phase.

[c] At the end of each ramp the cathode surface was briefly and partially stripped anodically to remove surface deposits, and Cu was added to the electrolyte dissolved in LiOD.

[d] On closer examination this noise resolved into signal as discussed below.

[e] The scale factor M is not relevant to the cross correlation function. The adjustable parameters x° and i° are heavily constrained by physical reality,

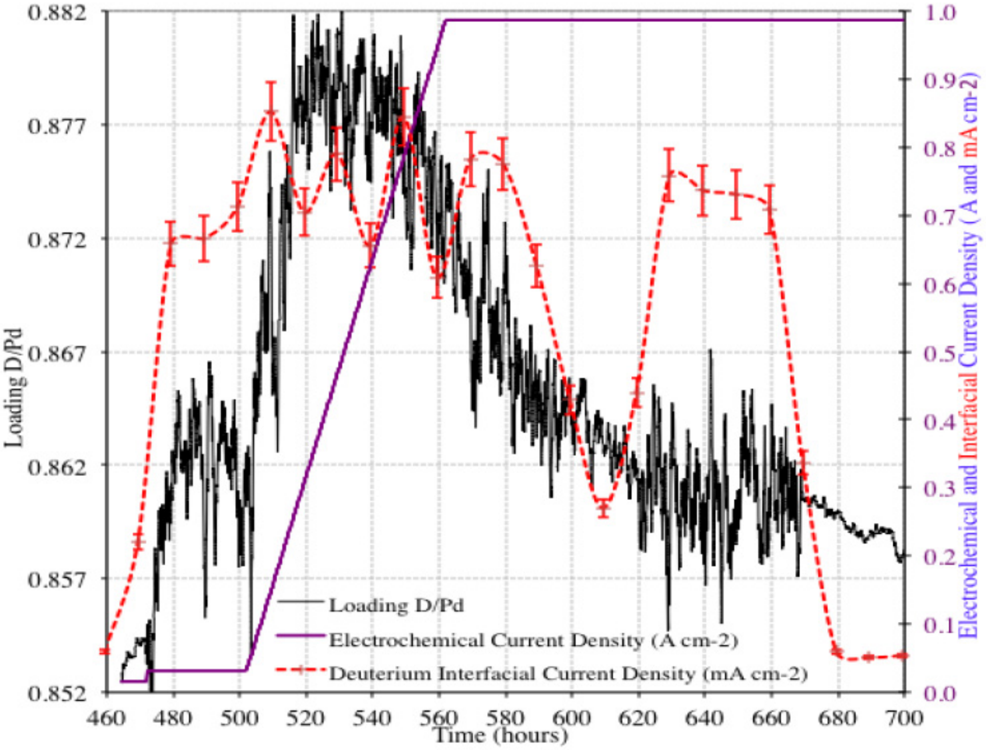

Figure 1. The response of loading and interfacial deuterium flux to a ramped increase in electrochemical current density in experiment M4.

of equation [1]. In fact, since the current is constant during most of the duration of excess power, the primary drivers are the slow decline of the average loading value, and the oscillation of loading (the dc and ac effects of loading, see Fig. 1). It is this data set, together with several subsequent sets primarily using 1 mm dia. wires and 50 μm thick foils[f] that prompted us to consider the deuteron flux as a variable in excess heat production, and to attempt to find means to stimulate it.

First, what is the nature of the loading oscillation, and what is its range of amplitude? In the 24-hour period from 610 to 634 h there was no change in current density and very little change in average loading with a slight declining trend. Despite this the measured excess power rises from near zero values ($\sim$30 mW cm^{-3}) between the peak values shown in Fig. 2, to more than ten times this value at 634 h. Details of the loading variation and excess power can be seen in this period in Fig. 3. The loading oscillation at constant electrochemical current density appears in the shape of a rough sinusoid (with some harmonic distortion), with fixed period $\sim$2 h, and spontaneous variation in amplitude. It is this internally generated amplitude modulation that affects the last term in equation [1] and dominates the variability of excess power in this interval.

Why 2 h? Once inside the Pd metal phase the D atoms diffuse with critical dimension 0.05 cm determined by

---

[f] Data from foils are not as easily handled for planar cathodes which invariably have non-uniform current distributions and non-uniform loading that results in a measured average value that may be well below the points of maximum loading where presumably the excess heat effects take place.

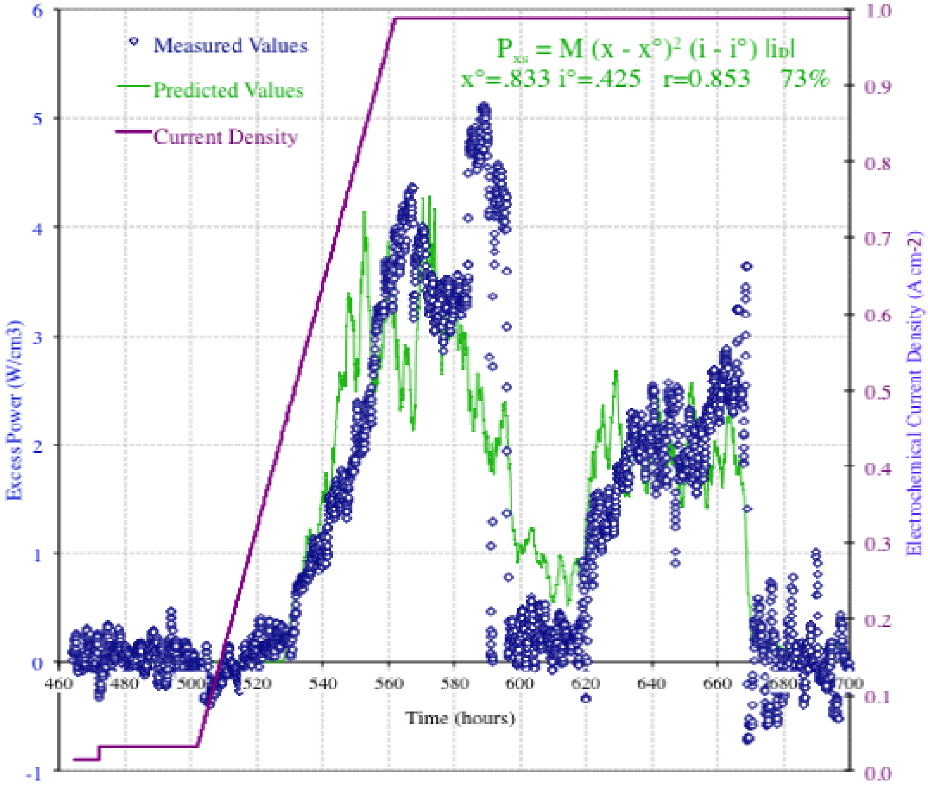

Figure 2. The observed and calculated excess power from Eq. (1) for a ramped increase in electrochemical current density in experiment M4.

the radius of the 1 mm dia. wire. There are approximately 14 peaks and valleys in the loading in Fig. 3 so that the average period is 1.71 h. Calculating the diffusion coefficient from this time constant for a penetration depth of 0.05 cm yields a value of $D_\mathrm{D} = 2 \times 10^7$, exactly that of deuterium at high concentration in palladium. It appears that what was happening, *without our control or even knowledge at the time*, was that the cathode spontaneously absorbed D at a rate determined by the electrochemical kinetic control of the surface monolayer coverage (D surface activity). At the point that the cathode was "full", and the inward flux no longer sustainable, either a condition of stress inside the lattice or an effect that reduced the deuterium surface activity causes the flux to reverse and complete the cycle. In the interval of Fig. 3 excess power is controlled by the amplitude of this oscillation. After many years we still do not know what caused the amplitude (and thus excess power density) to change.

What is happening and how can we affect it? The dashed red line in Fig. 1 plots the 10-hour averaged value of the flux of deuterium across the cathode interface that is required to cause the variation in bulk average loading[g]. Note the three order of magnitude difference in scale between i_D (the deuteron interchange flux expressed in mA cm^{-2}) and i (the applied electrochemical current density expressed in A cm^{-2}). This scale difference indicates that essentially all

---

[g] For convenient reference this flux is plotted as a current density although the exchange of surface-adsorbed and bulk-absorbed D atoms is a chemical not electrochemical process.

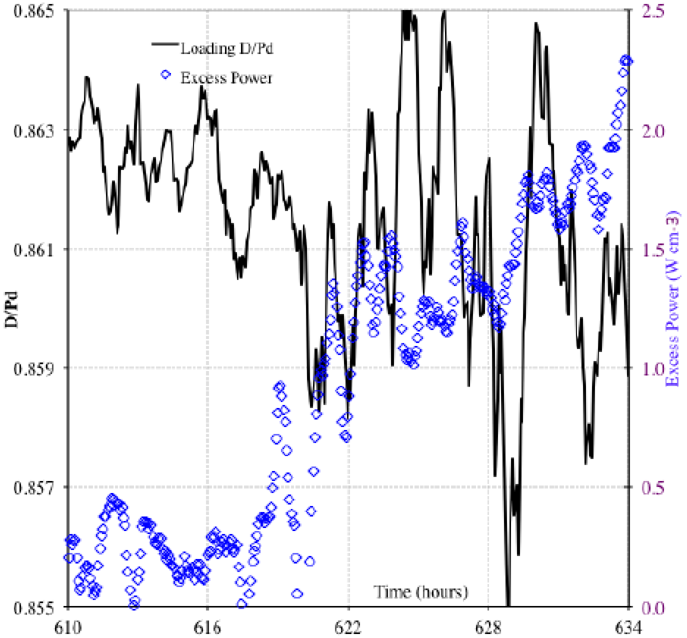

Figure 3. Detail of the spontaneous loading and excess power fluctuations in M4.

of the applied current results in D_2 molecule formation not loading. Despite this, the exchange flux of nearly 1 mA cm^{-2} is quite surprising, especially since in light of the fit to equation [1] in Fig. 2 this flux appears to control the rate of excess heat production in well-loaded cathodes after the incubation period.

This brings us to the central question: how can we take advantage of this knowledge to increase the reproducibility of our experiments and the power and energy density of the effect? The total excess energy produced in the two peaks (Fig. 2) of Ramp 3 was 82.5 ± 27 kJ, a 3 sigma effect but more would be desirable. After brief stripping and a third Cu addition a fourth ramp was commenced at 758 h. The loading during Ramp 4 was better than Ramp 3 with D/Pd reaching a maximum of 0.898 ± 0.001 but the loading fluctuation seen in Figs. 1 and 3 was not present. An attempt was made to stimulate loading fluctuations electrochemically by modulating the current with increasing amplitude about a fixed cathodic point ultimately reaching a maximum of 3.1 ± 1.0 A. This condition was maintained for 24 h but resulted in very little forced loading variation, a relatively rapid net loss of loading down to D/Pd∼0.82, and no excess power. The calorimeter maintained thermal balance with $P_{\mathrm{XS,\,Max}} = 0 \pm 40$ mW and $E_{\mathrm{XS}} = 4 \pm 26$ kJ in the approximately 300 h process of Ramp 4.

At 1077 h the cathode was stripped and 2 cm^3 of 1 M LiOD with 200 ppm Al was added to the cell, followed by 1 cm^3 of D_2O, with flowing D_2. At 1078 h the cell was pressurized to ∼ 5 psig, the D_2 flow stopped and manifold sealed, and the current density was returned to 16 mA cm^{-2}. At 1174 h the fifth current ramp was started from 0.1 to 3.1 A at 25 mA/h. At 1334 h a further attempt was made to induce loading variation by switching the current on alternate measurement cycles (5 min) between 3.1 A cathodic and 0.001 A anodic. During the initial ramp the loading reached a maximum loading of D/Pd = 0.918 ± 0.001 The introduction of cathodic/anodic pulsing at 1334 h produced a variability in loading, as desired, but the flux response was small, the net loading declined and the excess power and energy was within the calorimeter experimental uncertainty accuracy ($P_{\mathrm{XS,\,Max}} = -25 \pm 25$ mW and $E_{\mathrm{XS}} = -4 \pm 8$ kJ).

Before the declared end of experiment M4 a total of 26 further attempts were made to find a waveform or pulse sequence that would allow us to induce a loading variability and thus a flux of D across the interface, while maintaining above-threshold loading. None was found [6] and a number of experiments were designed and operated over the next few years with similar null results. Although high loadings could be achieved with suitable electrochemical control and robust Pd metallurgy, and high loading variabilties could be achieved with some current schemes and scupulous control of the elelctrochemical interface, these two criteria were not met simultaneously with any waveform employed by us until 2003.

The paper delivered by El Boher at ICCF10 in 2003 with principal author Dardik remains one of the most interesting and important works in the CMNS field [8]. Two aspects of novelty were introduced by Energetics Technologies Inc. (ETI) in this paper:

(1) The use of a palladium glow discharge in deuterium gas that produced 6.7 times more thermal output than input electrical energy in a well designed mass flow calorimeter.
(2) Implementation of a highly novel multi-periodic waveform that the inventors designated as a “SuperWave”.

Not only were ETI scientists able by means of this SuperWave to (presumably) load and stimulate the Pd/D-plasma interface to achieve significant levels of excess energy production at useful temperatures[h], they were also able to use this function to load and modulate the loading in electrolytic Pd/D_2O cells. As a result of this an extended and successful campaign of experimentation was mounted to explore the use of SuperWaves in loading Pd with D in electrolytic cells and excess heat production by ETI in Israel, SRI in the US and ENEA (Frascati) in Italy [9].

What is a SuperWave and what is it good for? SuperWaves are a new class of function, somewhat related to Brown Noise, generated by the self similar superposition of higher frequency replicates of a kernel function on itself according to the following rule. As the amplitude of the kernel function increases, the frequency and amplitude of the superimposed higher frequency replicate also increase. This generates a new kernel function; this recursion process can be replicated as many times as desired but from experience with electrochemical systems little benefit is gained beyond the fourth or fifth modulation level. What results is a function with lowest frequency determined by the period of the initial kernel, highest frequency governed by the selected scaling factors[i], and all frequencies in between (and all amplitudes) are represented in the function. Figure 4 shows this process in operation using a $\sin^2$ function as a kernel (the dark blue line).

The function shown in Fig. 4 and closely similar functions generated using varied parameters has been widely explored at SRI in the past decade for loading and excess heat generation. Another way of representing the SuperWave mathematically is as follows,

$$F(t) = A_0\sin^2(\omega_0 t)[1 + A_1\sin^2(\omega_1 t)][1 + A_2\sin^2(\omega_2 t)][1 + A_3\sin^2(\omega_3 t)]\ldots \tag{2}$$

More than 1000 experiments have been performed in the laboratories mentioned above[j] to test the power and benefits of SuperWaves in electrochemical and other systems. The advantages are best shown by example. Figure 5 shows the use of a SuperWave in an electrochemical cell and calorimeter of ETI design [9,10] during a DARPA-sponsored replication activity [11]. In this case the cathode was a 50 μm thick foil of area 8.6 cm^2 prepared by Violante at ENEA (Frascati) and the electrolyte was 0.1 M LiOD with no deliberate additions. The red data points plot the average,

---

[h] The water in the mass flow calorimeter was raised to the boiling point and the temperature inside in the plasma was obviously much higher.

[i] The highest frequency is practically constrained by the ability of power systems to deliver signal to the system under test, and the ability of the measurement system to interrogate and resolve the input and output signals.

[j] Primarily by ETI in Israel which is now constituted as the Sidney Kimmel Institute for Nuclear Renaissance (SKINR) at the University of Missouri, Columbia.

maximum and minumum loading obtained during the 20-minute SuperWave cycle[k] of experiment ETI 035-7. It can easily be seen that the SuperWave allows or facilitates loading up to extreme values for this cathode, and that this high loading persists to both for long times and at high currents. The maximum loading observed during the 540-hour interval of Fig. 4 was an impressive value of $\mathrm{D/Pd_{Max.}} = 1.010$ with a maximum 20-minute average value of $\mathrm{D/Pd_{MAv.}} = 0.982$, both at the maximum average current of 1.75 A or electrochemical current density of 203 mA cm^{-2}.

Connecting the minima and maxima of D/Pd for each SuperWave cycle is a bidirectional flux of deuterium through the large surface area. Although scattered, the black circle points in Fig. 5 show the very impressive response of a highly facile electrochemical interface. The largest response of over 4 mA cm^{-2} of deuterium interfacial flux occurred at ~160 h when the cathode was deliberately partially stripped and at intermediate currents of 470 mA or 55 mA cm^{-2}. An analysis of the excess power measured in this experiment in terms of Eq. (1) yeilded the following constants [11]: $x^\circ = 0.875$ D/Pd; $i^\circ = 35$ mA cm^{-2}. That is, in terms of Eq. (1), the foil cathode in experiment ETI 035-7 behaved very similarly to the wire cathode of experiment M4 dicussed above, but with a significantly lower current threshold (35 cf. 450 mA cm^{-2} for M4) and a very much lower proportionality constant M (10^3 cf. 3×10^6 for M4). Both factors suggest that a much smaller fraction of the total surface area was involved in excess heat production for the foil cathode. The reasons for this are reasonably well understood and described in reference [11], but are beyond the scope of this work.

---

[k] 20 minutes or 1200 s corresponds to a frequency of 0.83 mHz which is below the lowest frequency at which mass transport processes (the slowest relevant electrochemical process) are relevant.

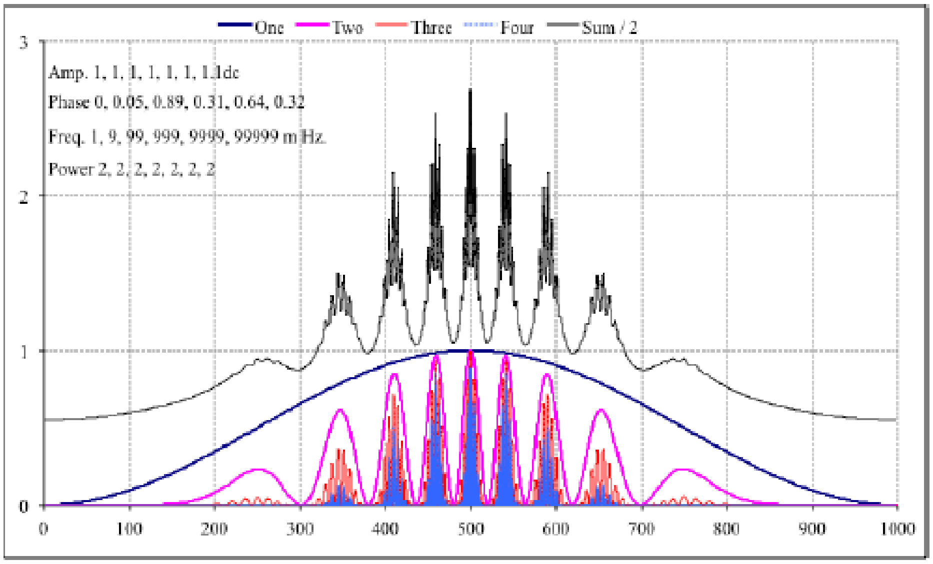

Figure 4. Generation of a SuperWave of 1000 second period, covering the range 1 mHz. to 100 Hz. with dc offset for electrochemical use.

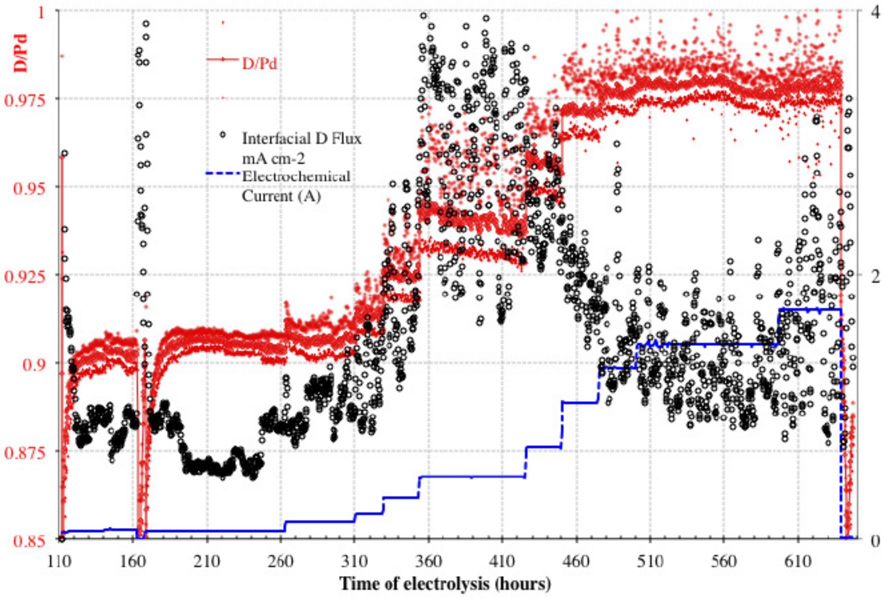

Figure 5. The interfacial impedance of an excess heat-producing Pd cathode 4 mm in dia. and 4.5 cm long at 1000 psig of D_2 pressure and 4°C using 1.0 M LiOD.

3. Discussion

What is relevant here is the clearly demonstrated ability of SuperWaves to engender high loading and high flux at high currents in a well prepared cathode. Since these are three recognized conditions of excess heat production it is pertinent to ask why the SuperWave is capable of producing this result, especially since no other waveforms that we have evaluated are? What is the SuperWave speaking to in the electrochemical system? One clue possibly was revealed in very early results obtained of the electrochemical impedance response of cathodes capable of excess heat production. Figure 6 shows data obtained for SRI Cell P2 in 1989 that was first published at ICCF1 (ACCF) in 1990 [12]. The first quadrant near semi-circular response[l] is the expected behaviour of an electrochemical charge transfer impedance in parallel with the electrochemical double layer capacitance.

The appearance of a second semi-circle under the real axis at low frequencies[m] is a relatively rare feature in electrochemical systems. It is sometimes referred to as an “inductive loop” since it conforms to the mathematics of a low frequency inductor but this makes no physical sense as energy is not stored in magnetic fields in electrochemical systems. This feature is better thought of as a combination of negative capacitance and negative resistance indicating the presence of positive feedback. Each of the impedance loops in Fig. 6 has a characteristic frequency, the loop above the real axis at a few hundred Hertz, the loop below the real axis at a few hundred milli-Hertz. One conjecture is that the SuperWave used has sufficient and appropriate dynamics to modulate both of these resonances[n], one associated with electrochemical kinetics (loading) and the other associated with positive feedback (flux).

---

[l] Actually the fourth quadrant as the imaginary impedance axis (vertical) is plotted by convention as –X.

[m] Frequency is not an explicit variable in this type of plot but each point is generated at a different frequency with frequency decreasing logarithmically from kHz to mHz in a clockwise fashion.

[n] It is likely that several other resonances also are crucial in producing the FPHE in electrolytic systems.

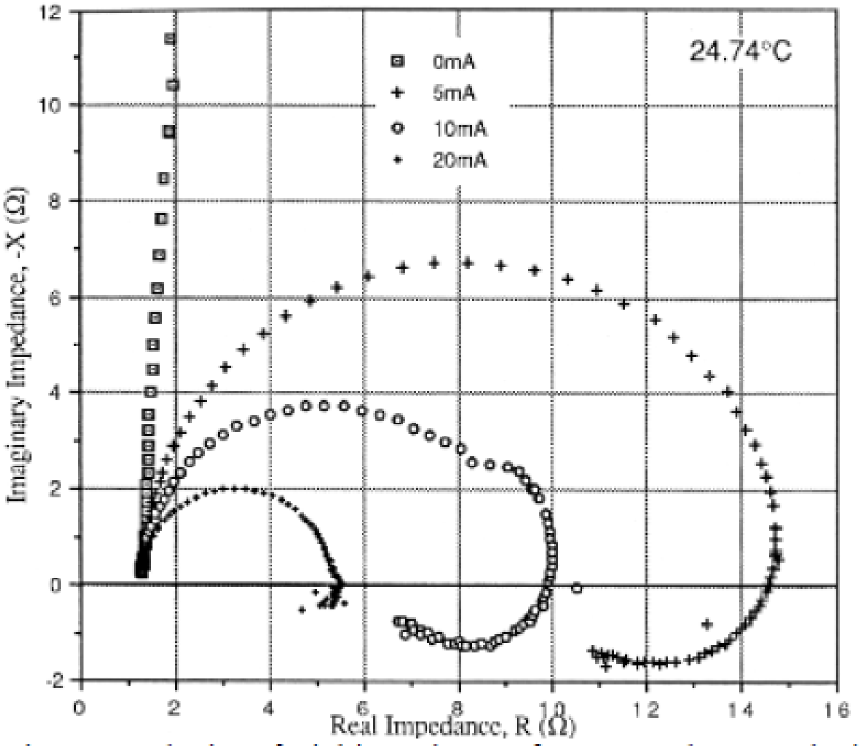

Figure 6. The interfacial impedance of an excess heat-producing Pd cathode 4 mm in dia. and 4.5 cm long at 1000 psig of D_2 pressure and 4°C using 1.0 M LiOD.

4. Conclusions

The empirical requirements of high loading, high current and high interfacial deuterium flux to produce the FPHE in electrolysis experiments are in mutual conflict. However, systems have been observed to exhibit spontaneous flux driven loading oscillations, and at least one function, the SuperWave proposed and developed by Dardik [8–11] and ETI (now SKINR), has been observed to be capable of meeting and sustaining these conditions synthetically. With regard to demonstrating and hopefully utilizing the FPHE it would appear to be important to understand the role of resonant effects in electrochemical kinetic processes, as well as other system resonances not discussed here. We are pursuing these concepts further in ongoing collaboration with Violante (ENEA) and La Gatta (TSEM) in Italy [13].

Acknowledgements

In addition to the SRI team the progress briefly outlined above has been critically dependent of the vision, courage and dogged tenacity of two individuals: Dr. Irving Dardik's novel conception and understanding of the basic form of the SuperWave and its potential role in FPHE studies; and Dr. Vittorio Violante's tireless pursuit of the metallurgical variables that control the ability of bulk palladium to accept and retain very high deuterium loadings. Both men were supported by highly capable research teams.

References

[1] M. Fleischmann, S. Pons and M. Hawkins, *J. Electroanalytical Chem.* **201** (1989) 301.

[2] M. McKubre, S. Crouch-Baker, A. Riley, S. Smedley and F. Tanzella, in *Frontier of Cold Fusion*, *Proc. ICCF3*, H. Ikegami (Ed.), Universal Academy Press, Tokyo, 1993, pp. 5–19.

[3] K. Kunimatsu, N. Hasegawa, A. Kubota, N. Imai, M. Ishikawa, H. Akita and Y. Tsuchida, in *Frontiers of Cold Fusion*, *Proc. ICCF3*, H. Ikegami (Ed.), Universal Academy Press, Tokyo, 1993, pp. 31–45.

[4] M. McKubre et al., EPRI TR-104195, 1994.

[5] M. McKubre, S. Crouch-Baker, A. Hauser, S. Smedley, F. Tanzella, M. Williams and S. Wing, *Proc. ICCF3*, S. Pons (Ed.), Antipolis Cedex, France, Monte-Carlo, Monaco, 1995, p. 17.

[6] M. McKubre et al., EPRI TR-107843-VI, 1998.

[7] M.C.H. McKubre and. F.L. Tanzella, *Proc. ICCF12,* A. Takahashi (Ed.), World Scientific, Singapore, 2005, pp. 392–403.

[8] I. Dardik, H. Branover, A. El-Boher, D. Gazit, E. Golbreich, E. Greenspan, A. Kapusta, B. Khachatorov, V. Krakov, S. Lesin, B. Michailovitch, G. Shani, G., and T. Zilov, *Proc. ICCF10*, P. Hagelstein (Ed.), World Scientific, Singapore, 2003, pp. 392–403.

[9] M.C.H. McKubre, F.L. Tanzella, I. Dardik, A. El-Boher, T. Zilov, E. Greenspan, C. Sibilia and V. Violante, in *Low-Energy Nuclear Reactions Sourcebook*, J. Marwan (Ed.), ACS Symposium Series 998, Oxford University Press, Oxford, 2008, p. 219.

[10] I. Dardik, T. Zilov, H. Branover, A. El-Boher, E. Greenspan, B. Khachatorov, V. Krakov, S. Lesin, S., and M. Tsirlin, in *Proc. ICCF11,* J.-P. Biberian (Ed.), World Scientific, Singapore, 2004, p. 84.

[11] M.C.H. McKubre and. F.L. Tanzella, *New Physical Effects in Metal Deuterides,* SRI Final Report to DARPA on contract HR0011-05-C-00879, 2007.

[12] M. McKubre, R. Rocha-Filho, S. Smedley, F. Tanzella, J. Chao, B. Chexal, T. Passell and J. Santucci, *Calorimetry and Electrochemistry in the D/Pd System, Proc. of the First Annual Conf. on Cold Fusion (ICCF1),* Salt Lake City, Utah, March 28–31, 1990.

[13] V. Violante, E. Castagna, S. Lecci, F. Sarto, M. Sansovini, T. D. Makris, A. Torre, D. Knies, D. Kidwell, K. Grabowski, D. Dominguez, G. Hubler, R. Duncan, A. El Boher, O. Azizi, M. McKubre, A. La Gatta, *Proc. ICCF18,* submitted.

J. Condensed Matter Nucl. Sci. 15 (2015) 11–22

Research Article

Nuclear Products of Cold Fusion by TSC Theory

Akito Takahashi*,†

Technova Inc., 1-1-1 Uchisaiwai-cho, Chiyoda-ku, Tokyo 100-0011, Japan

---

Abstract

Prediction of nuclear products both for metal–deuterium systems and metal protium systems is made on the basic physics of cold fusion by the Tetrahedral Symmetric Condensate (TSC) theory. This paper focuses on final state nuclear reactions of intermediate compound states as ^{8}Be* of 4D/TSC fusion and ^{4}Li* of 4H/TSC WS fusion. Prediction of final products is made by the nucleon-halo model of the highly excited intermediate compound states.

Keywords: BOLEP, 4D fusion, Final products, ^{4}He, ^{3}He, 4H WS fusion, n-Halo model, TSC theory

---

1. Introduction

Since 1989, there has been accumulated evidence of anomalous excess heat effects in correlation of 24MeV/^{4}He-generation (Miles [1], McKubre [2], and others) without correspondingly intense emission of particles (n, p, t, ^{3}He, γ) from experiments with Pd–D systems. Recently, another anomalous and long lasting excess heat effect at higher temperatures in Ni–H systems without easily detected nuclear products (the so-called ash) have been reported by Piantelli [3], Rossi [4], Celani [5], Kitamura–Takahashi [6] and some other groups. The level of observed anomalous excess heat looks too large to be explained by known chemical reactions. If the anomalous heat effect is of nuclear-reaction origin, why 'lethal' radiation (i.e., neutrons and gamma-rays) is not associated with the reaction is the big challenge to nuclear theory. The author has made serious efforts to establish theories to give consistent answers to the big question why so radiation-less heat results may happen in Pd–D and Ni–H systems. The summary conclusion of this paper is given in Table 1.

The Tetrahedral Symmetric Condensate (TSC)-related theory has been elaborated for 23 years since April 1989 [7] and the latest review paper [8] is given at ICCF17. The study of D(H)-cluster dynamics by using the quantum mechanical (QM) Langevin equation [9] has concluded that any transient entity (condensate state) as small as a few tens fm size will not be possible for the d–e–d and d–e–e–d systems, as well as 3D-cluster. 4D/TSC-neutral-cluster may make ultimate condensation to very small charge-neutral entity, as small as a few tens fm size or smaller to induce

---

*E-mail: akito@sutv.zaq.ne.jp

†Also at: Osaka University, 2-1 Yamadaoka, Suita, Osaka 565-0071, Japan.

Table 1. Major experimental claims of cold fusion and predictions by the TSC theories.

	Claims by experiments	Predictions by TSC models
Metal Deuterium Energy (MDE)	Heat: 24 ± 1 MeV/^{4}He (Miles [1], McKubre et al. [2])	4D fusion ash with low-E alphas (46 keV)
	Weak alpha peaks (Lipson [14], Roussetski [15], etc.)	Minor alpha-peaks by nucleon halo BOLEP minor decay channels
	Weak neutrons (Takahashi, Boss [16], etc.)	High-E neutron by minor triton emission BOLEP in ca. 1.5 keV
	X-rays burst (Karabut et al. [13])	
Metal Hydrogen Energy (MHE)	Heat w/o n and gamma	4H/TSC WS fusion
	Unknown ash	2–7 MeV ^{3}He and d
	(Piantelli [3], Takahashi–Kitamura [20], Celani [5], etc.)	Very weak secondary gamma and n: ca. 10^{-11} of ^{3}He and d yield

significant level reaction rates of nuclear strong interaction between deuterons. The condensation time for 4D/TSC is as short as 1.4 fs and the yield of 4D/TSC fusion per TSC is 1.0 (100%). Models of TSC formation sites on surface of metal nano-particle and fusion rate formulas with numerical estimations are given until now [8]. The model has been extended to the possible weak-strong simultaneous fusion for the 4H/TSC dynamic condensation [10]. However, to make some more definite predictions for final nuclear products and their secondary radiation-emitting interactions, the yet-to-study problem of final state interactions for the intermediate compound nuclei as ^{8}Be* (Ex = 47.6 MeV) and ^{4}Li* (Ex = 4.62 MeV) should be challenged. A trial study based on the nucleon-halo model by Takahashi–Rocha [11] is a starting point.

2. Three Steps of Nuclear Reaction

In any theoretical model treating nuclear (strong/weak) interactions, we should make explicit approach to the three steps, namely the initial state interactions, the intermediate nuclear excited state and the final state interactions, as shown by the chart in Fig. 1.

To make any nuclear reaction rate meaningfully observable (far more than 1 event per second, on/in condensed matter), pairing (d–d, p–p, for instance) and cluster (4d, 4p, 6d, etc. for instance) quantum mechanical (QM) wave-functions of interacting particles should have enough quantitative weight at the interaction surfaces of strong (about 1.4 fm, 1.4E-15 m, inter-nuclear distance) or weak (about 2 am, 2.0×10^{-18} m, inter-nuclear distance) interaction effective-domain [8]. Some special conditions of dynamic chemical (Coulombic or electro-magnetic EM) trapping potentials of D(H)-cluster may be realized in some mesoscopic catalytic conditions [12]. This is the initial state interactions under the EM force field. The nuclear interaction by strong (charged-pion/isospin exchange) or weak (weak boson/weak-isospin exchange) force field with the EM field pairing/cluster QM wave-function weight (as given by the Fermi's first golden rule [8]) is also the component of the initial state interactions.

Usually, the EM field motion and the strong/weak field reaction can be treated adiabatically by the Born–Oppenheimer wave-function separation. Almost all theoretical models ever proposed treat the initial state interaction only under crude assumptions. The intermediate compound states after the initial strong/weak nuclear interactions and the final state interactions to release excited energy by the mass-defect energy (ΔMc^2) as free energies of emitted 'ground-state' particles have not been properly/explicitly treated in the past proposed theories by many people, except for a few examples as the n-halo model analysis by Takahashi–Rocha [11].

In almost all cases of possible intermediate compound states (to be thought from any nuclear reaction process as proposed by anybody, although only a few models have treated the state properly and most models are blind or ignoring those nuclear physics states), the nuclear excitation energy is known easily by the mass-defect energy (ΔMc^2) but spin-

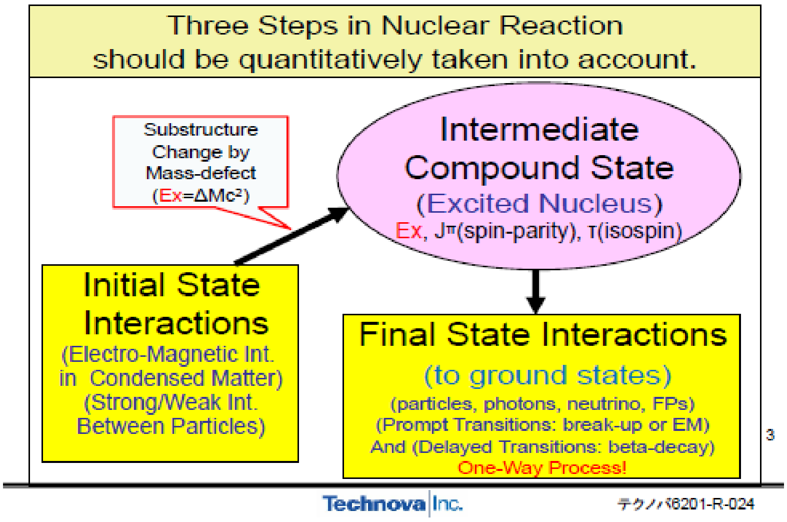

Figure 1. Three steps of nuclear reactions to be treated by any cold fusion theories.

parity and iso-spin are hard to know. So, we need some consistent modeling for the intermediate and the final state interactions to make predictions of the final nuclear products.

The flow from the initial state to the intermediate state is irreversible (a one-way process) due to the drastic change of substructure of composite particle (compound state) by the mass–energy defect: there happens a large entropy (randomness of sub-particles order) increase and the reverse projection to the initial state becomes no-solution (chaotic) mathematics. Therefore, we have to treat the intermediate compound state properly to know the final state interaction products: the process from the intermediate state to the final state products which are stable isotope or particle states with carrying kinetic energies is also irreversible.

Most theories have been proposed by people who are ignorant of the three-step irreversible process. They sometimes make wrong short-cuts ‘wishfully’ from the initial interaction directly to the final ‘selected-by-will’ products; an example is the wish of ^{64}Ni + p to ^{65}Cu (g.s.) + Q without prompt (lethal) gamma-rays from the intermediate excited state ^{65}Cu(Ex)*. Such a primitive mistake should be avoided in any nuclear reaction theory.

An illustration of the three steps of condensed matter-nuclear-reactions (CMNR) is shown in Fig. 2 for the 4D/TSC theory.

3. Final Products by MDE

Experimental claims [1,2] show that the final nuclear products of the excess heat phenomenon are ^{4}He atoms with 24±1 MeV/^{4}He-generation and thermal energy without ‘hard radiation’. Karabut et al. [13] has made an astonishing claim that they observed very intensive burst of photons in the soft X-ray energy region (1.5 keV in average), the integrated burst energy of which may be corresponding to the total released energy ca. 24 MeV per reaction. There have been no reports of observation of intense high energy alpha-particles corresponding to the anomalous excess heat evolution. However, very weak line-like spectra of alpha particles have been observed in the energy region less than about 17 MeV by Lipson et al. [14] and Roussetski et al. [15]. Boss et al. observed over 14 MeV neutron tracks in CR39 as scarce events [16] probably by the some secondary d–t reaction neutron emission. This work discusses in the

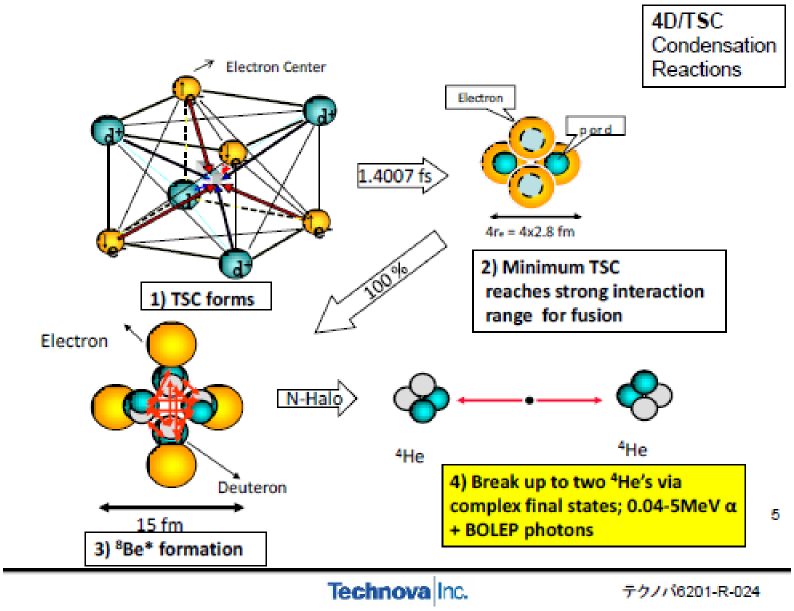

Figure 2. Three steps of 4D/TSC fusion; (1) and (2) are two adiabatic sub-states of EM and strong interactions in the initial state interaction, (3) is the intermediate compound state and (4) is the final state interaction.

following that these typical claims may match with the prediction of n-halo model of the final state interaction for the ^{8}Be* state of 4D/TSC fusion.

The details of modeling the final state interaction for the ^{8}Be* state after the 4D/TSC initial state interaction are given in the Takahashi–Rocha paper [11]. Here we present an overview. In Fig. 3, the image of n-halo model of ^{8}Be* is given in comparison with the n-halo model image of ^{8}Li(g.s). The n-halo-state of ^{8}Li has known to have a 'very long life time' of 838 ms. It is modeled as a core of t–h coupling with two neutron halos. Here h denotes helion (^{3}He nucleus as three-body binding nucleons in nucleus) and t denotes triton (also three-body binding of nucleons). In our image, there exists a vibration between h and t core clusters and additional vibrations between core clusters and neutron halos. In addition, there is rotational freedom between n-halos and core clusters. Such a combination of rotation and vibration would make the life time of ^{8}Li very long; as long as 838 ms. As ^{8}Li is at ground state, there is no freedom to make EM transitions (photon emitted transitions), but the very slow nuclear transition by the weak interaction is possible: the ^{8}Li(g.s.) makes beta-decay to ^{8}Be* (Ex = 3.06 MeV; 2+) state which makes prompt decay to break up to two 1.58 MeV alpha particles [11]. We know that the ^{8}Be(g.s) is of two-alpha cluster state [17] and image is given by the left-hand side figure of Fig. 4.

However, the highly excited state ^{8}Be* as Ex = 47.6 MeV after 4D-multibody-simultaneous fusion may come to the n-halo state as given in Fig. 3 (left-hand side figure), and may have 'very' long life time as that of ^{8}Li(g.s.), because of ca. 15,000 modes/nodes of very finely deformed spherical harmonics states in vibration/rotation boson-state-coupling between core h–h clusters and two-n-halo states [11]. The average nuclear-phonon energy of such complex bosonic coupling states under vibration/rotation nodes was estimated ca. 1.5 keV. The very highly excited energy (Ex = 47.6 MeV) of ^{8}Be* just after a 4D/TSC fusion may make 'avalanche' multiple photon emission via bosonic nuclear phonon coupling to damp its nuclear excited energy by the BOLEP (burst of low energy photons) process, like black-body radiation, to go out to the ground state of ^{8}Be(g.s.) which is known to make prompt two alpha break up with 46

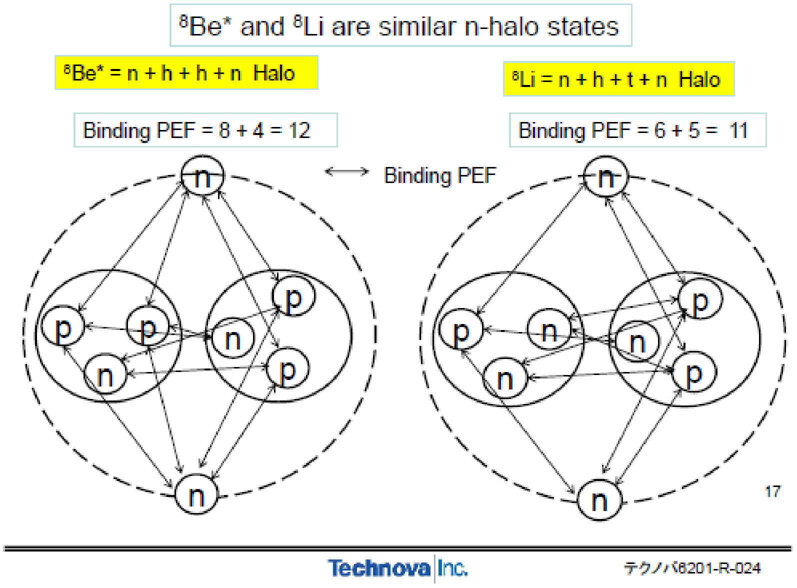

^{8}Be* and ^{8}Li are similar n-halo states

^{8}Be* = n + h + h + n Halo

Binding PEF = 8 + 4 = 12

^{8}Li = n + h + t + n Halo

Binding PEF = 6 + 5 = 11

Figure 3. The image of n-halo model of ^{8}Be*, compared with the image of ^{8}Li which has very similar n-halo state with ca. 0.8 s life time.

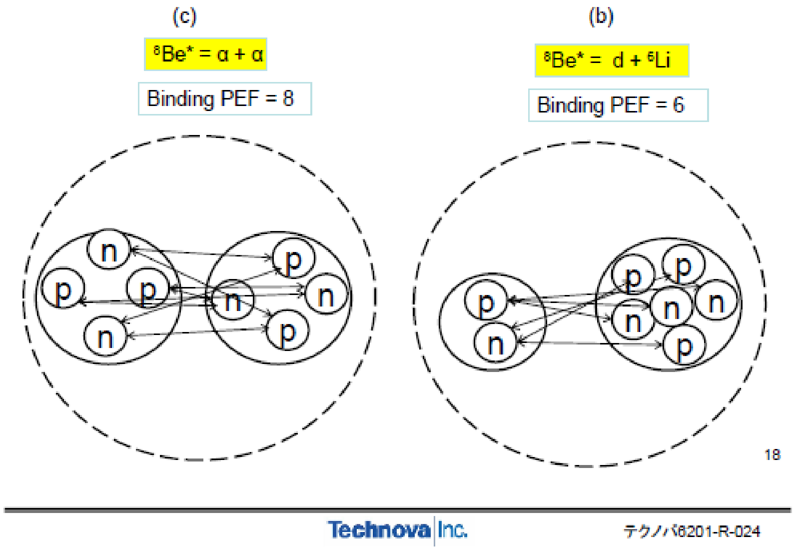

(c)

^{8}Be* = α + α

Binding PEF = 8

(b)

^{8}Be* = d + ^{6}Li

Binding PEF = 6

Figure 4. Typical cluster model of lower excited ^{8}Be*; two-alpha cluster and d–^{6}Li cluster.

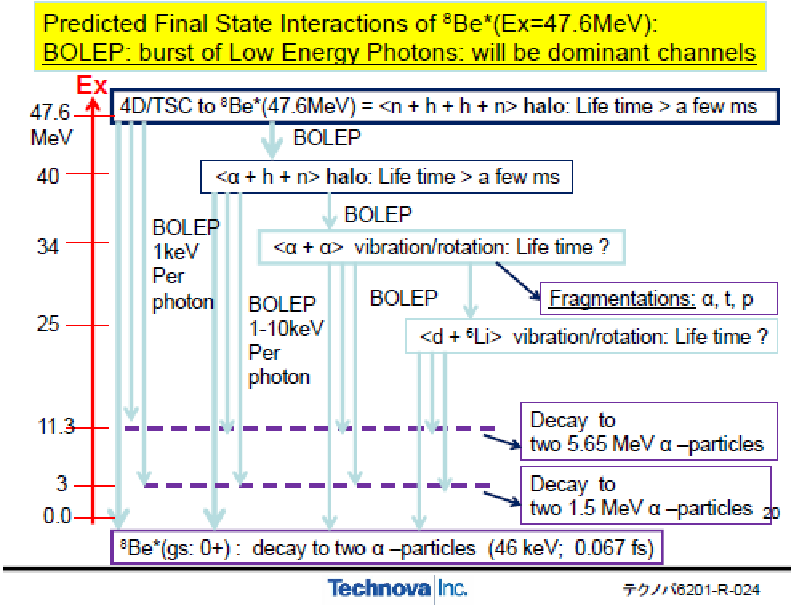

Figure 5. Predicted decay scheme of ^{8}Be*(Ex = 47.6 MeV) after 4D/TSC fusion .

keV/^{4}He in 6.7×10^{-17} s. This BOLEP process was regarded as the major channel of final state interactions.

As possible minor decay channels from the ^{8}Be* (Ex = 47.6 MeV) state, Takahashi–Rocha [11] considered intermediate state traps by two-alpha cluster vibration states. The scaling law of excitation energy as a function of effective nuclear binding force (as scaled by PEF, charged pion exchange force number) is used for various possible inner nucleus cluster-halo states. They estimated possible intermediate two-alpha cluster states as given in Table 2. $Ex = 34$ MeV is the upper limit of α–α cluster state excitation [11].

A simplified decay scheme of ^{8}Be*(Ex = 47.6 MeV) of 4D/TSC fusion is shown in Fig. 5. which omits the intermediate two-alpha states at 34, 27.5, 22.98, 22.0, 20.1 and 16.6 MeV levels for making the figure visible for major BOLEP channels.

Table 2. Possible two-alpha decay channels from ^{8}Be*

4D?→^{8}Be* (47.6 MeV) → BOLEP +^{8}Be*(34 MeV) and possible intermediate states which decay to 2α (*Note*: only 11.4 and 3.04 MeV states are drawn in Fig. 5)			
Ex (MeV)	Spin-parity	Isospin (T)	KE of α-particle (MeV)
34	(O+)	(0)	17
27.5	0+	2	13.8
22.98	(0+)	(0)	11.5
22.0	2+	0	11
20.1	2+	0	10.05
16.6	2+	0	8.3
11.4	(2+)	0	5.7
3.04	2+	0	1.55
–0.092 (gs)	0+	0	0.046

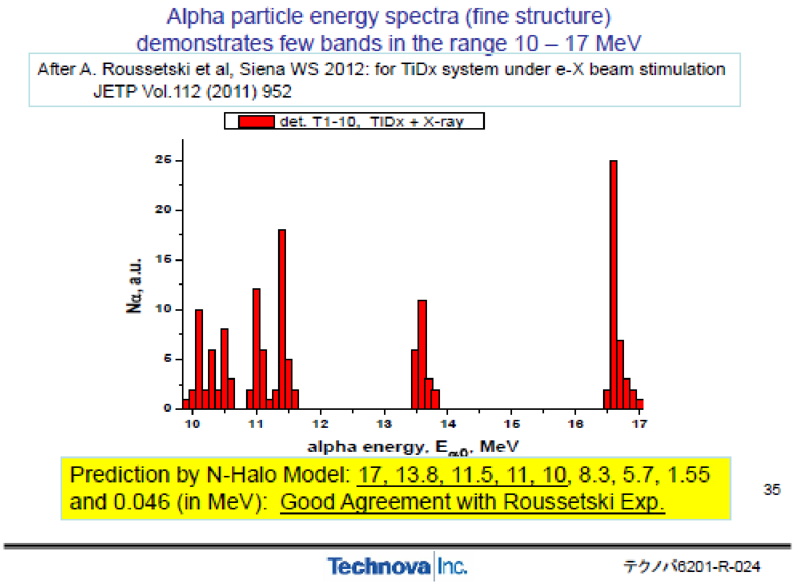

Alpha particle energy spectra (fine structure) demonstrates few bands in the range 10 – 17 MeV

After A. Roussetski et al, Siena WS 2012: for TiDx system under e-X beam stimulation
JETP Vol.112 (2011) 952

Prediction by N-Halo Model: 17, 13.8, 11.5, 11, 10, 8.3, 5.7, 1.55 and 0.046 (in MeV): Good Agreement with Roussetski Exp.

35

Technova Inc. テクノバ6201-R-024

Figure 6. Alpha line spectra observed by Roussetski agree almost completely with the n-halo model decay channels of ^{8}Be* (Ex = 47.6 MeV).

A fragmentation channel from the Ex = 34 MeV may emit 5.2 MeV triton via ^{4}He* (Ex = 20.2 MeV) of asymmetric fragmentation [11] and may induce the secondary d-t reaction which produces 9–19 MeV high energy neutron. Boss et al. [16] may have detected this neutron by CR39 triple tracks.

The predicted alpha-particle kinetic energies as minor channels gave beautifully coincident agreement with the Roussetski experiment (but for TiD system) as shown in Fig. 6.

Such a completely consistent agreement with many alpha-lines seems very difficult to explain by most other theoretical models proposed for cold fusion, except as a consequence of the TSC theory. This also seems to be strong evidence that the TSC mechanism may work as cold fusion physics. The broad alpha-particle peak at around 15 MeV observed by Lipson et al. [14] in PdD electrolysis system is another example as shown in Fig. 7.

It could be that the most important circumstantial evidence of BOLEP energy damping can be seen by comparing with Karabut et al. [13] result of ca. 1.5 keV ‘X-ray’ bursts, as shown in Fig. 8. The BOLEP by the n-halo model of ^{8}Be* decay may well correspond to the observed behavior of many burst-like soft-X-ray bursts with very intense counts.

The author expects that similar BOLEP-like photon-burst observation will be done for PdD electrolysis and gas-loading systems.

4. Nuclear Products by MHE

Recently many groups have claimed anomalous excess heat by Ni–H gas loading at higher temperature systems. The excess heat by Ni–H is reported to last much longer and with higher power than the PdD system [3–6]. If the observed anomalous heat is originated by nuclear reactions, missing hard radiation is far more mysterious and challenging to theoretical modeling. The author has made a trial explanation [18] based on the TSC theory. Additional discussions on the final state interaction of the 4H/TSC WS fusion which goes to the intermediate compound state of ^{4}Li* (*Ex* = 4.62 MeV) are given below.

According to the formula of QM-Langevin equation, the velocity of condensation (time-dependent) is inversely proportional to the square-root of mass of confined particle. Therefore, 4H/TSC will condense in 1.0 fs to the small size region of a few tens fm. However, there is no strong-fusion interaction (PEF = 0) between four protons of TSC to finally destroy the TSC state. We conceive that 4H/TSC can condense further to be as ultimately small 4H/TSC-minimum state as a few fm size (2.4 fm p–p distance is the limit, due to hard core of proton with 1.2 fm radius). The problem there is how long the 4H/TSC-minimum state can survive [8,10].

Once a proton-to-neutron transition is generated by the electron capture, we expect instantaneous strong interaction between just born neutron and closely available three protons within the Compton wave length of charged pions 1.4 fm (PEF = 3) as illustrated in step (3) of Fig. 10. As the pion range 1.4 fm is within the Heisenberg Uncertainty in distance, the n + 3p reaction takes place by 100 % with $\langle W \rangle$ value of PEF = 3 (comparable to d–t fusion) [9].

$$\mathrm{3p + n} \to {}^4\mathrm{Li}^*(Ex = 4.62\ \mathrm{MeV}). \tag{1}$$

The intermediate compound $^4\mathrm{Li}^*$ has two break-up channels.

$${}^4\mathrm{Li}^*(Ex = 4.62\ \mathrm{MeV}) \to {}^3\mathrm{He} + \mathrm{p} + 7.72\ \mathrm{MeV}, \tag{2}$$

$${}^4\mathrm{Li}^*(Ex = 4.62\ \mathrm{MeV}) \to \mathrm{2p + d} + 2.22\ \mathrm{MeV}. \tag{3}$$

The branch (2) is thought to be a major out-going channel and we will expect ^{3}He as main nuclear product.

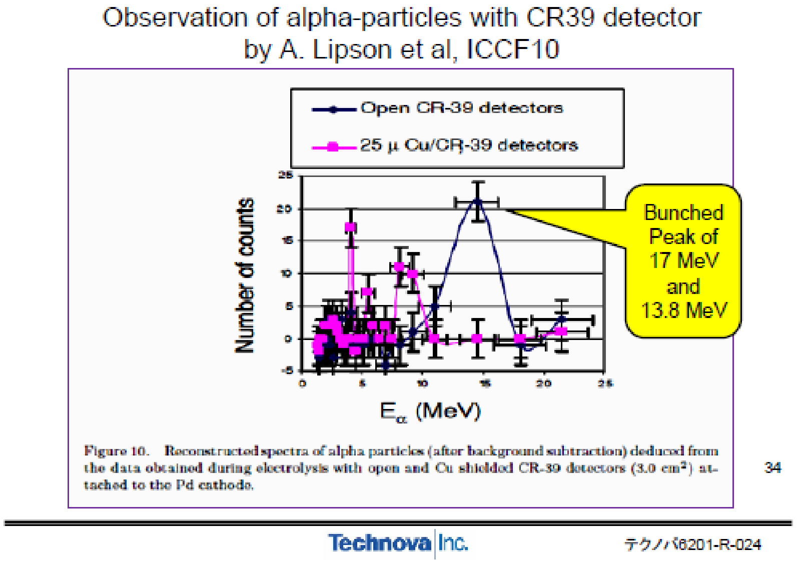

Observation of alpha-particles with CR39 detector
by A. Lipson et al, ICCF10

Figure 10. Reconstructed spectra of alpha particles (after background subtraction) deduced from the data obtained during electrolysis with open and Cu shielded CR-39 detectors (3.0 cm^2) attached to the Pd cathode.

34

Technova Inc. テクノバ6201-R-024

Figure 7. Lipson's 15 MeV alpha-peak may be a bunched peak of 17 and 13.8 MeV of the n-halo decay of ^{8}Be*.

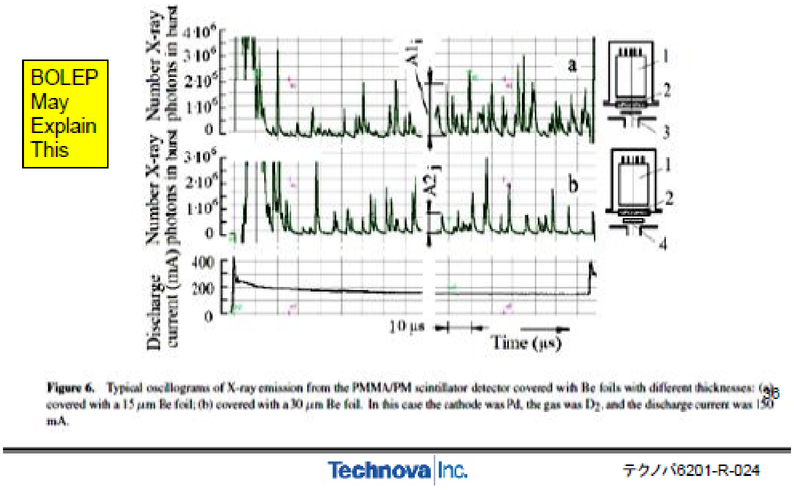
BOLEP May Explain This

Figure 6. Typical oscillograms of X-ray emission from the PMMA/PM scintillator detector covered with Be foils with different thicknesses: (a) covered with a 15 μm Be foil; (b) covered with a 30 μm Be foil. In this case the cathode was Pd, the gas was D_2, and the discharge current was 150 mA.

36

Technova Inc. テクノバ6201-R-024

Figure 8. Observed X-ray bursts by Karabut et al. .

And 5.79 MeV proton will produce secondary neutron by Ni(p, n) reactions with higher mass Ni isotopes, on the order of 10^{-13} of ^{3}He production rate and Ni(p, γ) secondary gamma-rays on the order of 10^{-11} per 5.79 MeV proton.

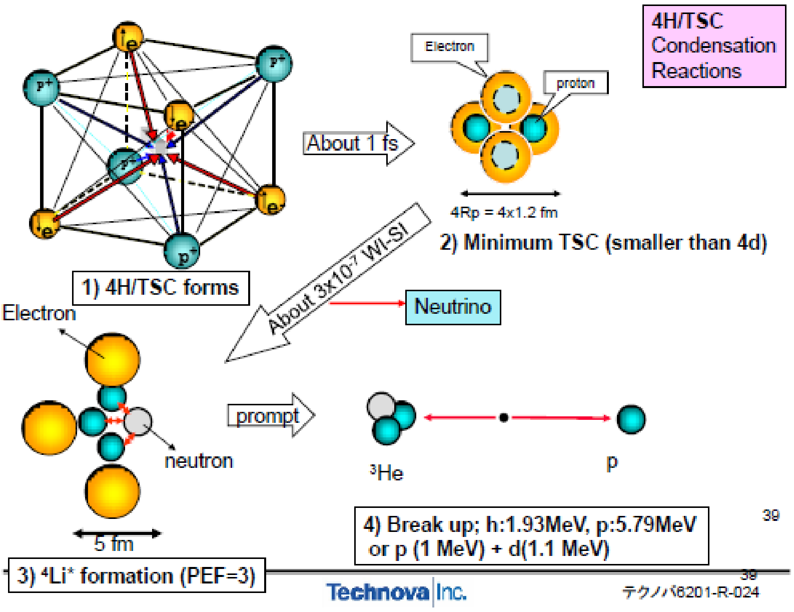
4H/TSC Condensation Reactions

1) 4H/TSC forms

2) Minimum TSC (smaller than 4d)

3) ⁴Li* formation (PEF=3)

4) Break up; h:1.93MeV, p:5.79MeV or p (1 MeV) + d(1.1 MeV)

39

Technova Inc. テクノバ6201-R-024

Figure 9. Brief view of 4H/TSC condensation and 4H weak-strong fusion interaction.

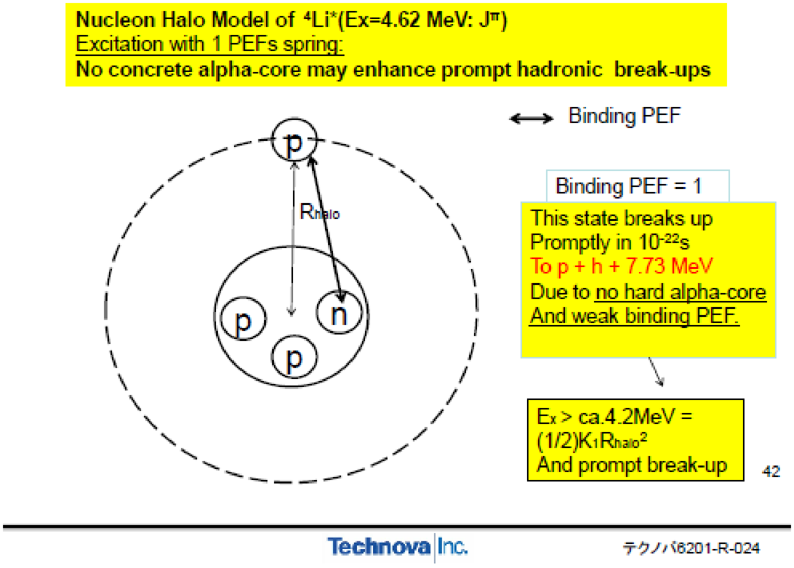

Nucleon Halo Model of ^{4}Li*(Ex=4.62 MeV: J$^\pi$)
Excitation with 1 PEFs spring:
No concrete alpha-core may enhance prompt hadronic break-ups

↔ Binding PEF

Binding PEF = 1

This state breaks up
Promptly in 10^{-22}s
To p + h + 7.73 MeV
Due to no hard alpha-core
And weak binding PEF.

E_x > ca.4.2MeV = $(1/2)K_1R_{halo}^2$
And prompt break-up

Figure 10. p-halo model of ^{4}Li* by 4H/TSC WS fusion.

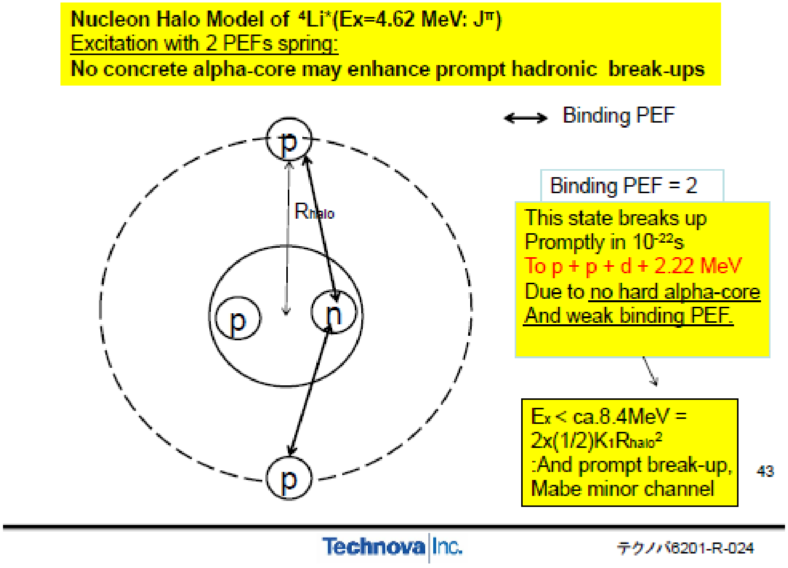

Nucleon Halo Model of ^{4}Li*(Ex=4.62 MeV: J$^\pi$)
Excitation with 2 PEFs spring:
No concrete alpha-core may enhance prompt hadronic break-ups

↔ Binding PEF

Binding PEF = 2

This state breaks up
Promptly in 10^{-22}s
To p + p + d + 2.22 MeV
Due to no hard alpha-core
And weak binding PEF.

E_x < ca.8.4MeV = $2x(1/2)K_1R_{halo}^2$
:And prompt break-up,
Mabe minor channel

Figure 11. p-halo-d-core sate of ^{4}Li* by the 4H/TSC WS fusion .

Characteristic X-rays (PIXE) from Ni ionization by the proton are also expected.

However, we do not know the branching ratio to the branch (3) which will not produce secondary neutrons and gamma-rays at all. So far detection of ash has been difficult.

The three steps of a nuclear reaction of 4H/TSC WS fusion are shown in Fig. 9. The adiabatic sub-steps (1) and (2) are of initial state interactions.

The excited energy of the intermediate compound state ^{4}Li*(*Ex* = 4.62 MeV) is rather low. However, we may apply the nucleon halo model here too.

Figure 10 shows the p-halo image with h-cluster core for ^{4}Li*. This halo state is similar to the n-halo state with h-cluster core for ^{4}He* (*Ex* = 23.8 MeV) [11] which is well evaluated (see TUNL Nuclear Data library: http://www.tunl.duke.edu/nucldata/index.shtml) as the prompt break-up channel of n + ^{3}He + 3.25 MeV. The p + t + 4.02 MeV break-up channel is thought to be the final state interaction from the p-halo state with t-cluster core for ^{4}He*(*Ex* = 23.8 MeV) and to be a nuclear equivalent state to the p-halo with h-cluster core for ^{4}Li*. From these comparable halo-states between ^{4}Li* and ^{4}He*, the life time of ^{4}Li* is estimated to be on the same order of that (namely 1.0×10^{-22} s) for ^{4}He*. Therefore, the BOLEP type EM transition is not possible to have competing branch for ^{4}Li*.

Obviously the very weak PEF binding (effective PEF = 1) makes the prompt scission of ‘p-bond’ to break up to p + ^{3}He + 7.72 MeV final state break-up. There seem to be no mechanisms plausible to make its life time longer. The life time of ^{4}Li* is considered to be on the order of 1.0×10^{-22} s, very short as nuclear reaction time. Another halo-state would be the two-p halo with d-core as shown in Fig.11.

The binding PEF = 2 is larger than that of Fig.10, but the binding to the d-core is not strong enough to prevent the prompt three body break-up to d + p + p + 2.22 MeV channel. The life time of this state might be a little bit longer than the case of p-h halo state (Fig.11), so that the ^{3}He + p + 7.72 MeV channel looks major channel. However, we do not know the exact branching ratio.

We have reported that fission products from Ni + 4p fission are predicted to be clean stable isotopes mostly, by the selected channel scission theory [12]. As discussed in the previous section, the life time of 4H/TSC-minimum state may be much longer than we conceived previously, and the size of its neutral entity is much smaller than the past image, the strong interaction with Ni nucleus would be selective to the Ni + 4p capture and 1p to 3p capture processes will be neglected.

Fission products are considered to be mostly from the near symmetric fragmentations of Ge* intermediate compound state. In the past, there were reports on production of foreign elements (‘transmutation was thought’) by several authors. Miley–Patterson data was analyzed by TSC-induced fission in [19]. Mass spectral analysis for samples before and after use is recommended for Ni-H system experiments as being done by Piantelli-group, Kobe-Technova-group (Sakoh et al.) and Celani-group (INFN).

5. Conclusions

The Final State Interactions of ^{8}Be* by 4D/TSC are qualitatively/semi-quantitatively discussed. Nucleon-Halo State of ^{8}Be* may have rather long life time as rotation of halo-nucleon coupled with vibration motion of alpha- and h-(t-) cluster, and would have narrow spaced energy-band structure, from where EM transition photons (1—10 keV: BOLEP: agreed with X-ray burst by Karabut exp.) damp ^{8}Be*(47.6 MeV) to ^{8}Be(g.s.:0+), as major final state channels.

Direct many hadronic break-up channels may compete with the nucleon-halo state transition, but as minor_channels with discrete α-peaks which agreed very well with Roussetski’s experiment and rather well with Lipson’s experiment. Quantitative QM studies are to be expected for BOLEP. Simultaneous (very rapid cascade) weak and strong interaction may be predicted in the final stage of 4H/TSC condensation. About 20 W (or more)/mol-Ni heat with ^{3}He and d products is predicted (Clean Heat). Heat level depends on 4H/TSC generation rate probably on surface mesoscopic catalyst sites of binary nano-particles as Cu–Ni [20] and on-going experimental study will provide important hints to elaboration of theoretical models for the Ni–H gas loading systems.

PIXE X-rays (ca. 8 keV) by proton will be detected if the p + ^{3}He + 7.72 MeV is the major final state channel. About 0.2 n per one joule heat will be detected. This is corresponding to the order of 10^5 neutrons/s per one mega-watts of heat level. About four gammas by Ni(p,γ) per joule will be. So, neutron and gamma levels will be very weak and practically very clean (serious radiation protection is not necessary for presumed Ni–H reactor devices).

The 4D simultaneous fusion (^{4}He: ash) and the 4H simultaneous weak-strong fusion (^{3}He, d: ash) are the consequence of the TSC theory that the author has developed until now. The concluding remarks are summarized at the beginning of this paper in Table 1.

Acknowledgment

The author is grateful to Technova colleagues A. Kitamura, R. Seto and Y. Fujita for their support.

References

[1] M. Miles et al., The science of cold fusion, Italian Physical Society, 1991. pp. 363–372.

[2] M. McKubre et al., The emergence of a coherent explanation for anomalies observed in D/Pd and H/Pd systems, Evidence for ^{4}He and ^{3}H production, *ICCF8 Conf. Proc.,* Vol. 70, Italian Physical Society, 2000, pp. 3–10.

[3] F. Piantelli et al., Some results from the Nichenergy laboratory, *presentation at the 10th Int. Workshop*, Siena, April 2012 (see ISCMNS web site).

[4] A. Rossi, see his web-site *Journal of Nuclear Physics*.

[5] F. Celani et al., Cu–Ni–Mn wires with improved submicrometric surfaces used as LENR device by new transparent dissipation-type calorimeter, Proc. *ICCF17*, to be published.

[6] H. Sakoh et al., Hydrogen isotope absorption and heat release characteristics of a Ni-based sample, *Proc. ICCF17*, Daejeon, Korea, August 2012, to be published (see also two papers on Ni–H systems by A. Takahashi, A. Kitamura et al., in this ICCF18 Conference).

[7] A. Takahashi, *J. Condensed Matter Nucl. Sci.* **4** (2011) 269–281.

[8] A. Takahashi, Physics of cold fusion by TSC theory, *Proc. ICCF17*, August 12–17, 2012, Daejeon, Korea (see also downloadable preprint at http,//vixra.org/author/akito_takahashi).

[9] A. Takahashi, The basics of deuteron cluster dynamics as shown by Langevin equation, *ACS LENRSB* **2** (2009) 19–217.

[10] A. Takahashi, 4HTSC fusion by simultaneous weak/ and strong interactions, *Proc. JCF12*, Dec. 2011, Kobe, 2012, pp. 115–122.

[11] A. Takahashi and D. Rocha, Nucleon halo model of ^{8}Be*, *Proc. JCF-13*, 2013, pp. 10–31, http,//jcfrs.org/file/jcf13-proceedings.pdf.

[12] A. Takahashi et al., Mesoscopic catalyst and D-cluster fusion, *Proc. JCF11*, 2011, pp. 47–52, JCFRS web-site (in Ref. [11]).

[13] A. Karabut et al., *J. Condensed Matter Nucl. Sci.* **6** (2012) 214.

[14] A. Lipson et al., Phenomenon of an energetic charged particle from hydrogen/deuterium loaded metals, *Proc. ICCF10*, Condensed Matter Nuclear Science, World Scientific, Singapore, 2006, p. 539.

[15] A. Roussetski et al., Siena WS 2012, for TiDx system under e-X beam stimulation See also, *Russian J. Exp. Theor. Phys.* **112** (2011) 952.

[16] P. Boss et al., *J. Condensed Matter Nucl. Sci.* **6** (2012) 13.

[17] R. B. Wiringa et al., *Phys. Rev. C* **62** (2006) 14001.

[18] A. Takahashi, *J. Condensed Matter Nucl. Sci.* **9** (2012) 108.

[19] A. Takahashi, TSC-Induced nuclear reactions and cold transmutations, *J. Condensed Matter Nucl. Sci.* **1** (2007) 86–96.

[20] A. Takahashi, A. Kitamura et al., Anomalous exothermic and endothermic data observed by Nano-Ni-composite samples, *Proc. ICCF18*, U. Missouri, July 20–27, 2013.

J. Condensed Matter Nucl. Sci. 15 (2015) 23–32

Research Article

Anomalous Exothermic and Endothermic Data Observed by Nano-Ni-Composite Samples

Akito Takahashi*,†, A. Kitamura‡, R. Seto and Y. Fujita
Technova Inc., 1-1-1 Uchisaiwai-cho, Chiyoda-ku, Tokyo 100-0011, Japan

Taniike and Y. Furuyama
Graduate School of Maritime Sciences, Kobe University, Kobe 6580022, Japan

T. Murota and T. Tahara
Santoku Corp., Kobe 6580013, Japan

Abstract

To study the anomalous heat effect of Ni-based binary-metal-nano-powder samples by gas-phase hydrogen isotope absorption/desorption, three kinds of samples CNZ, CNZ-II and NZ were tested for the temperature range 300–573 K. The highest excess heat power, ca. 2W/g-Ni was obtained with CNZ at 573 K. A peculiar H(D)-isotopic effect and sudden endothermic events caused by abrupt H(D)-desorption were observed. The heat phenomenon appears to be happening on surface of nano-particles.

Keywords: D(H)-gas absorption, Excess heat, Higher temperature, 2W/g-Ni, Ni-based nano-particle

1. Introduction

Gas-phase hydrogen isotope absorption/adsorption experiments have been performed since 2008 at Kobe University to elucidate the underlying mechanism of anomalously large heat releases [1–5]. This paper reviews recent results by summarizing the observations of anomalous data on excess heat, D(H)-loading and abrupt endothermic desorption in Ni-based-nano-composite samples under D(H)-gas charging at both room temperature and elevated temperatures, done by Kobe–Technova group in 2012–2013.

Referring to our JCF12 paper [6] on Pd_1Ni_7/ZrO_2 samples, the optimum small fraction of Pd ad-atoms to Ni-core of binary Pd–Ni nano-particles would have made the Pd–Ni binary nano-particles a very active catalyst for D(H)-gas

---

*E-mail: akito@sutv.zaq.ne.jp
†Also at: Osaka University, 2-1 Yamadaoka, Suita, Osaka 565-0071, Japan.
‡Also at: Graduate School of Maritime Sciences, Kobe University, Kobe 6580022, Japan.

adsorption/absorption at room temperature and would have caused very high D(H)/Ni loading ratio such as 3.0 and anomalously high dynamic sorption energy with enhanced isotopic effect for D-gas charging. We have considered that the effect of Pd ad-atoms may be taking place also by other element ad-atoms such as Cu. Our trial experimental procedure and results reported for Ni/ZrO_2, $Cu_{0.21}Ni_{0.21}$/ZrO_2 and $Cu_{0.08}Ni_{0.36}$/ZrO_2 samples (partially reported in our ICCF17 paper by Sakoh et al. [7]) will be summarized in this report. We have reanalyzed time-dependent data for speculative heat releasing mechanisms during the long (several weeks) lasting phase of D(H) loading into nano-metal. It seems that competing processes of D(H)-gas sorption and desorption at the surface of nano-powders may be attributed to the mechanism as discussed in this paper.

Burst-like heat peaks of η-values (in unit of eV per D(H)-take-in/out) were observed with anomalously high values reaching 600 eV/H-sorption, and with smaller η-values for isotopic D-sorption than H-sorption, at 573 K. Integrated heat values for several-week runs were reached at the levels of ca. 800 eV/atom-Ni for $Cu_{0.08}Ni_{0.36}$/ZrO_2 samples, which were about 10 times larger than those of Ni/ZrO_2 samples and about four times larger than those of $Cu_{0.21}Ni_{0.21}$/ZrO_2 samples, at temperatures of 523–573 K.

In the pre-treatment runs at 573 K, very anomalous abrupt desorption phenomena with rapid decrease of loading ratio and heat-level (an endothermic phenomenon) were repeatedly observed for all nano-Ni composite samples. Observed endothermic energy per D(H)-desorption was around 50–80 eV, which is too large to be explained by H(D)-bonding energy to any metal. Displacement/knock-on of plural Ni-atoms by a proton/deuteron desorption might cause ca. 40 eV per Ni-displacement for energy absorption. If so, we may speculate that vacancies/defects would be formed in Ni-core-lattice and multi-atomic H(D)-clusters would be trapped there in the post-pre-treatment D(H)-charging runs. (These clusters might be seeds to induce the anomalous heat effect, which might be some nuclear origin, for further main runs of D(H) charging by elevating temperature above room temperature.)

After the pre-treatment, we took data by elevating the temperature from 373 up to 573 K. We did not observe the anomalous ‘abrupt’ endothermic events by desorption and we did observe excess power showing steady, continuous evolution. We need further repeated experiments to conform the phenomenon.

No visible increase of neutron counts (by ^{3}He counter) over natural background has been observed until now. A very slight increase of gamma-ray counts (by NaI counter) was sometimes recorded, but we need spectral and heat-cross-correlation-based confirmation in further scaled-up experiments (see our report from A. Kitamura et al. in this Conference [12]).

2. Experimental Apparatus and Procedure

In Fig. 1 (Photo 1), a view of experimental twin apparatus seen from a window of the room in our facility is shown. The A1 chamber is for H-gas loading experiments, and the A2 chamber is for D-gas loading experiments. We run simultaneously H- and D-gas charging with conditions as similar as possible in the twin systems. Calorimetry of this higher temperature experiment is made by the isoperibolic (isothermal) method, without using water-cooing of reaction chambers which are installed inside the A_1/A_2 outer evacuated thermal isolation chambers being always cooled with spiral water pipes wound the surface of A_1/A_2 chamber (see also Fig. 2). The coolant water temperature is regulated to $24\pm0.1°C$. The air temperature of the room is also regulated to $24\pm0.1°C$ by a spindle-type air conditioner installed outside the room.

A schematic diagram of one of the systems of the twin system is shown in Fig. 2 The samples are put in the reaction chamber, and the outer chamber is evacuated for thermal insulation during hydrogen isotope absorption/adsorption. Sheath heaters with resistance of 37.9 and 53.8 Ω wound around the reaction chambers in the A_1 and A_2 systems, respectively, are used for sample heating in the cases of baking preconditioning runs and D(H)-gas charging absorption runs at elevated temperatures. Alumel-chromel thermocouples are used to measure temperatures. Surface temperatures of a reaction chamber are monitored with these three K-type thermocouples (Ts, To and Td in Fig. 2). The calibration

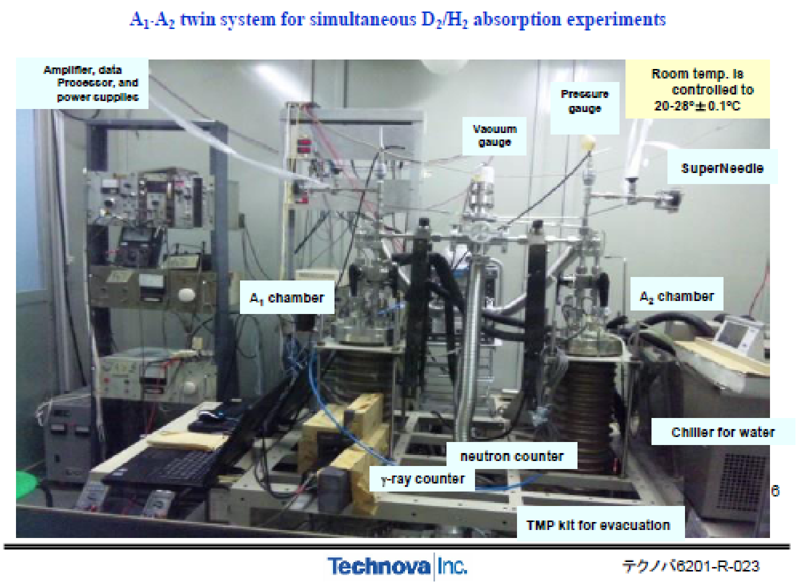

A_1-A_2 twin system for simultaneous D_2/H_2 absorption experiments

Technova Inc. テクノバ6201-R-023

Figure 1. (Photo): A window view of apparatus for the twin D(H)-gas loading experiment with metal-composite nano-powders.

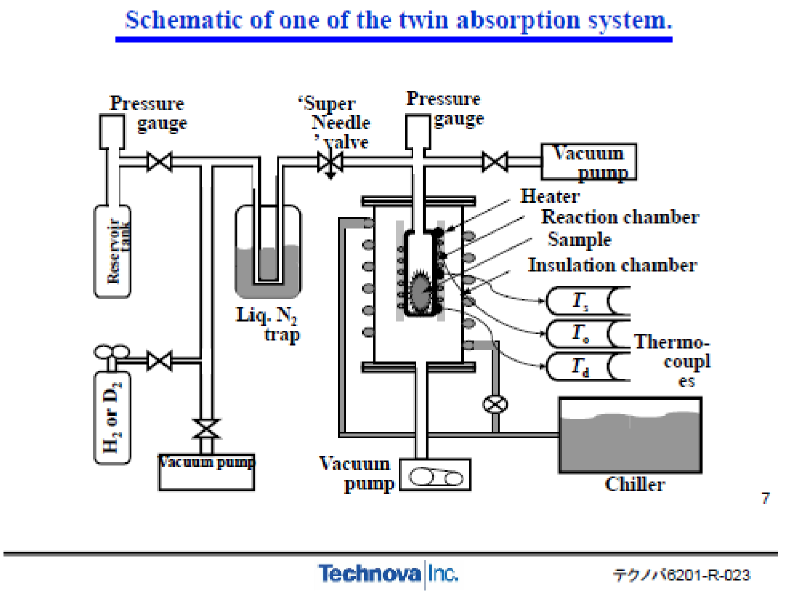

Schematic of one of the twin absorption system.

Technova Inc. テクノバ6201-R-023

Figure 2. Schematic diagram of one system of the twin system for D(H)-charging experiments with metal nano-composite powders.

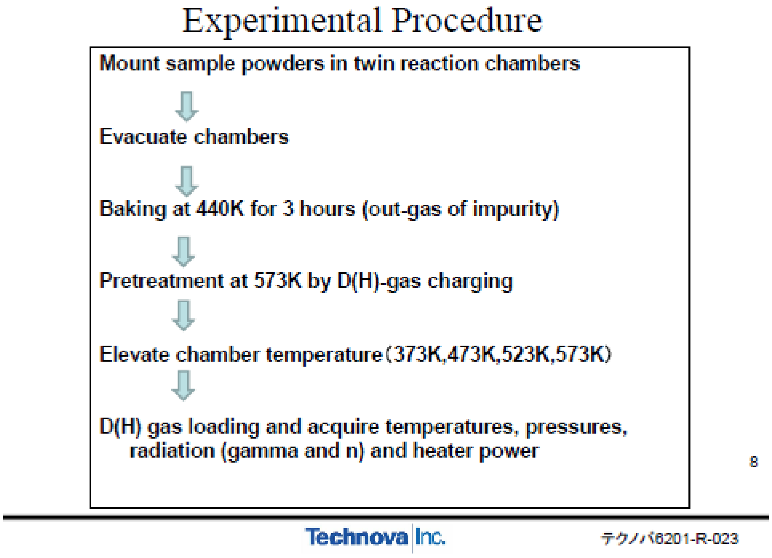

Experimental Procedure

Mount sample powders in twin reaction chambers

Evacuate chambers

Baking at 440K for 3 hours (out-gas of impurity)

Pretreatment at 573K by D(H)-gas charging

Elevate chamber temperature (373K,473K,523K,573K)

D(H) gas loading and acquire temperatures, pressures, radiation (gamma and n) and heater power

8

Technova Inc. テクノバ6201-R-023

Figure 3. Standard procedure of D(H)-gas charging experiments with nano-metal composite powders.

curve of heat-power vs. reaction chamber-surface temperature was obtained for the average of three TC data as a function of input heater-power by sheath heaters, under He-gas charged condition instead of D(H)-gas. Correction of difference in convection heat removal components between D(H)-gas and He-gas was done by using the difference of specific heat data of D(H)-gas and He-gas. Variation of heater input power was monitored every second and used for correction: this correction was less than ±0.5 W for a month long runs of experiment. A slight change of room temperature gave a slight effect (less than ±0.2W) on power level data of reaction chamber and was used for correction. We have done such corrections for power level determination as much as we could consider. The accuracy of excess heat-power level is estimated to be good with error bar of less than ±0.5 W.

The standard procedure for the gas-charging experiment is shown in Fig. 3. The D(H)-gas charging was started with 0.9–0.6 MPa pressure of source cylinder (reservoir tank) and fed through the super-needle valve with several s/m initial flow rates adjusted for the A_1/A_2 chambers.

We have used three kinds of Ni-based nano-composite samples for this series of experiments. Specification data of three samples are shown in Table 1. Based on the X-ray diffraction spectroscopy (XRDS) and the transmission-type electron microscope (TEM) picture analysis, initial particle sizes are around 24 nm for Ni-particles similarly for NZ, CNZ and CNZ-II samples. The particle size of Cu-particles was around 7 nm for CNZ and around 20 nm for CNZ-II. Used sample-weights were 20, 10 and 20 g, respectively, for NZ, CNZ and CNZ-II samples. We have assumed that only Ni-component is active to H(D)-absorption and relevant excess heat effect. Net weights of Ni components were 5.4, 2.07 and 2.44 g, respectively, for NZ, CNZ and CNZ-II samples.

After some runs of H(D)-charging, we plan to speculate about the formation of shell-core structured binary Cu–Ni nanoparticle [11]. We need to wait for TEM images of post-run samples to do this.

Table 1. Specification data of NZ, CNZ and CNZ-II samples.

	NZ20 (g)			CNZ10 (g)			CNXII20 (g)		
	Cu	Ni	Zr	Cu	Ni	Zr	Cu	Ni	Zr
Average grain size (nm)	–	23.5	–	6.8	24.5	–	24.2	18.2	–
Molar fraction (%)	0	35.8	64.2	7.9	36	56.1	21.4	21.5	57.1
Weight content (g)	–	5.4	14.6	0.49	2.07	7.44	2.64	2.44	14.9
Specific surface area (m^2/g)	27.6			43.5			44.2		

CNZ compared with NZ samples: Effect of *Cu* substitution for Pd on absorption at *elevated temperature.*

3. Results and Discussion

3.1. Comparison of base-temperature dependence of excess heat for Ni-base three samples

In Figs. 4–6, we show the results of observed excess heat-power data, respectively for NZ, CNZ-II and CNZ samples. D(H)-gas pressure data and D(H)/Ni dynamic loading ratio data are also included in figures. At room temperature for base-temperature, we have observed no visible increase of D(H)/Ni-dynamic loading ratios and we did not detect excess heat-power. A common trend for the three kinds of samples is: excess heat-power level becomes visible for higher base-temperatures than 473 K (200°C), and becomes larger as the base-temperature increases (up to 573 K, data were taken).

Excess heat-power levels are largest for CNZ sample, data for CNZ-II sample is next higher, and the data for NZ sample (namely without Cu) is the lowest. Another common trend is the evolution of larger excess heat-power levels for H-gas charging than those for D-gas charging. This trend is astonishing, but other research groups as Piantelli et al. [8] and Celani et al. [9] have claimed to observe the same effect. We have thought traditionally deuteron-induced cold fusion, especially for Pd–D systems at room temperature of base-temperature, is the easiest occurring nuclear effect in condensed matter. Why the reversed effect has happened for H-loading is of a new great mystery. One of us (Takahashi) has discussed some plausible reasons [10] for the recovery time (annealing) difference of damaged structures of nano-powders between the D-induced nuclear heat-source as by the 4D/TSC fusion events and the H-induced nuclear heat-source as by the 4H/TSC weak/strong (WS) fusion events. Released energy (47.6 MeV) by 4D fusion is one order larger than that (7.72 MeV) by 4H/TSC WS fusion [10,11]. Therefore, the lattice-damage by atom-displacement may be two orders of magnitude larger for D-system in Ni than that for H-system. For more discussions about the damage recovery effect, please see Ref. [11].

The largest heat-power level in this series of experiments was ca. 2W/g-Ni by CNZ sample at 573 K. The integrated value (total excess heat) was ca. 800 eV/Ni-atom. It is too large to explain by known chemical heat source for used materials [6,7].

3.2. Dynamic H(D)-sorption/desorption energy data

Next, we discuss time resolved parameters. The time-resolved specific sorption energy, or differential heat of hydrogen uptake, $\eta_{D(H)}$, is defined as the output energy per one hydrogen isotope atom absorbed/adsorbed [2];

$$\eta(t) \equiv \frac{\int_t^{t+\Delta t} W_{\text{true}}(t)\,\mathrm{d}t}{L(t+\Delta t) - L(t)}. \tag{1}$$

The formula holds for H(D)-desorption too. Typical calculated values of $\eta_{\mathrm{D(H)}}$ data for CNZ sample are shown in Figs. 7 and 8, respectively, for base-temperature of 523 and 573 K.

We have observed 'burst-like' data of η-values as seen in Figs. 7 and 8. The largest η-value is ca. 600 eV/H. It is anomalously large value, in the sense of chemistry or solid state physics. We need to consider possible mechanisms to release such large free energy by some nuclear processes such as discussed in our papers [9–11].

Another interesting feature of dynamic heat release is: as seen the data shown in Fig. 7, exothermic bursts are taking place for both of dynamic change of D(H)-sorption and D(H)-desorption, and especially exothermic (not endothermic) bursts happened for D(H)-dynamic desorption. This phenomenon depicts that the excess heat generating events are taking place at around surfaces of Ni or Cu–Ni binary nano-particles. Our theoretical prediction based on the surface mesoscopic catalysis effect to induce D(H)-cluster fusion [9–11] might match to the observed fact. However, we need further confirmation study from various angles based on future experiments using various kinds of nano-powders.

3.3. Abrupt endothermic events caused by H(D)-desorption

Typical data is shown in Fig. 9 for the CNZ-II sample. In the pretreatment runs at 573 K (see Fig. 3), we have observed an anomalous phenomenon of abrupt burst-like D(H)-desorption and corresponding endothermic reaction with anomalously large amplitudes for all three of the samples.

In the latter runs at 573 K or lower temperatures, the evolution of excess heat-power level was observed continuously and persistently and the abrupt endothermic events were not observed. What is the reason for such a drastic change of D(H)-absorption/excess-heat episodes from the initial pretreatment run to the final long lasting persistent excess heat runs? When the abrupt desorption happened, average η-values were ca. –50 to –80 eV/H(D)-desorption. We consider the highest possible H(D)-bonding energy to metal atom is on the order of a few eV, so that –50 eV/H(D) is too large to explain by the H(D)-absorption/desorption energy. Some peculiar events should happen in these circumstances.

One event that might be considered would be a single or plural Ni-atoms kick-out (displacement) induced by the abrupt H(D)-desorption, for we know from the radiation damage study of hot-fusion materials that metal atom displacement energy from lattice is on the order of 40 eV. Figure 10 is a speculative image of a plausible process.

Why do samples after the pretreatment become ‘gentle’ for persistent excess heat generation? We have no definite answer yet. We might consider that two separate nano-particles of Cu (6.8 nm, initially) and Ni (24.5 nm, initially)

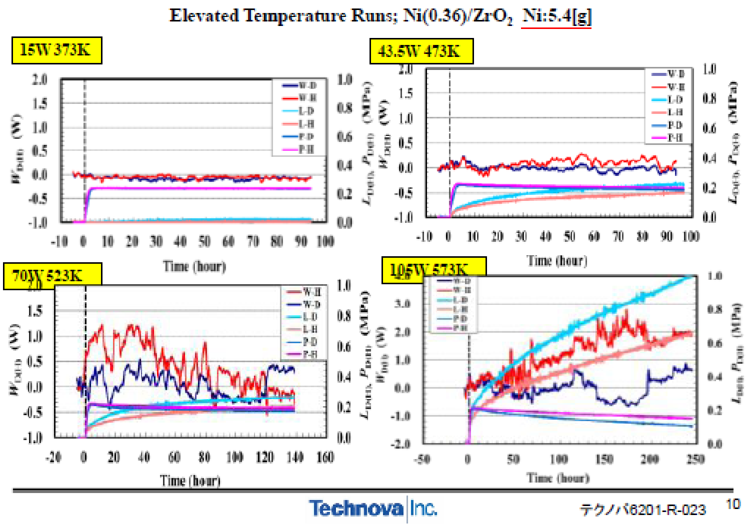

Figure 4. Base-temperature dependence of excess heat-power taken for NZ sample. Here W denotes excess-power (red for H and blue for D), p pressure and L loading ratio.

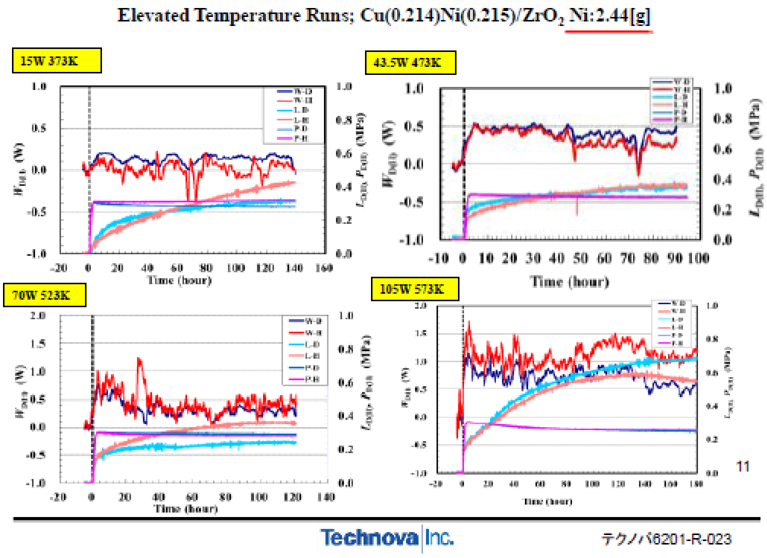

Figure 5. Base-temperature dependence of excess heat-power taken for CNZ-II sample. Here W denotes excess-power (*red* for H and *blue* for D), p pressure and L loading ratio.

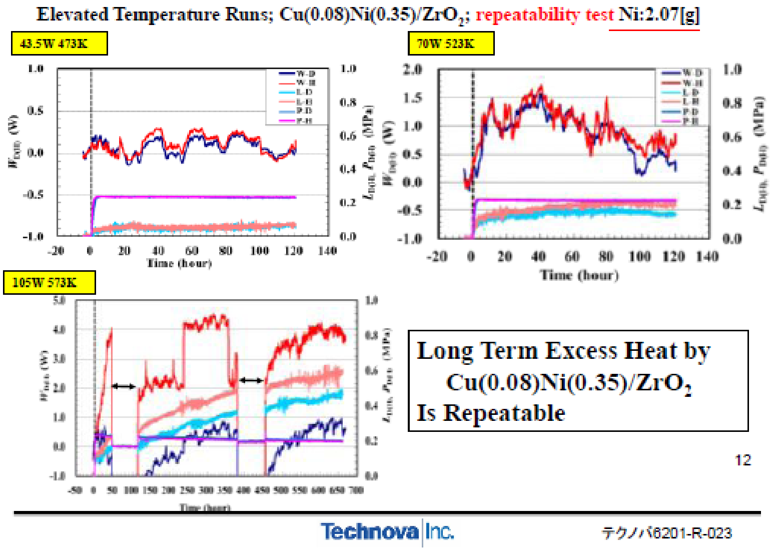

Figure 6. Base-temperature dependence of excess heat-power taken for CNZ sample. Here W denotes excess-power (*red* for H and *blue* for D), p pressure and L loading ratio.

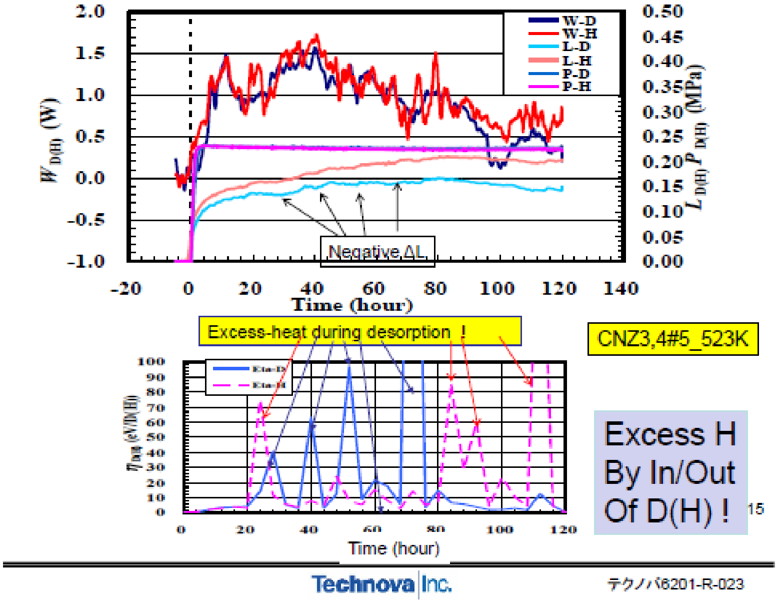

Excess-heat during desorption !

CNZ3,4#5_523K

Excess H
By In/Out
Of D(H) !

Figure 7. Data of dynamic H(D)-sorption/desorption energy for CNZ.

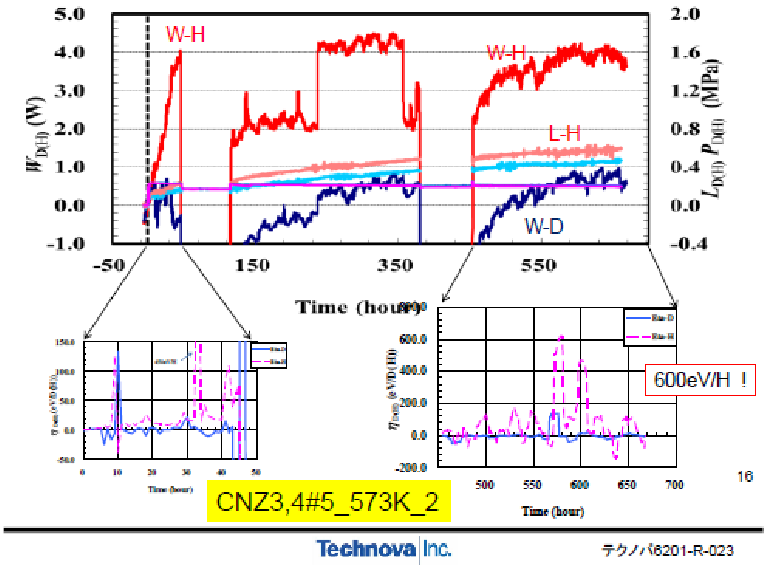

600eV/H !

CNZ3,4#5_573K_2

Figure 8. Data of dynamic H(D)-sorption/desorption energy for CNZ.

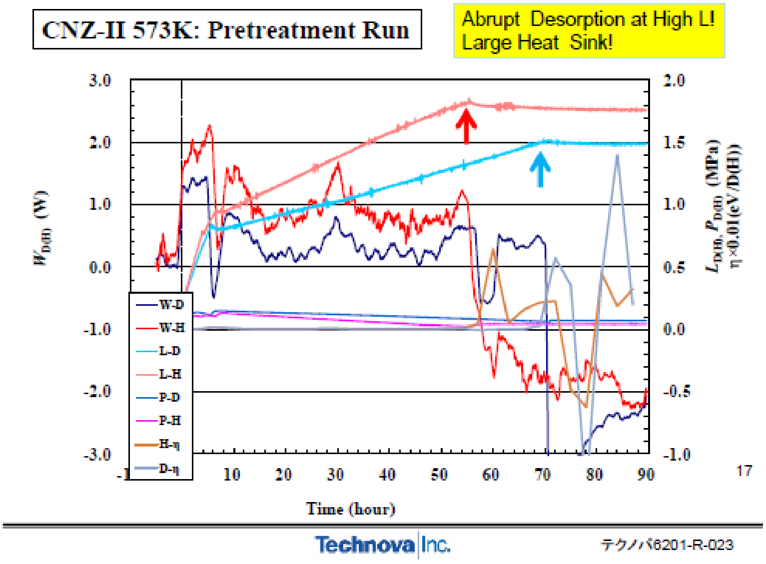

Figure 9. Data showing abrupt endothermic H(D)-desorption observed in the initial pretreatment run of CNZ-II sample (see points of arrows and data around time 10 h). Here P denotes pressure, L loading and W excess power .

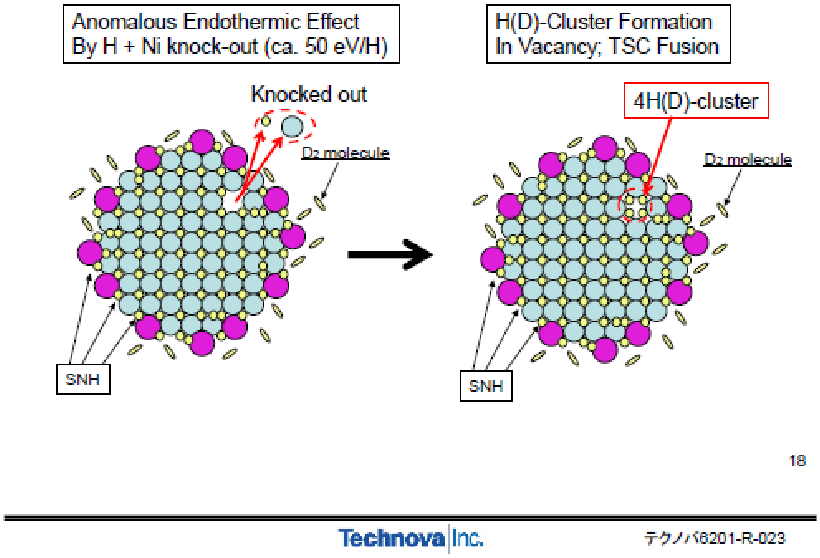

Figure 10. An image of plausible mechanism for the abrupt endothermic reaction with H(D) and Ni-atom kick-out. Here smaller circles with green color depict Ni atoms, and purple larger circles depict Cu atoms. .

might merge to make a Ni-core/Cu-outer shell structure as drawn in right figure of Fig. 10 to be a strong mesoscopic catalyst [11]. However, this is speculative.

4. Conclusion

The present three kinds of Ni-nano-composite samples gave anomalous and long-lasting excess heat data at elevated base-temperature (523, 573 K) conditions. Cu–Ni–Zr nano-composite samples gave several fold larger heat level than Ni–Zr nano-composite sample. A Cu additive seems to work as a strong catalyst for Ni-core particle to absorb D(H)-gas and releasing anomalously large excess heat. However, we have not yet studied why H_2 gas loading produced much more heat than D_2 gas loading. It is an interesting mystery.

The 8% Cu-added Ni-nano sample showed ca. 4-fold larger heat level per g-Ni than that of 21.4% Cu-added Ni-nano sample and such data were repeatedly observed. In pretreatment runs, an anomalous abrupt desorption/endothermic effect was repeatedly observed for all of the three kinds of samples. The mechanism of such an abrupt change is interesting, but has not yet been studied. At 573 K, η-values were anomalously as large as 100–600 eV/H, and integrated heat was 800 eV/atom-Ni for CNZ samples. This seems to indicate the existence of non-chemical reaction heat, but there is still no explanation by definite nuclear mechanism. Further confirmation experiments about the presently observed anomalous exothermic and endothermic phenomena are expected, using scaled-up devices.

References

[1] A. Kitamura, T. Nohmi, Y. Sasaki, A. Taniike, A. Takahashi, R. Seto and Y. Fujita, *Phys. Lett. A* **373** (2009) 3109–3112.

[2] A. Kitamura, Y. Miyoshi, A. Taniike, A. Takahashi, R. Seto and Y. Fujita, *J. Condensed Matter Nucl. Sci.* **4** (2011) 56–68.

[3] A. Kitamura, Y. Miyoshi, H. Sakoh, A. Taniike, A. Takahashi, R. Seto and Y. Fujita, *J. Condensed Matter Nucl. Sci.* **5** (2011) 42–51.

[4] H. Sakoh, Y. Miyoshi, A. Taniike, A. Kitamura, A. Takahashi, R. Seto and Y. Fujita, Proc. 12th Meeting of Japan CF Research Society, *JCF* **12** (2012) 10–18.

[5] A. Takahashi, A. Kitamura, Y. Miyoshi, H. Sakoh, A. Taniike, R. Seto and Y. Fujita, *16th Int. Conf. Condensed Matter Nuclear Science*, Chennai, India, 2011, Session of New Energy Technology, 241st ASC National Meeting, Mar. 2011.

[6] Y. Miyoshi, H. Sakoh, A. Taniike, A. Kitamura, A. Takahashi, R. Seto, Y. Fujita, T. Murota and T. Tahara: Proc. JCF-12 (2012) 1: visit http://jcfrs.org/file/jcf12-proceedings.pdf.

[7] H. Sakoh, Y. Miyoshi, A. Taniike, A. Kitamura, A. Takahashi, R. Seto and Y. Fujita, *17th Int. Conf. Condensed Matter Nucl. Sci.*, Daejeon, Korea, Aug. 2012.

[8] F. Piantelli et al., Some results from the Nichenergy laboratory, presentation at the 10th Int. Workshop, Siena, April 2012 (see ISCMNS web site).

[9] F. Celani et al., Cu–Ni–Mn wires with improved submicrometric surfaces used as LENR device by new transparent dissipation-type calorimeter, *Proc. ICCF17*, to be published.

[10] A. Takahashi, Nuclear products of cold fusion by TSC theory, *Proc. ICCF18*, to be published.

[11] A. Takahashi et al., Mesoscopic catalyst and D-cluster fusion, *Proc. JCF11* (2012)47-53, http://jcfrs.org/file/jcf11-proceedings.pdf.

[12] A. Kitamura, A. Takahashi, R. Seto, Y. Fujita, A. Taniike and Y. Furuyama, A mass-flow-calorimetry system for scaled-up experiments on anomalous heat evolution at elevated temperatures, *Proc. ICCF18*, to be published.

J. Condensed Matter Nucl. Sci. 15 (2015) 33–43

Research Article

Energetic Particles Generated in Earlier Pd + D Nuclear Reactions

D.Z. Zhou[*], C. Wang, Y.Q. Sun, J.B. Liang and G.W. Zhu
National Space Science Center, Chinese Academy of Sciences, Beijing 100190, China

L.P.G. Forsley
JWK International Corp., Annandale, VA 22003, USA

X.Z. Li
Department of Physics, Tsinghua University, Beijing 100084, China

P.A. Mosier-Boss
Massachusetts Institute of Technology, Cambridge, MA 02139, USA

F.E. Gordon
Navy Senior Executive Service, San Diego, CA 92122, USA

Abstract

Energy of low energy nuclear reactions (LENRs) is clean, cheap, sustainable and can solve all environmental problems. Linear Energy Transfer (LET) spectrum method using CR-39 detectors is the best method to investigate particles generated in LENRs. This paper introduces LET method and presents LET spectra and energy distributions for particles produced in Pd + D reactions obtained by re-analyzing the original data measured with CR-39 detectors by SPAWAR group using LET spectrum method.

Keywords: CR-39 detectors, Energy distributions, LENR particles, LET method, LET spectra

---

1. Introduction

Condensed Matter Nuclear Science (CMNS) is a multi-disciplinary academic field which combines nuclear physics and condensed matter physics and targets clean and sustainable nuclear fusion energy. CMNS consists of multiple subjects, including LENRs. The word “low” in LENRs refers to the input energies to the reactions, the output energies may be low or high, depending on the different reactions designed.

---

[*] E-mail: dazhuang.zhou@gmail.com

CR-39 plastic nuclear track detectors are the most useful track detectors in research. An important physical quantity in CR-39 work is the linear energy transfer (LET) lost by a charged ionizing particle traveling through matter, with units of keV/μm CR-39 or water. CR-39 detectors are sensitive to high LET particles ($\geq$ 5 keV/μm water) and can measure charged particles directly and neutrons through secondary charged particles. The LET spectrum method using CR-39 detectors is the best one for high-LET particles research. CR-39 detectors have been used for research on CMNSs, including LENRs

Experiments of LENRs indicated that a great variety of charged particles and neutral particles can be generated in LENRs at room temperature. For Pd + D experiments using CR-39 detectors, in addition to the primary charged particles – protons, tritons, ^{3}He and α particles, secondary charged particles with high LET can be produced by neutrons and high energy protons in the CR-39 detectors and can make an important contribution for the detected charged particles. All the primary protons and α particles with high LET and secondary high LET particles can be measured with CR-39 detectors. Another advantage to use CR-39 detectors is that the primary charged particles and neutrons can be fully separated by changing the thickness of absorbing film attached to the surfaces of CR-39.

The energetic particles from LENRs were observed with CR-39 detectors for the gas-loading Pd + D system used by the Tsinghua University and co-deposition Pd + D system used by the SPAWAR group. The gas-loading approach can avoid the high temperature problem at the boiling point existed for the deposition approach.

The successful Pd + D experiments conducted by the Tsinghua University group [1–7] and US SPAWAR group [8–13] using CR-39 detectors have accumulated abundant experimental data and if a better method of data analysis is applied the brand new results will be obtained.

However, due to the limitation of previous methods for data analysis, the physical results for the Pd + D reactions before are mainly photos of nuclear tracks in CR-39 detector, track cone comparisons and statistics of track parameters, all these results cannot provide us with important physical quantities – energy loss, energy and charge for the LENR particles. Therefore, in order to obtain quantitative results for LENR experiments, LET spectrum method using CR-39 detectors should be introduced and data re-analysis should be conducted. LET spectrum method using CR-39 has been widely used for research on radiation at aviation altitudes and in space [14–16]. Radiation at aviation altitudes dominated by atmospheric neutrons ($\sim$ 0.1 – 20 MeV) was successfully measured with LET method. This is a convincing reason to employ the LET method in LENR research. For our LET work, the original data of LENR particles were scanned and provided by the previous US Navy SPAWAR group, data analysis was conducted by Zhou at NASA-JSC using LET spectrum method [16]. Research on the properties and physical quantities of LENR particles is an important task in LENR research. The re-analysis work using LET spectrum method for the SPAWAR data was conducted successfully and some brand new results were obtained, including LET value,

2. Concepts on CR-39 Track Detectors

2.1. CR-39 nuclear track detectors

With chemical components $C_{12}H_{18}O_7$, CR-39 detectors are sensitive to particles with high LET ($\geq$5 keV/μm water). High LET particles are charged particles (primary and secondary). In LENR experiments, primary particles are produced by LENRs. Secondary charged particles are short range recoils and fragments produced in nuclear reactions. Therefore, CR-39 detectors can measure high-LET charged particles directly and neutrons through secondary charged particles. To decrease background radiation and to protect the surface of CR-39, a thin polyethylene film (hereafter referred as PE film) of $\sim$ 60 μm is covered on the surface of CR-39.

2.2. Physical principle of CR-39 detectors

When charged particles pass through CR-39 detector, they break molecular bonds of CR-39 polymer to form high chemical reactive paths along their trajectories. The particle trajectories can be revealed as etched cones in CR-39 detectors by chemical etching of CR-39 plates. Nuclear tracks form ellipse openings on CR-39 surfaces.

LET spectrum and other physical quantities can be determined with LET method using CR-39 detectors, based on LET calibration for the CR-39 detectors. The LET threshold of CR-39 detectors is about 5 keV/μm water, enabling protons of energy up to $\sim$ 10 MeV and, high charge and high energy particles (HZEs) to be detected directly. Secondary charged particles produced by high energy protons and neutrons with high LET are also detectable.

2.3. Restricted energy loss (REL)

The restricted energy loss is the portion of the total energy loss that produces delta rays of energy less than specified value, E_0 and only this part of energy loss is relevant to the nuclear track formation. The Benton model of restricted energy loss in CR-39 detector [17] takes into account the secondary ionizations produced by low energy delta rays and is given by

$$\left(\frac{\mathrm{d}E}{\mathrm{d}x}\right)_{E<E_0} = \frac{C_1 Z_{\mathrm{eff}}^2}{\beta^2}\left[\ln\left(\frac{w_{\max}E_0}{I^2}\right) - \beta^2 - \delta - U\right],$$

where C_1, I and δ are the detector constants, Z_{eff} the effective charge of incident particle, $w_{\mathrm{max}} = 2mc^2\beta^2\gamma^2$, m the electron mass, $\beta = v/c$, *ve* particle velocity, U low velocity correction and E_0 is usually taken as 200 eV for CR-39.

Quantity $(\mathrm{d}E/\mathrm{d}x)_{E<E_0}$ is also called Linear Energy Transfer (LET). Studies have shown, a critical LET exists below that etchable tracks are not formed. LET spectrum method will adopt the REL model to generate LET calibration. The restricted energy loss is often written as LET_{Δ} and the unrestricted energy loss as LET_{∞}.

2.4. Bulk etch and etch rate ratio

Define bulk etch B as the thickness etched off on one surface of the CR-39 detector. Bulk etch can be calculated with the Henke formula [18].

Define the track etch rate as $V_T = L_0/t$, where L_0 is the length from pre-etch surface to the cone tip measured along the particle's trajectory, t is the etch time. Similarly, bulk etch rate is defined as $V_B = B/t$ and the etch rate ratio is $S = V_T/V_B$. The etch rate ratio can be calculated with the Somogyi formula [19]:

$$S = \sqrt{1 + 4\left(\frac{D}{2B}\right)^2 \Big/ \left[1 - \left(\frac{d}{2B}\right)^2\right]^2},$$

where D and d are the ellipse major and minor axes of the track cone opening on the CR-39 surface.

3. LET Method Using CR-39 Detectors

The LET spectrum method using CR-39 detectors have been used for research on radiation at aviation altitudes and in space [14–16, 20–24]. The LET spectrum method using CR-39 detectors is as below: experimental design for particles exposures and measurements; exposures of CR-39 detectors to radiation particles to be detected; detectors recovery; chemical etch for CR-39 detectors; measurements and calculations for bulk etch and etch rate ratio; events recognition, data scan and acquisition with optical microscope; data analysis and calculation to obtain differential and integral LET spectra (fluence, etc.) and other important physical quantities.

3.1. Experimental designs

Detector configuration should satisfy the experimental requirements. The issue of the PE film on CR-39 surface should be considered carefully, the film can be removed before experiment or remained. If the film was removed, the LENR particles will incident on the CR-39 surface directly, therefore, the incident energy equals to the observed. If the film is remained, the LENR particles must pass through the film before hitting CR-39 surface, therefore, the energy incident on the film is the energy observed with CR-39 plus the energy absorbed by the film. In order to measure as many LENR particles as possible the film should be removed. PE films can also be used for separating charged particles and neutrons.

3.2. Chemical etch of CR-39 detectors

After exposures to LENR energetic particles, CR-39 detectors were chemically etched with NaOH solution, the temperature, solution concentration and the etching time can be adjusted so as to obtain better etching effects.

3.3. Data scan and acquisition

Data scan can be conducted with optical microscope, events were identified and the major and minor axes of track cone opening on the CR-39 surface were measured and collected. The collected events from CR-39 detectors exposed in LENR experiments include LENR particles and background radon α particles. Comparing to LENR particles, background is very low and can be ignored.

3.4. Data analysis and LET spectra generating

For each scanned event the LET value was calculated using LET calibration for CR-39, LET value was binned, then differential spectrum of fluence was generated. The differential fluence for LENR particles recorded with CR-39 detectors can be simplified and expressed as

$$F = \mathrm{d}N(i)/[A \times \mathrm{d\,LET}(i)],$$

where F is in 1/(cm^2.keV/μm CR-39), A is the scanned area of CR-39 detector, d$N(i)$ is the number of particles in the ith LET bin LET(i) with a bin width of dLET(i). The net differential fluence is obtained by subtracting the background from the total differential fluence.

3.5. Charge and energy distributions

The LET values for protons, α particles and particles with higher charges are different, therefore particle's charge can be classified by LET. After the determination of LET and charge, the particle's energy can be calculated. Then, the LET spectrum, charge distribution and energy distribution can be obtained.

3.6. LET Calibration for CR-39 detectors

LET calibration – the relationship between LET$_{200}$ CR-39 and etch rate ratio S, is a key part in LET spectrum method and can be obtained by exposing CR-39 detectors to accelerator-generated protons and heavy ions and the LET calibration of CR-39 detectors obtained by NASA-JSC (Johnson Space Center) researchers [21] can be used.

4. Low Energy Nuclear Reactions

Different LENRs were observed since 1990s [1–13]. The approach used by the Tsinghua University group and US Navy SPAWAR group is the Pd + D system.

Electrochemical reactions occurring at the cathode:

$$\mathrm{Pd}^{2+} + 2\,\mathrm{e}^- \to \mathrm{Pd}^0,$$

$$\mathrm{D_2O} + \mathrm{e}^- \to \mathrm{D}^0 + \mathrm{OD}^-.$$

The result is, metallic Pd is deposited in the presence of evolving D_2. A variety of different particles can be produced in the Pd + D experiments. The primary reactions that occur in DD fusion are:

$$\mathrm{D} + \mathrm{D} \to \mathrm{T}\ (1.01\ \mathrm{MeV}) + \mathrm{p}\ (3.02\ \mathrm{MeV}),$$

$$\mathrm{D} + \mathrm{D} \to \mathrm{n}\ (2.45\ \mathrm{MeV}) + {}^3\mathrm{He}\ (0.82\ \mathrm{MeV}).$$

The secondary reactions in plasma fusion are:

$$\mathrm{D} + \mathrm{T}\ (\le 1.01\ \mathrm{MeV}) \to \alpha\ (6.7\text{–}1.4\ \mathrm{MeV}) + \mathrm{n}\ (11.9\text{–}17.2\ \mathrm{MeV}),$$

$$\mathrm{D} + {}^3\mathrm{He}\ (\le 0.82\ \mathrm{MeV}) \to \alpha\ (6.6\text{–}1.7\ \mathrm{MeV}) + \mathrm{p}\ (12.6\text{–}17.5\ \mathrm{MeV}).$$

In addition to the primary high-LET charged particles, secondary high-LET charged particles (short range recoils and target fragments – heavy charged particles) may be generated through nuclear interactions of protons with higher energies ($>\sim$10 MeV) and neutrons in the CR-39 detectors. All the primary and secondary charged particles with high LET can be detected with CR-39 detectors. After the experiment, the PE film was removed and the CR-39 detectors were chemically etched. The etched CR-39 detector was scanned using an automated scanning track analysis system.

5. Results of Pd + D Experiments

5.1. Photos of nuclear tracks in CR-39 detectors

Figure 1 shows photos of nuclear track cones on CR-39 surfaces produced by particles from Pd + D experiments.

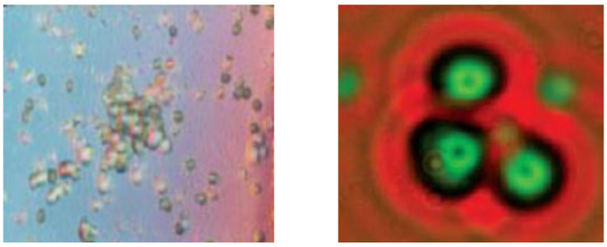

Figure 1. Photos of nuclear tracks in CR-39 produced by LENRs. (a) (*left*) All particles (Tsinghua University) [1–7]. (b) (*right*) Triple alphas (SPAWAR) [8–13].

5.2. LET Spectra of energetic charged particles

The original data of nuclear tracks in CR-39 were scanned from CR-39 detectors employed for 10-5-07 and 10-6-07 experiments, the scanned surfaces are denoted as "bottom" – facing the cathode or near the cathode and "top" - far from the cathode, the scanned area is 2.7×10^{-3} cm^2 and the LET bin width is 0.25 keV/μm CR-39.

Figure 2a,b shows LET spectra of differential fluence for detected charged particles. The conjunction point of LET around the maximum LET for protons and the minimum LET for alphas was determined as 31 keV/μm CR-39 using the minimum range of protons – the bulk etch of 8–9 μm and the maximum energy 17.2 MeV of alphas (the maximum energy of neutrons). Therefore, in the figures particles with LET $\leq$ 31 keV/μm CR-39 are protons and particles with LET $\geq$31 keV/μm CR-39 are α particles. Figure 2 indicates that LET values of protons and α particles measured is from $\sim$ 3 to $\sim$ 150 keV/μm CR-39; LET spectrum for protons has several peaks and the major peak is at $\sim$ 3.25–3.50 keV/μm CR-39.

Number of charged particles observed with CR-39 detectors for the Pd + D experiments are collected in Table 1. Data indicate that: (a) for the bottom surface of CR-39 detectors, the average ratio of events number is $\sim$ 96.3%

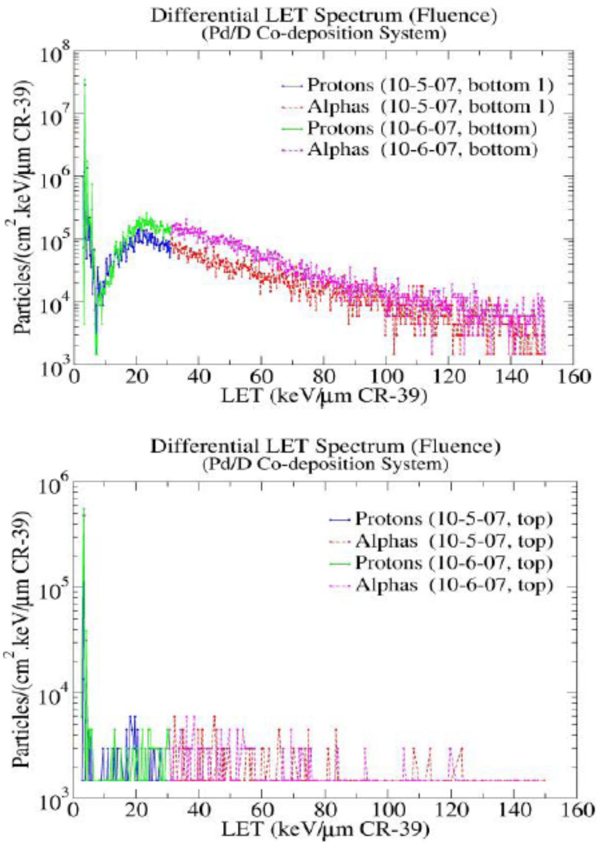

Figure 2. (a) LET spectra of differential fluence (bottom surfaces of CR-39 detectors). (b) LET spectra of differential fluence (top surfaces of CR-39 detectors).

Table 1. Events observed for different experiments.

Detector	Surface	Number of events			
		N_1 (Z= 1)	N_2 (Z= 2)	N_3 ($Z \geq 3$)	N (Total)
10-5-07	Bottom 1	26 516	63 07(	1431	34 254
	Bottom 2	5995	1438	312	7745
	Top	448	198	104	750
10-6-07	Bottom	33815	12 241	1357	47 413
	Top	511	210	111	832

(Z= 1,2) and $\sim$ 3.7% ($Z \geq 3$); (b) for the top surface of CR-39 detectors, the average ratio of events number is $\sim$ 86.4% (Z = 1,2) and $\sim$ 13.6% ($Z \geq 3$).

The differential LET spectra of fluence presented in Fig. 2, the data on events number and particle's charge collected in Table 1 indicate that LENR experiments of the Pd + D co-deposition system were repeated excellently.

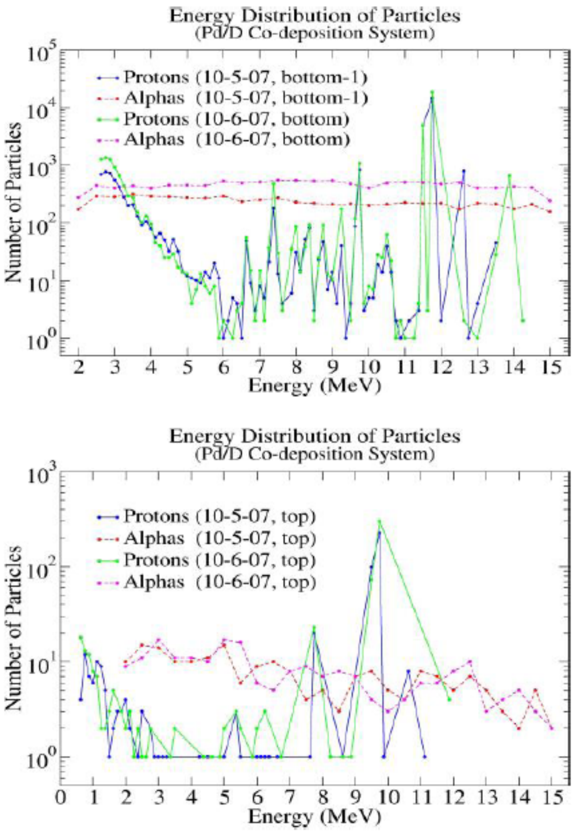

Figure 3. (a) Energy distribution of particles (bottom surfaces of CR-39, total energy). (b) Energy distribution of particles (top surfaces of CR-39, observed energy).

Table 2. Energies carried by observed particles

Detector	Surface	Energy of particles (MeV)			Ratio (%)	
		E_1 (Z = 1)	E_2 (Z = 2)	$E = E_1 + E_2$	E_1/E	E_2/E
10-5-07	Bottom 1	266279	50548	316827	84	16
	Bottom 2	59547	11224	70771	84	16
	Top	3596	1388	4984	72	28
10-6-07	Bottom	327263	103823	431086	76	24
	Top	4090	1283	5373	76	24

5.3. Energy distributions of energetic particles

As showed by above results, LENR particles measured with CR-39 are mainly protons and α particles, therefore, particle's energy can be calculated through LET.

Figure 3a,b shows the energy distributions of particles produced by Pd + D experiments and measured with CR-39. In the figures energy is total for the bottom CR-39 surfaces and observed for the top CR-39 surfaces.

There was a PE film with a thickness of $\sim$60 μm between the cathode of the Pd + D system and the surface of CR-39 detector, when protons and α particles produced in LENRs pass through the film, the energy loss $\sim$2 MeV/n, i.e., the minimum energy needed to pass through the film is $\sim$2 MeV for protons and $\sim$8 MeV for α particles. This fact indicates that α particles observed in CR-39 detectors are secondary particles produced by high energy primary protons and neutrons. Therefore, in Fig. 3(a) for the bottom surfaces, the energy for protons is total (the minimum energy of 2 MeV + energy observed) and the energy for α particles is observed.

For top surfaces of CR-39, energy absorption by CR-39 must be considered. The CR-39 thickness is $\sim$1000 μm, and the minimum energy needed to pass through CR-39 is $\sim$10 MeV for protons and 40 MeV for α particles. If particles observed at the top surfaces of CR-39 are primary charged particles, the total energy (minimum energy absorbed by PE film + minimum energy absorbed by CR-39 + observed energy) for both protons and α particles will be too high and contradict with the theoretical predictions. Therefore, majority particles observed at top surfaces of CR-39 detectors must be secondaries and energy for both protons and α particles in Fig. 3(b) are values observed.

There are some peaks for proton number in Fig. 3, the major peak is at $\sim$11.5–12 MeV for the bottom CR-39 surfaces and $\sim$9.75 MeV for the top CR-39 surfaces, consistent with the theoretical predictions for the LENRs of Pd + D system. The distribution of α particles is nearly uniform because they are mainly secondary particles. The energies carried by the energetic LENR particles can be calculated precisely based on the energy distributions. For the 10-5-07 and 10-6-07 experiments, the calculated energies for the measured protons and α particles are collected in Table 2. The total energies of protons and α particles observed in an area of 2.7 $\times$ 10^{-3} cm^2 are 3.2 $\times$ 10^5, 4.3 $\times$ 10^5, 5.0 $\times$ 10^3 and 5.4 $\times$ 10^3 MeV for 10-5-07 (bottom1), 10-6-07 (bottom), 10-5-07 (top) and 10-6-07 (top), respectively.

Because those particles scanned and analyzed are only part of the total particles generated in LENRs, the actual total energy carried by all LENR particles with high LET should be much higher than that calculated from the scanned events. Now considering the factor that part of the detected charged particles are produced through the interactions between neutrons and CR-39 material, and that detection efficiency of CR-39 detectors for neutrons with energies from $\sim$ 1 to 20 MeV is $\sim 10^{-4}$ to 10^{-3}, the actual number of particles entered the CR-39 detector is then much higher than the number showed in Fig. 3.

If protons and neutrons can be separated completely, the total energy carried by charged particles and neutrons can be calculated separately and accurately. Results presented in this section on the LET spectra, the energy distributions and the energies carried by the LENR particles are strong evidence for the generation of energetic particles and energy in LENRs.

6. Events of Triple Alpha Particles

Triple tracks originated from the same incident particle were observed with CR-39 detectors for the particles produced in the Pd + D co-deposition experiments. Triple α particles can be produced through the nuclear interaction between high energy neutrons and carbon nuclei of CR-39 material. For the triple track events reported [9,11], the LET and energy calculated with LET method are presented and discussed briefly as below.

(1) LET of triple particles are from $\sim$115 to $\sim$135 keV/μm CR-39, too high to be generated by protons with range larger than bulk etch value of $\sim$9 μm and the only reasonable explanation is that triple tracks are α particles.
(2) The total energy of the three α particles are $\sim$7.5 MeV, considering the threshold energy of 9.6 MeV for nuclear reaction ^{12}C(n,n')3α [25], the total energy of the parent neutron incident on the CR-39 detector is $\sim$17.1 MeV, consistent very well with the theoretical predictions made for LENRs of Pd + D system. The results obtained using LET method indicate that high energy neutrons are produced in the Pd + D system and these neutrons can shatter carbon nuclei in CR-39 to form triple α particles.
(3) Because the energy required for generating triple α particles is near the highest energy for neutrons generated by Pd + D system and that probability to produce triple alphas is low, therefore triple track events are very few.
(4) Triple α particles can also be generated from nuclear reaction ^{12}C(p,p')3α with a threshold energy of $\sim$12.7 MeV [26], in which 3.1 MeV is the Coulomb potential energy. Therefore, for the same triple tracks observed, if generated by protons, the total proton energy is (7.5 + 12.7) = 20.2 MeV, higher than the maximum value 17.5 MeV for protons in Pd + D system. This is why triple α particles are generated by high energy neutrons with energies of $\sim$17.1 MeV, not by protons $\leq$ 17.5 MeV.

The analysis for triple α tracks observed with CR-39 detectors convinced us that high energy neutrons are produced in Pd + D experiments. This is definitely another very strong evidence for the generation of LENRs.

7. Conclusions and Discussions

(1) LET spectra and energy distributions for particles produced by LENRs of Pd + D co-deposition system were obtained with the LET method using CR-39 detectors.
(2) All the results (LET and spectra, energy and distributions, high energy protons and neutrons and triple alphas are agree well with those predicted theoretically and then are very strong evidences for the energy generating from D + D and Pd + D nuclear reactions.
(3) The LET method using CR-39 detectors and the results measured for LENRs are reliable and can used for the quantitative data analysis on energetic LENR particles.

As mentioned earlier, radiation at aviation altitudes is dominated by atmospheric neutrons, as showed in Fig. 4 [27,28]. In the figure, radiation is calculated with LUIN (solar minimum, high latitude). To satisfy measurements for radiation field dominated by neutrons, CR-39 and other detectors were selected and the radiation field was successfully measured using LET and other methods by the international co-operation team supported by the European Commission for a completed solar cycle [14–16,28–31]. Results measured with CR-39 are consistent well with those measured by other methods and simulated theoretically using FLUKA [14], LUIN and CARI [32]. CR-39 results were also inter-compared every year with results from other detectors for the CERN-CERF neutron reference field which is dedicatedly designed to simulate radiation field at aviation altitudes. These investigations prove that CR-39 detectors are the best passive detectors sensitive to neutrons, protons and heavy ions and can be used for research on the energetic particles from LENRs.

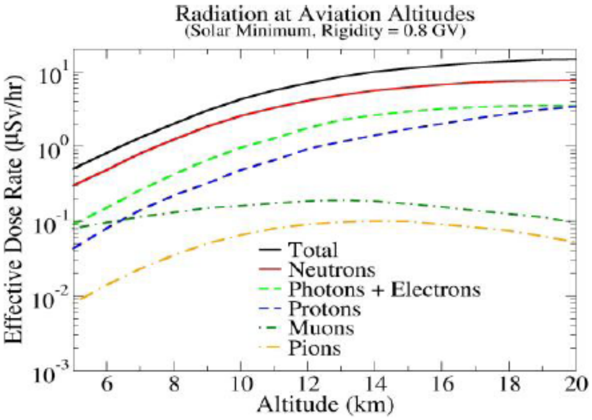

Figure 4. Components and variation of radiation at aviation altitudes.

References

[1] X.Z. Li, S.Y. Dong, K.L. Wang et al., *AIP Conf. Proc. 228*,Anomalous Nuclear Effects in Peuterium/Solid Systems, Provo, UT, US, Jones, SE (Ed.), 1990, pp. 419–429.

[2] X.Z. Li, D.W. Mo, L. Zhang et al., Anomalous nuclearphenomena and solid state nuclear track detector, *Nucl. Tracks Radiat. Meas.* **22** (1993) 599–604.

[3] G.S. Qiao, X.L. Han and L.C. Kong, Nuclear Products in a Gas-Loading D/Pd and H/Pd System, *Proc. 7th Int. Conf. on Cold Fusion*, Eneco Ed., Vanco., Canada, 1998, pp. 314—318.

[4] A.G. Lipson, A.S. Roussetski, G.H. Miley et al., *Proc. of the9th Int. Conf. on Cold Fusion*, X.Z. Li (Ed,) Tsinghua Univ. Press, Beijing, China, 2002, pp. 218–223.

[5] A.G. Lipson, A.S. Roussetski, G.H. Miley et al., *10th Int. Conf. Cold Fusion*, *Condensed Matter Nuclear Science*, MA, USA, 2003, http://www.LENR-CANR.org

[6] S.Y. Dong, K.L. Wang, Y.Y. Feng et al., Precursors to cold fusion phenomenon and the detection of energetic charged particles in deuterium/solid systems, *Fusion Technol.* **20** (1991) 330—333.

[7] Z.M. Dong., C.L. Liang, B. Liu et al., *J. Cond. Matter Nucl. Sci.* **5** (2010) 1–13.

[8] P.A. Mosier-Boss, S. Szpak, F.E. Gordon et al., Use of CR-39 in Pd/D co-deposition experiments, *Eur. J. Appl. Phys.* **40** (2007) 293–303.

[9] P.A. Mosier-Boss, S. Szpak, F.E. Gordon et al., Triple tracks in CR-39 as the result of Pd/D co-deposition: evidence of energetic neutrons, *Naturwissenschaften* **96** (2009a) 135–142.

[10] P.A. Mosier-Boss, S. Szpak, F.E. Gordon et al., Characterization if Tracks in CR-39 Detectors Obtained as a Result of Pd/D Co-deposition, *Eur. Phys. J. Appl. Phys.*, 46, pp. 30901-30912, 2009b.

[11] P.A. Mosier-Boss, J.Y. Dea, L.P.G. Forsley et al., Comparison of Pd/D co-deposition and DT neutron generated triple tracks observed in CR-39 detectors, *Eur. Phys. J. Appl. Phys.* **51** (2010) 20901–20911.

[12] P.A. Mosier-Boss, It's not low energy – but it is nuclear, *17th ICCF,* South Korea, Aug. 2012.

[13] L.P. Forsley, P.A. Mosier-Boss et al., Charged particle detection in the Pd/D system: CR-39 SSNTD vs. real-time measurement of charged particle stimulated Pd K shell X-rays, *Electronchimeca Acta* **88** (2013) 373–383.

[14] D. O'Sullivan, D. Zhou et al., Cosmic rays and dosimetry at aviation altitudes, *Radiat. Meas.* **31** (1999) 579–584.

[15] D. O'Sullivan, D. Zhou et al., Dose equivalent, absorbed dose and charge spectrum investigation in low Earth orbit, *Adv. Space Res.* **34** (2004) 1420–1423.

[16] D. Zhou, *Invited book CR-39 Plastic Nuclear Track Detectors in Physics Research*, Nova Science, New York, 2012.

[17] E.V. Benton, On latent track formation in organic nuclear charged particle track detectors, *Radiat. Effects* **2** (1970) 273–280.

[18] R.P. Henke and E.V. Benton, On geometry of tracks in dielectric nuclear track detectors, *Nucl. Instr. Meth.* **97** (1971) 483–489.

[19] G. Somogyi, Processing of plastic track detectors, *Nucl. Track Detect.* **1** (1977) 3–18.

[20] D. Zhou, D. O'Sullivan, E. Semones et al., Radiation field of cosmic rays measured in low Earth orbit by CR-39 detectors, *Adv. Space Res.* **37** (2006) 1764–1769.

[21] D. Zhou, E. Semones, M. Weyland et al., LET calibration for CR-39 detectors in different oxygen environments, *Radit. Meas.* **42** (2007) 1499–1506.

[22] D. Zhou, D. O'Sullivan, E. Semones et al., Radiation dosimetry for high LET particles in low earth orbit, *Acta Astron.* **63** (2008) 855–864.

[23] D. Zhou, E. Semones, D. O'Sullivan et al., Radiation measured for Matroshka-1 experiment with passive dosimeters, *Acta Astron.* **66** (2010) 301–308.

[24] D. Zhou, D. O'Sullivan, E. Semones et al., Radiation of cosmic rays measured on the international space station, *32nd ICRC* (Beijing, China, Aug. 2011), *Proc.: #1248.*

[25] S.A.R. Al-Najjar, A. Abedel-Naby and S.A. Durrani, Fast neutron spectrometry using the triple-reaction in the CR-39 detector, *Nucl. Tracks* **12** (1986) 611–615.

[26] A.M. MacLeod and G.R. Milne, Proton nuclear reaction cross sections in carbon and the ^{12}C(p,p'3α) reaction mechanism at 13 MeV, *Phys. A: Gen. Phys.* **5** (1972) 1252–1261.

[27] K. O'Brien, The exposure of aircraft crews to radiation of extraterestrial origin, *Radiat. Prot. Dosim.* **45** (1992) 145–162.

[28] K. O'Brien, LUIN 97, Personal Communication, 1997.

[29] G. Reitz, Radiation environment in the stratosphere, *Radiat. Prot. Dosim.* **48** (1993) 5–20.

[30] D. O'Sullivan, D. Zhou, Overview and present status of European commission research programme, *Radiat. Prot. Dosim.* **86** (1999) 279–284.

[31] D. Zhou, Radiation of cosmic rays at aviation altitudes and dosimetry, Ph.D. Thesis, Dept. of Experimental Physics, University College, Dublin, National University of Ireland.

[32] K. O'Brien, CARI, 2013: http://jag.cami.jccbi.gov/cariprofile.asp

J. Condensed Matter Nucl. Sci. 15 (2015) 44–54

Research Article

Excess Power during Electrochemical Loading: Materials, Electrochemical Conditions and Techniques

V. Violante,* E. Castagna, S. Lecci, F. Sarto, M. Sansovini, T.D. Makris and A. Torre
ENEA, Unità Tecnica Fusione, C.R. Frascati, Frascati, Italy

D. Knies, D. Kidwell, K. Grabowski and D. Dominguez
Naval Research Laboratory (NRL), Washington, DC, USA

G. Hubler, R. Duncan, A. El Boher and O. Azizi
SKINR, University of Missouri, Columbia, MO, USA

M. McKubre
SRI International Menlo Park, CA, USA

A. La Gatta
Consorzio Veneto Ricerca-TSEM Padova, Italy

Abstract

The critical role of the electrode material characteristics in increasing the probability of observing excess power during electrochemical loading of palladium cathodes with deuterium is investigated, and excess power production obtained using palladium material with these identified characteristics is reported. Characterizations have been performed by using SEM and AFM microscopy as well as electrochemical analysis and XPS. The emerging scenario suggested by these results is that poor control in achieving the identified material status is reflected in the reproducibility of the excess heat phenomenon.

Keywords: Deuterium, Electrolysis, Excess Power, Materials, Palladium

---

*E-mail: vittorio.violante@enea.it

1. Introduction

A significant body of research has been carried out to have a controlled mass transfer of deuterium into palladium cathodes in order to reproducibly exceed the loading threshold [1,2] required to observe excess power production during electrochemical loading [3–6].

The experimental data shows that loading up to about D/Pd = 0.9 (atomic fraction) is a fundamental necessary condition; additional conditions required to observe the onset of the effect [7–9] are enhanced mass transfer, crystal orientation, and specific surface morphology.

Different lots of palladium, most of them from the same producer, gave completely different behavior above the loading threshold D/Pd = 0.9. Three different behaviors have been identified:

(1) Large excess power (>100% of the input power).
(2) Low excess power (<20% of the input power).
(3) No excess power.

The excess heat effect was observed by using also $Pd_{90}Rh_{10}$ cathodes. Some specific features were identified for the active electrodes with both materials. The active palladium electrodes had mostly (100) orientation of the polycrystals, enhanced hydrogen (deuterium) diffusivity, average grain size around 100 microns and a well-defined surface morphology identified by means of the power spectral density function (PSD).

Active $Pd_{90}Rh_{10}$ cathodes have a high diffusivity and a surface morphology, in terms of PSD, very similar to the one belonging to the active Pd samples. The differences are a mixed orientation of the crystals and a lower grain size, typically some ten's of microns. Doping with contaminants has been performed for both Pd and $Pd_{90}Rh_{10}$ cathodes in order to achieve the material characteristics belonging to samples producing excess power.

2. Materials

The most significant evidence related to the cathode behavior in terms of excess power production is the different spectrum of contaminants. It is well known from physical metallurgy that contaminants may have several effects on the metal characteristics:

- Contaminants may act on: grain size, crystal orientation and grain boundaries.

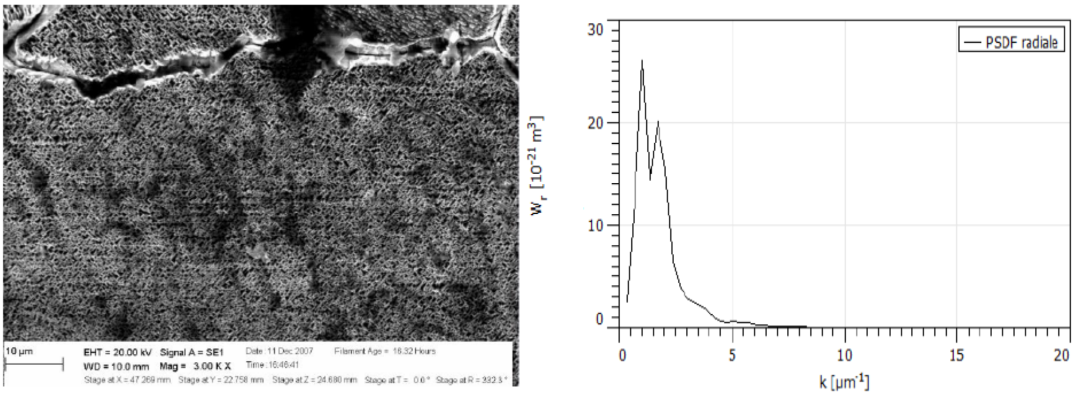

Figure 1. (a, *left*) SEM of the surface of #64 electrode giving up to 3500%. (b, *right*) PSD #64 cathode surface

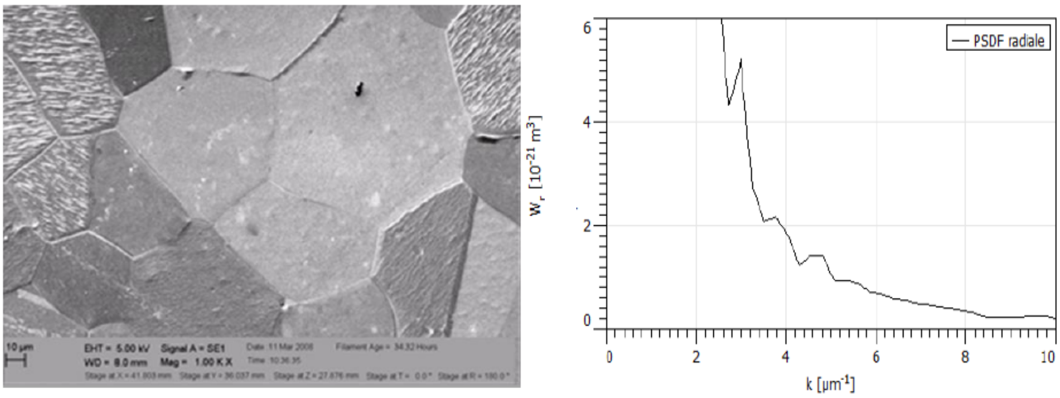

Figure 2. (a, *left*) SEM of a non-active electrode surface. (b, *right*) PSD of non-active electrode surface.

- It is well known from the literature [10] that contaminants modify the effect of chemical etching on surface morphology.

A scanning electron micrograph (SEM) of the surface of #64 cathode that produced up to 3500% excess power reveals what we call a labyrinth morphology as shown in Fig. 1a. This sample displayed the PSD shown in Fig. 1b and we have determined that the PSD and excess power are correlated – they are proportional so the higher the PSD peaks the greater the excess power. By contrast, non-active samples have a very low PSD signal as shown in Fig. 2a,b.

Fabrication of a Pd cathode characterized by crystals mainly (100) oriented, with average grain size around 100 μm and with a surface morphology reproducing a PSD with more than two peaks with decreasing amplitude from the left to the right as in Fig. 1b is not easily achieved. It was understood that materials having a larger concentration of Pt as contaminant gave more often a labyrinth structure such as the one shown in Fig. 1a after the chemical etching with aqua regia. For this reason, two palladium cathodes obtained by using a starting Pd able to give (100) orientation and proper grain size but unable to give the labyrinth structure after etching, were sputtered with a few nanometers of Pt

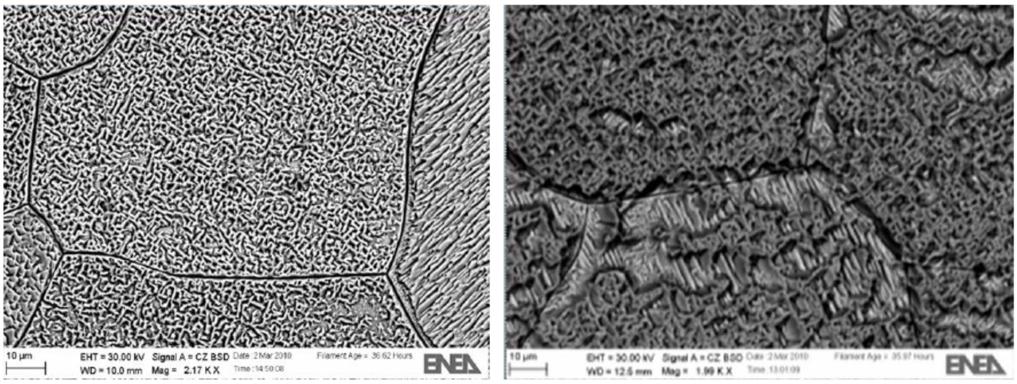

Figure 3. SEM of the surfaces of two Pd samples, doped by adding Pt on the surface and etched with Aqua Regia 50%.

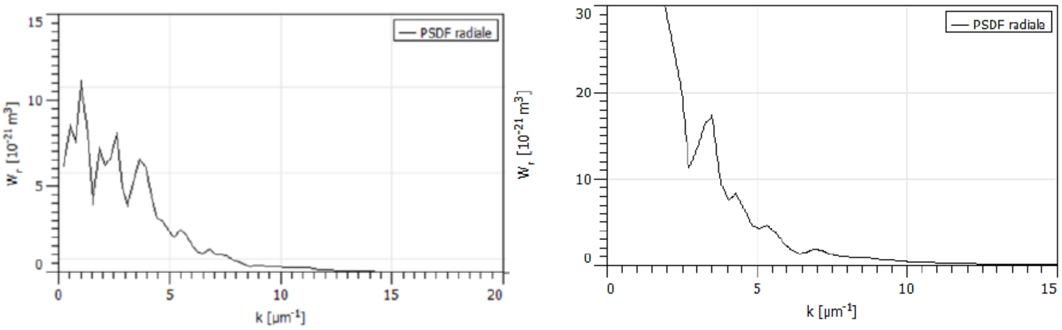

Figure 4. PSD for two Pd samples after Pt deposition, annealing and etching in aqua regia.

and annealed at 850°C. After the thermal treatment the two samples were etched, which produced the required surface morphology as shown in Fig. 3.

The PSD for both the samples were substantially modified compared to the one etched without the deposited Pt (Fig. 2b) as seen in Fig. 4.

These two samples were electrolytically loaded with deuterium in 0.1 M LiOD in two different mass flow calorimeters and both gave excess power up to 25% of the input power. The results are shown in Fig. 5 where power in and power out in milliwatts are plotted versus time in seconds.

A similar study was carried out on $Pd_{90}Rh_{10}$ cathodes prepared by applying the protocol developed at NRL [11]. Palladium and Rhodium have been melted at 90/10 atomic ratios in an alumina crucible by using a hydrogen-oxygen torch. The melted material was annealed at 900 ˚C and then cold rolled to a thickness of 50 μm. After rolling the sample was annealed again at 850°C and then etched with Aqua Regia. Figure 6 shows the surface of sample L119(20–60) after the chemical etching.

A second sample (L119(100–140) was prepared from the produced $Pd_{90}Rh_{10}$ alloy. Both the samples have been analyzed by EDX and we observed some content of Si (Silicon oxide) on the surface of L119(20–60). Figure 7 shows the PSD of the surface of L119(20âĂŞ-60) before electrolysis. We may observe that the PSDF spectral shape is absent. Figure 8 shows the energy dispersive X-ray spectrum (EDX) for sample L119(20–60) where Si is clearly evident.

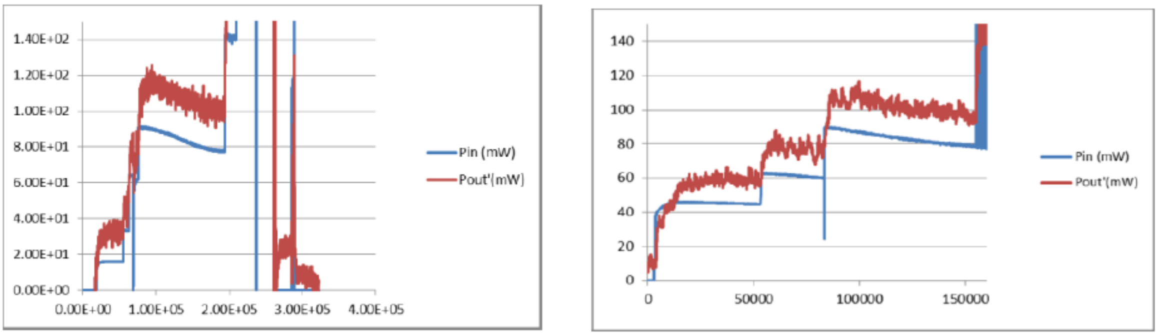

Figure 5. Data showing excess power up to 25% produced by each of the Pd cathodes doped on the surface with Pt before annealing and etching.

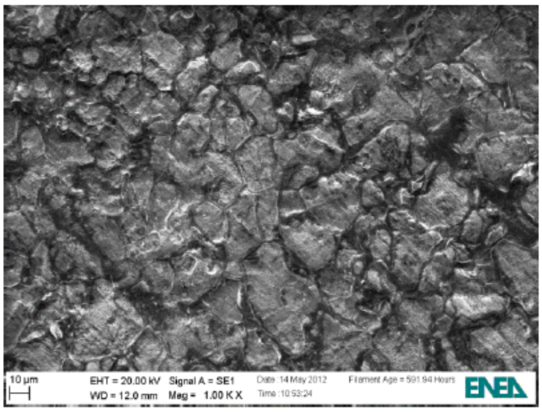

Figure 6. Surface of the L119(20-60) Pd90Rh10 sample.

A calorimetric study on sample L119(20–60) was performed by using the differential calorimeter developed at NRL [12] and the time history of power in and power out is shown in Fig. 9a.

We can observe in Fig. 9a that the excess power spontaneously develops after ∼2,90,000 s elapsed time and was stable for about 12 h. We assumed the effect to be a bias shift of the calorimetric system which was checked by inverting the current to deload the cathode and after deloading an input power level was applied close to the one existing before changing the polarity. After the thermal transient (with some adjusting of the input power at the required level) a perfect balance of power in equals power out was observed (the output curve was overlapping the input curve (see Fig. 9a). This confirmed that the signal was a real effect. The polarity was then reversed again and PdRh was reloaded

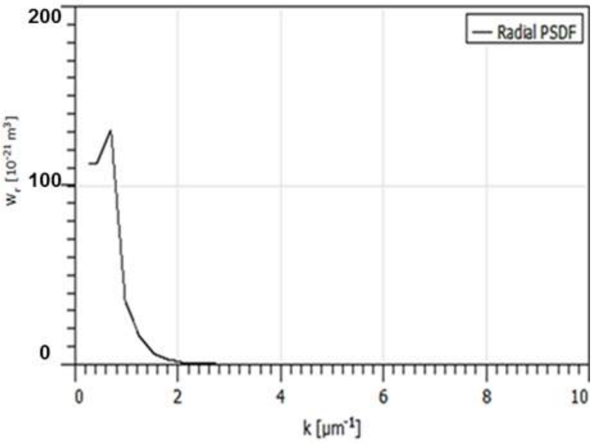

Figure 7. Power spectral density of L119(20-60).

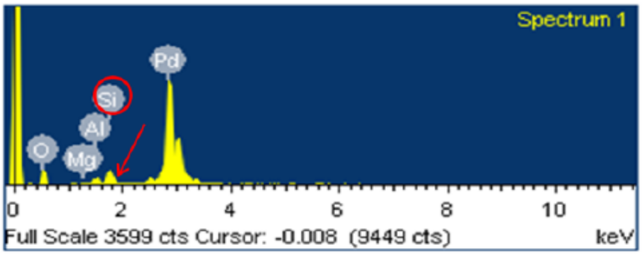

Figure 8. EDX of sample L119(20-60). Si is the most abundant contaminant on the surface.

at a higher current value. As soon as the cathode was reloaded (∼3,55,000 s elapsed time) the system gave again an excess that was larger than the previous one.

Figure 9b shows the same calorimetric run after 5,30,000 s. After ∼5,80,000 s it was decided to perform Galvanostatic Electrochemical Impedance Spectroscopy (GEIS) using the Biologic VP 200 Galvanostat-Potentiostat electrochemical spectrometer that was controlling the experiment. This operation was performed in order to extract, in situ, new information concerning the status of the electrochemical interface in terms of an equivalent circuit.

Five impedance spectra were acquired during the excess but Nyquist plots during the excess gave scattered points, revealing a significant disturbance during the effect; however, one plot was clearly readable after removing the noise. The EIS was carried out within the frequency range 200 kHz–20 Hz and the Nyquist plot is shown in Fig. 10 with frequency decreasing from left to right in the plot. The equivalent circuit during the excess is also shown in the inset in Fig. 10. The Nyquist plot clearly has resonating component inside. The applied DC current during the measurement was 90 mA with 7 mA sine probe amplitude.

The current was then reduced to 30 mA DC and a sufficient time was allowed to elapse (some hours) to complete the thermal transient of the calorimetric equipment (roughly within the time interval 5,90,000—6,50,000 s). The excess power disappeared as can be seen from Fig. 9b and a new impedance analysis was performed and 25 Nyquist plots were acquired within the frequency range 400 kHz–10 Hz. Most of the plots were unstable, yielding very scattered points as during the excess. In some cases it was possible to extract a signal from the noise. Two of them are shown in Figs. 11a,b.

In Fig. 11a the proper fitting of the impedance spectrum was achieved by inserting a typical RLC within the circuit with a resonant frequency of 166 Hz. Figure 11b shows another GEIS plot carried out after switching off the excess and we may see that an equivalent circuit quite similar to the one obtained during the excess power by reducing the current to 30 mA. In this case the equivalent circuit includes LCR components having a resonating frequency of about 200 kHz. After that the current was set to zero for a few seconds and the GEIS was performed again by maintaining the DC current at 30 mA and by applying 3 mA sine wave. The Nyquist plot is shown in Fig. 12. It is clear that RLC component disappeared as soon as input power was set to null.

The surprising result, even if preliminary, is that the excess power is characterized by a specific electrochemical structure of the interface (equivalent circuit) that remains also after switching off the effect by reducing the current, but such a structure is destroyed if the system is more strongly perturbed by reducing the current to zero.

The inductive behavior in Fig. 12 (negative imaginary component) at high frequencies is due to the wiring and connection of the cell and perfectly reproduces the tests performed with dummy circuits.

Even if the results have to be considered as preliminary and need to be replicated, it is clear that the electrochemical interface substantially changes during the production of excess and that the presence of LRC components are suggestive

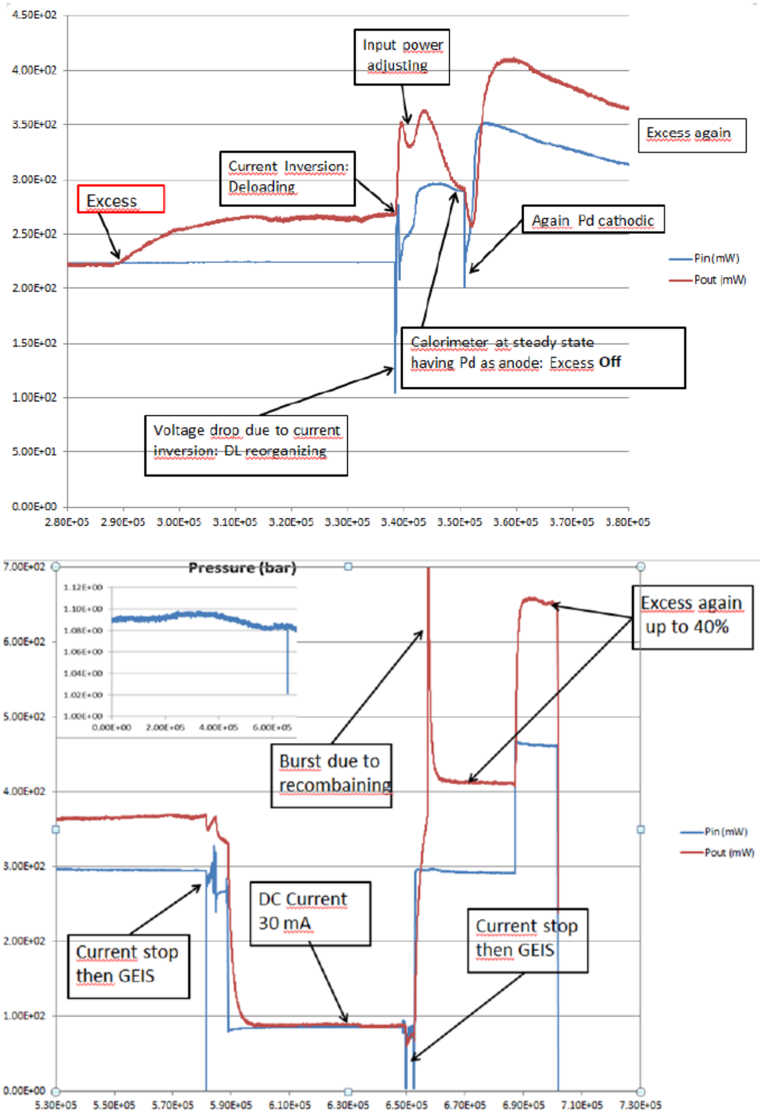

Figure 9. (a, *top*) Excess power occurs (∼2,90,000–3,55,000 s) and is switched off by current inversion. Restoring the original cathodic polarization restarts the power excess. (b, *bottom*) Excess power for the same run as in Fig. 9a at longer time.

of a resonant mechanism at the interface.

By comparison Fig. 13 shows a GEIS at two different current levels performed on an inactive Pd cathode.

As soon as the GEIS was completed, the cell current was increased again to 90 mA and the excess power restarted at a somewhat higher level as can be seen in Fig. 9b. There is a big power spike after increasing the current due to D_2 and O_2 gas recombination as the catalyst restarted as is confirmed by the negative pressure spike in the cell pressure

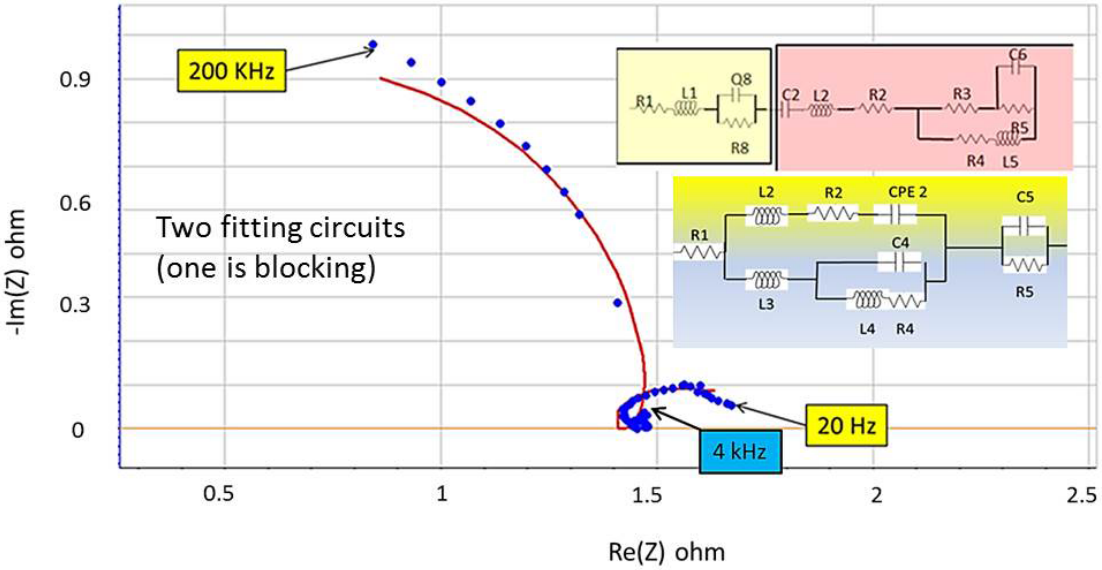

Figure 10. In situ Electrochemical impedance Spectroscopy on Sample L119(20–60). Excess-on.

plot (top left Fig. 9b). Further increasing the current produced greater excess power up to approximately 40% of the input. A small oscillation of both current and potential was observed during the excess.

The cell was switched off during the excess in order to physically investigate the status of the sample surface during an excess power event. Figure 14a shows an SEM image of the electrode surface as it was during the excess. Figure 14b shows the PSD. The most significant peaks are always in the region of k up to about 5 μm^{-1}. EDX revealed that during the excess, Fe, Cu and Pt were on the electrode surface.

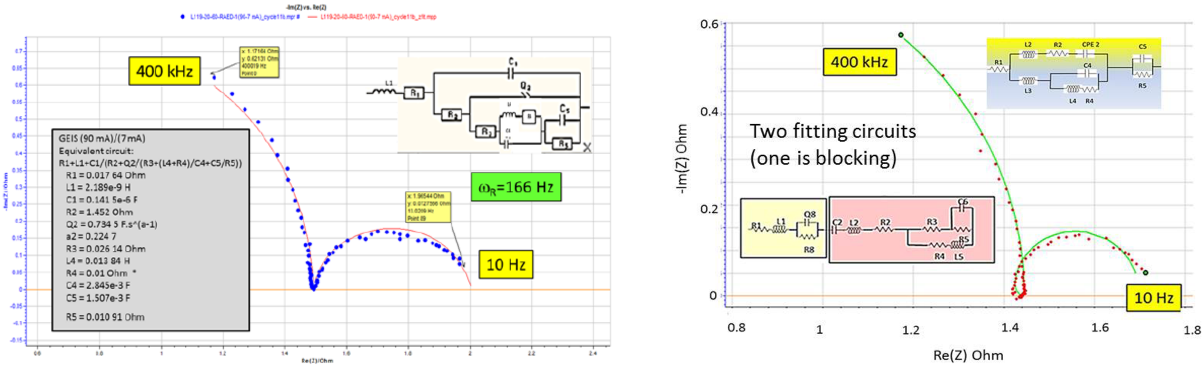
GEIS (90 mA)/(7mA)
Equivalent circuit:
R1+L1+C1/(R2+Q2/(R3+(L4+R4)/C4+C5/R5))
R1 = 0.017 64 Ohm
L1 = 2.189e-9 H
C1 = 0.141 5e-6 F
R2 = 1.452 Ohm
Q2 = 0.734 5 F.s^(a-1)
a2 = 0.224 7
R3 = 0.026 14 Ohm
L4 = 0.013 84 H
R4 = 0.01 Ohm *
C4 = 2.845e-3 F
C5 = 1.507e-3 F
R5 = 0.010 91 Ohm

Figure 11. (a, *left*) In situ Electrochemical impedance Spectroscopy on Sample L119(20–60). Excess-off. (b, *right*) In situ Electrochemical Impedance Spectroscopy on Sample L119(20–60). Excess-off.

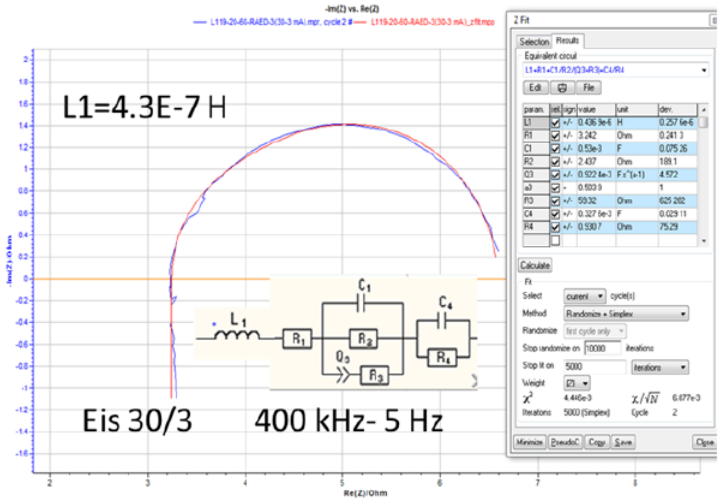

Equivalent circuit: L1+R1+C1/R2/(Q3+R3)+C4/R4

param.	sel.	sign	value	unit	dev.
L1	☑	+/-	0.436 9e-6	H	0.257 6e-6
R1	☑	+/-	3.242	Ohm	0.241 3
C1	☑	+/-	0.53e-3	F	0.075 26
R2	☑	+/-	2.437	Ohm	189.1
Q3	☑	+/-	0.922 4e-3	F.s^(a-1)	4.572
a3	☑	-	0.503 9		1
R3	☑	+/-	59.32	Ohm	625 282
C4	☑	+/-	0.327 6e-3	F	0.029 11
R4	☑	+/-	0.930 7	Ohm	75.29
	☐				

Fit
Select: current cycle(s)
Method: Randomize + Simplex
Randomize: first cycle only
Stop randomize on 10000 iterations
Stop fit on 5000 iterations
Weight: |Z|
χ^2 4.446e-3 $\chi/\sqrt{N}$ 6.677e-3
Iterations 5000 (Simplex) Cycle 2

Figure 12. GEIS, 30mA/3mA 400 kHz–5 Hz: Excess-Off, anode as reference.

Two additional samples from the sample PdRh lot were investigated and were found to be totally inactive regarding the appearance of excess power.

No evidence of specific surface contaminants was observed on these two samples. Since Si was absent from the surface of the inactive samples, a new lot of PdRh was prepared by intentionally adding Si as a contaminant. One sample was investigated in the differential calorimeter mentioned above.

Figure 15 shows the occurrence of excess power up to 16% with sample L133 (40–80) Si doped. The XPS analysis reveals that Si is in oxide form. The burst continued for 10 h. The large band of the input power before and after the event is due to a superwave current modulation [13]. While we do not have a statistical basis for a conclusion, we may consider that such a result suggests that the presence of specific contaminants on the surface of the electrodes is important to observe excess power.

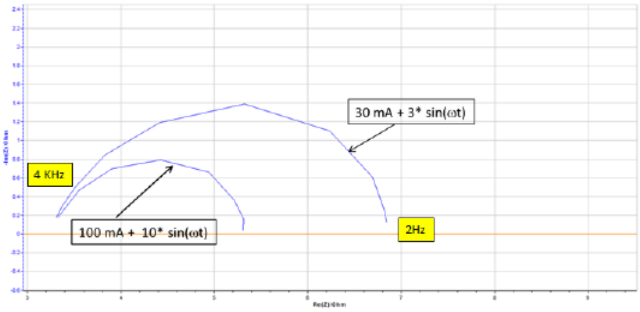

Figure 13. GEIS performed on inactive Pd electrode at two different current levels.

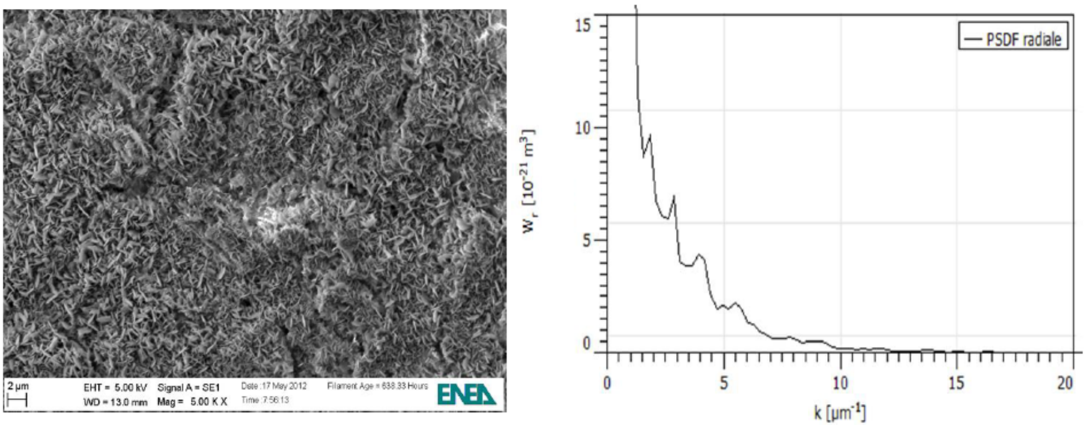

Figure 14. (a, *left*) SEM image of the electrode surface as it was during the production of excess power. (b, *right*) PSD of the surface shown in (a).

3. Conclusions

This paper describes experiments that reveal new information regarding the status of deuterium loaded Pd cathodes during production of excess power in electrolytic cells (0.1 M LiOD, Pt anode, PdRh alloy cathode).

First, electrochemical impedance spectroscopy (EIS) during excess power production reveals the presence of resonances at the surface/electrolyte boundary that requires an LRC component in the circuit diagram to reproduce the Nyquist plot. Second, the LRC component of the Nyquist circuit diagram is still present when the input power is reduced and no excess power is present. Third, the voltage and current during excess power events and after excess power events at reduced input power are unstable causing the EIS to be indecipherable at most times. Forth, as shown previously (reference) there is a strong correlation between the position and strength of peaks in the power spectral density (PSD) of those cathodes that produce excess power. Fifth, though not conclusive, this work suggests that the presence of specific contaminants (Si, perhaps others) on the cathode surface are important for observation of the

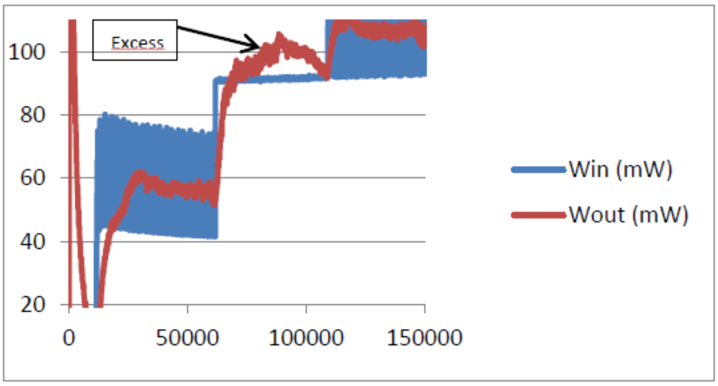

Figure 15. L133 (40–80), Pd90Rh10 Si doped, up to 16% excess power.

excess power. Sixth, this work points to the importance of materials science to achieve the surface morphology, alloy composition, contaminant control and grain orientation [7,8] necessary for the observation of excess power in these material systems.

References

[1] K. Kunimatsu, N. Hasegawa, A. Kubota, N. Imai, M. Ishikawa, H. Akita and Y. Tsuchida, Deuterium loading ratio and excess heat generation during electrolysis of heavy water by a palladium cathode in a closed cell using a partially immersed fuel cell anode, *Proc. Third Int. Conf on Cold Fusion,* Nagoya (Japan), October 20–25, 1992, p. 31.

[2] M.C.H. McKubre, S. Crouch-Baker, A.M. Riley, S. I. Smedly and F. L. Tanzella, Excess power observation in electrochemical stusies of the D/Pd system; the influence of loading, *Proc. Third Int. Conf on Cold Fusion,* Nagoya (Japan), October 20–25, 1992, p. 5.

[3] A. Adrover, V. Violante et al., Stress induced diffusion of hydrogen in metallic membranes, Cylindrical vs. planar formulations I, *J. Alloys and Compounds I* **358**(1) (2003) 268–280.

[4] A. Adrover, V. Violante et al., Stress induced diffusion of hydrogen in metallic membranes, Cylindrical vs. planar formulations II, *J. Alloys and Compounds I* **358**(1) (2003) 157–167.

[5] A. Adrover V. Violante et al., Effects of self-stress on hydrogen diffusion in Pd membranes in the coexistence of α and β phases, *J. Alloys and Compounds* II **368**(1) (2003) 287–297.

[6] V. Violante et al., Consequences of lattice expansive strain gradients on hydrogen loading in palladium, *Phys. Rev. B* **56**(5) (1997) 2417–2420.

[7] V. Violante et al., Material science on Pd–D system to study the occurrence of excess of power, *Proc. ICCF-14*, Washington DC, Vol. 2, 2008, pp. 429–436.

[8] V. Violante et al., Evolution and progressin material science for studying the Fleishmann and Pons effect (FPE), *Proc. ICCF-15*, Oct. 5–9 2009, Rome, Italy, 2009, p. 1.

[9] V. Violante et al., The study of the Fleishmann and Pons effect through the materials science development, *Proc. of the XVI Int. Conf. on Condensed Matter Nuclear Science,* Chennai, India, Feb. 6–11 2011, p. 313.

[10] M.A. Gosàlvez and R.M. Nieminen, *New J. Phys.* **5** (2003) 100.

[11] D.D. Dominguez et al., Are oxides interfaces necessary in Flaischmann and Pons type experiments? *Proc. of the XVI Int. Conf. on Condensed Matter Nuclear Science*. Chennai, India, Feb 6—11, 2011, p. 53.

[12] D. Knies et al., Differential thermal analysis calorimeter at the naval research laboratory, *Proc. ICCF-15,* Oct. 5–9 2009, Rome, Italy, 2009, p. 11.

[13] I. Dardik et al., Intensification of low energy nuclear reactions using superwave excitation, *10th Int. Conf. on Cold Fusion*, Cambridge (MA), USA, 24-29/08/ 2003, p. 61.

J. Condensed Matter Nucl. Sci. 15 (2015) 55–65

Research Article

Conservation of E and M, Single Cavitation Heat Events

Roger S. Stringham*

First Gate Energies, P.O. Box 1230, Kilauea, HI 96754, USA

Abstract

Experiments spread over a period of 24 years create a model for sonofusion. An explanation of results will influence new paths for its further development. Cavitation produced z-pinch target-foil implanting jets produce SEM photos of single event ejecta sites equal to the binding energy differences, E_b, for alpha production.

Keywords: Alpha, Cavitation, Jets, Photons

---

1. Introduction

The initial D_2O cavitation work started in March of 1989 with a 20 kHz resonator adapted from Heat Systems Inc., and resulted in a melted and discolored Pd target foil. In 1993, work with Ti target foils in 46 kHz systems produced a standing wave of 2.3 mm λs approximating the 1.6 MHz frequency that was adopted in 2003 and has been in use since.

In measured systems, calorimetric data corresponds with survey counts of ejecta site craters, ejs, in scanning electron microscope, SEM, photos of target foils. SEM photos at three frequencies of exposed targets were especially compelling. Figure 1a (2003) shows a newer Pd foil exposed at 1.6 MHz with single event ejs of E_b, Eq. (1) [1,2], where ejs debris is expelled with velocity and mass of 20 ±10 MeV. Figure 1b (1993) shows a Pd foil exposed at 46 kHz, with multiple 23.8 MeV, E_b, events 1993 [1], Figure 1c shows the standing wave on a Ti foil and the associated nodal lines of E_b distribution 1993 [2,3]. Surveys of target foils indicated a strong correlation between the size and number of ejecta sites and the excess heat generated, with the estimated energy of 20 ±10 MeV, close to the binding energy difference, E_b, of $2D^+ \rightarrow \alpha$, Eq. (1).

$$B(2\mathrm{D}^+;\alpha) = B - (2\mathrm{p},2\mathrm{n};\alpha) - 2B(\mathrm{p},\mathrm{n};\mathrm{D}^+) = 28.3 - 2\times 2.25 = 23.8\,\mathrm{MeV} = E_\mathrm{b}. \quad (1)$$

This indicated an event occurring at time $t' = 0$, during a picosecond timeframe, in which a dense deuteron condensate, $M = n\mathrm{D}^+$, becomes a two particle system, α and M', where M' is an expanding center of mass (COM)

---

*E-mail: firstgate@earthlink.net

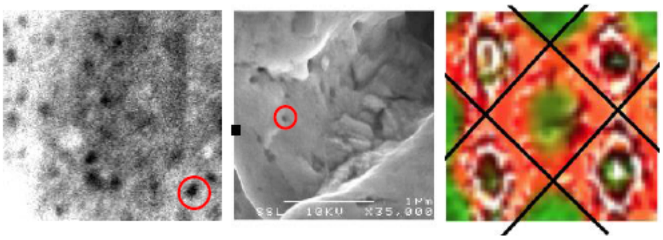

Figure 1. (a) Left :Pd foil, 1.6 MHz 1 μm^2. (b) Middle: Pd foil, 46 kHz 2 μm^2. (c) Right: TiOx nodal lines 46 kHz, .33 cm^2.

of residual deuterons, Eq. (2).

$$M \rightarrow M' + \alpha + E_\mathrm{b}/c^2 \text{ kg mass}; M' = M - 2\mathrm{D}^+, \tag{2}$$

While ^{4}He measurements of early kHz systems influenced development of the model, most of the data in this paper comes from the more recent 1.6 MHz system, Fig. 1a. Section 2 describes the experimental design used to collect flow-through calorimetry data. Section 3 presents the data that provides a basis for the model in Section 4, which complies with the laws of conservation of energy and momentum.

2. Experimental Design

The polycarbonate resonator was divided into three parts. "A" is the cap, which serves as a window and seals "B" enclosing the resonant volume, including a 1 g/s D_2O flow, a target foil, a calibration heater, a piezo-electric transducer, and a seal to "C". "C" allows for the Ar pressure balance for "B" and across the piezo thickness to "C", where the oscillator's electric connections for acoustic input, Q_a, are made, Fig. 2.

The power supply to the oscillator, Q_i, was connected into the 120 V 60 cycle utility. The D_2O had a residence time of 0.5 s in the 0.5 cm^3 volume resonator. Connections for the 12 W resistance calibration heater are within the resonator volume. The target foil was configured to be 1 mm from the 1.6 MHz PZT piezo disk (2 mm thick and 10 mm radius). The circulating system was on a duty cycle of 120 s off and on. Duty cycles of 60–200 s were also used. The temperature data was taken each second, and measurements were made at the beginning of the off-mode and extrapolated back to the last point of the on-mode. This process avoided a potential radio frequency interference of thermocouple ΔT data from the 1.6 MHz Q_a oscillator.

A D_2O flow system, Fig. 3, circulated D_2O at 1 g/s with an FMI constant mass-flow pump measured by the flow meter. D_2O passes through a filter, proceeding to a light box that contains a resonator, target foil, calibration heater, and a variable Q_a oscillator input. In the resonator are thermocouples measuring T in and out, ΔT. Photomultipliers and multipixel photon counters (MPPC) from Hamamatsu measured photon emission (PE) that is the sum of sonoluminescence (SL) of collapsing bubbles, as well as any non-absorbed Bremsstrahlung (Br) photons [2]. The flow continues to a flow-meter, a heat exchange coil, and a bubbler. The bubbler, connected to a vacuum line, controls the pressurized Ar gas saturating 20 ml of circulating D_2O and a gas sampling valve system. The bubbler separates any in-line circulation bubbles and has a direct connection back to the FMI pump completing the D_2O cycle.

3. Data Collection

Calorimetric data, supported by calibration heater Figs. 2 and 3, of the 1.6 MHz systems showed excess heat, Q_x, generated relative to acoustic input, Q_a. Surveys of SEM images of exposed target foils indicated 10^7 events/cycle, each producing E_b, the sum corresponding to measured Q_x. Also relevant to the model, intermittent ^{4}He mass spectrum, MS, measurements from the early 20 kHz systems showed some correspondence to Q_x and suggested inefficient cavitation. The introduction of multipixel photon counting, MPPC, Hamamatsu technology allowed for the use of PE signals as feedback for adjusting Q_a input to produce efficient cavitation. MPPC data shows an active zone of 100 ns, establishing a basis for a model timeline.

3.1. Some calorimetric data

Figure 4 shows flow-through calorimetry data from a 20 g 1.6 MHz resonator, which was used many times to generate data. The table in the upper right lists, in chronological order, a series of 10 data points at 1 atm. of Ar saturated D_2O circulating at 60 g/min. The data was produced by varying the input Q_i, where the oscillator's acoustic input, $Q_\mathrm{a} = .3Q_i$, thus changing the total heat output, Q_o, and excess heat, Q_x. The numerical values were collected for Q_a, Q_o, and Q_x were measured at 1 s intervals.

$$Q_\mathrm{o} - Q_\mathrm{a} = Q_x \text{ and } Q_\mathrm{a} = .3Q_i. \tag{3}$$

The D_2O rate of mass flow, F, through the resonator multiplied by ΔT was used to calculate the calorimetric Q_o measured heat as $\Delta T \times F$ calories [1,2]. Figure 4 plots showes a tipical result. The system, running at maximum Q_a,

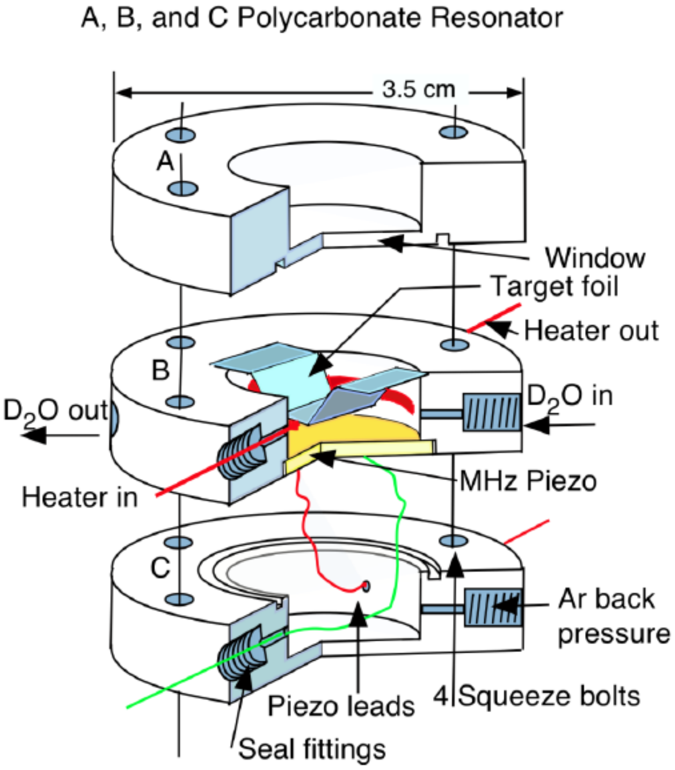

Figure 2. One view of a three-piece polycarbonate piezo resonator.

was at also at maximum Q_x for pressure, temperature, Q_a, and PE that were the controlling parameters. The data also shows straight line increase of Q_x vs Q_o and Q_a W, linking PE increases [4], see Fig. 5. The measured ΔT°C was used to calculate Q_o, and a watt-meter Q_a, see Fig. 3 [2].

3.2. SEM images

The removal of the exposed 100 μm thick Pd target foils from the 1.6 MHz resonator allowed for a leisurely SEM analysis of the craters, ejecta sites, on its surface. The red circles in Fig. 1a,b highlight 50 nm ejecta sites, corresponding to single events and occurring in both the older 46 kHz and newer 1.6 MHz resonators [1,2]. Figure 1a shows the uniformity of 50 nm ejecta sites in the 1.6 MHz resonator, in contrast with range of sizes indicating mostly multiple with single events in the older 46 and 20 kHz resonators [1]. Figure 1c shows the standing wave nodal plane of a Ti target foil surface exposed at 46 kHz, with ejecta sites distributed along the nodal lines as indicated [3]. Additional

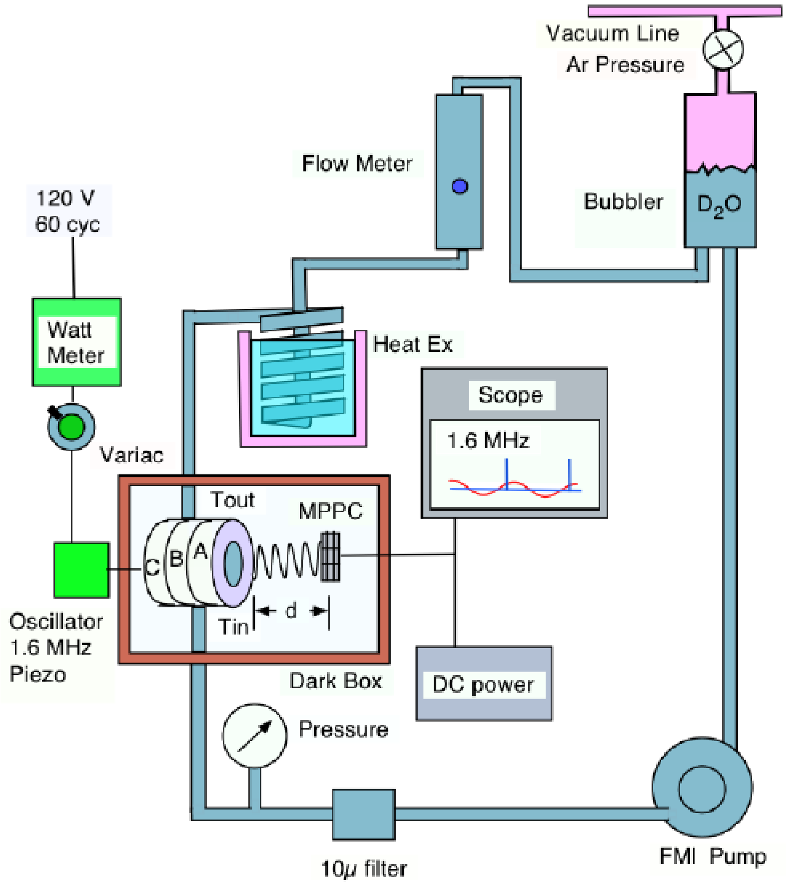

Figure 3. Flow system of D_2O through the resonator.

photos and videos are in possession of the author, showing slight to catastrophic foil damage depending on the thickness, element composition, and resonant frequency and amplitude of Q_a [1,3].

The 1.6 MHz single event ejecta sites were observed and counted in an area of 1 μm^2, Fig. 1a. The ejecta site count was extrapolated to its nodal plane area, which was one-hundredth of the 1 cm^2 target foil. The number of ejecta sites for one cycle was estimated at 10^7, each producing E_b, 23.8 MeV or 3.82 $\times$ 10^{-12} J. These numbers support 38 W of Q_x production at a 15 W Q_a input [5]. These photos and the calorimetry data support the occurrence of target foil events 25 nm below the foil surface, ejecting from the surface in expanding spherical heat pulses, E_b/s = Q_x [1].

3.3. The helium measurement

Helium measurements for early kHz cavitation systems were carried out in three laboratories: in 1991, by Dave Thomas at Stanford Research Institute (SRI); in 1992–1993 by Dr. Davidson of the US Bureau of Mines in Amarillo, TX; and in 1994-5, samples taken at Los Alamos National Laboratory (LANL) were analyzed by Brian Oliver at the Department of Energy, DOE, facility at Rocketdyne, CA. Brian Oliver also used MS measurements to track a sample of Ti target foil gases that change over time, showing decay of T to ^{3}He at the rate of the disintegration constants confirming the origin of the growing ^{3}He [3]. The Appendix at the end of this paper provides details on these measurements .

Reproducibility in He measurements suggested inefficient cavitation due to small variations in temperature, pressure, and acoustic input parameters. Thus, subsequent versions of resonators introduced the MPPC, new technology from Hamamatsu, which measures PE and couples it with significant changes to the MHz acoustic input, Q_a, suppressing small effects in resonator's T and P. This innovation in the MHz system produced better photon cavitation tracking. The MHz calorimetry, with no costly He measurements, was the basis for the Q_x determination.

3.4. SL and Br photon emission data

Figure 5 shows a typical 10,000 ns of MPPC data set at the following conditions: distance (d) of 8–16 cm from resonator to MPPC with a Q_a = 4.2 W. The PE signal, in blue, is coupled with the acoustic Q_a pulse, in red. PE is

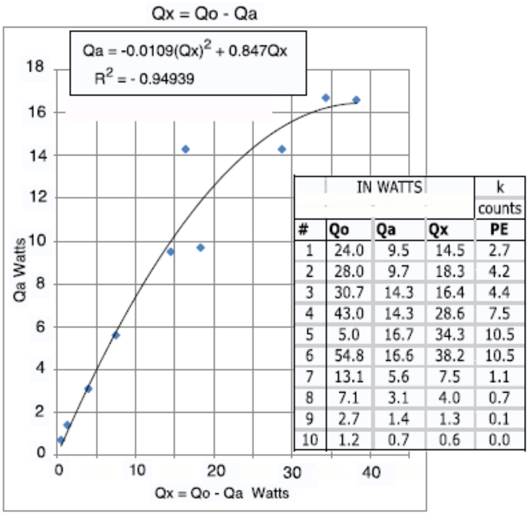

IN WATTS				k counts
#	**Qo**	**Qa**	**Qx**	**PE**
1	24.0	9.5	14.5	2.7
2	28.0	9.7	18.3	4.2
3	30.7	14.3	16.4	4.4
4	43.0	14.3	28.6	7.5
5	5.0	16.7	34.3	10.5
6	54.8	16.6	38.2	10.5
7	13.1	5.6	7.5	1.1
8	7.1	3.1	4.0	0.7
9	2.7	1.4	1.3	0.1
10	1.2	0.7	0.6	0.0

Figure 4. The relation between Q_o, Q_a, Q_x, and PE (photon emission).

produced by the SL of 10^6 collapsing bubbles and as Br photons not absorbed as heat during the distribution of E_b. Some unabsorbed Br photons degraded to low energies, and pass through to MPPC, registering in the PE measurement. The sum of Br photons less than .01% of Q_x, Fig. 5.

The MPPC's 1 mm^2 sensing area measures an average of 10^9 photons over time intervals of 100 ns, occupying less than 10% of each acoustic cycle [5]. This suggests future work could reduce the period of non-activity, perhaps by applying higher frequencies. The model in Section 4 describes the events in this 100 ns of activity zone, from the time the bubbles collapse through Q_x generation. This event sequence for α production will be shown to comply with the conservation of energy and momentum.

4. The Model: Timeline 100 ns

4.1. The cavitation bubble

A 20–50 g resonator via an oscillator driven piezo-electric transducer produces MHz cavitation bubbles in the flow of Ar saturated D_2O. From the spectrum of generated bubble sizes, only those bubbles that match physical size, pressure, temperature, and frequency will resonate [6]. The bubbles in resonance rapidly grow isothermally, increasing in mass and size to maximum radius R_o [1]. While in the acoustic positive phase the bubble adiabatically collapses in a few ns to the final bubble radius, R_f. Bubbles respond to the magnitude of the Q_a pressure wave. Bubbles of resonant size will oscillate in the acoustic field for millions of cycles, when Q_a is a few tenths of an atmosphere. Increasing Q_a to several atmospheres, the bubble will collapse in a single acoustic cycle. Its surface will accelerate toward its center at Mach 10 velocity [7], releasing SL and a z-pinch jet, with target foil implant ns later.

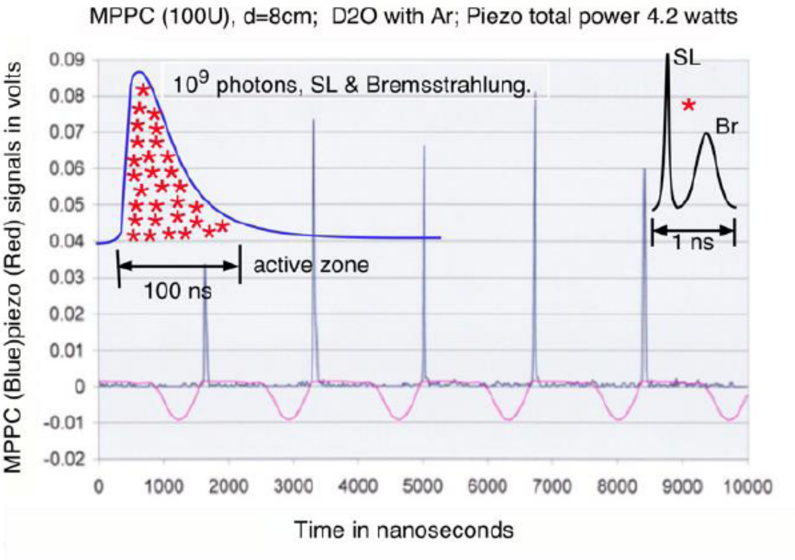

Figure 5. The 100 ns MPPC signal is the coupled activity zone. The inset, upper right, looks at a 1 ns speculated PE of SL and Br for one bubble, before photon absorption by the polycarbonate resonator's 350 nm cut-off. A major part of the sequence producing M clusters.

4.2. The z-pinch jet

The plasma contents of the bubble have become rearranged such that a high density deuteron plasma is confined and compressed by the electromagnetic pressure of a sheath of electrons carried over from the bubble's interface. The jet's velocity will be higher than the bubble's interface velocity of Mach 10 [7]. An encircling and squeezing B field further compresses the jet, narrowing its radius and further accelerating the jet's sheath electrons [8]. In the absence of intervention, this pressure will narrow the jet's radius until it disintegrates entirely, an effect that has frustrated Tokamak type research directions. In sonofusion systems, z-pinch provides an initial compression of the deuteron plasma, which is then implanted in a Pd target lattice before z-pinch collapses the jet.

When the jet implants the lattice, the much larger Ar^+ and O^{-2} ions are held at the surface. In fact, Figure 1c shows the iridescent TiOx films, which EDS and EDX measurements found to be of varying thicknesses [4].

4.3. The *M* condensate

When the z-pinch jet implants the lattice, the outside sheath electrons of the z-pinch jet are implanted first as a highly mobile free electron cloud, followed by the equally small but more massive and less mobile deuterons. Each implantation captures a number, n, of deuterons in a dense compressing condensate, $M = n\mathrm{D}^+$. Each z-pinch jet implant or viable bubble produces a number of M condensates that varies from 2 to 100, for a total of 10^7 M clusters from 10^6 viable bubbles, 10^{13} clusters/s [9]. This implantation process produces a charge separation of picosecond duration between the *M* condensate and its surrounding electron cloud.

4.4. Image charge pressure

Lawandy [9] shows that like charged particles will attract via an image charge under rare conditions: at separations, d, below 10^{-10} m; and between interface boundaries with permittivity differences of 1000. Image charge refers to the attractive force between one particle and its similarly charged neighbor's image, reflected on the opposing side of an interface. The extreme picosecond densities of free electrons form boson charged particles, Cooper Pairs, CP, that work together to squeeze M.

The permittivity factor β across the interface is calculated with the formula in Fig. 6, and must be between –0.5 and –1 for image forces to be effective. With a mass 1800 times that of its surrounding CP electrons, the M condensate of D^+ has a corresponding difference in relative mobility, so the permittivity factor β between the M condensate and its surrounding CP electrons approaches the –1 limit [9,10].

Having satisfied these rare conditions, CP with like charges have energies of attraction across a mutual phase boundary, the interface in Fig. 6, via an image charge of –2. The interface distance to its image charge was d and to its image in M was also d for a total of $2d$, see Fig. 6 right corner, where the immediate Pd is in a plasma state. M is in compression as x shrinks and squeezes the M interface. The shrinking triangle formed by $2d$, S, and x produce this pressure as a spherical compression piston [7].

4.5. The picosecond EM pulse

The magnetic field B runs parallel to the spherical interface of the M condensate and perpendicular to the attractive force, further containing M. This magnetic field together with the centrally focused electric field produces a picosecond electromagnetic pulse that compresses M. Deuteron separation becomes less than that of muon fusion, leading directly to the moment of event formation at $t' = 0$. This produces a 2-particle system of M' and α, with their respective energy and momentum, dispersing E_b/s of 23.8 MeV/s into the lattice and the circulating $\mathrm{D_2O}$.

4.6. Conservation of energy and momentum

The picosecond squeeze of the M condensate results in Eq. (2) at t' = 0, where heat is transported to the circulating D_2O by two particles, α and M', both originating in M. In a classical system, during the compression of M, its center is considered stationary. At $t' = 0$, M' rapidly expands with its center of mass, COM, momentum opposed to the connected α momentum, with a sum of 0. Equations for conservation of energy (4) and momentum (5) yield non-relativistic calculations for $v_{M'}$ and v_α, with E_b = 23.8 MeV and m_α at 6.64477×10^{-27} kg.

$$E_\mathrm{b} = .5(m_{M'}v_{M'}^2 + m_\alpha v_\alpha^2), \tag{4}$$

$$0 = m_{M'}v_{M'} - m_\alpha v_\alpha. \tag{5}$$

Table 1 gives m_M', v_M' , and v_α for M' = 98 D^+, 38 D^+, 18 D^+, 4 D^+, and 0 D^+.

The last line of this table, M' = 0 D^+, requires a relativistic calculation. It is included here to show that the lower limit produces results approaching muon fusion. Figure 7 illustrates the conservation of energy and momentum for different sizes of M condensates, including the lower kg limit.

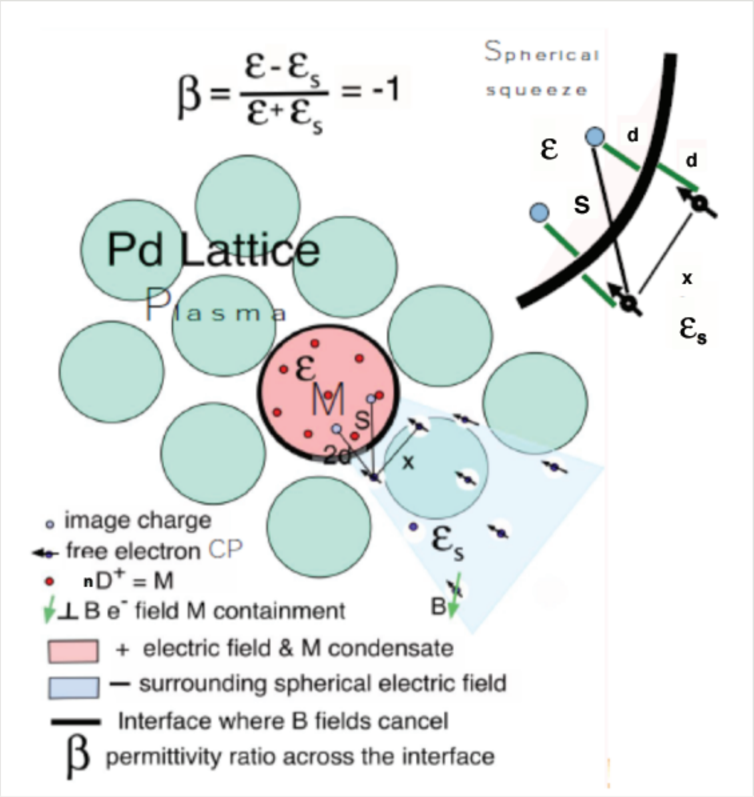

Figure 6. The interface M and CP squeeze system, accelerating e- in a D^+ E field.

Table 1. Velocities of *M'(COM)* and *alpha* in m/s

$M' = M - \alpha - E_b/c^2$kg	v_α(m/s)	$v_{M'}$ (m/s) (COM)	E_b (J)	Mom = 0 (kg/s)
3.2767×10^{-25}	33569687.1	680752.294	3.8×10^{-12}	0
1.2706×10^{-25}	33055015.2	1728709.02	3.8×10^{-12}	0
6.0184×10^{-26}	32178489.4	3552725.94	3.8×10^{-12}	0
6.6871×10^{-27}	24014821.5	23862966.6	3.8×10^{-12}	0
4.2398×10^{-29}	2699950.44	423151027	3.8×10^{-12}	0

4.7. Distribution of heat via Bremsstrahlung degradation

Each 100 ns cycle of 10^7 events melted the Pd target lattice (melting point 1825 K), as evidenced by the ejecta sites in the SEM images. As the spherical heat pulse reaches the target foil surface, an expanding hemispherical heat footprint transports heat through the Pd lattice to the circulating D_2O. The charged particles, D^+, lose their KE to the lattice via Bremsstralung cooling [4], in which high energy particles lose energy incrementally as they are bent by electromagnetic fields

With each new cycle, the molten Pd sub-surface erases the previous cycle's ejecta sites. This continuous refreshing of the Pd surface provides a new implanting surface for the next cycle's 100 ns deluge of E_b events. Within the ejecta site population there are some events that lay far enough from the nodal line to avoid the next cycle of surface heat ablation of ejecta sites. Such ejecta sites may persist for several cycles.

4.8. $2H^{++}$ Boson and M system

In 1992–1993, experiments run with H_2O showed similar target foil melting characteristics that are found in D_2O and some low calorimetry measured Q_x heating. The hope was that these experiments would serve as zero points for Q_x measurements. This was not the case, but the results were interesting. In keeping with the model, H_2O systems would produce some M condensates originating as a z-pinch implant of H_2^+. With a spin 1, H_2^+ would exhibit the bosonic character common to systems with attractive image charges. However, condensates with H^+, with a spin of $1/2$, lack the necessary bosonic character and would not compress sufficiently. This explains the lower Q_x for H_2O systems than D_2O systems. Temperature and density parameters also affect H_2^+ system in H_2O sonofusion.

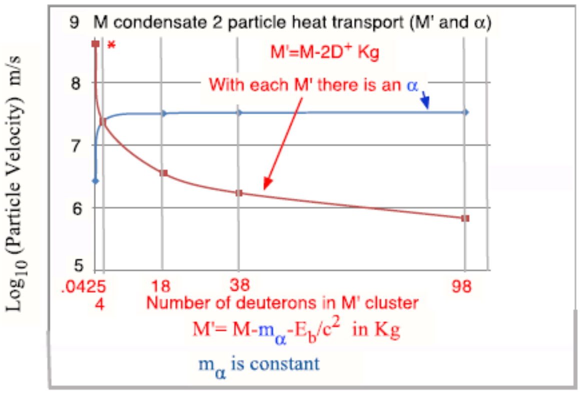

Figure 7. Velocities of COM of M' and α in m/s.M' clusters vary from 3.28 to 0.0423×10^{-27} kg or 98 to 0 D^+.

5. Conclusions

23.8 MeV, E_b, is the binding energy difference, B, for the α and M' event, Eq. (1). Q_x, measured calorimetrically, is equivalent to the sum of single E_b, 23.8 MeV, events, as surveyed from the SEM images, Fig. 1, Eq. (6).

$$\sum E_\mathrm{b}/\mathrm{s} = 23.8 \times 10^{13}\ \mathrm{MeV/s} = 38.2\ \mathrm{W} = Q_x \tag{6}$$

When the cavitation induced z-pinch jet implants the lattice, a charge separation occurs between free electrons and the M condensate of $n\mathrm{D}^+$. The spherical squeeze from the collective image charge of dense CPs on the interface compresses the condensate. Furthermore, this squeeze is spherically tangent to the interface, and thus acts as a magnetic containment. This picosecond pressure produces single 23.8 MeV, E_b, events, 10^7 events/cycle, 10^6 cycles/s, corresponding to calorimetrically measured Q_x. SEM images of target foils show clear evidence of events with temperatures reaching the Pd melting point of 1825 K, Fig. 1, [1]. Also, it can be shown that these single events conform to the Lawson Criteria [12].

In addition, the model complies with the laws of conservation of energy and momentum. These calculations, Eqs. (4) and (5), show increased velocity for M' COM with decreased number of deuterons in the M condensate. A relativistic calculation is required when the number of deuterons in the M condensate reaches 4.23×10^{-29} kg, and the system behaves like muon fusion.

The frequencies used to power piezos were changed over a span of 24 years from the initial 20–46 kHz, to the latest 1.6 MHz system. Comparisons of frequency results show that these systems have the same energy density but differ in the bubble size, number, and target foil crater production. High frequencies reduced bubble size by a factor of 1000, but the number of resonant bubbles increased by the same factor, so the energy density of ΣE_b, Q_x, remains the same [1]. Future development of sonofusion technology may suggest even higher frequencies, 20 MHz, which could shorten the time between 100 ns active zones, Fig. 5, to occupy a greater percentage of the MHz cycle.

Appendix

Dave Thomas, SRI Menlo Park, CA, 1991–1992, analysis used an adapted low mass, 1–6 mass units, KEV MS, to measure ^{4}He in Ar. The gas in vacuum conditions was passed through 60 g of heated CuO powder removing hydrogen. The gas passed from the bubbler to an evacuated 25 ml glass sample volume, Fig. 3. The cleansed gases were passed through a LN trap, removing Ar and D_2O, and into the MS for analysis. A possible 2 sigma value for ^{4}He was found.

Dr. Davidson, US Department of Interior, US Bureau of Mines Amarillo, TX, 1993–1994 specialized in ^{4}He MS analysis. Gas samples analyzed for ^{4}He in collected pre-treated gases as in the above SRI method returned positive results of ^{4}He at 20 ppm. The ^{4}He in the Ar supply was less than 2 ppm well below the 5 ppm that is the generally accepted value for helium in background air. ^{4}He atoms measured were 1/2 of the total atoms produced using vacuum line $pv = nRT$ [3].

In 1994, May and June, at Los Alamos National Laboratory, seven different target foil runs, gases from the bubbler filled evacuated 50 ml stainless steel sample volumes. There was no pre-treatment of the collected gases at measured pressures P_1 and then expanded to P_2 in V_2. See photo of sample volume [3]. Experiments were done using the M-2 resonator, 20 kHz. The gas samples were analyzed by Brian Oliver the at DOE ^{4}He and ^{3}He MS facilities. A report was produced, "Helium analysis of target metals", B.M. Oliver, 1995, Rockwell, International, Canoga Park, CA 91309. Analyses showed several positive results for ^{4}He and ^{3}He. Oliver used a 12 inch long $^1\!/_4$ inch diameter charcoal packed column in LN to absorb hydrogen and freeze out Ar before admission into a MS injection chamber. Using the chamber's gases, small aliquots, measuring about 5% of the chambers gas, were measured. Using the ideal gas law, several reproducible measurements were made. The total ^{4}He in resonator volume is determined from the fraction of gas collected from the free expansion of gases from resonator volume into an evacuated 50 ml valved sample volume.

Product gases, were calculated using $P_1V_1 = P_2V_2 = nkT$ to determine the ppm of ^{4}He in each aliquot delivered to the injection chamber. Three determinations were made ± 1 ppm.

This was complemented by the calorimetric measurement of 65 watts for the 19 hour run, matching the counted number of α, 552 ± 1 ppm [11]. The P_2 expansion into the sample volume contains ^{4}He in ppm that corresponds to the Q_xE_b events, Eq. (4).

Acknowledgements

I thank several individuals who helped with discussions and editing: Julie Wallace, Kim Nunlist, and Richard Spitzer.

References

[1] [1] R.S. Stringham, When bubble cavitation becomes sonofusion, *J. Condensed Matter Nucl. Sci.* **6** (2012) 1–12.

[2] Bremsstrahlung radiation http://heasarc.gsfc.nasa.gov/xstar/docs/html/node117.html

[3] R.S. Stringham, *ICCF 11 Proc.*, J. P. Biberian (Ed.) Marseilles, France, 31 Oct.–5 Nov. 2004, pp. 238–252.

[4] R.S. Stringham, Ti produces tritium that decays to helium three, *ICCF 15 Proc.*, V. Violante and F. Sarto (EDs.), Rome, Italy, 5–9 Oct. 2009, pp. 57–60. Standing wave, TiOx EDX, Tritium, 46 kHz.

[5] T.G. Leighton, *The Acoustic Bubble*, Academic Press, London, 1994, pp. 136–139.

[6] A. Bass, S. Ruuth, C. Camara, B. Merriman and S. Putterman, Molecular dynamics of extreme mass segregation in a rapidly collapsing bubble, *Phys. Rev. Lett.* **101** (2008) 234301.

[7] R.S. Stringham, Low-energy nuclear reactions sourcebook, Vol. 2, Jan Marwan and Steve Krivit (Eds.), *ACS Publications*.

[8] R.S. Stringham, The cavitation micro accelerator, *ICCF 8, Proc.*, F. Scaramuzzi (Ed.), Lerici, LaSpezia, Italy, 21–26 May 2000, pp. 299–304.

[9] N.M. Lawandy, Interaction of charged particles on surfaces, *Appl. Phy. Lett.* **95** (2009) 234101-1-3.

[10] Permittivity; un-dated explanation of http://www.princeton.edu/∼achaney/tmve/wiki100k/docs/Permittivity.html

[11] R.S. Stringham, *ICCF 17 Proc.*, S. Park and Frank Gordon (Eds.), 2012, Aug.12–17, to be published.

[12] Amasa S. Bishop, *Project Sherwood*, Addison-Wesley, 1958, pp. 12.

J. Condensed Matter Nucl. Sci. 15 (2015) 66–80

Research Article

Amplification and Restoration of Energy Gain Using Fractionated Magnetic Fields on ZrO_2–PdD Nanostructured Components

Mitchell Swartz*, Gayle Verner, Jeffrey Tolleson, Leslie Wright and Richard Goldbaum
JET Energy Inc., Wellesley Hills, MA 02481, USA

Peter Hagelstein
Massachusetts Institute of Technology, Cambridge, MA 02193, USA

Abstract

Lattice Assisted Nuclear Reactions (LANR) (CF) activated nanocomposite ZrO_2–PdNiD CF/LANR components are capable of significant energy gain over long periods of time with reproducibility and controllability. We report the response of such active components to steady and dynamic applied magnetic field intensities up to ~1.5 T changing with a 0.1 ms rise time. Power gain was determined by the triple verified system of dT/P_{in}, HF/P_{in}, and calorimetry. Fractionated magnetic fields have a significant, unique amplification effect. Residual, late-appearing effects are complex. Importantly, at higher input electrical currents, high intensity fractionated magnetic fields demonstrate their own, new optimal operating point (OOP) manifold curve. This suggests that cold fusion (LANR) is the first stage, and may be mediated by other than phonons.

Keywords: Fractionated magnetic fields, Magnetic field intensities, ZrO_2PdD, Magnetic fields and CF/LANR

---

1. Introduction

1.1. Lattice Assisted Nuclear Reactions (LANR)

Clean, high efficiency energy production is critically important today, and in the foreseeable future, whatever the source may be. Lattice assisted nuclear reactions [LANR] enable deuterium fusion under difficult-to-achieve conditions in very highly hydrided Group VIII metals [1–23] in both aqueous [1–14] and nanomaterial systems [19–23]. This paper reports a method of increasing the excess heat output from such preloaded nanomaterial systems [19–23] (Fig. 1).

In the case of LANR in Pd and in some Ni and Ti systems, the apparent "excess" energy is heat which comes from the fact that there can rarely occur, in a lattice under special conditions, the fusion of two heavy hydrogen nuclei to form a helium nucleus [6,15–18]. The product helium, ^{4}He, is created new and fresh, generated directly from

---

*E-mail: mica@theworld.com

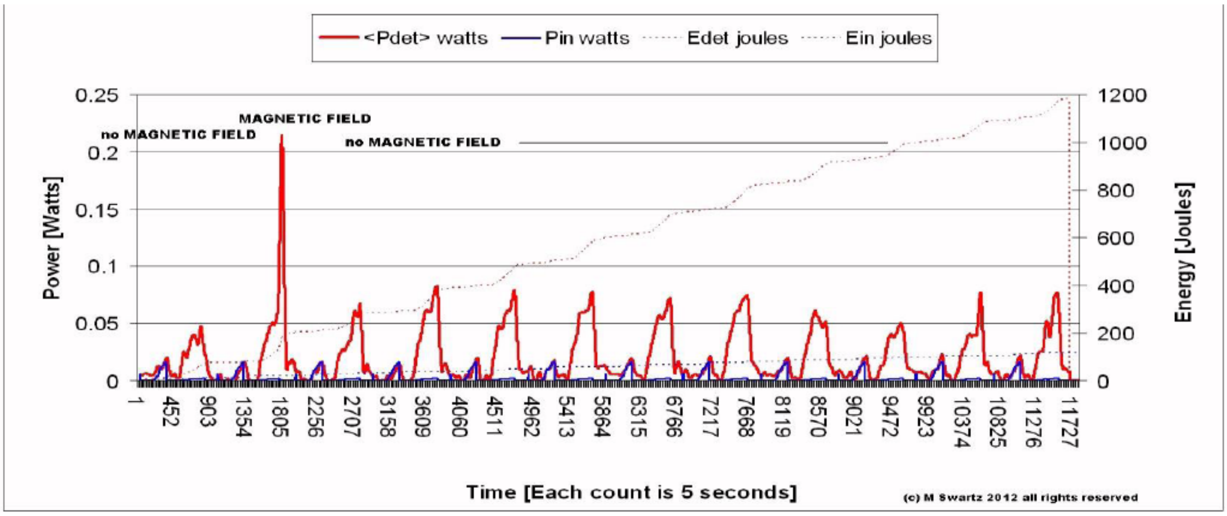

Figure 1. Impact of an applied Magnetic Field on a NANOR-type LANR component – Shown is the calorimetric response of a NANOR-type LANR component to the single application of a series of time-varying repeated high intensity H-field pulses (fractionated treatment between counts 1000 and 2000). The electrical input, and output, power and shown which reveal activity of the preloaded NANOR increasing during the fractionated treatment. Also shown are alternating thermal control, as well as background and calibration pulses. Power is read off of the left hand *y*-axis. The much lighter energy curves (dots) are read off of the right hand *y*-axis. Note the synchronous amplification of the NANOR power output induced by the magnetic field; this is not seen in the ohmic control. There is metachronous, longer-lasting, behavior which is no longer simply evanescent.

two, driven by more, deuterons physically located within the loaded palladium, nickel or one of their nanostructured materials. We speculate that the same, or similar, reactions occur here. Some of these materials have now been preloaded and made into high gain components, to create heat and other reactions with a very large energy density [19–23]. What is important is that the energy density of these CF/LANR components is quite considerable. Using the typical observed outputs, as described in this paper, the energy density and power density are orders of magnitude larger than conventional energy storage devices (Fig. 2).

Figure 2 shows the energy density and power density of these preloaded cold fusion, lattice assisted nuclear reaction components, in comparison to conventional, and recent, energy storage devices. These include the supercapacitor, nickel cadmium battery, lithium ion battery, lead acid battery, and fuel cell which are on the left-hand side of the graph.

As a result, LANR will play a critical role in all future technologies with potential revolutionary applications to all energy issues – robotics, transportation, electricity production, artificial internal organs, and space travel [1]. Most importantly, the product made by systems using CF/LANR is helium, which is environmentally safe and does not produce contamination.

1.2. Previous CF/LANR experiments

These reactions were first reported as aqueous systems called CMNS, LANR, LENR or cold fusion. Today, they involve palladium and/or nickel alloyed lattices or nanomaterials where the process occurs, generally irregularly at low efficiency. However, successful LANR requires engineering of multiple factors including loading, adequate confinement time (sometimes weeks), loading rate, and prehistory (with careful avoidance of contamination and materials and

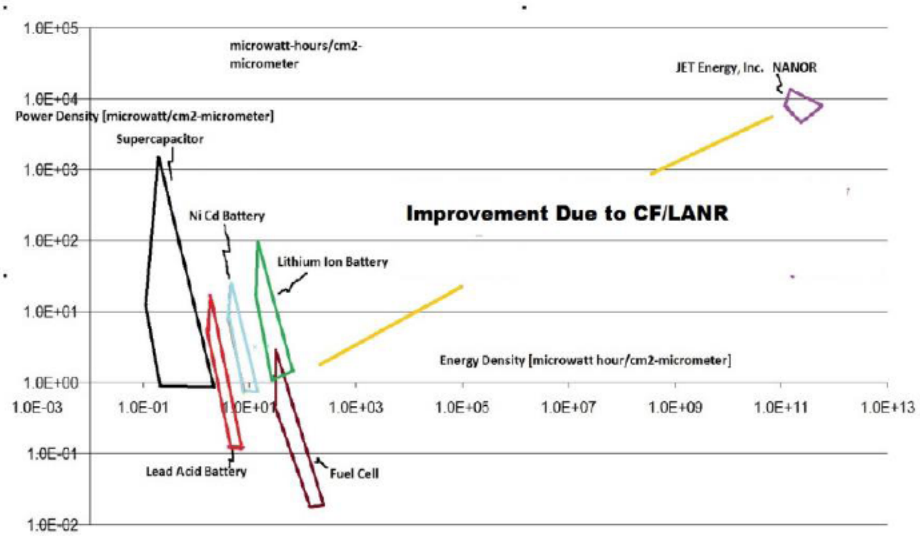

Figure 2. The energy density and power density of several energy production devices compared with the NANOR-type of CF/LANR component. Lattice Assisted Nuclear Reactions (LANR) have very high energy production densities .

operational protocols which quench performance). For example, we previously demonstrated this improvement of success in LANR aqueous systems, linked to high solution resistance (impedance) and shaped-metamaterial PHUSOR®-type LANR devices, with power gains more than 200–500%; and a wide range of power gains using codepositional high impedance devices DAP (Dual anode Phusor®-Type LANR device; Pd/D$_2$O, Pd(OD)$_2$/Pt–Au have reached ~8000% compared to input power and to input power transferred to control dissipative devices (100%) [8–14].

However, our greatest findings so far, are that specifically, nanostructured materials, metamaterials, and their controlled operation improve success of both likelihood and power gain magnitude [15–18]. This paper presents the response of a new generation of preloaded LANR (CF) activated nanocomposite NANOR$^{\circledR-\text{type}}$ZrO$_2$–PdNiD CF/LANR components, or devices, capable of significant energy gain [19–23] to dynamic applied magnetic field intensities.

1.3. Applied magnetic field intensities in CF/LANR

Magnetic and radiofrequency electromagnetic effects have been reported in aqueous CF/LANR systems [2–5,24]. In aqueous CF/LANR systems, steady magnetic fields have a small effect which include a decrease in cell electrical conductivity, if perpendicular to the direction of electrical current flow [24]. We report the first evidence of a fractionated magnetic field producing activation and rejuvenation of nanostructured CF/LANR material, reviving the output to higher levels than previously seen.

For this paper, we examined the impact of applied steady and dynamic ($\mathrm{d}H/\mathrm{d}t$) applied magnetic field intensities on NANOR-type CF/LANR devices during their significant energy gain. Controls included background, ohmic thermal controls, and long-term tests for time invariance and linearity, with and without the applied magnetic field intensities (~1.5 T with 0.1 ms rise time × 1–5000 pulses).

One issue examined in particular was to determine that if there was an effect, the next question would be: is it similar to the near infrared (NT-NIR) emitted from active LANR materials and nanostructured materials, and to the impact of optical and IR irradiation on LANR cathodes, where in both cases it was previously discovered and reported that such effects are maximized exactly when the CF/LANR devices are active at their peak optimal operating point [OOP; 12,14,15–18].

1.4. Active NANOR(R)-type LANR components

The two-terminal, NANOR®-type LANR devices are a new generation of active LANR (CF) preloaded, self-contained, reproducibly active, nanostructured nanocomposite ZrO_2–PdNiD CF/LANR devices capable of significant, reproducible excess heat from applied electric fields [19–23], and which have had portability enabling a range of investigations not previously possible. By self-contained, it is meant that the fuel is preloaded without the need for additional D sources, in liquid or gas. By portability, we refer to the fact that previously running a complete working CF/LANR system (aqueous high impedance PdD) required at least the equivalent of two desk sized volumes. In contrast, that requirement has now, with the preloaded NANOR-type CF/LANR component, been reduced to less than ∼one desktop surface equivalent. Thus, there is superior handling properties because of the fact that there are several types of additional equipment which are no longer required (to load before activation). This eliminates gas tanks, regulators, some types of power supplies and loading systems with their requisite temperature control, supplies of loading material, components holders, leads, electrical and gas connectors. They have all been made moot by the preloading of this component.

Their active CF/LANR core is ZrO_2–(PdNiD) and the like, loaded with additional D and H, yet dry and glued into an electrically conductive, sealed, configuration (Fig. 3a). The left figure shows two last-generation NANOR-type CF/LANR components revealing the core nanomaterial in a transparent way. The present NANOR has ZrO2–PdNiD nanostructured material at the core.

One such NANOR system was driven for more than a year with careful evaluation for energy gain under a variety of conditions, including during the January, 2012 IAP MIT Course on CF/LANR, and later during a long term low-power open demonstration at MIT which ran from Jan. 30, 2012 through mid May 2012 [20]. The NANOR®-type

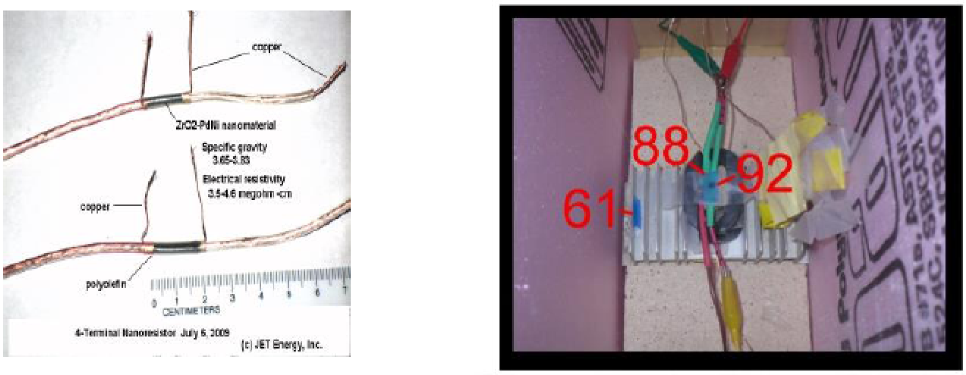

Figure 3. (a) The left figure shows two last-generation NANOR-type CF/LANR components revealing the core nanomaterial in a transparent way. The present NANOR has ZrO_2-PdNiD nanostructured material at the core. (b) The right hand side shows the physical arrangement used for exposure of a functioning Series VI NANOR and an ohmic control to the high intensity fractionated applied magnetic field. To show the arrangement and locations, the calorimeter was stripped of all thermal ballast, thermal conductive layers, electrical connectors, temperature sensors, probes, heat flow sensors, and insulating layers (both thermal and electrical) to reveal the physical arrangement of the CR-39 chips, the NANORő, the ohmic control, the housing and shielding .

preloaded LANR device openly demonstrated clearcut energy gain and features including its convenient size and its superior handling properties which arise because loading has been separated from activation. Over several weeks, time integration with calibration by the ohmic controls revealed that the NANOR®-type LANR device demonstrated more reproducible, controllable, energy gain (COP) which ranged generally from 5 to 16 (14.1 ($\sim$1412%) in the steady state ($\sim$hour) while the MIT IAP course was ongoing).

The NANOR® used for this work is a sixth generation CF/LANR device, smaller than 2 cm, with less than a gram of active material. However, this is actually a matter which is not *de minimus* because the LANR excess power density was more than 19,500 W/kg of nanostructured material. The later-designed preloaded NANOR®s can be fashioned into easily activated LANR (CF) Integrated Circuits which enable an entire new generation of ZrO_2–PdNiD preassembled IC electronic devices. The importance is that they enable LANR devices and their integrated systems to now be fabricated, transported, and then activated. They are the future of clean, efficient energy production.

1.5. Electronic properties of CF/LANR nanomaterials

Close up, in ZrO_2–PdNi-D LANR/CF nanostructured materials, the lattice of Pd is expanded by Zr, and less so, by the H and D. In addition, there are other major changes secondary to the oxidation of the Zr. We speculate that the nanomaterial, ZrO_2–(Pd_xNi_{1-x}), is a composite distribution of nanostructured ferromagnetic "islands" separated among a vast dielectric zirconia "ocean". We surmise that the dielectric zirconia embeds uncountable numbers of nanostructured metal ternary alloy islands of the material containing now NiPdD. The appearance is like a chocolate chip cookie on the nanoscale. The "chips" are composed of hydrided palladium nickel metallic alloy embedded in a zirconium oxide dielectric matrix ("cookie").

Electrically, the response of the CF nanostructured material is complex. The zirconia dielectric matrix is insulating at low voltage and it keeps the nanoscale metal islands electrically separated. It also prevents the aggregation of the islands. Each nanostructured island acts as a short circuit element during electrical discharge. These allow deuterons to form what is believed to be a hyperdense D-state in each island, where the deuterons are able to be sufficiently close together and "locked in".

In addition, CF/LANR nanomaterials are characterized by complicated polarization/transconduction phenomena including an "avalanche (transconduction electrical breakdown) effect" which has a critical role in excess heat generation [19–23]. We previously reported sudden changes of, and generally large, electrical impedances of such NANOR®-type devices containing nanostructured materials. Several were $\sim$3 mΩ when lower voltages were applied, but then as the voltage was increased to $\sim$24 V, the impedance suddenly decreased to very low values. It was shown theoretically that this sudden reduction can be attributed to an "avalanche effect" that is typical of the current–voltage behavior that occurs in Zener diodes. Keys to achieving success in CF/LANR include electrical engineering (continuum electromechanics and the Navier–Stokes equation to handle flow) as well as material science and metallurgy. Control of the breakdown states and quenching tendencies has been critical. Great difficulties have had to be surmounted including assembly of apomaterials of very high electrical resistivity (impedance), as high as 300 gΩ, creating several serious problems.

2. Experimental

2.1. Materials – active LANR nanostructured materials

We have surmounted many of these problems and previously reported the manufacture of NANOR®s and the production of excess heat using nanomaterial palladium, nickel, and newer alloyed compounds, such as ZrO_2PdNi. However, on the difficult side, to make preloaded nanocomposite LANR/CF materials into dry electronic circuit devices requires preparing active nanostructured materials from improved very pure materials, control and avoidance of low-threshold breakdown of states and the quenching tendencies of nanostructured materials, and surmounting their extremely high electrical resistances and "avalanche (transconduction electrical breakdown) effect" [19–23].

For these NANOR-type LANR devices, it is believed that the fuel for the nanostructured material is contained within the core is palladium deuteride, itself within the zirconia nanostructured material. Nanostructured powders, such as Zr 67% Ni 29% Pd 4% (by weight before the oxidation step), absorb a very large number of deuterons for each and every nickel and palladium nuclei. There are reports of numbers in the order of 3.5, and perhaps higher. These include ZrO_2–PdNiD, ZrO_2–Pd, ZrO_2–NiD, and the like. The NANOR-type of LANR device is designed to contain the active ZrO_2/PdD nanostructured material in its core volume, or chamber. At JET Energy, Inc., the core that have been developed and used is ZrO_2–(PdNiD) with augmented processing including entrapping additional D and H using several proprietary processes and apparatus. The deuterons are tightly packed ("highly loaded"). The additional D yields apparent indicated loadings (ratio to Pd) of more than 130% D/Pd, but shallow traps are not ruled out. For simplicity, all of these nanostructured materials in the core, in their range of deuterations, will henceforth simply be referred to as ZrO_2–PdD.

This preloading system has achieved impressive results of excess heat over many months. Most importantly, the activation of the desired LANR reactions is, for the first time at room temperature, separated from the loading of the LANR substrate.

It is a long, expensive, arduous, effort to prepare these preloaded nanocomposite dry CF/LANR devices, whose development has required control of their breakdown states and quenching tendencies. The path to development has not been easy. There are important issues also involving particle size, electrical conductivity, and aggregation, that will be mentioned briefly, and some involve a large literature, beyond the scope of this publication. First, the size of nanostructured materials is key. The desired nanostructure islands of NiPdD have characteristic widths of 2–70 nm size, with the theoretical being less than the observed by imaging. The vibrations of nanostructured materials are believed to be very important for successful CF/LANR activity, and are reported to be maximized with softening of the material; and are important because they do couple the excited state of ^{4}He* to the ground state, and because they might also be of such amplitude that they can cause a sudden structural phase change to a lower free energy state.

Second, preparation of active nanostructured materials, able to undergo preloading, requires very pure materials. Contamination remains a major problem, with excess heat potentially devastatingly quenched. Contaminants can appear from both electrode and container degradation and leeching, from atmospheric contamination, especially after temperature cycling. Furthermore, the heavy water and D_2 are hygroscopic, therefore must be kept physically isolated from the air by sealing.

Third, potential toxicity must be considered. Nanostructured and nanocomposite materials have potential human and environmental health hazards. The large number of particles, and greater specific surface area, yield increased absorptive risk through the skin, lungs, and digestive tract. The preloaded nanostructured material is placed into the hermetically sealed enclosure which is specially designed to withstand pressure, minimize contamination, enable lock on of wires connecting to it. The enclosure is tightly fit with the electrodes. This is important because contamination is a potential problem, and because of the potential toxicity issue. In briefest summary, the production of the preloaded core material involves preparation, production, proprietary pretreatment, loading, post-loading treatment, activation, surmounting the extremely high electrical resistances, and then adding the final structural elements, including holder and electrodes. These are assembled to create the complete preloaded LANR nanomaterial package. When done properly, the result is a very useful and more reproducible nanostructured preloaded ZrO_2–PdD device which can be thereafter, remotely, easily activated, driven by an electrical circuit and controlled by an electrical driver. The component weighed about 80 times the weight of the core active material.

2.2. Methods – electrically driving the materials

The LANR preloaded, stabilized NANOR®s are driven by a high voltage circuit up to 3000 V rail voltage, which is the high voltage that can be delivered in any run to either the NANOR or the ohmic control. The duty cycle was split with half going to a control portion consisting of a carefully controlled electrical DC pulse into an ohmic resistor which was used to thermally calibrate the calorimeter. Input power is defined as $V \times I$. There is no thermoneutral correction in denominator. Therefore, the observed power is a lower limit. The instantaneous power gain [power amplification factor (non-dimensional)] is defined as P_{out}/P_{in}. The energy is calibrated by at least one electrical joule control [ohmic resistor] used frequently, and with time integration for additional validation. The excess energy, when present, is defined as $(P_{output} - P_{input})$ * time.

2.3. Methods – Thermometry and DAQ

Data acquisition is taken from voltage, current, temperatures at multiple sites of the solution, and outside of the cell, and even as a 4-terminal measurement of the NANOR®'s internal electrical conductivity. Data acquisition sampling is at data rates of 0.20–1 Hz, with 24+ bit resolution (e.g. Measurement Computing (MA) USB-2416, or a Omega OMB-DaqTemp or equivalent; voltage accuracy $0.015^{\pm 0.005}$ V, temperature accuracy <0.6°C). All connections are isolated when possible, including where possible with Keithley electrometers, or their equivalent, for computer isolation. All leads are covered with dry, electrically insulating tubes, such as medical grade silicone, Teflon, and similar materials, used to electrically isolate wires. To minimize quantization noise, if necessary, 1 minute moving averages may be used for some signals. The noise power of the calorimeter is in the range of ∼1–30 mW. The noise power of the Keithley current sources is generally ∼10 nW.

2.4. Methods – verifiable calorimetry

The amount of output energy (and therefore, both power, and energy, gain) is determined from the heat released producing a temperature rise, which is then compared to the input energy. Observed signals are determined by parallel diagnostics including thermometry, focused heat flow measurement, and isoperibolic calorimetry, and then semiquantitively repeatedly calibrated by an ohmic (thermal) control located next to the NANOR®. The result is heat measurement of this preloaded NANOR®-type LANR three (3) ways ending in calorimetry, input-power-normalized ΔT (dT/P_{in}), and input power normalized heat (HF/P_{in}).

The output of the NANOR® is compared to the output of the precisely driven ohmic control (Fig. 4a). The instantaneous power gain is kinematically determined by the ratio of the input power normalized temperature increase to the input electrical power (P_{in}), called by the symbol '$\Delta T/P_{in}$' referring to the increase of temperature (ΔT) divided by the input electrical power. Also, the output of the NANOR® is independently derived by kinematically evaluating the heat flow, using the ratio of the input power normalized heat flow to the input electrical power (P_{in}), called by the symbol 'HF/P_{in}' referring to the heat flow (HF) divided by the input electrical power. The third method is examination by calorimetry, calibrated by the thermal ohmic control and thermal waveform reconstruction, and confirmed by long-term time integration. These three methods of verification are pooled to derive very useful information, including the energy produced ("excess energy") and sample activity ("characteristic or largest incremental power gain over an ohmic control").

2.5. Methods – applied magnetic field intensity

For this paper, we examined the response of NANOR®-type preloaded LANR devices containing active ZrO_2–PdD and ZrO_2–PdNiD nanostructured materials to steady state (continuous) magnetic fields, and then dynamic, rapidly

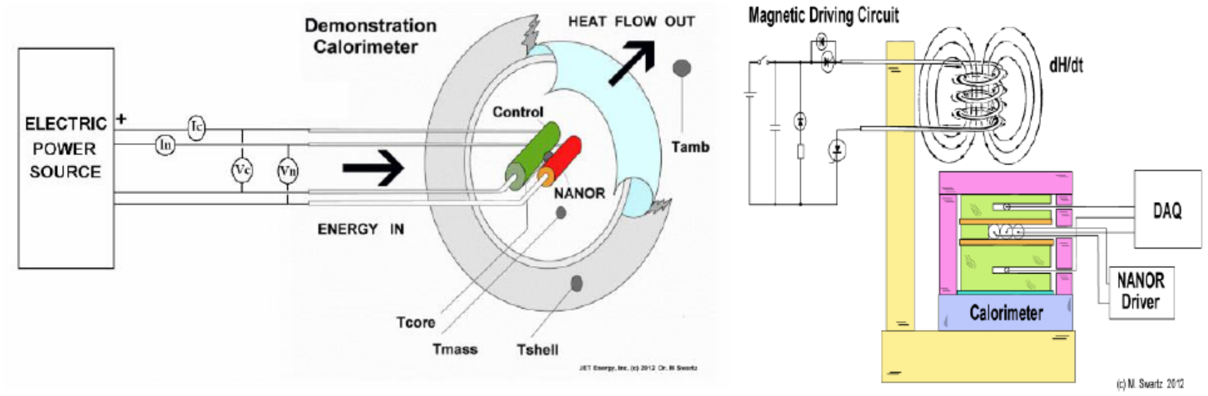

Figure 4. (*Left*) Schematic electric driver and calorimeter showing parallel diagnostics consisting of heat flow measurement and temperature, and the ohmic (thermal) control. (*Right*) Two terminal NANORő-type devices containing active ZrO_2–PdNiD nanostructured material at their core, with DAQ under the applied (off axis) dynamic magnetic field intensity. Next to it are the ohmic control, a temperature measurement device. The ballast with additional temperature measurements and calorimeter are shown only figuratively .

changing and then successively reapplied (fractionated) magnetic field (H-field) intensities. In the latter, the CF/LANR system ran while an H-field pulse sequence was delivered (dH/dt $\sim$1.5 T with 0.1 ms rise time × 1000–5000 pulses). The set-up is shown in Fig.3b and Fig 4b. Figure 3b shows the calorimeter stripped of said thermal materials and probes to reveal the physical arrangement of the CR-39 chips, the NANOR®, the ohmic control, the housing and shielding. The NANOR® and its active site are marked at #92. #88 labels the ohmic control. #61 labels the nearby control CR-39 chip, partially shielded by aluminum. The thermal materials *et alia* were replaced for the experiments. In Fig. 4b, the magnetic field lines continue into the housing and into and about the NANOR and the ohmic control. They are not shown in the diagram of Fig. 3b for convenience. The NANOR Explorer (the driver) is not shown. The fractionation refers to the sequence of multiple pulses, which in this case had rise times listed above.

Controls included background, ohmic thermal controls, tests for time invariance, with and without the applied magnetic field intensities. As controls, we ran simultaneous ohmic systems, and also used previous long term checks of the system and CF/LANR NANOR®-type component without fractionated (and static) H-fields, including with calibrations, and evaluations, along with the previous reports at ICCF-17. These reported on the importance of careful paradigms, intercalated controls, and demonstrated reasonable time invariance and linearity (except during the infrequent outgassing condition also reported, also reported where the excess power goes to zero).

Each pulse sequence was delivered at 1 Hz to the control and NANOR, but with the electrical current drive to the thermal ohmic control and then the NANOR®. This enabled determining the impact of the H-field upon the background, and upon the control, and upon the NANOR®. Times of these experimental cycles were longer compared to those discussed at ICCF-17 or used at the MIT IAP demonstration system because it was felt that long time constants might be involved (e.g. magnetization, possible additional energy transfer). A proprietary autonomous system was used to run the NANOR® continuously alternating with background and an ohmic thermal control. This was used to control the system which included a complementary, surrounding calorimeter. The proprietary microprocessor-controlled system semiquantitatively examines and drives the NANOR®, examining it for heat-production activity, linearity, time-invariance, and even the impact of additives and applied fields.

Power gain was determined by dT/P_{in}, HF/P_{in}, and calorimetry, but did not include the impact of the H for two reasons. First, it was transient, and not present in the vast amount of data. Second, it was also impinging upon the controls which were monitored for the impact of the H-field upon it (ohmic resistor) at the same distance location, next to the NANOR®, and with electrical currents also going through it.

3. Results

3.1. DC magnetic fields

Static applied ("DC") magnetic fields have an small effect upon the active NANOR®-type nanomaterial CF/LANR systems, increasing power gain, especially at higher input electrical currents. Under that condition, and not seen in the controls, the applied static magnetic field intensities did produce a small to moderate increase gain (Fig. 5). They also produced some low intensity long-term (called 'metachronous') effects. These metachronous changes were reflected as a slight loss of near time-invariance. This effect was increased irregularity in the CF/LANR excess power output, post applied steady magnetic fields (and as discussed below, was also seen with the application of dynamic magnetic fields. As will be shown below, this is a minor effect compared to what was wrought by the applied high intensity fractionated magnetic fields, which will be shown to create both simultaneous and late (metachronous) major effect (*vide infra*).

3.2. d*H*/d*t* Magnetic fields – synchronous effects

In this case, it was discovered that high intensity, dynamic, repeatedly fractionated magnetic fields have a major, significant and unique synchronous amplification effect on the preloaded NANOR®-type LANR device under several

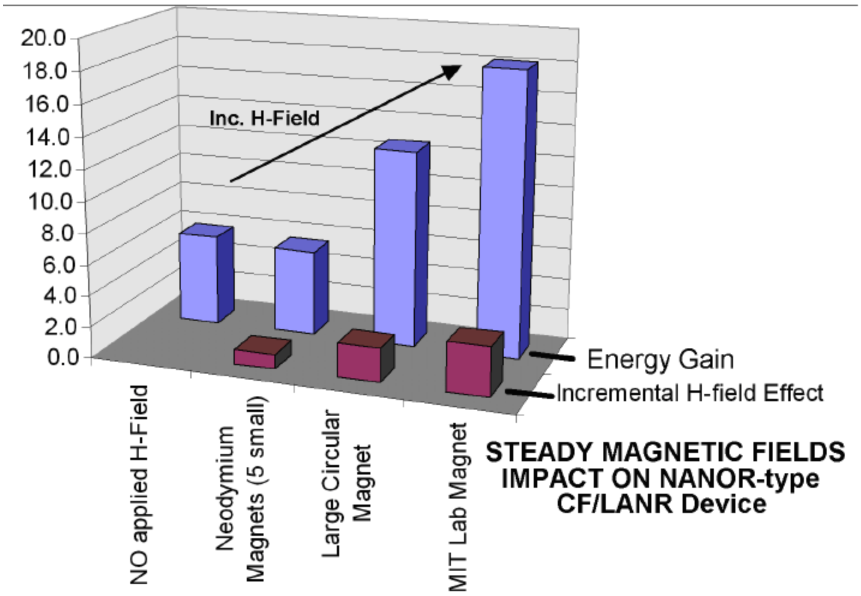

Figure 5. Impact of DC H-field Intensity on NANOR®-type LANR component – Energy gain and incremental H-field amplification for the LANR NANOR® Output as effect by an applied steady (DC) magnetic field intensity.

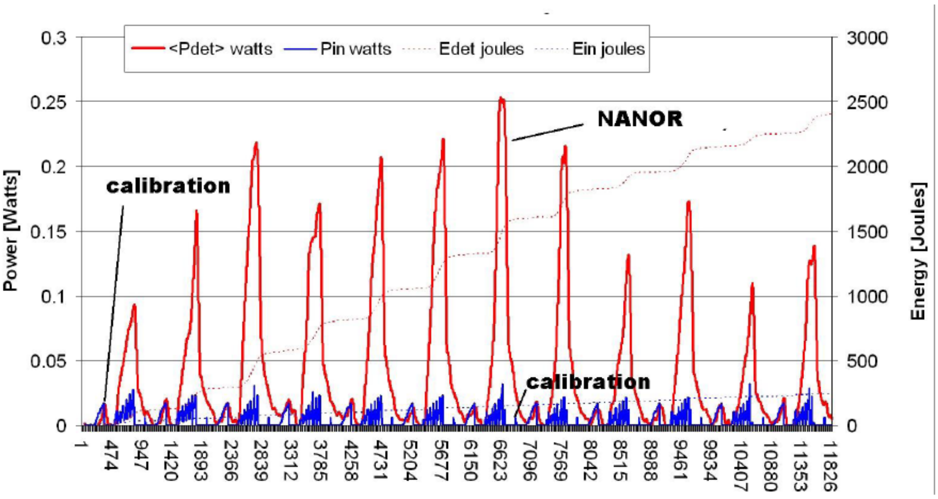

Figure 6. Input power and output heat flow normalized to input electrical power of a self-contained CF/LANR quantum electronic component at 124 V peak input voltage. There is also enhanced improvement of CF/LANR (which is synchronous), and there is improved of CF/LANR which is metachronous and longer-lasting.

conditions of operation. Synchronous effects are those caused by the applied high intensity fractionated magnetic field imposed upon the NANOR during the NANOR®s power gain during the run.

The magnetically treated preloaded NANOR®-type LANR devices had significant incremental power gain, and had – over a prolonged amount of time – higher efficiency excess heat production. This incremental gain was a significant improvement over all previous NANORs, and in fact, was an increase in power gain which is significant and far beyond that of CF/LANR alone.

For example, previously, the preloaded nanostructure devices [NANOR®s] had a significant energy gain, such as in the MIT 2012 demonstration unit (Energy gain $\sim 14\times$). By contrast, now, in this series of experiments involving investigating the possible impact of dH/dt, the CF/LANR NANOR® components demonstrated even higher gains. The incremental impact of the applied high intensity fractionated magnetic field treatments yielded a major synchronous effect on the power gain as determined by $\mathrm{d}T/P_{\mathrm{in}}$, HF/$P_{\mathrm{in}}$, and calorimetry. The peak power gain was ranged from 22 to up to $\sim$80 times input electrical power or more beyond the control, as determined by calorimetry.

The input power provided to produce the H-field was not included, because consistent with this approximation it should be noted that there was no change in the output of the ohmic control, or with the background, and that the was no further H-field input beyond the first hour. Further evidence that the H-field has negligible input by energy is revealed by the negligible change in currents to the ohmic control and background (no electrical input) regions.

Most importantly, there was an increase over ordinary active cold fusion operation of these NANOR-type systems. The application of dH/dt created an increase of 4–10 times the peak power gain over “conventional” CF/LANR, “conventional” means the observed output of the same NANOR-type system before said application of repetitively fractionated magnetic field.

It is important to note that this effect was not observed in the controls through which currents are also applied during their share of the duty cycle. This effect was not observed for NANOR®s in place with no additional current driving them. This major level of impact only seen for the preloaded NANOR®-type LANR device when it was already putting out excess energy. This major level of impact was not observed for static magnetic fields.

3.3. Residual (metachronous) effects

Other effects were noted. Astonishingly, it has now been discovered that high intensity, dynamic, repeatedly fractionated, magnetic fields have an incremental major, significant and unique, complex, metachronous amplification effect on the preloaded NANOR®-type LANR device (cf. Figs. 6 and 1).

It is important to consider this *de novo* magnetic behavior. Perhaps this is expected for the nickel containing NANORs, but it is somewhat surprising for the palladium NANORs. Nickel is ferromagnetic and the induction of magnetization is to be expected. Not so normally for palladium.

However, under some conditions involving vacancies, the conversion of Pd from paramagentic to ferromagnetic behavior has been reported [25–28]. Palladium, like platinum, have potential as exchange-enhanced paramagnetic materials. When the Stoner criterion is satisfied, in response to external stimuli such as applied E-field, they exhibit unconventional magnetic responses – they become exchanged-enhanced ferromagnetic.

Palladium exhibits a strong Stoner enhancement. Pd has been reported, positioned between ultrathin ferromagnetic films, to become ferromagnetic [25]. With Pt, an electric gate voltage can induce an anomalous Hall effect (AHE) in the Pt thin film. The applied electric field can induce a magnetic moments as large as $\sim 10\ \mu$B in materials which can self interact, as described by the Langevin function [26]. Theoretically, this is supported by density-functional calculations [27]. The Fermi-level density of states drives the transition at the surface to an itinerant ferromagnetic state above a critical applied electric field intensity, E_c, and follows a square-root variation with electric field. This appears to be driven by vacancies in Pd (theoretically, up to 15% calculated using the SCR Korringa–Kohn–Rostoker coherent potential approximation method, which predicts a magnetic at $\sim 10\%$ vacancies) [28]. We have recently begun to image the induced domains [29].

There has been long term metachronous impact wrought upon the treated CF/LANR NANORs, long after the treatment, heralded as increased power and energy gain as determined by $\mathrm{d}T/P_{\mathrm{in}}$, HF/$P_{\mathrm{in}}$, and calorimetry. There was also an improvement of CF/LANR activity which was metachronous – and that means longer-lasting. Metachronous effects are those physical changes wrought by the applied high intensity fractionated magnetic field upon the function of the NANOR®s power and energy gain *after* the run. This is in addition to the enhanced improvement of CF/LANR operation by the dynamic magnetic treatment which is synchronous.

These wrought late-appearing, long lasting complex effects, including variable changes in activity, are significantly important. Operationally, the application of these high intensity fractionated magnetic fields had significant long term effects, which eliminate the previous near linearity of the output.

Instead there appear further time-complex findings, including the demonstration of increased irregularity and time variance of the energy gain, and what appear to have a component of cyclical changes in activity, rather than the simple exponential falloff seen previously extending over weeks [19–23].

This amplification of CF/LANR by dynamic magnetic fields and especially the significant, residual post-applied fractioned magnetic fields effects (which are complex and demonstrate variable, including cyclic, changes in activity) suggest a new CF/LANR material science/nuclear interaction.

3.4. New optimal operating point manifold

Now that both synchronous and metachronous effects have been discussed, it is important to shift to consider the incredible, newly discovered changes in optimal operating point (OOP) operation of the CF/LANR components. Previously, all cold fusion systems and the NANOR®s have always shown a single optimal operating point manifold for excess heat operation. That is no longer accurate after only a single treatment to a high intensity fractionated magnetic field. Instead, there now appear, uniquely, two OOP manifolds (Fig. 6).

Figure 7 shows the two OOP manifolds, as well as the ohmic control ("normal") response (defined here as '100%') and conventional CF/LANR operation ("cold fusion"), and the synchronous and metachronous impacts of a fractionated magnetic field intensity. There is an amplified (phonon) OOP bigger than before, and an entirely new, *de novo* (magnon?) OOP. By this terminology, the authors mean an OOP enabling successful control of CF/LANR which is itself "catalyzed" by phonons (and magnons, respectively) in that de-excitation from the 24 MeV excited ^{4*} can only occur by an adequate number of coherent phonons which constitute a lossy enabling cohort.

Note that in the figure, conventional CF/LANR operation is shown above the output of ohmic controls ("normal"). Now, what was once extraordinary CF/LANR output from an active component, now appears to have been the only the 'first stage' CF/LANR.

Importantly, located at higher driving input electrical currents, the high-intensity fractionated magnetic fields treated NANOR®s (M-NANORs) demonstrate their own novel magnetic-induced optimal operating point (M-OOP) manifold curve which is located to the "right" (at higher input electrical currents) of the conventional CF/LANR OOP.

Attention is now directed to the two (2) OOP manifolds. The composite two-maximum OOP manifold of dH/dt-treated NANOR®s is complex and reflects an amplified original optimal operating point manifold AND a new OOP, apparently linked to the input electric current or power in a complex way. On close inspection, there is the development of an entirely new OOP manifold by the applied fractionated magnetic field intensity AND a modification of the previous "original" OOP manifold. The result is that there is now an amplified (phonon) OOP and a *de novo* second (magnon?) OOP manifold – these are the two OOP manifolds.

The set of several (new) dual OOP manifolds also present BOTH the synchronous and the metachronous impacts of a fractionated magnetic field intensity. Note that M-OOP for NANOR®s have different OOP characteristics, and different behavior, than conventional OOPs for NANOR®s. This suggests that these might actually reflect different methods of coupling through the lattice to the ^{4}He*. It does this by showing both the generated amplified phonon OOP and the *de novo* magnon OOP which continues during its application, and somewhat after its treatment of the CF/LANR device. These findings suggest that there are two possible paths for successful cold fusion results. Or in the

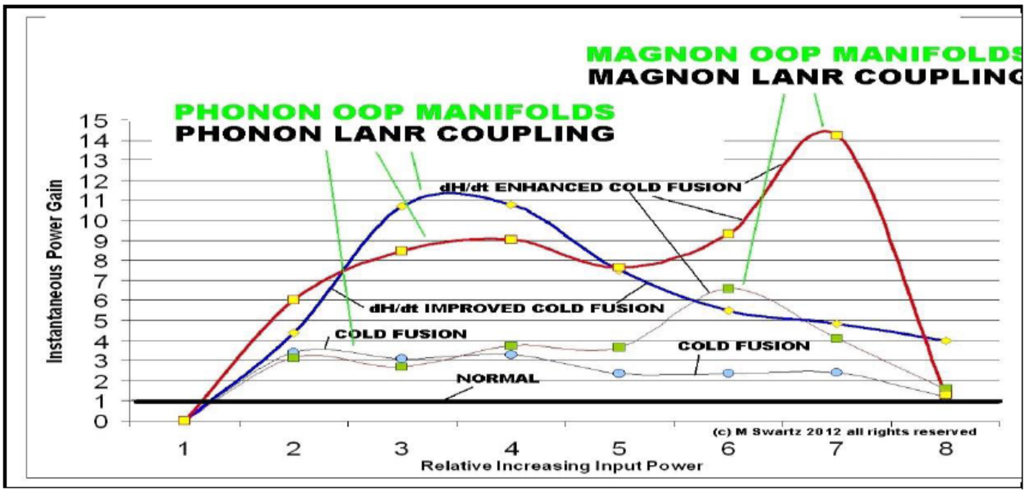

fo

Figure 7. Amplification of, and Residual Impact upon, a NANORő-type LANR Device – Instantaneous power gain for the preloaded NANORő-type LANR device under several conditions of operation. There is development of a new optimal operating point (OOP) manifold by the applied fractionated magnetic field intensity. There is also enhanced improvement of CF/LANR (which is synchronous, and here called "enhanced"), and there is improved of CF/LANR which is metachronous and longer-lasting, which is here called "improved". Conventional cold fusion and conventional ohmic thermal operation ("normal", characterized by a power gain of 1 or less) are also shown.

alternative, the magnon OOP is important because it is a 'gateway' to an entire new level of CF/LANR operation - a second stage.

3.5. dH/dt Magnetic fields can damage equipment

High intensity magnetic fields can damage equipment. There is a danger of equipment breakdown even with only 3 minutes of dH/dt treatment. This is also reflected in the electronic signals delivered.

4. Conclusion

4.1. Interpretation

It is clear that magnetically activating these preloaded nanostructured CF/LANR devices is very useful. Attention is directed to the just-discovered synchronous and metachronous impacts of a fractionated magnetic field intensity, associated with strong evidence of two (2) OOP manifolds. Astonishingly, it was discovered that there is also enhanced improvement of CF/LANR (which is synchronous), and there is improved of CF/LANR which is metachronous and longer-lasting.

The peak power gain of such treated NANOR®s (M-NANOR®s) ranged from 22 to up to ∼80 times input electrical power or more beyond the control, as determined by calorimetry. There was also an increase in energy gain, and increased incremental power gain, over ordinary cold fusion. The application of dH/dt created an increase of 4–10 times the peak power gain over conventional CF/LANR with the same system.

These treated magnetically poled NANOR®-type nanostructured LANR devices (M-NANOR®s) have functioned for more than many months after treatment, at more than one location. They are conveniently preloaded, mountable as easily activated LANR (CF) components into integrated circuits. They are activated by applied electric fields and applied fractionated magnetic fields, and are a new generation of activated CF/LANR nanocomposite ZrO_2–PdNiD electronic devices. These can be used as an effective very clean, highly efficient, energy production system, apparatus, and processes. They are integrable into microprocessor controlled integrated circuits providing a new generation of CF/LANR quantum optical devices containing preloaded nanostructured LANR materials.

Tomorrow, preloaded CF/LANR nanostructured materials and devices will be high power, high-efficiency, self-contained, auto-controlled, energy production devices. They will enable remote powering of electronic, bioelectronics, robotic, propulsion, space and avionic, and off-grid systems.

4.2. Future plans and implications

The two different OOP manifolds suggest an entirely new material science/nuclear interaction and technology. These complex responses remind one of ferro-, ferri, and antiferromagnetism, and the range of dielectric materials which are known to exist for other materials, and which are now possible here, too.

Furthermore, there may be special effects when the field is perpendicular to the direction of current through the NANOR® at the time of operation, and more work is needed to determine this with statistical certainty over clinical report.

Acknowledgements

The authors would like to thank Alex Frank, Allen Swartz, Charles Entenmann, Dennis Cravens, Dennis Letts, Brian Ahern, Jeff Driscoll, Larry Forsley, Pamela Mosier-Boss, Frank Gordon, Robert Smith, Robert Bass, David Nagel, Linda Hammond, and JET Energy and New Energy Foundation for support. NANOR® and PHUSOR® are registered

trademarks. NANOR®-technology, and PHUSOR®-technology, and other discussed IP herein, are protected by U.S. Patents D596724, D413659 and several other patents pending.

References

[1] Swartz, M., Survey of the observed excess energy and emissions in lattice assisted nuclear reactions, *J. Sci. Exploration* **23** (4) (2009) 419–436.

[2] Szpak, S., P.A. Mosier-Boss and F.E. Gordon, Further evidence of nuclear reactions in the Pd/D lattice: emission of charged particles, *Naturwissenschaften,* 94 (2007) 511–514.

[3] Bockris, J. O'M., R. Sundaresan, D. Letts and Z.S. Minevski, Triggering and structural changes in cold fusion electrodes, *Proc. ICCF4*, Maui, Hawaii, 1993.

[4] Cravens, D., Factors, Affecting success rate of at generation in CF cells, *Proc. ICCF-4,* Maui, Hawaii, USA, 1993.

[5] Bockris, J.O'M., R. Sundaresan, D. Letts and Z.S. Minevski, Triggering and structural changes in cold fusion electrodes, *ICCF4*, Maui, Hawaii, 1993, to be published.

[6] Miles, M.H., Hollins, R.A., Bush, B.F., Lagowski, J.J. and R.E. Miles, Correlation of excess power and helium production during D_2O and H_2O electrolysis, *J. Electro-analytical Chem.* **346** (1993), 99–117; Miles, M.H. and Bush, B.F., Heat and helium measurements in deuterated palladium, *Trans. Fusion Technol.* **26** (1994) 156–159.

[7] Swartz, M., Three physical regions of anomalous activity in deuterided palladium, *Infinite Energy* **14**(61) (2008) 19–31.

[8] Swartz, M., Excess power gain using high impedance and codepositional LANR devices monitored by calorimetry, at flow, and paired stirling engines, *Proc. ICCF-14*, 10–15 August 2008, Washington, D.C. ISBN: 978-0-578-06694-3, 123, (2010).

[9] Swartz, M. and G. Verner, Excess at from low electrical conductivity avy water spiral-wound Pd/D_2O/Pt and Pd/D_2O–$PdCl_2$/Pt devices, *Condensed Matter Nuclear Science*, *Proc. ICCF-10*, P. Hagelstein and S. Chubb (Eds.), World Scientific, NJ, ISBN 981-256-564-6, 29-44; 45-54 (2006).

[10] Swartz. M., The Impact of avy water (D_2O) on nickel-light water cold fusion systems, *Proc. 9th Int. Conf. on Cold Fusion (Condensed Matter Nuclear Science)*, Beijing, China, Xing Z. Li (Ed.), May 2002, pp. 335–342.

[11] Swartz, M. and G. Verner, The Phusor®-type LANR cathode is a metamaterial creating deuteron flux for excess power gain, *Proc. (ICCF-14),* 10–15 August 2008, Washington, D.C. ISBN: 978-0-578-06694-6,3, 458, (2010).

[12] Swartz, M., Photoinduced excess at from laser-irradiated electrically-polarized palladium cathodes in D_2O, *Condensed Matter Nuclear Science, Proc. ICCF-1*0, Peter L. Hagelstein and Scott Chubb (Eds.), NJ, ISBN 981-256-564-6, 213-226 (2006).

[13] Swartz, M., Can a Pd/D_2O/Pt device be made portable to demonstrate the optimal operating point? *Condensed Matter Nuclear Science, Proc. of ICCF-10*, Peter L. Hagelstein and Scott, R. Chubb (Eds.), World Scientific, NJ, ISBN 981-256-564-6, 29-44; 45-54 (2006).

[14] Swartz, M., G.Verner and A.Weinberg, Non-thermal near-IR emission from high impedance and codeposition LANR devices, *Proc. of the 14th Int. Conf. on Condensed Matter Nuclear Science and the 14th Int. Conf. on Cold Fusion (ICCF-14),* 10–15 August 2008, Washington, D.C. David J. Nagel and Michael E. Melich (Eds.), ISBN: 978-0-578-06694-3, 343, (2010).

[15] Swartz, M., Optimal operating point manifolds in active, loaded palladium linked to three distinct physical regions, *Proc. of the 14th Int. Conf. on Condensed Matter Nuclear Science and the 14th Int. Conf. on Cold Fusion (ICCF-14)*, 10–15 August 2008, Washington, D.C. David J. Nagel and Michael E. Melich (Eds.), ISBN: 978-0-578-06694-3, 639, (2010).

[16] Swartz, M., Quasi-one-dimensional model of electrochemical loading of isotopic fuel into a metal, *Fusion Technol.* **22**(2) (1992) 296–300.

[17] Swartz. M., Consistency of the biphasic nature of excess enthalpy in solid state anomalous phenomena with the quasi-1-dimensional model of isotope loading into a material, *Fusion Technol.* **31** (1997) 63–74.

[18] Swartz. M., Generality of optimal operating point behavior in low energy nuclear systems, *J. New Energy* **4**(2) (1999) 218–228.

[19] Swartz, M.R., G. Verner and J. Tolleson, Energy gain from preloaded ZrO_2–PdNi–D nanostructured CF/LANR quantum electronic components, *Proc. of the 17th Int. Conf. on Condensed Matter Nuclear Science and the 17th Int. Conf. on Cold Fusion (ICCF-17; pending)* (2012).

[20] Swartz. M. and P.L.Hagelstein, Demonstration of energy gain from a preloaded ZrO_2–PdD nanostructured CF/LANR quantum electronic device at MIT, *Proc. ICCF17* (2012).

[21] Swartz, M., LANR nanostructures and metamaterials driven at their optimal operating point, *Third Volume of the LANR/LENR Sourcebook*, October 21, 2011.

[22] Swartz. M., P. Mosier-Boss, P.L. Hagelstein, G, Verner, J, Tolleson, L. Wright and R. Goldbaum, Imaging of an active LANR quantum electronic component using CR-39 confirmation of LANR nuclear activity and emission of penetrating ionizing radiation temporally, spatially, and by imaging, *Proc. of the 18th Int. Conf. on Condensed Matter Nuclear Science and the 18th Int. Conf. on Cold Fusion (ICCF-18)*, Minnesota, 2013.

[23] Swartz. M., Incremental high energy emission from a ZrO_2–Pd-D nanostructured CF/LANR quantum electronic component, *Proc. of the 18th Int. Conf. on Condensed Matter Nuclear Science and the 18th Int. Conf. on Cold Fusion (ICCF-18)*, Minnesota, 2013.

[24] Swartz, M.R. Impact of an applied magnetic field on the electrical impedance of a LANR device, *Proc. of JCMNS*, Vol. 4, March 2010, *New Energy Technology Symposium* held at the 239th American Chemical Society National Meeting and Exposition in San Francisco (2011).

[25] Santos, D.L.R., P. Venezuela, R.B. Muniz and A.T. Costa, Spin pumping and interlayer exchange coupling through palladium, *Phys. Rev. B* **88** (2013) 054423.

[26] Shimizu, Sunao, Kei S. Takahashi, Takafumi Hatano, Masashi Kawasaki, Yoshinori Tokura, and Yoshihiro Iwasa, Electrically tunable anomalous hall effect in Pt thin films, *Phys. Rev. Lett*. **111** (2013) 216803.

[27] Sun, Y., J.D. Burton and E.Y. Tsymbal, Electrically driven magnetism on a Pd thin film, *Phys. Rev.* B **81** (2010) 064413.

[28] Takanol, N., T. Kai2, K.Shiiki2 and F.Terasakil, Effect of copious vacancies on magnetism of Pd, *Solid State Commun.* **97**(2) (1996) 153–156.

[29] Swartz, M, Magnetic imaging of a NANOR using a horizontal translated hall effect sensor, (2014) in preparation.

J. Condensed Matter Nucl. Sci. 15 (2015) 81–91

Research Article

Imaging of an Active NANOR®-type LANR Component using CR-39*

Mitchell R. Swartz[†], Gayle Verner, Jeffrey Tolleson, Leslie Wright, Richard Goldbaum
JET Energy Inc., Wellesley Hills, MA 02481, USA

Pamela Mosier-Boss and Peter L. Hagelstein
Research Laboratory of Electronics, Massachusetts Institute of Technology, Cambridge, MA 02139, USA

Abstract

This effort examined CR-39 chips exposed to a ZrO_2-PdD NANOR®-type CF/LANR component exhibiting significant energy. There was a fall-off in pit count with increasing distance from the operating system. Most interestingly, the CR-39 over the device essentially imaged the active CF/LANR device at very low resolution. Large tracks were the most effective for imaging. Smaller and mid-sized tracks appear to be useful for measuring fall off of the chip irradiation as a function of distance. The conclusion is that CF/LANR is a nuclear process, and for this system at this power level, the quantitative amount is measurable in a spatial, controllable, pattern.

Keywords: CR-39 Imaging, Imaging CF/LANR Systems, Preloaded CF/LANR component, ZrO_2PdD

---

1. Introduction

1.1. CF/LANR high energy emissions

Lattice assisted nuclear reactions (LANR) enable deuterium fusion under difficult-to-achieve conditions in hydrided Group VIII metals. Although LANR is a nuclear process, gamma emission is actually isospin forbidden by electric dipole transitions (both in charge independent [1] and dependent [2] analyses of the nuclear force). However, for hot fusion, the forbidden restriction is “lifted” by the high temperature, and so penetrating gamma emission is significantly observed. However at lower temperature, only rarely have charged particles, gamma radiation, and neutrons also been detected [3]. Past diligent efforts with autoradiography and CR-39 have heralded the recording of rare, high energy penetrating radiation emitted from cold fusion (LANR) materials in their active state; confirmed by autoradiography

---

[*] Confirmation of CF/LANR nuclear activity by emission of low level penetrating ionizing radiation which is temporally and spatially linked.

[†] E-mail: mica@theworld.com

or CR-39 chips over periods of days. Miles (China Lake, USN) and M. Srinivasan (Bhabha Atomic Research Center (BARC) independently used dental X-ray film autoradiography on the outside of the cells which revealed fogging heralding low energy X-ray production [4,5]. Srinivasan reported neutrons in 1989 as the current increased beyond 100 A, neutron signals, in bursts, resulted in 6 of 11 cells. Thereafter, energetic charged particles were detected by CR-39 in gas LANR systems [6] and in aqueous codeposition systems [7]. X. Z. Li (Tsinghua U) first used CR-39 in his 1990 Pd gas loading experiments to detect energetic charged particles [8].

Mosier-Boss et al. [7] reported CR-39 tracks which indicate possible neutron interactions, including carbon shattering. Some tracks herald D–D and DT reactions. Etching suggests uniformity in the 2–8 MeV range. The triple tracks, found in ∼5–10% of their experiments, indicate energetic neutrons have shattered carbon atoms. Also observed in LANR systems are mini-explosions, ionizing radiation, and neutron production, and tritium production. These observations of significant quantities of high energy charged particles, and emissions, in LANR systems, suggests that, although very few investigators have looked with adequate equipment, there is accumulating, near overwhelming, evidence that nuclear reactions in, and assisted by a lattice, are initiated at low energies. This paper describes how to image these systems (Fig. 1).

2. Experimental

2.1. Survey of problems

The first problem with quantitation by a detector is that only very low numbers of neutrons and charged particles with short range are emitted. The second problem is that if the emissions are similar to the near infrared (NT-NIR) emission (see Section 4.1) from active LANR materials, then such penetrating high energy emission should only occur when the CF/LANR devices are active at their optimal operating point (OOP). Third, the output from CF/LANR devices are

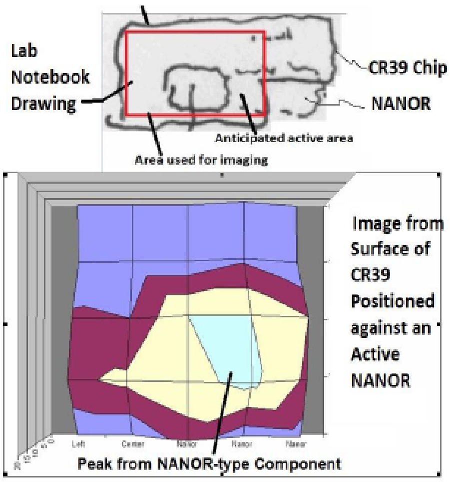

Figure 1. (a) (*left, top*) The location of the CR-39 chip over the NANOR®-type CF/LANR quantum electronic component. The ohmic control was at the top. (b) (left, *bottom*) This shows the distribution looking down the vertical axis, similar to the drawing above it. The very low resolution image of the NANOR® was obtained by pixel counting in the 2D record of large tracks on the CR-39 chip which was left vicinal to the NANOR®-type CF/LANR component. Another view is in Fig. 6b. There was no image from the ohmic control which was physically located just above the CF/LANR component, or in either of the two control CR-39 chips.

very low level and can be interfered with by environmental contamination (including people with ^{40}K). Therefore, a pretested NANOR®-type system was used at a number of input powers [8], run autonomously over days examined by Geiger Muller tube and CR-39, a polyallydiglycol carbonate polymer used as a time-integrating, solid state, nuclear track detector.

2.2. Materials

Nanostructured materials are important, unique and relevant to LANR and the future of LANR devices. They are used both as CF/LANR materials and produced in codeposition structures [9,3]. They have been observed producing non-thermal near infrared emissions when active [10], and exhibiting LANR excess heat correlated with the size of the Pd–D nanostructures [9]. Nanostructured materials have been used in LANR using palladium black [11] in a double structure (DS)-cathode. Today, second and third generation nanostructured ZrO_2–PdD and ZrO_2–PdNiD powders, such as Zr 67% Ni 29% Pd 4% (by weight before the oxidation step), absorb a very large number of deuterons for each and every nickel and palladium nuclei; with loading circa 3.5, and perhaps higher. LANR (CF) preloaded nanocomposite ZrO_2–PdNiD NANOR®-type CF/LANR components are capable of significant energy gain [12,14]. The ZrO_2–(Pd Ni)D is prepared with complicated processes of oxidizing and adding deuterons to the complicated mixture of zirconium oxide surrounding metallic palladium, nickel, or Pd-Ni islands. The air bake temperature and time, and final proprietary dopants and processing appear to have critical importance.

2.3. Methods – NANOR-type LANR device fabrication

We previously reported on the design and utilization of a new generation of active LANR (CF) preloaded nanocomposite ZrO_2–PdD and ZrO_2–PdNiD CF/LANR materials to fabricate NANOR®-type devices (Fig. 2) capable of significant, reproducible excess heat from applied electric fields [9,12,13]. These self-contained, two-terminal NANOR®-type LANR devices feature new composition, structure, and superior handling properties enabling portability and transportability. The NANOR®-type of LANR device used here contained active ZrO_2/PdD nanostructured material loaded with additional D. The deuterons are tightly packed (“highly loaded”). The additional D yields apparent indicated loadings (ratio to Pd) of more than 130% D/Pd, but shallow traps are not ruled out. For simplicity, all of these nanostructured materials in the core, in their range of deuterations, will henceforth simply be referred to as ZrO_2–PdD.

It is a long, expensive, arduous, effort to prepare these preloaded nanocomposite dry CF/LANR devices, whose development has required control of their breakdown states and quenching tendencies. The NANOR used for this work is a sixth generation CF/LANR device, smaller than 2 cm length, with less than a 50 mg of very active LANR material.

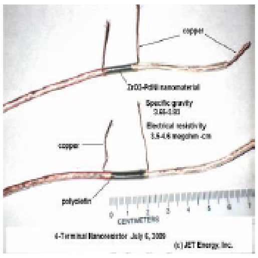

Figure 2. The source of the CF/LANR radiation which was imaged here, and detected by the irradiated CR-39 chip, is shown here. Two of these two terminal NANOR®-type devices containing active ZrO_2–PdNiD nanostructured material at their core are shown.

Although small in size, this is actually not *de minimus* because the LANR excess power density was more than 19,500 W/kg of nanostructured material [12]. The NANOR® system was driven for more than a year with careful evaluation for energy gain under a variety of conditions, including during the January, 2012 IAP MIT Course on CF/LANR, and later during a long term low-power open demonstration at MIT which ran from Jan. 30, 2012 through mid-May 2012 [12,13]. The NANOR®-type preloaded LANR device openly demonstrated clear cut energy gain and features including its convenient size and its superior handling properties. Over weeks, the NANOR®-type LANR device demonstrated reproducible, controllable, energy gain (COP) which ranged generally from 5 to 16 (e.g. 14.1 (∼1412%) while the MIT IAP course was ongoing [13]).

2.4. Methods – electronic properties of nanomaterials

Close up, in ZrO_2–PdD LANR/CF nanostructured materials, the lattice of Pd is expanded by Zr, and less so, by the H and D. In addition, there are other major changes secondary to the oxidation of the Zr. Some are electrical and very important. The nanostructured material is a composite distribution of nanostructured ferromagnetic “islands” separated among a vast dielectric zirconia “ocean”. The dielectric zirconia embeds uncountable numbers of nanostructured metal ternary alloy islands of the material containing now PdD. Electrically, the response of the CF/LANR nanostructured material is complex and characterized by complicated polarization/transconduction phenomena including an “avalanche effect” (transconduction electrical breakdown) which has a critical role in excess heat generation [9,12]. This occurs because the zirconia dielectric matrix is insulating at low voltage and it keeps the nanoscale metal islands electrically separated. We previously reported sudden changes of, and generally large, electrical impedances of such NANOR®-type devices containing nanostructured materials [9,12]. Several were ∼3 MΩ when lower voltages were applied, but then as the voltage was increased to ∼24 V, the impedance suddenly decreased to very low values. It was shown theoretically that this sudden reduction can be attributed to an “avalanche effect” that is typical of the current–voltage behavior that occurs in Zener diodes. Control and avoidance of low-threshold breakdown of states, the quenching tendencies of nanostructured materials, surmounting their extremely high electrical resistances and their complicated polarization/transconduction phenomena including said “avalanche effect” has a critical role in excess heat. Great difficulties had to be surmounted including assembly of apomaterials of very high electrical resistivity (impedance), as high as 300 GΩ, creating several serious problems. Therefore, a proprietary controlling system was used. This was designed with a complementary, surrounding calorimeter and a unique driving system whose design, autonomy, and interconnection implementations in conjunction with the NANOR®, have made portability of the system to MIT, and elsewhere, possible. The proprietary microprocessor controlled system semiquantitatively examines and drives the NANOR, examining it for heat-production activity, linearity, time-invariance, and even the impact of additives and applied fields.

The LANR preloaded, stabilized NANOR®s were driven by a high DC voltage circuit up to 1000^+ volts rail voltage. The duty cycle was split with half going to a control portion consisting of a carefully controlled electrical DC pulse into an ohmic resistor which was used to thermally calibrate the calorimeter [12].

2.5. Methods – Data acquisition

Data acquisition (DAQ) was taken from voltage, current, temperatures at multiple sites of the solution, and outside of the cell, and even as a 4-terminal measurement of the NANOR’s internal electrical conductivity [12,14]. Data acquisition sampling is at data rates of 0.20–1 Hz, with 24+ bit resolution; voltage accuracy of $0.015^{\pm 0.005}$ V, temperature accuracy <0.6°C). All connections are isolated when possible, including where possible with Keithley electrometers, or their equivalent, for computer isolation. The noise power of the calorimeter is in the range of ∼1–30 mW. The noise power of the Keithley current sources is generally ∼10 nW.

2.6. Methods – power and energy considerations

Input power is defined as $V \times I$. There is no thermoneutral correction in denominator. Therefore, the observed power is a lower limit. The instantaneous power gain (power amplification factor (non-dimensional)) is defined as $P_{\text{out}}/P_{\text{in}}$. The energy is calibrated by at least one electrical joule control (ohmic resistor) used frequently, and with time integration for additional validation. The excess energy is defined as $(P_{\text{output}} - P_{\text{input}}) \times$ time.

2.7. Methods – calorimetry

The amount of output energy (and therefore, both power, and energy, gain) is determined from the heat released producing a temperature rise, which is then compared to the input energy. Observed signals are determined by parallel diagnostics including thermometry, focused heat flow measurement, and isoperibolic calorimetry, and then semiquantitively repeatedly calibrated by an ohmic (thermal) control located next to the NANOR® [12].

The output of the NANOR® is compared to the output of the precisely-driven ohmic control. The instantaneous power gain is kinematically determined by the ratio of the input power normalized temperature increase to the input electrical power (P_{in}), called by the symbol 'HE/P_{in}' referring to the increase of temperature (ΔT) divided by the input electrical power. Also, the output of the NANOR® ΔT is independently derived by kinematically evaluating the heat flow, using the ratio of the input power normalized heat flow to the input electrical power (P_{in}), called by the symbol 'HF/P_{in}' referring to the heat flow (HF) divided by the input electrical power. The third method is examination by calorimetry, calibrated by the thermal ohmic control and thermal waveform reconstruction, and confirmed by long-term time integration. These three methods of verification are pooled to derive very useful information, including the energy produced ("excess energy") and sample activity. The result is heat measurement of this preloaded NANOR®-type LANR three ways ending in calorimetry, input-power-normalized ΔT ($\mathrm{d}T/P_{\text{in}}$), and input power normalized heat ($\mathrm{HF/P_{in}}$) [10].

2.8. Methods – setup

The CR-39 chips in this study were adjacent to, and were exposed to, a NANOR®, driven as a CF/LANR device Figs. 1a and 3). There was no pre-exposure of the chips to either O_2 or CO. A sample of chips had been exposed, on one corner, to a known alpha source, to ascertain that those induced tracts look consistent with expectations, confirming sensitivity and response. The track etch rate, used later after exposure, was determined from the known energy alpha track diameters (here, ^{241}Am, at ~5.4 MeV less 256 keV lost traversing the oxide protective layer (e.g. Fig. 4b)). The resultant track diameters were, at their maximum, ca. 5–10 μm.

The entire setup was driven autonomously for several days to minimize exogenous irradiation of the chips. During LANR exposure, three CR-39 chips were used at different distances, and one was placed directly over the NANOR® during the irradiation sequence over several days. One CR-39 was partially shielded by several millimeters of aluminum within the chamber.

2.9. Methods – difficulties of working with CR-39

Many of the problems which exist in CR-39 analysis are partially surmounted here. These include relative insensitivity (which requires irradiation over long times), difficulty in resolving precise moieties, the need for electronic equilibrium including buildup (rarely considered), the possible interference by oxygen radicals generated near electrodes and by recombinant materials, heterogeneity over the CR-39, as well as a distribution including data recorded at different depths, and other various types of induced damage to the irradiated CR-39.

Therefore, for this experiment, long irradiation times were used (several days), buildup was achieved in part by the NANOR®s cylindrical shell, electrical insulation was made from all electrodes, and the active LANR nanomaterial was dry with the detectors positioned over the potential emitter. After sectioning the image of the processed plate, the heterogeneity was used to image the device. Because there is information at a variety of levels (i.e. important information lies deep in the irradiated CR-39 chip), a system was engineered to extract this which will be a subject of a future paper. This permitted examination of the irradiated chip below additional "noise" secondary to irregular surfaces and changes wrought by the etching and handling of the chip.

2.10. Activity of the NANOR during monitoring

The driven NANOR did show excess energy during the experiment [15]. An M-NANOR® was used to maximize the likelihood of seeing some type of emitted output.

2.11. Quantifying the irradiated CR-39 chip

After the experiment, etching was performed using 6.5 Mol NaOH at 65°C for 8 h by Dr. Mosier-Boss. The surface noise was minimized by standard etching protocol to remove ∼6–10 μm from the CR-39 surfaces. The etch time created a distribution of maximum track diameters of circa ∼5–10 μm.

Examination of the processed CR-39 chips was done by optically sectioning each chip into 24 sectors away from the edges to remove handling errors. Large circular characteristic deep tracks, and paired large tracks, were counted. Counts were done by conventional optical microscopy and with side imaging which separates out surface noise from deeper tracks, and with a proprietary system which separates out surface noise from deeper tracks. The goal was to glean the information which lies deep in the chip below what appears to be a significant amount of "noise" secondary to irregular surfaces.

Figure 3. (a) (*left*) A look into the calorimeter which, for the photograph, has been stripped of thermal materials and probes to show the physical arrangement of the chips. For this image to show the location, all thermal ballast, addition thermal sensors, flow sensors, and addition insulation (both thermal and electrical) were removed. Shown are the NANOR® (beneath chip ′23, at the active site marked at #92, and the nearby chip, ′21, at site #61, which was partially shielded by aluminum. The NANOR is shown below the chip, with the darkened black region (site #92) believed to be the active area at the time. The CR-39 chip was placed above the NANOR, and then thermal materials and probes replaced before the experimental run. (b) (*right*) The three CR-39 chips with their ID numbers, hence forth ′23,′ 21, and ′25 (left in the lab notebook).

3. Results

3.1. Falloff with distance of irradiation of CR-39 chips

The collected, treated, examined chips did show incremental change, consistent with LANR activity, after they were scored (Figs. 4a and 5a,b). There was a fall-off in distance from the operating system (Figs. 5 and 6a).

3.2. Imaging of CCR-39 chips

For this system at this power level, the quantitative amount is measurable, and can give a spatial image (Figs. 1 and 6) if long periods of time are permitted in conjunction with control chips. This combination is used to remove the impact of exogenous sources of CR-39 irradiation, such as from environmental ^{40}K, environmental alphas, and spallation neutrons from irregularly irregular cosmic rays.

Large tracks were the most effective for imaging. Smaller and mid-sized tracks appear to be useful for measuring fall off of the chip irradiation as a function of distance.

3.3. Imaging of a CR-39 chip by an LANR component

Most interestingly, the CR-39 over the device had a final regional count post as shown in the figures below. Twenty-four pixels were used. Pixel by pixel, counts were made. In the figures below, the spatial homology is preserved except for rotation so that the back rows can be seen. It has essentially imaged the active CF/LANR device at very low resolution. The scalar count of the largest and paired tracks over the pixels, as we have done previously with positron

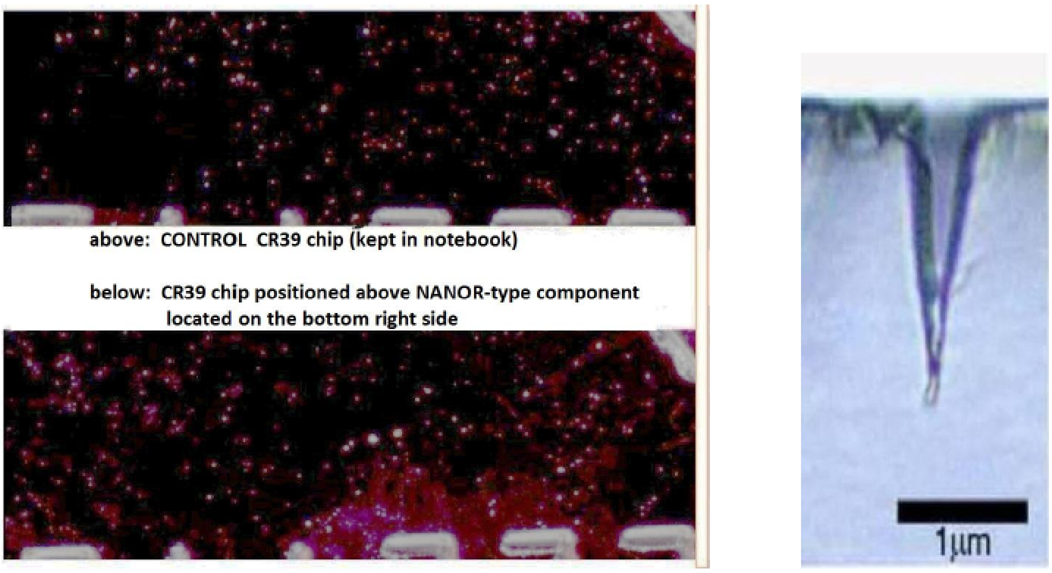

Figure 4. (a) (*left*) Actual images of two of the CR-39 chips (control kept in the notebook (*top*), and the one above the active NANOR (*bottom*). The NANOR was located on the bottom right. For this printing, there has been substantial image processing to brighten the image which would otherwise be too dark. The circles are the tracks seen in Fig. 4b in cross-section. (b) (*right*) Viewed from the side, an alpha track after etching on a CR-39 chip (after Yoshioka et al. [16]).

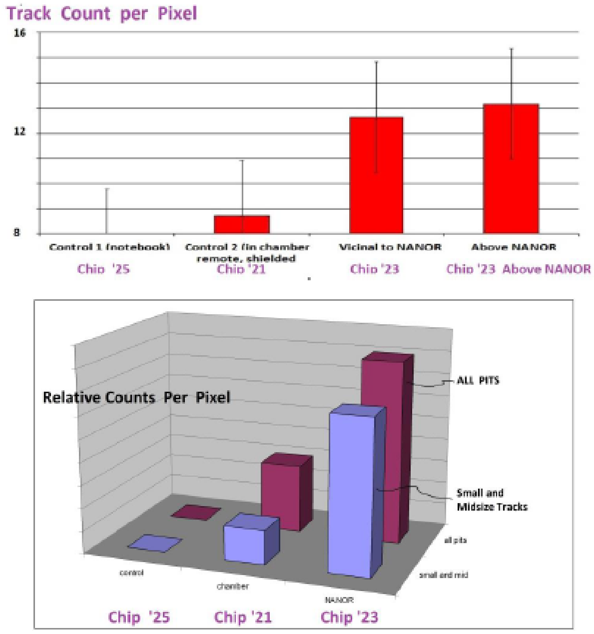

Figure 5. (a) (*top*) Histogram of small and medium sized circular defect densities (number per pixel) in the CR-39 chips which were located at a control location (notebook), in the chamber away from the NANOR®-type CF/LANR component and partially shielded by aluminum, and over the entire CR-39 chip covering the NANOR and nearby volume (defined 'vicinal'), as well as the area only directly above the NANOR. The error bars are 1 SD. (b) (*bottom*) Qualitative histogram of small and medium sized circular defects (blue) and all tracks (maroon) in the CR-39 chips. The counts are normalized to the control chip which was in the notebook .

emission tomography of tumors [17], reveals an "image" of the LANR/CF device elicited only after etching the CR-39 to derive the information "written" thereon.

4. Conclusions

4.1. Interpretation

LANR, as wrought by the NANOR®-type component, is a nuclear process. Furthermore, integrating emission-sensitive elements can, henceforth, be used to image the active site(s) of LANR systems, components, nanostructured materials and devices. It may also be useful for their study and development.

4.2. Questions to be answered

How much resolution can be obtained? How can it be offset with duty cycle? Can separate OOP manifolds now be measured for output and imaging? Do they occur at different locations in the NANOR or other CF/LANR component?

4.3. Possible etiology of the tracks in the CR-39

What is precisely the source of the tracks in the CR-39? Although it is relatively insensitive to gamma rays there could be additional contributions. A. Meulenberg has suggested that gammas energetic enough to create electron–positron

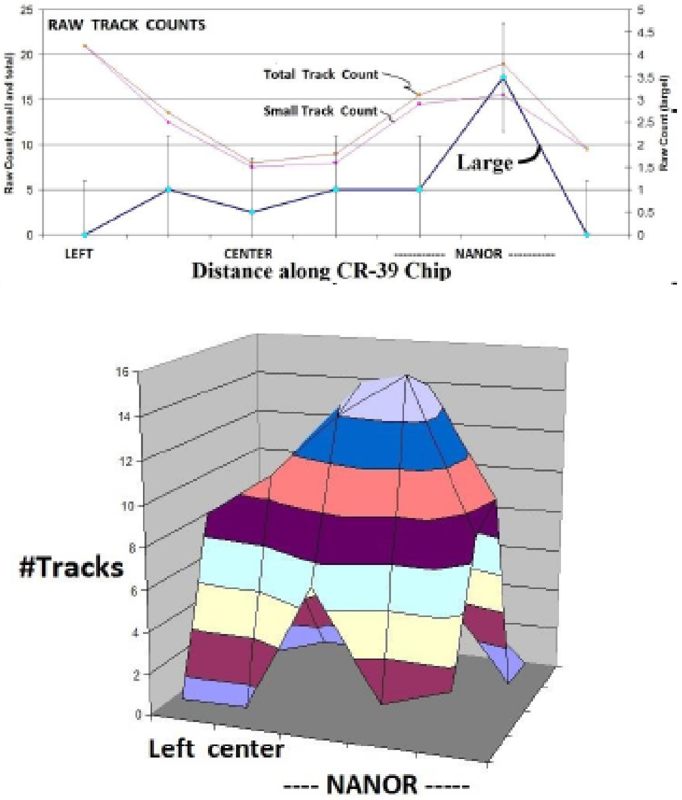

Figure 6. (a) (*top*) The distribution of the density of track counts of small tracks, all tracks, and large tracks as a function of location along a single chip place above the NANOR and the region around it. The NANOR was at the lower left of the flat chip. Importantly, it can be seen that large tracks may be the most useful in imaging CF/LANR systems. (b) (*bottom*) The distribution of density of the large tracks, pixel by pixel, is made over the surface of the CR-39 chip which covered the NANOR and its nearby region, as the NANOR ran continuously over days. Shown is a 3D representation of that large track density count, at this very low resolution pixel number, with the magnitude of the count shown by the height looking up the *y*-axis. With the same information, Fig. 1 shows the result of rotating this distribution and it shows how it looks directly down that *y*-axis. Also, confer Fig. 1b which shows the distribution from the vertical axis perpendicular to the long axis of the chip.

pairs might give a knock-on proton sufficient energy for a very short ionization path in the CR-39.

P. Mosier Boss and L. Forsley suggest an additional source might be triplet production [7]. In addition, a neutron can transfer half its energy to a proton, creating lengthy tracks. Furthermore, in rare conditions, tritium production has been seen [18,5]. However, tritum is unlikely etiology for three major reasons. First, because of the distance, second because of the very small amount which was ever producible, and third because the OOP manifolds are separate and the He-heat producing OOP manifold was mainly driven [19].

Could the results be due to IR or UV emission? Dr. Stan Szpak (SPAWAR) et al. reported the emission of infrared from LANR codeposition devices [20]. However, they did not use a control or calibration [10]. In 2008, Swartz demonstrated that two controls are needed, including normalization of NIR emission intensities to both non-energized background and to ohmic control areas.

In experiments involving a variety of LANR metamaterial spiral-wound and other Phusor®-type lattice assisted nuclear reaction (LANR) systems, including high impedance palladium [$Pd/D_2O/Pt,Pd/D_2O/Au$], codepositional ($Pd/Pd(OD)_2/Pt$) heavy water, and nickel ($Ni/H_2O_xD_2O_{1-x}/Pt,Ni/H_2O_xD_2O_{1-x}/Au$) light water Phusor®-type LANR devices. Swartz demonstrated that the emission of near-IR from the electrodes coupled with LANR operation is only observed when active electrodes operated at their optimal operating point, and that there was a linkage of excess power gain and heat flow with simultaneous NT-NIR emission [10].

Most importantly, NT-NIR is coupled and specific to the LANR devices' excess heat production and not its physical temperature. However, CR-39 is not effected by this low energy electromagnetic radiation unless sufficient to melt the material. Although that was not the case, high energy penetrating emission linked to CF/LANR excess heat, and transitions was the case, here.

Acknowledgements

The authors would like to thank Dr. Alex Frank, Alan Weinberg, Allen Swartz, Larry Forsley, Dr. Frank Gordon, Brian Ahern, Jeff Driscoll, Linda Hammond, Charles Entenmann, and Andrew Meulenberg for their suggestions. This effort was supported by JET Energy Inc. and New Energy Foundation. NANOR® and PHUSOR® are registered trademarks of JET Energy, Incorporated. NANOR®-technology, and PHUSOR®-technology are protected by U.S. Patents D596724, D413659 and several other patents pending.

References

[1] Radicati, L.A., *Phys. Rev*. **85** (1952) 962.

[2] Szydilik, P.P., Shell-model analysis of the excited states of ^{4}He, *Phys. Rev. C* **1** (1970) 1.

[3] Swartz, Mitchell M., Survey of the observed excess energy and emissions in lattice assisted nuclear reactions, *J. Scientific Exploration* **23**(4) (2009) 419–436.

[4] Miles, M. et al., Correlation of excess power and helium production during D_2O and H_2O electrolysis using palladium cathodes, *J. Electroanal. Chem.* **346** (1993) 99–117.

[5] Srinivasan, M. et al., Observation of tritium in gas/plasma loaded titanium samples. in anomalous nuclear effects in deuterium/solid systems, *AIP Conference Proceedings 228*, 1990. Brigham Young Univ., Provo, UT: American Institute of Physics, New York.

[6] Li, X.Z. et al., The precursor of cold fusion phenomenon in deuterium/solid systems, *AIP Conference Proceedings 228*, Brigham Young University, Provo, UT, New York, 1990.

[7] Mosier-Boss, P.A., Szpak, S., Gordon, F.E. and Forsley, L.P.G., Use of CR-39 in Pd/D co-deposition experiments, *Euro. Phys. J.–Appl. Phys.* **40** (2007) 293–303.

[8] Swartz, Mitchell R., Incremental emission from ZrO_2–Pd–D nanostructured CF/LANR quantum electronic component, *ICCF-18*, Missouri, USA, 2013.

[9] Swartz, Mitchell R., LANR nanostructures and metamaterials driven at their optimal operating point, *LANR/LENR Sourcebook*, Vol. 3, October 21, 2011.

[10] Swartz, Mitchell R., G. Verner and A. Weinberg, Non-thermal near-ir emission from high impedance and codeposition LANR devices, *Proc. ICCF-14*, Washington DC, USA, ISBN: 978-0-578-06694-3, 343, (2010).

[11] Arata, Y. and Y.C. Zhang, Observation of anomalous heat release and helium-4 production from highly deuterated palladium fine particles, *Jpn. J. Appl. Phys.* **38** (1999) L774–L776, Part 2, No. 7A, 1 July (1999).

[12] Swartz, Mitchell R., G. Verner and J. Tolleson, Energy gain from preloaded ZrO_2–PdNi–D nanostructured CF/LANR quantum electronic components, *ICCF17*, Daejeon, Korea, 2012.

[13] Swartz, Mitchell R. and P.L.Hagelstein, Demonstration of energy gain from a preloaded ZrO_2–PdD nanostructured CF/LANR quantum electronic device at MIT, *ICCF17*, Daejeon, Korea, 2012.

[14] Swartz, Mitchell R., Excess power gain using high impedance and codepositional LANR devices monitored by calorimetry, heat flow, and paired stirling engines, *Proc. ICCF-14*, Washington DC, USA, ISBN: 978-0-578-06694-3, 123, (2010)).

[15] Swartz, Mitchell R., P.L. Hagelstein et al., Amplification and restoration of energy gain using fractionated magnetic fields on ZrO_2–PdD nanostructured CF/LANR quantum electronic component, *ICCF-18*, Missouri, USA, 2013.

[16] I. Yoshioka, I Tsuruta, H. Iwano and I Danhara, *NucI. Instr. Method. Phys. Res. A* **555** (2005) 386.

[17] Kairento, A-E., G. Brownell, D. Elmaleh and Swartz, M.R., Comparative Measurement of Regional Blood Flow, oxygen and glucose utilisation in soft tissue tumour of rabbit with positron imaging, *Br. J. Radiology* **58** (1985) 637–643. .

[18] Iyengar, P.K. and M. Srinivasan, Overview of BARC studies in cold fusion, in *The First Annual Conference on Cold Fusion*, University of Utah Research Park, Salt Lake City, Utah: National Cold Fusion Institute, 1990.

[19] Swartz, Mitchell R., Optimal operating point manifolds in active, loaded palladium linked to three distinct physical regions, *Proc. ICCF-14*, Washington DC, USA, ISBN: 978-0-578-06694-3, 639, (2010).

[20] Swartz, Mitchell R., Codeposition of palladium and deuterium, *Fusion Technol.* **32** (1997) 126–130.

J. Condensed Matter Nucl. Sci. 15 (2015) 92–101

Research Article

Incremental High Energy Emission from a ZrO_2–PdD Nanostructured Quantum Electronic Component CF/LANR

Mitchell Swartz*

JET Energy, Inc., Wellesley Hills, MA 0248, USA

Abstract

In situ measurement for possible incremental penetrating ionizing radiation output from an activated nanocomposite ZrO_2–PdD CF/LANR component revealed a barely detectable, incremental emission when there was significant energy gain. The autonomous driver minimized background radiobiological interference. This effort demonstrates that CF/LANR is relatively safe, with penetrating ionizing emissions, at these power levels, of lower biological impact than typical background sources.

Keywords: High energy CF/LANR emission, Preloaded CF/LANR component, quantum electronic cold fusion component, ZrO_2–PdD CF/LANR nanostructure

---

1. Background

1.1. Introduction

Lattice assisted nuclear reactions (LANR) use hydrogen-loaded alloys to create heat and other reactions with an energy density 'off the chart' [1,2]. They are an energy multiplier because the energy density of LANR reactions is ten million times that of gasoline. In the case of LANR, there can rarely occur, in a lattice under special conditions, the fusion of two heavy hydrogen nuclei to form a helium nucleus at near room temperature. LANR will play a critical role in many future technologies with potential revolutionary applications to all energy issues – robotics, transportation, electricity production, artificial internal organs, and space travel [1]. So for quality assurance it is important to ascertain the safety of these systems (Fig. 1) in order to evaluate risk/benefit and possible shielding and occupancy issues.

---

*E-mail: mica@theworld.com

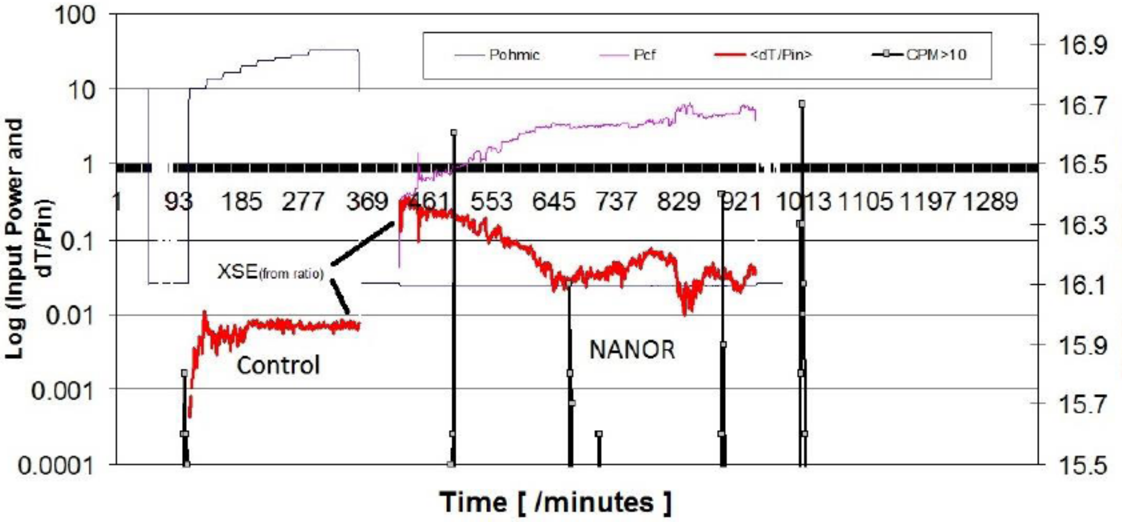

Figure 1. Input power, calorimetry, and gamma measurements of background, thermal control and a CF/LANR system – Shown are the Input Power in milliwatts and Resulting delta-Temperature normalized to the electrical input power (presented as the logarithm on the left hand y-axis), and the 10 min averaged output from the CPM (right hand y-axis) Geiger Müller tube (СИ29БГ tube and TTL serial converter), which was vicinal to a self-contained CF/LANR quantum electronic component containing active preloaded ZrO_2–PdD nanostructured material at its core. The curves are shown as a function of time in minutes ("Counts"). The activity (excess power gain) of the active CF/LANR system is obtained from the ratio of dT/P_{in}(NANOR) to dT/P_{in}(Control)).

1.2. Penetrating radiation and particle emissions

Although LANR is a nuclear process, gamma emission is actually forbidden, both in CF/LANR and in hot fusion as well. For hot fusion, the forbidden restriction is "lifted" by the high temperature, and so penetrating gamma emission is really observed. However at lower temperature, the equations indicated a decrease of forward directed penetrating radiation [3,4] which is observed, and so for cold fusion, (excess) heat and ^{4}He are the usual products, and only rarely have charged particles, gamma radiation, and neutrons also been detected [1]. Diligent efforts with autoradiography and CR-39 have heralded the recording of rare, high energy penetrating radiation emitted from cold fusion (LANR) materials in their active state; in the past usually confirmed by autoradiography or CR-39 chips over periods of days. Miles (China Lake, USN) and M. Srinivasan (Bhabha Atomic Research Center (BARC)) independently used dental X-ray film autoradiography on the outside of the cells which revealed fogging heralding low energy X-ray production [5,6]. M. Srinivasan (BARC) reported neutrons in 1989 as the current increased beyond 100 amperes, neutron signals, in bursts, resulted in 6 of 11 cells [7]. Thereafter, energetic charged particles were detected by CR-39 in gas LANR systems [8] and in aqueous codeposition systems [8]. X.Z. Li (Tsinghua U) first used CR-39 in his 1990 Pd gas loading experiments to detect energetic charged particles [9]. Forsley and Mosier-Boss (SPAWAR) reported CR-39 tracks which indicate possible neutron interactions, including carbon shattering. Some tracks herald D-D and DT reactions. Etching suggests uniformity in the 2–8 MeV range. The triple tracks, found in ∼5–10% of their experiments, indicate energetic neutrons having shattered a carbon atom. Also observed in LANR systems are post LANR mini-explosions, ionizing radiation, and neutron production, and tritium production. These observations of significant quantities of high energy charged particles, and emissions, in LANR systems, suggests that, although very few investigators have looked with adequate equipment, there is accumulating, near overwhelming, evidence that nuclear reactions in, and assisted by a lattice, are initiated at low energies.

2. Experimental

2.1. Problems

The first problem with quantitation of possible emissions by a detector (Geiger Müller tube, for example) is that very low numbers of neutrons and charged particles appear to be emitted. The second problem is that such penetrating ionizing radiation emissions might be similar to the near infrared (NT-NIR) emissions [10] from active LANR materials which only occur when the CF/LANR devices are active near their optimal operating point (OOP) [11,12]. Third, the output from CF/LANR devices are very low level and can be interfered with by environmental contamination. People with ^{40}K and uranium and thorium in their bodies each contribute ∼0.4 mSv/year. Cosmic rays, radon progeny and terrestrial sources each contribute 0.3, 0.2, and 0.6 per year. Therefore, the only source which could interfere (and irregularly interfere) was removed. A pretested NANOR®-type system was therefore used at a number of input powers [13,14], and it was run autonomously over several weeks.

2.2. Materials

LANR (CF) activated nanocomposite ZrO_2–PdNiD and ZrO_2–PdD CF/LANR quantum electronic components are capable of significant energy gain [13,2]. They are produced in codeposition structures [15] and have been observed producing non-thermal near infrared emissions when active [10], and exhibiting LANR excess heat correlated with the size of the Pd–D nanostructures [15]. Nanostructured materials used in LANR include palladium black [16] in a double structure (DS)-cathode, and today, second and third generation nanostructured ZrO_2–PdD and ZrO_2–PdNiD powders, such as Zr 67% Ni 29% Pd 4% (by weight before the oxidation step). For NANOR®-type LANR devices, the fuel for the nanostructured material resides, ready in the core, and is deuterium (Fig. 2).

The component used here is self-contained, two-terminal NANOR®-type LANR device that features new composition, structure, and superior handling properties enabling portability and transportability. It contains active ZrO_2–PdD nanostructured material loaded with additional D. The deuterons are tightly packed ("highly loaded"). The additional D yields apparent indicated loadings (ratio to Pd) of more than 130% D/Pd, but shallow traps are not ruled out. For simplicity, all of these nanostructured materials in the core, in their range of deuterations, will henceforth simply be

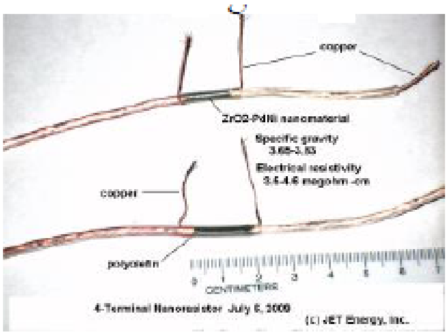

Figure 2. The source of the GM irradiation were NANOR CF/LANR devices. Shown are two terminal NANOR®-type devices containing active ZrO_2–PdD nanostructured material at their core. Used for this study was an M- NANOR®.

referred to as ZrO_2–PdD. The enclosure is tightly fit with the electrodes. It is a long, expensive, arduous effort to prepare these preloaded nanocomposite CF/LANR devices, whose development has required control of their breakdown states and quenching tendencies. The NANOR® component used for this work is a sixth generation CF/LANR device, smaller than 2 cm length, with less than 50 mg of active LANR material. Although small in size, this is actually not *de minimus* because the LANR excess power density was more than 19,500 W/kg of nanostructured material [11,13].

2.3. Methods – electronic properties of nanomaterials

We previously reported sudden changes of, and generally large, electrical resistances of such NANOR®-type devices containing nanostructured materials [13,15].The proprietary microprocessor controlled system semiquantitatively examines and drives the NANOR, examining it for heat-production activity, linearity, time-invariance, and even the impact of additives and applied fields. The LANR preloaded, stabilized NANORs were driven by a high DC voltage circuit up to 1000^+ V rail voltage. The duty cycle was split with half going to a control portion consisting of a carefully controlled electrical DC pulse into an ohmic resistor which was used to thermally calibrate the calorimeter [13, 17–19]. The NANOR® system used had previously been driven for more than a year with careful evaluation for energy gain under a variety of conditions, including during the January, 2012 IAP MIT Course on CF/LANR, and later during a long term low-power open demonstration at MIT which ran from Jan. 30, 2012 through mid-May 2012 [12,14]. The NANOR®-type preloaded LANR device openly demonstrated clear cut energy gain (COP) which ranged generally from 5–16 (e.g. 14.1 ($\sim$1412%) while the MIT IAP course was ongoing, 11). In order to measure the incremental increase of penetrating ionizing radiation output of an active nanocomposite ZrO_2–PdD LANR material, the NANOR was driven at its well-characterized optimal operating point. The system was previously well characterized over many months at MIT.

2.4. Methods – power and energy considerations

Data acquisition was taken from voltage, current, temperatures at multiple sites of the solution, and outside of the cell, and even as a 4-terminal measurement of the NANOR's internal electrical conductivity [13, 19,16–18,11]. Data acquisition sampling was at data rates of 0.20–1 Hz, with 24+ bit resolution; voltage accuracy $0.015^{\pm 0.005}$ V, temperature accuracy <0.6°C. The noise power of the calorimeter is in the range of $\sim$1–30 mW. The noise power of the Keithley current sources is generally $\sim$10 nW. Input power is defined as $V \times I$. There is no thermoneutral correction in denominator. Therefore, the observed power is a lower limit. The instantaneous power gain [power amplification factor (non-dimensional)] is defined as $P_{\text{out}}/P_{\text{in}}$. The energy is calibrated by at least one electrical joule control (ohmic resistor) used frequently, and with time integration for additional validation. The excess energy, when present, is defined as $(P_{\text{output}} - P_{\text{input}}) \times$ time.

The amount of output energy (and therefore, both power, and energy, gain) is determined from the heat released producing a temperature rise, which is then compared to the input energy. Observed signals are determined by parallel diagnostics including thermometry, focused heat flow measurement, and isoperibolic calorimetry, and then semiquantitively repeatedly calibrated by an ohmic (thermal) control located next to the NANOR [10,11,15–17]. The output of the NANOR is compared to the output of the precisely driven ohmic control. The result is heat measurement of this preloaded NANOR®-type LANR three (3) ways ending in calorimetry, input-power-normalized ΔT (dT/P_{in}), and input power normalized heat (HF/P_{in}) [11]. These three methods of verification are pooled to derive very useful information, including the energy produced ("excess energy") and sample activity.

2.5. Methods – ionizing radiation detection

In order to maximize the likelihood of detecting any possible incremental increase of penetrating ionizing radiation output of an active nanocomposite ZrO_2–PdD LANR material, the NANOR® was driven directly next to a vicinal, in situ Geiger–Müller tube, embedded in the calorimeter (Fig. 3a). A second custom DAQ was used. In addition, the tube chosen was a (SI29BG) Russian military tube (also called SI29BG). It is comparatively small and sensitive to both β and γ ionizing radiation. Here, the military standard СИ29БГ Geiger–Müller tube was chosen over the more popular СБМ-20 (SBM-20) tube because of the shorter minimum Dead Time of 95 μs, and four times greater sensitivity. The ÑÈ29ÁÃ has a Gamma Sensitivity to ^{60}Co (cps/mR/h) of 44–52. Therefore, the conversion factor

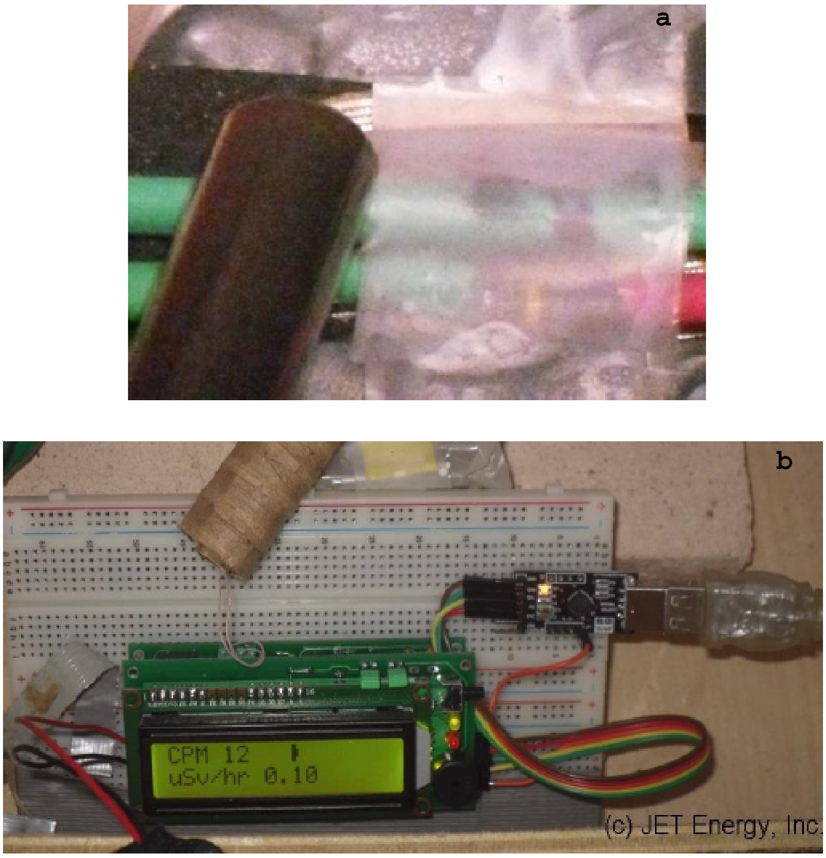

Figure 3. (a) Shown is the central region within the calorimeter. The horizontally directed NANOR-type quantum electronic component, containing active ZrO_2–PdD nanostructured material, is located within the upper green cylinder. The Geiger Müller tube is shifted off of the active site (rectangular appearing black area located just above the ohmic resistor (to the right of its yellow-colored band;, and off to the right from the center) and shown moved about twice its width to the left from its normal location for the photograph. The Geiger–Müller tube is just outside of the tape and to left for the photograph. In addition, the holders, thermal ballasts, thermal conduction materials, vicinal detectors, and electrical insulation, have been removed to more clearly show this. (b) The modified Arduino delivered 500–700 V to the GM tube while also recording GM output, integrating that to CPM, and a 10 min running average of CPM, and converting to microSv/h. The output was delivering (including tube voltage) to the USB to the second DAQ, and to a charlieplexed digital output over the Arduino (shown with background levels).

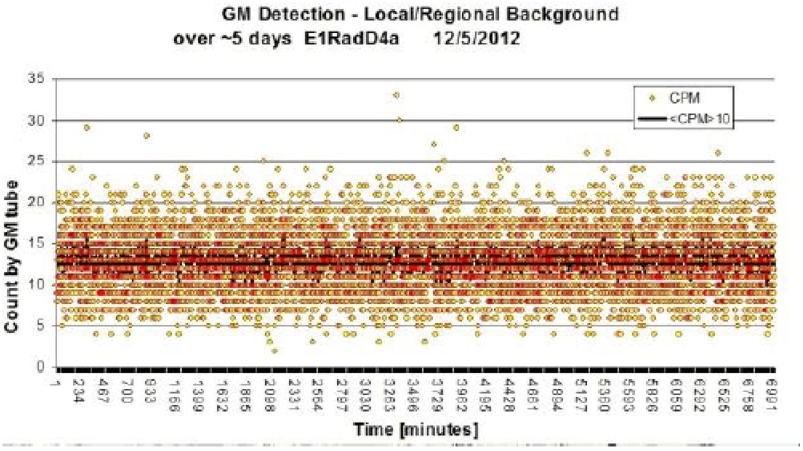

Figure 4. A five-day collection of background data. Shown is the 10 min moving average of the CPM, $\langle$CPM$\rangle$10, as a function of time (Fig. 5). For this long measurement, the LANR NANOR, the ohmic control, and the electrical driving system was in place but remained electrically off, for the entire time.

used was 123.147 cpm/μSv/h. A TTL serial converter based on SILABS CP2102 chip was necessary to connect the GM board to PC. The Geiger Müller system was calibrated both for microprocessor function and detection sensitivity.

In order to minimize the impact of environmental contamination, we used very long, autonomously-run, times for the measurements. An ATMEGA328 autonomous system was used to remove interaction with, and contamination from, ^{40}K, because humans are a major cause of incident background radiation. Also used were an Arduino [ATMEGA328 processor] driven/controlled Geiger counter dosimeter, with confirming LCD shield tube (simultaneously displaying the Count Per Minute (CPM) and equivalent dose rate of radiation in μSv/h) and USB connection to a second logging computation system. The Arduino sketch was designed to record to computer via serial port the counter outputs CPM, μSv/h and the voltage across the tube, as data in 1 min intervals. The GM count was taken each minute, and the 10 min moving average of that is designated $\langle$CPM$\rangle$10. In order to minimize the likelihood of cross-talk and other sources of error, the Geiger–Müller in situ dosimeter's computer and power connections were separate from the normal DAQ and driving circuits. The Geiger detector and ATMEGA328 required 5.5 and 16 mA, respectively, for a total of 22 mA. Because the verification LCD backlight, when connected pushed the total current required to 41 mA, therefore a separate computer system was used. Recalibration of the calorimetry was performed prior to the experiment in a control, and normal CF/LANR sequence. Thereafter, the NANOR drive system (NANOR® EXPLORERTM) and the vicinal Geiger–Müller tube СИ29БГ(SI29BG) detector operated over months through a series of background, thermal controls, and LANR drive sequences, and LANR components.

3. Results

3.1. Background

First, we measured the background over several weeks. Shown below is 5 days of that control (Figs. 4 and 5). The long-term time-averaged detected background was $12.68^{\pm 3.40}$ nanosieverts/h.

3.2. Derivation of "High Pass Filter"

Then, a high pass filter was used on the counts per minute, especially the 10 min average to maximize detection. An example is in Fig. 5. Examination revealed the following: For example, $\langle \mathrm{CPM} \rangle 10$ only went above 16.0 thrice in 5 days, and $\langle \mathrm{CPM} \rangle 10$ never went above 16.4. However, during the shorter time that the NANOR was driven, $\langle \mathrm{CPM} \rangle 10$ did exceed that level four times, and two of those events were higher than 16.5.

3.3. Incremental increase from CF/LANR

Next, we determined the incremental increase from the CF/LANR device. The long-term time-averaged emission was determined by subtracting the detected background from the observed output when the device was active. This became $13.11^{\pm 3.72} - 12.68^{\pm 3.40}$ with the CF/LANR component in peak active mode. There was a maximum (peak incremental difference observed of ~2.5 nanosieverts/h. This should be compared with the background irradiation from internal irradiation sources within every person, mainly from internal ^{40}K and uranium and thorium, which contributes ~46 nanosieverts/h.

3.4. Irregularly irregular emissions

This method of analysis with a high pass filter derived from the running 10 min average of the CPM by a Geiger–Müller tube located vicinal to the self-contained NANOR®-type CF/LANR quantum electronic component, containing active preloaded $\mathrm{ZrO_2}$–PdD nanostructured material at its core was used with isoperibolic calorimetry, calibrated by ohmic controls. Shown in Figs. 1 and 6 are the results, including one which occurred during some additional very low level thorium irradiation. In the figures below, the 10 min average CPM is shown on the right hand y-axis. Three types of regions are shown including background, thermal ohmic heating (labeled "control"), and the active LANR device (labeled "NANOR") which is operated at a variety of electrical input powers, as was the thermal ohmic control. (The 2% thoriated electrodes, discussed below in a separate experiment, were not present here.) For clarity, the periods without any input are not labeled.

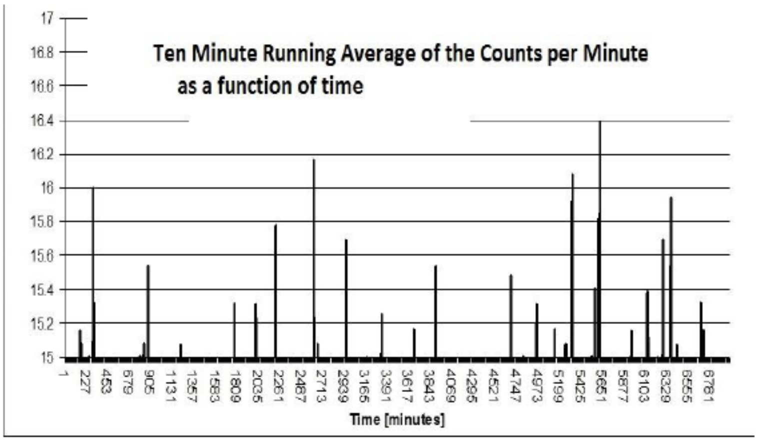

Figure 5. A five-day collection of "high-pass" background data. Shown is $\langle \mathrm{CPM} \rangle 10$, as a function of time, but only shown are those events which exceeded $\langle \mathrm{CPM} \rangle 10$ greater than 15. In the following, a high pass filter was used which only "passes" the $\langle \mathrm{CPM} \rangle 10$ which are greater than ~15.5.

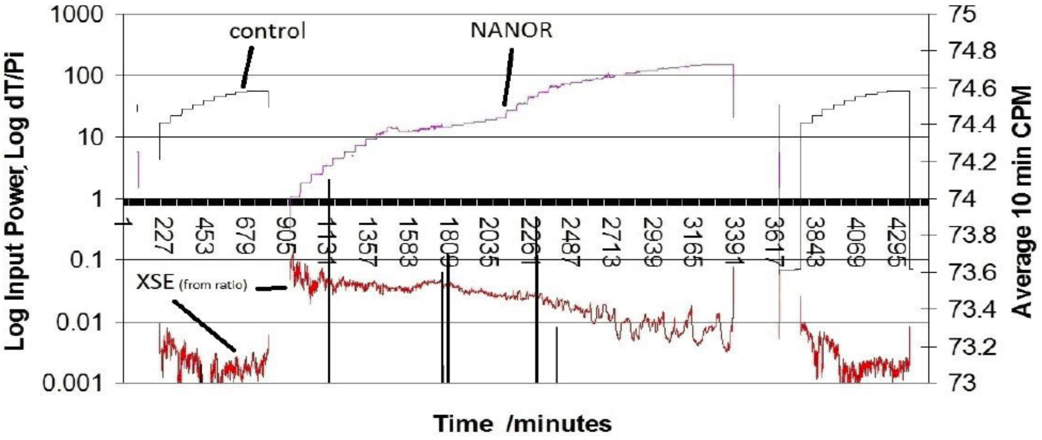

Figure 6. Calorimetry and gamma measurements of background, thermal control and a CF/LANR system. with a 2% Thoriated Rod nearby – Shown are the Input Power in milliwatts, Resulting delta-Temperature rise which is input power normalized [as the logarithm on the left], and the 10 minute average output count by a Geiger Müller tube, which was located vicinal to the self-contained CF/LANR quantum electronic component containing active preloaded ZrO_2–PdD nanostructured material at its core. The activity of the active CF/LANR system is XSE (obtained from the ratio of dT/P_{in} (CF/LANR) to dT/P_{in} (control)).

Attention is directed to the observation of very rare, irregularly spaced, distinguishing emissions were observed with LANR compared to background, and compared to the ohmic thermal control). These are distinguishing emissions of penetrating radiation or other emissions (e.g. gammas) observed with LANR NANORs driven at their OOP compared to background and compared to the ohmic thermal control. These peak bursts are in the range of ~24.6 nanosieverts/h momentarily during these emissions, which are infrequent and irregularly irregular. Correcting for the irregular and infrequent nature of the emission, this time averages out to become an incremental output of circa ~0.14 nanosieverts/h for this functioning demonstration NANOR device. Considering the electrical input power, this time averages out to become circa ~8.5 nanosieverts/h/W incremental output penetrating radiation for this functioning demonstration device very close up to the NANOR without any shielding.

3.5. Impact of additional thorium irradiation

In order to determine if additional irradiation by ionizing irradiation to the NANOR might increase or change the output of the NANOR®-type LANR component (Fig. 2) and as an additional control, a series of long term runs over weeks were also made with several vicinal 2% thoriated tungsten electrodes (*Sylvania*; not connected to any power source). This active NANOR®-related differential even occurred during the thorium irradiation examination.

In an experimental run similar to that shown in Fig. 1, there was for this run, extending over a long time, a continuous background irradiation of the LANR device (during background, control, and its active state) from 2% thoriated-tungsten electrodes which were not electrically connected to anything. This is shown in Fig. 6. Attention is directed to the observation of, again, very rare, irregularly spaced, distinguishing emissions were observed with LANR compared to background, and compared to the ohmic thermal control.".

Additionally, note that there was no increase in excess heat OR incremental penetrating output observed for the LANR system by the additional irradiation from the nearby 2% thoriated electrodes. There was still a NANOR®-related differential in output which persisted during the thorium irradiation, even with the much higher CPM secondary to the additional thorium irradiation (due to the alpha and other decays).

4. Conclusion

4.1. Interpretation

There is an incremental outputs associated with CF/LANR at the active point of the OOP manifold for very brief and irregular times. These are not seen as frequently, if at all, during the control sequences involving background. These results are not from a cosmic ray shower because similar groups of these bursts did not occur during background runs (Fig. 3), nor during thermal controls. These results demonstrate that the incremental output of gamma by this CF/LANR device heralds a nuclear reaction controlled by applied electric field intensities using preloaded deuterides.

Further corroborating that this is a real effect, attention is directed to the fact that when the excess heat disappeared, so did the bursts. Of special note is the fact that the bursts did occur sometimes immediately after the calibration pulse, or the run, of the NANOR.

In conclusion, this is further confirmation that LANR is indeed an important nuclear process. The maximum burst output, during one of the irregularly irregular peaks and very infrequent, is, for this functioning demonstration device, $\sim$ 2.7 μsieverts/h-W. This may be the result of this being an M-NANOR® rather than a conventional NANOR® component since new CF/LANR pathways appear to be available through the second OOP manifold.

In addition, considering the electrical input power, but also correcting for the irregular and infrequent nature of the emission, this time average then becomes circa ~8.5 nanosieverts/h-W incremental output in penetrating radiation emissions for this functioning demonstration device.

Thus, for this system and electrical drive, the emitted radiation is quantitatively measurable, biologically insignificant, and therefore safe. The output should be compared with the background irradiation from people, each of which with their internal ^{40}K and uranium and thorium in their bodies, emits $\sim$ 46 nanosieverts/h. In retrospect, it was fortunate and necessary to have made the equipment autonomous given these findings.

4.2. Future plans

What remains to be determined is the exact nature of the source of the incremental counts and its energy spectrum. These peaks are most likely gamma emission because GM tubes are relatively insensitive to neutrons, however, the GM walls and nearby materials could be a source of additional collision-created ions capable of registering a pulse from neutrons (A. Meulenberg). Some amount of consideration of occupancy, shielding, etc. should now be considered for any very high power CF/LANR device.

5. Acknowledgements

The author is especially grateful to Gayle Verner and Jeffrey Tolleson for their meticulous help in the manuscript and in several idea developments, and to Alex Frank, Peter Hagelstein, Brian Ahern, Jeff Driscoll, Larry Forsley, Pamela Mosier-Boss, Frank Gordon, David Nagel, Robert Smith, Allen Swartz, Charles Entenmann, Val Zavarzin, Ron Kita, Andrew Meulenberg, Ed Pell, and JET Energy and New Energy Foundation for support. NANOR® and PHUSOR® are registered trademarks of JET Energy, Incorporated. NANOR®-technology, and PHUSOR®-technology, and other discussed IP herein, are protected by U.S. Patents D596724, D413659 and several other patents pending.

Bibliography

[1] Swartz, Mitchell R., Survey of the observed excess energy and emissions in lattice assisted nuclear reactions, *J. Scientific Exploration* **23**(4) (2009) 419–436.

[2] Swartz, Mitchell R., P. Hagelstein et al., Amplification and restoration of energy gain using fractionated magnetic fields on ZrO_2–PdD nanostructured CF/LANR quantum electronic component, *Proc. ICCF-18*, Missouri, USA, 2013.

[3] Swartz, Mitchell R., Phusons in nuclear reactions in solids, *Fusion Technol.* **31** (1997) 228–236.

[4] Swartz, Mitchell R. and G. Verner, Bremsstrahlung in hot and cold fusion, *J. New Energy* **3**(4) (1999) 90–101.

[5] Iyengar, P.K. and M. Srinivasan, Overview of BARC studies in cold fusion. in the first annual conference on cold fusion, University of Utah Research Park, Salt Lake City, Utah, National Cold Fusion Institute, 1990.

[6] Miles, M. et al., Correlation of excess power and helium production during D_2O and H_2O electrolysis using palladium cathodes, *J. Electroanal. Chem.* **346** (1993) 99–117.

[7] Srinivasan, M. et al., Observation of tritium in gas/plasma loaded titanium samples. in anomalous nuclear effects in deuterium/solid systems, *AIP Conferencpe Proceedings 228*, American Institute of Physics, New York, 1990.

[8] Li, X.Z. et al., The precursor of cold fusion phenomenon in deuterium/solid systems. in anomalous nuclear effects in deuterium/solid systems, *In AIP Conference Proceedings 228*, American Institute of Physics, New York, 1990.

[9] Mosier-Boss, P.A., Szpak, S., Gordon, F.E. and Forsley, L.P.G., Use of CR-39 in Pd/D co-deposition experiments, *Eur. Phys. J.–Appl. Phys.* **40** (2007) 293–303.

[10] Swartz, Mitchell R., G. Verner and A. Weinberg, Non-thermal near-IR emission from high impedance and codeposition LANR devices, *Proc. ICCF-14*, D.J. Nagel and M. Melich (Eds.), Washington DC, USA, ISBN: 978-0-578-06694-3, 343, (2010).

[11] Swartz, Mitchell R., Consistency of the biphasic nature of excess enthalpy in solid state anomalous phenomena with the quasi-1-dimensional model of isotope loading into a material, *Fusion Technol.* **31** (1997) 63–74.

[12] Swartz, Mitchell R., Optimal operating point manifolds in active, loaded palladium linked to threedistinct physical regions, *Proc. ICCF-14*, D.J. Nagel and M. Melich (Eds.), Washington DC, USA, ISBN: 978-0-578-06694-3, 639, (2010).

[13] Swartz, Mitchell R., G. Verner and J. Tolleson, Energy gain from preloaded ZrO2–PdNi–D nanostructured CF/LANR quantum electronic components, *Proc. ICCF-17,* 2012.

[14] Swartz, Mitchell R. and P.L. Hagelstein, Demonstration of energy gain from a preloaded ZrO_2–PdD nanostructured CF/LANR quantum electronic device at MIT, *Proc. ICCF-17,* Daejeon, Korea, 2012.

[15] Swartz, Mitchell R., LANR nanostructures and metamaterials driven at their optimal operating point, *J. Condensed Matter Nucl. Sci.* **6** (2012) 149.

[16] Arata, Y. and Zhang, Y.C., Anomalous production of gaseous ^{4}He at the inside of DS-cathode during D_2-electrolysis, *Proc. of the Japan Academy Series B*, 75, 281; Arata, Y. an Zhang, Y.C. (1999). Observation of anomalous heat release and helium-4 production from highly deuterated fine particles, *Jpn. J. Appl. Phys.* **38**(2) (199) L774; Arata, Y. an Zhang, Y., The establishment of solid nuclear fusion reactor, *J. High Temp. Soc.* **34**(2) (2008) 85.

[17] Swartz, Mitchell R., Can a Pd/D_2O/Pt device be made portable to demonstrate the optimal operating point?, *Condensed Matter Nuclear Science, Proc. ICCF-10*, P.L. Hagelstein and S.R. Chubb (Eds.), Cambridge, MA, USA, World Scientific, NJ, ISBN 981-256-564-6, 29-44; 45-54 (2006).

[18] Swartz, Mitchell R., Excess power gain using high impedance and codepositional LANR devices monitored by calorimetry, heat flow, and paired stirling engines, *Proc. ICCF-14*, D.J. Nagel and M. Melich (Eds.), Washington DC, USA, ISBN: 978-0-578-06694-3, 123, (2010).

[19] Swartz, Mitchell R. and G. Verner, Excess heat from low electrical conductivity heavy water spiral-wound Pd/D_2O/Pt and Pd/D_2O–$PdCl_2$/Pt devices, *Condensed Matter Nuclear Science, Proc. of ICCF-10*, Peter L. Hagelstein and Scott S.R. Chubb (Eds.), Cambridge, MA, USA, World Scientific, NJ, ISBN 981-256-564-6, 29-44; 45-54 (2006).

J. Condensed Matter Nucl. Sci. 15 (2015) 102–105

Research Article

Entrepreneurial Efforts: Cold Fusion Research at JET Energy Leads to Innovative, Dry Components

Mitchell R. Swartz*

Nanortech Inc., P.O. Box 81135, Wellesley Hills, MA 02481, USA

Abstract

Dry, preloaded NANOR®-type technology makes cold fusion (LANR) reactions more accessible. These self-contained, two-terminal nanocomposite components have at their core PdD and NiD nanostructured material. Their CF/LANR/CF activation is separated from their loading, and yields up to 20 times input; characterized by reasonable reproducibility and controllability. With an excess power density of 19,500 W/kg, and zero-carbon footprint, could these ready-to-be-activated NANOR®-type LANR components/systems/materials be the future of clean efficient energy production?

Keywords: Dry cold fusion component, NANOR, Preloaded cold fusion component, Preloaded energy production

---

1. Making CF/LANR Technology Available

1.1. Growing challenges

Everyone wants a better source of energy. Consumers know what they want, and that is clean, non-radioactive power for homes, heating, water, and cars. They also want less dependence on oil and commercial viability of its successor is neither wind nor solar – because they are unreliable. A thriving, expanding way of life needs a low cost solution using advanced technology to wean ourselves from petroleum to clean, efficient, energy production from CF/LANR nanomaterials.

1.2. The light at the end of the tunnel

Dry, preloaded NANOR® technology makes some LANR reactions accessible. This technology uses a new vista of advanced materials and processes resulting in these preloaded, dry, ready-to-go devices. They deliver the desired reactions from proprietary complex hydrogen-loaded alloys and engineering systems to create quite a bit of heat. The

---

[*] E-mail: mica@theworld.com

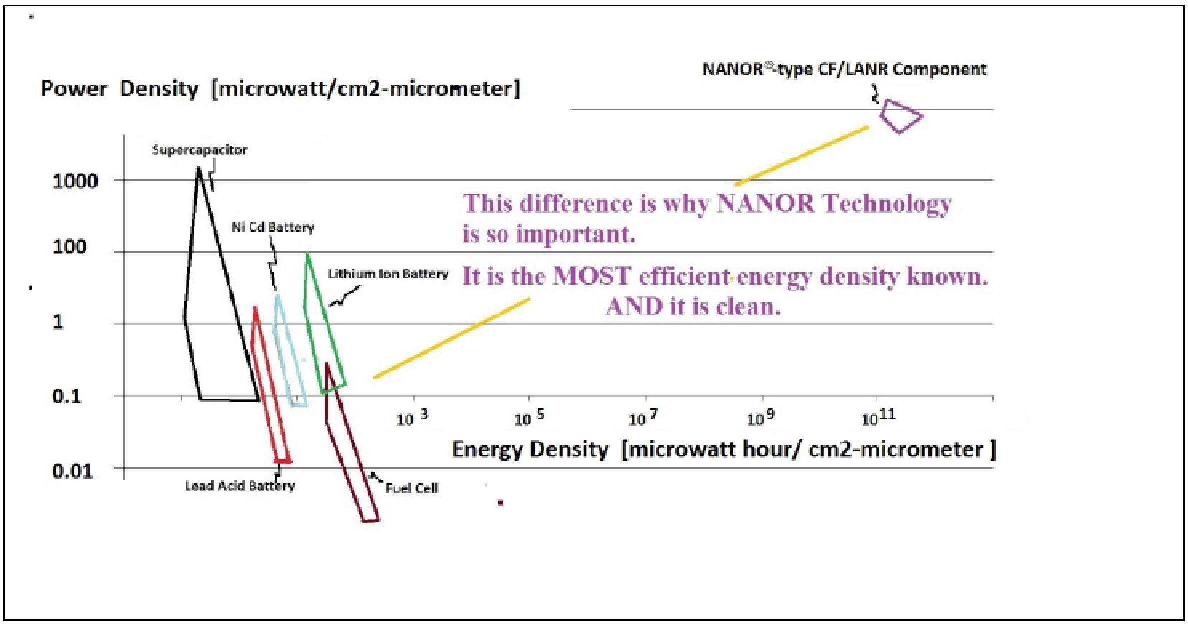

Figure 1. Shown is a Rangone plot quantitatively presents both the power density and energy density of typical energy production (and energy storage/energy conversion) sources and the NANOR-type cold fusion (lattice assisted nuclear reaction) quantum electronic component. The latter is one of the most efficient energy density devices known, and it has zero carbon footprint.

excess energy gain compared to driving input energy is up to 20 times (or more). The carbon footprint is zero, and the next generation will have higher power, and ultimately produce electricity.

This technology is a superior quality, “must have”, material, post-processing technique, and sought-after apparatus which makes “turn key” use of proprietary materials and processes to deliver a fairly reproducible LANR system.

1.3. The NANOR and NANOR Explorer

In the first decade of the 21st Century, JET Energy invented, developed, then publicly demonstrated a new type of energy production device – the NANOR®-type CF/LANR component. It is a new solid-state device, containing palladium, nanoparticles embedded in zirconium oxide insulation and preloaded with deuterium, which greatly enhances repeatability and was at the heart of the 2012 Demonstration unit shown at MIT. This received worldwide attention then, and continues to do so, now.

2. Business Model

2.1. Technology transfer program

On July 1, 2013, Nanortech Inc. was launched in the Commonwealth of Massachusetts to solely focus on advancing and producing the NANOR®-type LANR quantum electronic component and its associated controlling platform. Nanortech is developing the first line of these LANR products.

Our Goal is to Make NANOR® technology and NANOR® -type CF/LANR components and systems available as unique, high efficiency, clean, energy production platforms.

Nanortech, Inc.

Figure 2. Light at the ‘End of the Tunnel’.

Dry NANOR®-type Clean Abundant Energy Technology
Energy gain of up to ∼20 times more than is put in
The Carbon Footprint is zero
Confirmed technology
Unique and with high power gain
Status/post two open demonstrations at MIT
Several Avenues of R&D Ongoing
Developing M-NANOR® systems
Quality assurance techniques
Variety of activation methods

The NANOR®-type CF/LANR technology will, with the NANOR® and NANOR Explorer, enable others to perform better work in their labs. It also gives others the capacity to test their theories, ideas, and supplemental technologies.

The goal is to make NANOR®s technology and NANOR®-type CF/LANR components and systems available as unique, high efficiency, clean, energy production platforms. Now, with these devices and technology, others, too, will experience the thrill of generating even more excess heat with their own innovations! Simply put, these technologies give the valued luxury of the proverbial “ticket” to join in the exploration of this exciting, newly opened frontier.

The excess energy gain compared to driving input energy is up to 20 times (or more). The carbon footprint is zero, and the next generation will have higher power, and ultimately produce electricity. The energy and power densities of cold fusion are so large (Fig. 1) that insertion of this healing technology may be the 'light at the end of the tunnel' (Fig. 2) [1,2].

References

[1] M.R. Swartz, G. Verner and J. Tolleson, Energy gain from preloaded ZrO_2–PdNi–D nanostructured CF/LANR quantum electronic components, *ICCF-17*, Daejeon, Korea, 2012.

[2] M.R. Swartz and P.L. Hagelstein, Demonstration of energy gain from a preloaded ZrO_2–PdD nanostructured CF/LANR quantum electronic device at MIT, *ICCF-17*, Daejeon, Korea, 2012.

J. Condensed Matter Nucl. Sci. 15 (2015) 106–116

Research Article

Femto-Helium and PdD Transmutation

A. Meulenberg*

S-2 Supriya Residency, 93/8 4th Main, 12th Cross, Malleswaram, Bangalore 560003, India

---

Abstract

Extensive evidence exists for cold fusion to produce transmutation products as well as excess heat. This paper deals with the palladium–deuteride (PdD) structure that is generally modeled with a deuterium-to-helium (D + D ⇒ ^{4}He) cold-fusion process. How this process results in transmutation is based on the extended-lochon model that predicts deep-orbit electrons that are tightly bound to the ^{4}He nucleus and thus make the equivalent of a neutralized alpha particle. This model is compared with the NiH system (H + H ⇒ D, $H_2^{\#\#}$, or 2H$^{\#}$) described earlier and distinguishes long-range from short-range transmutation (distance from the fusion site) as well as the relative excess energies from fusion vs. transmutation. The model predicts the probable transmutation process(es) and products in the palladium system and explains other observed results of cold-fusion experiments.

Keywords: Femto-atoms, Femto-molecules, Deep-Dirac levels, Neutral-alpha, Selective fusion

---

1. Introduction

Cold fusion, CF, is distinguished from the conventionally accepted D–D fusion process by production of ^{4}He rather than of fragmentation products (protons, neutrons, tritium, and ^{3}He). Therefore, CF (with deuterium) is most commonly modeled with a D + D⇒^{4}He process. The present Lochon [1] and Extended-Lochon Models [2] of CF predict deep-atomic electrons as a mediator for cold fusion. In particular, deep-Dirac levels (DDLs are atomic levels with relativistic electrons having femtometer orbits and a binding energy >500 keV), as predicted by relativistic quantum mechanics and the Dirac equations [3], can be populated in this pre-fusion process. The extended-lochon model states that this electron energy (high-binding and kinetic) comes from the potential energy (mass) of the proton binding it. The energy release, associated with electron decay from ground-state-atomic to deep-Dirac levels, cannot come from normal dipole radiation because there is insufficient angular momentum to form photons. Low-probability second-order effects, such as the double-photon process or interaction with lattice electrons and phonons, must be expected instead. Low electron-transition probability to the DDLs is proposed as the limiting factor in cold fusion processes.

In the deuterium system, tunneling through the D-?-D Coulomb barrier, but beneath the ^{4}He fragmentation levels [2], is suppressed because there are no resonant nuclear states available to assist in the process at the energies involved. When fusion does occur, the deuterons (or their component parts) are in an excited condition, but not at any resonant levels.

---

*E-mail: mules333@gmail.com

Therefore, while EM fields can be produced by the accelerating protons and by the tightly bound electrons, no specific-energy gamma radiation results from any de-excitation. Furthermore, since neither the protons nor the electrons have any quantized angular momentum ($\ell = 0$) or any lower energy states (and the ground state has zero angular momentum), EM emission is further limited to the low-probability double-photon emission (zero-to-zero angular-momentum-state transitions are highly forbidden). This low-probability radiation mode can provide the necessary angular momentum for photons and still conserve the zero angular momentum of the system. With normal decay paths blocked, alternative (perhaps also forbidden) pathways, which are generally not considered, must be evaluated [4].

These limitations to the dissipation of nuclear energy greatly increase the time needed for an excited ^{4}He* nucleus to reach the ground state. However, the presence of the DDL electrons (forming a $^4\mathrm{He}^{\#\#}$ atom, with each superscript # representing a DDL electron) provides the best path for this decay [4]. There are consequences of both this pathway and the longer time required for it to dissipate the excess nuclear energy from the fusion process.

During the $^4\mathrm{He}^{\#\#}$ decay process, and before the electrons are ejected with the remaining nuclear energy, the composite structure of two protons, two neutrons, and two DDL electrons is an excited 'femto-helium' atom [5,6]. Because of its small DDL orbital radii, the femto-helium atom is only slightly larger than an alpha particle. While discussing its nuclear interactions with lattice nuclei, we will call this small, neutral, body a 'neutral alpha'. Its interactions will be like a super-low-energy, charge-free, alpha collision, with the additional aspects of the DDL electrons, the 'loosely bound' nucleons, and the remaining nuclear energy of the decaying ^{4}He* nucleus. Alternatively, it can be considered to be an excited multi-femtometer size 'atom', $^4\mathrm{He}^{\#\#}$, that decays slowly to the ^{4}He ground state unless/until fusion processes with adjacent nuclei either absorb or release its energy or component parts. The decay to ground state has been addressed earlier [4,6] and is perhaps the most probable scenario. The fusion products, formed with nearby lattice nuclei, would be a clear signal of any CF nuclear process(es) and their nature. That interaction with lattice nuclei and its consequences is the topic of this paper.

The number of subsequent fusion products for such a neutral-alpha interaction with lattice nuclei is disproportionately large relative to that from neutron activation or even transmutation from femto-hydrogen [7]. This 'option' of multiple transmutation products greatly increases the total interaction cross section with nuclei near to the CF source and perhaps the energy released to the lattice. The large energy input to a lattice nucleus (i.e., the addition of four nucleons) also makes nuclear fission quite likely. The evidence for induced-fission reactions (e.g., some of Mizuno's work [8]) as a major contributor to excess energy of CF reactions in PdD and its consequences will be addressed in a future paper.

Femto-ions, -atoms, and -molecules are highly mobile in the lattice because of their near-nuclear size. On the other hand, neutral alphas have a finite lifetime that, in matter, limits the possible range from its source by more than just the effects of chance interactions with lattice nuclei. The relatively short range of these neutral alphas provides a couple of unique signatures for the PdD system relative to the Ni-H system.

A number of representative transmutations, with their energy and radiation release, are described to illustrate the neutral-alpha model. A feature of the Femto-hydrogen model is its selectivity for radioactive isotopes. It is expected that to a lesser degree (because of lower mobility) the neutral-alpha will display a similar selectivity. A discussion of the applicability of this model to the PdD system will address the proposed transmutation spatial 'profile' and its comparison with the NiH system.

2. Differences between NiH and PdD Systems ($\mathrm{H}_2^{\#\#}$ vs. $^4\mathrm{He}^{\#\#}$)

Ni-based systems appear to produce more heat when loaded with H than with D. Pd-based systems appear to produce more heat when loaded with D than with H. Why?

To first order:

(1) The p+e+p ⇒ D + neutrino fusion reaction [9] gives much less excess energy (1.44 MeV) than does the

D+D$\Rightarrow^4$He (+ up to 24 MeV excess) reaction.

  (a) Being a 3-body reaction, the p–e–p fusion is less common in the sun than the 2-body p–p reaction.
  (b) Being a weak interaction, neither the p–e–p nor the p–p fusion reactions are very probable under most circumstances.
  (c) Under the high-density conditions of a collapsing star, both reactions become many orders of magnitude more rapid.

(2) Other options include cold fusion processes (where # indicates a DDL electron and the deep-orbit electron places the protons and electron(s) very close together – as in 1.c.):

  (a) H+H $\Rightarrow$ 2 $H^{\#}$, or $H_2^{\#+}$ + e, or $H_2^{\#\#}$
  (b) D+D $\Rightarrow$ 2 $D^{\#}$ ($D_2^{\#\#}$, $D_2^{\#+}$, or $^4He^{\#+}$and $^4He^{\#\#}$ are probably very short-lived)
  (c) all cold fusion reactions are unlikely unless conditions are right.

(3) Transmutation from interaction of a femto-atom with a lattice atom:

  (a) $H^{\#}$ produces 6–8 MeV (assuming addition of a nucleon),
  (b) 2 $H^{\#}$, or $H_2^{\#+}$, or $D^{\#}$ produces 12–16 MeV (assuming addition of two nucleons),
  (c) $^4He^{\#\#}$ produces up to 30 MeV (assuming addition of four nucleons at 6–8 MeV per nucleon plus the nuclear energy dissipated by the deuterons prior to collision with a heavier nucleus). However, a stable alpha configuration within a nucleus may reduce the average individual energy-gain per added nucleon.
  (d) Fission induced by these interactions could provide even more excess nuclear energy.

(4) Palladium plus $^4He^{\#\#}$ has more options to cause transmutation than does Pd + $H_2^{\#}$, or Pd + $D^{\#}$, or Pd + $H^{\#}$.
(5) Experimentally, $^4He^{\#\#}$ (hence $D^{\#}$+$D^{\#}$) produces less excess heat in Ni than in Pd. This could relate to a difference in actual fusion rates and/or to the fact that induced fission of the heavier lattice nuclei in the PdD CF reactions could produce more excess energy.
(6) $H^{\#}$ (hence H+H) produces less excess heat in Pd than in Ni. This could relate to actual fusion rates being lower in the larger lattice and/or to the lower average energy from adding nucleons to the heavier lattice nuclei (having fewer transmutation options than the $^4He^{\#\#}$ ‘neutral alpha’ (see below) may mean less average energy per fusion.
(7) $D^{\#}$+ $D^{\#}$ should always be the dominant heat generator, because the excess energy of the D+D $\Rightarrow^4$He reaction is generally greater than other combinations of transmutations available by the proton or neutron addition to a nucleus.

However, some ‘second-order’ effects may dominate.

3. Second-order Effects

(1) In the lochon model, matched-electron pairing effects may be critical [5]
(2) In the linear-molecule model [10], strong phonon effects depend on single-species linear sub-lattices
(3) Both above models depend on deep-electrons to produce fusion and femto-molecules. Filling of the DDLs depends on oscillation amplitude of the hydrons (protons, deuterons, or tritons) involved as well as their proximity. Both effects are dependent on symmetry of the species.
(4) Phonon effects may be limited by the asymmetry of the deuteron electric dipole-moment orientation and its center of mass. This can affect oscillation amplitudes and the effect may be stronger in nickel-based than in palladium-based systems. Thus, mixed-species operation (i.e., D+H and p+n (d vs. p only)) is probably less efficient in CF than is any pure-species operation.

3.1. Long-range ($H^{\#}$, $D^{\#}$, or $H_2^{\#\#}$) vs. short-range ($^4He^{\#\#}$) transmutation

(1) Most CF energy may come from direct fusion, but, transmutation (from failed direct-fusion products) may be a major contributor.
(2) Because of angular momentum (centrifugal forces), hydrons may not fuse directly. They can co-rotate in metastable orbits.
(3) Co-rotating hydrons either fuse with each other or with lattice nuclei, as they wander from their source region at thermal velocities.
(4) H+H direct fusion is retarded by the time required to form neutrons (weak interaction).
(5) D+D direct fusion is retarded by the decay time from $D^{\#}$ + $D^{\#}$ or $4He^{\#\#}$ to ^{4}He ground.
(6) $H_2^{\#\#}$, with 2–3 fm electron orbits may be semi-stable (greater than picosecond half-life?)
(7) $D_2^{\#\#}$, with 2–3 fm electron orbits are unstable (neutrons couple, inducing fusion – less than femto-second half-life?)
(8) $H^{\#}$and $D^{\#}$, if formed in failed fusions, are stable and *long-ranged*. Because of much stronger DD bonds and the presence of neutrons, DD-fusion failure (resulting in $D^{\#}$ atoms) is uncommon.
(9) Long-range (microns?) travel of femto-H atoms means mainly lattice atoms are transmuted. However, any radioisotopes (natural or created) in the lattice and any impurities with greater interaction cross-sections are preferentially transmuted.
(10) $H_2^{\#\#}$ and $^4He^{\#\#}$ have short half lives and are thus *short-ranged*.
(11) Short-ranged (nm?) means most transmutations are with lattice atoms and with prior transmutations, where both are near to the source of femto atoms.

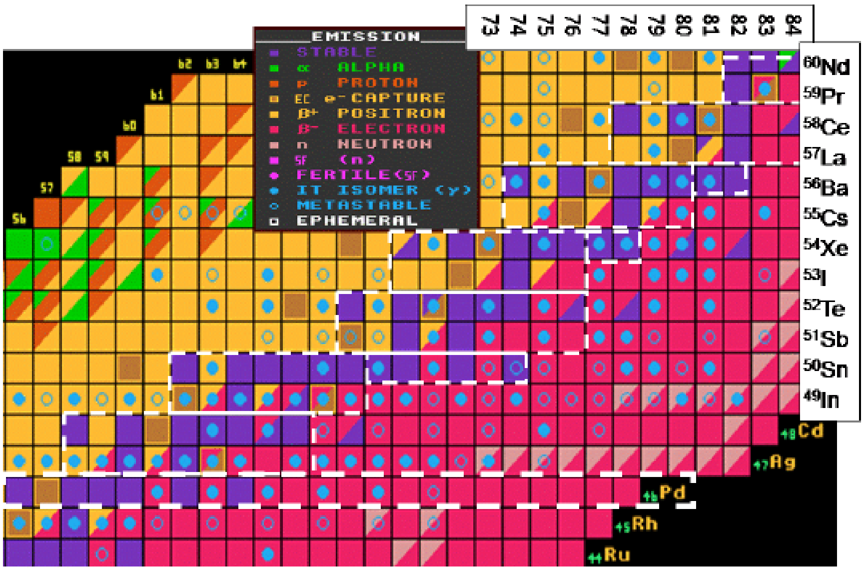

Figure 1. Probable isotopes of transmutations leading from ‘neutral alpha’ interactions with a Pd lattice and subsequent transmutations (protons on ordinate, neutrons on abscissa).

3.2. Short-range transmutation processes

Long-range transmutation processes, involving $H^{\#}$in the Ni–H system, were described in an earlier paper [7]. The present paper describes the short-range fusion processes in the PdD system. The colored chart below (Fig. 1) identifies the probable transmutation-isotope range of the ‘neutral alphas’ interaction (dashed boxes) with the Pd lattice and the local buildup of transmuted elements about a nuclear active environment, the NAE. The preferred mode is:

$$^{A}\mathrm{N}_{Z} +^{4}\mathrm{He}^{\#\#} \Rightarrow\ ^{A+4}\mathrm{N}_{Z+2} \tag{1a}$$

If this mode is not available (i.e., not producing a stable nucleus), then additional options include

$$^{A}\mathrm{N}_{Z} +^{4}\mathrm{He}^{\#\#} \Rightarrow\ ^{A+4}\mathrm{N}_{Z} + 2\ \text{neutrinos}, \tag{1b}$$

$$\Rightarrow\ ^{A+4}\mathrm{N}_{Z+1} + 1\ \text{neutrino}, \tag{1c}$$

$$\Rightarrow\ ^{A+3}\mathrm{N}_{Z+1} + 1\mathrm{p} + 1\mathrm{e}, \tag{1d}$$

$$\Rightarrow\ ^{A+3}\mathrm{N}_{Z+2} + 1\mathrm{n}, \tag{1e}$$

$$\Rightarrow\ ^{A+2}\mathrm{N}_{Z+2} + 2\mathrm{n}, \tag{1f}$$

$$\Rightarrow\ ^{A+2}\mathrm{N}_{Z+1} + 1\ \mathrm{p} + 1\mathrm{n} + 1\mathrm{e}, \tag{1g}$$

$$\Rightarrow\ ^{A+2}\mathrm{N}_{Z} + 2\mathrm{p} + 2\mathrm{e}, \tag{1h}$$

$$\Rightarrow\ ^{A+1}\mathrm{N}_{Z+1} + 2\ \mathrm{n} + 1\mathrm{p} + 1\mathrm{e}, \tag{1i}$$

$$\Rightarrow\ ^{A+1}\mathrm{N}_{Z} + 1\mathrm{n} + 2\mathrm{p} + 2\mathrm{e}, \tag{1j}$$

$$\Rightarrow\ ^{A}\mathrm{N}_{Z-1} + 1\ \text{neutrino} + 2\mathrm{n} + 2\mathrm{p} + 1\mathrm{e}, \tag{1k}$$

$$\Rightarrow\ ^{A}\mathrm{N}_{Z-2} + 2\text{neutrino}\ + 2\mathrm{n} + 2\mathrm{p}. \tag{1l}$$

(1m)

The neutrons and protons coming out of the transmutation may be as individuals or as composites (such as alphas). Most of these examples are demonstrated below. Other combinations exist; but, they would depend on having the correct starting isotope, a stable product, and an exothermic reaction. The point is that the DDL electrons allow a multi-nucleon body to enter a nucleus for fusion, fission, or transmutation.

Figure 1 shows the partial range of options available to the neutral alpha ($^{4}\mathrm{He}^{\#\#}$) as it encounters different nuclei. There is no intention to provide all of the options, nor to be quantitative about them. This is an initial training exercise, that can be changed dramatically by a single data set (just as the Ni–H model was improved with the Defkalion ^{61}Ni data [11]).

Starting with $^{102}\mathrm{Pd}_{46}$ (Fig. 2), the six first order reactions expected (in order of probability) are:

$$^{102}\mathrm{Pd}_{46} +^{4}\mathrm{He}^{\#\#} \Rightarrow^{106}\mathrm{Cd}_{48} \qquad \text{(no weak interactions)}$$

$$\Rightarrow^{104}\mathrm{Pd}_{46} + 2\mathrm{p} + 2\mathrm{e} \qquad \text{(no weak interactions)}$$

$$\Rightarrow^{105}\mathrm{Pd}_{46} + 1\text{neutrino} + 1\ \mathrm{p} + 1\mathrm{e} \qquad \text{(1weak interaction), 1p} \Rightarrow \text{1n)}$$

$$\Rightarrow^{103}\mathrm{Rh}_{45} + 1\mathrm{p} + 2\mathrm{n} + 1\mathrm{e} + 1\text{neutrino} \qquad \text{(1weakinteraction, 1p} \Rightarrow \text{1 n)}$$

$$\Rightarrow^{106}\mathrm{Pd}_{46} + 2\text{neutrinos} \qquad \text{(2weak interactions, 2p} \Rightarrow \text{2n)}$$

$$\Rightarrow^{102}\mathrm{Ru}_{44} + \text{alpha} + 2\text{neutrinos} + 2\mathrm{e} \qquad \text{(2weak interactions, 2p} \Rightarrow \text{2n)}$$

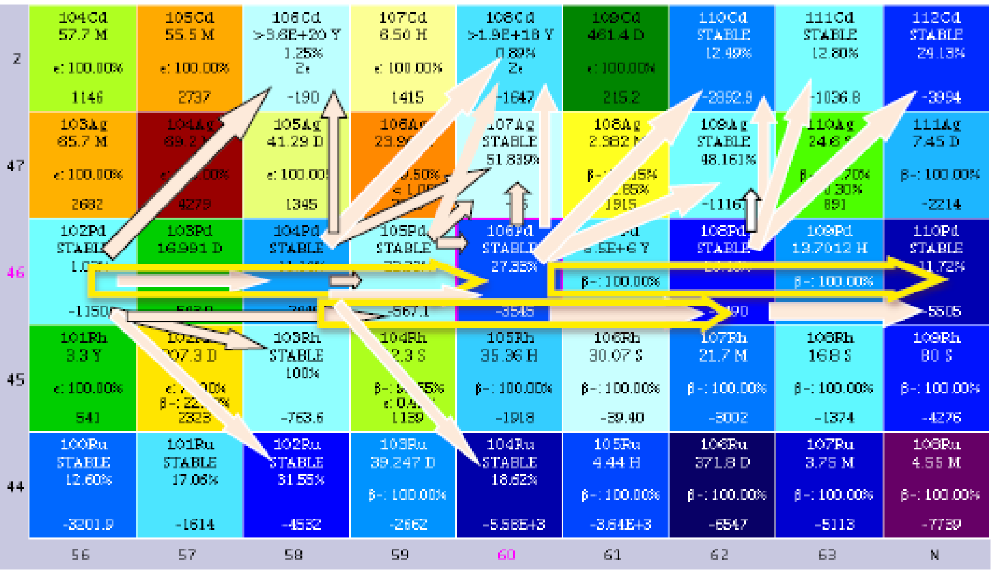

Z	104Cd 57.7 M ε: 100.00% 1146	105Cd 55.5 M ε: 100.00% 2737	106Cd >3.6E+20 Y 1.25% 2ε -190	107Cd 6.50 H ε: 100.00% 1415	108Cd >1.9E+18 Y 0.89% 2ε -1647	109Cd 461.4 D ε: 100.00% 215.2	110Cd STABLE 12.49% -2892.9	111Cd STABLE 12.80% -1036.8	112Cd STABLE 24.13% -3994
47	103Ag 65.7 M ε: 100.00% 2682	104Ag 69.2 ε: .00% 4279	105Ag 41.29 D ε: 100.00 1345	106Ag 23.9 .50% < 1.0	107Ag STABLE 51.839%	108Ag 2.382 M β-: .15% .85% 1915	109Ag STABLE 48.161% -1116	110Ag 24.6 β- .70% 0.30% 891	111Ag 7.45 D β-: 100.00% -2214
46	102Pd STABLE 1.0 -1150	103Pd 16.991 D	104Pd STABLE	105Pd STABLE -567.1	106Pd STABLE 27.33%	Pd .5E+6 Y β-: 100.00%	108Pd STABLE 90	109Pd 13.7012 H β-: 100.00%	110Pd STABLE 11.72% -5505
45	101Rh 3.3 Y ε: 100.00% 541	102 07.3 D ε: .00% β-: 22. % 2323	103Rh STABLE 100% -763.6	104Rh 2.3 S β-: .55% ε: 0.4 1139	105Rh 35.36 H β-: 100.00% -1918	106Rh 30.07 S β-: 100.00% -39.40	107Rh 21.7 M β-: 100.00% -3002	108Rh 16.8 S β-: 100.00% -1374	109Rh 80 S β-: 100.00% -4276
44	100Ru STABLE 12.60% -3201.9	101Ru STABLE 17.06% -1614	102Ru STABLE 31.55% -4532	103Ru 39.247 D β-: 100.00% -2662	104Ru STABLE 18.62% -5.58E+3	105Ru 4.44 H β-: 100.00% -3.64E+3	106Ru 371.8 D β-: 100.00% -6547	107Ru 3.75 M β-: 100.00% -5113	108Ru 4.55 M β-: 100.00% -7739
	56	57	58	59	60	61	62	63	N

Figure 2. Transmutation of lower mass stable palladium nuclei via femto-helium (neutral alphas). Multiple pathways to stable isotopes are displayed as preferred paths. (Some arrows are outlined only for clarity.)

The normally preferred reaction, $^{102}\mathrm{Pd}_{46}+^{4}\mathrm{He}^{\#\#} \Rightarrow {}^{106}\mathrm{Cd}_{48}$, may be suppressed because that particular Cd isotope would like to get rid of positive charge. However, it is extremely long lived, so it might still provide the strongest transmutation path. The weak interaction probability (p ⇒ n by electron capture) is greatly enhanced by the continued proximity of the DDL electron(s) during the interaction of the $^{4}\mathrm{He}^{\#\#}$ with the lattice nucleus.

It is clear that a major difference in the present model and conventional views of alpha-induced nuclear reactions has to do with the binding energies of the constituent parts and the presence of the tightly bound electrons. If nuclear collisions occur while the paired deuterons are still high in the common nuclear-potential well, the neutral alpha readily splits into multiple parts that can interact with the target nucleus in many ways. As the deuteron pair decays toward the $^{4}\mathrm{He}$ groundstate, the probability of separating the nucleons is reduced and that of separating the DDL electrons from the nucleus is increased. Thus, the preferred transmutation paths may be dependent on the extent of the $^{4}\mathrm{He}^{\#\#}$decay at the time of interaction.

In Fig. 2, transmutation of $^{104}\mathrm{Pd}$ by the $^{4}\mathrm{He}^{\#\#}$ reaction has a (nearly) stable target isotope ($^{106}\mathrm{Cd}_{48}$) that can be reached by double neutron emission. Even though this cadmium isotope is nearly stable, its preferential decay mode (double positron emission) is so similar to the reverse of the process needed to reach it from $^{104}\mathrm{Pd}$ that the probability of that path relative to the transition to $^{108}\mathrm{Cd}_{46}$ would appear to be negligible. The seven 'easy' transmutations to stable isotopes in this interaction are:

The $^{105}\mathrm{Pd}$ isotope has only three options for ready transmutation to stable (or very long-lived) isotopes via neutral alphas. Of these three stable nuclides, perhaps only $^{107}\mathrm{Ag}$ is spin compatible with the neutral alpha transmutation of the $^{105}\mathrm{Pd}$ isotope. (This comment is based on the observed lack of heat generated by the $^{61}\mathrm{Ni}$ isotope in CF reactions [11].) If true, then this observation could lead to a test of the present model.

The $^{106}\mathrm{Pd}$ isotope has a preferred path, from $^{106}\mathrm{Pd}$ to $^{110}\mathrm{Cd}$, a completely stable isotope (Fig. 3). Therefore, unless something else interferes (e.g. isotopic spin), the present model would predict this path as the main transmutation for

$^{104}\mathrm{Pd}_{46}+{}^{4}\mathrm{He}^{\#\#}$ $\Rightarrow$ $^{108}\mathrm{Cd}_{48}$ (no weak interactions)
$\Rightarrow$ $^{107}\mathrm{Ag}_{47} + \mathrm{p} + \mathrm{e}$ (no weak interactions)
$\Rightarrow$ $^{106}\mathrm{Pd}_{46} + 2\mathrm{p} + 2\mathrm{e}$ (no weak interactions)
$\Rightarrow$ $^{105}\mathrm{Pd}_{46} + 2\mathrm{p} + 1\mathrm{n} + 2\mathrm{e}$ (no weak interactions)
$\Rightarrow$ $^{106}\mathrm{Cd}_{48}$ + 2 neutrons (no weak interactions)
$\Rightarrow$ $^{108}\mathrm{Pd}_{46}$ + 2 neutrinos (two weak interactions, $2\mathrm{p} \Rightarrow 2\mathrm{n}$)
$\Rightarrow$ $^{104}\mathrm{Ru}_{44}$ + alpha + 2 neutrino (two weak interactions, $2\mathrm{p} \Rightarrow 2\mathrm{n}$)

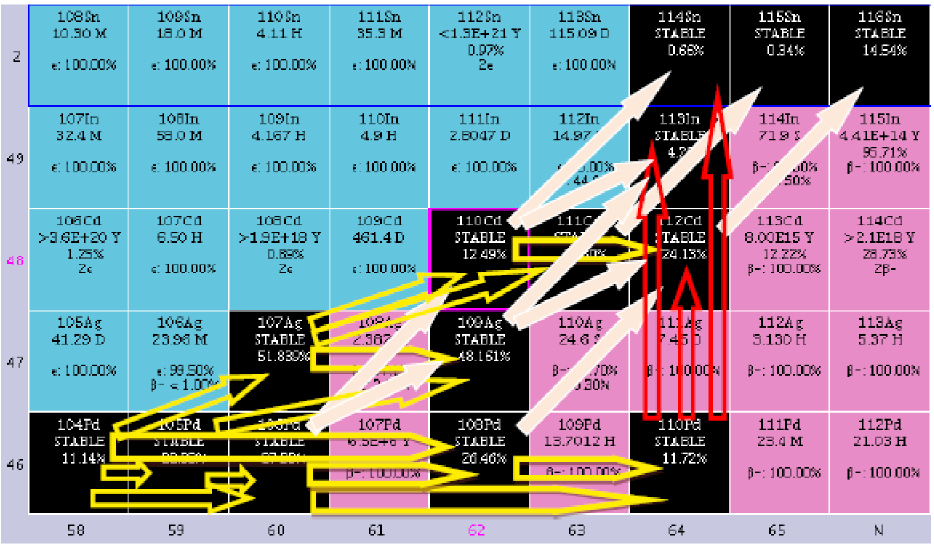

Figure 3. Transmutation of stable nuclei via femto-helium (neutral alphas) toward higher atomic and mass number.

^{106}Pd. On the other hand, if the DDL electrons cannot dissipate the added nuclear energy quickly enough, ejection of one or two protons would also leave the result as a different stable nucleus. This begins the strong growth in transmutations to the higher atomic number nuclides in this family. The probability of the different pathways could be statistical or it could be highly sensitive to various nuclear conditions. CF data from isotopically pure Pd sources could provide a sensitive test for involvement of nuclear physics in this field as such testing of Ni isotopes has been.

The red arrows in Fig. 3 indicate a possible new dominant process (induced-beta decay). In this case: The ejection

$^{110}\mathrm{Pd}_{46}+{}^{4}\mathrm{He}^{\#\#}$ $\Rightarrow$ $^{112}\mathrm{Cd}_{48}$ + 2 neutrons (no weak interaction)
$\Rightarrow$ $^{113}\mathrm{In}_{49}$ + 1 neutron + 1 neutrino + 1 beta^{-} (electron) (1 weak interaction, $\mathrm{n} \Rightarrow \mathrm{p}$)
$\Rightarrow$ $^{114}\mathrm{Sn}_{50}$ + 2 neutrinos + 2 betas (electrons) (2 weak interactions, $2\mathrm{n} \Rightarrow 2\ \mathrm{p}$)

of neutrons is not a problem and the induced decay of one or more neutrons is natural. Nevertheless, the possible slowness of the presented weak interactions (despite the DDL electron proximity) could severely retard the latter two reactions.

If an alpha were to be absorbed by the ^{110}Pd, it would go to ^{114}Cd$_{48}$, which would double-beta decay to ^{114}Sn$_{50}$. The fact that the ^{4}He$^{\#\#}$ could induce this action in a single step, because of the presence of DDL electrons, is not a surprise. Similarly, the ^{110}Pd$_{46}$+^{4}He$^{\#\#}$ to the long-lived ^{113}Cd$_{48}$ would perhaps lead to a direct transmutation to ^{113}In$_{49}$via induced beta decay. According to the model presented here, transmutation to a radioactive isotope via ^{4}He$^{\#\#}$ is not an expected interaction, given other options, and thus the unusual direct double-beta decay to ^{114}Sn$_{50}$would be a preferred path. If this were a natural pathway for CF-induced transmutation of ^{110}Pd$_{46}$, then observation of double-beta decay would be a test for the model and the possibility of observing a neutrino-less double-beta decay [12] would be greatly improved. A potential problem with such a test is the uncertainty in output energies from the multi-body interaction presented. Furthermore, the near-simultaneous de-orbiting of the DDL electrons would provide a source of energetic electrons that would interfere with measurements of double-beta decay coincidence measurements.

The remainder of the predicted neutral-alpha transmutation chain, from Ag thru Xe, follows this same pattern (Fig. 3). Stable isotopes generally lead to stable isotopes, if possible. This is always possible for neutral alphas in this range. Sometimes unstable isotopes can result, but they are unlikely to decay before they are transmuted again into a stable isotope.

Since alpha bombardment of most of these isotopes yields only a few MeV per nucleon, it is clear that the major excess energy in CF in the DD system is from the formation of ^{4}He and not from any transmutations. The increase in ‘energy added per nucleon’ for lower atomic number nuclides indicates a need for considering further the contribution of fission in the analysis [8].

4. Selective Fusion

At ICCF-17, in an attempt to account for the negligible rates of energetic radiation from neutron-activated transmutations that would normally produce high levels, two mechanisms were invoked. Both involve the presence of DDL electrons, but at different stages of the initial fusion process. The presence of DDL electrons has been used to describe the initial-decay process of ^{4}He* in D–D fusion [4]. Since the transfusion process described here involves Femto-atoms and molecules, such DDL electrons must also be incorporated into (or about) the transmuted nucleus during/after fusion with a femto-atom or molecule. With such incorporation, these deep-orbit electrons would provide a much more rapid decay path, via near-field coupling of the nuclear energy to the DDL electron(s) and then from the DDL electrons to the lattice atomic electrons [4]. This accounts for the reduction or elimination of radiation from fusion products that are highly radioactive, if produced by only the addition of neutrons.

The second mechanism is a bit less obvious; but, if valid, of major importance to CF and the observed results. Mentioned in the ICCF-17 posters, but not described in detail in the published version [7], is the selective-attraction of the femto-atoms to radioactive nuclei. In [4], I use Maxwell’s equations to indicate the relative E-field strengths generated by nuclear protons, DDL electrons, atomic electrons, and radio-nuclides. The fact that radio-nuclides have energetic protons that ‘want’ to give away energy and the DDL electrons of femto-atoms can receive it (at nuclear frequencies) means that work can be done. This provides an attractive potential between the two.

Using Feynman’s description of the H-molecular ion, the Yukawa exchange potential, and his extension to the photon as the mediator of the Coulomb potential, one may provide a mathematical and conceptual basis, for sufficient attraction between femto-hydrogen atoms to fuse or to form femto-molecules. (The draft of that paper is already 10 pages long.) Formation of the femto-hydrogen atoms and molecules, because of their ability to liberate 6–8 MeV per incident nucleon in fusion leading to transmutation, could be an important contributor to excess-heat generation in the Ni–H and Pd–H systems. These two systems have their own transmutation profiles that partially overlap with that of the femto-helium system described here and that of the femto-hydrogen described earlier. Femto-deuterium molecules may be unstable, rapidly decaying to short-lived ^{4}He$^{\#\#}$, so that only transmutation via the ^{4}He$^{\#\#}$ atoms is considered here.

5. Consequences

Long-range transmutation in the NiH system via femto-hydrogen atoms or molecules is a meaningful contributor to the excess heat observed. It may actually dominate the contributions from direct p–e–p or p–e–e–p fusion reactions in that regard. The transmutation results are spread over a large area around a source region and primarily shifts the isotopic distribution of nickel in the lattice rather than producing new elements. This may be important if the source of the excess-energy production and femto-atoms (e.g., a nuclear-active environment – or NAE) is dependent on the integrity of a nickel structure.

It is unlikely that the isotopic nature of the nickel would alter the production of direct p–e–p or p–e–e-p fusion reactions or femto-nuclei. Nevertheless, the negative results for ^{61}Ni may belie that statement [11]. These results, which may be explained in terms of isotopic-selection rules, could point to which is the major source of excess energy. Since ^{61}Ni is only a small percentage of the isotopes in the natural material, this unexpected result has little impact on the heat producing capability of the Ni–H system. Even as the levels of the isotope build up, if it does not interfere with the production of the femto-hydrogen, then the long-range of these femto-structures would find a nearly infinite supply of productive Ni isotopes.

In the Pd–H system, the femto-hydrogen created could transmute Pd to silver (Ag) in the source region. Even if long ranged, this addition of Ag to the Pd lattice could 'poison' the CF action (or it could help it by raising the Fermi level in the local lattice). However, if the source of femto-hydrogen is local, the concentration of transmutation products would be highest in the source region. Creating an alloy in the NAE of a PdD system could be a severe, life-limiting problem for CF activity.

Short-range transmutation in the PdD system is another story. Because the production of ^{4}He generates a majority of the excess heat in this D–D fusion system, creation of 'neutral alphas' is not critical to the system's heat-production function. However, their creation presents a problem. Being short range, they will alter not just the isotopic distribution in the source region; they will quickly alter the elemental composition of the source region itself.

Assuming that the new elements created interfere with the activity within the NAE, this effect would appear to be a severe limitation to CF in the PdD system. The NAE sites would rapidly destroy themselves with their own by-product. The only redeeming feature is that the neutral alphas are short ranged because they are short lived. Thus, while high concentrations of new elements may accumulate about an NAE (until it ceases to function), the actual rate of transmutation may be low.

How does the short-range transmutation affect the Ni–H system? As with the Ni–H system, where most of the transmutations are to other Ni isotopes, the Ni–D system would behave in the same manner. The path out of the Ni isotopes would be primarily via ^{64}Zn and ^{66}Zn, although ^{63}Cu and ^{65}Cu might be available as well. The consequences of these elements in the NAE region are still to be determined.

In the Ni–H system, isotopic selection rules appear to retard production of the Cu isotopes. This might, or might not, be the case for the Ni–D system. If nothing retards the formation of the heavier elements from the fusion with the short-range neutral alphas, then the Ni NAEs might lose their effectiveness faster in the Ni–D system, than in the Ni–H system. These effects may also apply to the PdH and PdD systems. How they affect the transmutation of lattice and impurity nuclides is still to be determined. The present model fits the available CF data and appears to be highly predictive. Time will tell.

6. Conclusions

The present model indicates that transmutation occurs in varying amounts and distributions in tested Cold Fusion Systems (Pd–H, Pd–D, Hi–H, and Ni–D). I believe that the deep-Dirac level electron is the only mechanism that can overcome the Coulomb barrier of lattice nuclei without invoking neutrons that would produce results incompatible with well-known neutron-activation products. The common belief that neutrons are the only low-energy mechanism that can produce transmutation has blocked acceptance of both CF results and models for many years.

The existence of DDL electrons, proposed to account for the ability to produce ^{4}He as the primary product of D–D fusion, also explains the available CF transmutation data. This paper, explaining the direct-transmutation products of the Pd–D system, via the neutral femto-atom concept, complements the prior work on the Ni–H system. It is not the whole story, which must include both transmutation of the Pd lattice nuclides and any contaminants or dopants included. It also must include the fission of these nuclides and their fusion products. These parts of the story must await a future effort.

The proposed model suggests transmutation from both short-range femto-deuterium molecules and long-range femto-hydrogen atoms and molecules. The former is likely to alter (by saturating a region with multiply-transmuted atoms), and ultimately inactivate, its source regions (assuming the validity of a concept of nuclear-active environment sites). The latter, by widely distributing the transmuting species, has much less effect on the sources of femto-hydrogen. In fact, the majority of transmutations would be to higher mass Ni or Pd isotopes and thus have no effect on the CF process.

A final mechanism, selective attraction of femto-atoms to radio-nuclides (that affects the short-range and long-range transmutations differently) is addressed. This effect reduces (possibly eliminates) residual radioactivity from the transmutation process or from radioactivity introduced into the lattice. The effect further concentrates transmutations about the ^{4}He$^{\#\#}$ sources and to a lesser extent about the femto-hydrogen sources.

The careful work by Mizuno [8] indicated that transmutation and subsequent fission may play a major role in the excess energy from cold fusion in PdD lattices. The processes leading to the many transmutations in PdD described here could also lead to fission in the same manner as would neutrons.

Acknowledgement

This work is supported in part by HiPi Consulting, New Market, MD, USA, by the Science for Humanity Trust, Bangalore, India, and the Science for Humanity Trust, Inc, Tucker, GA.

References

[1] K. Sinha and A. Meulenberg, A model for enhanced fusion reaction in a solid matrix of metal deuterides, in *ICCF-14, Int. Conf. on Condensed Matter Nuclear Sci.*, 2008., Washington, DC., 2009, Vol. 2, pp. 633–638.

[2] A. Meulenberg and K. Sinha, Tunneling beneath the ^{4}He*fFragmentation energy, *J. Cond. Matter Nucl. Sci.* **4** (2010) 241–255; also A. Meulenberg and K.P. Sinha, Lochon and extended-lochon models for LENR in a lattice, *Infinite Energy Magazine* **112** (2013) 29—32.

[3] J. Maly and J. Va'vra, Electron transitions on deep Dirac levels I, *Fusion Technol. (US)* **24**(3) (1993).

[4] A. Meulenberg and K.P. Sinha, Deep-orbit-electron radiation emission in the decay from 4H*^ to 4He, 17th Int. Conf. On Cond. Matter Nucl. Sci., Daejeon, Korea, 12–17 Aug, 2012 (to be published in JCMNS).

[5] A. Meulenberg and K.P. Sinha, Deep-electron orbits in Cold Fusion, 17th Int. Conf. on Condensed Matter Nuclear Science, Daejeon, Korea, 12–17 August, 2012 (to be published in JCMNS).

[6] A. Meulenberg, From the naught orbit to He^4 ground state, *16th Int. Conf. on Condensed Matter Nuclear Science*, Chennai, February 6–11, 2011, *JCMNS-10*, 2013, pp. 15–29.

[7] A. Meulenberg, Femto-molecules and transmutation, *17th Int. Conf. on Condensed Matter Nuclear Science*, Daejeon, Korea, 12–17 August, 2012 (to be published in *JCMNS*); also A. Meulenberg, Femto-atom and femto-molecule models of cold fusion, *Infinite Energy Magazine,* **112** (2013) 41–45.

[8] Mizuno, T., Isotopic changes of elements caused by various conditions of electrolysis, American Chemical Society, Salt Lake City, Utah, March 22, 2009. Mizuno, T., T. Ohmori, and M. Enyo, Isotopic changes of the reaction products induced by cathodic electrolysis in Pd, J. New Energy, 1996. **1**(3): p. 31. http://newenergytimes.com/v2/library/2009/2009Mizuno-1-ACS-Isotopic-Changes.pdf.

[9] http://en.wikipedia.org/wiki/Proton-proton_chain#The_pep_reaction

[10] A. Meulenberg, K.P. Sinha, Composite model for LENR in linear defects of a lattice, ? 18th Int. Conf. on Condensed Matter Nuclear Science, Columbia, Missouri, 25/07/2013

[11]] J.Hadjichristos, M. Koulouris, A. Chatzichristos, Technical characteristics & performance of the Defkalion's Hyperion pre-industrial product, 17th Int. Conf. on Condensed Matter Nuclear Science, Daejeon, Korea, 12-17 August, 2012.

[12] http://en.wikipedia.org/wiki/Double_beta_decay#Neutrinoless_double_beta_decay

J. Condensed Matter Nucl. Sci. 15 (2015) 117–124

Research Article

Pictorial Description for LENR in Linear Defects of a Lattice

A. Meulenberg[*]

S-2 Supriya Residency, 93/8 4th Main, 12th Cross, Malleswaram, Bangalore 560003, India

Abstract

This note provides a pictorial description of several new concepts in low energy nuclear reactions (LENR) and thereby provides an image for both theoreticians and experimentalists to better grasp the differences with the old. Recent work on the concept of a 'linear hydrogen molecule within a lattice defect' is emphasized by showing how the interatomic spacing of the unusual molecule is no longer bound by the lattice spacing. A concept of the nature of the Coulomb potential for finite-sized charges at nuclear distances is pictured so that people stop clinging to the point- and separated-charge descriptions that are no longer appropriate. A known force, spin-spin coupling, may be important when dimensions approach those of the nucleus. The strong magnetic moment of the electron, indicating the importance of this effect at larger distances, is also pictured.

Keywords: Cold fusion, Coulomb potential, Linear array, Nuclear Coulomb potential, Spin–spin coupling Variable lattice spacing

1. Introduction

Too often technical papers are full of equations, with which many experimentalists are not comfortable, or full of data with no expressed consolidating theme with which to draw the results together. Cold fusion (CF) is more often rejected because of 'known' physics than because of new ideas required to explain the experimental observations. It is hoped that some pictures might help to explain things.

The concept of lattice spacing is one of the foundations of solid state physics. This concept, including the lattice and Coulomb barriers preventing hydrogen atoms from approaching one another in a lattice, is a major argument against the possibility of proximity-induced fusion. The standard view is that H atoms are bound to specific sites and vibrate within that location. The Einstein oscillations [1] about a central point fixed in the lattice are small compared to the fixed spacing between adjacent sites. Thus, the thermal effects (even collectively as phonons) are never adequate to bring H atoms close enough together to account for the heat or fusion rates observed experimentally. A linear-defect mechanism has been proposed that overcomes this limitation [2–4]. However, the first of these papers to identify a change in lattice spacing as the solution to this problem provided only a mathematical model as to how this would overcome the Coulomb barrier in this manner. It did not provide a mechanism for achieving this change in lattice spacing. The second of these papers [3] identified a location (a specific type of defect) that could be the source or site of

---

[*] E-mail: mules333@gmail.com

CF within a material. The author, Ed Storms, being a chemist was unable to present a convincing story to the physicists of the CMNS community. In some cases, he was facing the problem of 'things too-well known'. In others, it was his inability to use the concepts that were a common language to the physicists. The third paper [4] sought to bring these theoretical and 'practical' concepts together, along with some concepts introduced by Schwinger in the early 1990s [5]. This present paper will provide pictorial representations to help visualization of the distinction between the standard view and the new, and perhaps necessary, concepts for bringing hydrogen atoms close enough together for fusion rates predicted by observed CF results.

Another issue that will be expressed pictorially has no meaning for most physicists. It can be expressed; but it still leaves questions. How does the Coulomb potential change when an electron is within the nuclear-potential region? At what point do paired fermions become a boson? What is the meaning of 'radius' for electrons and protons?

The third issue that will be expressed pictorially, spin-spin coupling, has not been raised/expressed in the context of CF. In atomic physics and chemistry, spin-orbit coupling [6] is a weak magnetic interaction between an electron's magnetic moment and the magnetic field resulting from its orbital motion. It is an important feature of electron interactions at this level. At nuclear dimensions, where the nuclear magnetic moments and possible orbits are much smaller, this coupling may be important for nucleons.

Spin-spin coupling [7] is the interaction of the magnetic fields associated with the spin of separate charged particles. At atomic orbital distances, this may be a barely noticeable effect. At nuclear distances, even the low-magnetic-moment nucleons can interact in this manner. However, at the intermediate distances between the atomic orbitals and the nucleus, the strong magnetic moment of the electrons can produce a very important force between electron pairs. This could greatly alter the interaction of colliding atoms, if the atomic electrons drop deeper into the charge potential well during the collision. This picture influences the expectations for both the Lochon [8] and the Linear-Hydrogen Molecule Models of CF [4].

2. Variable Lattice Spacing

The fixed lattice spacing, ℓ, of conventional solid state theory is displayed in Fig. 1A with the Einstein oscillations (with amplitude 'a') superimposed. The linear array indicates the spacing between of a vertical array of atoms in a lattice.

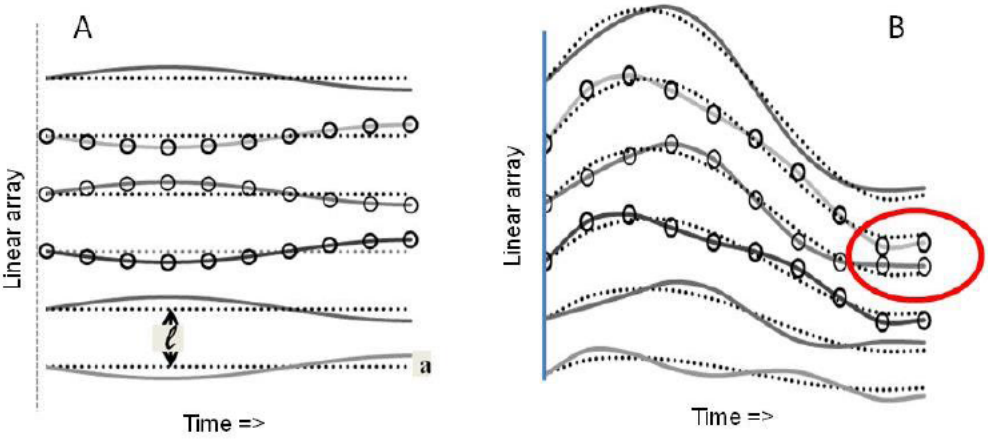

Figure 1. Fixed and changing lattice spacing. (A) Einstein oscillations about *fixed* lattice points. (B) Oscillations with *varying* lattice spacing.

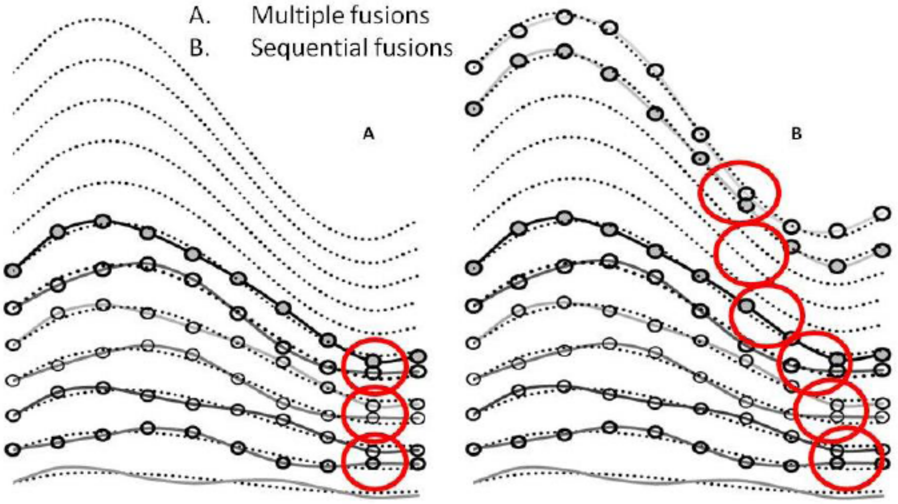

Figure 2. Variable Lattice spacing (displayed as dotted lines for a vertical lattice array stepped in time). (A) Multiple fusions. (B) Sequential fusions.

This array is propagated to the right with steps in time. The oscillations about the fixed lattice represent longitudinal optical photons with adjacent atoms 180° out of phase. This means that the distance of closest approach between atoms is $\ell - 2a$. The circles (of radius δ) represent the interaction distance about the atoms (not to scale) at which fusion has a high probability.

Figure 1B is similar except that the lattice spacing, ℓ', is now allowed to vary with time. If a lattice spacing varies in an oscillatory manner, and the oscillations can increase in amplitude with time, then there will be a point (e.g., circled region) where the variations in lattice and Einstein oscillations are properly phased so that $\ell' - 2(a) < 2\delta$ and fusion will occur.

The difference in Figs. 1A and B represents the differences in sub-lattice atomic arrays that are confined by the rigid structure of a 3-dimensional lattice and linear arrays that are only confined laterally. The linear array can vary its interatomic spacing; but this capability is seldom modeled in physical structures. It cannot occur in a normal 3-D lattice. This is an important point that Storms made – based on his study of the CF experiments and data over many years. This is not to say that the lattice does not affect the defect-isolated linear array. It says that the lattice influence does not dominate the phonon-induced motion along the array.

If the number of atoms in the linear array is increased (from Fig. 1B), then it is possible to have multiple fusions occurring at the same time (circles in Fig. 2A). In fact, multiple fusions can occur sequentially at different points along the linear array (Fig. 2B). It is possible that the energy released by a single fusion can boost the rest of the array into a more confined configuration that would create fusion reactions of many or most of the atoms in that region of the array. This could account for the ‘thermal craters’ often observed in solid-Pd electrodes that have produced excess heat.

2.1. Consequences of Change in Lattice Spacing

Figures 1 and 2 provide a picture of the variable-lattice array changing its spacing as a function of time and identify points at which fusion can occur. Mechanistically, it indicates the proximity coupling of lattice phonons with the nuclear potential (Schwinger model [5]). The phonons drive both the Einstein oscillations and the lattice oscillations.

The oscillation amplitude can grow in time. It can be stable, but then be 'triggered' by some event over a threshold. If the nuclei get close enough together, the nuclear potential can provide an impulse that can increase the amplitude of oscillation. This is equivalent to an increase in the number of phonons. These new phonons are generated from the nuclear potential energy. Since phonons are bosons, they seek to get into the same state (including phase) and this would result in greater amplitudes of the respective modes. This is a positive feedback mechanism that would ultimately result in fusion of H atoms in the linear array.

A major contribution to this scenario by Schwinger was the concepts that the nuclear potential must be included in the Hamiltonian of the linear array and that this energy source could be used to increase the specific phonon modes driving the array into close-spaced positions. He could not convince his fellow physicists of this new approach, despite his use of quantum mechanics, being a Nobel Laureate, and being one of the best theoretical physicists of his time.

3. Coulomb Potential at Nuclear Distances

Fifty years ago, in his Lectures on Physics, Feynman wrote (in paraphrase) "the Coulomb potential has been shown to be valid up to the nucleus." The understanding among some mathematical physicists seems to be that it is valid to $r = 0$. They seem to ignore that, if this is true, then every particle with a potential obeying this $1/r$ potential must be a singularity (with infinite energy). However, they reject a solution of the Dirac equations that is singular at $r = 0$. Since Cold Fusion results violate many theoretical arguments, let us examine this one more closely.

Starting with the creation of an electron-positron pair from a finite energy photon (1022 keV $< E_\gamma < \infty$), we can assume that the combined relativistic mass of the pair is less than infinite. Thus, the Coulomb potential fails at $r = 0$. Yet, nearly all quantum mechanics Hamiltonians, using the $(1/r)$ Coulomb potential, do so without comment. This seldom causes a problem since throwing out any solution that does not go to zero at $r = 0$ appears to be an appropriate process. For over 50 years, anytime someone suggests (in a journal) that perhaps the 'anomalous' solution of the Dirac equations (non-zero at $r = 0$) should not be thrown away, papers are immediately published showing that solution to be invalid. In the 21st century, it may not be possible to even publish a paper indicating that the anomalous solution may be valid. In 2005, Jan Naudts was able to get such a paper[a] posted in the 'arXiv' [9]. However, while his paper could not be published in a journal, two papers rejecting his work were able to be published in an established physics journal (Physics Letters A). An earlier paper [10], which gave a finite value at $r = 0$ for a Coulomb-like potential in the Dirac equations, was published in Fusion Technology (not a journal that mathematical physicists would read) and only received rejecting papers from a single source. However, the rejection was not based on the normal mathematical 'niceties'. It was based on a physical reason: the low probability of the anomalous solution having any observable effect.

With this background, let us examine the potentials in the nuclear region. We start with an assumption: the Coulomb potential cannot exceed the mass of the particle producing it. This would mean that the potential energy for an electron cannot exceed 511 keV. (Assume also that any relativistic mass is electromagnetic and therefore not contributing to the charge mass.) In the far field, the electrostatic potentials of a proton and electron are identical, $V_\mathrm{p} = V_\mathrm{e}$. In the near field (i.e., inside the nucleus), the electrostatic potential can continue to grow until limited by the mass and/or effective radius ($R_\mathrm{p} =\sim 0.88$ fm). The potential of the electron loses its $1/r$ dependence at a larger radius ($R_\mathrm{e} =\sim 2.8$ fm), below which $V_\mathrm{p} > V_\mathrm{e}$. Details of this development of a mass-dependent potential are the subject of a different paper.

3.1. Shapes of electrons and protons

When using the concept of size for a proton or electron, there is a lot of ambiguity. For a proton, the radius is considered to be on the order of 0.88 fm. The measured nuclear potential is the primary (and logical) determinant of this dimension.

---

[a] He used the Klein–Gordon equation rather than the Dirac equations. However, the intent and result is the same.

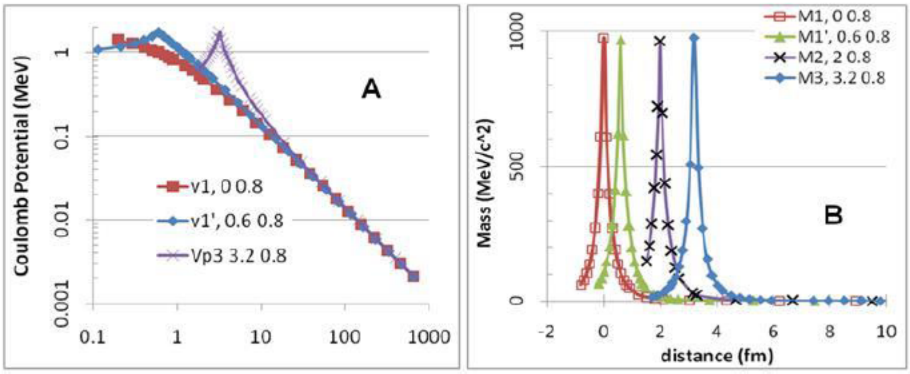

Figure 3. Proton ‘shapes’ for (A) potential and (B) mass energies of protons at various distances (0, 0.6, 3.2 fm) from the origin.

If we were to consider the electrostatic potential to define the radius, then there is a possible problem since there is no well-defined edge to measure. In Fig. 3 we have defined the shapes to be finite at $r = 0$. The electron has a maximum potential energy of 511 keV at $r = 0$ with a ‘turnover’ at the classical radius. The proton has a larger maximum; but, as a compound structure, its energy density integrated over the effective volume must still be that of its mass.

Figure 3A gives the shape of this potential on a log-log plot for three different locations. The shape is not symmetric on this type plot. However, it indicates that the far-field ($>$ 30 fm) potential is not very sensitive to the shape and location of the charge within this nuclear range.

The shape and magnitude of electrons and protons, based on charge potential, are identical in the far field. So in some sense, it could be said that they are the same size. Only within the 10 fm range (for this model) do they differ. Often the electron radius is defined by its Compton radius ($\sim$ 380 fm). In this figure, the potential at that dimension corresponds to about 0.1% of the peak value. If, instead of the potential, we select the mass energy of the proton as the determining factor, then Fig. 3B (a linear plot) provides some examples based on the sub-fermi electrostatic-potential shape of Fig. 3A. We could as easily select a shape that would give 95%, or 99%, of the total field-mass energy to be within the measured radius.

The present model would indicate that protons in a nucleus would repel one another at the $\sim$ 1 MeV level because of their charge. The fact that the addition of an electron’s charge (by replacing a proton with a neutron) reduces the nuclear mass by $\sim$ 0.7 MeV supports this value.

Figure 4A presents the potential of a closely located electron proton pair ($V_\mathrm{p} + V_\mathrm{e}$) on a log-log plot. The absolute value of the negative electron potential is plotted for better comparison with the proton charge potential. Outside of the nucleus, the sum of the two potentials drops off as $\sim 1/r^3$, as should a dipole potential.

Figure 4B presents the electric-field-energy density of closely-located electron-proton pairs on a log-lin plot. Since the modeled potential is finite at $r = 0$, the electric field and its energy density is zero at this point. Beyond about 30 fm, the energy densities have little effect on one another. Within 10 fm, the electron is only a ‘bump’ on the side of a proton. Since the electron is moving around the proton, this bump is ‘smeared’ out and thus is reduced even more. To apply the uncertainty principle to an electron within this range of a proton would make little sense. The question arises, “at what point does a pair of fermions become a boson?”

When an electron comes within a fermi of a proton (with seriously overlapping energy densities), there is no means of identifying the electron as an individual entity. The strong fields and thus the high energy density are now between the pair. If stabilized in a weak interaction, the pair can become a neutron. This presents the next question: does the

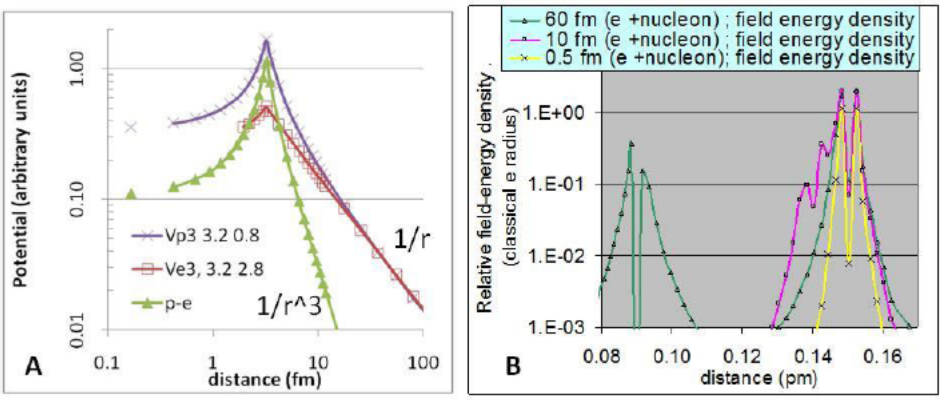

Figure 4. Proton 'shapes' for (A) potential and (B) field-energy densities of protons and electrons at various separation distances (0, 0.5, 10, and 60 fm).

pair of fermions become a boson before it is changed into another fermion, the neutron?

There are many unknowns about the nature and interactions of particles in the fermi range. Cold fusion may be able to contribute to the knowledge of this region. There is also an effect at larger distances that is seldom mentioned, because it is in the transition range between the more-stable nuclear and the atomic phenomena. The spin–spin interaction between intrinsic electron magnetic fields may be critical to CF models invoking the 'slow' collapse and fusion of linear or paired H molecules.

4. Electron spin–spin coupling

Electrons have magnetic moments ('**m**' in Fig. 5) resulting from the current (I) with (near) circular motion (rotation) of an effective-charge density. Magnetic fields (**B**) of electrons interact. These interactions are attractive when the magnetic moments of electron pairs are counter-aligned and repulsive when aligned. However, their effects are a 'mixed-bag' when misaligned. When the electrons are moving, the dynamic coupling is more complicated. When in orbital and/or relativistic motion, the near-field coupling is even further complicated.

The magnetic fields provide a dipole–dipole interaction. However, the amplitude of that interaction depends on the relative dipole-moment orientation and that is dynamic. In the far-field (atomic scale), the magnetic interaction is small relative to the Coulomb interaction; but it does provide ordering of the electron-shell filling. Because of the $1/r^4$ dependence of the dipole–dipole force, if the magnetic moments of two electrons are fully counter-aligned, then the

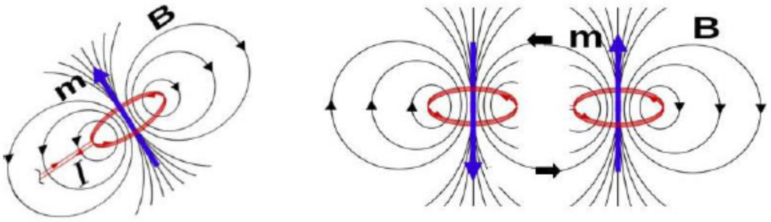

Figure 5. Magnetic fields from electron spin and their interaction.

spin–spin attraction [11] is comparable to the Coulomb repulsion when separated by the Compton radius. The attractive force will lower the total energy of the system providing an attractive potential (Fig. 6) and seeking to maintain the counter-alignment of electron spins. Nevertheless, the angular momentum of the electrons (orbital and spin) will prevent the continued counter alignment of the moments unless a resonance happens to provide such a mechanism.

In addition to the interaction of the electron's spin, external magnetic fields, and the proton magnetic moments (while small relative to those of the electrons) can influence the alignment of the electrons' moments.

Altering the relative alignment of the moments will change both the strength and direction of the interaction. This change can occur at each pass and will randomize the influence of the magnetic interaction. Furthermore, if the protons move closer together and the electrons move deeper into the protons' potential well, the increased electron velocity can introduce a relativistic contribution to the alteration of the spin vector directions. Thus, as the electrons move closer to the protons, such effects grow and the electron–electron interactions become less important relative to those with the proton(s). This should prevent an attractive magnetic potential from ever getting as strong as the Coulomb repulsion between the electrons. This attraction may even weaken with proximity to the proton(s) (or each other) so that it is small near the points of nuclear fusion or of deep Dirac orbits [10]. As a complex multi-body system, it may not have a steady-state solution for the equations of motion. But, it may be chaotic, rather than random. Nevertheless, the variable attractive potential between the electrons could greatly increase their time spent between protons only picometers apart and thus the attractive force drawing the protons together. Since the situation envisioned for this interaction is not steady state, but transient, perhaps just estimating the probability of aiding fusion by this mechanism is possible. However, longer-term interactions in deep-Dirac levels could be strongly affected by these magnetic dipole effects.

5. Summary

(1) The capability of changing H sub-lattice spacing is a potential answer to the cold fusion question of how to achieve H–H proximity and H–H penetration of a Coulomb barrier.

(2) For Coulomb potentials at nuclear distances:

  (a) The electron peak potential is probably limited by mass energy

  (b) The proton peak electrostatic potential is probably limited by its field-energy 'distribution'

(3) Electron spin–spin coupling may be critical to some CF models:

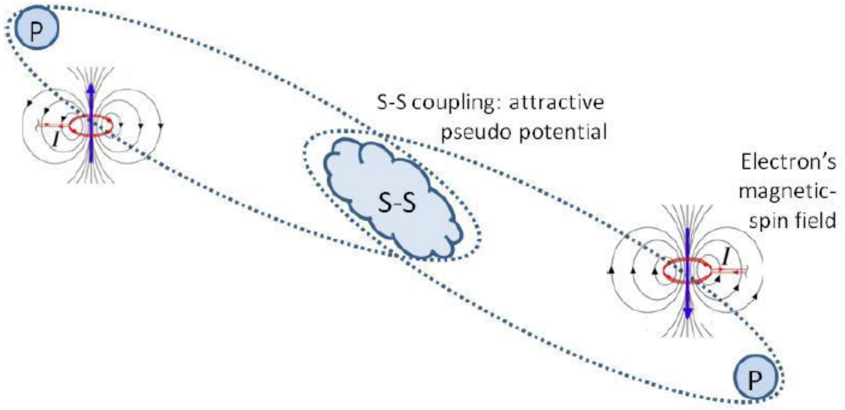

Figure 6. Magnetic field interactions producing a spin–spin attractive potential between electrons.

(a) Spin–spin attraction between electrons could exceed Coulomb repulsion for charge spacing within 300 fm.
(b) It provides an attractive pseudo-potential that is centered between the electrons.
(c) Spin alignment, perturbation, and relativistic velocities of magnetic dipoles in deep passes or orbits about protons make determination of spin–spin coupling difficult.
(d) The influence of these effects needs to be explored in terms of the Dirac equations and their anomalous solution.

Acknowledgement

This work is supported in part by HiPi Consulting, New Market, MD, USA; by the Science for Humanity Trust, Inc, Tucker, GA, USA, and by the Indian National Science Academy. The author would like to thank Daniel Rocha for helpful discussions of the spin-spin interactions.

References

[1] http://en.wikipedia.org/wiki/Einstein_solid
[2] K.P. Sinha, A theoretical model for low-energy nuclear reactions in a solid matrix, *Infinite Energy* **29** (1999) 54.
[3] E.K. Storms, An explanation of low-energy nuclear reactions (cold fusion), *J. Cond. Matter Nucl. Sci.* **9** (2012) 86–107.
[4] A. Meulenberg and K.P. Sinha, Composite model for LENR in linear defects of a lattice, *ICCF-18, 18th Int. Conf. on Cond. Matter Nuclear Science*, Columbia, Missouri, 25/07/2013.
[5] J. Schwinger, Nuclear energy in an atomic lattice, in the First Annual Conference on Cold Fusion, 1990.
[6] http://en.wikipedia.org/wiki/Spin-orbit_coupling
[7] http://en.wikipedia.org/wiki/Spin-spin_coupling#Spin-spin_coupling
[8] K. Sinha and A. Meulenberg, A model for enhanced fusion reaction in a solid matrix of metal deuterides, in *ICCF-14 Int. Conf. on Condensed Matter Nuclear Sci*. 2008., Washington, DC., Proc. , 2009, Vol. 2, pp. 633–638.
[9] J. Naudts, On the hydrino state of the relativistic hydrogen atom, arXiv preprint physics/0507193, 2005.
[10] [10] J. Maly and J. Va'vra, Electron transitions on deep Dirac levels I, *Fusion Technol.* **24**(3) (1993) 307.
[11] http://en.wikipedia.org/wiki/Magnetic_dipole-dipole_interaction

J. Condensed Matter Nucl. Sci. 15 (2015) 125–136

Research Article

Radiation Coupling: Nuclear Protons to Deep-Orbit-Electrons, then to the Lattice

A. Meulenberg*

S-2 Supriya Residency, 93/8 4th Main, 12th Cross, Malleswaram, Bangalore 560003, India

---

Abstract

This paper [1] explores the properties of the tightly bound electrons predicted by the anomalous solution to the Dirac equations. Starting with the assumption that electrons can exist in these deep-Dirac levels (DDLs) with orbits in the femtometer range and ~ 500 keV binding energies, the electromagnetic radiation fields and their coupling to both nuclear and atomic-electrons are identified. The shapes of both the nuclear potentials and the potential at the bottom of the Coulomb regime have a major role in the coupling between excited nucleons and the DDL electrons. The many orders-of-magnitude differences in frequency of the nucleons, the DDL electrons, and the atomic electrons account for the small interactions under normal circumstances. The changes in these frequencies in radioactive nuclides and for excitation of the DDL electrons account for many of the observed phenomena in cold fusion.

Keywords: Cold fusion, Deep-Dirac levels, Non-photonic coupling, Nucleon radiation, Potential shapes

---

1. Overview

The process of nuclear energy transfer from excited nuclei to the outside world is commonly by way of gamma radiation, particle emission, and neutrino emission. All processes require conservation of energy and angular momentum. The various decay paths are generally competitive and depend on the ‘state’ of the excited nucleus. This paper [1] will look at a non-standard process of nuclear-energy coupling to the lattice via the deep-Dirac level (DDL) electrons proposed as a primary pathway [2] in at least one decay mode of low-energy nuclear reaction: that of deuteron fusion, D–D to ^{4}He*.

The existence of [3] and processes of populating [4–7] these DDLs have been addressed in earlier papers. In this paper, we will assume that they exist (perhaps short-lived in the normal sense, e.g. femto-seconds) and that they can exist about an excited nucleus. In our energy-transfer process, without particle decay, nuclear-energy coupling to the lattice involves near-field (less than a wavelength) electromagnetic EM coupling of energy from energetic charged nuclei to deep-Dirac level electrons. From there, the energetic electrons couple energy (via near-field and far-field radiation) into adjacent free and bound electrons in the lattice. This coupling causes intense local ionization and perhaps energetic

---

*E-mail: mules333@gmail.com

(multi-keV) electrons, but little or none of the energetic EM radiation normally observed from excited nuclei. There will be soft X-radiation from bound and free electrons decaying back into the emptied orbits of the lattice atoms. The resulting decays of the ionized and highly destabilized lattice atoms produce a greatly ‘broadened’ spectrum of photonic radiation with energies up to the binding energies of those electrons (eV to multi-keV level).

The ratios of the various energy transfer modes, nuclear to DDL, nuclear to lattice, and DDL to lattice have been explored in an earlier paper in terms of Maxwell’s equations for the **E**-field strengths produced by the acceleration of the various charges involved [8]. This paper will spend more time on the coupling between the charges and therefore on the energy-transfer nature and probabilities. Many details, such as magnetic coupling and the differences between protons and neutrons within the nucleus, are not included here.

2. Radiation

2.1. Maxwellian

The ‘Bible’ for electromagnetic (EM) radiation studies is Maxwell’s equations. However, Maxwell did not believe in photons and he certainly did not know about atomic-electron orbitals. Nevertheless, his equations hold up today, nearly a century and a half after he proposed them. They are continuing to be used (and misused) today. Their far-field component has been used to explain photons. But then quantum mechanics claim that only QM can explain why they stop radiating and why matter does not collapse as all bound electrons spiral into their nuclei. There are better reasons (see below [9]); but Maxwell’s equations and the concept of non-photonic bound-radiation fields are fundamental to the development explored herein.

2.2. Atomic

Transitions between atomic-electron orbitals are the source of most of our observed light radiation. QM describes the basis for discreet orbitals as the mechanical resonance of an electron in a Coulomb potential well. It does not include

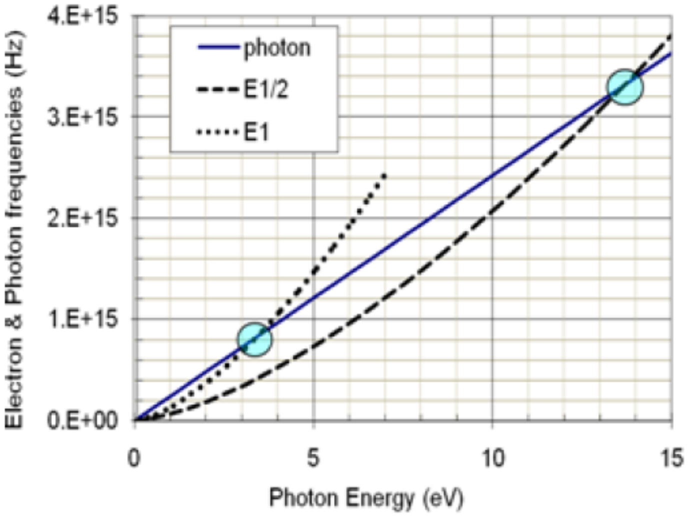

Figure 1. Relationship between hydrogen–electron and generated-photon frequencies and energies.

the EM radiation in those calculations. It simply states that the radiation matches the differences in the predicted energy levels and therefore the QM calculations are correct. They *are* correct, but they do not explain the mechanism of EM radiation caused by the 'fall' from one orbit into one deeper in the potential. Maxwell says that charge has an associated electric vector field, **E**. A uniformly moving charge also has a magnetic vector field, **B**. A cyclically moving charge has an EM field. He never mentioned the fields leaving. All of these fields are bound to the charge and cannot leave accept under special circumstances.

What are the special circumstances for radiation to occur from an atomic electron? Fig. 1, for a hydrogen atom, indicates the relationship between photon frequency E_γ and the electron orbital frequency (ν_e) that is proportional to $E^{3/2}$ [9]. The photon curve indicates the linear relationship between the photon frequency and its energy ($E_\gamma = h\nu_\gamma$). The E1 curve represents the electron frequency that corresponds to the photon energy at that frequency. Note that the resonance point ($\nu_\mathrm{e} = \nu_\gamma$) is at $\sim$ 3.3 eV, which corresponds to the $n = 2$ level of H at $\sim$ 3.34 eV. The $n = 1$ ground state (13.6 eV) is identified by resonance with the $E_{1/2}$ curve. This curve represents one-half the frequency associated with the electron orbit [9]. Of importance here is the special frequency relationship between the electron and the photon that permits a photon to form about, and depart from, the atom.

The departure of a photon does not eliminate the bound EM-field. It is constantly being generated, even when an electron is in the ground state. The EM-field is part of the electron and contributes to the effective mass that must be used to calculate its kinetic energy [10]. This EM-field is confined as an evanescent wave; it can be considered to be a virtual photon [11]. What keeps the electron in the ground state from emitting a photon? QM says that the electron is at an energy minimum and cannot lose any more energy. Yet we know that an electron at 1 fm from a proton charge center has energy in the MeV range. So the atomic ground state is not a minimum energy. It is a local minimum, a resonance, as are all of the orbitals. The real reason is that it takes angular momentum of h to form a photon and the ground state electron does not have that amount to donate. Even if it did have sufficient angular momentum, the frequency mismatch between the electron and forming photon would prevent formation of the required resonant EM state called a photon.

2.3. Nuclear

Transitions between nuclear levels are similar to those of the atomic electrons and produce gamma rays. In this case, the charge oscillators are the nuclear protons and not an electron. While protons do not radiate as efficiently as electrons (when in the same accelerating field), a proton in a MeV field could radiate more than will an electron in a multi-eV field. There are major differences though [8]. While the nuclear frequencies and accelerations are much higher than those of the atomic electrons, the dipole moment is 4–5 orders of magnitude smaller. Other important differences are explored in the section on potentials.

2.4. Bound vs. unbound radiation

Decay transitions between energy levels require a release of energy from the local system. Both before and after the transition, the bound radiation field about the bound electron/proton pair is present. This is also true for the nuclear protons. Maxwell's equations (and their extension) give values to the bound **E**-field strengths resulting from the charge acceleration [8]. These EM fields are radiated out from the dipole-charge center, but are not released. They are evanescent waves that do not convey energy unless there is an absorber present. They are 'standing' waves with as much energy entering the dipole source as leaving. These evanescent waves 'reach out' and can interact with charges in the vicinity. Since, unexcited atoms are conservative systems, these interactions are reversible. If a photon can form and depart or be absorbed, this is an irreversible process. (It is reversible by the inverse operation with an incident photon.) However, there are other irreversible processes that a do not involve photons. These involve the bound EM waves in a direct energy-exchange process. We will discuss both processes below.

3. Radiation Coupling

3.1. Resonance

Energy exchange is almost always a resonance phenomenon. We will describe it in our system from a classical viewpoint of coupled oscillators. Two coupled oscillators, with different resonant frequencies, ν_1 and υ_2 will generate additional frequencies that depend on both resonants (e.g., $\nu_1 \pm \nu_2$). The process of finding the 'common' frequency classically is to establish the system of linear equations for both oscillators and then, after putting it into a matrix, to diagonalize the matrix. This is the basis of the Heisenberg matrix mechanics. And, since it has been proven that the Heisenberg formulation is equivalent to the Schrodinger wave formulation and thus QM, we will stick to the more-intuitive classical oscillator model for the present.

Consider a system consisting of the electron and its EM field. Since energy transfer is more efficient when the two oscillators are resonant (and both are resonant with the common frequency), we can see the resonant condition for photon formation, $1/(E_1 - E_2)$ comes directly from this condition, $1/(\nu_1 - \nu_2)$. Recognize that $1/(E_1 - E_2) = 1/(h\nu_1 - h\nu_2)$ is not valid in general. However, in a Coulomb potential, the kinetic energy KE of a non-relativistic orbital electron is equal to the photon energy E_γ that was released in the formation of the orbit by bringing the electron from infinity. Thus, KE $= E_\gamma = h\nu_\gamma$ and this is also the binding energy BE of that energy level. The equality, $1/(E_1 - E_2) = 1/(\nu_1 - h\nu_2)$, is a nice way of keeping track of both the energy relationships and resonances. It ties the electron-energy levels to the photon release that can create the deeper orbits.

The derivation for the Bohr orbits, using classical resonance relationships between the electron and photon frequencies [9], speaks of a 'nascent' photon. This is the EM field that is approaching both the energy and frequency conditions for the photon that might be emitted. While the description identifies the conditions for both absorption and emission of photons, it does not emphasize the fact that the photon is an energy 'coupler' between the electrons of two atoms.

3.2. Couplers

In the simplest picture, consider an electron far from a proton. If bound to the proton, its orbital frequency and generated EM field is very low. As an oscillator, coupled to its EM field that is another oscillator, the electron can move its orbit closer to the proton by transferring energy to the field (if a photon can escape). In the process, it will increase its orbital frequency and its EM-field energy and frequency. If no photon is released, as in the inward portion of a non-radiating elliptical orbit, the EM field grows but then returns energy to the electron as it moves back out to its original position. Just as observed in coupled simple-harmonic oscillators that only change their amplitudes over time (at the common coupled frequency), the electron and EM field change their amplitudes; but, in a Coulomb potential, they also vary their frequencies over time. Since the photon has a single frequency for a given energy, but an infinite possible set of energies, its formation must depend on resonances with the electron. At these resonant frequencies, energy can be transferred quickly enough to allow a photon to 'complete' itself, become an independent soliton [12], and leave. During the emission process, there are three coupled resonators involved: the electron, its bound EM field, and the photon. This is an important factor that needs to be further explored.

The reverse process, photo-absorption, again depends on the resonance between the incident photon and the bound electron (and its EM field). In this case, the photon interacts with the electron by 'loading' energy into the electron's EM field. With a greatly enhanced EM field, the balance between the oscillators (EM field and bound electron) is shifted and the electron has its radius increased. Thus, it slows down and decreases its orbital frequency.

Unlike a simple harmonic oscillator that keeps the same frequency independent of the energy input, an electron in a Coulomb potential experiences changes in both its orbital and its EM-field frequencies. These changes are reflected in the anomalous dispersion relationship (Fig. 2) for resonant frequencies at the macroscopic levels. At the atomic level, the variations in the dispersion relationship are more extreme. The importance of resonance between the electron's

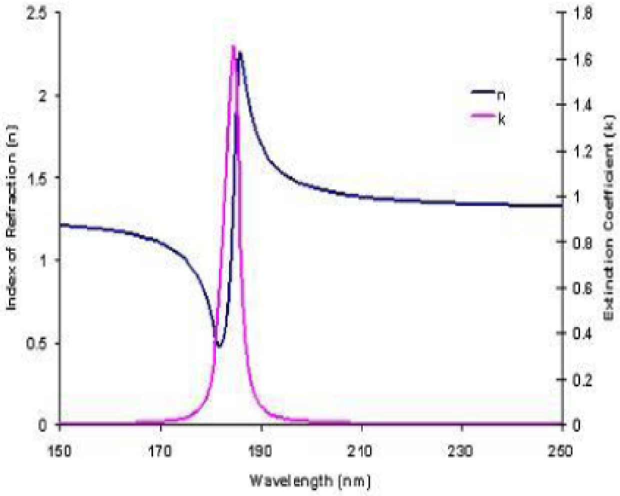

Figure 2. Anomalous dispersion curves showing the extinction coefficient *k* (related to absorption) and the refractive index (*n*, showing the local fluctuation in speed of light).

orbital frequency and the photon frequency is seen in the local high refractive index (*n*) at resonance. This high n, as in a lens, focuses the large-diameter photon (e.g., micron size) into the smaller atomic region (Angstrom size). The change in frequencies during the energy exchange is important also. The rates of change in orbital and field frequencies (inversely related to the wavelengths shown in the figure) alter the effective frequency of the incident photon. Again, interactions of '3-body' coupled resonances must be explored in detail (but not here).

We will make another assumption at this point that affects the later sections of this paper.

Assumption: Just as the electron and its bound EM-field are coupled and frequency-related during the variations (oscillations) of the electron orbit within an atom, these two oscillators are coupled and frequency-related to the energy and frequency of a third coupled oscillator, the photon, during the emission or absorption of that photon.

This assumption is an attempt to explain the observations and physical 'laws' that state the photon to be the coupling mechanism between atoms. If this assumption is correct, and the relative frequencies of the three resonators alters the absorption and emission probabilities, then the nature of the potential well that a charge 'inhabits' will also affect the probability of transitions and even their nature.

3.3. Coupler dependence on the shape of potential

All atomic spectra are generated by electrons in a Coulomb potential (although one that may be influenced by its environment). This is not necessarily the case for gamma rays and, as will be seen, not always the case for an electron in the deep Dirac levels. Figure 3 illustrates a model of a useful nuclear potential (Woods–Saxon) [13], showing the different regimes, and an experimentally determined potential showing application of the model to a real nucleus (that includes the Coulomb barrier). The model has a harmonic oscillator regime, where a change in energy does not alter the nucleon frequency. It also displays a square-well regime where the frequency of a nucleon increases as it is raised in the potential well (and is lowered as the nucleon drops deeper into the well). A regime not shown explicitly is the

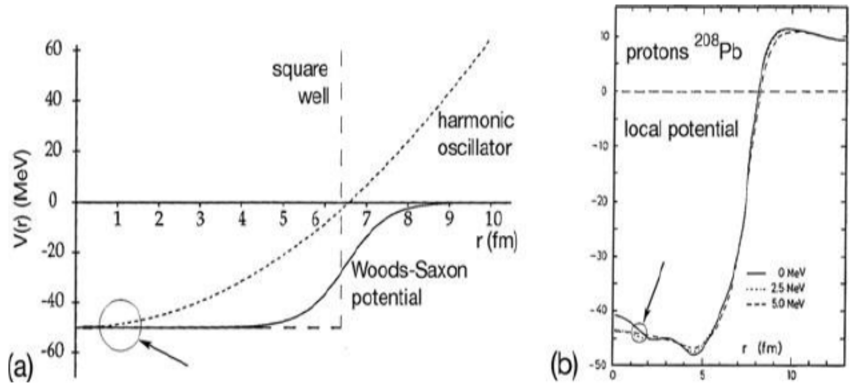

Figure 3. (a) A nuclear-potential model and two simplifying approximations. (b) A measured nuclear-potential profile.

region near the escape energy where the shape of the potential 'turns over' and is much closer to that of a Coulomb potential. In this region, the nucleon frequency decreases as it is raised in the well and increases as it drops into the well.

Since the nuclear forces are short-ranged (< 1 fm), the inner nucleons of a multi-nucleon nucleus contribute little to the shape at its edge. Thus, a low-Z nucleus would have little or no 'flat' region in its center (unlike the high-Z nuclei of Fig. 3). The nuclear radius ($R = r_{\mathrm{o}}A^{1/3}$, with $r_{\mathrm{o}} = 1.25$fm) is much smaller.

If the assumption in the last section is valid, then protons near escape velocity of the nuclear potential can more readily produce photons than those much deeper in the well. They are moving faster and have a stronger acceleration (thus greater EM field), because of the square-well potential further in. This ready emission of energy would be a means of 'containing' protons within the nuclear potential. If in a region of the potential where photons are not readily formed, then a nucleon tunnelling out of the nuclear potential well (through the Coulomb barrier) may be the dominant mode of changing nuclear energy levels. Other nuclear decay modes also can become dominant. The potential-dependent coupling described above now leads to the question of the electron's deep-Dirac levels (DDLs) that are at the bottom of their Coulomb potential [14]. What are the real shapes of the local potentials and the consequences of that shape?

4. Radiation to and from Deep Dirac Levels (DDLs)

Normal atomic electron orbitals are narrow minima (resonances) within a Coulomb potential. The bound electrons are moving around in an Angstrom-size well with perhaps a low Fermi-size hard-core center. Deeper levels have much smaller radii. To go to a lower orbit (from an excited state) and maintain the 'closed' orbit of an integer number of the deBroglie wavelengths, the electron must increase both its kinetic energy and momentum. The change in energy required is larger at the lower orbitals. At high levels, near ionization, the orbits widen out rapidly and the energy levels come closer together.

Figure 4 gives the electron kinetic energy (KE in meV) as a function of distance from a proton [5]. The dips (minima) in the curve represent various resonances, known and possible. The depth of the dips is not real, only representative. Does a resonance actually change the KE? It changes the probabilities, but does that represent a potential? The single Compton wavelength should generate a resonance with a corresponding local minimum in the electron's energy level. Has this level ever been seen? The deep-Dirac levels for hydrogen have been predicted at a binding energy, BE $=\sim 500$ keV. Is there a resonance there? There appears to be a change in the shape of the potential, because now the centrifugal barrier is a large portion of the available potential well. To get this much energy from the Coulomb potential alone, the

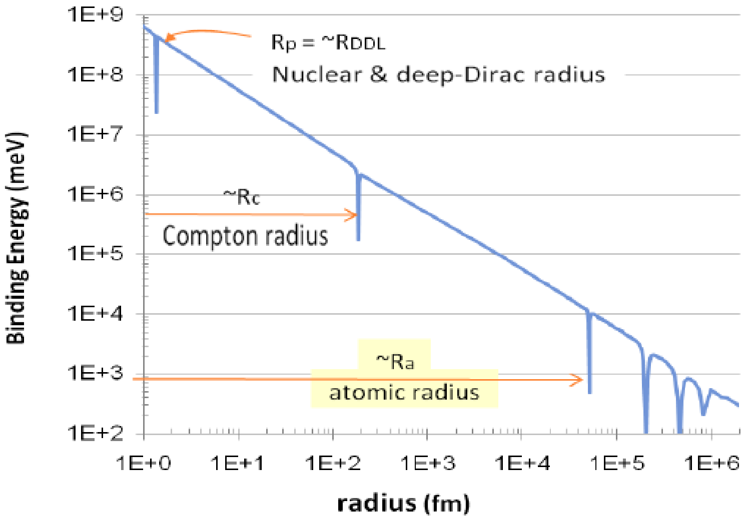

Figure 4. Ranges for kinetic energy vs. radii of nuclear, DDL, and atomic-electron orbitals.

electron must be within a Fermi of the center of the proton. The spin coupling between the electron and proton may allow the orbit to be larger. However, there are presently too many unknowns in this region to properly predict levels.

Nevertheless, much can be suggested about the DDL orbits. They are at or near a true minimum (the maximum kinetic energy in Fig 4). The energy predicted by the Dirac equations [7] can only be order of magnitude, since the $1/r$ Coulomb potential is not assumed to be valid to below 1 fm and no nuclear magnetic moment has been included in the Hamiltonian. The centrifugal barrier confines the electron to near-circular orbits and prevents formation of 'normal' s-orbitals that would pass closer to the proton center. Classically, relativistic orbits with too little angular momentum would simply 'spiral-in' to the proton center (whatever the nature of that center). The only paper to calculate details of the DDLs, gives the DDL ground state to be an $n = 2$ orbit, nevertheless Maly and Va'vra [3] still classify it as an s-orbit (its angular momentum is less than h so that $\ell = 0$).

Maly and Va'vra also find additional, deeper, orbits with higher angular momentum (high ℓ implies more circular orbit) and kinetic energy. This is reasonable since the lowest ℓ values produce rosette orbits (orbital paths oscillating between a non-zero inner and an outer limit). More circular orbits can have a smaller average distance from the proton center and therefore their average distance from the proton(s) may be deeper in the Coulomb potential. The asymptotic limit is 511 keV. This added energy goes into relativistic mass that increases the angular momentum of the circular orbit. At some point, the mass increases faster than does the relativistic velocity. The reduction in average orbital radius with addition of energy increases the electron frequency, but no resonances have been considered on this inner branch away from the DDL ground state. (Magnetic Landau levels and the neutron may be options on this branch.)

It is this ability to increase frequency with added energy that makes the DDL such an important 'tool' in the cold fusion story. This trait, impossible in a Coulomb potential, is also that of the photon. Thus, the DDL electron can act as a coupling medium between the nuclear protons, which might be in the Coulomb-like regime of the nuclear potential well of a femto-atom [15,16], and the lattice electrons.

4.1. Nuclear to DDL energy transfer

A nucleon, in a square-well portion of a potential, will decrease its frequency as it decays from a more energetic state. As, or if, it moves to the bottom of a nuclear well, a particle becomes a simple harmonic oscillator (SHO) that will not change its frequency as it changes its energy. No nuclear potential well will be as conducive to forming photons as the atomic potential, since the high mass and small dipole moments of nucleons more than compensate for the strong acceleration field of the nuclear potential. However, the nuclear square well and SHO further impede photon formation because the inverted changing of resonance frequency of a nuclear proton and that of a nascent photon would appear to play a major role. This difference in change of resonant frequency with particle kinetic energy is critical to the following discussion.

From the nuclear-potential model (Fig. 3), as an excited nuclear proton decays from the quasi-Coulomb potential region, it moves into the square-well type region ($r = < 1$ fm?) and its ability to form photons will diminish. In these deeper parts of a nuclear potential, where the nucleon frequencies decrease as their kinetic energy decreases, photon formation and emission is less likely.[a] Therefore, internal conversion or other mechanisms become the dominant decay modes [2].

If DDL electrons are present about a nucleus, the situation is different. Proximity makes the excited-proton EM field very strong for the full DDL electron orbit (not just a small portion of it) and excited-nucleon and DDL-electron frequencies are comparable. Direct proton EM coupling to an electron in the DDL Coulomb branch is thus a rapid decay path for excited nuclei in the middle regions of the nuclear potential well.

The point to remember is that, because DDL electrons have two branches through which they can absorb energy, they are able to readily and directly draw energy from excited nuclear protons *regardless* of which nuclear-potential regime they inhabit. The inner branch leads to formation of neutrons, if sufficient energy is available in this mode. Whether this neutron formation bypasses, or simply accelerates, the weak interaction is still to be determined.

4.2. DDL electrons to atomic electrons

The next step is similar. The DDL electron(s), now with excess energy from a decaying proton, is able in turn to transfer energy to the bound electrons of the host lattice atoms. Nevertheless, the method of energy transfer to the lattice electrons is not through the expected modes.

Proximity coupling, via photons from relativistic electrons, could predict extremely high transfer rates. However, the very small dipole moments and extremely high frequencies of the DDL orbits prevent this. Furthermore, if a DDL electron has absorbed energy directly from a proton in a nuclear-Coulomb mode, then the DDL electron would be excited into the near-nuclear (inner) mode. It would have increased its frequency to try to match that increase of the decaying proton. If in turn, the excited DDL electron tries to lose that excess energy, its decay mode from the inner branch is *not* compatible with photon production.

Figure 5 gives some perspective on the relationship between the nucleon, DDL electron, and atomic-electron frequencies. The DDL- and nuclear-orbital frequencies are only rough approximations, since the values depend on the model selected. Nevertheless, because of the near square-well nuclear potential, excited nucleons have frequencies even

---

[a] Some physicists will insist that an electron or nucleon changing state will annihilate at state A and be recreated at state B. I, agreeing with Feynman, will insist that the particles move continuously along a path from one state to another. If this is so, then the EM-field, always present with charged particles in motion, will reflect the variations in potential along that path. These variations in the EM-field are critical to the formation and departure of a photon [9]. Extending this logic, the shape of the potential well will alter the nature and probability of a transition. It will alter the preferred mechanism for a particular transition. It is in this spirit that I discuss the energy transfer between excited nucleons and the DDL electrons. Under these conditions, fixed energy levels need not be considered. The transfer of energies by a non-photonic EM-radiation mechanism is possible and much more probable than by any other mechanism.

closer to those of the DDL electrons than those of nucleons in the ground state. Thus, energy transfer is increasingly more efficient for the excited nucleons. It can be seen that because of the difference in frequency, the coupling between nuclear protons and atomic electrons would be negligible. The situation is worse for DDL and atomic electrons. This is why the DDL population is so low. The DDLs and atomic levels cannot readily communicate. However, electrons in those levels can transfer energy in other ways.

How does a DDL electron, with excess energy from a decaying proton, transfer energy to the bound electrons of the host lattice atoms. The inner branch is compatible with direct stimulation of the atomic electrons. In this regard, the DDL electron is like the photon and would be a case of a fermion, rather than a boson, being the mediator between two fermions.

The extreme difference in frequency between the DDL and atomic-orbit electrons does not present an insurmountable problem since an s-orbital lattice electron quickly passes close to its nucleus at relativistic velocities. The strong DDL electric fields from the same or adjacent deep-orbit atoms will perturb lattice-electron paths during this period of velocity matching in a non-linear region (near its nucleus) and allow significant direct energy transfer. This process is like that of a baseball bat rather than like resonant photon transfer. Stable resonant states are not required for such energy transfer.

4.3. The DDL baseball bat

As an example of a DDL electron's influence on a nearby s-orbit atomic electron, assume that the DDL electron's **E**-field (at $> 10^{23}$ Hz, Fig. 5) is strong enough to accelerate an electron to an average velocity of 10^8 m/s for a fifth of a DDL electron cycle (2×10^{-24} s). The atomic electron will deviate from its path by 2×10^{-16} m or 0.2 fermi. Normally, during a whole DDL-electron cycle, the atomic electron will fluctuate by this amount and never be affected. If, however, it is shifted this much during perigee, when it might be as close as 10 fermi from its nucleus, this much shift in its orbit may change the atomic electron's orbit by 2 keV. (See Fig. 4, where the electron energy at 10 fm is $\sim$ 80 keV and at 8 fm $E =\sim 100$ keV. Divide this difference of 20 keV by 10, to approximate a 0.2 fm shift, to get a $\sim$ 2 keV shift in energy.)

A 2 keV shift would not be the most common energy transfer. But it is not a maximum either. Each neighboring lattice atom has multiple s-orbit electrons and they transit their nuclear region in the $> 10^{16}$ times per second range. Many more next-neighboring lattice atoms are not as strongly affected, but might absorb 100s of eV per s-orbit pass.

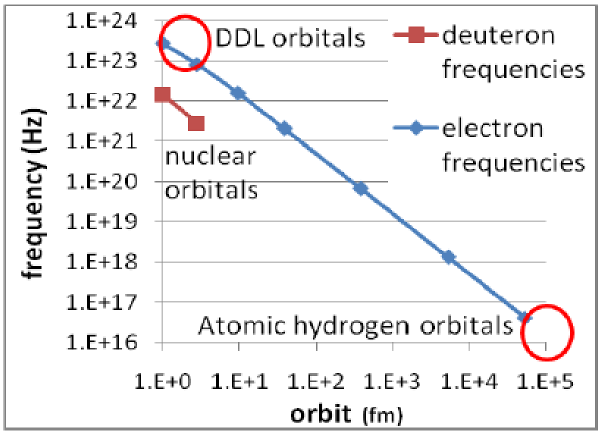

Figure 5. Ranges for frequencies and radii of nuclear, DDL, and atomic-electron orbitals.

Most of the time the phases between the DDL and atomic electrons would not be ‘right’ for such large energy transfers. Furthermore, the energy added to, and subtracted from, the s-orbit electrons is only accumulated on a statistical basis. Nevertheless, energy can be transferred from the nucleus to the DDL electron and on to the lattice at a very high rate. The transfer is at a rate that would cause ionization and yet not cause damage to the lattice.

4.4. Observables

The interaction between the excited nuclei and the DDL electrons would not be directly observable except in a few cases. The case when a pair of femto-hydrogen atoms (hydrogen with DDL, instead of normal, electrons) [8] join and produces a deuterium atom would probably also produce a neutrino. Neither a single deuteron nor the neutrino could be easily identified nor as being correlated or even attributable to the same event.

The keV excitations of bound lattice atomic s-orbit electrons would lead to X-rays that have been observed in cold fusion experiments. There would be two types of X-rays. There would be those, with a broad range of energies, from Bremsstrahlung produced by energetic electrons ejected by the initial ‘kick’ from the DDL electron that far exceeded the ionization energy. There would also be nearly monoenergetic X-rays from electrons falling into the emptied s-orbits. Nevertheless, the severe local disturbance (ionization and strong EM fields) might still spread such normally spectral energies beyond identification. Since there are higher-n s-orbital electrons, a whole range of lower-energy EM radiation would also be available. But, they might be even harder to observe, if the events were not taking place on the surface and an appropriate ‘window’ or internal spectrophotometer were not available.

5. Summary

From this author’s last year’s and this year’s ICCF papers, we can draw a fairly complete picture of interactions and events assuming the predicted properties of a DDL electron and the known properties of nuclear protons. This paper dwells on the energy transfer between excited nucleons and the DDL electrons and then to the bound electrons of the lattice atoms. Many of the properties of this exchange process are described below. Note that both the nucleons and the DDL electrons have two frequency-dependent modes.

5.1. Protons to DDL electrons

- **Processes to increase energy transfer (no large effects)**
  - (a) Excited nuclear protons (in the square-well potential regime) have higher frequencies (closer to DDL electron’s resonance frequencies) than do ground-state protons.
  - (b) Decaying protons (in the attractive Coulomb-like nuclear-potential regime) may significantly decrease their orbital radius during this process and thereby increase orbital frequency, acceleration, and radiation field. This increases their net coupling to DDL electrons being excited into the inner branch, which also increase their frequency as they gain energy.
  - (c) Exciting DDL electrons into their Coulomb branch will lower their frequencies and bring them closer to the nuclear-proton’s resonant frequencies.
  - (d) Energy added to DDL electrons, in the Coulomb regime, increases R_{DDL}, and thus their dipole moments. This increases coupling to nucleons.
- **Processes to decrease energy transfer**
  - (a) Protons that are lower in the square-well regime have lower frequency. This reduces their radiation field intensity and moves them further from DDL frequencies.

(b) Decaying protons, in the square-well regime, lower their frequency as they lose energy. This lowering reduces their radiation field intensity and their coupling to forming photons and to DDL electrons in the inner branch, which increase their frequency with added energy.

5.2. DDL electrons to lattice electrons

- **Processes to increase energy transfer**
  (a) Collisions of DDL electrons with lattice valence electrons approaching a nucleus transfer energy directly.
  (b) Collisions give DDL electrons angular momentum that allows them to radiate photons (not possible before).
  (c) Exciting DDL electrons into the Coulomb branch lowers their frequency (closer to that of bound lattice-electron's orbital resonances).
  (d) As DDL electron excess energy (from excited nucleons) approaches its binding energy, its frequency overlaps with lattice atomic-electron states.
  (e) At close to DDL-electron ejection, both frequency and spatial overlap occurs with the more numerous d-orbital lattice electrons.
  (f) DDL-electrons, with higher binding energy, have greater EM radiation fields and thus are in a better transfer regime with respect to free lattice electrons.
  (g) Energy added to DDL electrons, in the Coulomb branch, increases R_{DDL}, and thus their dipole moments.
- **Processes to decrease energy transfer**
  (a) Increasing R_{DDL}lowers DDL electrons' acceleration and thus their EM field (large effect)
  (b) Excited DDL electrons in the Coulomb branch have lower velocities and thereby a reduced relativistic term (3–4× effect)

Acknowledgement

This work is supported in part by HiPi Consulting, New Market, MD, USA; by the Science for Humanity Trust, Inc, Tucker, GA, USA, and by the Science for Humanity Trust, Bangalore, India.

References

[1] Based on Poster Paper by A. Meulenberg, Radiation Coupling: Nuclear protons to deep-orbit-electrons, then to the lattice, *ICCF-18, 18th Int. Conf. on Cond. Matter Nucl. Sci.*, Columbia, Missouri, 25/07/2013. http://hdl.handle.net/10355/36501

[2] A. Meulenberg, From the naught orbit to He^4 ground state, *16th Int. Conf. on Cond. Matter Nuclear Sci.,* Chennai, February 6–11, 2011, *J. Cond. Matter Nucl. Sci.* **10** (2013) 15–29.

[3] J. Maly, and J. Va'vra, Electron transitions on deep Dirac levels I, *Fusion Technol.* (US) **24** (1993) 307–318.

[4] A. Meulenberg and K. Sinha, Tunneling beneath the 4He* fragmentation energy, *J. Cond. Matter Nucl. Sci.* **4** (2010) 241–255.

[5] A. Meulenberg and K. Sinha, New visions of physics through the microscope of cold fusion, *J. Cond. Matter Nucl. Sci.* **13** (2014) 378–390.

[6] A. Meulenberg and K.P. Sinha, Composite model for LENR in linear defects of a lattice, *ICCF-18, 18th Int. Conf. on Cond. Matter Nucl. Sci.*, Columbia, Missouri, 25/07/2013 http://hdl.handle.net/10355/36818.

[7] A. Meulenberg and K.P. Sinha, Lochon and Extended-lochon models for lenr in a lattice, *Infinite Energy Magazine*, pp. 29–32, Issue 112, November/December 2013.

[8] A. Meulenberg and K.P. Sinha, Deep-orbit-electron radiation emission in the decay from 4He* to 4He, *J. Cond. Matter Nucl. Sci.* **13** (2014) 357–368.

[9] A. Meulenberg, Creation and fusion of photons, Paper 8121-29, SPIE Optics + Photonics 2011, 21–25 August 2011, San Diego, CA, United States.

[10] C.A. Mead, Collective *Electrodynamics: Quantum Foundations Of Electromagnetism*, 2nd printing, MIT Press, Cambridge, MA, 2000, p. 21.

[11] A. Meulenberg, Virtual and real photons, Paper 8121-38, presented at SPIE Optics + Photonics 2011, Conf. 8121 The Nature of Light: What are Photons? IV, 21–25 Aug. 2011, San Diego, CA, USA.

[12] http://en.wikipedia.org/wiki/Soliton_

[13] http://en.wikipedia.org/wiki/Woods%E2%80%93Saxon_potential

[14] A. Meulenberg and K.P. Sinha, Deep-electron orbits in cold fusion, *J. Cond. Matter Nucl. Sci*. **13**(2014) 368–377.

[15] A. Meulenberg, Femto-atom and femto-molecule models of cold fusion, *Infinite Energy Magazine*, pp. 41–45, Issue 112, November/December 2013.

[16] A. Meulenberg, Femto-molecules and transmutation, *J. Cond. Matter Nucl. Sci*. **13** (2014) 346-357.

J. Condensed Matter Nucl. Sci. 15 (2015) 137–148

Research Article

Revisiting the Early BARC Tritium Results

Mahadeva Srinivasan*,†

Bhabha Atomic Research Centre, Trombay, Mumbai, India

Abstract

Within days of the F&P announcement of 1989, several groups at BARC embarked on a program to look for the generation of neutrons and tritium when deuterium (or hydrogen) is loaded into metals such as Pd, Ti and Ni. Electrolytic, gas and plasma loading techniques were deployed. Post run electrolyte samples were analyzed for tritium content using standard liquid scintillation techniques. In the case of gas and plasma loaded "dry" samples, surface tritium content was measured directly using windowless beta counters. Autoradiography was deployed as a very effective tool to monitor the spatial distribution of tritium in the near surface layers of test samples. The first confirmation of copious tritium generation was obtained on 21 April 1989 in a commercial "Milton Roy" Pd–D_2O electrolytic cell. The results obtained during the first year of the BARC Cold Fusion campaign were presented at ICCF 1 in March 1990 where we reported observing tritium generation in 22 different electrolytic cells, which were set up totally independently by diverse research groups. The present paper revisits the early BARC tritium results obtained in a variety of experimental configurations during the period 1989–1996.

Keywords: Autoradiography, BARC Studies, Deuterium gas loading, Electrolysis experiments, Ni–H experiments, Plasma focus, Tritium measurements

---

1. Introduction and Scope of BARC Studies

A four-line news item on the Fleischmann and Pons (F&P) announcement carried by the 24 March 1989 issue of the Times of India newspaper, triggered a flurry of activity at the Bhabha Atomic Research Centre (BARC) in Mumbai. Within days, groups with expertise in a variety of disciplines such as hydriding of metals, electrochemistry, isotope exchange processes in upgrading heavy water, fusion plasma experiments and neutron and tritium measurements, set up electrolytic cells with widely different geometrical configurations, in order to verify the nuclear origin of the F&P effect. Because neutrons and tritium were the commonly expected products of fusion reactions, these were the signatures that the BARC experiments sought. BARC, being the premier nuclear R & D centre in India with more than 50 divisions and 3500 scientists and engineers, had the expertise and equipment readily available for study of every aspect of nuclear science.

---

*E-mail: chino37@gmail.com

†Retired.

Details of the various electrolytic cells setup and the results of the neutron and tritium measurements carried out in the early years are documented in [1–4]. The first publication on the confirmation of generation of neutrons and tritium in the BARC Cold Fusion experiments was presented at the Fifth International Conference on Emerging Nuclear Energy Systems (ICENES V), held in Karlsruhe during July 1989 [1]. A comprehensive paper with 50 authors, published in the August 1990 issue of Fusion Technology [4], describes in great detail the Cold Fusion experiments conducted at BARC during the first year following the F&P announcement, inclusive of the gas/plasma-loaded Ti samples studies [5]. An interim progress report, titled "BARC Studies in Cold Fusion," covering the period April to September 1989 [2] unambiguously confirming the occurrence of nuclear reactions at room temperature in deuterided Pd and Ti samples was published around the same time as the highly negative findings of the report of the Energy Research Advisory Board Cold Fusion Panel set up by the US Department of Energy and played a key historical role in helping keep interest in the subject alive. During 1992–1995, additional experiments were carried out with Ni–H systems, and these also indicated the production of tritium [7–9].

1.1. Measurement of tritium levels in solution samples

Tritium levels in the electrolyte samples collected after operation of the cells for some time were measured by specialist groups of the Isotope and Health Physics divisions of BARC using well-known liquid scintillation counting techniques applicable for low energy beta emitters, taking the following precautions: (a) ^{40}K free counting vials were employed to minimize background counts; (b) For higher count rate cases, 0.1–2.0 ml of sample was added to the scintillator, while for low count rate samples, $\approx$10 ml was used. In the higher concentration samples, pH was reduced by diluting with double distilled water, in order to minimize chemiluminescence as well as quenching effects. If warranted, micro-distillation of the samples was resorted to before the addition of scintillation cocktail. Whenever possible, the measured tritium values were cross-checked with results obtained after chemiluminescence cooling; and (c) Instagel scintillation cocktail was used as solvent to minimize chemiluminescence interference effects. Samples of the electrolyte saved prior to the commencement of electrolysis were counted along with the test samples drawn from the operating cells. To compute the excess tritium produced in each run, the following points were considered: (i) Initial tritium concentration in the stock D_2O. (This was typically a few Bq/ml.) (ii) To be on the conservative side, the tritium carried away by the D_2 gas stream during electrolysis was neglected and (iii) Dilution effects from the periodic make-up of D_2O were accounted for.

1.2. Measurement of tritium on surface of solid samples

Tritium which has a half life of 12.3 years, emits a low energy β having a maximum energy of 18.6 keV corresponding to an average energy of 5.7 keV only. The range of the maximum energy β being as small as 9 mg/cm^2, tritium located only within this depth can be detected through direct beta particle counting. Since these βs are stopped even by the 'thin' windows of most nuclear particle detectors, for direct counting of tritium windowless detectors have to be employed. In the case of titanium samples, the upper half of the β spectrum is able to excite the characteristic Kα (4.5 keV) and Kβ (4.9 keV) X-rays of titanium. (This does not happen in Pd.) The mean free path of 4.9 keV soft X-rays in titanium metal being $\sim$10 mg/cm^2 tritium present in deeper layers of the titanium also can get detected through measurement of its characteristic K X-rays.

1.3. Autoradiography

Autoradiography is a simple technique to establish the presence of radiation emitting zones and has been used very effectively at BARC to study the spatial distribution of near surface tritium in solid cold fusion samples. To achieve good spatial resolution the samples are kept in close contact with medical X-ray film and exposed in a dark room for times ranging from a few hours to a few days. In the case of titanium samples, fogging is due to the combined effect of tritium βs and the Ti K X-rays. To rule out the suspicion that image formation could be due to mechanical (scratching of films) or chemical reduction effects caused by the deuterium (or hydrogen), exposures were carried out with a stack of two films in contact with some samples, and it was confirmed that the second (or outer) film also gave a similar but fainter image indicating that image formation is due to nuclear particles only. While autoradiography has the advantage that it gives spatially resolved images of the distribution of tritium (or other radiation emitting substances), quantitative estimates are unreliable due to the saturation characteristics of image formation in photographic films. Highly localized regions of tritium ("hot spots") containing ≈ 0.2 kBq of activity or 10^{11} atoms of tritium each can be barely detected through a 100 h exposure.

2. Electrolysis Experiments during 1989–90 [1–4]

As mentioned earlier, several groups at BARC set up electrolytic cells using whatever samples of Pd they could get hold of, within days of the F&P announcement. The Neutron Physics Division had a head-start because, coincidentally, on 24 March 1989, a large cathode surface area (300 cm^2) Pd–D_2O electrolytic cell with 5 M NaOD electrolyte was all set and ready to be switched on! This off-the-shelf, ultra-pure hydrogen generator with 16 Pd–Ag alloy tubular cathodes arranged along a circle (inner and outer nickel cylinders constituted the anode) had been procured from Milton Roy Co. of Ireland for generating oxygen-free deuterium gas for plasma focus hot fusion experiments. On receipt of the F&P announcement, two different neutron monitors were moved on either side of the cell, while a third neutron detector bank placed over a meter away served as background monitor. The first evidence of neutron emission was obtained on 21 April 1989 when both the foreground neutron detector channels gave a dozen coincident peaks of varying magnitude during a four hour run when the cell current was being slowly ramped up. Four hours after commencement there was a huge neutron burst and the cell operation got automatically terminated by its protection circuit. (A couple of the Pd cathode tubes even got ruptured during this incident due to overheating.) A sample of the electrolytic solution which was later analyzed for tritium content indicated that the tritium concentration had attained a high level of 55.6 kBq/ml (1.5 μCi/ml), corresponding to a total tritium yield during the whole run of 13.9 MBq ($\sim 8.10^{15}$ atoms of T). The post run tritium concentration of the electrolyte was $\sim$ 20,000 times the initial value.

Table 1 summarizes details of eight electrolysis experiments in which both neutron and tritium production were observed. The quantum of tritium observed in the electrolytes of 11 additional cells, in which neutron production was not monitored, are summarized in Table 2 of [3]. The magnitude of tritium generated in the various BARC cells (22 cells in all) was in the range of a few kBqs to a few MBqs.

Table 1. Electrolysis experiments in which both neutrons and tritium generation were observed.

Division	Cathode				Yield		Ratio
	Material	Geometry	Area (cm^2)	Anode	Neutron yield	Tritium yield	(n/T)
1. Desalin *	Ti	Rod	104	ss pipe	$3\times10^{+7}$	$1.4\times10^{+14}$	2.1×10^{-7}
2. Neut Phy.*	Pd–Ag	Tubes	300	Ni Pipes	$4\times10^{+7}$	$8\times10^{+15}$	5×10^{-7}
3. HWD*	–	–	300	–	$9\times10^{+7}$	$1.9\times10^{+15}$	5×10^{-7}
4. HWD*	–	5 Disks	78	Porus Ni	$5\times10^{+4}$	$4.1\times10^{+15}$	1.2×10^{-9}
5. Anal. Ch$^{@}$	Pd	Hol Cyl.	5.9	Pt Mesh	$3\times10^{+6}$	$7.2\times10^{+13}$	4×10^{-8}
6. ROMg $^{@}$	–	Cube	6.0	–	$1.4\times10^{+6}$	$6.7\times10^{+11}$	1.7×10^{-4}
7. ROMg $^{@}$	–	Pellet	5.7	–	$3\times10^{+6}$	$4\times10^{+12}$	1×10^{-4}
8. App. Chem$^{@}$	–	Ring	18	–	$1.8\times10^{+8}$	$1.8\times10^{+11}$	1×10^{-3}

Electrolyte: *5 M NaOD $^{@}$ 0.1 M LiOD.

Table 2. Tritium production in deuterium gas loaded Pd samples.

Experiment	No. 1	No. 2	No. 3	No. 4	No. 5
Nature of sample	Pd black powder	Pd–Ag Foil	Pd–Ag Foil	Pd–Ag Foil	Pd–Ag Foil
Mass(g)	20	0.96	10.9	10.8	0.43
Date of loading	20 June 89	24 Aug. 1989	19 Sept.19 89	7 Mar. 1990	18 Sept. 19 89
Vol. of D_2 absorbed (ml)	1325	34.5	518.4	222	20.2
(D/Pd) ratio	0.63	0.46	0.45	0.20	0.45
Equilibriation time (h)	16	16	240	40	240
Water used for extraction (ml)	50	6	50	50	5
Tritium activity of water (Bq/ml)	8.1	5.9	8.5	12.5	32.6
T/D ratio in Pd	32×10^{-11}	1.1×10^{-11}	8.7×10^{-11}	3.4×10^{-11}	8.3×10^{-11}
Absolute tritium activity (Bq)	410.7	370	429.2	717.8	159.1
Total tritium atoms in Pd	2.31×10^{11}	2.02×10^{10}	24×10^{11}	$4.1.\times10^{11}$	8.96×10^{11}
Tritium atoms per g Pd	1.2×10^{10}	21×10^{10}	2.2×10^{10}	3.8×10^{10}	20.8×10^{10}

2.1. Deuterium gas loaded Pd samples [4]

In these experiments conducted by the Chemistry Division of BARC, D_2 gas was generated by reducing D_2O with Na in vacuum and stored under pressure in an SS dewar with liquid nitrogen cooling, in the presence of activated charcoal. The stock D_2O used had an initial tritium content of 0.075 nCi/ml (2.8 Bq/ml), corresponding to a (T/D) isotopic ratio of 3×10^{-14}.

Pd samples either in the form of Pd black powder or Johnson & Matthey Pd–Ag foils, were placed in an SS reaction vessel connected to a vacuum system (10^{-5} mm) through a buffer tank of 1 litre volume equipped with a pressure gauge. After degassing and cooling under vacuum, D_2 gas at 1 atm pressure was let into the buffer tank and the system sealed off for equilibration with the Pd contained in the reaction vessel for several hours or days at times. From the pressure drop observed the quantity of gas absorbed in the Pd could be deduced. The deuterated Pd samples were later immersed inside a measured quantity of distilled water for a few hours. The concentration of tritium in this water was then measured through standard liquid scintillation counting techniques. The tritium content in the Pd was deduced there from knowing the gram moles of D_2 absorbed in Pd as well as the relevant equilibration constant (K).

Table 2 summarizes the results. The tritium activity measured in the distilled water was a fraction of a nCi/ml (5–30 Bq/ml). The total quantity of tritium estimated to have been generated in the Pd foils was in the region of 10^{10} –10^{11} atoms. It is observed that the (D/Pd) ratios attained following D_2 absorption are in the region of 0.20–0.63. The amount of tritium produced per gram of Pd sample varied widely, from $\sim$1.2 to 20.8×10^{10} atoms/g. As may be expected the higher values are generally consistent with the longer duration of equilibration time (240 h) between D_2 gas and Pd, but the large Pd foil (column No. 3) which was also equilibrated for 240 h has given only 2.2×10^{10} atoms of tritium per gram of Pd. In all cases the finally attained (T/D) ratios which were in the range of 0.3×10^{-11} – 8.3×10^{-11} are two to three orders of magnitude higher than that of the initial gas which was 3×10^{-14}. Thus fresh tritium amounting to about 10^{10}or 10^{11} atoms appears to have been generated in the Pd, presumably following "cold fusion" reactions. It is not possible to conclude whether the tritium was produced during the gas absorption phase or during the subsequent "curing" or equilibration process with water.

2.2. Aged TiD targets [4]

Several groups in BARC had procured deuterated titanium targets on copper backing during 1972–1986 for dosimetry studies with accelerator based neutron sources. Thirteen such targets were available, nine procured from M/s. Amersham International of UK and four fabricated in-house by the Isotope Division of BARC. In view of the ongoing studies involving deuterated titanium targets it was conjectured that "cold fusion" reactions might have occurred in these "aged" targets over a period of 4–18 years and if so, it was argued, they should contain detectable amounts of tritium. In order to check this hypothesis these aged targets were counted as well as autoradiographed for establishing the magnitude of tritium if any present in them employing the techniques described above. The details of the targets, measurements and results are described in [4]. It was confirmed that all 13 targets indicated the presence of tritium, the absolute content varying between 0.3 and 150 MBq. Inquiries with the suppliers of these targets indicated that while inadvertent contamination during manufacture to the extent of a few hundred Bq was in principle a likely possibility, contamination levels in the MBq region is difficult to explain. The tritium levels in these aged TiDx targets expressed in terms of the (T/D) isotopic ratios was seen to vary in the range of $0.07\text{–}3.5 \times 10^{-4}$. For comparison the tritium activity of the D_2O moderator of a CANDU type power reactor is at most 30 Ci/1 even at saturation, corresponding to a (T/D) ratio of 10^{-5}. Besides, the (T/D) ratio of fresh D_2O from a production plant is typically in the region of $10^{-14}\text{–}10^{-13}$ only. It is therefore postulated that the unexpectedly high tritium levels in aged deuterated Ti targets must most probably be due to the occurrence of "cold fusion" reactions over the intervening years.

2.3. Cone and disc-shaped Ti samples subjected to RF heating in D_2 atmosphere

In these experiments, chemically cleaned machined targets of Ti were individually heated to temperatures of up to 900°C in a glass chamber using a surrounding induction heating coil (1–2 MHz frequency, 3–6 kW power). The glass chamber was connected to a vacuum system as well as H_2 and D_2 gas bottles. Degassing was initially carried out at 900^oC for 7 h until a vacuum of 10^{-5} mm was maintained steadily. The Ti samples were then heated to 600^oC in H_2 atmosphere of a few mm pressure. The induction heater was subsequently switched off and the target allowed to cool absorbing H_2 in the process. At least three cycles of H_2 absorption/desorption was given to create active sites for D_2 absorption. Three such heating/cooling cycles were then repeated with D_2 gas. The pressure drop recorded by an oil manometer indicated the quantity of gas absorbed during each cooling cycle. It was observed that the quantity of gas absorbed increased with each cycle, saturating in the third or fourth cycle. The targets typically absorbed $< 10^{19}$ molecules of D_2. Since the mass of Ti was a few hundred milligrams, this corresponds to a gross (D/Ti) ratio of hardly 0.001. However, we have reason to believe that most of the absorption would be confined to a "skin depth" in the surface region and the (D/Ti) ratio there would be substantially higher. (It is common knowledge that when a metallic object is heated by induction heating, the current distribution and heating rate falls off exponentially with increasing depth.)

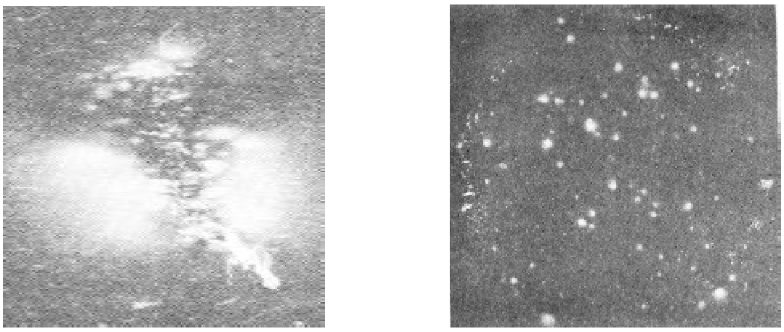

Figure 1. Autoradiographs of a deuterated Ti cone and a disc target .

After loading, all the targets were subjected to various tests such as autoradiography, K X-ray counting etc discussed earlier, in search of tritium. Although several dozen targets were successfully loaded with D_2 gas, only a few of them gave positive evidence for the presence of tritium. Interestingly the samples which soaked up large amounts of D_2 gas did not give any positive results. The best results were obtained from a disc shaped button (10 mm dia × 2 mm thick) and a couple of conical pieces meant for use as electrodes. Figure 1 depicts the autoradiographs of a deuterated cone and disc respectively. The radiographs show large numbers of "hot spots" randomly distributed within the boundary. The occurrence of spots all along the rim of the machined disc is significant. It is estimated that each spot corresponds to about 10^9–10^{10} atoms of tritium. The total number of tritium atoms in the whole target works out to be $\sim 10^{11}$. If this is compared with the 10^{19}–10^{20} atoms of D absorbed in all by the Ti, targets it points to a gross (T/D) ratio of $\sim 10^{-9}$. But if only the D present in the "hot spot zones" are considered, the corresponding (T/D) ratio would be significantly higher.

It is noteworthy that these autoradiographs are distinctly spotty as against those of the aged targets discussed earlier which were uniform. This difference may be attributed to the fact that the above Ti targets were subject to severe cold working causing defect sites during fabrication (prior to loading) whereas the aged targets were produced through vacuum deposition of titanium thin films onto a copper backing with no cold work involved.

2.4. TiDx shavings subject to thermal shock caused by liquid nitrogen [9]

In the experiments described below, anamolous generation of tritium when deuterated Ti lathe turnings (or chips) were subject to a thermal shock following dunking in liquid nitrogen (LN) was investigated, in a variation of the Frascati type experiment wherein the production of sharp bursts of neutrons had earlier been reported in similar experiments. Prior researchers had made attempts to measure tritium production by degassing the thermally shocked chips and recombining the released gases to form tritiated water. In contrast, in our experiments, the surface tritium content in individual TiDx chips following LN treatment, was measured directly. We speculated [10] that when a single sharp burst of say 100 neutrons is produced within a short duration of less than a 100 μs from a cylinder containing thousands of chips, such a burst must most probably be emanating from a single chip. This is because it is very difficult to conceive of any physical process or mechanism by which several individual chips can interact (or communicate) with each other on this short a time-scale so as to generate a neutron-burst simultaneously ("like a symphony orchestra"). Based on the anomalously large (10^8) tritium-to-neutron ratio observed in earlier CF experiments, both at BARC and elsewhere, we speculated that atleast 10^{10} tritium atoms ($\sim$20 Bq of activity) must be present in a few individual TiDx chips.

In the experiments reported here Titanium metal shavings or chips (a few mm long, ∼ 1 mm wide and 0.2–0.5 mm thickness) were machined out of a 20 mm diameter rod. A few thousands of these chips weighing about 10 g in all, were chemically cleaned with H_2SO_4, HCl, etc. before being charged into a stainless steel chamber. The chamber was then heated for 2 h at 800°C under a vacuum of 10^{-5} torr by means of a resistance heater placed around it. During cooling of the chamber, when the temperature cooled down to around 600°C, deuterium gas was admitted. The total quantum of deuterium gas absorbed by the chips during further cooling was estimated from the pressure drop recorded by an oil manometer.

With the objective of causing thermal shock in the deuterated chips, they were dropped directly into liquid nitrogen contained in an aluminum cylinder. After complete evaporation of the LN, when the chips had almost attained room temperature, the container was again refilled; this cycle was repeated 4 or 5 times for each batch of chips. The chips were then analyzed for presence of tritium using a thin window NaI gamma detector. Lots of about 100 chips each from the LN treated and untreated stock of TiDx chips were uniformly spread on the top window of a vertically mounted NaI detector, in such a way as to minimize self shielding effects. While the counts with the untreated chips corresponded to background only, all the lots of the shock treated batch indicated activity above background. Through a process of sub-dividing the active lots into smaller batches and counting again, four highly active chips could be isolated from a

Table 3. Tritium activity in highly active Ti chips

Chip ID No[1]	NAI Counter[2]		Gas Counter[2]		Ratio
	Count Rate (N_{cps})	Tritium activity (MBq)	Count rate (B_{cps})	Tritium activity (kBq)	($N_{\text{cps}}/B_{\text{cps}}$)
F6	0.12	0.02	475	4.75	2.5×10^{-4}
F55	0.11	0.02	460	4.6	2.5×10^{-4}
Z1	63.5	10.7	34665	346	1.8×10^{-3}
Z2[3]	9.7	1.7	–	–	
Z3[4]	89.2	15.2	–	–	
Z4	140.9	23.9	42415	424	3.3×10^{-3}

[1] Indicates a specific number assigned to each of the individually counted chips.

[2] Tabulated count rates are the maximum value averaged over several measurements, corrected for background.

[3] Lost during analysis.

[4] Due to coil shape of this chip, it was not possible to fit in the drawer of the beta detector.

total of more than 1000 TiDx chips. The activity with different orientations of these four active chips varied by factors of 3–5 with the maximum count rates being in the range of 9.7–140.9 cps as listed in Table 3 (chip Nos Z1–Z4).

All the TiDx chips were again counted in lots of 15–20, by placing them inside the drawer of a windowless 2π geometry gas flow type proportional β counter. The results of this gross counting were consistent with the NaI detector measurements. Some of the virgin metal shavings as well as the deuterated but untreated titanium chips were also counted in the detector but none of them gave any counts over the background. Other batches of TiDx chips, cycled later, also failed to show any detectable activity. The four 'high' activity chips were also counted individually with the windowless β detector, but in view of their very high activity there was considerable dead time counting losses. The statistical variation in the activity of single chips was studied by counting some of the chips individually from a few of the randomly selected active lots. Of the 66 chips so counted, at least 50% gave count rates more than twice the background.

A careful scrutiny of the X-ray-counts to β-counts ratio for the low and high activity chips, indicated a clear difference between them. Superimposed on the observation of the differences in shapes of the β-spectra between the high and low activity chips, we inferred that tritium in the low activity chips is closer to the surface than in the high activity chips leading to the conclusion that only four (or perhaps a few more chips) had actually "produced" tritium

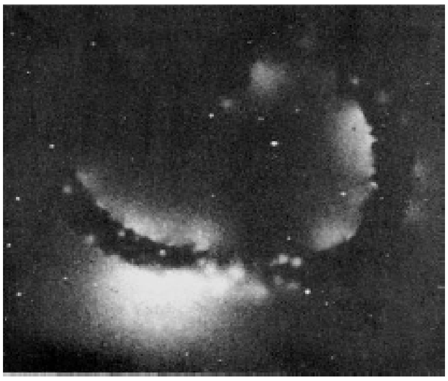

Figure 2. Autoradiograph of chip # Z4.

during the thermal shock treatment whereas most of the other chips must have picked up the tritium as contamination during the LN treatment. The justification for this line of argument is spelt out in detail in our original paper [9].

Autoradiography of the four highly active chips was carried out with a view to gain some insight into the spatial distribution of the tritium on the surface. The test chip was sandwiched between two X-ray films to image the active zones on both sides of it. Fig. 2 which is the autoradiograph of chip No. Z4 for an exposure time of 17 h indicates the presence of about 35–40 hot spots. The radiograph of the other side also gave a similar image but with a lesser number of spots, implying different activity distributions on the two sides, a feature observed during β and X-ray counting also. The hot spots in all these radiographs are similar to those observed earlier at BARC in the autoradiographs of other deuterated titanium targets. However one remarkable feature of the autoradiographs of these chips worth highlighting is the so called "shadowgram effect" resulting in the outline of the chip boundary being clearly visible.

3. Plasma focus experiments [11]

In a plasma focus device a coaxial plasma gun (Fig. 3) is used to produce a dense hot ($\approx$1 keV temperature) "plasma focus" a few cm long and a few mm in diameter, just above the central electrode. The chamber is filled with deuterium gas at a pressure typically in the range of 1–20 mbar. The device is driven by a fast capacitor bank charged to 12 kV (stored energy of 2 kJ). When the spark gap switch is fired, a surface discharge is first initiated along the surface of the lower glass insulator which then develops into a radial current sheath that is accelerated by J × B forces axially between the electrodes, sweeping and 'snow plowing' the gas ahead of it. On reaching the upper end of the central anode, the current sheath turns around on itself forming a quasi-cylindrical implosion, resulting in a dense hot "plasma focus" just above the electrode tip. The focus itself lasts for less than a microsecond, but before its disintegration it produces an intense burst of neutrons of a few tens of ns duration. The neutron yield in a PF device depends on the quality of focus formation and typically varies in the range of 5×10^5 –10^8, depending on the filling pressure and other factors. Since the fusion reactions result from internally accelerated deuterons impinging on a hot deuterium plasma "target", it is basically a hot fusion (beam-target) process and as such roughly equal numbers of neutrons and tritium atoms are generated.

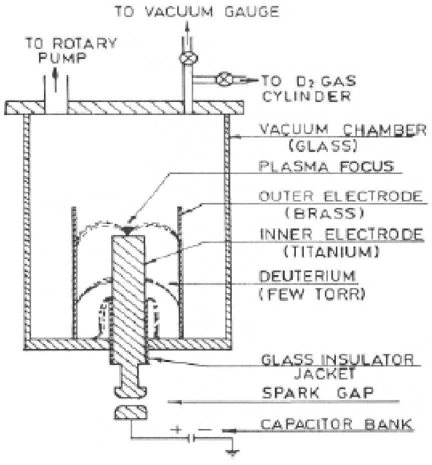

Figure 3. Schematic of a PF device.

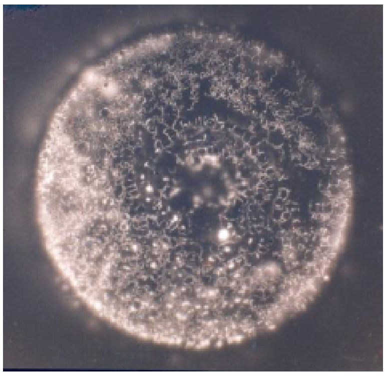

Figure 4. Autoradiograph of Ti anode TA1.

In January 1990 as part of a program to study the influence of anode material on the characteristics of the formed plasma focus, experiments with a central Ti rod electrode were carried out. This first titanium electrode (TA1) was exposed to 50 charge/discharge shots at different deuterium gas filling pressures. The electrode was then removed and scanned using a NaI detector. It was found to contain a surprisingly large activity of more than 10 MBq (10^{16} atoms) of tritium. The overnight autoradiograph taken on 9 Feb. 1990 confirmed this and gave a truly spectacular image (Fig. 4). The image revealed a large number of randomly distributed tritium bearing hot spots. Two kinds of structures are discernible in the image : the first type is sharp worm-like lines which appear to be created by betas emanating from the surface. The second variety are diffused spots, which could be attributed to soft X-rays emanating from deeper layers.

In order to ascertain whether positive voltage operation or negative voltage operation gives better results, two fresh titanium electrodes (TA2 & TA6) were exposed to 25 discharge shots each of opposite polarities. The reversed polarity shots were conducted following speculation that some of the energetic deuterons which are the cause of neutron production in a PF device may get directed towards the central electrode and get implanted in it. Both these anodes which were then scanned using the NaI detector. TA2 subjected to positive voltage shots gave 0.3 MBq while TA6 which was given negative voltage shots had 0.07 MBq. This was somewhat puzzling as one would have expected reverse polarity shots to give better results on the basis of improved deuteron implantation. The autoradiographs of these electrodes however indicated only faint images, confirming the presence of less tritium activity as compared to TA1 anode.

As mentioned already the 2 kJ Plasma Focus device typically produces 10^7neutrons/shot. In the present experiments assuming 100 shots as upper limit, not more than 10^9 neutrons could therefore have been produced in all, with each electrode. Since the tritium-to-neutron branching ratio in conventional (d–d) reactions is unity, the same number, namely 10^9 tritium atoms would have been produced at the most as a result of the hot fusion reactions. Besides it is totally unrealistic to expect that all of this tritium would have succeeded in getting absorbed on the top surface of the central Ti electrode. Thus the 10^{14} (TA2) to 10^{16} (TA1) atoms of tritium measured on the end faces of the Ti anodes cannot be attributed to known PF type hot fusion processes. Besides the initial tritium content of the deuterium gas used in these experiments which was measured to be < 27 Bq/l too cannot account for the large amounts of tritium measured on the top surface of these Titanium anodes. It is concluded that anomalous "cold fusion" type nuclear reactions would appear to be the most likely source of this high a level of tritium generation in these titanium electrodes.

3.1. Ni hydrogen electrolysis experiments [7–9]

Experiments were initiated with light-water electrolytic cells using Ni cathodes and K_2CO_3 solutions as electrolyte, following reports of observation of excess heat in such systems by Mills and Kneizys [12] and other groups in the early 1990s. Although observation of excess heat in open electrolysis cells with Ni cathodes and K_2CO_3electrolyte was reported by us at ICCF 3 in Nagoya in 1992 [7], we subsequently came to the conclusion that the apparent excess heat reported at that time can be attributed to hydrogen-oxygen recombination effects within the open cell. We were, however, probably the first to report observation of tritium in light water electrolytic cells. At Nagoya, we reported that 18 out of 29 cells indicated tritium levels in the range of 46–3390 Bq/ml after a few weeks of cell operation. The high value of 3390 Bq/ml was produced in a cell in which D_2O was added to the extent of 25%, but three other identical cells with 25% D_2O did not give any tritium. One cell with enriched Li_2CO_3 in H_2O (54% enriched ^6Li) gave 1454 Bq/ml, whereas two others with the same type of cathode and electrolyte gave no tritium whatsoever. Cell no. OM-3 with online sampling facility showed a steady increase of tritium level, reaching a value of 224 Bq/ml over four weeks; further operation of this cell however showed a saw tooth type variation of the tritium activity (see Fig. 5).

Some skepticism was expressed even within BARC circles regarding the reliability of low level tritium measurements in light water cells. Suspicion was voiced that the result could have been either from cross-contamination at the tritium measurements lab, where samples from different research groups were handled, or from “tritium in the BARC atmospheric air”. Hence, starting in June 1993, a completely new set of Ni light water cells were set up and operated at two separate laboratory sites, over a three month period. Six cells were set up at the Chemical Engineering Division, and 17 cells (five at a given time) at the Process Instrumentation Division, specifically for the purpose of verifying tritium production. This time, a new captive liquid scintillation counting facility was installed in the Chemical Engineering Division and extra caution observed to avoid any possible external contamination. All electrolyte samples were micro-distilled, with researchers taking adequate precautions to avoid alkali carry over before mixing with the scintillation cocktail for counting. With these procedures, tritium levels down to 0.5 Bq/ml could be measured. Details regarding these repeat measurements are presented in [7]. In all, 10 of 23 of the new cells showed low levels of tritium in the 0.5–4.8 Bq/ml range. In three of the Chemical Engineering Division cells, from which electrolyte samples could be drawn online without disturbing cell operation, an intriguing saw-tooth oscillatory variation of tritium levels of the electrolyte was observed. This observation, pointing out, with cross references, that such oscillatory behavior of tritium levels in electrolyte has been observed by other laboratories also in Pd–D_2O cells are discussed in [7].

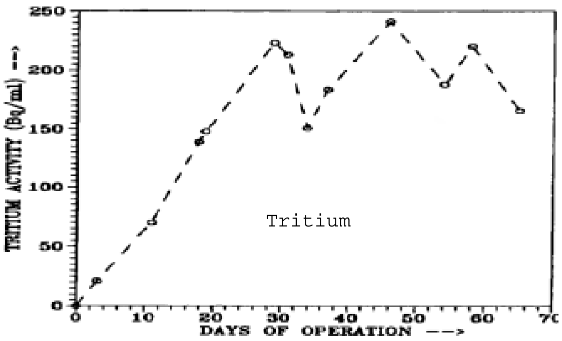

Figure 5. Variation of tritium activity in electrolyte of Ni cathode light water cell No. OM-3.

3.2. Tritium in H_2 gas loaded Ni wire experiments [8]

During 1994–1995, experiments were also conducted with self-heated thin Ni wires in a hydrogen gas atmosphere by subjecting the wires to several cycles of hydrogen absorption–desorption. The wires were then cut into 1 cm bits and analyzed for tritium content after dissolution. The results again showed, as in the case of titanium, a non-uniform production of tritium along the length of the wire, with some sections showing no tritium and others containing significant amounts; one bit had as much as 2,333 Bq. Details are given in [8].

4. Conclusions

This paper gives a brief overview of the variety of experiments conducted independently by many different groups at BARC during the period 1989–1996 wherein the anomalous generation of tritium in selected metallic deuterides/ hydrides was confirmed. The experiments spanned both electrolysis studies as well as gas/plasma loading techniques in which Pd, Ti and Ni were used as the host metal. Production of tritium was confirmed both in Pd–D systems as well as Ni–H configurations, and in each case with both electrolysis as well as gas/plasma loading. The fact that all the dozen groups who set up electrolytic cells totally independently and confirmed finding tritium in the electrolyte, as well as in a variety of gas/plasma loaded target studies, is very significant.

Looking back, BARC can perhaps claim credit for being the *first* to report the following experimental findings:

(1) Production of tritium in Pd–D_2O electrolytic cells (Prof. Bockris has conceded this in private correspondence).
(2) Tritium production is over a million times more probable than neutrons (so called “branching ratio anomaly”)
(3) Generation of tritium in Ni–H_2O electrolytic cells.
(4) With machined Ti targets tritium production invariably occurs in isolated hot spots (first hints of NAE concept ?).
(5) Use of a Plasma Focus device for loading and triggering anomalous tritium production.
(6) Application of autoradiography as a very effective tool to record the spatial distribution of tritium in Titanium targets.
(7) Lastly observation of neutron emission in “bunches” in a non Poissonian manner, leading to the speculation that micro-nuclear explosions may be occurring. This aspect is dealt with in detail in [10].

Acknowlegements

The author gratefully acknowledges the very significant contributions made by all the co-authors of the BARC papers cited here, to the successful conduct of the various experiments reviewed.

References

[1] P.K. Iyengar, Cold fusion results in BARC experiments. In *Proc. Fifth Int. Conf. on Emerging Nucl. Energy Systems,* Karlsruhe, Germany, July 1989, p. 291.
[2] P.K. Iyengar and M. Srinivasan (Eds.), *BARC Studies in Cold Fusion, BARC-1500,* Atomic Energy Commission, Government of India, Bombay, 1989.
[3] P.K. Iyengar and M. Srinivasan , Overview of BARC studies in cold fusion, In *The First Annual Conference on Cold Fusion, Salt Lake City,Utah.* National Cold Fusion Institute: University of Utah Research Park, Salt Lake City, Utah, 1990.
[4] P.K. lyengar et al., Bhabha Atomic Research centre studies in cold fusion, *Fusion Technol.* **18** (1990)32.
[5] M. Srinivasan et al., Observation of tritium in gas/plasma-loaded titanium samples, In *Proc. Int. Workshop on Anomalous Nuclear Effects in Deuterium/Solid Systems,* Brigham Young University, Provo, Utah, 1990, American Institute of Physics, New York, 1991, pp. 519–534.

[6] M. Srinivasan et al., Tritium and excess-heat generation during electrolysis of aqueous solutions of alkali salts with nickel cathode. In *Frontiers of Cold Fusion: Third International Conference on Cold Fusion, Nagoya, Japan*, 1992,H. Ikegami (Ed.), Universal Academy Press, Tokyo, Japan, 1992, p. 123.

[7] T.K. Sankaranarayanan et al., Investigation of low-level tritium generation in Ni–H_2O electrolytic cells, *Fusion Technol.* **30** (1996) 349.

[8] T.K. Sankaranarayanan et al., Evidence for tritium generation in self- heated nickel wires subjected to hydrogen gas absorption/desorption cycles, In *Proc. of the 5th Int. Conf. on Cold Fusion,* Monte Carlo, Monaco, 1995, B.S. Pons (Ed.), IMRA Europe, Sophia Antipolis, Valbonne, France, 1995, p. 173.

[9] T.C. Kaushik et al., Preliminary report on direct measurement of tritium in liquid nitrogen treated TiDx chips, *Indian J. Technol.* **28** (1990) 667.

[10] Mahadeva Srinivasan, Neutron emission in bursts and hot spots: signature of micro-nuclear explosions? *JSCMNS* **4** (2011) 168.

[11] R.K. Rout et al., Detection of high tritium activity on the central titanium electrode of plasma focus device, *Fusion Technol.* **19** (1991) 391.

[12] R.L. Mills and K. Kneizys, *Fusion Technol.* **20** (1991) 65.

J. Condensed Matter Nucl. Sci. 15 (2015) 149–161

Research Article

Piezonuclear Fission Reactions Simulated by the Lattice Model

A. Carpinteri,* A. Manuello and D. Veneziano

Politecnico di Torino, Department of Structural, Geotechnical and Building Engineering, Corso Duca degli Abruzzi, 24–10129 Torino, Italy

N.D. Cook†

Kansai University, Department of Informatics, Takatsuki, Osaka 569-1095, Japan

Abstract

Recent experiments conducted on natural rocks subjected to different mechanical loading conditions have shown energy emissions in the form of neutrons and anomalous chemical changes. In the present study, a numerical model is used to simulate the anomalous nuclear products according to the fission interpretation. Specifically, the reactions were simulated by means of a nuclear lattice model assuming that nucleons are ordered in an antiferromagnetic face-centered-cubic (fcc) array. The simulations indicate that small and middle-sized nuclei can be fractured along weakly bound planes of the lattice structure. It is argued that the simulations provide theoretical support for the experimentally-observed reactions and, moreover, that the probabilities calculated for various low-energy fissions can be used to explain the stepwise changes in the element abundances of the Earth's crust, evolved from basaltic to sialic composition over geological time.

Keywords: Earth crust composition, Lattice model, Nuclear cold fusion, Piezonuclear fission reactions

1. Introduction

In the last few years, numerous experiments have been conducted on natural non-radioactive rocks, such as granite, basalt, magnetite and marble, by subjecting them to different mechanical loading conditions. The experiments were always accompanied by energy emissions and anomalous chemical changes [1–8] and provided repeatable evidence concerning a new kind of nuclear reaction that may take place during quasi-static or cyclic-fatigue tests at low (2 Hz), intermediate (200 Hz) and high (20 kHz) loading frequencies [8]. Such evidence indicates that mechanical pressure waves, suitably exerted on an inert medium of stable nuclides, can generate neutron emissions and nuclear reactions of a new type [1–14].

Very recently, theoretical interpretations have been proposed by Widom et al. in order to explain neutron emissions as a consequence of nuclear reactions taking place in iron-rich rocks during brittle micro-cracking and fracture [13,14].

---

[*] E-mail: alberto.carpinteri@polito.it

[†] E-mail: cook@res.kutc.kansai-u.ac.jp

Several evidences show that iron nuclear disintegrations are observed when rocks containing such nuclei are crushed and fractured. The resulting nuclear transmutations are particularly evident in the case of magnetite rocks and iron-rich materials in general. The same authors argued that neutron emissions may be related to piezoelectric effects and that fission of iron may be a consequence of the photodisintegration of the same nuclei [13].

Those experimental results together with the evidence of so-called low-energy nuclear reactions (LENR) [15–17] strongly suggest that knowledge of nuclear structure is not a "closed chapter" in Physics. Moreover, recent studies on piezonuclear fission reactions, occurring in the Earth's crust and triggered by earthquakes and brittle rocks failure, provide a good opportunity for old questions concerning nuclear structure to be addressed once again in the light of new phenomena suggestive of low-energy nuclear reactions [12]. Even small deviations from conventional assumptions, e.g., concerning the condensation density of nuclear matter or the concept of an average binding energy per nucleon [15,18–22], could have significant implications. Based on the experimental evidence concerning piezonuclear fission, it would suffice to assume that a nuclear structure failure occurs along weak lattice planes within the nucleus, similar to the cleavage fractures known to occur in very hard and strong rocks [6–8].

The nuclear lattice model has been advocated by Cook and Dallacasa as a unification of the diverse models used in nuclear structure theory [17–19,23–30], but, remarkably, the basic lattice structure was first proposed by the originator of the well-established independent-particle model, Eugene Wigner, in 1937 [31] – work that was explicitly cited in his Nobel Prize notification. The lattice model has previously been used to simulate (i) the mass of fission fragments produced by thermal fission of the actinides, and (ii) the transmutation products found on palladium cathodes after electrolysis, as reported in various experimental studies [20,29,30,32]. With regard to the underlying nuclear lattice model, the antiferromagnetic face-centered-cubic (fcc) lattice with alternating proton and neutron layers is the most suitable model for various reasons: (i) from theoretical research on nuclear matter, it is known to be the lowest-energy solid-phase packing scheme of nucleons ($N = Z$) [17–19,22]; (ii) the lattice structure reproduces the quantum number symmetries of the independent particle model (IPM) (the entire n-shell and j-lm-subshells of the shell model), while being based on the local interactions of the liquid drop model (LDM) [17,21,22]; (iii) because of the identity between the nuclear lattice and the IPM, the approximate nucleon build-up procedure is known and implies a specific 3D structure for any given number of protons and neutrons with known quantum numbers, which can be represented in Cartesian space [17].

Several decades of development of the lattice model suggest that the gaseous, liquid, and cluster-phase models of conventional nuclear structure theory can be unified within a specific lattice model. Moreover, the lattice lends itself to straightforward application in explaining different fission modes [17,21,22]. The earlier simulation results were concerned with fission fragments from uranium nuclei and transmutation products from palladium isotopes (experimentally reported by Mizuno in 1998 and 2000 [20,32]). In the present simulations, the Nuclear Visualization Software (NVS) [17] was used to simulate the anomalous nuclear reactions recently observed by Carpinteri et al. [1–11] and to numerically reproduce the nuclear products observed after fracture and fatigue experiments. The results lead to the conclusion that the anomalous nuclear reactions, emerging from Energy Dispersive X-ray Spectroscopy (EDS) analysis of fractured specimens and from the evolution of the continental Earth's crust, can be well explained by the nuclear lattice model. In addition, the lattice approach allows one to compute a probability related to each possible fission reaction. The probability values obtained for the anomalous reactions can then be used to interpret the evolution of the abundance of product elements in the Earth's crust, ocean and atmosphere.

2. Reproducing Anomalous Fission Fragments using the Lattice Model

The nuclear lattice model proposed by Cook and Dallacasa [17–19,23–28] can be used to simulate the piezonuclear fission reactions by constructing individual isotopes, in accordance with the lattice build-up procedure, and then simulating the cleavage of the lattice along various lattice planes. The starting points for the simulations are therefore the nuclear structures of the elements and those known to be abundant in the Earth's crust today and in previous eras [6–12]. Although other nuclear structure models have been developed since the 1930s, the fcc lattice is the most suitable to simulate the anomalous reactions recently discovered because of its clear structural implications. The simulation begins with a 3D lattice structure of specific isotopes based on the total number of neutrons N and protons Z. By simulating the fission of the nucleus as a fracture occurring along a certain section plane across the lattice, "fragments" are produced, and correspond to the post-fission daughter nuclei.

The quantum mechanical foundations of the lattice model and its relation to the Schrödinger wave-equation have been discussed elsewhere, but, for the purposes of the simulation, it is sufficient to describe the lattice structure in Cartesian space. That is, the mean position of each nucleon can be defined in relation to its quantum numbers by means of the following equations [17]:

$$x = |2m| \, (-1) \, (m + 1/2) \, , \tag{1}$$

$$y = (2j + 1 - |x|) \, (-1)^{(i+j+m+1/2)} \, , \tag{2}$$

$$z = (2n + 3 - |x| - |y|) \, (-1)^{(i+n-j-1)} \, , \tag{3}$$

where n, m, j, s, and i are the quantum numbers that describe the energy state for a given nucleon [21,22]. Equations (1)–(3) are deduced from a rigorous, self-consistent representation of the IPM in three-dimensional space [17]. In accordance with the known quantum mechanics of nuclear states, each nucleon is characterized by a unique set of five quantum numbers, which define the precise energy state of the nucleon, as described by the Schrödinger equation [17,21,22]. The spatial origin of this wave is a function of the three coordinates x, y, z. Hence, for any isotope, knowing that each nucleon belongs to a certain energy level given by the values of its quantum numbers, it is possible to consider the 3D lattice of nucleons as a representation of its quantum mechanical state [17,21,22].

Piezonuclear reactions cannot be defined as traditional fission reactions, since temperature and energy conditions are not equivalent to those involved in thermal neutron-induced fission. For this reason, it is convenient to verify that these anomalous reactions may be correctly described in the NVS simulations. To simulate this new kind of fission, we assumed that fractures occur in the nuclear lattice along their crystal planes. Following this approach, two distinct fragments are produced from any considered reaction. Their characteristics are given by the NVS in terms of fragment stability, fission threshold energy along a certain fracture plane, and the number of protons and neutrons in each fragment. The resulting elements can be deduced from the characteristics of the fragments obtained at the end of the simulation. The analysis of the nuclear characteristics is described in the next section along with the isotopes obtained from the piezonuclear reactions. Important considerations are made on the neutron emissions from the anomalous nuclear reactions measured during the experiments. They may be deduced by investigating the stability of the resulting fragments. We assume that unstable isotopes with an excess of neutrons are likely to induce neutron emissions, depending on local binding characteristics, in order to reach more stable nuclear states. These emissions deduced from the model are then compared with the experimental results reported by Carpinteri et al. [1–11].

3. Simulations and Results

The NVS simulates lattice structures up to 480 nucleons and calculates fission results along 17 different section planes for each given nuclide (Table 1). In fact, many more lattice planes are available for simulation, but the electrostatic repulsion between the protons in the two fragments is much greater for lattice planes that break the lattice structure into

Table 1. Fission planes and their identification number in the NVS.

Fracture plane	Equations
1	$x = 2$
2	$x = 0$
3	$x = -2$
4	$z = -2$
5	$z = 0$
6	$z = 2$
7	$y = 2$
8	$y = 0$
9	$y = -2$
10	$-x + y + z + 1 = 0$
11	$-x + y + z - 1 = 0$
12	$x - y + z + 1 = 0$
13	$x - y + z - 3 = 0$
14	$-x - y + z - 1 = 0$
15	$-x - y + z + 3 = 0$
16	$x + y + z - 1 = 0$
17	$x + y + z + 3 = 0$

approximately symmetrical fragments, so that many low-repulsion, asymmetrical fission events are ignored. A single simulation consists in fracturing the nucleus along one single plane at a time, breaking only the bonds that connect the two fragments [17]. It is understandable that the choice of the fracture planes is affected by the lattice structure and, therefore, by the position of the nucleons with respect to the x, y, z axes. Being a lattice model drawn from crystallography implies that all the planes used for the simulations correspond to the principal crystallographic planes [17]. In particular, the seventeen planes used by the NVS are parallel to the horizontal, vertical and inclined (45°) planes passing through or near the origin of the axes. Each plane is identified by a number from 1 to 17, as shown in Table 1.

Eighteen reactions derived from direct and indirect experimental evidence were simulated by means of the NVS along different fission planes and each considering a different starting element (Table 2). As mentioned in Section 1, the elements known to be involved in the piezonuclear reactions were considered in the numerical simulations. Such reactions are strictly connected to: (i) the experimental results obtained from the EDS analyses performed after fracture tests on natural rock specimens, or (ii) the compositional changes in the Earth's crust evolution during the last 4.57 billion years [5–12]. As recently reported [9–12], the evolution of the Earth's crust and atmosphere, the formation of oceans and greenhouse gases, and the origin of life are phenomena deeply related to piezonuclear reactions [1–12]. This was the motivation for undertaking the simulation of fission reactions according to a non-traditional methodology [19].

These reactions were simulated using two build-up procedures for nuclear structure. The first one generates a default nucleus where each nucleon has a pre-assigned position and quantum numbers that give the lattice a regular, densely-packed, polyhedral structure. The second procedure uses the "picking function", which is the most convenient way for constructing a nucleus from a set of nucleons with specific quantum numbers and coordinates [17]. The picking function was applied only when the lattice structures using the default configuration were inappropriate due to the weak bonding of the last few nucleons. In particular, once a specific default nucleus has been constructed and displayed, usually the last two protons or neutrons were individually moved from one energy-state to another to find the configuration that best reproduces the (fission) product elements.

All 18 reactions reported in Table 2 are simulated by the NVS and the results are summarized in Table 3. For

Table 2. Piezonuclear reactions obtained as direct evidence from EDS analysis of fractured specimens, or conjectured considering the continental Earth's crust evolution.

Earth's crust evolution	
(1)	$\mathrm{Fe}_{26}^{56} \rightarrow 2\ \mathrm{Al}_{13}^{27} + 2$ neutrons
(2)	$\mathrm{Fe}_{26}^{56} \rightarrow \mathrm{Mg}_{12}^{24} + \mathrm{Si}_{14}^{28} + 4$ neutrons
(3)	$\mathrm{Fe}_{26}^{56} \rightarrow \mathrm{Ca}_{20}^{40} + \mathrm{C}_{6}^{12} + 4$ neutrons
(4)	$\mathrm{Co}_{27}^{59} \rightarrow \mathrm{Al}_{13}^{27} + \mathrm{Si}_{14}^{28} + 4$ neutrons
(5)	$\mathrm{Ni}_{28}^{59} \rightarrow 2\ \mathrm{Si}_{14}^{28} + 3$ neutrons
(6)	$\mathrm{Ni}_{28}^{59} \rightarrow \mathrm{Na}_{11}^{23} + \mathrm{Cl}_{17}^{35} + 1$ neutron
Atmosphere evolution, ocean formation and origin of life	
(7)	$\mathrm{Mg}_{12}^{24} \rightarrow 2\mathrm{C}_{6}^{12}$
(8)	$\mathrm{Mg}_{12}^{24} \rightarrow \mathrm{Na}_{11}^{23} + \mathrm{H}_{1}^{1}$
(9)	$\mathrm{Mg}_{12}^{24} \rightarrow \mathrm{O}_{8}^{16} + 4\mathrm{H}_{1}^{1} + 4$ neutrons
(10)	$\mathrm{Ca}_{20}^{40} \rightarrow 3\mathrm{C}_{6}^{12} + \mathrm{He}_{2}^{4}$
(11)	$\mathrm{Ca}_{20}^{40} \rightarrow \mathrm{K}_{19}^{39} + \mathrm{H}_{1}^{1}$
(12)	$\mathrm{Ca}_{20}^{40} \rightarrow 2\mathrm{O}_{8}^{16} + 4\mathrm{H}_{1}^{1} + 4$ neutrons
Greenhouse gas formation	
(13)	$\mathrm{O}_{8}^{16} \rightarrow \mathrm{C}_{6}^{12} + \mathrm{He}_{2}^{4}$
(14)	$\mathrm{Al}_{13}^{27} \rightarrow \mathrm{C}_{6}^{12} + \mathrm{N}_{7}^{14} + 1$ neutron
(15)	$\mathrm{Si}_{14}^{28} \rightarrow 2\ \mathrm{N}_{7}^{14}$
(16)	$\mathrm{Si}_{14}^{28} \rightarrow \mathrm{C}_{6}^{12} + \mathrm{O}_{8}^{16}$
(17)	$\mathrm{Si}_{14}^{28} \rightarrow 2\mathrm{C}_{6}^{12} + \mathrm{He}_{2}^{4}$
(18)	$\mathrm{Si}_{14}^{28} \rightarrow \mathrm{O}_{8}^{16} + 2\mathrm{He}_{2}^{4} + 2\mathrm{H}_{1}^{1} + 2$ neutrons

each simulation, the plane that allows the anomalous fission is indicated. Each fragment is identified by the number of protons (Z), the number of neutrons (N), and the corresponding isotope. In addition, when the fragment is unstable, NVS displays the experimentally known decay time of that fragment. In the case of unstable fission fragments, the number of neutrons exceeds the stable condition and neutron emissions may occur from that fragment in order to achieve stability. It is interesting to note that, from the NVS results, it is possible to reproduce the neutron emissions of piezonuclear reactions, in addition to the product elements (fragments).

For the first simulation, the Fe_{26}^{56} nucleus was chosen as the starting element and the lattice of this nucleus is shown in Fig. 1. Its characteristics assigned by the software are as follows: Protons: 26; Neutrons: 30; n-values: 0, 1, 2, 3; j-values: 1/2, 3/2, 5/2, 7/2; m-values: ±1/2, ±3/2, ±5/2, ±7/2, according to the literature [17,21,22].

Once the nuclear structure is modified with the picking option, the lattice is "fractured" along fission planes that cut all nucleon–nucleon bonds connecting the two fragments (Fig. 2). Among the 17 planes of fission, six of them are relevant for reactions (1)–(3) of Table 2, whereas the remaining 11 produce results unrelated to the empirical data (Table 2). Specifically, the simulation results related to reaction (1) occur along the fission planes 2 and 8, which are the *yz* and the *xz* plane in Cartesian space respectively (see Table 1 and Fig. 2). As shown in Table 4, the fragments produced from the fissions along planes 2 and 8 possess the same characteristics as those described in the piezonuclear reaction (1) (Table 2). The two fragments correspond toAl_{13}^{27}, andAl_{13}^{29}. The former is stable, whereas the latter is unstable as it contains two neutrons in excess, which are weakly-bound to the lattice fragment and are presumably emitted when the reaction occurs. Assuming the emission of these two neutrons, the fission can be considered as symmetric with respect to both planes 2 and 8.

The second simulation was run in accordance with reaction (2) (see Table 2 and Table 3). In this case, the lattice structure forFe_{26}^{56} is produced using the picking option [17]. The fragments obtained from the fission simulated by

Table 3. Fracture of the Mg^{24} lattice along plane 2; broken bonds are represented in red between the fragments of reaction (7) in Table 3.

Reaction	Plane	Fragment 1					Fragment 2					Neutron Emission	Fission Probability (%)
		Z	N	A	Isotope	Decay time[1]	Z	N	A	Isotope	Decay time[1]		
(1)[2]	2	13	14	27	Al^{27}	Stable	13	16	29	Al^{27}	6.6 (m)	+2n	23.22
	8	13	14	27	Al^{27}	Stable	13	16	29	Al^{27}	6.6 (m)	+2n	
(2)[2]	14	12	12	24	Mg^{24}	Stable	14	18	32	Si^{28}	172(y)	+4n	40.74
	16	12	12	24	Mg^{24}	Stable	14	18	32	Si^{28}	172(y)	+4n	
(3)[2]	1	6	7	13	C^{12}	Stable	20	23	43	Ca^{40}	Stable	+4n	36.04
	3	20	22	42	Ca^{40}	Stable	6	8	14	C^{12}	5730(y)	+4n	
(4)	2	13	14	27	Al^{27}	Stable	14	18	32	Si^{28}	172 (y)	+4n	100
	8	14	16	30	Si^{28}	Stable	13	16	29	Al^{27}	6.6 (m)	+4n	
(5)[2]	2	14	16	30	Si^{28}	Stable	14	15	29	Si^{28}	Stable	+3n	32.60
(6)[2]	12	11	13	24	Na^{23}	14.95(h)	17	18	35	Cl^{35}	Stable	+n	67.40
(7)[2]	2	6	6	12	C^{12}	Stable	6	6	12	C^{12}	Stable		11.26
(8)[1]	9	11	12	23	Na^{23}	Stable	1	0	1	H^1	Stable		31.01
(9)[2]	4	8	12	20	O^{16}	13.5(s)	4	0	4	$4H^1$	Stable	+4n	(57.73)
	6	0	4	4			12	8	20	$O^{16}+4H^1$	0.1(s)	+4n	
	7	4	4	8	$4H^1$	0.07(fs)	8	8	16	O^{16}	Stable	+4n	
	8	8	9	17	O^{16}	Stable	4	3	7	$4H^1$	0.07(fs)	+4n	
(10)[2]	1	2	2	4	He^4	Stable	18	18	36	$3C^{12}$	Stable		10.28
(11)[2]	1	1	0	1	H^1	Stable	19	20	39	K^{39}	Stable		58.46
(12)	1	4	4	8	$4H^1$	0.07(fs)	16	16	32	$2O^{16}$	Stable	+4n	31.26
	3	16	16	32	$2O^{16}$	Stable	4	4	8	$4H^1$	0.07(fs)	+4n	
	7	4	4	8	$4H^1$	0.07(fs)	16	16	32	$2O^{16}$	Stable	+4n	
	9	16	16	32	$2O^{16}$	Stable	4	4	8	$4H^1$	0.07(fs)	+4n	
(13)[2]	13	6	6	12	C^{12}	Stable	2	2	4	He^4	Stable		100
(14)	2	6	7	13	C^{12}	Stable	7	7	14	N^{14}	Stable	+n	100
(15)	2	7	7	14	N^{14}	Stable	7	7	14	N^{14}	Stable		14.66
	8	7	7	14	N^{14}	Stable	7	7	14	N^{14}	Stable		
(16)	10	6	6	12	C^{12}	Stable	8	8	16	O^{16}	Stable		35.89
	12	6	6	12	C^{12}	Stable	8	8	16	O^{16}	Stable		
	14	6	6	12	C^{12}	Stable	8	8	16	O^{16}	Stable		
	16	6	6	12	C^{12}	Stable	8	8	16	O^{16}	Stable		
(17)	9	12	12	24	$2\,C^{12}$	Stable	2	2	4	He^4	Stable		15.06
(18)	1	2	3	5	He^4	0.76(zs)	12	11	23	$O^{16}+He^4+2H^1$	11.3(s)	+2n	34.38
	8	8	9	17	O^{16}	Stable	6	5	11	$2He^4+2H^1$	20.385(m)	+2n	
	13	12	11	23	$O^{16}+He^{4+}2H^1$	11.3(s)	2	3	5	He^4	0.76(zs)	+2n	

[1] Decay time of the isotope (half life): zepto-seconds, 10-21 (zs); femto-seconds, 10–15 (fs); seconds (s); minutes (m); hours (h); days (d); years (y)

[2] Picking Option

NVS are summarized in Table 5. The results of the simulation show that the fragments are consistent with those of reaction (2) for fissions occurring along two different planes: 14, 16 (see Table 5 and Fig. 3). It is remarkable that the fragments from the fission along plane 14 are identical to those along plane 16. The simulation produces an isotope

Table 4. Fragments(2 $Al_{13}^{27} + 2$ neutrons)from the simulation of reaction (1).

Fission plane	Fragment 1				Fragment 2					Partial fission probability (%)
	Z_1	N_1	A_1	Isotope	Z_2	N_2	A_2	Isotope		
2	13	14	27	Al^{27}	13	16	29	Al^{27}	+ 2n	10.65
8	13	14	27	Al^{27}	13	16	29	Al^{27}	+ 2n	12.56

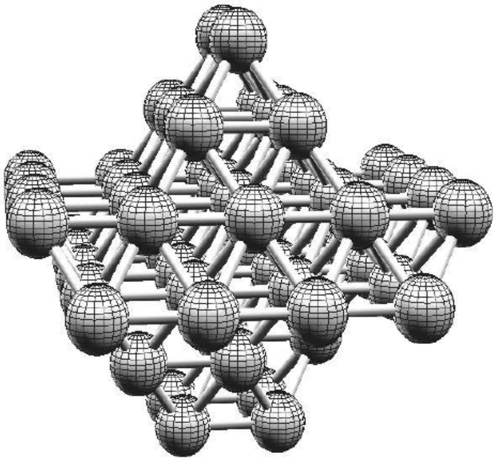

Figure 1. Screenshot of the 3D ^{56}Fe lattice structure built using NVS, which is downloadable from www.res.kutc.kansai-u.ac.jp/ cook.

of Mg and an isotope of Si, which are identified as Fragments 1 and 2. In each case, Fragment 1 is stable, whereas Fragment 2 is unstable. In particular, Fragment 1 is a stable nucleus of Mg^{24} and Fragment 2 is a nucleus of Si^{32}, unstable, which contains four neutrons that can be emitted when reaction (2) occurs.

Considering the data from the Earth's crust and the indirect piezonuclear evidence, reactions (7) and (12) are particularly significant for their implications concerning atmosphere evolution and ocean formation, respectively [9–12]. The simulation results of these reactions are summarized in Table 3. The simulation of piezonuclear reaction (7) produces as fragments two nuclei of C^{12} with no excess of neutrons (Figs. 4 and 5). Therefore, the simulation describes a symmetrical fission that does not entail neutron emissions according to piezonuclear reaction (7).

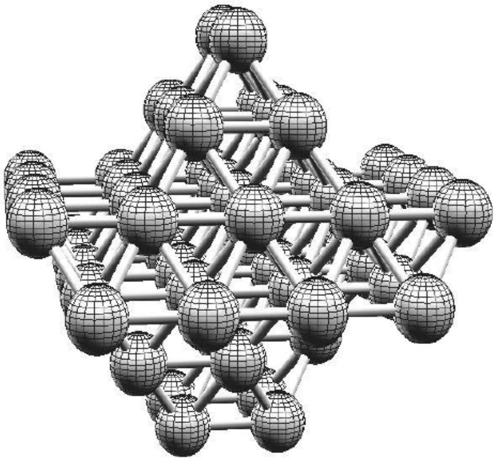

Figure 2. Fracture of the ^{56}Fe lattice along planes 2 ($x = 0$) and 8 ($y = 0$); broken bonds in red between Al fragments of reaction (1) in Table 3.

Table 5. Fragments (Mg^{24}_{12} + Si^{28}_{14}+ 4 neutrons) from the simulation of reaction (2).

Fission plane	Fragment 1				Fragment 2					Partial fission probability (%)
	Z_1	N_1	A_1	Isotope	Z_2	N_2	A_2	Isotope		
14	12	12	24	Mg^{24}	14	18	32	Si^{28}	+4n	20.37
16	12	12	24	Mg^{24}	14	18	32	Si^{28}	+4n	20.37

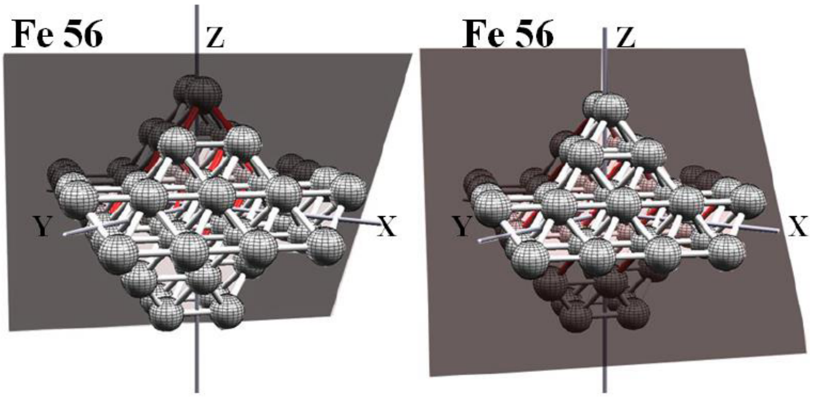

Figure 3. Fracture of ^{56}Fe lattice along planes 14 ($-x - y + z = 1$) and 16 ($x + y + z = 1$); broken bonds in red between Mg and Si Fragments of reaction (2) in Table 3.

On the other hand, as observed in the case of reactions (1), (2), and (12), there are unstable fragments. In particular, for every plane (Table 3) that allows for the products $2O^{16}_{8}$ + $4H^{1}_{1}$ of piezonuclear reaction (12), at least one of the two fragments obtained from each simulation is unstable. This result suggests that neutron emission is favored in many of the lattice fission events (Figs. 6 and 7).

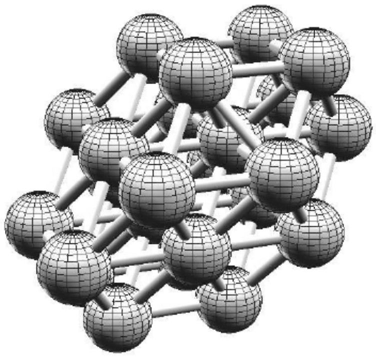

Figure 4. ^{24}Mg nuclear lattice structure.

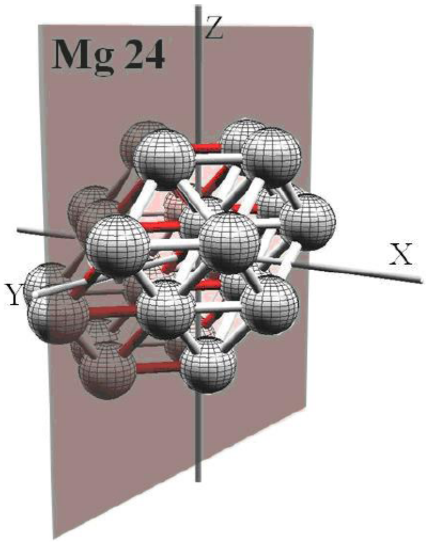

Figure 5. Fracture of the ^{24}Mg lattice along plane 2; broken bonds are represented in red between the fragments of reaction (7) in Table 3.

4. Binding Energy and Probability of Alternative Piezonuclear Fission Reactions

As described above, the nucleus is represented as a lattice where the nodal positions are occupied by the nucleons. A given nuclear lattice in its ground-state has a certain total binding energy (BE) that generally depends on the number and type of nearest-neighbor nucleon–nucleon bonds, thus on the number of constituent nucleons [21,22]. The binding energy is usually expressed as average binding energy per nucleon (BE/nucleon) or average binding energy per bond

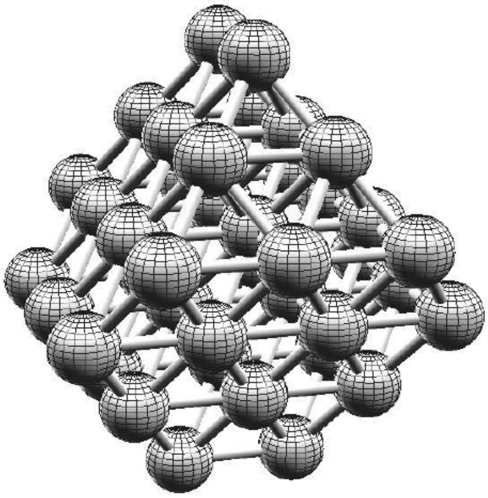

Figure 6. ^{40}Ca nuclear lattice structure.

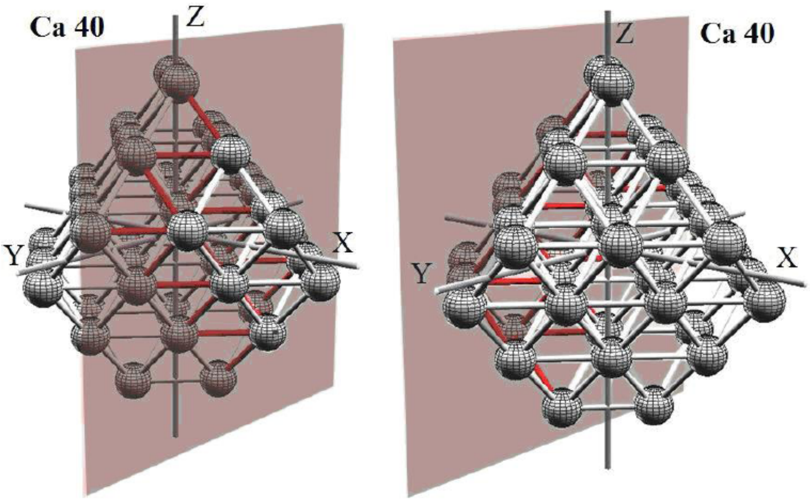

Figure 7. Fracture of ^{40}Ca along planes 1 and 3; broken bonds in red between the fragments of reaction (12) in Table 3.

(BE/bond), which represents a mean value of the energy distribution among the bonds in the nucleus [21,22]. According to the lattice model, the bonds are not all equivalent and are formed by various combinations of nucleon states (as specified by quantum numbers *n, j, m, s* and i). Specifically, the dipole–dipole interactions of nucleon pairs are attractive (singlet-pairs) for all nearest-neighbor PP and NN combinations, but there are both attractive and repulsive dipole combinations for PN pairs (triplet- and singlet-pairs, respectively). As a consequence, the antiferromagnetic fcc lattice with alternating proton-neutron layers implies the existence of lattice planes that are either strongly or weakly bound, depending on the character of the bonds in the lattice plane. It is the internal structure of the nucleon lattice that leads directly to the prediction of lattice fragments of various masses and probabilities.

In order to assess the probability of fission occurring in a given nucleus, it is necessary to know the binding force of the nuclear lattice structure: the lower is this force the higher is the probability of fission. This can be evaluated in terms of binding energy of the lattice structure through a specific plane. In particular, the binding energy of the bonds between nearest-neighbor nucleons crossed by a fracture plane minus the Coulomb repulsion through the same plane represents the residual binding energy. Inverting this value yields a ratio (MeV^{-1}) that is defined as proportional to the probability of fission ($P_{fission}$) [17]:

$$P_{\text{fission}}(Z,N) = \frac{1}{\left(\beta \sum_{m}^{A_{\text{f1}}} \sum_{n}^{A_{\text{f2}}} b_{m,n} - \sum_{j}^{Z_{\text{f1}}} \sum_{k}^{Z_{\text{f2}}} Q_{j,k}\right)}, \tag{4}$$

where Z, N, and A are the number of protons, neutrons and the total number of nucleons contained in the atomic nucleus; f1 and f2 stand for the two resulting fragments of the given reaction; β is an experimental value of the nucleon–nucleon binding force. Between nearest-neighbor nucleons this value changes according to the different nature of the bond; $b_{m,n}$ is the number of bonds across the fission plane taken into consideration and so the number of broken nucleon–nucleon bonds along the fracture plane; $Q_{j,k}$ is the Coulomb repulsive contribution between the protons in the two fragments defined by the fission plane.

Using the parameter P_{fission}, the probabilities of piezonuclear reactions (1) and (2) were calculated as shown in detail in Tables 4 and 5 and summarized in Table 3. The Fission Probability is expressed as a normalized percentage of the cases studied for each element reported in Table 2 with their relevant fission planes, and a given binding force value β is assumed (approximately comprised in the range between 2 and 4 MeV) [17]. From Table 4, the simulation of piezonuclear reaction (1) results in two cases of the 17 possible fission planes, with a total P_{fission} of $\sim$23%, whereas from Table 5 it is observed that reaction (2) results in two cases having a total P_{fission} of $\sim$41%. According to these considerations, it is of interest that these probabilities reproduce the known abundances of the Al^{27}, Mg^{24} and Si^{28} elements in the Earth's crust [9–12]. The probability that a nucleus of Fe^{56} produces Magnesium and Silicon (piezonuclear reaction (2) in Table 2) is significantly larger (ratio: 1.74) than that implying the symmetrical nuclear fission of Fe^{56} into two Al^{27} atoms (reaction (1) in Table 2). This is in agreement with the evidence regarding the compositional changes in the evolution of the Earth's crust. In fact, the total decrease in Fe^{56} over the last 4.57 Billion years of about 11% seems to be consistently counterbalanced by the increases in Mg, Si and Al, where the contribution of Mg^{24} and Si^{28} $\sim$7% is a little less than twice that of the Al^{27} increase, $\sim$4% [9–12]. The ratio of the normalized P_{fission} of reaction (2) to that of reaction (1) is approximately 1.75, as the ratio of Mg and Si ($\sim$7%) increase to the increase in Al ($\sim$4%) in the Earth's crust. It is also interesting to note that reaction (3) involving Fe as the starting element and Ca and C as the resultants can be obtained by the NVS simulation. This reaction, not so frequent in the Earth's crust system, could be recognized as a fundamental reaction during the application of ultrasound to sintered Ferrite (α-Iron) and steel bars, as recently reported by Cardone et al. [33]. This evidence indicates that the NVS is able to reproduce different piezonuclear fission reactions also belonging to different systems and experiments at different scales (Earth's crust or ferrite bar).

The results obtained from the Ca-based reaction simulations also showed consistency with the findings reported in [9–12]. During the evolution of the Earth's crust, Ca decreased by about $\sim$4%, while K increased by about $\sim$2.7%, according to reaction (11). The total Ca depletion may be almost perfectly counterbalanced considering the increases in O and H (H_2O) that together correspond to an increment of about 1.3% [9–12]. This means that more than two thirds of the Ca depletion resulted in potassium and approximately one third in H_2O. On the other hand, considering the probability of fission computed for reactions (10)– (12) by NVS (Table 3), the piezonuclear reaction involving K as the product, reaction (11), returned a normalized probability of $\sim$58.4%. The normalized probability of the simulation of reaction (12), involving H and O as products, is about 31.2% (see Table 3) [9–12]. The ratio of the fission probability of reaction (11) to that of reaction (12) is about two, which is in good agreement with the evidence concerning the Earth's crust [9-12].

The consistency with the evidence drawn from the Earth's crust can be verified also in the case of Mg as the starting element of the anomalous reactions (7)–(9). In particular, we find a global Mg decrease ($\sim$7.9%) that is counterbalanced by a $\sim$2.7% increase in Na in the Earth's crust and by increases of $\sim$2.0% and $\sim$3.2% in H_2O and C, respectively, in the ancient atmosphere. The evidence of the Na increase is supported by the NVS simulation that returns a normalized probability percentage for reaction (8) equal to $\sim$31.0%. With regard to the other reactions, involving C, O and H as resultants, we obtained a total normalized probability percentage of about $\sim$69%. These last two percentages are in good agreement with the considerations concerning the evolution of the Earth's crust composition as about two thirds of the Mg decrease can be ascribed to the formation of gaseous elements such as C and H_2O that formed in the proto-atmosphere of our planet [9–11,34].

5. Conclusions

The simulations conducted using the NVS reproduced the piezonuclear reactions assumed and observed in both laboratory tests and Earth's crust by Carpinteri et al. [1–12]. The results were obtained using the approach recently proposed by Cook and co-workers to provide a fully quantum mechanical unification of the different models of nuclear structure [17,20].

It is true that the full comprehension of the mechanisms is yet to be achieved. However, a possible, yet not intuitive, way to explain the nuclear evidence is to consider the fracture as the origin of the phenomena of neutron emission and isotopic changes, but not the direct cause. Acoustic emissions sources, at very high frequencies (THz), generated by micro and macro-cracks during damage, could be considered as the generating mechanism. The achievement of the acoustic resonance of the atom could lead to the nuclear anomalies in fracture experiments phenomena encountered.

The simulations suggest that neutron emissions can be favored when the product fragments present unstable conditions. From this point of view, the recent evidence provided by fracture and fatigue experiments indicates neutron emissions far in excess of the background level [1–12]. This may be correlated to piezonuclear fission of nuclei along specific weak planes of the lattice structure. Furthermore, the presence of relatively weakly-bound planes within the lattice can be assumed as an indicator of the lattice behavior, through a given plane, calculated by means of the Fission Probability. This implies that certain piezonuclear reactions may occur with a higher probability than others. In particular, the total decrease in Fe^{56} over the last 4.57 billion years of about 11% consistently counterbalanced by an increase in Mg^{24} and Si^{28} ($\sim$7%), and by that in Al^{27} ($\sim$4%), is confirmed by the normalized fission probabilities of the relevant reactions computed by the lattice model. Analogously, similar numerical results obtained by NVS supported the decreases in Ca and Mg and the increases in K, Na, C and H_2O, contributing to explain the Earth's crust evolution together with the proto-atmosphere compositions and the formation of the oceans under the light of the piezonuclear conjecture.

Finally, the current version of the NVS simulates the fission of nuclei assuming an average value of the nuclear binding force. More precise results could be obtained in the case of these reactions using an improved version of the NVS that is able to consider the binding energy between nucleons as a function of the different nucleon states. Such improvements will be implemented in future research in order to take into consideration a more realistic distribution of the binding energy across the nucleus.

References

[1] A. Carpinteri, F. Cardone and G. Lacidogna, Piezonuclear neutrons from brittle fracture: Early results of mechanical compression tests, *Strain* **45** (2009) 332–339; Atti dell'Accademia delle Scienze di Torino, Torino, Italy **33** (2009) 27–42.

[2] F. Cardone, A. Carpinteri and G. Lacidogna, Piezonuclear neutrons from fracturing of inert solids, *Phys. Lett.* A **373** (2009) 4158–4163.

[3] A. Carpinteri, F. Cardone, G. Lacidogna, Energy emissions from failure phenomena: Mechanical, electromagnetic, nuclear, *Experimental Mechanics* **50** (2010) 1235–1243.

[4] A. Carpinteri, O. Borla, G. Lacidogna and A. Manuello, Neutron emissions in brittle rocks during compression tests: Monotonic vs. cyclic loading, *Physical Mesomechanics* **13** (2010) 268–274.

[5] A. Carpinteri, G. Lacidogna, A. Manuello and O. Borla, Energy emissions from brittle fracture: Neutron measurements and geological evidences of piezonuclear reactions, Strength, *Fracture and Complexity* **7** (2011) 13–31.

[6] A. Carpinteri, G. Lacidogna, A. Manuello and O. Borla, Piezonuclear fission reactions: Evidences from microchemical analysis, neutron emission, and geological transformation, *Rock Mechanics and Rock Engineering* **45** (2012) 445–459.

[7] A. Carpinteri, G. Lacidogna, , O. Borla, , A. Manuello and G. Niccolini, Electromagnetic and neutron emissions from brittle rocks failure: Experimental evidence and geological implications, *Sadhana* **37** (2012) 59–78.

[8] A. Carpinteri, G. Lacidogna, A. Manuello and O. Borla, Piezonuclear fission reactions from earthquakes and brittle rocks failure: Evidence of neutron emission and nonradioactive product elements, *Experimental Mechanics*, doi: 10.1007/s11340-012-9629-x (2012c).

[9] A. Carpinteri, A. Chiodoni, A. Manuello and R. Sandrone, Compositional and microchemical evidence of piezonuclear fission reactions in rock specimens subjected to compression tests, *Strain* **47**(2) (2011) 267–281.

[10] A. Carpinteri and A. Manuello, Geomechanical and Geochemical evidence of piezonuclear fission reactions in the Earth's Crust, *Strain* **47** (2011) 282–292.

[11] A. Carpinteri and A. Manuello, An indirect evidence of piezonuclear fission reactions: Geomechanical and geochemical

evolution in the Earth's crust, *Physical Mesomechanics* **15** (2012) 14–23.

[12] N.D. Cook,A. Manuello, R. Sandrone, S. Guastella, O. Borla, G. Lacidogna and A. Carpinteri, Neutron emissions and compositional change evidence in piezonuclear reactions during fracture of granite, basalt and magnetite fracture tests (This issue).

[13] A. Widom, J. Swain and Y.N. Srivastava, Photo-disintegratin of the iron nucleus in fractured magnetite rocks with magetostriction, arXiv: 1306.6286v1 (2013).

[14] A. Widom, J. Swain and Y.N. Srivastava, Neutron production from the fracture of piezoelectric rocks, *J. Phys. G: Nucl. Part. Phys.* **40** (2013) doi:10.1088/0954-3899/40/1/015006.

[15] P.W. Bridgman, The breakdown of atoms at high pressures, *Phy. Rev*. **29** (1927) 188–191.

[16] E. Storms, *Science of Low Energy Nuclear Reaction: A Comprehensive Compilation of Evidence and Explanations About Cold Fusion* (World Scientific, Singapore, 2007).

[17] N.D. Cook, *Models of the Atomic Nucleus* (Springer, Hideldburg, 2^{nd} Ed., 2010).

[18] N.D. Cook and V. Dallacasa, Face-centered-cubic solid-phase theory of the nucleus, Phy. Rev. C **35** (1987) 1883.

[19] N.D. Cook and V. Dallacasa, LENR and nuclear structure theory, *Proc. ICCF-17*, August 12–17, 2012, Daejong, Korea.

[20] T. Mizuno, Nuclear Transmutation: The reality of cold fusion, Tuttle, Concord NH (1998).

[21] J. Lilley, *Nuclear Physics: Principles and Applications* (Wiley, New York, 2001).

[22] K.S. Krane, *Introductory Nuclear Physics* (Wiley, New York, 1987).

[23] N.D. Cook, An FCC lattice model for nuclei, *Atomkernenergie* **28** (1976) 195.

[24] N.D. Cook, Quantization of the FCC nuclear theory, *Atomkernenergie* **40** (1981) 51.

[25] V. Dallacasa and N.D. Cook, The FCC nuclear model (II), *Nuovo Cimento II* 97 (1987) 157.

[26] N.D. Cook, Computing nuclear properties in the FCC model, *Computers in Phys.* **3** (1989) 73.

[27] N.D. Cook, Nuclear binding energies in lattice models, *J. Phys. G* **20** (1994) 1907.

[28] N.D. Cook, Is the lattice gas model a unified model of nuclear structure? *J. Phys.* **25** (1999) 1.

[29] N.D. Cook, Toward an explanation of transmutation products on palladium cathodes, *Proc. ICCF-14*, 2008, Rome, Italy.

[30] N.D. Cook, Simulation of palladium fission products using the FCC lattice model, *Proc. ICCF-16*, 2010, Chennai, India.

[31] E. Wigner, On the consequences of the symmetry of the nuclear hamiltonian on the spectroscopy of nuclei, *Phy. Rev.* **51** (1937) 106.

[32] T. Mizuno, Experimental confirmation of the nuclear reaction at low energy caused by electrolysis in the electrolyte, *Proc. Symp. on Advanced Research in Energy Technology,* 2000, pp. 95–106.

[33] F. Cardone, A. Carpinteri, A. Manuello, A. Mignani, R.A. Sepielli and M. Petrucci, Ultrasonic Piezonuclear Reactions in Iron, This issue.

[34] L. Liu, The inception of the oceans and CO_2-athmosphere in the early history of the Earth. Earth Planet, *Sci. Lett.* **227** (2004) 179–184.

J. Condensed Matter Nucl. Sci. 15 (2015) 162–182

Research Article

Hydrogen Embrittlement and Piezonuclear Reactions in Electrolysis Experiments

A. Carpinteri*, O. Borla, A. Manuello and D. Veneziano
Politecnico di Torino, Department of Structural, Geotechnical and Building Engineering, Corso Duca degli Abruzzi, 24–10129 Torino, Italy

A. Goi

Abstract

A great deal of evidence of anomalous nuclear reactions occurring in condensed matter has been observed using electrolysis, fracture (with solids), and cavitation (with liquids). Despite the large amount of experimental results from so-called cold nuclear fusion and Low Energy Nuclear Reaction research activities, researchers still do not understand these phenomena. On the other hand, as reported by most of the articles devoted to Cold Nuclear Fusion, one of the principal features is the appearance of micro-cracks on the electrode surfaces after the experiments. In the present paper, a mechanical explanation is proposed considering a new kind of nuclear reactions, the piezonuclear fission, which is a consequence of hydrogen embrittlement of the electrodes during electrolysis. The experimental activity was conducted using a Ni–Fe anode and a Co–Cr cathode immersed in a potassium carbonate solution. Emissions of neutrons and alpha particles were measured during the experiments and the electrode compositions were analyzed both before and after the electrolysis, revealing the effects of piezonuclear fissions occurring in the host lattices. The symmetrical fission of Ni appears to be the main and most evident feature. Such a reaction would produce two Si atoms or two Mg atoms with additional fragments as alpha particles.

Keywords: Cold nuclear fusion, Electrolysis, Hydrogen embrittlement, Piezonuclear fissions

---

1. Introduction

During the last two decades a great deal of evidence of anomalous nuclear reactions occurring in condensed matter has been observed [1–34]. These tests were characterized by significant neutron and alpha particle emissions as well as by extra heat generation. At the same time, appreciable variations in the chemical composition after embrittlement or during fatigue fracture were detected [35–40].

Most relevant papers on so-called Cold Nuclear Fusion describe broad experimental activities conducted on electrolytic cells powered by direct current and filled with ordinary or heavy water solutions. In particular, in 1989, Fleischmann and Pons proposed the first experiment reproducing Cold Nuclear Fusion by means of electrolysis [6].

---

*E-mail: alberto.carpinteri@polito.it

They asserted that the palladium electrode reacted with the deuterium coming from the heavy water solution [6]. Later works reported that Pt and Ti electrodes had also been electrolyzed with D_2O to produce extra energy and chemical elements previously absent [26,28,29]. Extra energy has been also produced from electrolysis with Ni cathodes and H_2O-based electrolyte [13]. Furthermore, it was affirmed that a voltage sufficient to induce plasma generates a large variety of anomalous nuclear reactions when Pd, W, or C cathodes are adopted [16, 21–25].

In many of these experiments, the generated heat was calculated to be several times the input energy and the neutron emissions rate, during electrolysis, was measured to be about three times the natural background level [6]. In 1998, Mizuno presented the results of the measurements conducted by means of neutron emission detectors and compositional analysis techniques related to different electrolytic experiments [22]. Relevant heat generation was observed when the cell was supplied with high voltage, with an excess energy of 2.6 times the input one. Remarkable neutron emissions were revealed during these tests, as well as a considerable amount of new elements, i.e. Pb, Fe, Ni, Cr, and C, with the isotopic distribution of Pb deviating greatly from the natural isotopic abundances [22]. These results suggested that nuclear reactions took place during the electrolysis process [22]. Later, in 2002 Kanarev and Mizuno reported the results obtained from the surface compositional analysis of iron electrodes (99.90% of Fe) immersed in KOH and NaOH solutions [34]. After the experiments, EDX spectroscopy revealed the appearance of several chemical elements previously absent. Concentrations of Si, K, Cr, and Cu were found on the surfaces of the operating cathode immersed in KOH. Analogously, concentrations of Al, Cl, and Ca were noticed on the iron electrode surfaces operating in NaOH. These findings are evidence of compositional changes occurring during plasma formation in electrolysis of water [34]. In 2007, Mosier-Boss et al. [31,33] obtained important proofs of anomalous measurements in experiments conducted by electrolytic co-deposition cells. More in detail, anomalous effects observed in the Pd/D system include heat and helium-4 generation, tritium, neutrons, gamma/X-ray emissions, and transmutations [7,12,31,33].

Preparata wrote: “despite the great amount of experimental results observed by a large number of scientists, a unified interpretation and theory of these phenomena has not been accepted and their comprehension still remains unsolved” [6–9,26,27].

Very recently, theoretical interpretations have been proposed by Widom et al. in order to explain neutron emissions as a consequence of nuclear reactions taking place in iron-rich rocks during brittle micro-cracking and fracture [41,42]. A great deal of evidence shows that iron nuclear disintegrations are observed when rocks containing such nuclei are crushed and fractured. The resulting nuclear transmutations are particularly evident in the case of magnetite rocks and iron-rich materials in general. The same authors argued that neutron emissions may be related to piezoelectric effects and that fission of iron may be a consequence of the photodisintegration of the same nuclei [41].

On the other hand, as shown by most articles devoted to Cold Nuclear Fusion, one of the principal features is the appearance of micro-cracks on electrode surfaces after the tests [26,27]. Such evidence might be directly correlated to hydrogen embrittlement of the material composing the metal electrodes (Pd, Ni, Fe, Ti, etc.). This phenomenon, well-known in metallurgy and fracture mechanics, characterizes metals during forming or finishing operations [43]. In the present study, the host metal matrix (e.g. Pd) is subjected to mechanical damaging and fracturing due to external atoms (deuterium or hydrogen) penetrating into the lattice structure and forcing it apart during gas loading. Hydrogen effects are largely studied especially in metal alloys, where the presence of H free atoms in the host lattice causes the metal to become more brittle and less resistant to crack formation and propagation. In particular, hydrogen generates an internal stress that lowers the fracture stress of the metal so that brittle crack growth can occur under a hydrogen partial pressure below 1 atm. [43,44].

Some experimental evidence shows that neutron emissions may be strictly correlated to fracture of non-radioactive or inert materials. From this point of view, anomalous nuclear emissions and heat generation had been verified during fracture in fissile materials [2–4] and in deuterated solids [5,8,30]. The experiments recently proposed by Carpinteri et al. [36–39] represent the first evidence of neutron emissions due to piezonuclear fissions observed during failure of inert, stable, and non-radioactive solids under compression, as well as from non-radioactive liquids under ultrasound cavitation [37,38]. In the present paper, we analyze neutron and alpha particle emissions during tests conducted on an electrolytic cell, where the electrolysis is obtained using Ni–Fe and Co–Cr electrodes in aqueous potassium carbonate solution. Voltage, current intensity, solution conductivity, temperature, alpha and neutron emissions were monitored. The compositions of the electrodes were analyzed both before and after the tests. Strong evidence suggest that so-called Cold Nuclear Fusion, interpreted under the light of hydrogen embrittlement, may be explained by piezonuclear fission reactions occurring in the host metal, instead of by the nuclear fusion of H isotopes adsorbed in the lattice. These new kind of fission reactions have recently been observed from the laboratory to the Earth's crust scale, when particular stress waves originate from fracture or fatigue phenomena, as they do corresponding to an impending earthquake [5–40].

2. Experimental Set-up and Measurement Equipment

2.1. The electrolytic cell and the power circuit

Over the last 10 years, specific experiments have been conducted on an electrolytic reactor (owned by Mr. A. Goi et al.). The aim was to investigate whether the anomalous heat generation may be correlated to new type of nuclear reactions during electrolysis phenomena. The reactor was built in order to be appropriately filled with a salt solution of water and potassium carbonate (K_2CO_3). The electrolytic phenomenon was obtained using two metal electrodes immersed in the aqueous solution. The solution container, named also reaction chamber in the following, is a cylinder-shaped element of 100 mm diameter, with 150 mm high and 5 mm thick. For the reaction chamber, two different materials were used during the experiments: Pyrex glass and Inox AISI 316L steel. The two metallic electrodes were connected to a source

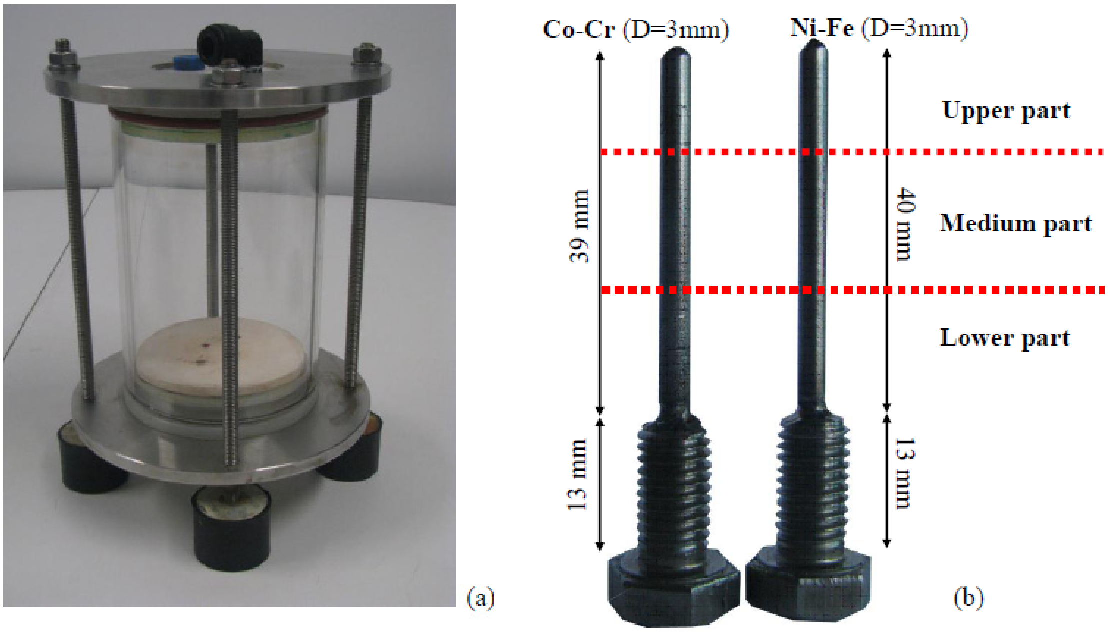

Figure 1. The reaction chamber is a cylinder-shaped element of 100 mm diameter, 150 mm high and 5 mm thick (a). The two electrodes presented a height of about 40 mm of the operating part and a diameter of about 3 mm. The threaded portions and the base are 13 and 5 mm long, respectively (b).

of direct current: an Ni–Fe based electrode as positive pole (anode), and a Co–Cr based electrode as negative pole (cathode) (see Fig. 1b).

With regard to the experiment described in the present paper, after approximately 10 operating hours, the generation of cracks was observed in the glass container, which forced the authors to adopt a more resistant reaction chamber made of steel. Teflon lids are sealed to both the upper and the lower openings of the chamber. The reaction chamber base consists of a ceramic plate preventing the direct contact between liquid solution and Teflon lid (see Fig.1a). Two threaded holes host the electrodes, which are screwed to the bottom of the chamber, which is then filled with the solution. A valve at the top of the cell allows the vapor to escape from the reactor and condense in an external collector. Externally, two circular Inox steel flanges, fastened by means of four threaded ties, hold the Teflon layers. The inferior steel flange of the reactor is connected to four supports isolated from the ground by means of rubber based material. As mentioned before, a direct current passes through the anode and the cathode electrodes, provided by a power circuit connected to the power grid through an electric socket. The components of the circuit are an isolating transformer, an electronic variable transformer (Variac), and a diode bridge linked in series (Fig. 2).

2.2. Measurement equipment and devices

Different physical quantities were measured during the experiments, such as voltage, current, neutron and alpha particle emissions.

Electric current and voltage probes were positioned in different parts of the circuit as it is shown in Fig. 2. The voltage measurements were performed by a differential voltage probe of 100 MHz with a maximum rated voltage of 1400 V. The current was measured by a Fluke I 310S probe with a maximum rated current of 30 A. Particular attention was paid to the data obtained from the current and voltage probes positioned at the input line powering the reaction chamber (probes 7 and 8 in Fig. 2) in order to evaluate the power absorbed by the cell. Current intensity and voltage measurements were also taken by means of a multimeter positioned at the input line. From the turning on to the switching off of the electrolytic cell, current and voltage were found to vary in a range from 3 to 5 A and from 20 to

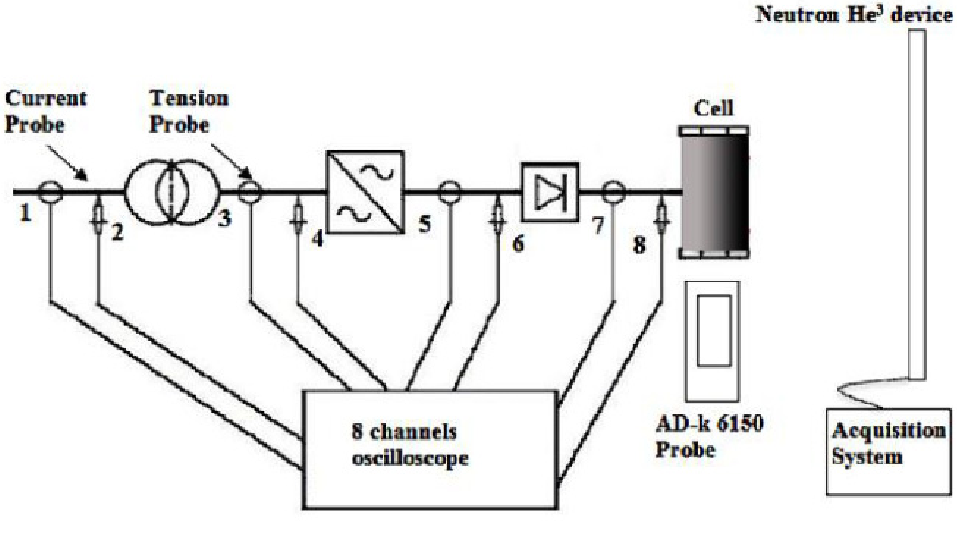

Figure 2. Scheme of the experimental set-up adopted and disposition of the measurement equipment employed during the tests.

120 V, respectively. For convenience and clarity, these values are considered as a benchmark to be compared to further measurements which will be reported in future works.

Regarding the neutron emission measurements, since neutrons are electrically neutral particles, they cannot directly produce ionization in a detector, and therefore cannot be directly detected. This means that neutron detectors must rely upon a conversion process accounting for the interaction between an incident neutron and a nucleus, which produces a secondary charged particle. Such charged particle is then detected and the neutron's presence is revealed from it. For an accurate neutron evaluation a He^3 proportional counter was employed. The detector used in the tests is a He^3 type (Xeram, France) with pre-amplification, amplification, and discrimination electronics directly connected to the detector tube. The detector is supplied by a high voltage power (about 1.3 kV) via NIM (Nuclear Instrument Module). The logic output producing the TTL (transistor–transistor logic) pulses is connected to a NIM counter. The logic output of the detector is enabled for analog signals exceeding 300 mV. This discrimination threshold is a consequence of the sensitivity of the He^3 detector to the gamma rays ensuing neutron emission in ordinary nuclear processes. This value has been determined by measuring the analog signal of the detector by means of a Co-60 gamma source. The detector is also calibrated at the factory for the measurement of thermal neutrons; its sensitivity is 65 cps/$n_{thermal}$ (±10% declared by the factory), i.e., the flux of thermal neutrons is one thermal neutron/s cm^2, corresponding to a count rate of 65 cps.

For the alpha particle emission, a 6150AD-k probe with a sealed proportional counter was used, which does not require refilling or flushing from external gas reservoirs. The probe is sensitive to alpha, beta, and gamma radiation. An electronic switch allows for the operating mode "alpha" to detect alpha radiation only, such that in this mode the radiation recognition is very sensitive because the background level is much lower. A removable discriminator plate (stainless steel, 1 mm) distinguishes between beta and gamma radiation detection. An adjustable handle can be locked to the most convenient orientation. During the experiments the 6150AD-k probe was used in the operating mode alpha to monitor the background level before and after the switching on of the cell.

Finally, before and after the experiments Energy Dispersive X-ray spectroscopy has been performed in order to recognise possible direct evidence of piezonuclear reactions that can take place during the electrolysis. The elemental analyses were performed by a ZEISS Auriga field emission scanning electron microscope (FESEM) equipped with an Oxford INCA energy-dispersive X-ray detector (EDX) with a resolution of 124 eV @ MnKa. The energy used for the analyses was 18 keV.

3. Experimental Results

3.1. General remarks and preliminary stage

In Fig. 1b, the two electrodes used for the tests are shown. The initial measurement phase implied the use of the Energy Dispersive X-ray spectroscopy (EDX) technique to obtain measurements useful to evaluate the chemical composition of the two electrodes before the experiments. In particular, a series of measures were repeated in three different regions of interest for each electrode in order to obtain a sufficient amount of reliable data. Such regions are the upper, the middle and the lower part of the single electrode, as reported in Fig. 2b.

Table 1. EDX spectroscopy of the K_2CO_3 salt used for the aqueous solution.

Element	Weight%	Atomic%	Compd%	Formula
C	13.02	22.05	47.72	CO_2
K	43.40	22.57	52.28	K_2O
O	43.58	55.38		
Total	100.00			

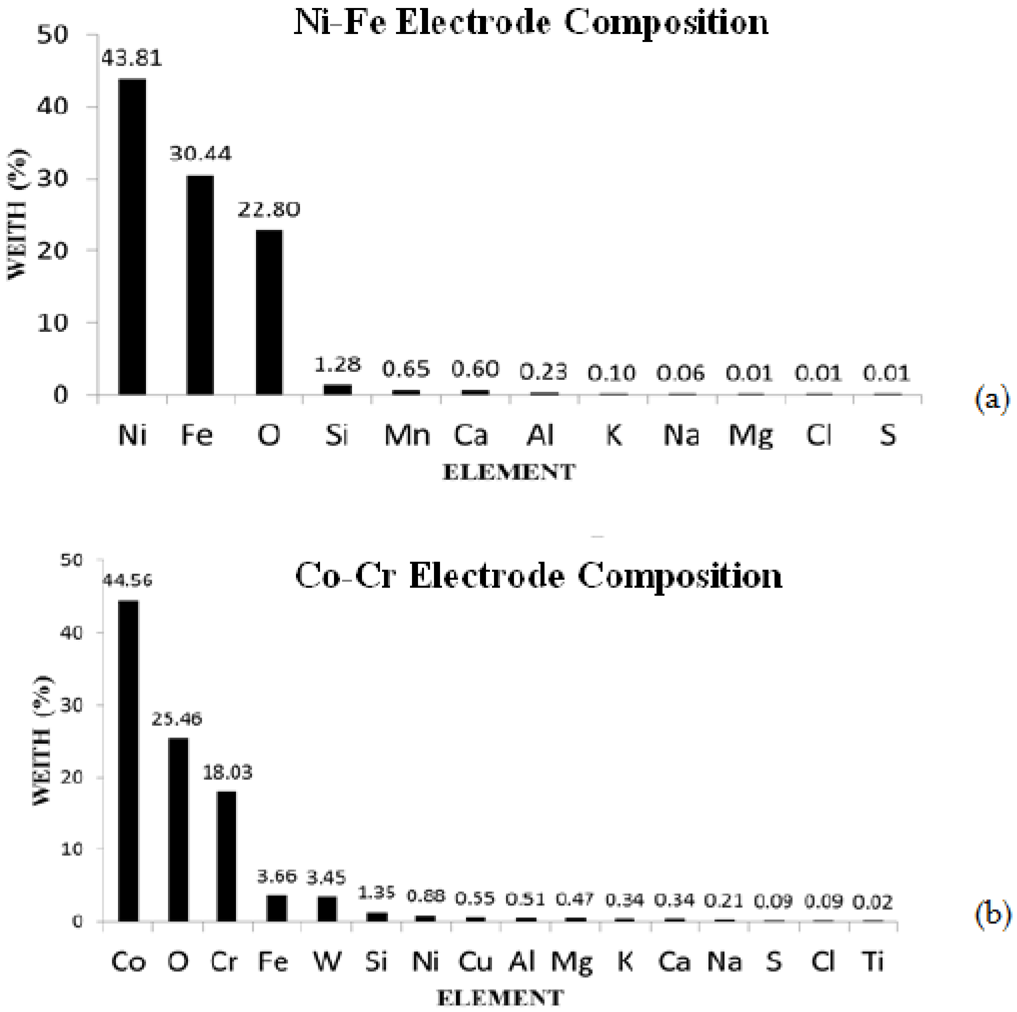

Figure 3. Mean element concentrations of the two electrodes used for the electrolysis.

In Figs. 3a and b, the average element concentrations of the electrodes used for the electrolysis are shown. In the initial condition the Ni–Fe electrode (anode) is composed by approximately 44% in Ni, 30% in Fe, and 23% in O. The remaining percentage includes contents of Si, Mn, Ca, Al, K, Na, Mg, Cl, and S, observable only in traces (Fig. 3a). On the other hand, the Co–Cr cathode is composed approximately by 44% in Co, 18% in Cr, 4% in Fe, 25% in O, and traces of other elements such as Si, Al, Mg, Na, W, Cu, and S (Fig. 3b). Table 1 summarizes the results for the compositional

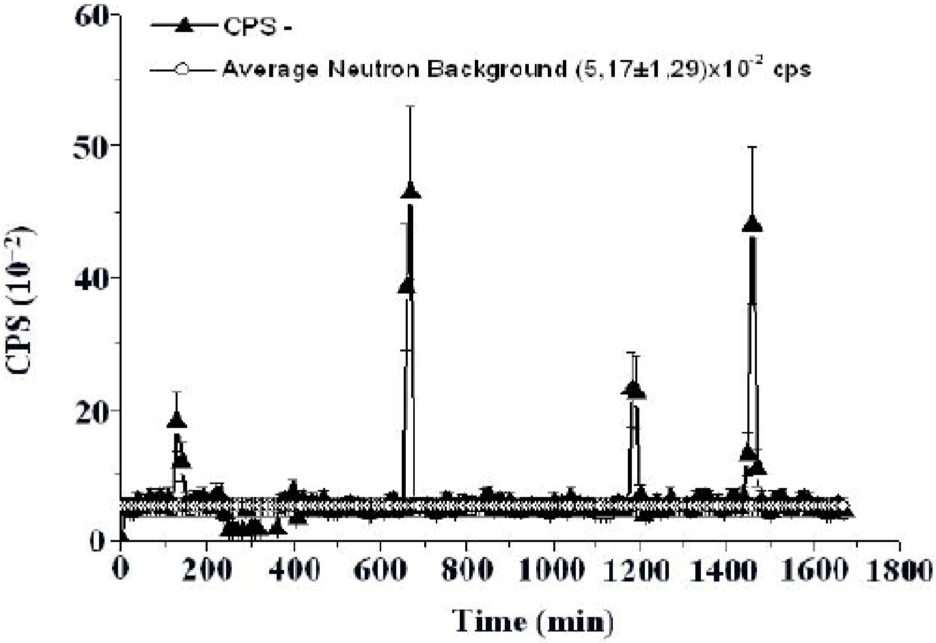

Figure 4. Neutron emission measurements. emissions between 4 and 10 times the background level have been observed during the experiments.

analysis conducted on the K_2CO_3, the salt used for the aqueous solution (K_2CO_3+H_2O), where the solute to solvent ratio was approximately 40 g/l.

3.2. Neutron and alpha particle detection during the experiment

Neutron emission measurements performed during the experimental activity are represented in Fig. 4. The measurements performed by the He^3 detector were conducted for a total time of about 26 h. The background level was measured for different time spans before and after switching on the reaction chamber. These measurements reported an average neutron background of (5.17 ±1.29) $\times 10^{-2}$ cps. Furthermore, when the reactor is active, it is possible to observe that after a time span of more than 3 h (200 min) neutron emissions of about four times the background level may be observed. After less than 11 h (650 min) from the beginning of the measurements, it is possible to observe a neutron emission level of about one order of magnitude greater than the background level. Similar results were observed after 20 h (1200 min) and 25 h (1500 min) when neutron emissions of about 5 times and 10 times the background were measured, respectively.

In Figs. 5a and b, alpha particle emissions are shown. The data are related to an alpha emission level monitored by means of the 6150AD-k probe set to the operating mode "alpha". The measurements shown in Fig. 5a are referred to the data acquired for a time interval equal to 60 minutes when the reaction chamber was operating (cell on). The data in Fig. 5b represent the alpha particle emissions corresponding to the background level and are obtained by measurements acquired, also in this case, for a 60 min (cell off) time interval. From these figures, it can be noticed that the number of counts per second acquired by the probe increased considerably when the electrolytic cell was operating (cell on) (Fig. 5a). In addition, the mean values of two alpha emission time series were computed, one when the cell was switched

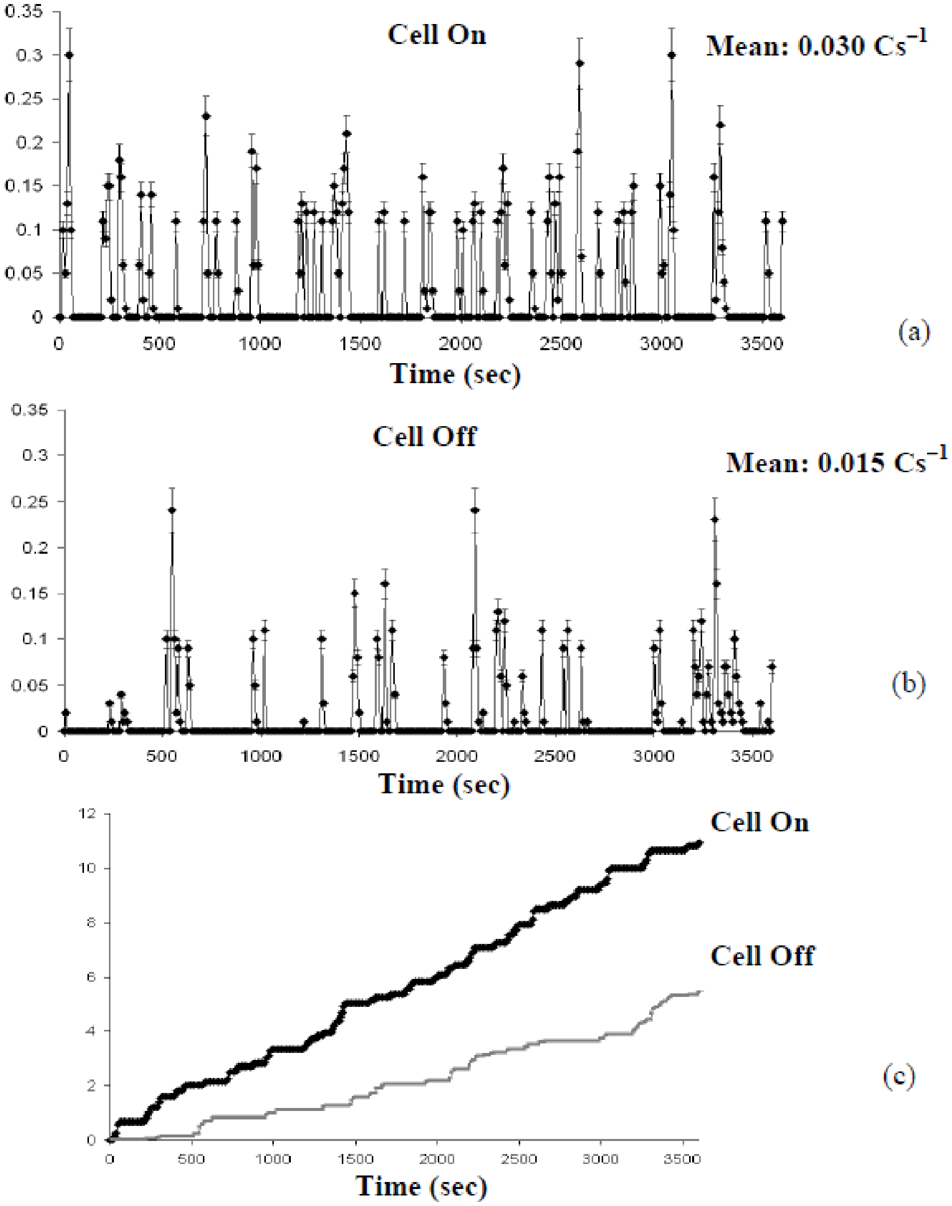

Figure 5. Data acquired for a time interval equal to 60 min when the reaction chamber was operating (a). The alpha particle emissions corresponding to the background level (b). Cumulative curves for the alpha emissions (c).

on and the other when the cell was off. The first time series, showed an average alpha emission of about 0.030 c/s (count per second), whereas the second one provided the background emission level in the laboratory with a mean value of about 0.015 c/s. It is evident that the average alpha particle emission during the electrolysis is two times the background level. These results, together with the evidence of neutron emissions reported in Fig. 4, are particularly interesting when considering the compositional variation described in the following, and will be useful to corroborate the hypothesis of piezonuclear fission for the chemical elements constituting the electrodes. In Fig. 5c, the cumulative curves for the alpha emission counts are reported. It is evident that the total counts value, monitored when the cell was operating (cell on), is approximately twice the value measured for the background level (cell off).

3.3. Compositional analysis of the electrodes

As reported in the previous section, Energy Dispersive X-ray Spectroscopy was performed in order to recognise possible direct evidence of piezonuclear reactions taking place during the electrolysis. In Figs. 6a and b two images of the Co–Cr electrode surface respectively before the experiment and after 32 h from the beginning of it are reported. It is shown that the electrode after several operating hours presented micro-cracks and cracks visible on its external surface (see Fig. 6b).

The experimental activity was developed in three different phases in order to investigate possible compositional variations on the electrode surface. A first analysis was carried out to evaluate the composition of the electrodes before they underwent the electrolysis experiment (0 h) (see Table2). The second analysis was conducted after an initial operating time of the electrolytic cell of about 4 h (see Table 2). After this, a third and a fourth step analyses were performed. For these two steps, the cell operated for 28 and 6 h, respectively, corresponding to a cumulative working time of 32 (4 h+28 h) and 38 h (4 h+28 h+6 h) (see Table2). In the case of the Ni–Fe electrode, the resulting mean concentrations of Ni, Si, Mg, Fe, and Cr are reported for each step, see Table 2. In Figs. 7–11, the EDX measurements for each element are reported considering the four steps previously mentioned (Figs. 7a, 8a, 9a, 10a, and 11a). At the same time, the evolution of the mean values of each time series along with their respective standard deviations, corresponding to 0, 4, 32, and 38 h, are reported by histograms (Figs. 7b, 8b, 9b, 10b, and 11b). After 38 h, the appearance of Cr, before absent, was detected as reported in Table 2 and in Fig. 11a. In particular, the Ni concentration showed a total average decrease of 8.6% from 43.9% to 35.3% after 38 h (see Table 2 and Figs. 7a and b). This Ni depletion is one fourth of the initial Ni concentration. A mean increment in Si concentration after 32 h of 3.9% and an average increment in Mg concentration after 38 h, starting from 0.1% up to 4.8%, can be observed from the data reported in Table 2, Figs. 8 and 9. Similar considerations may be done also for Fe and Cr concentrations. The average Fe content decreased of 3.2%, changing from 30.5% to 27.3% at the end of the experiment (see Table 2 and Fig. 10). On the other hand, the Cr concentration appeared only in the last phase with an appreciable increase of 3.0% (see Table 2 and Fig. 11). Such decreases in Ni and Fe seem to be almost perfectly counterbalanced by the increases in other elements: Si, Mg, and Cr. In particular, since the analysis excluded Ni content variations on the other electrode, the balance: Ni (–8.6%) = Si (+3.9%) + Mg (+4.7%) can be reasonably explained only by the following symmetrical piezonuclear fissions:

$$\mathrm{Ni}_{28}^{59} \rightarrow 2\mathrm{Si}_{14}^{28} + 3\ \text{neutrons}, \qquad (1)$$

Table 2. Ni–Fe Electrode, Element concentration before the experiment, after 4, 32 and 38 h of the test. The values reported for the mass % of each element are referred as the mean value of all the effectuated measurements.

	Ni (%)	Si (%)	Mg (%)	Fe (%)	Cr (%)
Before the experiment	43.9	1.1	0.1	30.5	–
After 4 h	43.6	1.1	0.4	30.7	–
After 32 h	35.2	5.0	0.2	27.9	–
After 38 h	35.3	1.5	4.8	27.3	3.0

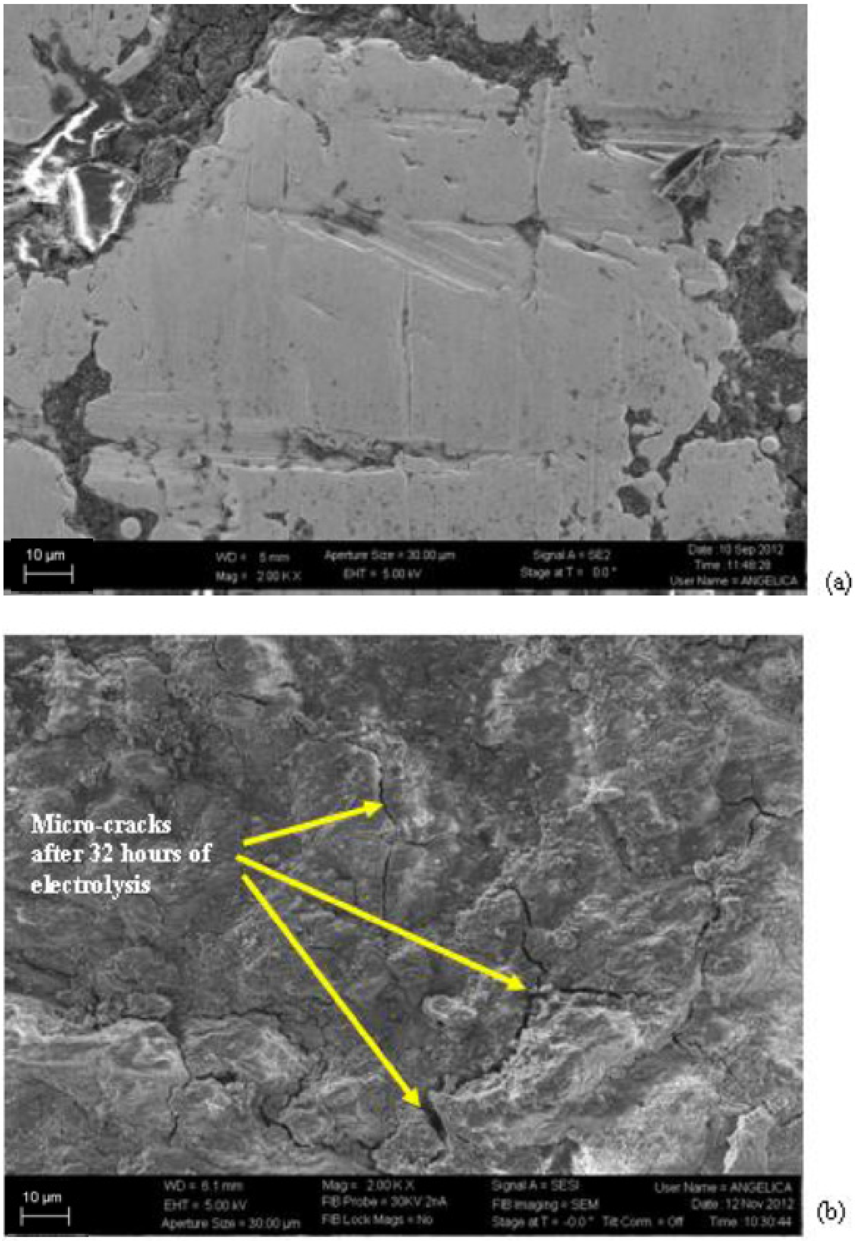

Figure 6. Image of the Co–Cr electrode surface before the experiment (a). The electrode after many operating hours presented cracks and micro-cracks visible on the external surfaces (b).

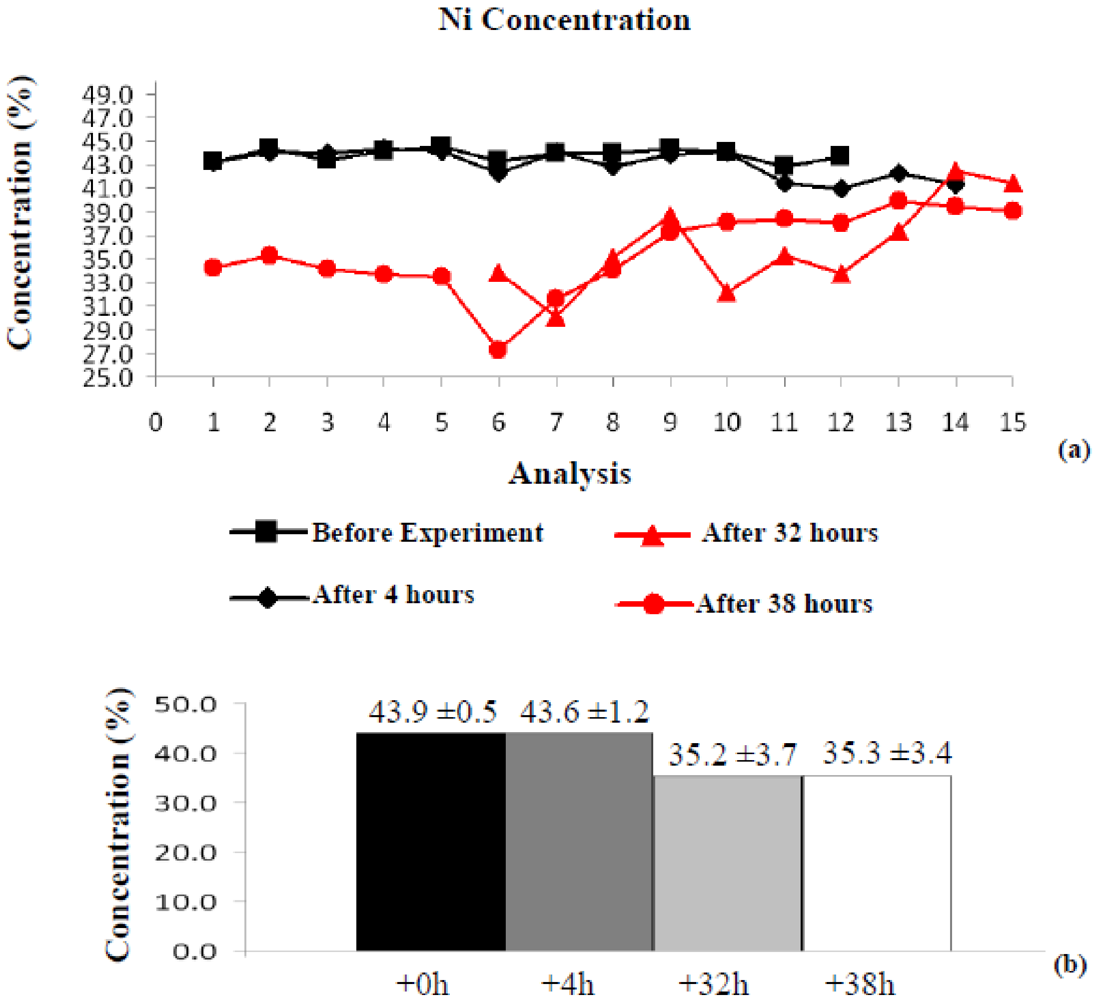

Figure 7. Ni concentration before the experiment, after 4, 32 and 38 h (a). The average values of Ni concentration change from a mass percentage of 43.9% at the beginning of the experiment to 35.2 and 35.3% after 32 and 38 h, respectively (b).

$$\mathrm{Ni}_{28}^{59} \rightarrow 2\mathrm{Mg}_{12}^{24} + 2\mathrm{He}_{2}^{4} + 3\ \text{neutrons}. \qquad (2)$$

At the same time, the balance Fe (–3.2%) ≅ Cr (+3.0%) may be explained by the reaction:

$$\mathrm{Fe}_{26}^{56} \rightarrow \mathrm{Cr}_{24}^{52} + \mathrm{He}_{2}^{4}\ . \qquad (3)$$

It is very interesting to notice that reactions (1) and (2) imply neutron emissions, as well as reactions (2) and (3) imply the emissions of alpha particles.

As far as the Co–Cr electrode is concerned, it is possible to observe variations even more evident in the concentrations of the most abundant constituting elements. In particular, the average Co concentration decreased by 23.5%, from an

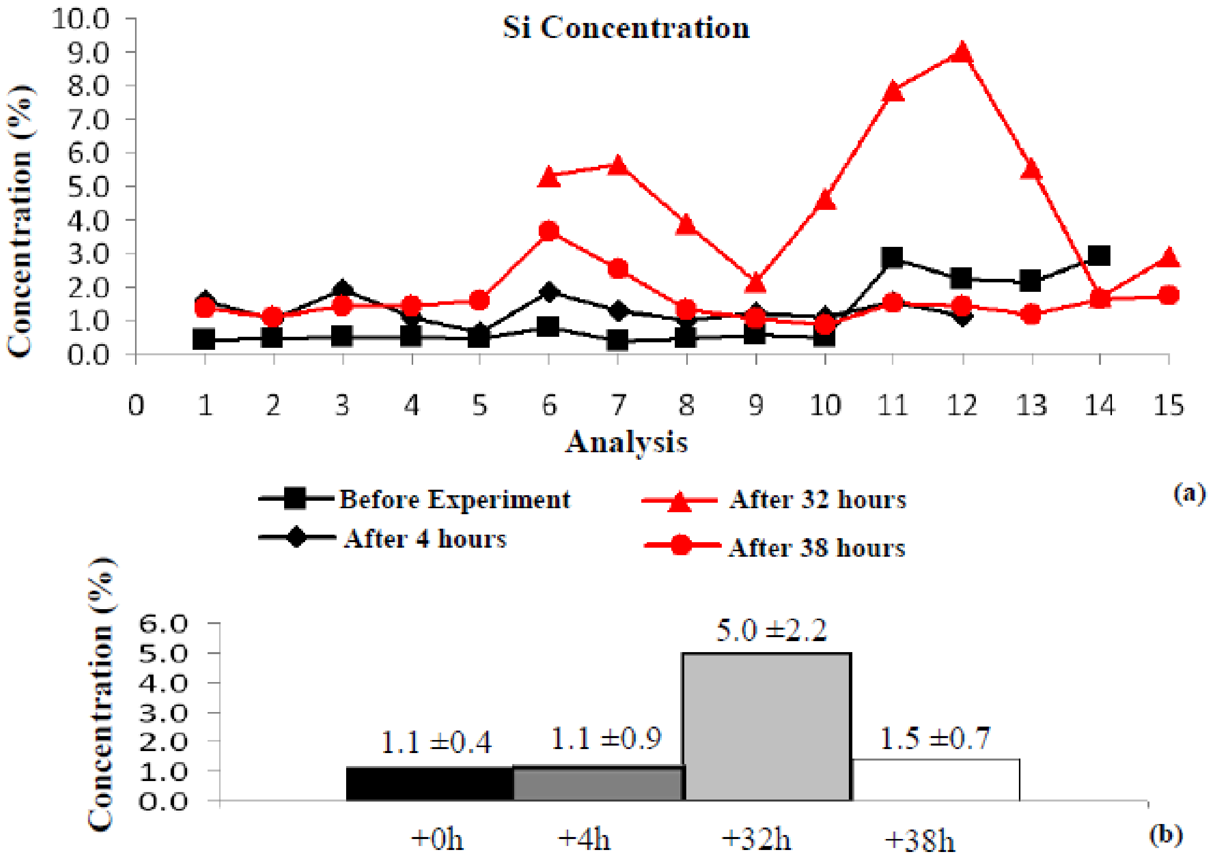

Figure 8. Si concentration before the experiment, after 4, 32 and 38 h (a). The mean values of Si concentration change from a mass percentage of 1.1% at the beginning of the experiment to 5.0 and 1.5% after 32 and 38 h, respectively (b).

initial percentage of 44.1% to a concentration of 20.6% after 32 h (see Table 3 and Figs. 12a and b). At the same time an increment of 23.2% can be observed in the Fe content after 32 h, changing from 3.1% before the experiment to 26.3% at the end of the second phase (see Table 3 and Figs. 13a and b). It is rather impressive that the decrease in Co and the increase in Fe are almost the same: Co (–23.5%) ≅ Fe (+23.2%). According to the compositional analysis on the Ni–Fe electrode no Co concentration was found that could lead us to consider the chemical migration to explain its depletion in the Co–Cr electrode, thus the following reaction seems the most reasonable possibility:

$$\mathrm{Co}^{59}_{27} \rightarrow \mathrm{Fe}^{56}_{26} + \mathrm{H}^{1}_{1} + 2\ \text{neutrons}. \tag{4}$$

In Table 3 and in Figs. 14 and 15, Cr and K concentrations are reported for the different phases of the experiment. The K increase by about 12.4% after 32 h may be only partially counterbalanced by the decrease in Cr (8.1%) according to reaction (5). The remaining increment of K (4.3%) could be considered as an effect of the K_2CO_3 aqueous solution deposition at the end of the third step.

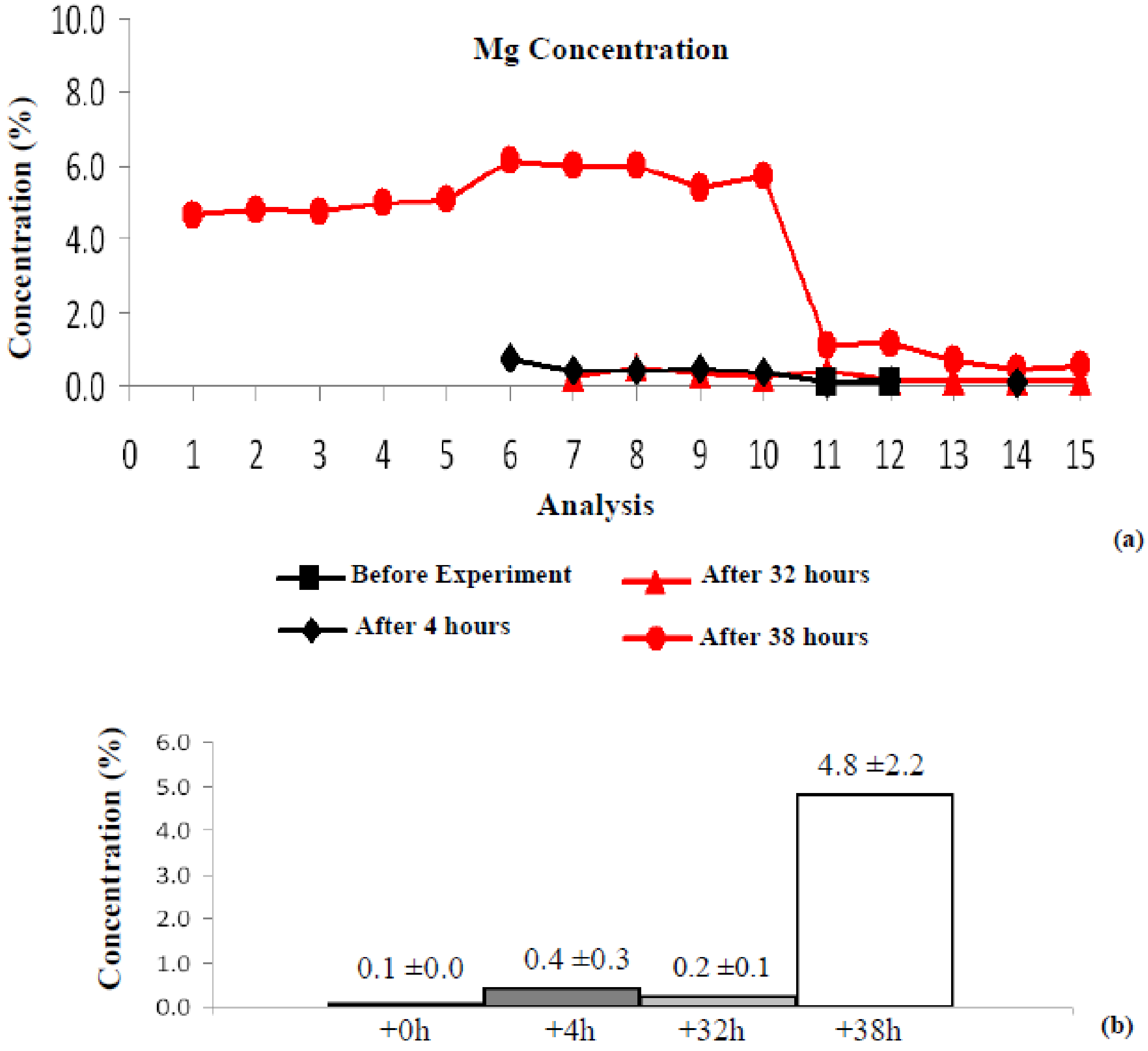

Figure 9. Mg concentration before the experiment, after 4, 32 and 38 h (a). The mean values of Mg concentration change from a mass percentage of 0.1% and 0.4% at the beginning of the experiment to 4.8% after 38 h (b).

Considering these variations also the following piezonuclear reaction, involving Cr as the starting element and K as the resultant could be considered:

$$\mathrm{Cr}^{52}_{24} \rightarrow \mathrm{K}^{39}_{19} + \mathrm{He}^{1}_{1} + 2\mathrm{He}^{4}_{2} + 4 \text{ neutrons}. \qquad (5)$$

Also in this case, it is remarkable that both reactions (4) and (5) imply neutron emissions, while reaction (5) implies also the emission of alpha particles.

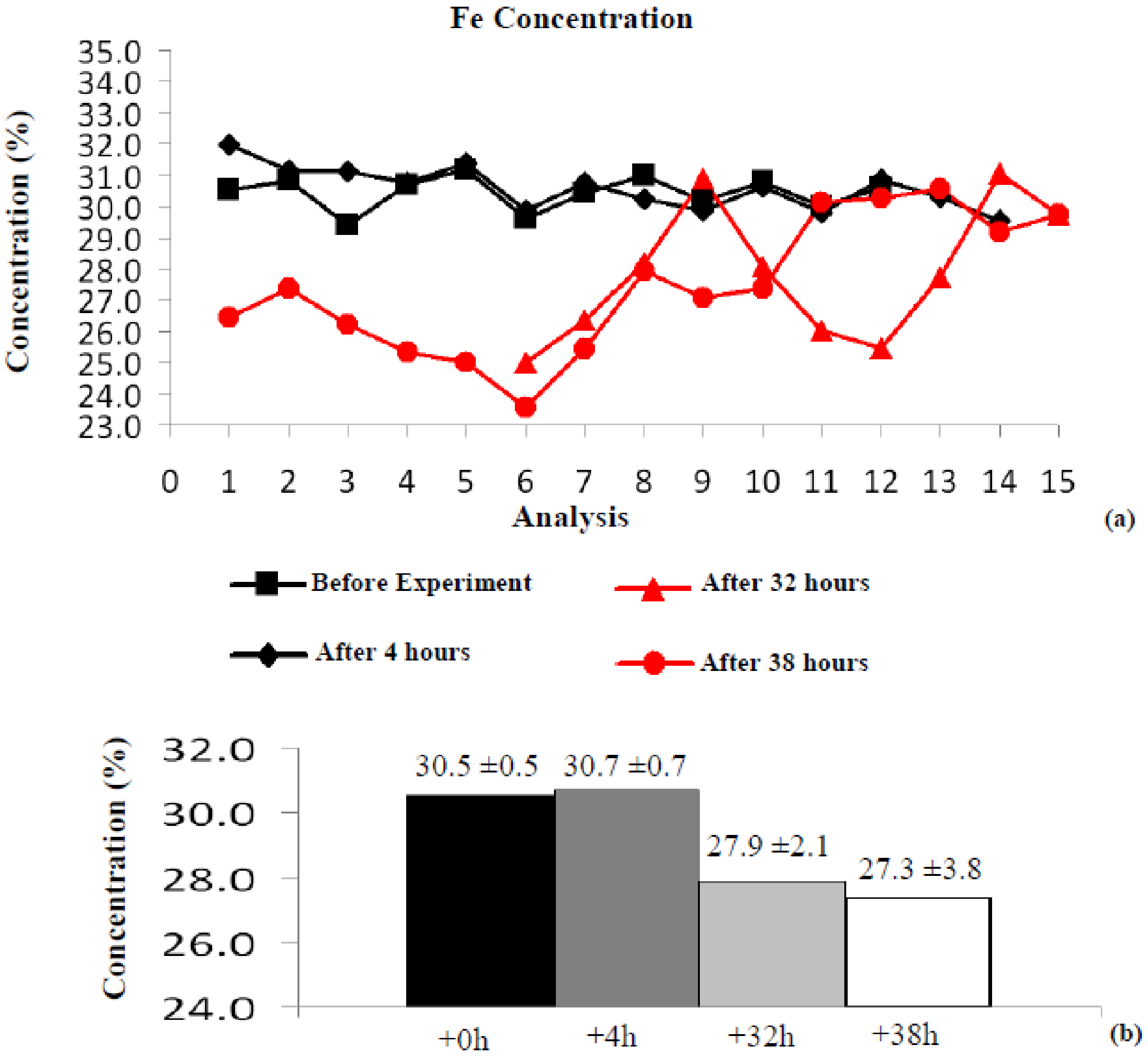

Figure 10. Fe concentration before the experiment, after 4, 32 and 38 h (a). The mean values of Fe concentration change from a mass percentage of 30.5% at the beginning of the experiment to 27.9% and 27.3% after 32 and 38 h, respectively (b).

It is important to consider that the balances reported, for Ni–Fe electrode (reactions (1)–(3)) and for Co–Cr electrode (reactions (4), (5)), were obtained considering the values of the second or third step corresponding to the larger variation for each element concentration (see Tables 2 and 3). Additional variations observed for some of these elements, such as Si, Co and Fe, between the second and the third step, may be explained considering other possible secondary piezonuclear reactions occurring on the electrode surface. Further efforts should be devoted to evaluate the evidence of these secondary fissions.

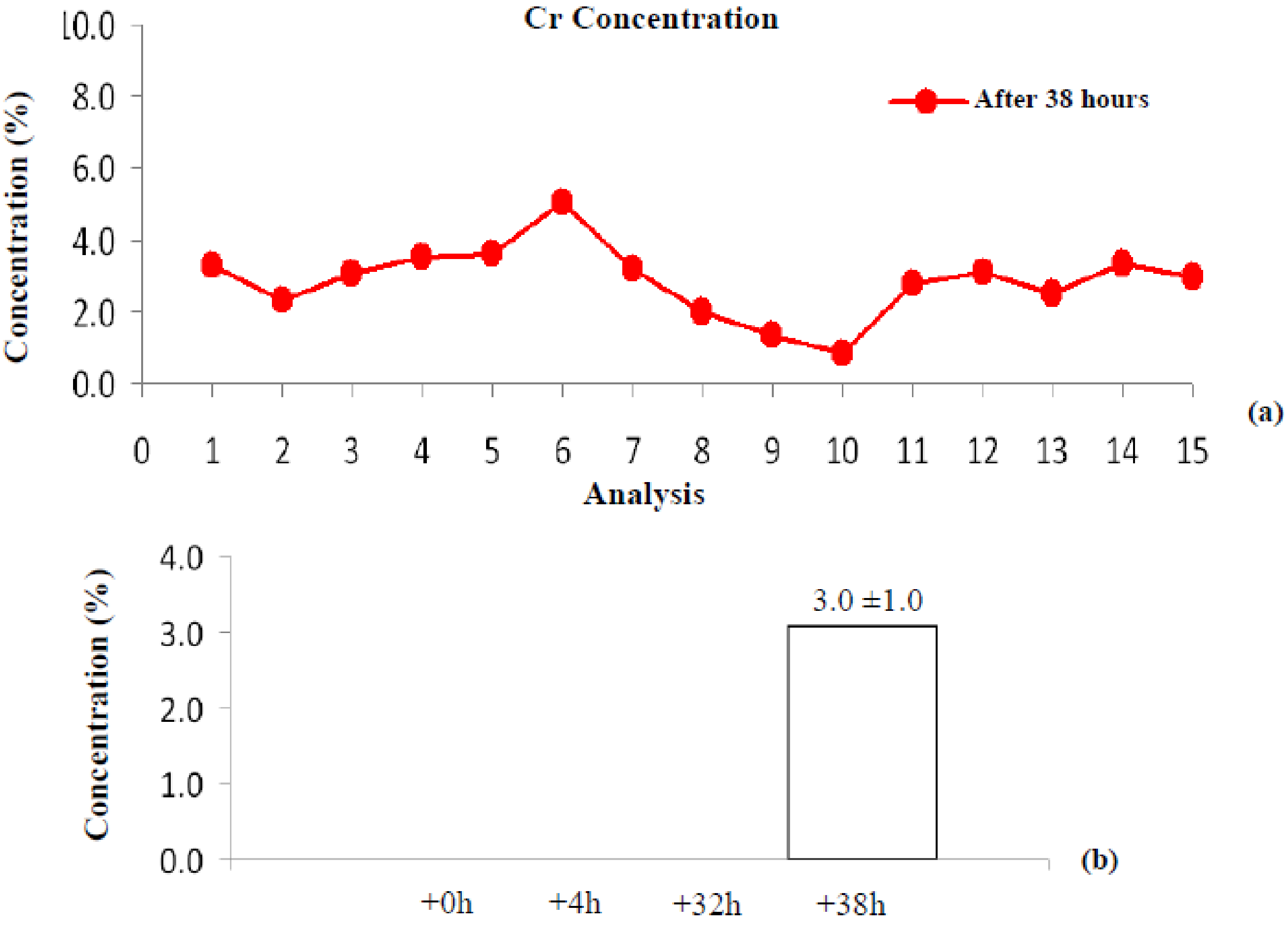

Figure 11. Cr concentration after 38 h (a). The mean value of Cr concentration changes from 0 % (absence of this element) to a mass percentage of 3.0% after 38 h (b).

All these results suggest that during gas loading, performed with hydrogen or deuterium, the host lattice is subjected to mechanical damaging and fracturing due to atoms absorption and penetration. Evidence of diffused cracking was identified also on the electrode surface after the experiments (see Fig. 6b). Based on this, we argue that the hydrogen, favoring the crack formation and propagation in the metal, comes from the electrolysis of water. In fact, because the electrodes immersed in a liquid solution, their surface is exposed to the formation of gaseous hydrogen due to the decomposition of water caused by the current passage.

4. Conclusions

Neutron emissions up to one order of magnitude higher than the background level were observed during the operating time of an electrolytic cell. In particular, after a time span of about 3 h, neutron emissions of about four times the

Table 3. Co–Cr Electrode, Element concentration before the experiment, after 4, after 32 and 38 h of the test. The values reported for the mass % of each element are referred as the mean value of all the effectuated measurements.

	Co(%)	Fe(%)	Cr(%)	K(%)
Before the experiment:	44.1	3.1	17.8	0.5
After 4 h	43.7	1.6	17.8	2.2
After 32 h	20.6	26.3	9.7	12.9
After 38 h	34.4	6.6	5.1	4.4

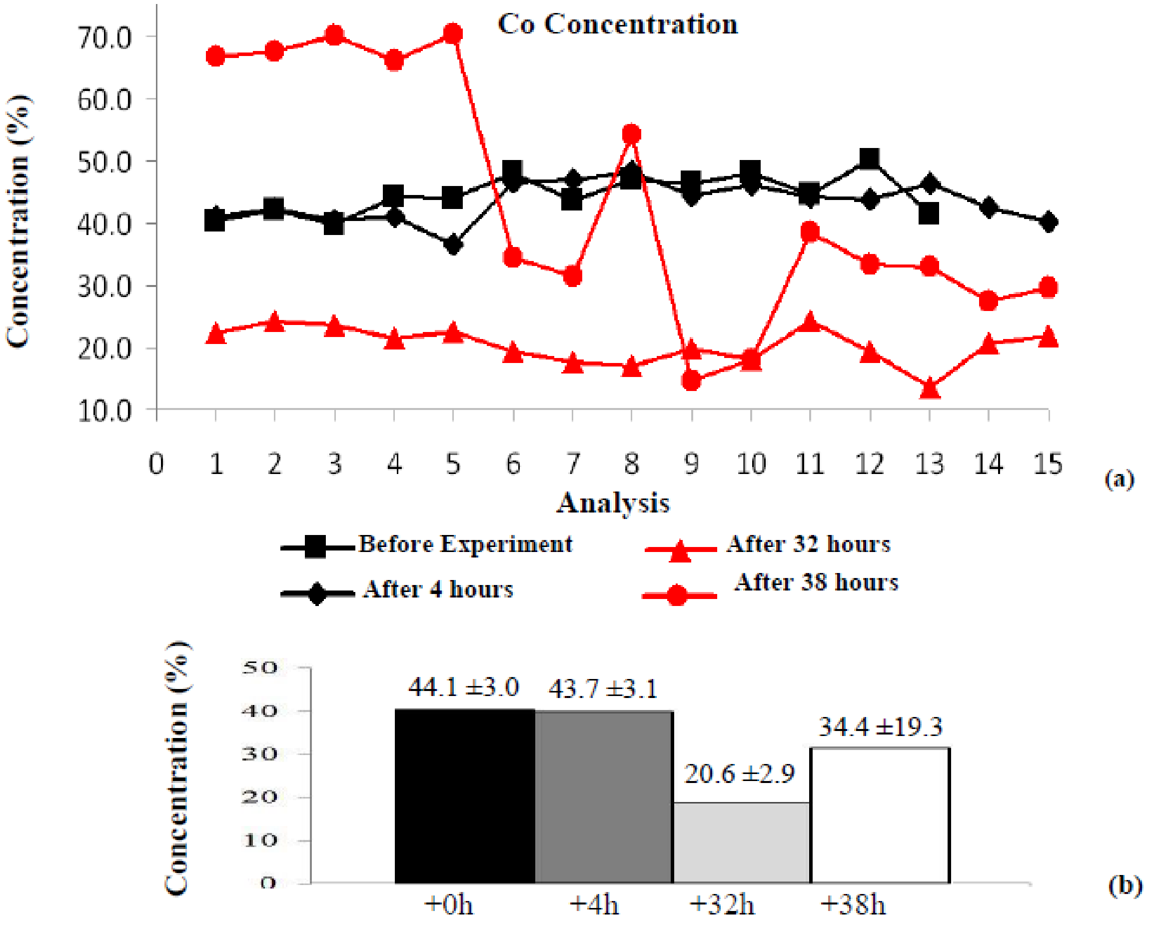

Figure 12. Co concentration before the experiment, after 4, 32 and 38 h (a). The mean values of Co concentration change from a mass percentage of 44.1% at the beginning of the experiment to 20.6 and 34.4% after 32 and 38 h, respectively (b).

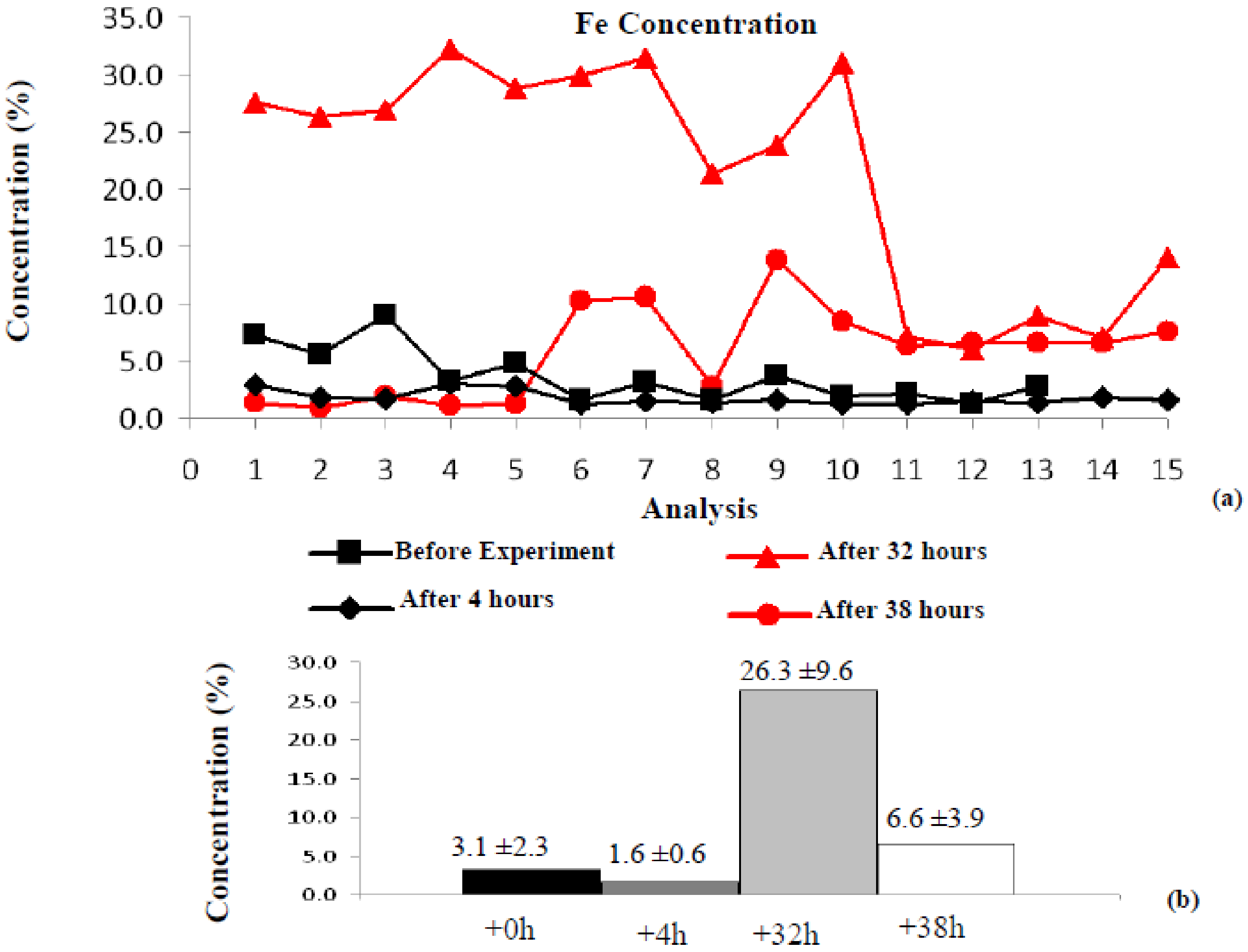

Figure 13. Fe concentration before the experiment after 4, 32 and 38 h (a). The mean values of Fe concentration change from a mass percentage of 3.1% at the beginning of the experiment to 26.3 and 6.6% after 32 and 38 h, respectively (b).

background level were measured. After 11 h, it was possible to observe neutron emissions of about one order of magnitude greater than the background level. Similar results were observed after 20 and 25 h.

When the cell was switched on, the average alpha particle emission was about 0.030 c/s for 1 h of measurement; this value corresponds to an alpha emission level of about two times the background measured in the laboratory before and after the experiment (0.015 c/s).

By the EDX analysis performed on the two electrodes in three successive steps, significant compositional variations could be recorded. In general, the decreases in Ni and Fe in the Ni–Fe electrode seem to be almost perfectly counterbalanced by the increases in lighter elements: Si, Mg, and Cr. In fact, the balance Ni (–8.6%) ≅ Si (+3.9%) + Mg

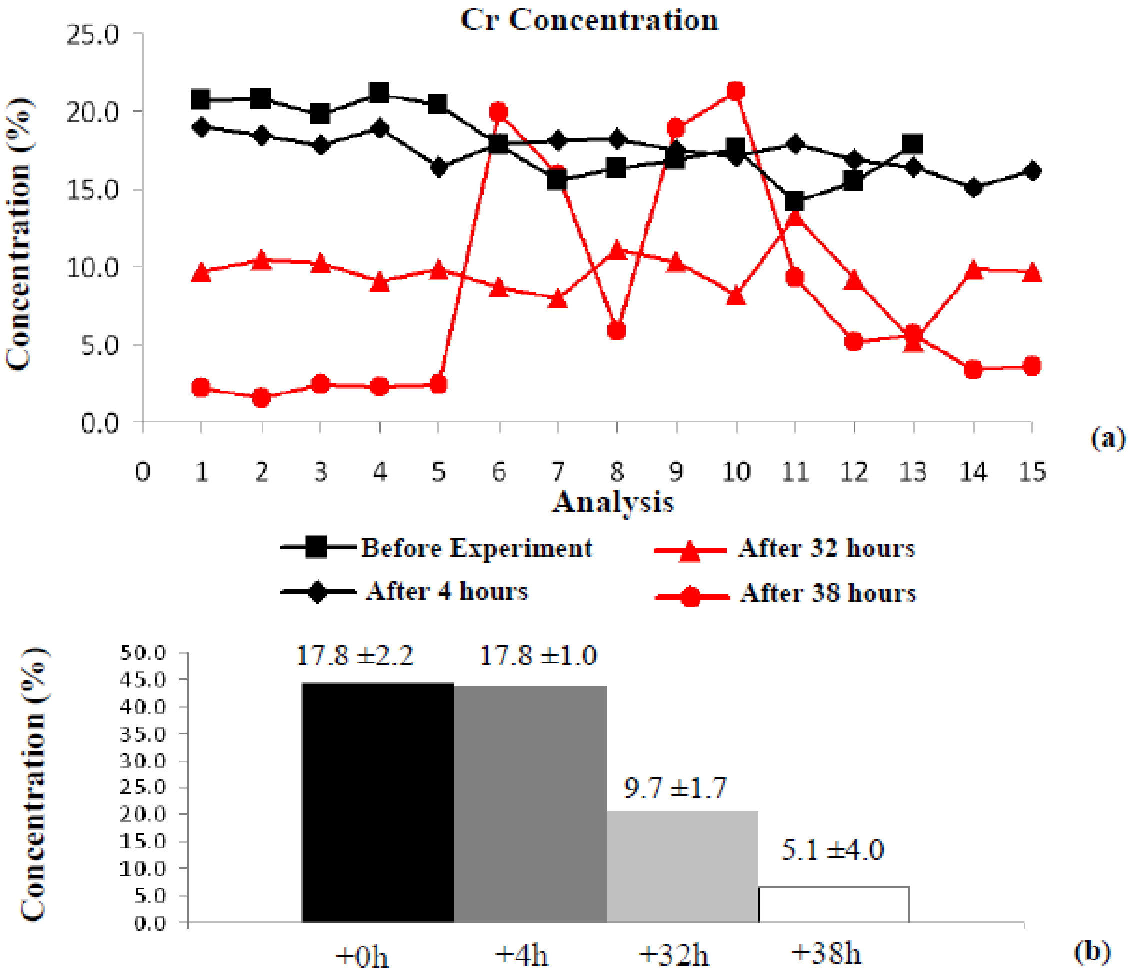

Figure 14. Cr concentration before the experiment after 4, 32 and 38 h (a). The Cr concentration changes from a mass percentage of 17.8% to 9.7% and 5.1% after 32 and 38 h (b).

(+4.7%) is satisfied by reactions (1) and (2). Specifically, Si could have also undergone further reactions, which would explain its drop in concentration observed at the third step. At the same time, the balance Fe (–3.2%) ≅ Cr (+3.0%) may be explained considering reaction (3).

As far as the Co–Cr electrode is concerned, the Co decrease is almost perfectly counterbalanced by the Fe increase: Co (–23.5%) ≅ Fe (+23.2%). This last evidence, which is really impressive considering the mass percentage involved, seems to be explainable only considering reaction (4). Finally, the Cr decrease and the K increase may be explained taking into account reaction (5) and the solution deposition. In particular, the K increase by about 12.4% may be only partially counterbalanced by the decrease in Cr (8.1%) according to reaction (5). The remaining increment in K (4.3%) could be considered as an effect of the K_2CO_3 aqueous solution deposition at the end of the third step.

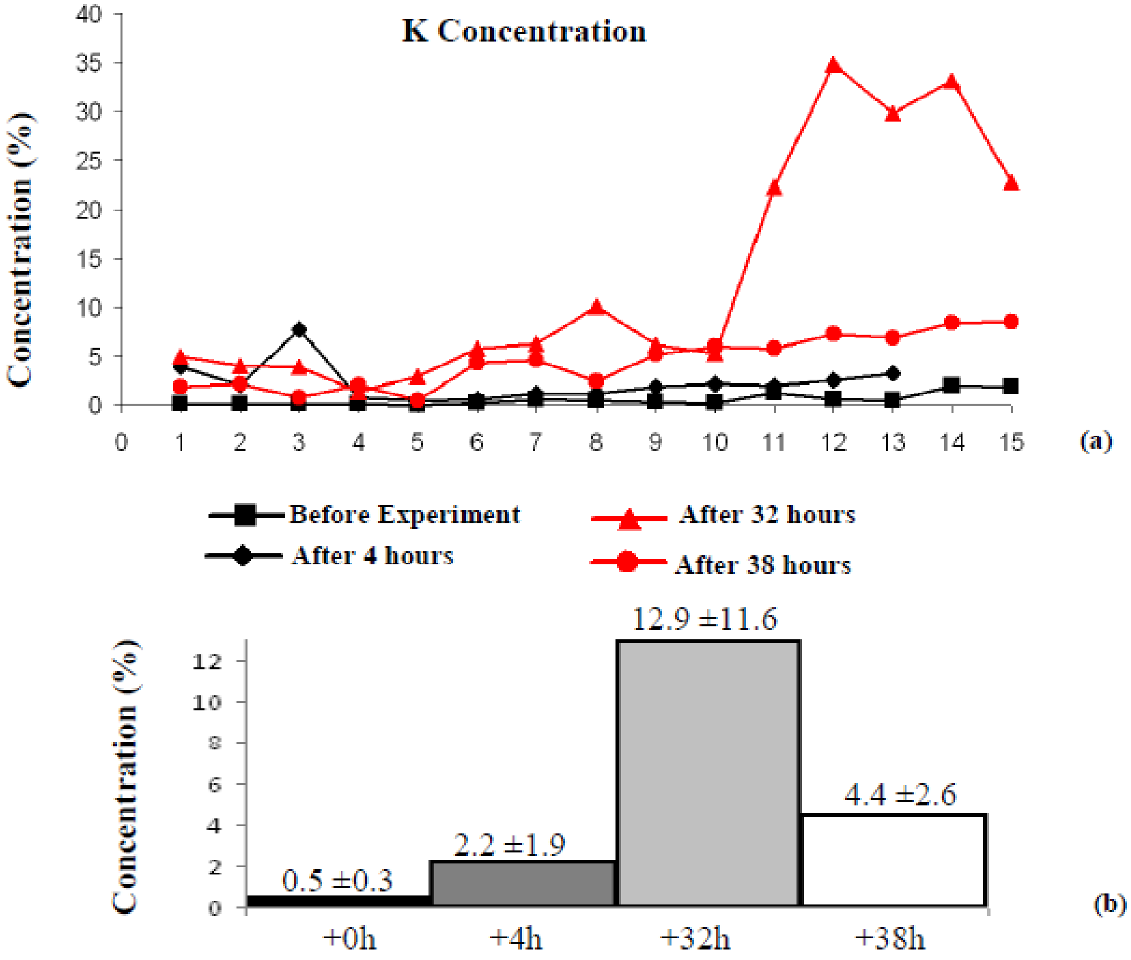

Figure 15. K concentration before the experiment after 4, 32 and 38 h (a). The K concentration changes from 0.5 and 2.2% after 4 h to 12.9 and 4.4% after 32 and 38 h (b).

Chemical variations and energy emissions may be accounted for direct and indirect evidence of mechano-nuclear fission reactions correlated to micro-crack formation and propagation due to hydrogen embrittlement. According to this interpretation of so-called Cold Nuclear Fusion, hydrogen, which is imputed to favor the crack formation and propagation in the electrodes, comes from the electrolysis of water. Being the electrodes immersed in a liquid solution, the metal surface is exposed to the formation of gaseous hydrogen due to the decomposition of water molecule caused by the current passage. In addition, the high current density contributes to the formation and penetration of hydrogen into the metal. So-called Cold Nuclear Fusion, interpreted under the light of hydrogen embrittlement, may be explained by piezonuclear fission reactions occurring in the host metal, rather than by nuclear fusion of hydrogen isotopes forced into the metal lattice.

Aknowledgements

Dr. A. Sardi and Dr. F. Durbiano are gratefully acknowledged for their help during the experimental set-up definition and for the assistance given during the measurements. Also Dr. A. Chiodoni is warmly acknowledged for the EDX spectroscopy analyses.

References

[1] Borghi, D.C. Giori, D.C. Dall'Olio, A., *Experimental Evidence for the Emission of Neutrons from Cold Hydrogen Plasma*, CEN, Recife, Brazil, 1957.
[2] Diebner, K., Fusionsprozesse mit Hilfe konvergenter Stosswellen – einige aeltere und neuere Versuche und Ueberlegungen, *Kerntechnik.* **3** (1962) 89–93.
[3] Kaliski, S., Bi-conical system of concentric explosive compression of D—T, *J. Tech. Phys.* **19** (1978) 283–289.
[4] Winterberg, F., Autocatalytic fusion–fission implosions, *Atomenergie-Kerntechnik* **44** (1984) 146.
[5] Derjaguin, B. V. et al., Titanium fracture yields neutrons? *Nature* **34** (1989) 492.
[6] Fleischmann, M. Pons S. and Hawkins M., Electrochemically induced nuclear fusion of deuterium, *J. Electroanal. Chem.* **261** (1989) 301.
[7] Bockris, J.O'M. Lin, G.H. Kainthla, R.C. Packham, N.J.C. and Velev, O., Does Tritium Form at Electrodes by Nuclear Reactions? *The First Annual Conference on Cold Fusion*. National Cold Fusion Institute, University of Utah Research Park, Salt Lake City, 1990.
[8] Preparata, G., Some theories of cold fusion: A review, *Fusion Technol.* **20** (1991) 82.
[9] Preparata, G., A new look at solid-state fractures, particle emissions and "cold" nuclear fusion, *Il Nuovo Cimento* **104A** (1991) 1259–1263.
[10] Mills, R.L. and Kneizys, P., Excess heat production by the electrolysis of an aqueous potassium carbonate electrolyte and the implications for cold fusion, *Fusion Technol.* **20** (1991) 65.
[11] Notoya, R. and Enyo, M., Excess heat production during electrolysis of H_2O on Ni, Au, Ag and Sn electrodes in alkaline media, *Proc. Third Int. Conf. on Cold Fusion*, Nagoya Japan, Universal Academy Press, Tokyo, Japan, 1992.
[12] Miles, M.H. Hollins, R.A. Bush, B.F. Lagowski, J.J. and Miles, R.E., Correlation of excess power and helium production during D_2O and H_2O electrolysis using palladium cathodes, *J. Electroanal. Chem.* **346** (1993) 99–117.
[13] Bush, R.T. and Eagleton, R.D., Calorimetric studies for several light water electrolytic cells with nickel fibrex cathodes and electrolytes with alkali salts of potassium, rubidium, and cesium, *Fourth Int. Conf. on Cold Fusion,* Lahaina, Maui. Electric Power Research Institute 3412 Hillview Ave., Palo Alto, CA 94304, 1993, p. 13.
[14] Fleischmann, M. Pons, S. Preparata, G., Possible theories of cold fusion, *Nuovo Cimento Soc. Ital. Fis. A* **107** (1994) 143.
[15] Szpak, S. Mosier-Boss, P.A. and Smith, J.J., Deuterium uptake during Pd–D codeposition, *J. Electroanal. Chem.* **379** (1994) 121.
[16] Sundaresan, R. and Bockris, J.O.M., Anomalous reactions during arcing between carbon rods in water, *Fusion Technol.* **26** (1994) 261.
[17] Arata, Y., Zhang, Y., Achievement of solid-state plasma fusion ("cold-fusion"), *Proc. Jpn Acad.* Ser. B **71** (1995) 304–309.
[18] Ohmori, T. Mizuno, T. and Enyo, M., Isotopic distributions of heavy metal elements produced during the light water electrolysis on gold electrodes, *J. New Energy* **1**(3) (1996) 90.
[19] Monti, R.A., Low energy nuclear reactions: Experimental evidence for the alpha extended model of the atom, *J. New Energy* **1**(3) (1996) 131.
[20] Monti, R.A., Nuclear transmutation processes of lead, silver, thorium, uranium, *The Seventh Int. Conf. on Cold Fusion*, ENECO Inc., Vancouver, Canada, Salt Lake City, UT, 1998.
[21] Ohmori, T. Mizuno T., Strong excess energy evolution, new element production, and electromagnetic wave and/or neutron emission in light water electrolysis with a tungsten cathode, *Infinite Energy* Issue **20** (1998) 14–17.
[22] Mizuno, T., Nuclear transmutation: the reality of cold fusion, Infinite Energy Press, 1998.
[23] Little, S.R. Puthoff, H.E. and Little, M.E., Search for excess heat from a Pt electrode discharge in K_2CO_3–H_2O and K_2CO_3–D_2O electrolytes, September (1998).

[24] Ohmori, T. and Mizuno, T., Nuclear transmutation reaction caused by light water electrolysis on tungsten cathode under incandescent conditions, *Infinite Energy* **5**(27) (1999) 34.

[25] Ransford, H.E., Non-stellar nucleosynthesis: transition metal production by DC plasma-discharge electrolysis using carbon electrodes in a non-metallic cell, *Infinite Energy* **4** (23) (1999) 16.

[26] Storms, E., Excess power production from platinum cathodes using the Pons–Fleischmann effect, *8th Int. Conf. on Cold Fusion*, Lerici (La Spezia), Italian Physical Society, Bologna, Italy, 2000, pp. 55–61.

[27] Storms, E., *Science of Low Energy Nuclear Reaction: A Comprehensive Compilation of Evidence and Explanations About Cold Fusion*, World Scientific, Singapore, 2007.

[28] Mizuno, T. et al., Production of heat during plasma electrolysis, *Jpn. J. Appl. Phys. A* **39** (2000) 6055.

[29] Warner, J. Dash, J. and Frantz. S., Electrolysis of D_2O with titanium cathodes: enhancement of excess heat and further evidence of possible transmutation, *The Ninth Int. Conf. on Cold Fusion,* Tsinghua University, Beijing, China, 2002, p. 404.

[30] Fujii, M. F. et al., Neutron emission from fracture of piezoelectric materials in deuterium atmosphere, *Jpn. J. Appl. Phys.* **41** (2002) 2115–2119.

[31] Mosier-Boss, P.A. et al., Use of CR-39 in Pd/D co-deposition experiments, *Eur. Phys. J. Appl. Phys.* **40** (2007) 293–303.

[32] Swartz, M., Three physical regions of anomalous activity in deuterated palladium, *Infinite Energy* **14** (2008) 19–31.

[33] Mosier-Boss, P.A., et al., Comparison of Pd/D co-deposition and DT neutron generated triple tracks observed in CR-39 detectors, *Eur. Phys. J. Appl. Phys.* **51**(2) (2010) 20901–20911.

[34] Kanarev, M. Mizuno, T., Cold fusion by plasma electrolysis of water, *New Energy Technol.* **1** (2002) 5–10.

[35] Cardone, F. Mignani, R., *Energy and Geometry*, World Scientific, Singapore, Chapter 10, 2004.

[36] Carpinteri, A. Cardone, F. Lacidogna, G., Piezonuclear neutrons from brittle fracture: Early results of mechanical compression tests, *Strain* **45** (2009) 332–339. *Atti dell'Accademia delle Scienze di Torino* **33** (2009) 27–42.

[37] Cardone, F., Carpinteri, A., Lacidogna G., Piezonuclear neutrons from fracturing of inert solids, *Phys. Lett. A*. **373** (2009) 4158-4163.

[38] Carpinteri, A. Cardone, F. Lacidogna G., Energy emissions from failure phenomena: Mechanical, electromagnetic, nuclear, *Experimental Mechanics* **50** (2010) 1235-1243.

[39] Carpinteri, A., Lacidogna, G., Manuello, A., Borla O., Piezonuclear fission reactions: evidences from microchemical analysis, neutron emission, and geological transformation, *Rock Mechanics and Rock Eng.* **45** (2012) 445–459.

[40] Carpinteri, A., Lacidogna, G., Manuello, A.,. Borla O., Piezonuclear fission reactions from earthquakes and brittle rocks failure: Evidence of neutron emission and nonradioactive product elements, *Experimental Mechanics* **53** (2013) 345–365.

[41] Widom, A., Swain, J., Srivastava, Y.N., Photo-disintegratin of the Iron Nucleus in Fractured Magnetite Rocks with Magetostriction, arXiv: 1306.6286v1 (2013).

[42] Widom, A., Swain, J., Srivastava, Y.N., Neutron production from the fracture of piezoelectric rocks, *J. Phys. G: Nucl. Part. Phys.* **40** (2013) doi:10.1088/0954-3899/40/1/015006.

[43] Milne, I. Ritchie, R.O. Karihaloo, B., *Comprehensive Structural Integrity: Fracture Of Materials From Nano To Macro*, Vol. 6, Chapter 6.02, Elsevier, Amsterdam, 2003, pp. 31–33.

[44] Liebowitz, H., *Fracture An advanced Treatise.* Academic Press, New York, San Francisco, London, 1971.

J. Condensed Matter Nucl. Sci. 15 (2015) 183–189

Research Article

Neutron Isotope Theory of LENR Processes

John C. Fisher[*]

600 Arbol Verde, Carpinteria, CA 93013, USA

Abstract

Neutron isotopes are characterized and their reactions with ordinary isotopes are described. A theory of LENR processes emerges.

Keywords: LENR, Neutron Isotope, Nuclear reaction, Theory

1. Initial Assumptions

The neutron isotope theory of low energy nuclear reactions (LENR) is based on the assumptions that no new fundamental particles are required, that quantum mechanics is the appropriate analytic tool, and that the coulomb barrier prevents LENR reactions between charged particles. It follows that every LENR reaction must involve at least one neutral reactant. Potential neutral reactants are limited to neutrons and to isotopes of the neutron. (Note that neutron isotopes, although not widely recognized or studied, are not new fundamental particles.) Finally the experimental scarcity of neutrons in LENR phenomena leaves neutron isotopes as the only candidate neutral reactants. The theory suggests that although rare in nature, neutron isotopes are captured and proliferated in LENR reactors [1,2].

2. Neutron Isotope Structure

I view the ground state of a neutron isotope containing an even number of neutrons as a structure of neutron pairs consisting of contiguous nested pockets or boxes, each box containing a pair of neutrons having opposite spins. The pairs surrounding each box are treated as a classical confining structure, and the neutrons in each box are treated quantum mechanically as independent particles in that box. The number of boxes is equal to the number of neutron pairs. The ground state energy of this system is taken to be the ground state energy for a pair of neutrons in a box, summed over all boxes in the isotope. For an isotope composed of an odd number of neutrons, I envision a similar structure in which one of the boxes contains a single neutron.

An excited neutron isotope can have more than one box that contains a single neutron, and can have neutrons excited to states above the ground state of a particle in a box. However in this analysis I consider only low temperatures for which such excitations can be neglected.

---

[*] E-mail: jcfisher@fisherstone.com

Neutron isotopes are unstable. They undergo beta decays in which one or more neutrons become protons. Because the fraction of protons is small for isotopes of interest, the structure of a mix of neutrons and protons is essentially the same as that of a neutron isotope: Pairs of nucleons of opposite spin occupy boxes in the overall isotope structure, except for isotopes with an odd number of nucleons which have one box that contains a single neutron or proton.

3. Liquid Drop Model

Neutron isotopes have different permutation symmetries than ordinary nuclei. Because neutrons are indistinguishable from each other the neutron isotope wave function remains unchanged by any permutation of them. When a neutron isotope undergoes beta decay in which a neutron is replaced by a proton, I assume that the wave function of the resulting hydrogen nucleus retains full permutation symmetry of nucleons in the neutron-proton mix. (In a more exact treatment the wave function would be slightly changed. But for now I neglect such changes except for the 0.78 MeV mass difference between a neutron and a proton and for the coulomb energies of multiply-charged nuclei.)

In what follows I refer to permutation-symmetric nuclei simply as symmetric nuclei, and I refer to atoms having symmetric nuclei as symmetric atoms. Preliminary analysis suggests that symmetric nuclei and atoms are a few MeV per nucleon more massive than ordinary nuclei and atoms.

For all charged isotopes I indicate the number of protons by the chemical symbols H, He, Li, and so on. In order to distinguish permutation-symmetric atoms from ordinary atoms I mark the permutation-symmetric atoms with a subscript "s" as in $\mathrm{H_s}$, $\mathrm{He_s}$, $\mathrm{Li_s}$, and so on. (As a symmetry reminder I also attach a subscript "s" to all multi-neutron isotopes, although lacking protons neutron isotopes are not chemical atoms.) And for all nuclei I indicate the total number of nucleons (neutrons and protons together) by a superscript to the left of the chemical symbol. In this notation a neutron isotope composed of 100 neutrons is represented by $^{100}\mathrm{n_s}$, a hydrogen atom with a permutation-symmetric nucleus that contains 100 nucleons including one proton is represented by $^{100}\mathrm{H_s}$, and a carbon atom with a permutation-symmetric nucleus that contains 500 nucleons including 6 protons is represented by $^{500}\mathrm{C_s}$.

Analysis of ordinary nuclei has shown that a liquid drop model can provide a good approximation of the masses of the various isotopes. I expect that similarly a liquid drop model can provide a good fit to the masses of neutron isotopes and their neutron-rich beta decay products. Here I propose such a model for the mass excesses of symmetric atoms, in which the expression Δ(X) stands for the mass excess of atom X in MeV. For the mass excess of a neutron isotope we have

$$\Delta(^{A}n_{\mathrm{s}}) = A\Delta(n) - a_{\mathrm{v}}A + a_{\mathrm{s}}A^{2/3}. \tag{1a}$$

The parameters a_{v} and a_{s} are expressed in MeV. They are independent of A and are chosen to fit the data insofar as possible. $\Delta(n)$ is the mass excess of a single free neutron; a_{v} is the binding energy per neutron in a large neutron isotope; and a_{s} is the reduction of binding energy per neutron at the surface of a neutron isotope. (Here the subscript "s" on a_{s} refers to "surface" rather than "symmetric.") For the mass excess of a symmetric hydrogen atom we have

$$\Delta(^{A}H_{\mathrm{s}}) = (A-1)\Delta(n) + \Delta(p) - a_{\mathrm{v}}A + a_{\mathrm{s}}A^{2/3}. \tag{1b}$$

The parameters a_{v} and a_{s} are independent of the mix of neutrons and protons. One neutron mass excess $\Delta(n)$ has been replaced by one proton mass excess $\Delta(p)$.

In general the mass excess of $^{A}\mathrm{Z_s}$ containing Z protons and $A - Z$ neutrons is

$$\Delta(^{A}Z_{\mathrm{s}}) = (A-Z)\Delta(n) + Z\Delta(p) - a_{\mathrm{v}}A + a_{\mathrm{s}}A^{2/3} + a_{c}Z(Z-1)A^{-1/3}. \tag{1c}$$

In this expression the term $a_{\mathrm{c}}Z(Z-1)A^{-1/3}$ is the reduction in binding energy associated with the Coulomb energy of the Z protons. The coefficient a_{c} is independent of A and Z. The parameters a_{v} , $a_{\mathrm{s},}$ a_{c} must be determined by the data. At present the only criterion available is that all reactions claimed to be exothermic in this analysis are indeed exothermic when using the current parameter values

$$a_{\mathrm{v}} = 2.60\ \mathrm{MeV}, \qquad a_{\mathrm{s}} = 4.12\ \mathrm{MeV}, \qquad a_{\mathrm{c}} = 0.1\ \mathrm{MeV}. \tag{1d}$$

These current values are expected to change and to improve as the theory matures.

4. Symmetric Atom Reactions

The theory suggests that interactions between neutron isotopes and deuterium (^{2}H) can support a family of LENR reactions that help maintain a concentration of ambient neutron isotopes within an active reaction volume. This is analogous to the interaction between neutrons and uranium that help maintain a concentration of ambient neutrons in an ordinary nuclear reactor.

I begin by considering the various microscopic reactions that might be expected between neutron isotopes $^A\mathrm{n_s}$ and deuterium. These reactions include neutron isotope growth with deuterium fuel and ordinary hydrogen ash that are capable of increasing the size of a neutron isotope without limit,

$$\begin{aligned}&^{A}\mathrm{n_s} + {}^2\mathrm{H} \rightarrow {}^{(A+1)}\mathrm{n_s} + {}^1\mathrm{H}, \qquad {}^{(A+1)}\mathrm{n_s} + {}^2\mathrm{H} \rightarrow {}^{(A+2)}\mathrm{n_s} + {}^1\mathrm{H},\\ &^{(A+2)}\mathrm{n_s} + {}^2\mathrm{H} \rightarrow {}^{(A+3)}\mathrm{n_s} + {}^1\mathrm{H}, \qquad {}^{(A+3)}\mathrm{n_s} + {}^2\mathrm{H} \rightarrow {}^{(A+4)}\mathrm{n_s} + {}^1\mathrm{H},\end{aligned} \tag{2}$$

and so on. They also include beta decays of symmetric atoms to other symmetric atoms containing one less neutron, one more proton, and one more electron,

$$^A\mathrm{n_s} \rightarrow {}^A\mathrm{H_s}, \qquad {}^A\mathrm{H_s} \rightarrow {}^A\mathrm{He_s}, \qquad {}^A\mathrm{He_s} \rightarrow {}^A\mathrm{Li_s}, \tag{3}$$

and so on until the build-up of nuclear charge makes further beta decay endothermic. In addition alpha decay with ^{4}He ash becomes possible for nuclear charge $Z \geq 2$,

$$^A\mathrm{He_s} \rightarrow {}^{(A-4)}\mathrm{n_s} + {}^4\mathrm{He}, \qquad {}^A\mathrm{Li_s} \rightarrow {}^{(A-4)}\ \mathrm{H_s} + {}^4\mathrm{He}\ , \qquad {}^A\mathrm{Be_s} \rightarrow {}^{(A-4)}\mathrm{He_s} + {}^4\mathrm{He}, \tag{4a}$$

and so on finally to ordinary helium tritium and neutron ash in reactions

$$^6\mathrm{He_s} \rightarrow {}^4\mathrm{He} + 2\mathrm{n}, \qquad {}^6\mathrm{H_s} \rightarrow {}^3\mathrm{H} + 3\mathrm{n}. \tag{4b}$$

Because reactions (2)–(4) do not increase the number of symmetric isotopes, there must be other reactions that do. Otherwise there could be no chain reaction to create and sustain the concentration of ambient neutron isotopes required for macroscopic LENR. The theory proposes that this function is served by neutron isotope fission reactions such as

$$\begin{aligned}&^{A+B+10}\mathrm{n_s} + {}^{40}\mathrm{Ca} \rightarrow {}^A\mathrm{n_s} + {}^B\mathrm{n_s} + {}^{50}\mathrm{Ca} + 39\ \mathrm{MeV},\\ &^{A+B+16}\mathrm{n_s} + {}^{58}\mathrm{Ni} \rightarrow {}^A n_\mathrm{s} + {}^B\mathrm{n_s} + {}^{74}\mathrm{Ni} + 43\ \mathrm{MeV},\\ &^{A+B+22}\mathrm{n_s} + {}^{104}\mathrm{Pd} \rightarrow {}^A\mathrm{n_s} + {}^B\mathrm{n_s} + {}^{126}\mathrm{Pd} + 38\ \mathrm{MeV}.\end{aligned} \tag{5}$$

The indicated reaction energies are approximations subject to revision as the theory matures. LENR can proceed provided such reactions increase the number of symmetric isotopes at a rate that exceeds the losses from reactions (4b) and from diffusion to beyond the reaction volume.

5. Heat After Death

In one of their experiments Pons and Fleischmann [3] boiled away the liquid from an operating electrolytic reactor until the reactor was dry, after which they observed that it continued to produce thermal energy with an intensity that persisted with a half-life of about an hour. This they termed "heat after death." In this experiment, all isotopes necessary for a chain reaction were present in the dry reactor (deuterium in the solid electrolyte residue and Pd in the cathode). Growth reactions (2) had terminated and the chain reaction had ceased. Yet thermal energy production continued from beta and alpha decays in reactions (3) and (4) as the population of symmetric isotopes shrank and finally disappeared via reactions (4b). The duration of heat after death is consistent with the rates of beta and alpha decay expected in reactions (3) and (4).

6. Heat and Helium

At steady state, four instances of reaction (2) consume $^{2}\mathrm{H}$ and generate $^{1}\mathrm{H}$ in the overall reaction

$$^{A}\mathrm{n_s} + 4(^{2}\mathrm{H}) \rightarrow\ ^{A+4}\mathrm{n_s} + 4(^{1}\mathrm{H}), \tag{6}$$

and two instances of reaction (3) together with one instance of reaction (4a) consume $^{A+4}\mathrm{n_s}$ and generate $^{4}\mathrm{He}$ in the overall reaction

$$^{A+4}\mathrm{n_s} \rightarrow\ ^{A}\mathrm{n_s} +\ ^{4}\mathrm{He}. \tag{7}$$

Together at steady state these amount to

$$4(^{2}\mathrm{H}) \rightarrow 4(^{1}\mathrm{H}) +\ ^{4}\mathrm{He} + 21\ \mathrm{MeV} \tag{8}$$

independent of the parameters a_v , $a_{\mathrm{s},}$ and a_c .

Neglecting the small energy contribution from fission reactions (5), and the compensating small energy loss of kinetic energy carried by neutrinos in reactions (3), the liberation of 21 MeV of energy per helium atom in (8) agrees with observation to within the experimental uncertainty.

7. Neutrons

It is a remarkable feature of LENR reactions that they produce negligible numbers of neutrons and gamma rays. Yet knock-on neutrons are expected from the impact of alpha particles from reactions (4a) on deuterium fuel in the reaction medium. Neutron isotope theory requires that such neutrons be eliminated before they can be detected, being absorbed in reactions of the form

$$\begin{aligned}
&\mathrm{n} +\ ^{A}\mathrm{He_s} \rightarrow\ ^{A-1}\mathrm{H_s} + \mathrm{p} + 0.2\ \mathrm{MeV},\\
&\mathrm{n} +\ ^{A}\mathrm{Li_s} \rightarrow\ ^{A-1}\mathrm{He_s} + \mathrm{p} + 0.4\ \mathrm{MeV},\\
&\mathrm{n} +\ ^{A}\mathrm{Be_s} \rightarrow\ ^{A-1}\mathrm{Li_s} + \mathrm{p} + 0.6\ \mathrm{MeV},\ \text{and so on,}
\end{aligned} \tag{9}$$

thus accounting for the absence of neutrons in LENR.

8. Gamma Rays

Most beta and alpha decays leave the final nucleus in an excited state, which decays by emission of one or more gamma rays in the range 0.1–10 MeV. Although gamma rays are expected from isolated reactions (3)–(5), the following analysis shows they are not expected in LENR reactions that support high densities of neutron isotopes.

Consider the reaction

$$ {}^{A}\mathrm{n_s} + {}^{40}\mathrm{Ca} \to {}^{A-10}\mathrm{n_s} + {}^{50}\mathrm{Ca} \tag{10a}$$

in which ten neutrons are transferred from a neutron isotope to ^{40}Ca. The resulting ^{50}Ca undergoes the beta decay

$$ {}^{50}\mathrm{Ca} \to {}^{50}\mathrm{Sc}^{*} \tag{10b}$$

with a half-life of 13.9 s. The star on Sc* indicates a transient excited state, lasting perhaps 10^{-9} s prior to gamma ray emission. Because of the high density of $^{A}\mathrm{n_s}$ isotopes in an LENR reaction it is likely that one will come in contact with the Sc* before it has a chance to emit a gamma ray. In that case we can have the reaction

$$ {}^{A}\mathrm{n_s} + {}^{50}\mathrm{Sc}^{*} \to {}^{A}\mathrm{n_s} + {}^{50}\mathrm{Sc}. \tag{10c}$$

In this reaction the excitation energy of the ^{50}Sc* is taken up by an increase in kinetic energy of the $^{A}\mathrm{n_s}$ and there is no gamma ray emission. This reaction is similar to internal conversion, in which the energy of an excited nucleus is given to an orbital electron and there is no gamma [4].

The ^{50}Sc is also beta unstable and decays to ^{50}Ti* with a half-life of 102.5 s,

$$ {}^{50}\mathrm{Sc} \to {}^{50}\mathrm{Ti}^{*} \tag{10d}$$

followed by

$$ {}^{A}\mathrm{n_s} + {}^{50}\mathrm{Ti}^{*} \to {}^{A}\mathrm{n_s} + {}^{50}\mathrm{Ti}, \tag{10e}$$

again without emission of a gamma ray. Overall in reactions (10a)–(10e) we have the transmutation of ^{40}Ca to ^{50}Ti without emission of gamma rays.

9. Transmutation of Ordinary Nuclei

Neutron isotopes can react exothermally with most ordinary nuclei, transmuting the ordinary nuclei to heavier elements. Transmutations occur in several steps. The first step transfers neutrons from a neutron isotope to a target ordinary nucleus, producing an ordinary neutron-rich isotope of the target element. An example from Section 8 is

$$ {}^{A}\mathrm{n_s} + {}^{40}\mathrm{Ca} \to {}^{A-10}\mathrm{n_s} + {}^{50}\mathrm{Ca} + 43\ \mathrm{MeV}. \tag{11}$$

In general the most probable number of transferred neutrons is the number that maximizes the energy released in the reaction (10 neutrons in this example).

Neutron transfer is followed by a series of beta decays of ordinary neutron-rich nuclei that ends when a stable transmutation product is reached. In this example

$$ {}^{50}\mathrm{Ca}(13.9\ s) \to {}^{50}\mathrm{Sc}(102.5\ s) \to {}^{50}\mathrm{Ti}. \tag{12}$$

The overall transmutation is $^{40}\mathrm{Ca} \to {}^{50}\mathrm{Ti}$. This transmutation has been observed by Iwamura [5], along with transmutations Sr → Mo [6], Cs → Pr [6], Ba → Sm [7], and many others.

10. Neutron Isotope Fission

Neutron isotope fission reactions are closely related to transmutation reactions. In general, to every transmutation reaction

$$ {}^{A+B+C}n_\mathrm{s} + {}^{D}Z \to {}^{A+B}n_\mathrm{s} + {}^{C+D}Z \tag{13}$$

there corresponds fission reaction

$$^{A+B+C}\mathrm{n_s} + {}^{D}\mathrm{Z} \rightarrow {}^{A}\mathrm{n_s} + {}^{B}\mathrm{n_s} + {}^{C+D}Z. \tag{14}$$

Transmutation reaction (13) is expected to be more exothermic than fission reaction (14) because (in a liquid drop model) the surface energy of a pair of droplets ($^{A}\mathrm{n_s} + {}^{B}\mathrm{n_s}$) is larger than that of the single droplet ($^{A+B}\mathrm{n_s}$) they form when combined.

Fission reaction (14) tends to be less probable than reaction (13) because it releases less energy; but it tends to be more probable because it provides an additional decay channel. Although the reaction energies and reaction probabilities are not yet well known, and are subject to determination and revision as the theory evolves, I note that the fission rate is positive provided that reaction (14) is exothermic.

In association with reactions (2), reactions (13) and (14) have other important implications for LENR. Growth reaction (2) increases by one the number of neutrons bound in symmetric nuclei. And each of reactions (13) and (14) decreases that number by C. If the rate of reaction (2) is less than C times the sum of the rates of reactions (13) and (14) the number of neutrons bound in symmetric nuclei will shrink, symmetric nuclei will shrink and disappear, and reaction will cease. In order for a chain reaction to exist the rate of reaction (2) must be greater than C times the rates of reactions (13) and (14) summed over every element Z in the reaction volume (there may be more than one such element Z). This requires that the concentrations of elements Z be sufficiently small. Under these conditions reaction (14) assures that there will remain a small net growth in the number of symmetric nuclei, and that a chain reaction can be established.

Reactions (2) and (5) are expected to be very rapid because they are not inhibited by the coulomb repulsions felt by reactions between charged reactants. Their mean free paths may be very small and the minimum size of an active reaction volume may be many orders of magnitude smaller than for an ordinary nuclear reactor.

11. Symmetric Atoms in Nature

I assume that large charged symmetric atoms exist in nature at very low concentrations, their rate of alpha decay suppressed by a large coulomb barrier. These atoms may be formed from time to time in natural reactors around the earth, much as natural uranium reactors have formed in the past [8].

Long-lived symmetric atoms may survive for months or years before a statistical excess of alpha decays (4a) reduces their charge to zero generating a neutron isotope $\mathrm{n_s}$. In this way decays of a long-lived isotope can randomly produce the rare $\mathrm{n_s}$ that can initiate LENR reaction in a suitable environment. The wait can be long in a laboratory that has not previously been exposed to active LENR. This offers an explanation for the fact that many initial attempts to observe LENR were abandoned.

But an initial reaction generates populations of long-lifetime isotopes that remain in the reactor or escape from the reactor and survive in the laboratory until a second LENR reaction is attempted. The wait for initiation of a second reaction is shorter than it was for the first, owing to the large number of medium lifetime precursors generated by the first reaction that survive in the equipment and laboratory.

12. Reactor Design

It is well known that shear deformation of a liquid speeds the rate of reaction between dissolved atoms. This happens because in liquids mechanical flow is much faster than diffusion for bringing potential reactants close enough to each other to react. The situation can be reversed in a solid material where the rate of mechanical flow is negligible relative to diffusion. It can also be reversed in a hot gas, where diffusion can mix reactants with great rapidity.

Various methods of reactant mixing can support various reactor designs. Two designs have had considerable success and others look promising.

In Fleischmann–Pons electrolytic reactors [9] deuterium released during electrolysis goes into solution in the electrolyte near a palladium cathode. As the deuterium concentration rises, bubbles form and grow. Bubble activity is usually concentrated at cathode surface imperfections that enhance the probability of bubble nucleation. The turmoil of bubble nucleation and growth increases the mixing rate in the bubble deuterium gas. LENR reaction is fast. The rates of growth reactions (1) and of fission reactions (5) are increased and a chain reaction is initiated. As the chain reaction heats the gas, the rising temperature increases the diffusive mixing rate exponentially in an explosive reaction.

In this way we can understand the sparkling flashes of thermal energy in the electrolyte that cover the surface of a cathode as reported by Szpak et al. [10]: Available ^{2}H is consumed in a flash of chain reaction in which growing bubbles, expanded by heat, accelerate the rate of mixing of nuclear reactants. The temperature can rise high enough to melt the cathode surface. The bubble nucleation site is blown free of electrolyte and of most gas, shutting down electrolysis at that site. Active electrolysis then must shift to other sites. In this way electrolysis is concentrated at "hot spots". After a flash of reaction there is a short period of time during which the bubble nucleation site cools down, electrolyte returns, and electrolysis resumes. New bubbles appear at the site of the old. The new bubbles grow and support new flashes of reaction. The active volume of the nuclear reaction is on order of perhaps 10^{-5} cc, confirming that an active LENR reaction volume may be many orders of magnitude smaller than for an ordinary nuclear reactor.

In Rossi-type reactors, on the other hand, the LENR reaction takes place in a large volume of deuterium gas (or deuterium-hydrogen mixture) that is heated to high temperature by an electric heater [11]. LENR then proceeds largely by diffusive mixing of neutron isotopes and deuterium. This process can be exponential from the start, controlled only by reducing the heater power until heater power and reaction power together are less than the loss of power by radiation and conduction from the surface of the reactor. If reduction of heater power is insufficient, the Rossi reaction power rises exponentially and the reactor melts, releasing the gas and terminating the reaction.

13. A Goal for Nuclear Power

One goal for LENR power production is red hot steam, as thick as kerosene, flowing at the speed of a pistol bullet out of a reactor into a steam turbine. This would be an ideal power source to compete with fossil fuels.

Acknowledgement

I thank the referee for a thorough and insightful review of the manuscript, which has been strengthened in response to his critical comments.

References

[1] J.C. Fisher, poster, ICCF-18, U. Missouri, July 22–26 (2013), google search: jcfisher@fisherstone.com

[2] J.C. Fisher, Outline of polyneutron theory, *8th Int. Workshop on Anomalies in H/D Loaded Metals*, Catania, Italy, 2007, p. 70: www.iscmns.org/Catania07/ProcW8.pdf

[3] S. Pons and M. Fleischmann, *Trans. Fusion Technol.* **26** (4T), Part 2 (1994) 87.

[4] K.S. Krane, Introductory Nuclear Physics, Wiley, New York, 1988, p. 341.

[5] Y. Iwamura et al., P*roc. ICCF-7*, Vancouver, Canada, April 19–24, 1998, p. 167.

[6] Y. Iwamura et al., *Proc. ICCF-9*, Beijing, China, May 19–24, 2002, p. 141.US2002/0080903A1, June 27, 2002.

[7] Y. Iwamura et al., *Proc. ICCF-11*, Marselles, France, Oct. 31–Nov 5, 2004, p. 339.

[8] Wikipedia.org/Natural_nuclear_fission_reactor

[9] M. Fleischmann, S. Pons and M. Hawkins, *J. Electroanal.Chem.* **261** (1989) 301 and errata in Vol.263, 1989.

[10] S. Szpak et al., Thermal behavior of polarized Pd/D electrodes prepared by co-deposition, *Thermochim. Acta* **410** (2004) 101.

[11] G. Levi et al., arXiv.org> physics> arXiv: 1305.3913, Indication of anomalous heat energy production in a Reactor device, June 7, 2013.

J. Condensed Matter Nucl. Sci. 15 (2015) 190–194

Research Article

Pressurized Plasma Electrolysis Experiments

Jean-Paul Biberian*
Aix-Marseille University, Marseille, France

Mathieu Valat
Martin Fleischmann Memorial Project

Walter Sigaut†
INP Grenoble, BP 53-38041 Grenoble Cedex 9, France

Pierre Clauzon and Jean-François Fauvarque
CNAM, 292 Rue Saint-Martin, 75003 Paris, France

Abstract

We have performed a plasma electrolysis experiment for the first time at a pressure of 5×10^5 Pa in a specially designed calorimeter. The cathode was a 2 mm tungsten rod, and the anode was a stainless-steel foil. The electrolyte was 0.6 mol K_2CO_3 in light water. In one instance, we observed excess heat of 20 W for 90 min.

Keywords: Cold fusion, Electrolysis, High pressure, Plasma

---

1. Introduction

In recent years, plasma electrolysis has gained much interest for several reasons: it is easy to implement at a low cost, and very spectacular when the plasma ignites in water. However, in spite of the easy implementation, the measurements call for a lot of care. Ohmori and Mizuno [1] demonstrated the production of excess energy, neutrons and transmutation in a plasma electrolysis experiment with a tungsten cathode in K_2CO_3 light water electrolyte. Mizuno et al. [2] confirmed excess heat production. Mizuno et al. also [3–5] showed an increase in the production of hydrogen by a factor of 80 compared to the Faraday law, due to thermal dissociation of water vapor at high temperature during plasma electrolysis. In some experiments they measured excess heat. Cirillo and Iorio [6], and Cirillo et al. [7] showed by

---

*E-mail: jpbiberian@yahoo.fr
†Also at: UCL, Louvain-la-Neuve, Belgium.

Scanning Electron Microscopy the formation of new elements on a tungsten cathode. Mizuno et al. [8], Fauvarque et al. [9] showed the production of excess heat. Cirillo et al. [10] have measured neutron emission during plasma electrolysis, but this was not confirmed by Faccini et al. [11].

This type of experiment has several attractive features: first of all it is very spectacular with the formation of bright plasma in water, which is a show by itself. Second, the cost is low, since it calls for ordinary water, inexpensive K_2CO_3 electrolyte, and standard tungsten welding rods. The power supply can be as simple as the main voltage coming from the wall rectified to produce a more or less direct current voltage.

The results obtained in the various experiments are of four kinds: excess heat; abnormal production of hydrogen; neutrons; and transmutation. Even though the experiments are easy to perform, the various parameters are not simple to measure. Because the plasma is unstable, at constant voltage the current varies greatly, and it becomes difficult to measure the electric input power. Also, it is complicated to measure the heat production, because it comes from the temperature rise of the electrolyte and its evaporation. One of the key issues is the risk of water droplets that are splashed out of the cell in liquid form, and then mistakenly accounted for as vapor, giving rise to a faulty excess heat. Measuring neutrons is not easy, since they are scarce, and they are absorbed by the water. They have been detected only by placing CR39 near the cathode. Finally, the presence of what appear to be new elements could very well

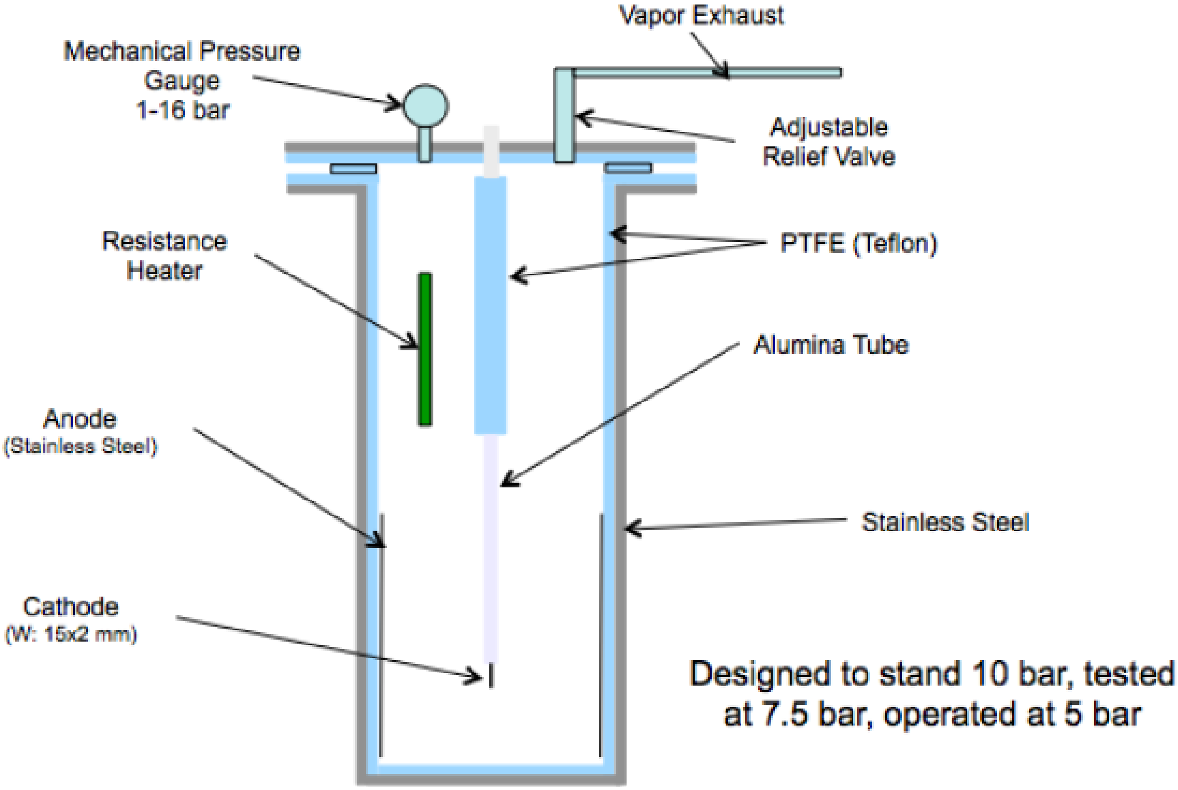

Figure 1. Schematic of the reaction chamber.

be due to contamination from the electrolyte or the various components in the reactor. Only isotopic analysis can be meaningful.

In our experimental work, we focused only on excess heat measurements. For that purpose, we have developed a unique calorimeter enabling us to measure with precision the power input and the heat produced. We assume positive feedback takes place with temperature, so our experimental set-up enables the cell to work under pressure, so that the water temperature is higher than 100°C.

2. Experimental

Figure 1 shows a schematic of the cell. The interior is all Teflon^{TM} covered, so that the electrolyte is never in contact with the external stainless-steel envelope. The lid contains the electrical feedthroughs for the anode, cathode and calibration resistor, a mechanical pressure gauge, as well as a mechanical relief valve that maintains the chamber at constant pressure, and therefore at constant temperature. There is no sensor to measure the temperature of the electrolyte. All measurements of excess heat are made when the pressure reaches a constant value, and a constant temperature is deduced from the pressure. In order to lower the heat loss by convection and conduction, the external stainless steel surface is covered with an insulating blanket.

The cell is positioned on a 6 kg Sartorius balance Signum 1 having a precision of 100 mg (see Fig. 2). The weight loss is converted in heat production assuming that all the water is escaping through the relief valve as dry vapor.

The electric power is measured with a wattmeter (Norma D6100), with a sampling rate of 70 kHz. The cell is operated at constant voltage with a Sorensen DCS 300-3.5E switching power supply, which produces up to 300 V and

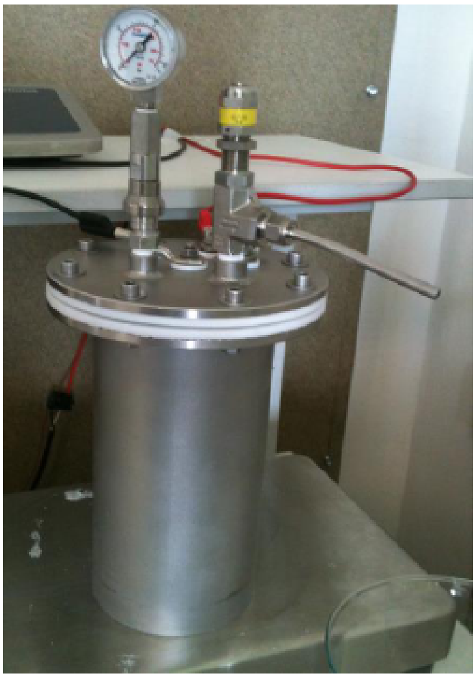

Figure 2. A view of the cell on the balance without the insulation blanket.

3.6 A. When larger voltages or currents were used, two of these power supplies were put in series, or in parallel.

At atmospheric pressure, the heat of vaporization of water is 2258 J/g, and the boiling temperature is 100°C. At five times the atmospheric pressure, the heat of vaporization is 2107 J/g and the boiling temperature is 152°C.

All the data were recorded on a PC with LabVIEW® software. In order to minimize the size of the data files, we averaged the values in 30-second intervals.

3. Calibration

The heat loss of the calorimeter was determined by placing a 300 W resistor in the cell. The difference between the power input and the heat measured through the weight loss corresponds to the heat lost through the walls of the calorimeter. At 5 bar of pressure, this loss was 92 W. In the actual experiments we added 92 W to the heat calculated from the weight loss.

4. Experiments

We have performed a large number of experiments at atmospheric pressure and at 5 bar. We have used tungsten rods of various diameters: 1, 2, and 4 mm. We tested tungsten with and without thorium (2%). We have also tested 2 mm nickel wires. We systematically employed K_2CO_3 as electrolyte. The electrolyte concentration varied between 0.01 and 0.06 mol/l.

Figure 3 shows that the vapor leaving the cell is dry. The condensation cloud forms about 6 mm away from the exit of the exhaust tube.

5. Preliminary Results

Not all experiments were positive. Many failed for various reasons: the cathode was often sputtered away and destroyed by the plasma. There are many parameters to take into account: electrode material; diameter and length of the electrode; concentration of the electrolyte; and voltage applied. At 5 bar, i.e. 152°C, with a 2 mm diameter, 2 cm long cathode, we measured an average excess heat of 19 W. With an average input power of 175 W, for 60 min, the COP is thus 1.11. The voltage was 305 V and the average current was 0.57 A.

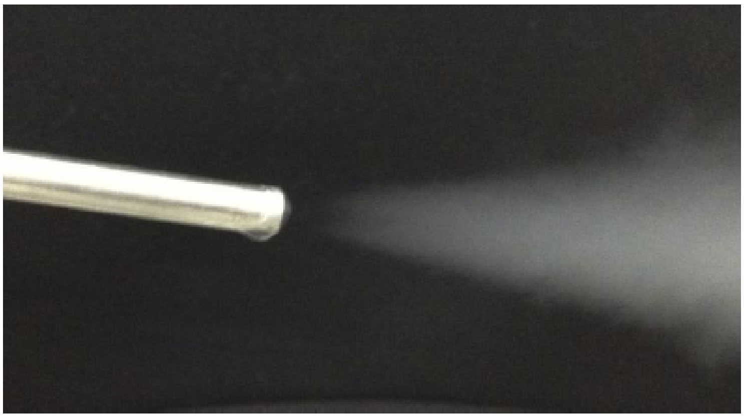

Figure 3. Dry steam coming out of the exhaust pipe.

6. Conclusion

This high-pressure calorimeter has a number of advantages: it operates at constant temperature, above 100°C and it can be easily changed by changing the pressure of operation. With our present design, we can work at up to 10 atm. of vapor pressure. Because the temperature is constant, the time constant of the system when input power changes is short. Our preliminary results confirm the production of excess heat, and we believe that it can be made much higher than what we have obtained so far after tuning the various parameters. Moreover, this design is very well adapted for finding deuterium in the gas if the reaction mechanism is $H + H \rightarrow D$.

There are some disadvantages linked to this design: the duration of the experiment is limited by the quantity of water in the cell, because we cannot add water during operation since we operate under pressure. Also, the cathode gets eroded most of the time, and this also limits the duration of the experiment.

References

[1] T. Ohmori, and T. Mizuno, Strong excess energy evolution, new element production, and electromagnetic wave and/or neutron emission in the light water electrolysis with a tungsten cathode, in *Proc. of the 7th Int. Conf. on Cold Fusion*, Vancouver, Canada, 1998.

[2] T. Mizuno, T. Ohmori, T. Akimoto and A. Takahashi, Production of heat during plasma electrolysis in liquid, *Jpn. J. Appl. Phys.* **39**(10) (2000) 6055–6061.

[3] T. Mizuno, T. Akimoto and T. Ohmori. Confirmation of anomalous hydrogen generation by plasma electrolysis, in *4th Meeting of Japan CF Research Society,* Iwate, Japan, Iwate University, 2003.

[4] T. Mizuno, Y. Aoki, D. Y. Chung and F. Sesftel, *Generation of heat and products during plasma electrolysis I liquids*, *Proc. ICCF11*, pp. 161–177.

[5] T. Mizuno, T. Akimoto, K. Azumi, T. Ohmuri, Y. Aoki and A. Takahashi, Hydrogen evolution by plasma electrolysis in aqueous solution, *Jap. J. App. Phys.* **44** (2005) 396—401.

[6] D. Cirillo and V. Iorio, Transmutation of metal at low energy in a confined plasma in water, *Proc. ICCF11*, pp. 492–504.

[7] D. Cirillo, E. Del Giudice, R. Germano, S. Sivasubrammanian, Y.N. Srivasata, V. Tontodonato, G. Vitiello and A. Widom, Water plasma modes and nuclear transmutations on the metallic cathode of a plasma discharge electrolytic cell, *Key Eng. Mat.* **495** (2012) 124–128.

[8] T. Mizuno, T. Ohmuri, T. Akimoto and A. Takahashi, Production of heat during plasma electrolysis in liquid, *Jpn. J. Appl. Phys*. **39**(10) (2000) 6055–6061.

[9] J.-F. Fauvarque, P. Clauzon, G. Le Buzit and J.-M. Lallevé, Abnormal excess heat observed during Mizuno-type experiments, *ICCF12 Proc.* Yokohama, Japan, 2005, pp. 80–85.

[10] D. Cirillo, R. Germano, V. Tontodonato, A. Widom, Y.N. Srivasata, E. Del Giudice and G. Vitiello, Experimental evidence of neutron flux generation in a plasma discharge electrolytic cell, *Key Eng. Mat.* **495** (2012) 104–107.

[11] R. Faccini, A. Pilloni, A.D. Polosa, M. Angelone, E. Castagna, S. Lecci, A. Pietropaolo, M. Pillon, M. Sansovini, F. Sarto, V. Violante, R. Bedogni and A. Esposito, Search for neutron flux generation in a plasma discharge electrolytic cell, arXiv: 1310.4749v1 [physics.ins-det] 17 October 2013.

J. Condensed Matter Nucl. Sci. 15 (2015) 195–202

Research Article

Numerical Modeling of H_2 Molecule Formation within Near-surface Voids in Pd and Ni Metals in the Presence of Impurities

O. Dmitriyeva,* R. Cantwell and M. McConnell

Coolescence, LLC, Boulder, CO, USA

Abstract

We have used density functional theory (DFT) to investigate crucial material parameters that can promote a low energy nuclear reaction (LENR). This approach significantly decreases the experimental burden involved into material fabrication and testing. It also provides the foundation for systematical study and optimization of important material properties. We focused on three characteristics to describe the LENR environment: (1) a high hydrogen isotope loading ratio, (2) the presence of dopants or impurities, and (3) material morphology. We chose two figures of merit to characterize those environments: hydrogen adsorption energy on metal surface and H_2 bond length. We showed that high hydrogen loading and the presence of impurities in Pd and Ni can lower the adsorption energy, thus increasing hydrogen surface mobility potentially improving the reaction rate. Another factor that would increase the fusion probability is the distance between two hydrogen atoms. We demonstrated that a hydrogen molecule can be formed in a near-surface void in Pd and Ni at the bond length of 0.70–0.74 Å.

Keywords: DFT, Impurities, LENR, Palladium, Surface, Vacancy

---

1. Introduction

Various aspects of the interaction between hydrogen isotopes and metals have been studied extensively because of the great technological role they play in hydrogen storage, gas separation/purification, catalyst design and energy applications. Numerous experimental studies that address the energetics and dynamics of hydrogen isotopes adsorption/absorption on metal surfaces and in bulk have been published. With the use of computational power, theoretical studies of metal hydrides have also contributed significantly to our understanding of the fundamental principles underlying hydrogen–metal interactions.

Deuterium and/or hydrogen loading in Pd and Ni materials under special conditions results in excess heat generation, transmutations and/or particle generation. This is known as low nuclear energy reaction (LENR) [1] . In our theoretical study we applied density functional theory (DFT) to investigate the properties of potentially active LENR materials. Our study does not explain or make any attempts to explain the theoretical basis for LENR, but rather we looked at a

---

[*] E-mail: olga@coolescence.com

chemical environment that was reported to favor a reaction. We based our study on successful LENR reports that have been made available over the past 25 years [1–3]. We chose three factors that seemed to play a crucial role in obtaining positive experimental results. Those factors were (1) a high deuterium /hydrogen loading ratio when each Pd or Ni atom has at least one corresponding D or H atom within the fcc crystal lattice (loading ratio 1:1) [4,5]; (2) the presence of impurities introduced to Pd or Ni either intentionally (alloys, powdered additions to electrolyte) or unintentionally (doping by impurities from environment during the fabrication step or from electrolyte during the experiment) [6,7]; (3) and material morphology: cathode surface and bulk defects [8,9].

Hydrogen and deuterium systems are equivalent within a self-consistent DFT frame; therefore from this point forward we will leave out deuterium of our discussion and operate with hydrogen only with the validity of the results towards a deuterium system implied. We chose two figures of merit to evaluate the results of our simulations. The figures of merit were (1) hydrogen adsorption energy (E_{ads}), and (2) H_2 bond length — namely hydrogen–hydrogen (H–H) separation distance, which we studied in the manner proposed in Ref. [9].

In our simulations we targeted the systems that promote the reduction of E_{ads} and closer H–H separation distance. These systems include palladium and nickel hydrides, and their near-surface alloys (NSA). In NSAs the dopants are concentrated in a sub-layer, which allows a decrease in adsorption energy while keeping the H_2 dissociation barrier low [10]. Weaker binding of atomic hydrogen to the surface of the metal can make the subsequent surface reaction step easier. In the case of LENR we were interested in the type of reaction that would bring two hydrogen atoms as close to each other as possible, within the metal lattice frame, to increase the transmission probability and thus the fusion rate. The standard hydrogen bond length in a vacuum is 0.74 Å. When hydrogen is adsorbed in Pd the distance between two H atoms is equal to approximately 2.3 Å, or the distance between the two adjacent octahedral sites. The large separation makes these hydrogen atoms relatively isolated within the lattice frame. The conditions that favor closer H–H separation distances in bulk palladium were studied by Peter Hagelstein and others [9]. Their calculations predicted the hydrogen molecule formation inside Pd monovacancy at the bond length of 0.77 Å. In this manuscript we explore the conditions in a chemical environment which will reduce the H_2 bond length even further. Our analysis is applicable to H_2 formation in palladium and nickel hydrides inside near-surface voids in the presence of impurities.

2. Simulation Approach and Validation

The simulations were performed in a Quantum Espresso simulation package [11]. We used periodic self-consistent DFT calculations that have shown predictive results for similar transition metal systems [12,13]. The total energies were calculated within a generalized gradient approximation (GGA). The GGA was chosen over local density approximation (LDA) to assure good agreement between the calculated and experimentally measured hydrogen adsorption energies. All simulations were done for hydrogen, but the results of self-consistent energy calculations can be extended to deuterium systems as well.

The metal surface was modeled as a 3D set of periodically repeating multilayer slabs of bulk material at (100) crystal plane orientation. The convergence of a slab's potential energy as a function of its thickness was evaluated for 4, 6, 8 and 10-slab layer constructions in the manner described in [14]. Starting with 6-layer slabs and thicker, the formation energy converged. The 6-layer slab configuration was adopted for further simulations with implementation of $6 \times 6 \times 1$ automatically generated k-point grid.

To avoid the interaction between periodically replicated slabs, we set the separation between the slabs to be 2.5 times larger than the lattice constants. For example, the Pd lattice constant in our model is 3.94 Å, which makes the vacuum gap in the slab construction to be 9.85 Å wide. The electron density falls off to near-vacuum level within 2 Å from the surface. Thus, the slabs were sufficiently separated and did not quantitatively affect surface processes.

We tested several models to verify that this simulation approach was sound and would give reasonable results for the system of interest. The immediate quantities of interest were binding energies and separation distances for simple

Table 1. Simulated configurations.

Dopant	Pd as a host	Ni as a host
F	Interstitial	Interstitial
O	Interstitial	Interstitial
Cl	Interstitial	Interstitial
C	Interstitial	Interstitial
Se	Interstitial	Substitutional
As	Interstitial	Substitutional
Li	Interstitial	Interstitial
B	Interstitial	Interstitial

molecules of H_2, PdH and Pd–H_2 complex. The binding energy for H_2 was found to be 4.97 eV at 0.75 Å separation (compare to known 4.52 eV at 0.74 Å). The binding energy for PdH was 2.12 eV at 1.57 Å separation (compare to 2.34 eV at 1.55 Å [15]). We found two stable states for Pd–H_2 complex in the manner described in [15,16]. For all three cases the results were in satisfying agreement with the referenced literature.

The next quantities we checked were the bulk lattice parameters for Pd and Ni and their hydrides. Based on our calculations the expansion of Pd lattice as a result of PdH formation is 4% from 3.94 to 4.10 Å (compare to 3.4% experimentally found 3.89 to 4.025 Å). For Ni to NiH transition the lattice expansion was found to be 7.8% from 3.46 to 3.73 Å (compare to 6% experimentally found 3.52–3.73 Å).

The last validation of our simulation approach was done for hydrogen adsorption energies on the surfaces of different metals and near-surface alloys (NSA). The calculations were done for Pd, Ni, Cu, and Pt. All three available adsorption sites were tested: four-folded, bridged and on-top. The upper two layers of the slab were relaxed in the direction perpendicular to the surface. After that, the atoms of the crystal lattice were fixed at their relaxed positions only hydrogen atom was allowed to move around the adsorption site in order to minimize the energy of the system. Hydrogen adsorption energy was calculated using the formula:

$$E_{\text{ads}} = E_{\text{surf+H}} - E_{\text{surf}} - \frac{1}{2}E_{\text{H}_2}.$$

The values reported in this paper are for four-folded adsorption sites only. The results are in good agreement with the experimental data and the other DFT studies [10].

In the near-surface configuration the dopants were included only in a sub-layer. The structures are described with the Y/X notation first introduced in Ref. [10], where X is a host and Y is a solute element.

The choice of interstitial versus substitutional configuration was justified by the energy minimization calculations. The configuration with lower total energy indicates the preferred system's state. The interstitial dopants were modeled using the expanded lattice parameter (4.10 Å for Pd and 3.73 Å for Ni). All simulated configurations and types of dopants are included in Table 1.

3. Results and Discussion

3.1. Role of hydrogen loading

As discussed in the introduction, hydrogen loading in palladium is known to decrease adsorption energy [17]. We replicated the calculations for the palladium surface and updated them with a similar study for Ni. Table 2 contains the hydrogen adsorption energy values for Pd and Ni materials loaded at different levels. The adsorption energy decreases with increases in the hydrogen loading.

Table 2. Hydrogen adsorption energy values for Pd and Ni hydrides.

Configuration	E_{ads} (eV)
Pure Ni	–0.684
Ni with one H atom in sub–layer*	–0.617
-Ni with 2 H atoms in sub–layer	–0.595
NiH fully loaded at 1:1 ratio	–0.592
NiH with additional H adsorbed in on–top position	–0.385
Pure Pd	–0.499
Pd with one H atom in sub-layer*	–0.397
Pd with 2 H atoms in sub-layer	–0.389
PdH fully loaded at 1:1 ratio	–0.382
PdH with additional H adsorbed in on-top position	–0.109

*Number of H atoms per unit cell. Unit cell consists of 12 host atoms: Pd or Ni.

The hydrogen adsorption energy was initially higher for pure Ni compared to pure Pd. E_{ads} decreased as increasing amount of hydrogen was absorbed in the metal. The adsorption process eventually stopped when the metal lattice was fully saturated with hydrogen and a hydrogen monolayer was formed on the surface.

3.2. Role of impurities

The inclusion of some dopants/impurities in the host metal lattice resulted in a similar hydrogenation effect: E_{ads} decreased in the presence of impurities. We modeled the presence of dopants in the metal lattice sub-layer in the manner described in [10]. The near-surface configuration can be experimentally achieved during the co-deposition of Pd in a heavy water-based electrolyte [18] or by a galvanic displacement of an add layer [19]. The E_{ads} values for Pd and Ni metals and their doped configurations are summarized in Table 3.

Table 3. Hydrogen adsorption energy for Pd and Ni slabs and their doped configurations.

Pure metal configuration	E_{ads} (eV)	Alloy configuration	E_{ads} (eV)
Pd	–0.499	H/Pd	–0.389
		O/Pd	–0.251
		C/Pd	–0.208
		Se/Pd	–0.160
		F/Pd	–0.243
		As/Pd	–0.083
		Cl/Pd	–0.070
		Li/Pd	–0.389
		B/Pd	–0.289
Ni	–0.684	H/Ni	–0.595
		O/Ni	–0.196
		C/Ni	–0.346
		Se/Ni	–0.614
		F/Ni	–0.274
		As/Ni	–0.482
		Cl/Ni	0.169
		Li/Ni	0.124
		B/Ni	–0.159
		Pd/Ni	–0.623

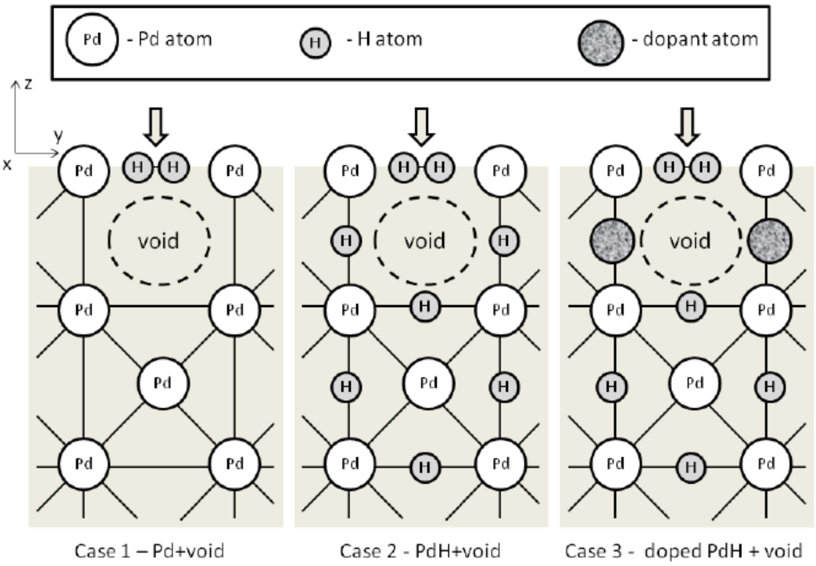

Figure 1. Pd slab with a void at a sub-layer. The hydrogen molecule is entering from the surface and traveling towards the void. Three cases represent: (1) undoped Pd, (2) PdH, and (3) doped PdH.

It follows from Table 3 that the E_{ads} for pristine metals is higher than for the doped material, meaning that hydrogen does not bind as strongly to the metal surface if near-surface impurities are present.

3.3. Role of vacancies

The near-surface void was modeled as an absence of the host atom in the sub-layer of a Pd or Ni slab. The hydrogen molecule entered the metal lattice through the four-fold adsorption site, penetrating the slab along the z-direction towards the void. At each point along the z-direction the H_2 molecule's z-coordinate was fixed, but the molecule was allowed to relax in the xy plane to minimize the total energy of the system. Figure 1 shows the 2D representation of the three different cases under investigation: (1) a pristine metal slab with the void, (2) a metal hydride slab with the void, and (3) a metal hydride slab with an interstitially doped sub-layer at the void.

We tested the verity of possible dopants or impurities that may be present in an experimental or industrial environment. Figure 2 shows the change in H–H separation as a function of the penetrating distance from the surface of Pd, PdH and F/PdH (fluorine atom as an interstitial dopant in PdH sub-layer).

The change in the electronic density as a result of hydrogenation promotes the formation of a hydrogen molecule inside the near-surface void at a 0.75 Å A separation distance. The same hydrogen molecule formed in pristine Pd metal will have a bond length of 0.80 Å. The presence of fluorine brings the electronic density even lower, reducing the separation distance to 0.74 Å. The calculations done for Ni showed a similar trend, with a minimum H–H separation distance of 0.70 Å inside the near-surface void in the presence of fluorine.

The H–H separation distances at the near-surface void were calculated for Pd and Ni metal slabs doped with F, O, Cl, Se, Rh, As, Li, and B. The results are summarized in Fig. 3. The impurities are arranged along the x-axis according to their electronegativity, with fluorine as the most electronegative element, and followed by the less electronegative dopants. Our calculations showed that the point of minimum H–H separation inside the crystal does not coincide with

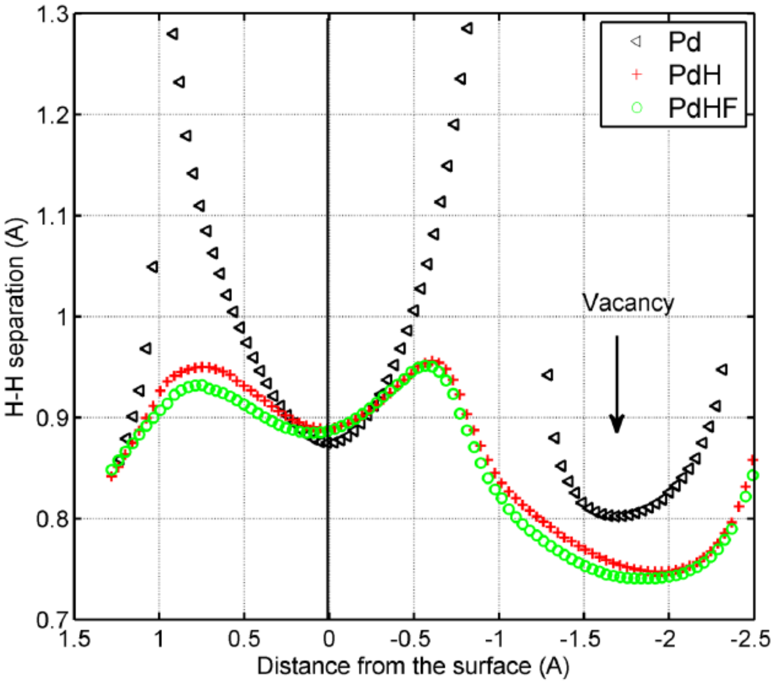

Figure 2. H–H separation as a function of the distance from the surface of the metal (located at zero). The positive values to the left correspond to the distances above the surface, while negative values to the right correspond to the distances beneath the surface. The vacancy is at -1.703 Å beneath the surface. Legend: *black* – pristine Pd metal (case I from Fig. 1), *red* – PdH (case II), *green* – PdH doped with F (case III).

the system total energy minimum. This means that this arrangement is not energetically preferable at the equilibrium state, and thus is unlikely. However, non-equilibrium processes such as mechanical stress of the crystal lattice due to hydrogen loading may promote a favorable environment for hydrogen molecule formation.

4. Conclusions

We investigated the mechanisms for hydrogen molecule formation in Pd and Ni within the near surface voids using the mean of the density functional theory. We used available experimental data to establish the important factors that are suggested to benefit LENR and modeled the chemical environment for those configurations. Those factors include: a high level of hydrogen loading, the presence of impurities and the presence of surface defects. Using adsorption energy as a figure of merit we demonstrated that a high level of hydrogen loading has an effect that is similar to the doping effect when hydrogen adsorption energy is reduced. Usually this implies the increase of a dissociation energy barrier. However, some near-surface alloy configurations offer a unique exception to this rule, providing both low adsorption energy and a low H_2 dissociation barrier. Weak binding of hydrogen to the surface can make the subsequent reaction steps easier. From the LENR point of view this could mean a monolayer of nearly free atomic hydrogen moving along the metal surfaces and encountering steps, dislocations or vacancies where the H_2 molecule can form at close separation distance. The near-surface void or vacancy could be a type of surface defect where two hydrogen atoms can bind together.

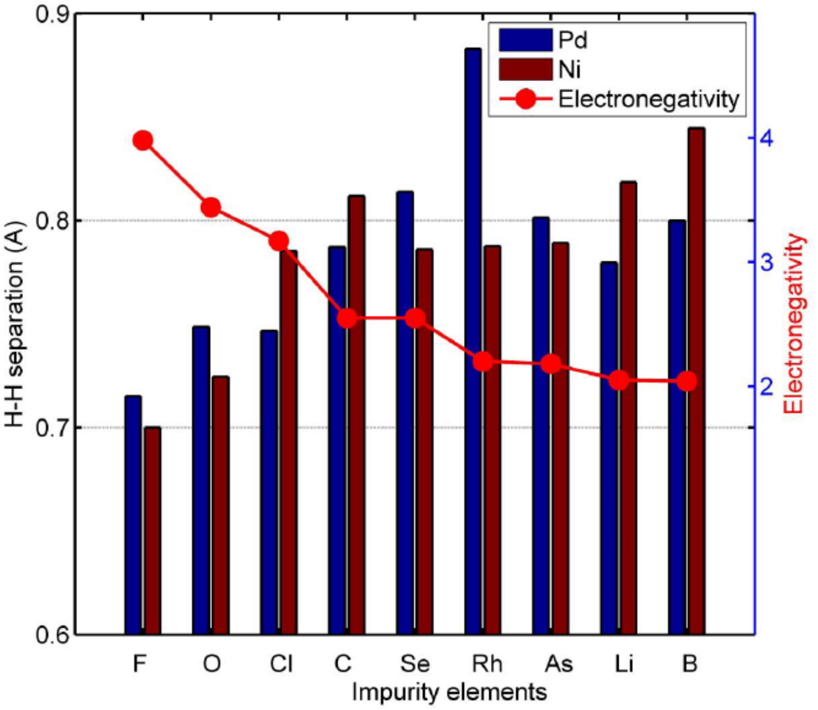

Figure 3. H–H separation at the near-surface void in the presence of different sub-layer impurities. Calculations were done for the Pd and Ni host structures using the procedure described in Section 2.

Since fusion probability depends strongly on the separation distance, we used H–H separation as another figure of merit to evaluate our model. The presence of hydrogen that has been absorbed in bulk changes the overall electronic density and allows the H_2 molecule to form a bond at shorter separation distance. This effect can be enhanced (and the separation reduced) through the introduction of high electronegative impurities.

References

[1] E. Storms, Status of cold fusion (2010), *Naturwissenschaften* **97** (2010) 861–881.
[2] C. Beaudette, *Excess Heat*, South Bristol, Maine, USA: Oak Grove Press, LLC, 2002.
[3] www.LENR-CANR.org, The library of papers about cold fusion.
[4] A. Kitamura, T. Nohmi, Y. Sasaki, A. Taniike, A. Takahashi, R. Seto and Y. Fujita, Anomalous effects in charging of Pd powders with high density hydrogen isotopes, *Phys. Lett. A* (2008) 3109–3112.
[5] M. McKubre, S. Crouch-Baker, R. Rocha-Filho, S. Smedley and F. Tanzella, Isothermal flow calorimetric investigations of the D/Pd and H/Pd systems, *J. Electroanalytical Chem.* **368** (1994) 55.
[6] E. Storms, The *Science of Low Energy Nuclear Reaction*, World Scienific, Singapore, 2007.
[7] V. Violante, E. Castagna, S. Lecci, F. Sarto, M. Sansovini, T. Markis, A. Torre, D. Knies, D. Kidwell, K. Grabowski, D. Dominguez, G. Hubler, R. Duncan, A. El Boher, O. Azizi, M. McKubre and A. La Gatta, Excess of power during electrochemical loading: materials, electrochemical conditions and techniques, in *Int. Conf. Condensed Matter Nuclear Science*, Columbia, MO, 2013.

[8] V. Violante, F. Sarto, E. Castagna, M. Sansovini, S. Lecci, D. Knies, K. Grabowski and G. Hubler, Material science on Pd–D system to study the occurance of excess power, in *Int. Conf. on Condensed Matter Nuclear Science*, Washington, DC, 2008.

[9] J. He, L. Dechiaro, D. Knies, G. Hubler, K. Grabowski, A. Moser, D. Dominguez, D. Kidwell and P. Hagelstein, Stability of a hydrogen molecule in a vacancy of palladium hydrides, *Int. J. Hydrogen Energy* **37** (2012) 12351–12357.

[10] J. Greeley and M. Mavrikakis, Alloy catalysts designed from first principles, *Nature Materials* **3** (2004) 810–815.

[11] P. Giannozzi, S. Baroni, N. Bonini, M. Calandra, R. Car, C. Gavazzoni, D. Ceresoli, G. Chiarotti, M. Cococcioni, I. Dabo, A. Dal Corso, S. Fabris, G. Fratesi, S. de Gironcoli, R. Gebauer, U. Gerstmann, C. Gougoussis, A. Kokalj, M. Lazzeri, L. Martin-Samos, N. Marzari, R. Mauri, R. Mazarello, S. Paolini, A. Pasquarello, L. Paulatto, C. Sbraccia, S. Scandolo, G. Sclauzero, A. Seitsonen, A. Smogunov, P. Umari and R. Wentzcovitch, QUANTUM ESPRESSO: a modular and open-source software project for quantum simulations of material, *J. Phys.:Condens.Matter* **21** (2009) 395502,19.

[12] J. Perdew, K. Burke and M. Ernzerhof, Generalized gradient approximation made simple, *Phy. Rev. Lett.* **77**(18) (1996) 3865–3868.

[13] I. Pasti, M. Gavrilov and S. Mentus, Hydrogen adsorption on palladium and platinum overlayers: DFT study, *Adv. Phy. Chem.* **2011** (2011) 1–8.

[14] R. Magyar, A. Mattsson and P. Schultz, Some practical considerations for density functional theory studies of chemistry at metal surfaces, in *Metallic Systems*, Boca Raton, FL, USA, Taylor & Francis, 2011, pp. 163–199.

[15] K. Balasubramanian, P. Feng and M. Liao, Electronic states and potential energy surfaces of PdH_2: Comparison with PtH_2, *J. Chem. Phys.* **88** (1988) 6955–6961.

[16] C. Jarque and O. Novaro, On the stability of the PdH_2 molecule, *J. Am. Chem. Soc.* **108** (1986) 3507–3510.

[17] M. Johansson, E. Skulason, S. Murphy, G. Nielsen, R. Nielsen and I. Chorkendorff, Hydrogen adsorption on palladium hydride at 1 bar, *Surface Sci.* **604** (2010) 718–729.

[18] S. Szpak and P. Mosier-Boss, Calorimetry of the Pd+D codeposition, *Fusion technol.* **36** (1999) 234–241.

[19] P. Ferrin, S. Kandoi, J. Zhang, R. Adzic and M. Mavrikakis, Molecular and atomic hydrogen interaction with Au–Ir near-surface alloys, *J. Phys. Chem. C* **113** (2009) 1411–1417.

[20] P. Hagelstein, Molecular D_2 near vacancies in PdD and related problems, 2013.

[21] M. Lischka and A. Grob, Hydrogen adsorption on an open metal surface; H_2/Pd(210), *Phys. Rev. B* **65** (2002) 075420.

J. Condensed Matter Nucl. Sci. 15 (2015) 203–230

Research Article

Possibility of Tachyon Monopoles Detected in Photographic Emulsions

Keith A. Fredericks*

Restframe Labs, W. Lafayette, IN 47906, USA

Abstract

Low-energy nuclear reaction experiments using photographic emulsions, including those by Urutskoev, et.al, Ivoilov, and others have shown unique particle tracks. Analysis of a sample population of these types of tracks suggests detection of magnetically charged particles with faster-than-light velocities. Particle kinetic energy was estimated from energy deposition and momentum was estimated from track curvature in magnetic fields. Measured values were plotted on a kinetic energy versus momentum graph and were found to fall in the $v > c$ region. Track curvature was found to be parabolic, which is a signature for monopoles. Using the classical theory of tachyons, the plane of parabolic curvature suggests electrically charged tachyons detected as slower-than-light monopoles. Preliminary lower limits for particle mass are found. Further study is suggested to broaden this search.

Keywords: Detection, Mass Estimate, Monopoles, Parabolic curvature, Photographic emulsion, Superluminal, Tachyons

---

1. Introduction

A recent preliminary analysis of unique particle tracks [1] is consistent with the possible detection of tachyons (faster-than-light particles) as shown by four signatures

1. Kinetic energy vs. momentum values are consistent with $v > c$ particles
2. A superluminal Lorentz transformation (SLT) rectifies particle mass and velocity confirming the particle as a tachyon
3. Parabolic curvature in applied magnetic fields is unique to monopoles, but the observed plane of curvature is incorrect
4. An SLT rectifies the orientation of the Lorentz force acting on the particle confirming the particle as a tachyon (monopole)

This result is testable by repeating one or more of the six experiments yielding particle tracks (in Section 2) in a perpendicular applied magnetic field followed by analysis of the parabolic curvature, kinetic energy and momentum

---

*E-mail: keith@restframe.com

of the particle tracks. Certain additional particle properties are considered and seen to fit within the framework of the classical theory of tachyons. As these types of particle tracks have been observed in experiments associated with Low Energy Nuclear Reactions (LENR), it is possible that these particles play a role in the as yet unknown mechanism of these reactions.

1.1. Background

A unique collection particle track effects has been observed in a variety of studies [1–13] since 1979. The same track effects have been observed in diverse experiments including bombardment by low-energy ions in glow discharge plasma processes [10,11], electric explosion of metallic wires and thin foils [2,3,6], low-energy discharges in water [4,5], electrolysis with Pd cathodes in H_2O [12,13], the search for monopoles of solar origin at the north pole [7], the supercompression of solid targets using electron beams [8,9], and exposure to human hands [1]. All experiments cited here recorded particle tracks using photographic emulsions except [8,9], which recorded tracks with MDS (metal–dielectric–semiconductor).

Our experiments [1], from 1979 observed track effects primarily under conditions where human fingertips were *exposed* to photographic emulsions. The use of amplified photographic emulsions in these experiments significantly enhanced the sensitivity to the track effects and facilitated the recording of a number of important effects not observed in other experiments and led to the largest and most comprehensive set of particle tracks with over 200 exposures and well over 1000 tracks.

The data generated in these experiments replicates very closely virtually all track effects observed in [2–11] and shares properties with [12,13]. The tracks exhibit certain properties in photographic emulsions and other materials and are characterized as to their curvature in magnetic fields, length, width, periodic structure, random motion, correlation, splitting, and vertex structure. These properties considered together begin to form a picture of a particle that creates unique tracks in photographic emulsions and other materials and that must represent a new type of elementary particle.

The paper is organized as follows:

- Section 2: Review of Studies
- Section 3: Particle Properties
- Section 4: ζ-Correction
- Section 5: Momentum
- Section 6: Energy Loss
- Section 7: Superluminal Lorentz Transformation
- Section 8: Discussion
- Section 9: Conclusion

2. Review of Studies

These unique track observations are shared between several studies. Most of these studies [2–6,8–13] fall into the category of LENR or CMNS (Condensed Matter Nuclear Science) [14–16]. Data from Fredericks [1] and Bardout [7] do not involve electrical discharges, but show the same tracks. The identity between the results of these two types of experiments is established [1] and it is possible that the particles creating these tracks are involved with LENR either as a catalyst or a by-product.

The amplification of photographic detectors used in Fredericks [1] yielded the most extensive collection of track types, including those shown in each of the LENR studies and therefore represents a super-set of all tracks. Track types were categorized and related to particle properties.

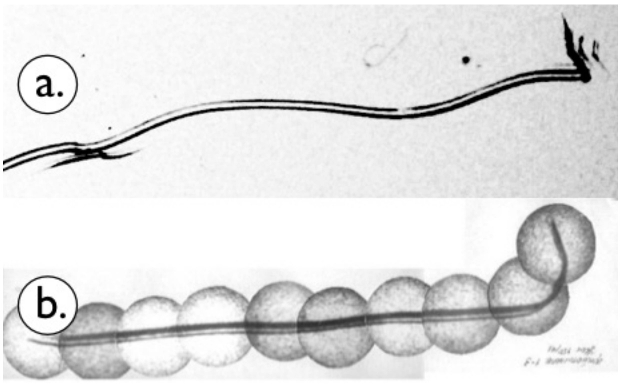

Figure 1. (a) Fredericks track in Polychrome Litho film. Compare with tracks in Section 3.10 and Fig. 6 in Priem et al. [6] (b) Urutskoev track. “Typical track" of Urutskoev and co-workers.

Each of the studies is briefly described and representative particle track images from each study are compared with matching images from Fredericks [1].

2.1. Urutskoev and co-workers

Urutskoev and co-workers [2] observed the transmutation of elements in a series of experiments using exploding wires and foils in liquids in reaction vessels. Fluoroscopic, radiographic and nuclear track emulsions were arranged at a distance from the reaction vessel or from samples of reaction by-products and were exposed for certain periods. Magnetic fields of $B \sim 20$ G were applied at the reaction site and $B \sim 1.2$ kG were applied at the detector.

They observed “strange radiation" on the emulsions and reported a number of track types, including *comets*, *spirals*, *gratings* and *caterpillar traces*.

Other properties observed were twin tracks, large-angle deflections, vertexes and track width that varied with distance from the source. Urutskoev and co-workers in collaboration with Georges Lochak forwarded a theory of *Lochak monopoles* [17] as a possible explanation of the particle track observations.

2.2. Ivoilov

Ivoilov [4] extended the work of Urutskoev and co-workers using low-energy discharges with carbon electrodes in liquids and excitation of beta-decay products in magnetic fields. The experimental setup was surrounded at a distance of 10–15 cm from the *source of the radiation*. Double-sided X-ray film was exposed in a perpendicular applied magnetic field for 3–10 min. during the discharge. Ivoilov observed long tracks up to 10 mm with regular periodic structure, large-angle deflections and curvature and states that the results were *completely identical* to those of Urutskoev and co-workers.

Ivoilov forwarded the important idea of internal reflection between the film base/gelatin and gelatin/air interfaces as responsible for the very long track lengths observed. Ivoilov was also the first to call attention to correlated tracks exhibiting rotational symmetry that Lochak called *chiral symmetry*. These types of tracks are shown in Figs. 2 and 17 and related to Figs. 24,23 and 19.

A connection is made between chiral tracks and north and south monopoles, but this is heuristic as there is no explanation of exactly *why* north and south monopoles would appear in opposite sides of $\sim 10\ \mu$m double-sided (presumably commercial) X-ray films (on polyester base) using “reflectors” of Al, glass, Ge or Si behind the film.

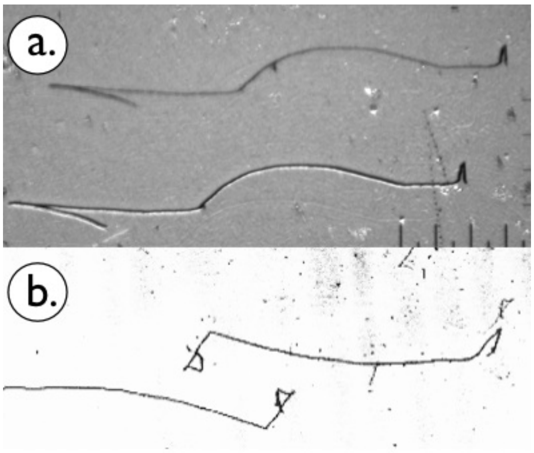

Figure 2. (a) Fredericks tracks. Correlated tracks in Kodak Kodalith type III film. Tracks are copies instead of mirror images or chirally transformed. (b) Iviolov “chiral" tracks. Multiple correlated tracks can be seen in the original image. The chirally transformed track is explained in the Ivoilov analysis as a reflected track which is recorded on the bottom emulsion facing an aluminum plate with polyester base material sandwiched between the two emulsion layers. Unspecified type of double-sided X-ray emulsion.

2.3. Rodionov and Savvatimova

Rodionov and Savvatimova [10] reviewed experiments where particle tracks were observed on photographic emulsions and surfaces of metal electrodes. They generated images in emulsions surrounding glow discharges in plasma and recorded track images on metal electrodes from the reaction vessel.

The tracks have widths usually about 10 μm, lengths of millimeters and more, repeated patterns *like tire treads or necklaces, continuous lines, groups of lines and parallel lines*.

Several images are shown of tracks in Pd cathodes and in Kodak BioMax (autoradiographic emulsion), RT-2 X-ray, and nuclear track emulsions. These images show large-angle deflections or vertexes where two tracks co-terminate, and tracks with regular periodic structure, some of which are labeled as spirals. A regular periodic structure *parabolic* track on a Pd cathode from this study is analyzed in our earlier paper [1].

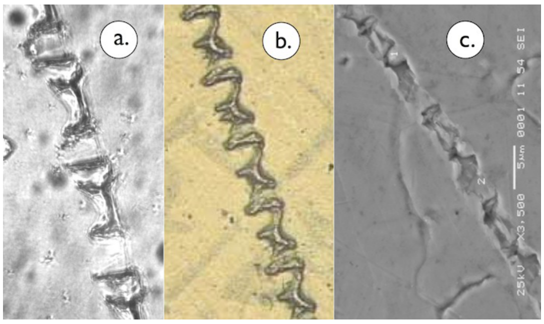

Figure 3. (a) Fredericks track on Polychrome litho film. (b) Rodinov and Savvatimova periodic structure track on nuclear emulsion. Note similarity to Fredericks track where “hourglass” structures are separated by flat structures. (c) Rodinov and Savvatimova periodic structure track on Pd cathode from scanning electron microscope.

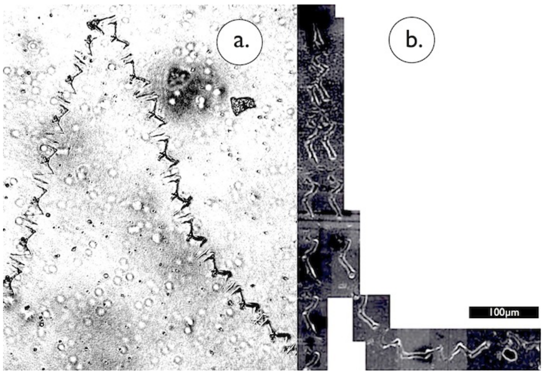

Figure 4. (a) Fredericks track (b) Adamenko and Vysotskii track evaporated in MDS showing parabolic curvature. Detail of track using high magnification.

2.4. Adamenko and Vysotskii

Adamenko and Vysotskiiadamenko.1,adamenko.2 use a method of supercompression of solids with a high-current vacuum tube diode leading to the transformation of nuclei. In these experiments, the authors find tracks on the surfaces of MDS (Metal Dielectric Semiconductor Al–SiO_2–Si sandwich) targets. The tracks created in the MDS are said to be *analogous* to the Urutskoev tracks in photographic emulsions.

Total energy required for the formation of the track was calculated to be $\approx -10^6$ GeV/cm. Particle mass is estimated based on the assumption of magnetic charge to be $\approx 10^{-23}$ g ($\approx$ 560 GeV). The authors suggest that the particle may fit within the framework of a magnetic monopole and in particular the Lochak monopole.lochak.equation

The particle track shown exhibits either a very large-angle deflection or the co-termination of two tracks. One half of the track shows a great deal of smooth curvature (much of which is parabolic). The very good micrographs give an unprecedented view of the almost perfectly correlated periodic structure of each part of the track leading up to the large-angle deflection.

2.5. Priem et al.

Priem et al. [6,18] replicated the experiments of Urutskoev [2] and found good agreement with their results related to both the by-products of the explosion of wires and the subsequent recording of particle tracks similar to

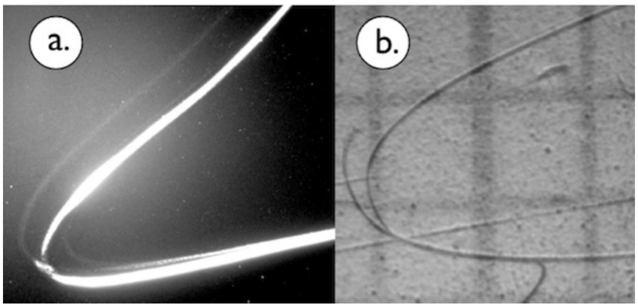

Figure 5. (a) Fredericks track. (b) Priem et al. track. On both tracks, parabolic curvature and splitting are seen.

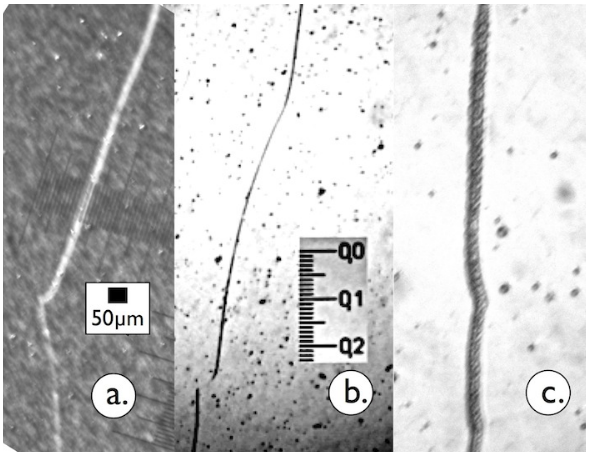

Figure 6. Tracks a and b are classic 2-tailed vertexes with convex curvature. The curved part of track b is difficult to see, but appears to be parabolic. Track a was measured to be parabolic. (a) Fredericks track in Kodak Kodalith type III film. (b) Bardout et al. track in Kodak Industrex MX125 (double-sided) film. (c) Related Lochak "laboratory" tracklochak.web showing regular periodic structure.

Urutskoev et al. Of primary interest are photographic observations of *parabolic tracks* (not noted as such in their work), tracks with regular periodic structure as in Urutskoev et al. [2] and tracks with random or "irregular" structure. Each of these track types correspond to a specific track type in our study.

2.6. Bardout et al.

Bardout et al. [7] reported on photographic results from an expedition to the North Pole where Lochak's prediction regarding the detection of monopoles traveling from the sun to the earth was tested. Three tracks, exposed on Kodak Industrex MX125, are shown. The authors note that the tracks are similar to those detected in Urutskoev et al. Large-angle deflections are seen in very long tracks with regular periodic [a] [19] internal structure. Tracks a and b in Fig. 6 are consistent with *two-tailed vertexes* shown in Section 3.11.

2.7. Matsumoto

Matsumoto [12,13] performed electrolysis experiments in glass cells wit platinum anodes and palladium cathodes in a solution of ordinary H_2O with 0.5 M K_2CO_3. The experiments were instrumented with 50 and 100 μm MA-7B Fuji Film nuclear emulsions. Matsumoto generated a series of images apparently distinct from other studies considered here, but similarities to our group of studies is seen in track structure and correlation.

The track structure in the *star* image in Fig. 7 of Matsumoto [13] shows distinct circular periodic structure similar to images of Fredericks [1]. In Matsumoto's *ring* images, nearly perfectly circular ring images are shown. Rotational symmetry is exhibited in images exposed on adjacent facing double-sided plates in Figs. 19 and 20. This type of symmetry appears to be related to observations by Ivoilov [4,5] and Fredericks [1]. Matsumoto attributed his unique images to ball lightning and microscopic black and white holes.

---

[a] G. Lochak, personal communication.

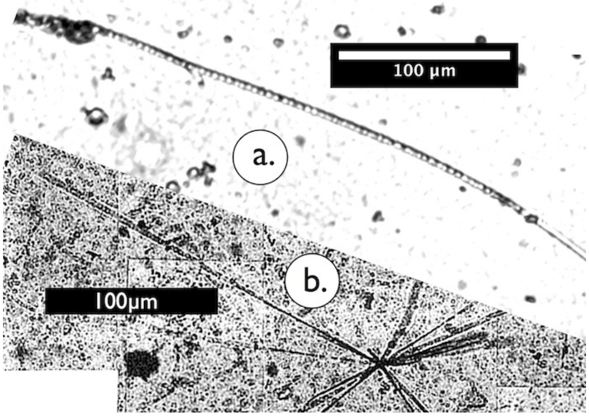

Figure 7. Both tracks exhibit regular periodic “circles” in tracks. (a) Fredericks track (b) Matsumoto *star* in Fujifilm MA-7B nuclear emulsion.

2.8. Fredericks

These experiments exposed human fingertips to emulsions for 2–30 min and many experiments were carried out with an applied magnetic field perpendicular to the plane of the emulsion. The effect was shown to occur independently of a dielectric isolator included between the fingertips and the photographic emulsion surface [1]. Film type, amplification and development were analyzed. The tracks were observed on six different film types using two different types of photographic development [1].

A special photographic amplification technique was employed, making possible a higher level of photographic sensitivity specifically for line and dot images, greatly enhancing track visibility [1].

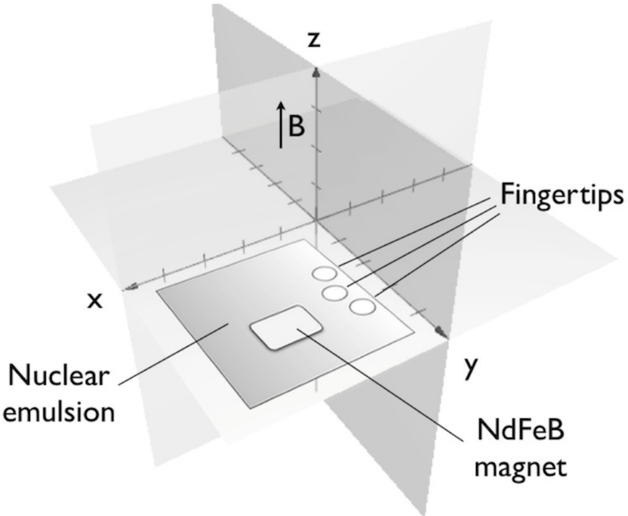

Figure 8. Experimental setup of Fredericks showing M3, a neodymium permanent magnet.

Track observations [1] included parabolic curvature in applied magnetic fields, strong correlation, regular periodic structure, numerous large-angle deflections, random motion, and correlated random motion.

2.9. Commentary

Bardout [7] and particularly Fredericks [1] stand out from the other studies due to the absence of any electrical explosions, discharges, their by-products or applied electric fields, which constitute in [2–6, 8–13] the assumed source (or catalyst) of the phenomena. It is remarkable with these differences in exposure conditions that Fredericks duplicates virtually all observed track types. The only track types specifically *not observed* were the Ivoilov [4,5] "chirals" and the Matsumoto [13] "rings." A relationship between all of the tracks in the present study is clearly established indicating a commonality of exposure, the mechanism of which is not clear. The studies in [2–9] and analyses by Lochaklochak.equation,lochak.lenr envision the *Lochak* monopole as responsible for these particle tracks, but without solid support for this hypothesis.

3. Particle Properties

3.1. Image formation

In the following we refer to the state of photographic development of the track image and the central track image in tracks with a border effect. Track images are formed on photographic film in one of three ways:

1. *Type 1.* Excitation of of the AgBr crystals via either ionization or light causing track images via developed AgBr crystals. This is referred to as "positive" or "normal exposure." This type of track image is seen on the emulsion as a dark line on a lighter background.
2. *Type 2.* Bleaching of the AgBr crystals via an unknown mechanism causing track images via the absence of developed crystals. This is referred to as "reversal" or "bleaching." This type of track image is seen on the emulsion as a white line on a darker background.
3. *Type 3.* Direct action on the gelatin and possibly the plastic base producing track images via the removal and/or deformation of plastic or gelatin. This is referred to as "evaporated." This category of track images can be clear, but visible due to the refraction of light and can also be accompanied by developed silver in the repeating patterns.

Type 3 image formation is unusual in the area of photographic science and indicates a non-standard action occurring in the emulsion. Regular periodic structures are seen on photographic emulsions, Pd cathodes, and MDS semiconductor surfaces. A connection may exist between the elevated energies required to expose tracks on metal or semiconductor surfaces and "evaporated" track images in the plastic base of emulsions.

3.2. Lines and dots

The tracks appear as dots and lines. Dots indicate angles of incidence of particles more perpendicular to the plane of the emulsion. Lines indicate angles of incidence more parallel to the plane of the emulsion. Dots appear in various sizes, generally corresponding to track cross section dimensions. Some dots are substantially larger and some are "smeared." Some of these smeared tracks correspond to the *comet* tracks of Urutskoev et al. (see Fig. 16a. in [2]).

3.3. Track width

Our track width measurements can be compared with studies by Urutskoev [2] and Iviolov [4] where 5–30 μm track widths were measured. They found that track width decreased as detector distance from the source was increased.

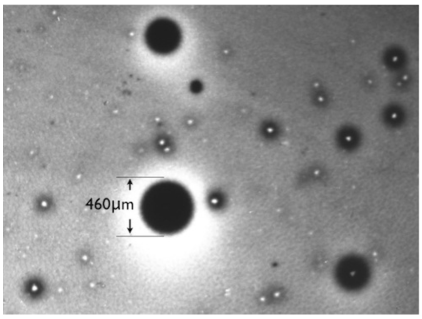

Figure 9. Micrograph at 25× of dots. Note the internal structure of all-black dots and dots with white centers. Kodak type NTB3 10 μm emulsion.

Track width has been measured to have a range of at least 5–110 μm (horizontal) and 5–460 μm (vertical).

In our studies, tracks have been observed with and without image amplification. In exposures with amplification, the inner track is surrounded by an edge, fringe or halo effect on both sides of the track, which increases the visibility of these images [1].

3.4. Track length

Figure 10 shows a 69 mm track. It is not clear if tracks have begun or ended in the emulsion. It is not immediately clear in what direction particles producing these tracks traveled although it may be possible to find track direction and charge by analyzing correlated pairs and groups of tracks in magnetic fields, which is the subject of future work.

There is tapering on both ends of the 69 mm track. Since a specific type of tapering is expected for monopoles [22], it may be of interest to analyze this tapering in detail.

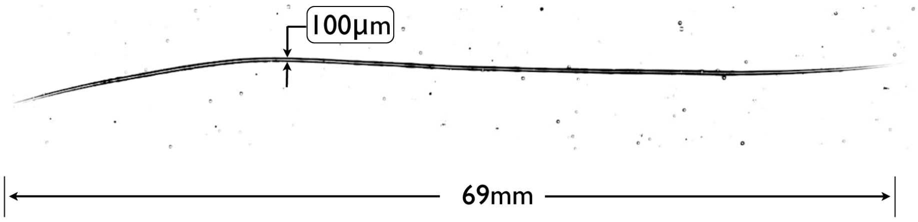

Figure 10. *69 mm* track in Kodak NTB3 type emulsion. The track width average is 91 μm.

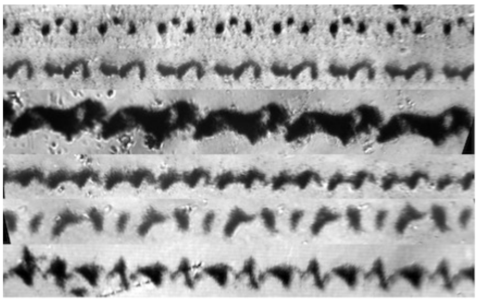

Figure 11. Different types of positive regular periodic structure tracks in Polychrome Litho film, no pre-exposure, developed with constant agitation.

3.5. Regular periodic structure

Under magnification, tracks with regular periodic structure are seen. Certain tracks have a completely periodic structure whereas other tracks change in mid-track from wholly saturated tracks to periodic tracks (and possibly back to wholly saturated). Some totally saturated tracks show underlying periodic structure suggesting an intrinsic periodic track structure.

Under low magnification, regular periodic structure tracks bear a closer resemblance to conventional charged particle tracks. These tracks however possess a much greater track length than conventional particles *and* a regular periodic structure as opposed to the random nature [23] of grain patterns in conventional nuclear track studies. Under higher magnification, regular periodic structure tracks show specific repeated patterns. Others have called these patterns “beaded necklaces” and “caterpillars.” The regular periodic structure is suggestive of helical trajectories or trajectories with some type of periodic, or possibly chaotic, spin component.

3.6. Reversed tracks

Tracks can appear as either exposure (black, positive) or bleaching (white, reversed) The percentage of positive tracks versus reversed tracks has not been measured.

“Reversed" tracks appear to have formed due to a process that tears down or bleaches the latent image rather than

Figure 12. Different types of “evaporated” regular periodic structure tracks in Polychrome Litho film, no pre-exposure, developed with constant agitation.

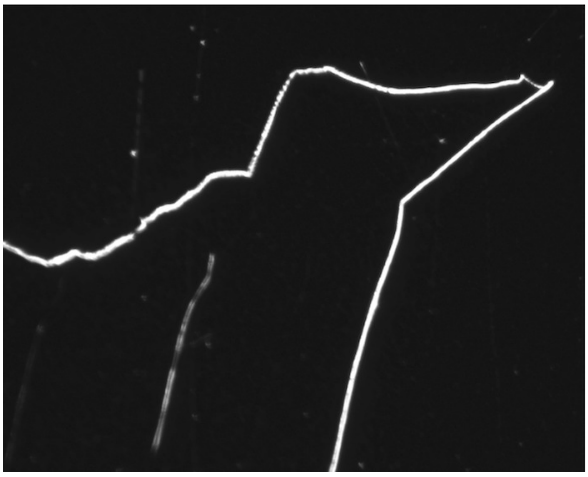

Figure 13. Photomicrograph of single track from Fig. 24, "Vector Swarm."

a process that creates a developable latent image. Other examples of such tracks are shown in Figs. 14 and 24. In photographic processes where this type of bleaching occurs, the mechanism is probably a reversal effect caused by rehalogenation of the latent image. When both positive and reversed tracks are observed on the same exposure, the different tracks may be due to particles with different energy levels.

3.7. Track curvature

Photographic nuclear track studies commonly require magnetic fields at least 100 times greater than those used in bubble chambers to produce measurable curvature in a photographic emulsion. In fact photographic emulsions are generally not used to observe charged particle curvature in applied magnetic fields. The observations considered here resemble tracks in bubble chambers more than tracks in photographic emulsions. This indicates highly penetrating particles and non-standard track exposure mechanisms.

In virtually all exposures where a perpendicular magnetic field was applied with respect to the plane of the emulsion, track curvature is observed to be *exactly parabolic*. See also Figs.23,26 and 28. Curve fitting in Section 5.1 shows parabolic curvature with high confidence. Particle momentum is estimated from track curvature in Section 5.2.

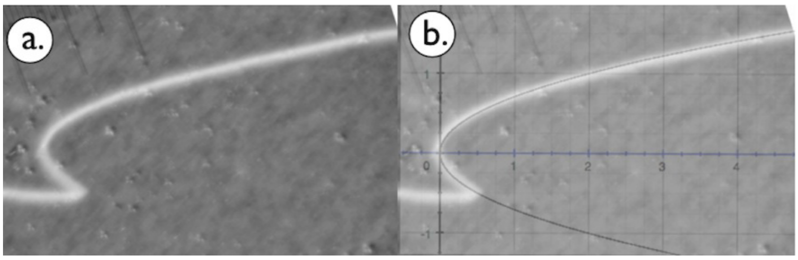

Figure 14. *Hook*, Curved track in Kodalith type III film. Applied magnetic field of permanent magnet M3. (a) Raw track. (b) Graph of parabola $x = y^2$ overlaid on track.

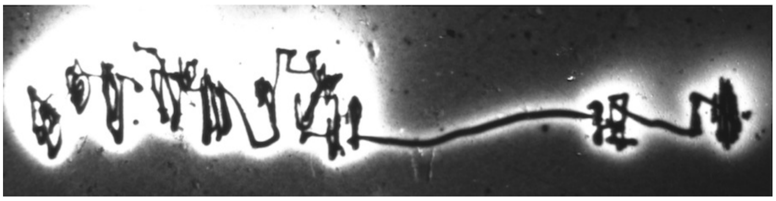

Figure 15. *squiggle2* Random motion type tracks in Kodak NTB3 10 μ nuclear emulsion. Extreme large angle deflections and continuous smooth curvature are shown. Minimum track width = 10 μm, track linear measure = 4.3mm.

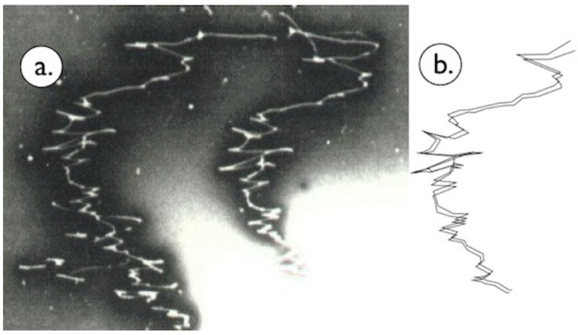

Figure 16. (a) Correlated random motion trajectories. Kodak 10 μm NTB3 emulsion. (b) Using a graphics editor, the tracks were traced from the original. The tracks when superimposed upon each other reveal very similar though not quite identical structure.

3.8. Random motion tracks

Large-angle deflections are very rare in photographic emulsions.powell In these tracks, with linear measure up to ~ 5 mm, large-angle deflections are numerous.

3.9. Correlated tracks

Correlated trajectories and correlated random motion trajectories have not been seen in any standard photographic nuclear track studies done to date.

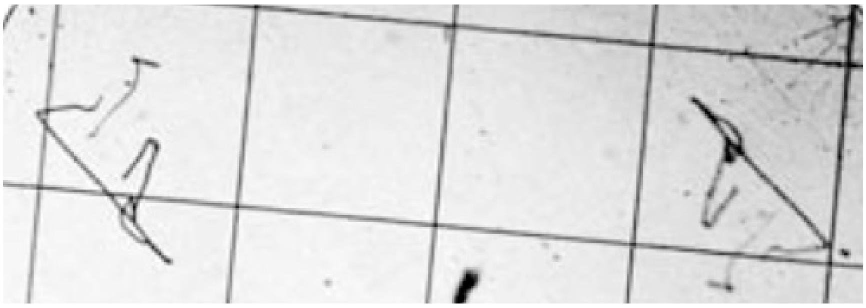

Figure 17. Ivoilov “chiral”" tracks in original orientation

Figure 18. Ivoilov "chiral" tracks where right track was flipped horizontally and vertically and overlaid on left track. Note correspondence on main track and misalignment on other tracks. Compare with Fredericks tracks in Fig. 16 where two correlated tracks are overlaid.

In images shown by Ivoilov [4] and analyzed by Lochak [17], tracks exhibit rotational symmetry. Ivoilov used glass, Al, and monocrystalline Ge and Si as *reflectors* behind double-sided X-ray film. These images can be overlaid with only minor differences between them, see Fig. 18.

In conjunction with Georges Lochak, Ivoilov proposed that the observations were due to the *Lochak* monopole [17] and further that the pairs of detected particles were *chirally symmetric*. Figure 19 in Matsumoto [13] has characteristics of Ivoilov correlations in that similar images are captured on two pieces of film, but the correlation may

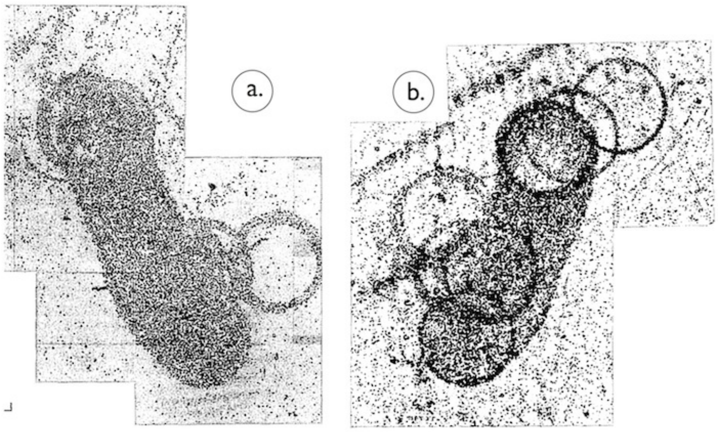

Figure 19. Matsumoto correlated tracks as presented in original publication.

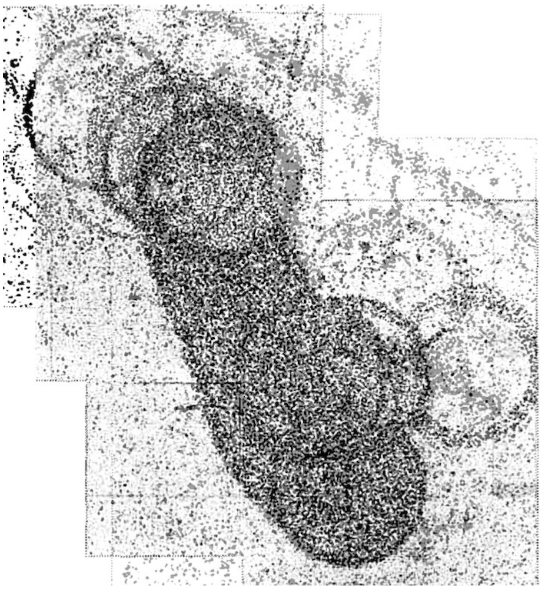

Figure 20. Matsumoto correlated tracks overlaid. The shape of the image and certain ring positions correspond.

be more closely related to translational type symmetry as in the Fredericks images rather than a rotational symmetry as in studies of Ivoilov.

Correlation of these particle tracks is the rule and not the exception. Particles often travel in pairs or groups, shown in the analysis as tracks with a very high degree of correlation, even in the case of extremely complex trajectories. Particles found to be correlated throughout each of their trajectories appear to be connected. It is tempting to view this condition as a correlated particle experiment with the correlated tracks a visualization of entanglement.

In addition to observations of tracks in pairs, tracks in groups are also seen. If a permanent magnet is used in the experiment, it is likely that correlated groups of tracks will appear. Effects due to a non-uniform applied magnetic field are seen in Figs. 21–24.

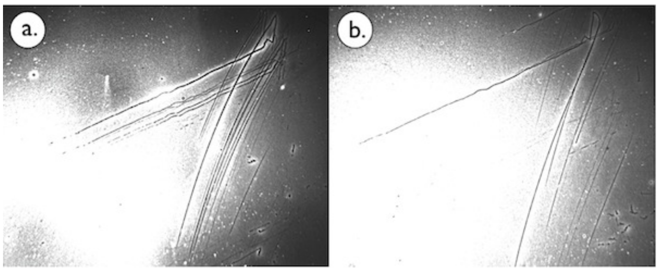

Figure 21. *Bobby pins* raw tracks in Kodak NTB3 10 μm emulsion. Tracks a and b are separated by a few millimeters on the film. Tracks have many of the same features, except that track a has a loop, i.e., the track crosses itself whereas track b does not. These tracks are correlated in position extremely well until the critical region (segment 19 in Fig. 22) when track a has a large angle deflection to the left and track b has a corresponding smoothly curving deflection to the right. Susceptibility to magnetic deflection appears to be overwhelming or twisting the correlation.

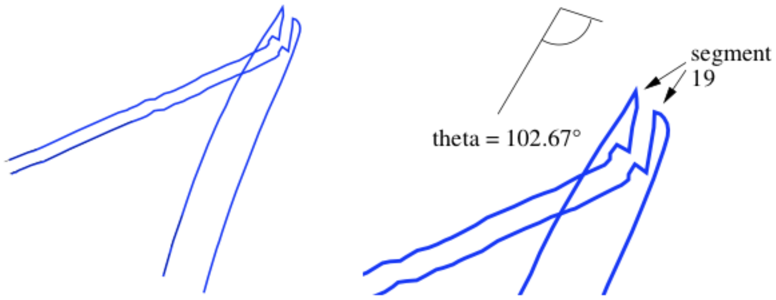

Figure 22. Digitized tracks from Fig. fig:bobby-pins

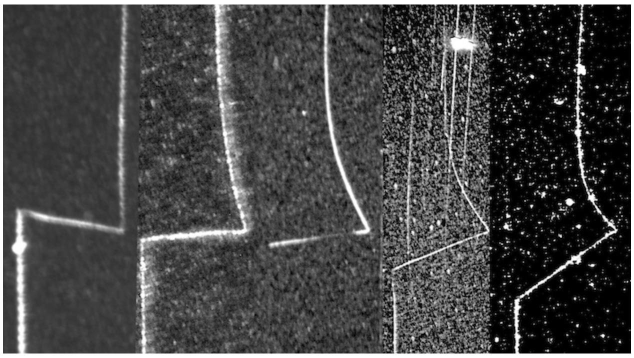

Figure 23. Progressive curvature seen in a correlated group of tracks from the same exposure.

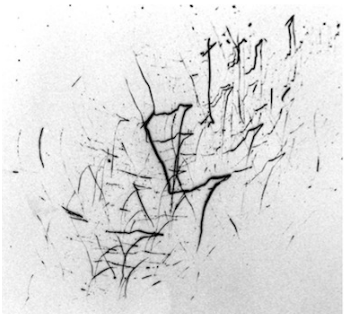

Figure 24. *Vector Swarm* Group correlation of tracks including random motion components. These tracks do not line up when overlaid. They change form with location, apparently due to relative position in the applied non-uniform magnetic field. A large number of the tracks in this exposure are correlated. A measure of corresponding line segments of matching groups of tracks reveals a macroscopic “central force,” which will be the subject of future work.

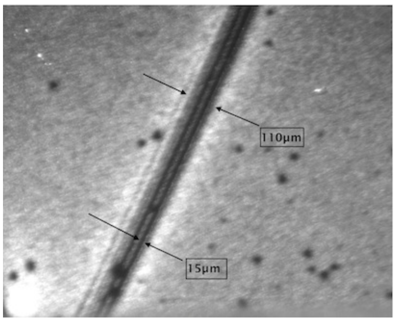

Figure 25. *Sub Tracks Detail* Micrograph at 45x magnification showing sub-track structure of the track bundle.

Turning to Fig. 24, a very interesting region of track exposures was found. As with certain of the previous exposures, correlation of track images was seen. But instead of an entire group of carbon copies, we see a field of complex track structures with the same set of line segments, but each set of line segments has its own unique individual geometric transformation.

The group of track exposures appears to be subject to a *geometric center* related to magnetic field strength. This may reconcile observations of rotational and translational symmetry as translations with respect to electromagnetic fields. Figure 24 shows conclusive evidence of a real particle effect and what can only be a group of "identical" correlated particles going through a series of quantum transitions in a non-uniform magnetic field.

3.10. Track bundles

Tracks with internal structure and large measured widths are observed to apparently split in places. In light of this, it is postulated that these particles can travel in bundles and that they can undergo various transitions such as splitting into correlated twins or swarms. Lower energy particles may be the result of the splitting of the higher energy bundle.

The result of Urutskoev et al. where they observed larger tracks closer to the source and smaller tracks at a further distance from the source may indicate that decay and splitting occurs for these particles over a one meter distance reducing a 30–5 μm track. It is noted that Urutskoev et al. [2] mentioned the idea that certain of the "ink blot" style tracks may be modeled as particle "clusters." If the particles are traveling in bundles, a computation of particle energy or mass needs correction with respect to the base particle mass. One way to do this correction is shown in Section 4.

3.11. Vertexes

In the set of all tracks, several types of vertexes are observed, but one type of vertex stands out. This is the two-tailed vertex. Of particular interest is where one of the track segments is curved and the other is straight. These structures are either singular or infrequent in long tracks. They very often have similar features and are seen in either *concave* or *convex* configurations. These types of vertexes have been observed also in other studies [2–5,7–11]. Eighteen of these *two-tailed* tracks were selected for track curvature and energy deposition measurements and are the subject of analysis in Sections 5.2–7.

4. ζ-Correction

Based on the observation that the particles are traveling in bundles, a correction factor is created

$$\zeta = \frac{w}{w_0}, \tag{1}$$

where w_0 is the actual smallest track width measured for a single particle and w is the measured track width of a given track. For this study $w_0 = 5\ \mu m.$ ζ was measured and utilized in computations for a number of tracks including the 18 sample tracks [1].

5. Momentum

Tracks appear in photographic emulsions much like they would be expected to appear in a bubble chamber, often with long (>cm) track lengths and smooth curvature in magnetic fields, so it is straightforward to make track curvature measurements on the tracks as is done for bubble chamber photographs. Initially it was thought that the curvature of these tracks was circular. (This error was also made in [6].) Using an overlay of a $y = x^2$ parabola, the tracks can be seen visually in Figs. 14,26 and 28 to be parabolic. Fitting curves to the 18 tracks, in Section 5.1, confirms this with excellent fits over the sample of tracks.

5.1. Parabolic curvature

In Fig. 27, parabolic curvature can occur for

(1) electrically charged particles in an applied *electric* field,
(2) magnetically charged particles in an applied magnetic field.

There is no applied electric field in any of our exposures and the curvature is observed in the x, y plane instead of *the* x, z *plane* where parabolic curvature is expected for a particle with magnetic charge.

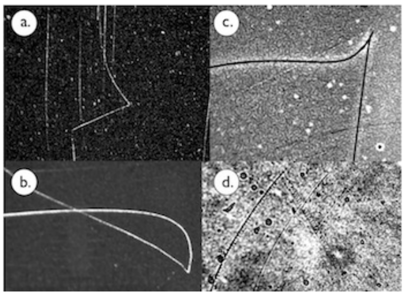

Figure 26. (a) One of a series of tracks with progressive curvature. Concave reversed track. Exact fit to parabola. (b) The classic vertex form. Convex positive track. Exact fit to parabola. (c) The concave form of the vertex. Reversed track. Exact fit to parabola. (d) Small convex form track using 400× magnification. Evaporated track. Exact fit to parabola.

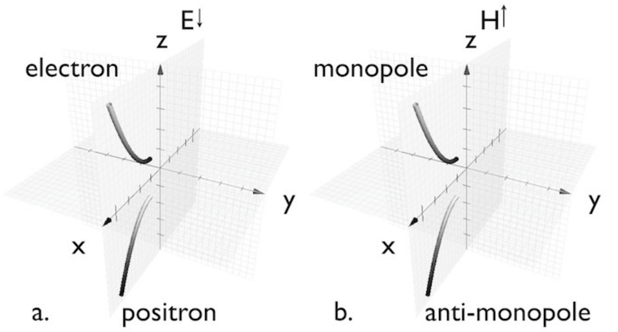

Figure 27. (a) An electric field, E is applied along the z-axis in the -z direction. Due to the E field, electrons curve upward and positrons curve downward in a parabola in the x, z plane. (b) A magnetic field, $\mathbf{H}$ is applied along the z-axis in the +z direction. Due to the $\mathbf{H}$ field, magnetic monopoles curve upward and anti-monopoles curve downward in the x, z plane.

The track x, y data for *bobby pins*, the example track, was digitized using the ImageJ package and fit to Eq. (2), of the generalized quadratic equations

$$y = \frac{\sqrt{-b + (b^2 - 4a(c - x))}}{2/a} \tag{2}$$

$$y = \frac{\sqrt{-b + (b^2 - 4a(c - x))}}{2/a} + \mathrm{o} \tag{3}$$

$$y = \frac{\sqrt{-b + (b^2 - 4a(c - x)))}}{2/a}, \quad \text{where}$$

$$y = \frac{x}{y} + \mathrm{o}, \tag{4}$$

which all describe parabolas, where a, b and c are coefficients and o is an offset. The fit target was the lowest sum of absolute square error. Lower numbers for both R-squared and RMSE means a better fit. The mean goodness-of-fit of the generalized quadratic equations to the plotted data is $\overline{R}^2 = 0.998$ [1].

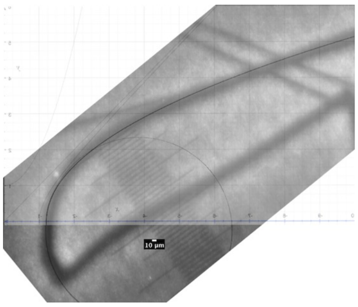

Figure 28. Track 4. *Bobby pins* was visually fit in this image to the parabola $y = x^2$ and a circle for comparison.

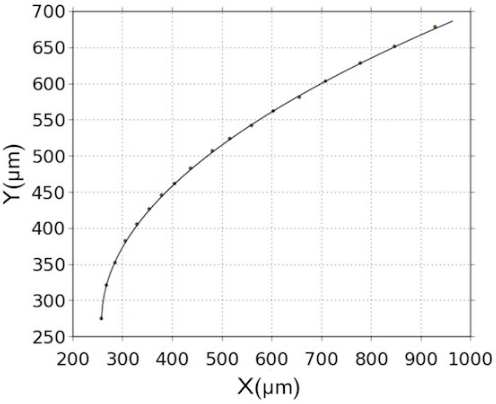

Figure 29. Track 4. *Bobby pins* fit to general quadratic equation (2).

Overall, this sample of tracks (and others in the study) show a nearly perfect fit to quadratic equations and therefore to parabolic trajectories. Parabolic curvature in the x, z plane with an applied magnetic field on the z-axis in searches for monopoles [25,26] is considered a strong signature for a magnetically charged particle [25, 27–29] since *parabolic curvature is unique*. But parabolic curvature is observed in the x, y plane with an applied magnetic field on the z-axis. A solution to this problem is shown in Section 7.

5.2. Momentum estimates

Momentum was estimated using 18 curved segments in two-tailed tracks using the following criteria:

(1) must be a two-tailed track with a vertex,
(2) one tail must have smooth curvature,
(3) must have a twin track,
(4) magnetic field strength is known.

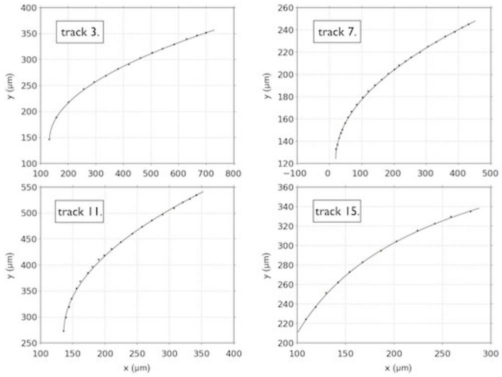

Figure 30. Tracks 3, 7, 11 and 15 curve fits to general quadratic equations (2)–(4) showing graphical fits to parabolas.

The computation below uses the kinetic energy, E_k computed with the general energy loss model in Section 6.1. For a magnetically charged particle, the analogous formula for parabolic electrostatic deflection for a particle traveling in the x direction in the x, y plane is used where

$$y = \frac{e|\mathcal{E}|x^2}{2mv_x^2}. \tag{5}$$

Substituting B, the magnetic field strength for $\mathcal{E}$, the electric field strength and $g = g_\mathrm{D} = (137/2)e$ (Dirac case) or $g = -e$ (Recami-Mignani [30] case), magnetic charge for e, electric charge, becomes

$$y = \frac{g|B|x^2}{2mv_x^2}, \tag{6}$$

where $mv = p$ and $v/c = \beta = pc/E$ where E is energy, v the velocity and p is the momentum. In natural units (where $c = 1$) momentum is given by

$$p_i = \sqrt{\frac{g|B|x^2}{2y/E}} \tag{7}$$

where p_i is the ith computed momentum value using known values for x, y and E in Eq. (7). Average momentum, $\overline{p}$ is estimated using

$$\overline{p} = \frac{1}{n}\sum_{i=1}^{n} p_i \tag{8}$$

6. Energy Loss

The energy loss in the emulsion is computed based on the number of developed (or bleached) AgBr grains in a cylindrical track [11]. The tracks are observed in the gelatin, between the gelatin/air interface and the gelatin/plastic base interface. This can be verified by viewing track sharp focus at different depths between these interfaces using a microscope at 100× (or more) magnification. There is no concrete idea of the mechanism of track formation due to either radiative or ionization mechanisms, so a general model of energy loss based on deposited energy will be used.

6.1. Generalized model

Katz and Kobetich [31] show that 63% of grains in an emulsion are developed (or bleached) when the energy is between 230 and 400 eV/grain. For our purposes here, it is estimated that ~90% of grains would be developed at a minimum of ~600 eV/grain producing a saturated track after our uniform pre-exposure energy of ~150 eV/grain.

In this model a track exposure of 600 eV/grain creates a saturated track. This is a preliminary simplified model of energy level per grain where it is assumed that energy loss is the same at all values of β and energy loss is based on ionization. Adjusting the value for eV/grain can accommodate other energy loss models such as radiative models. This can be also be improved in the future to better reflect known energy losses at different values of β and by including various energy loss levels.

Our example track is 1.33 cm and comprised of [1]

$$(1.15 \times 10^8 \text{ grains})(600 \text{ eV/grain}) = 6.9 \times 10^{10} \text{ eV}, \tag{9}$$

Table 1. Linear stopping power based on the general model, measured values of number of grains, N_{grains} and track length, L for sample tracks.

Track	cS (GeV/cm)	N_{grains}	L (cm)
"69 mm" fig:69mm	1051.0	1.2×10^{10}	6.90
"67 mm"	467.1	5.2×10^{9}	6.74
"hyper"	168.2	8.7×10^{8}	3.10
"short rev"	116.8	1.2×10^{8}	0.61
"rev caterpillar"	81.1	1.6×10^{7}	0.12
"bobby pins"	51.9	1.2×10^{8}	1.33
"curve swarm"	29.2	1.7×10^{7}	0.35
"birds"	13.0	5.2×10^{6}	0.24

and in general energy loss per unit path or linear stopping power is

$$\begin{aligned} S_{\text{linear}} &= \frac{\mathrm{d}E}{\mathrm{d}x} = \frac{6.9 \times 10^{10}\ \text{eV}}{1.33\ \text{cm}} = 5.187 \times 10^{10}\ \text{eV/cm} \\ &= 51.87\ \text{GeV/cm}, \end{aligned} \tag{10}$$

and with density, ρ of AgBr photographic emulsions at 3.82 g/cm^3, mass stopping power is

$$\begin{aligned} S_{\text{mass}} &= \frac{\mathrm{d}E/\mathrm{d}x}{\rho} = \frac{5.187 \times 10^{10}\ \text{eV/cm}}{3.82\ \text{g/cm}^3} \\ &= 1.36 \times 10^{10}\ \text{eV}\,\text{cm}^2/\text{g} \\ &= 13.6\ \text{GeV}\,\text{cm}^2/\text{g}. \end{aligned} \tag{11}$$

7. Superluminal Lorentz Transformation

The transformation from bradyonic (slower-than-light) inertial frames to tachyonic inertial frames allows us to shift between timelike and spacelike objects. The superluminal Lorentz transformation (SLT) [30,33,34] extends the special theory of relativity to superluminal frames and observers. Most importantly for our purposes, the SLT makes possible the interpretation of experimental data where superluminal objects are observed in subluminal frames.

The SLT is required to make sense out of observations made of superluminal objects from frame f' in the subliminal laboratory frame f.

7.1. Energy–momentum

Measured values of kinetic energy and momentum for our 18 tracks plotted on a graph in Fig. 31 fall in the area for $v > c$ particles. Measured values for kinetic energy, E_{k} and momentum, p are compared with known particles, i.e. electrons, protons and photons on this graph. Values for the Recami–Mignani model are shown here. Values for the Dirac model are shown in [1].

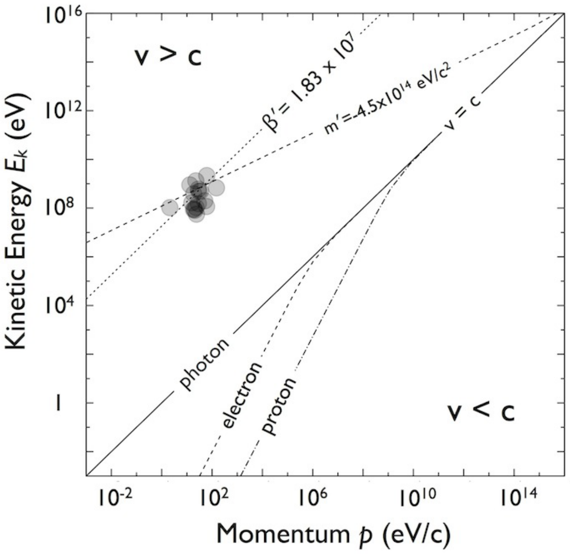

Figure 31. A Recami–Mignani tachyon monopole with monopole charge, $g = -e$ (in Gaussian units). Measured values for momentum and kinetic energy are clustered in the *faster-than-light* ($v > c$) area of the graph with a mass contour line computed with Eq. (17) intersecting the peak mass value of $|m| = 4.5 \times 10^5$ GeV/c^2. The velocity contour line intersects the SLT β value, $1/\overline{\beta} = \overline{\beta}'$ for our 18 tracks. Note also that as the SLT transforms $p' \rightleftarrows E_\mathrm{k}$, coordinate axes are reversed above $v = c$. Graph concept after Fraundorf [35].

Mass of particle tracks is estimated by inserting measured values of kinetic energy, E_k and momentum, p into the relativistic energy–momentum equation

$$c^2p^2 = E_\mathrm{k}^2 + 2E_\mathrm{k}mc^2 \tag{12}$$

solving for mass,

$$m = \frac{p^2c^2 - E_\mathrm{k}^2}{2E_\mathrm{k}c^2} \tag{13}$$

or, in natural units with $c = 1$

$$m = \frac{p^2 - E_\mathrm{k}^2}{2E_\mathrm{k}}. \tag{14}$$

This computation yields an average mass value of $|\overline{m}| = 227.58$ MeV/c^2 at an average velocity of $\overline{\beta} = 1.34\times10^{-6}$. The mass and velocity contours for the standard computation using Eq.(14) intersect in the wrong half (the $v < c$ half) of the graph and E_k is off by twelve orders of magnitude. The lack of agreement between the raw plotted data and mass computed using Eq. (14) inclines us to reject this particle mass result.

To estimate a *tachyon mass* the observables E_k and p need to be transformed from frame f to frame f' using an SLT of Eq. (14)

$$m' = -\frac{p'^2 - E_\mathrm{k}'^2}{2E_\mathrm{k}'}, \tag{15}$$

where the values of E and p are interchanged like $E'_\mathrm{k} = p$ and $p' = E_\mathrm{k}$ and the sign changes [1]. $\beta = p/E$ is transformed with an SLT as $\beta' = 1/\beta$.

Mass contours are found using

$$p = \sqrt{E_\mathrm{k}^2 + 2E_\mathrm{k} m} \tag{16}$$

for $v < c$ given values of m and E_k, and

$$p' = \sqrt{E_\mathrm{k}'^2 + 2E'_\mathrm{k} m'} \tag{17}$$

for $v > c$, given values of m' and E'_k.

Using Eq. (15) for Recami–Mignani tachyon monopoles gives $|\overline{m}'| = 7.29 \times 10^6$ GeV/c^2 and $\overline{\beta}' = 1.83 \times 10^7$. This mass estimate should be taken as a lower limit of particle mass as (we assume) less than the actual particle kinetic energy is deposited in the track.

Figure 31 features contour lines for both velocity and mass. While the "raw" E_k and p values are directly plotted on the graph, the contour lines β' and m' on the upper $v > c$ half of the graph were found using a superluminal Lorentz transformation. Since the SLT is a special transformation *only applied in the case of superluminal particles*, this corroborates the identification of this particle as superluminal.

The estimate of particle mass was made based on a mass contour line intersecting with the cluster of data points. The peak mass value of $|m'| = 4.5 \times 10^5$ GeV/c^2 for Recami–Mignani tachyon monopoles (see Ref. [1] was inserted into Eq. (17) for a range of energy and momentum values and plotted as the dashed mass contour line intersecting the cluster of points in Fig. 31. This agreement between the raw plotted E_k and p values, the SLT peak mass, m' computed with Eq. (15), and velocity, $\beta' = 1/\beta$ intersecting as contours, constitutes an independent check of the data.

The measured kinetic energy value depends on the estimate of energy loss per grain that was used in the computation. In the general model computation, a 600 eV/grain base energy was used with an additional assumption of 150 eV/grain for the supplemental pre-exposure energy. If a base energy of 50 eV/grain is used, putting the total energy per grain at 200 eV, which is below the minimum value (for 63% of grains to be developed) of 230 eV/grain [31], the minimum kinetic energy value is still well above 10^4 eV and still above the $v = c$ contour line.

Measured average momentum depends on Eq. (7), the measured kinetic energy and the computed value of the magnetic field. The average momentum values on the plot in Fig. 31 are over three orders of magnitude (eV/c) from the $v = c$ line in the case of the Recami–Mignani tachyon monopole [36].[b]

7.2. Electromagnetic field

Parabolic curvature in magnetic fields as shown in section section:parabolic-curvature is expected of magnetic monopoles, however the curvature is seen (paradoxically) in the x, y plane instead of the x, z plane as expected. The orientation of the magnetic field in our experiments (Fig. 8) is clearly perpendicular to the x, y plane.

---

[b] Assuming circular curvature in the Dirac model we found $\overline{p} \simeq 519$ eV/c.

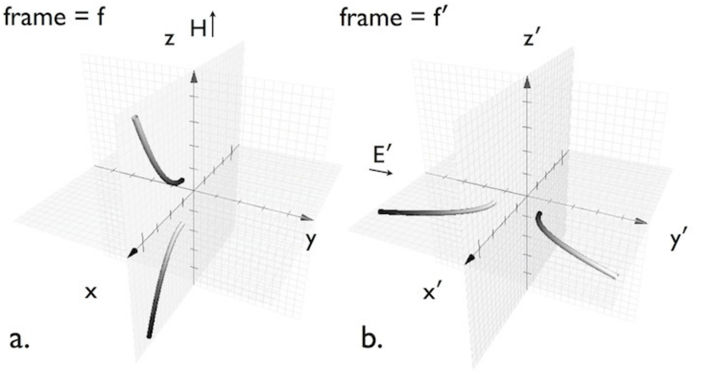

Figure 32. (a) Frame f where a magnetic field applied parallel to the z-axis is expected to cause parabolic curvature for magnetically charged bradyons in the x, z plane. (b) For *tachyons*, parabolic curvature occurs for electrically charged tachyons in the frame f' in the x', y' plane. For observables connected with electromagnetic fields, frame f' is related to frame f by a superluminal Lorentz transformation where $\mathbf{H}_z = \mathbf{E}'_y$.

Recami and Mignani show [32,33] the electrically charged tachyon in the bradyonic frame as possessing magnetic charge $g = -e$ (in Gaussian units) (as opposed to the "standard" $g = g_{\mathrm{D}} = e(137/2)$). This theory is symmetric between subluminal and superluminal frames with $v = c$ the partition between frames.

Superluminal particles in f' with electric charge behave as magnetic monopoles in our subluminal frame f, but to make sense of the observables in f we need to transform as $f \xrightarrow{\mathrm{SLT}} f'$ [30,33]. Since the velocity u, $(0 < u < c)$ of frame f differs from the velocity $U = c^2/u$, $(U > c)$ of frame f' as $U \to \pm\infty$, we use the *transcendent SLT* [30,33,37], recami.transcendent,recami.classical,recami.applications which rotates coordinate axes by either 90° or 270° as well as swapping $\mathbf{E}$ and $\mathbf{H}$.

By using this transformation we rectify the paradox of parabolic particle tracks observed in the plane perpendicular to the applied magnetic field. Thus it is possible to interpret our parabolic tracks in photographic emulsions as due to electrically charged tachyons. Measurement of the parabolic curvature of these tracks also importantly allowed us in Section 5.1 to estimate the particle momentum using Eq. (7).

7.3. Tachyon shape

Assuming that the tachyon has a spherical shape in its restframe, f', an SLT is applied to determine how the tachyon would appear to a subluminal observer in frame f. After application of the SLT, the tachyon shape becomes a *hyperbolic annulus* [33,38]. The intersection of this shape, orthogonal to the particle's motion is an annulus or a ring (or dot) comprised of the area between two concentric circles [39].[c]

This agrees with certain perpendicularly incident tracks seen in Fig. 9. This also coincides directly with some of the unusual track shapes (Figs. 19 and 35 shown in [13] studies and is of interest to replicate. Compare also with periodic circles in Fig. 7.

The intersection of the double hyperbolic annulus with a plane parallel to the tachyon motion appears as an x-shaped object as in Fig. 36a. This corresponds to a track in the plane of the emulsion. It is possible to simulate periodic tracks such as in Section 3.5 by constructing repeating conic sections as in Fig. 36b.

---

[c] See also Figs. 3, 5 and 6 of Ref. [38].

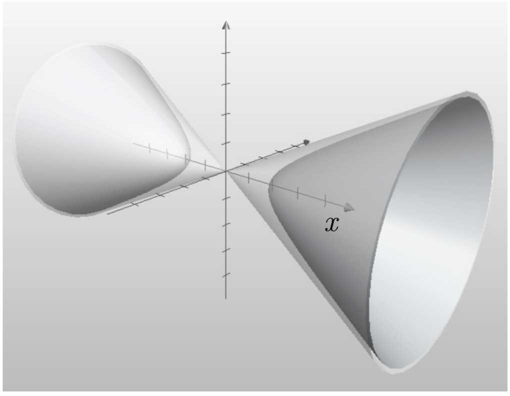

Figure 33. Shape of tachyon (between conic and hyperbolic surfaces) with motion in x direction after an SLT as a subluminal observer in frame f would see it.

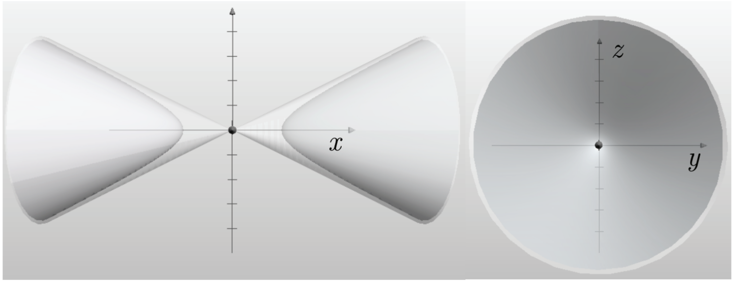

Figure 34. Top and end views of tachyon shape.

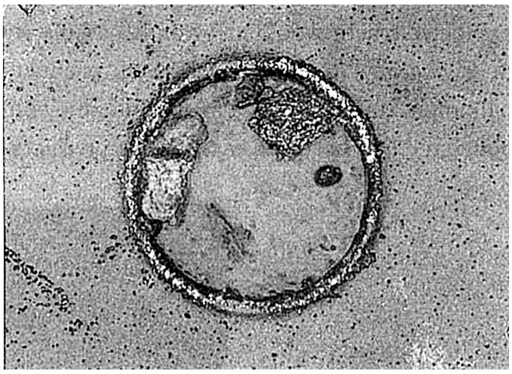

Figure 35. Ring track of Matsumoto

The horizontally incident tracks in this concept appear to be akin to a collective excitation and might be physically modeled by a series of tachyon creations and annihilations arising from *vacuum fluctuations* propogating in space [33]. See also Fig. 16 of Ref. [1] and Fig. 35 of [33].

7.4. Summary

We found values of E_k and p indicating superluminal particles. To find m and β consistent with the observables E_k and p, *an SLT was required.* Curvature of our sample tracks was found to be parabolic, indicating magnetic monopoles, but the plane of detection was perpendicular rather than parallel to the applied magnetic field. An SLT applied to the coordinate system shifts the $\mathbf{H}$ and $\mathbf{E}$ fields and rectifies the explanation of the particle as a tachyon monopole. Extending this analysis to certain particle tracks we find a possibility that tachyon shape, transformed using an SLT, may correspond with certain types of particle tracks.

8. Discussion

Analyzing the exposed area of a track in the emulsion Urutskoev and co-workers [2] estimated kinetic energy at $E\sim$700 MeV. This is one order of magnitude lower than the average non-ζ-corrected energy value for our 18 tracks of $E \simeq 1.7$ GeV, but much lower when compared with our longer (and thicker) tracks. Other tracks in Urutskoev and co-workers [2] and tracks in the other photographic studies [4–7,10,11] if examined for deposited energy (using ζ-correction) should all correspond within our limits.

Adamenko and Vysotskii [8,9] estimated an upper limit of kinetic energy at $E \sim -10^6$ GeV and particle mass at $\approx 10^{-23}$g ($\approx$ 560 GeV). Our peak mass values presented above fall above the 560 GeV value by two orders of magnitude. Our higest non-ζ-corrected energy values come in at 7.3×10^3 GeV, falling within the range below the upper limit of $E \sim -10^6$ GeV. Ivoilov [4] suggests that the particles may correspond to neutrinos of zero mass, which are monopoles [17] with a maximum value of $\sim$ 1 MeV. Our kinetic energy values are much greater than this and there is no agreement between our data and the Ivoilov energy data.

8.1. Further considerations

In the Recami–Mignani theory, the tachyon may be observed as a monopole in the ordinary subluminal laboratory frame. "Standard" monopole mass is estimated to be either on the order of the unification mass ($\approx 4\times10^{15}$ GeV)groom or, assuming the monopole has a radius equal to the classical electron radius, $m \approx 2.4$ GeV/c^2. Certain magnetic monopole searches have concentrated in the low to intermediate mass region [41] of 10^3 GeV/c^2 $< m_M <$ 10^{12} GeV/c^2. Our lower limit peak mass values of $|m| = 5.4 \times 10^4$ GeV/c^2 and $|m| = 4.5 \times 10^5$ GeV/c^2 are consistent with that range.

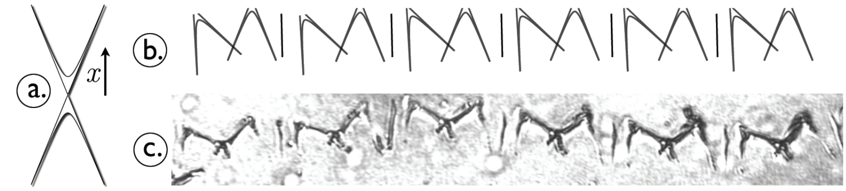

Figure 36. (a) Intersection of tachyon with plane parallel to particle motion on x axis. (b) Simulation of "M" components of track with periodic structure using conic sections. (c) Track from Fig. 4 exhibiting periodic structure.

The Recami–Mignani model however assumes a monopole charge of $g = -e$ (in Gaussian units) rather than the standard Dirac charge of $g = g_{\mathrm{D}} = (137/2)e$. For our purposes the difference in charge simply shifts the raw momentum and mass values lower by about an order of magnitude. Tachyons traveling as identical particles should behave as like charges that attract the same way as ordinary wires carrying electric current [38]. These tachyons could coalesce in bundles and split apart in applied electromagnetic fields.

In the model of Fried [42] where tachyons contribute to dark matter, tachyons are expected with masses on the order of 10^6–10^8 GeV. These tachyons are also expected to travel together over galactic distances in “lines” and “swarms.” Our lower limit mass estimate is in agreement with these values. Both of the above theoretical considerations fit with the observation of bundles and splitting shown in Section 3.10.

9. Conclusion

The analysis presented here suggests the detection of Recami–Mignani tachyon monopoles with a lower limit of $|m| \sim 4.5 \times 10^5$GeV/c^2 (or $|m| \sim 5.4 \times 10^6$GeV/c^2 in the case of Dirac tachyon monopoles) that can travel in bundles of “identical" particles with regular periodic trajectories and various modes, dependent on energy level. At lower energies, particles may go into random motion. Correlation of pairs and groups of these particles is observed frequently.

In Section 6 measured energy and momentum values for our sample tracks indicate superluminal particles. This result is supported by the requirement to transform the data using an SLT to yield consistent mass and velocity values. In Section 5 parabolic curvature is observed in an applied magnetic field as would be expected for a magnetic monopole, except that the parabolic curvature is in the x, y rather than the x, z plane. Parabolic curvature in the x, y plane *perpendicular* to an applied magnetic field suggests the detection of a magnetic monopole in our local frame, which as shown in Section 7 is how an electrically charged tachyon in a superluminal frame appears in the local frame.

Using tachyon shape derived using the SLT shows possible agreement with ring and periodic structure images which may be further associated with collective excitations or vacuum fluctuations. Further study of the image formation, energy deposition, curvature in magnetic fields, bundling, splitting, vertexes and correlation of these particles is indicated to get a clear picture of their properties.

Acknowledgments

The author thanks Leonid Urutskoev, Moses Fayngold, Matej Pavšič, Erasmo Recami, Anri Ruhkadze, Mark Davidson, Irina Savvatimova and Nikolay Ivoilov for helpful comments and kind interest.

References

[1] K.A. Fredericks, *Eng. Phys.* **6** (2013) 15; Eprint online (2013).
[2] L.I. Urutskoev, V.I. Liksonov and V.G. Tsinoev, *Ann. Fond. L. de Broglie* **27** (2002) 701; ArXiv Physics e-prints (2001), arXiv:physics/0101089.
[3] L.I. Urutskoev, *Ann. Fond. L. de Broglie* **29** (2004) 1149.
[4] N.G. Ivoilov, *Ann. Fond. L. de Broglie* **31** (2006) 115.
[5] N.G. Ivoilov and L.I. Urutskoev, *Ann. Fond. L. de Broglie* **29** (2004) 1177.
[6] D. Priem et al., *Ann. Fond. L. de Broglie* **34** (2009) 103.
[7] G. Bardout, G. Lochak and D. Fargueb, *Ann. Fond. L. de Broglie* **32** (2007) 551.
[8] V. Adamenko and V.I. Vysotskii, in *Proc. of the 14th Int. Conf. on Condensed Matter Nuclear Science and the 14th Int. Conf. on Cold Fusion (ICCF-14)*, 10–15 August 2008, Washington DC, D.J. Nagel and M.E. Melich (Eds.), New Energy Foundation Inc., 2008, p. 484.

[9] S.V. Adamenko and V.I. Vysotskii, A*nn. Fond. L. de Broglie* **33** (2008) 13.

[10] B. Rodionov and I. Savvatimova, in *12th Condensed Matter Nuclear Science*, Vol. 12 A. Takahashi, K.- I. Ota and Y. Iwamura (Eds.). 2006, pp. 421–429.

[11] I. Savvatimova and J. Dash, in *The 9th Int. Conf. on Cold Fusion, Condensed Matter Nuclear Science*, 2002. Tsinghua Univ., Beijing, China, Z.Z. Li (Eds.), Tsinghua Univ. Press, 2002.

[12] T. Matsumoto, *Fusion Technol.* **18** (1990) 356.

[13] T. Matsumoto, *Bulletin of the Faculty of Engineering,* Hokkaido Univ. No. 175 (1995), p. 73.

[14] E. Storms, *21st Century Sci. ang Technol. Winter*, 76 (2000).

[15] E. Storms, Student's Guide to Cold Fusion, revised (2012), lenr-canr.org.

[16] E. Storms, What is now known about cold fusion? (Ad- dendum to the Student's Guide) (2011), lenr-canr.org.

[17] G. Lochak, *Z. Naturforsch.* **A62** (2007) 231, arXiv:0801.2752 [quant-ph].

[18] D. Priem et al., *Ann. Fond. L. de Broglie* **33** (2008) 129.

[19] G. Lochak, personal communication.

[20] G. Lochak, Traces of monopoles observed in laboratory, (2013) lochak.com website.

[21] G. Lochak and L. Urutskoev, in Condensed Matter and Nuclear Science, *Proc. of the 11th Int. Conf. on Cold Fusion*, 31 October–5 November, Marseille, France, 2004, J. Biberian (Ed.), World Scientific, London, 2006, p. 421.

[22] [22] R. Katz and D.R. Parnell, *Phys. Rev.* **116** (1959) 236.

[23] T.E. Furtak and R. Katz, *Radiat. Effects* **11** (1971) 195; Eprint online (1971).

[24] C.F. Powell, *The Study of Elementary Particles by the Photographic Method*, Pergamon Press, London, 1959.

[25] W. Braunschweig et al., *Z. Phys. C* **38** (1988) 543, 10.1007/BF01624358.

[26] T. Gentile et al., *Phys. Rev. D* **35** (1987) 1081.

[27] A. Abulencia et al. (CDF Collaboration), *Phys. Rev. Lett.* **96** (2006) 201801.

[28] CDF (The CDF Collaboration), A direct search for dirac magnetic monopoles, (2004), the CDF Collaboration 2004, CDF note 7183.

[29] A. Aktas et al. (H1 Collaboration), *Eur. Phys. J.* **C41** (2005) 133, arXiv:hep-ex/0501039 [hep-ex].

[30] E. Recami and R. Mignani, *Nuovo Cimento* **4** (1974) 209.

[31] R. Katz and E.J. Kobetich, *Phys. Rev*. **186** (1969) 344.

[32] J. Beringer et al. (Particle Data Group), *Phys. Rev. D* **86** (2012) 010001.

[33] E. Recami, *Nuovo Cimento* **9** (1986) 1, 10.1007/BF02724327.

[34] L. Parker, *Phys. Rev.* **188** (1969) 2287.

[35] P. Fraundorf, A conservation-law view of everyday motion (2007), Department of Physics and Astronomy and Center for NanoScience at the University of Missouri in Saint Louis.

[36] Assuming circular curvature in the Dirac model we found $p \simeq 519$ eV/c.

[37] R. Mignani and E. Recami, *Il Nuovo Cimento A* **14** (1973) 169.

[38] A. Barut, G. Maccarrone and E. Recami, *Nuovo Cimento A* **71** (1982) 509, 10.1007/BF02770989.

[39] See also Figs. 3, 5 and 6 of Ref. [38].

[40] D.E. Groom, *Phys. Reports* **140** (1986) 323.

[41] G. Giacomelli, S. Manzoor, E. Medinaceli and L. Patrizii, *J. Phys. Conf. Ser.* **116** (2008) 012005, arXiv:hep- ex/0702050 [HEP-EX].

[42] H. Fried and Y. Gabellini (2007), arXiv:0709.0414 [hepth].

J. Condensed Matter Nucl. Sci. 15 (2015) 231–239

Research Article

A Mass-Flow-Calorimetry System for Scaled-up Experiments on Anomalous Heat Evolution at Elevated Temperatures

A. Kitamura[*,†], A. Takahashi[‡], R. Seto and Y. Fujita

Technova Inc., Japan

A. Taniike and Y. Furuyama

Kobe University, Japan

Abstract

A new mass-flow calorimetry system has been installed to investigate the excess-power phenomena at elevated temperatures with an increased amount of the sample. Calibration runs using alumina powder has revealed very good stability with very high heat recovery rate. The first trial runs with a silica-included Cu·Ni nano-composite sample containing 4 g of Ni mixed with 200 g of Al_2O_3 showed an anomalous increase in temperature of the sample, which could imply a long-lasting excess power of 5 W/g-Ni.

Keywords: Hydrogen gas absorption, Oil-cooling mass-flow calorimetry, Silica-included Cu·Ni nano-composite, 5 W/g-Ni

1. Introduction

We have been studying phenomena of anomalous heat evolution from hydrogen-isotope-loaded nano-composite samples at elevated temperatures as well as at room temperature using a $A_1 \cdot A_2$ twin absorption system [1,2]. Recent experiments have used Ni-based nano-composite samples; Pd_1Ni_7/ZrO_2 ("PNZ"), Ni/ZrO_2 ("NZ"), $Cu_{0.081}Ni_{0.36}/ZrO_2$ ("CNZ") and $Cu_{0.21}Ni_{0.21}/ZrO_2$ ("CNZII"). The results of measurements have been presented in the 12th Annual Meeting of the Japan CF-Research Society (JCF12), the 17th International Conference on Condensed Matter Nuclear Science (ICCF17) and the 13th Annual Meeting of the Japan CF-Research Society (JCF13), and have been/will be published in [3–5], respectively.

These are summarized, and the time-dependent data are re-analysed in another paper by A. Takahashi in this Conference [6] in a paper speculating about heat releasing mechanisms during the several-weeks-long phase of D(H)-loading into the nano-composite samples. As shown there, many interesting, even astonishing, features are involved:

---

[*] E-mail: kitamuraakira3@gmail.com

[†] Also at: Kobe University, Japan.

[‡] Also at: Osaka University, Japan.

burst-like heat release with anomalously high values of differential heat of sorption (η) reaching about 600 eV/atom-H; large values of integrated heat reaching about 800 eV/atom-Ni from the CNZ sample absorbing H; and abrupt desorption with absorbed energy of 50–80 eV/atom-Ni observed almost exclusively in the first 573-K run for each sample.

To confirm these interesting phenomena, repeated measurements with improved signal-to-noise ratio are required. Since the easiest way to accomplish this is to increase the amount of sample material being tested, we have fabricated a reaction chamber with ten-times-larger volume than the present one. Another important improvement is mass flow calorimetry applied to the system using an oil coolant with a boiling point of 390°C.

In the present paper we show the characteristics of this new oil-cooling mass-flow calorimetry system for observing anomalous heat evolution in H-gas charging to Ni-based nano-composite samples and for calibration runs using blank alumina sample.

2. Description of the System

The improvement has been done on the A_2 part of the $A_1 \cdot A_2$ twin system. The reaction chamber (RC) with a capacity of 50 cm^3 has been replaced with one with a capacity of 500 cm^3. A schematic of this new system, called the "C_1 system", is shown in Fig. 1.

On the outer surface of the RC, a coolant pipe and a 1-kW sheath heater are wound alternately for heat removal

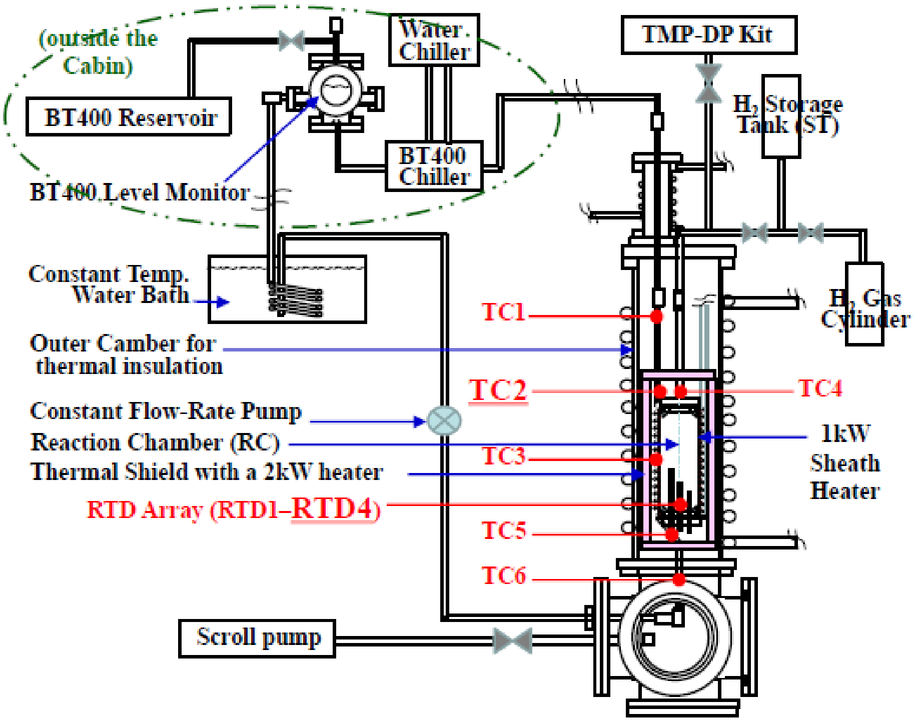

Figure 1. Schematic of the C_1 absorption system.

and sample heating, respectively. These are enclosed by a thin sheet of stainless steel for the purpose of thermal shield and close contact of the sheath heater to the side surface of the RC. All of these are supported by a stainless-steel pipe feeding H_2 gas to the sample in the RC, and surrounded again by a thermal shield made of ceramic fiber (Isowool 14C; Isolite Insulating Products Co. Ltd.) not only on the side but also on the top and the bottom. The power to the heater is fed from a DC power supply in a constant-current mode.

The coolant oil is an aromatic hydrocarbon (Barreltherm-400; Matsumura oil Co. Ltd.), which has a boiling point of 390°C and a practical maximum temperature of 330°C. The coolant is driven by a digital liquid tubing pump (Masterflex peristaltic pump) with a constant flow rate of 20 cm^3/min or 40 cm^3/min in the present work. The plastic peristaltic tube (the section that is squeezed by the rotor) is either Viton or Tygon. The coolant is fed to the RC from the bottom, and heated by the heater and the H-absorbing sample. After emerging from the top flange, the oil is cooled down to the ambient temperature, and fed back to the tubing pump through a water bath kept at a temperature of 24.0±0.1°C.

Seven thermocouples (TC) are deployed; 5 points on the surface of the coolant pipe; TC1, TC2, TC3, TC5 and TC6, on the gas feed pipe TC4, and TC0 for monitoring the ambient temperature. For flow calorimetry TC2 just behind the outlet from the RC is used. In addition to the TC's, four resistance temperature detectors (RTD; 3-terminal type) are deployed inside the RC to directly measure the sample temperature. These are located inside four sheaths penetrating and supported by the bottom ICF70 blank flange. The positions in the RC expressed as [radial position (mm), height (mm) from the bottom flange] are [10, 30], [0, 60], [10, 60] and [10, 90], respectively for RTD1, RTD2, RTD3 and RTD4.

The amount of H atom absorbed/adsorbed in the sample is deduced from decrease in the number of H_2 molecules calculated from pressure values at the storage tank (ST), P_s, and that at the RC, P_r, both measured with piezoelectric elements. Since one of the most important matters of concern is whether excess heat, if any, originates in nuclear effects or not, neutron and γ-ray counting rates are monitored steadily with a ^{3}He neutron dose rate meter and a NaI scintillation detector both located just outside the outer chamber.

All of the measured values mentioned above are processed with a "Measurement and Automation Explorer (MAX)" system, National Instruments. We are planning to make feedback control of the heater input power and the flow rate of the coolant to enable constant temperature operation in future.

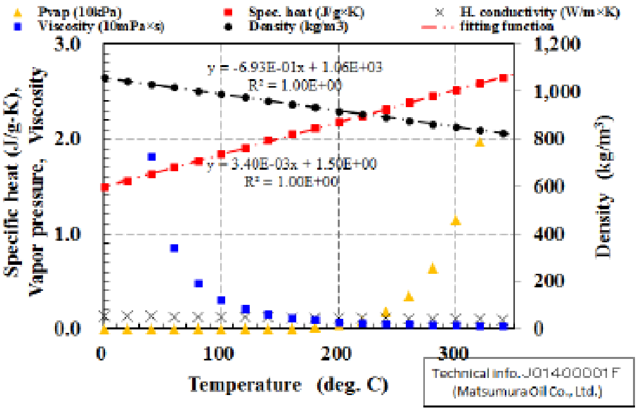

Figure 2. Physical properties of BarrelTherm-400.

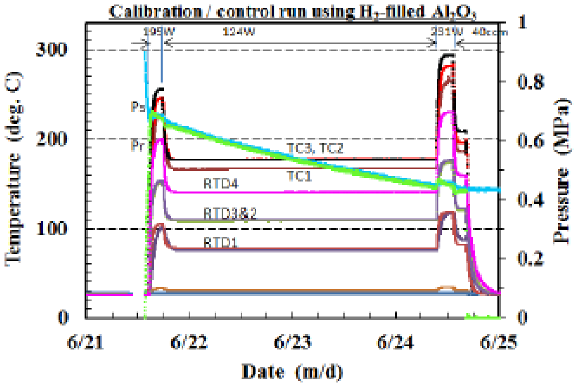

Figure 3. An example of functional fitting of the temperature change in the 195–124 W transition phase in the calibration run H–Al_2O_3.

The physical properties of the Barreltherm-400 are cited from Ref. [7], and shown in Fig. 2 as a function of temperature. It has rather strong temperature dependence of the viscosity. Although this might affect the flow rate of the coolant, the tubing pump is tough enough to send out the oil forcibly by the peristaltic rotors. The temperature dependence of the density and the specific heat are approximated by linear functions of temperature for the purpose of calculation of heat balance, etc.

3. Calibration

We have to know the heat conversion coefficient ($\mathrm{d}W/\mathrm{d}T$), the time constant (τ), and the heat recovery rate (R_h) beforehand using a dummy powder. We used a powder of alumina (Al_2O_3) with an average size of 60 μm for this purpose. Figure 3 shows temperature history during the calibration runs operated at heater input of 195, 124 and 231 W with a coolant flow rate of 20 and 40 cm^3/min.

After introduction of H_2 gas into the evacuated RC from the ST at [month/date hour:min] = [6/21 13:25], the pressures P_r and P_s begin to increase and decrease, respectively. The 195-W run was started at [6/21 14:22], when a discontinuous changes in pressure increase/decrease rate are observed as a result of temperature increase in the RC and resultant decrease in the pressure difference between the ST and the RC.

The heater power of 195 W was maintained for 3 h, during which the pressures and the temperatures reach almost saturated values. The power was changed to 124 W at [6/21 17:35], and a 231-W run followed at [6/24 9:16]. After about 4 h, the flow rate of the coolant was changed to 40 cm^3/min at [6/24 13:09]. This series of the calibration runs were finished by evacuating the RC at [6/24 16:05], followed by stopping the heater power supply at [6/24 16:20] and readjusting the flow rate to 20 cm^3/min at [6/24 16:26]. During the whole period of this calibration runs, the pressures P_s and P_r continue to decrease with almost constant rate. This should be due to some leak out of the ST–RC system. We have failed to fix it during the preliminary runs described in the following.

We see that the temperatures are very stable during the 2.5 days kept at 124 W; 178 $\pm 0.1°$C at TC2 and 141 $\pm 0.07°$C at RTD4. It is also important to note that the temperatures become almost saturated during each power phase with approximate time constant of 30 min. To calculate the heat conversion factor and the heat recovery rate, however, it is necessary to obtain the difference between each step as precise as possible. For this purpose, the temperature change is fitted to an exponential saturation function in each transition phase. An example of the fitting is shown in Fig. 4. Good fittings are obtained for both TC2 and RTD4.

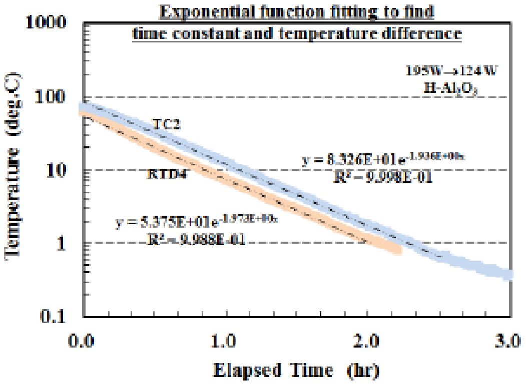

Figure 4. An example of functional fitting of the temperature change in the 195–124 W transition phase in the calibration run H–Al$_2$O$_3$.

The parameters thus deduced are summarized in Fig. 5 as a function of the input power. Although some dependence on the input power or the sample temperature could be deduced, we use in the following the average values; heat conversion coefficient dW/dT = (9.74 ±0.76)×10^{-1} W/°C, heat recovery rate R_{h} = (8.82 ±0.26)×10^{-1} with time constant τ = (2.98 ±0.12)×10^{1} min. Rather high value of the heat recovery rate is owing to high degree of thermal insulation for the RC.

4. Preliminary H-absorption run

A series of the trial runs have been conducted to find practical problems with use of a 50 g powder of silica-included Cu·Ni nano-composite, $Cu_{0.0071}Ni_{0.030}/SiO_2$ (“CNS”, Admatechs Co. Ltd.), which contains 4.1 g of Ni (mostly as NiO) and 1.1 g of Cu with particle sizes of 5–50 nm in effective diameter. An EDS photograph shows that a part of the particles contains both Cu and Ni, implying that Cu and Ni atoms are merged into single particles to form some compounds.

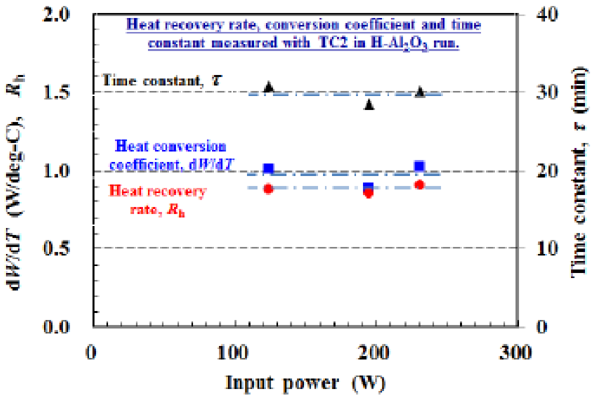

Figure 5. Heat conversion coefficient, recovery rate and time constant measured in the calibration run H–Al$_2$O$_3$.

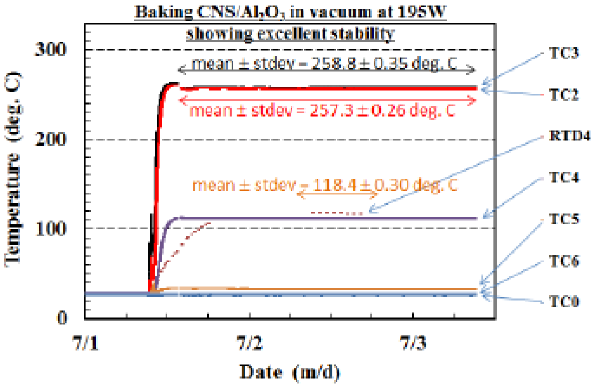

Figure 6. Baking process of the CNS/Al_2O_3 sample showing very stable temperatures everywhere in the system. The temperatures at RTD's were recorded manually in this period.

Since the 50 g sample of the CNS occupied only about 130 cm^3 in the RC volume, the RC was filled up with a mixture of the CNS and alumina that was used for the calibration/control run. The CNS/Al_2O_3 mixture was subjected first to vacuum baking at a heater input power of 196 W for about 2 days. The variation of the temperature during the baking process is shown in Fig. 6. Regrettably, due to a mis-setting of the RTD in the data acquisition system, we have the RTD data manually recorded for only several points.

The outer surface of the RC was kept at just below 260°C. In contrast, the sample temperature at RTD4 reached only 118°C even at the final stage of the baking process, when the pressure in the RC decreased down below 10^{-1} Pa. The reason for the relatively low temperatures at RTD's is relatively low heat conduction in the radial direction through the porous materials. In the case of the Al_2O_3 calibration run, H–Al_2O_3, we observed RTD4 showing 200°C, as has been described in the preceding section. This shows importance of the hydrogen gas at several atmospheres for heat conduction. Temperature, pressure and loading ratio in the run H–CNS/Al_2O_3.

Next we introduced hydrogen (protium) gas into the RC, and changed the heater input power from 195 W to 231

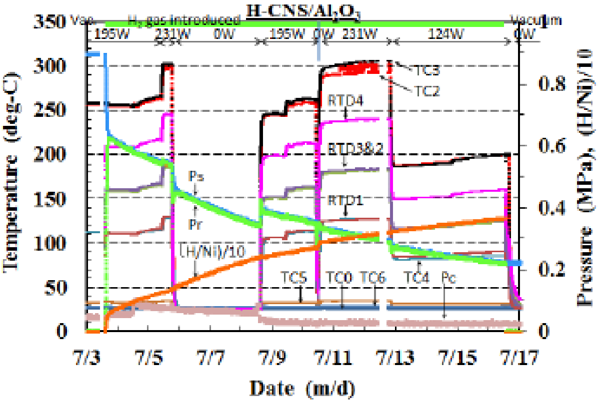

Figure 7. Temperature, pressure and loading ratio in the run H–CNS/Al_2O_3.

W, 0 W, 195 W and 231 W again, and finally to 124 W. The whole sequence of this run, H–CNS/Al_2O_3, is shown in Fig.7, where the traces of the temperatures, TC0–TC6 except TC1 and RTD1–RTD4, are shown together with the pressures, P_s, P_r, and P_c at the level monitor of BT400. Moreover, the amount of hydrogen atoms lost from the gas phase is shown as (H/Ni), the ratio of the number of the hydrogen atom absorbed/adsorbed to that of the host Ni atom, i.e., the so-called loading ratio. In the calculation of the number of hydrogen atoms in the gas phase from the measured pressures and temperatures together with the volumes of the ST and the RC, we assumed the representative temperature in the RC to be the mean temperature at RTD4 and TC3. Otherwise smooth variation of (H/Ni) was not reproduced.

The parameter (H/Ni) increases almost steadily throughout the whole run, which is thought to be caused by a leak out of the system as mentioned earlier. We also notice stepwise increases at the beginning when the gas is introduced into the RC, and just after the moment when the heater power is increased from 195 to 231 W. These should be due to real absorption/adsorption of hydrogen by the sample. Summing up the contributions, we obtain the loading ratio of 0.75 ± 0.05.

We notice that, in contrast to the control run H–Al_2O_3 shown in Fig. 3, the temperatures increase continuously under the constant input power of 195, 231 and 124 W. Moreover, almost stepwise increases are observed in the periods of 195 and 124 W. The increase was not observed in the control run H–Al_2O_3. As an example, the temperature evolutions in the 124 W phase of the H–CNS/Al_2O_3 run are compared with those of the H–Al_2O_3 run in Fig. 8. The comparison reveals temperature increase by 11–22°C at the TC2 and TC3, and by 9–20°C at the RTD4. If these increases can be attributed to the real increases in the power, they correspond to the "excess" powers of 11–22 W and 11–24 W, respectively. When evaluated in terms of the specific power, the "excess" amounts to about 5 W/g-Ni.

Similar values are deduced for the temperature increases in other periods of input power. Moreover, the assumed "excess" power is on the same order of magnitude as that claimed for the CNZ (Cu·Ni/Zi_2O_3) sample yielding an excess power of 2 W/g-Ni [6].

Before concluding there is excess power, we have to check for other possibilities. First, there might be a possibility that the temperature increase was due to a decrease in the flow rate of the coolant, which could be caused by a swelling of the coolant tube in the peristaltic pump tube section. Regarding this point, it should be noted that the Viton peristaltic pump tube was replaced by a Tygon one on July 8, after a leak in the Viton tube was found. We restarted the run with the new Tygon tube at a power of 195 W on the same day. It was not longer than one day before a similar temperature

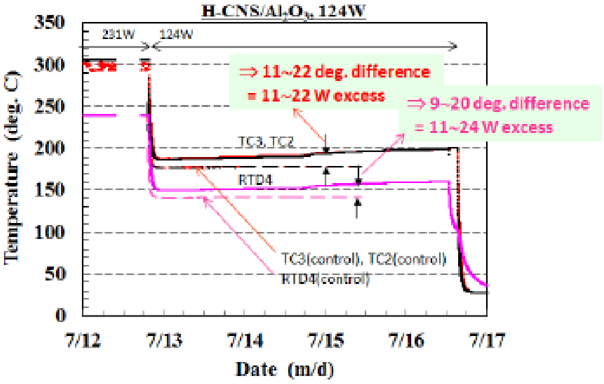

Figure 8. Comparison of the temperature change during the 124 W phase in the runs H–CNS/Al_2O_3 and H–Al_2O_3.

increase was observed. Therefore, it seems rather difficult to ascribe the temperature change to any deformation of the coolant tube.

Another possibility could be a transformation of the sample itself due to repeated cycle of heating. Agglomeration of the Cu·Ni particles or interwinding of the two kinds of the powders might occur. Both of these changes could increase the thermal conductivity of the sample to make the thermal flow from the heater to the sample bulk higher and raise the sample temperature. However, it appears to be difficult to explain by this mechanism the temperature increases at TC2 through TC4 by almost the same values as those at RTD1 through RTD4.

The system has a gas leak which could affect the calorimetry, since the heat transfer due to thermal conduction and/or convection, or heat loss via the top and bottom flanges, becomes less active as the pressure decreases. This effect is negligible in the present configuration, since the effect would cause a temperature decrease (not an increase) at the RTD's with decreasing pressure, since the RTD's are located near the heat sink. Moreover, we are comparing the temperature evolutions in the foreground (CNS) runs with those in the background (Al_2O_3) runs which also have the gas leak out of the system with a rate of the same order of magnitude as shown in Fig. 3.

Finally, we have to mention that no noticeable change was observed in either the γ-ray or the neutron counting rates, as is shown in Fig. 9. The heater power calculated from the measured voltage across the heater and the resistance at room temperature is also plotted in the figure. It is also clear that the fluctuation of the input power is not the origin of the temperature increases.

In short, it is reasonably plausible to ascribe the observed temperature increase to excess power from the sample. It is, however, also true that the increased amount is too small to rule out all other factors which could affect the temperature. We have designed the calorimeter system to hold an increased amount of the sample material, of the order of several hundred grams. Unfortunately, only 50 g of the CNS sample containing only 4.1 g of the active element Ni is available at the moment. We are planning to test the CNZ sample with an amount on the order of 100 g.

5. Conclusion

As for the calibration of the oil-mass-flow calorimetry using a dummy Al_2O_3 powder, we summarize the results as follows:

(A1) The coolant oil reached almost 300°C at the input heater power of 231W.

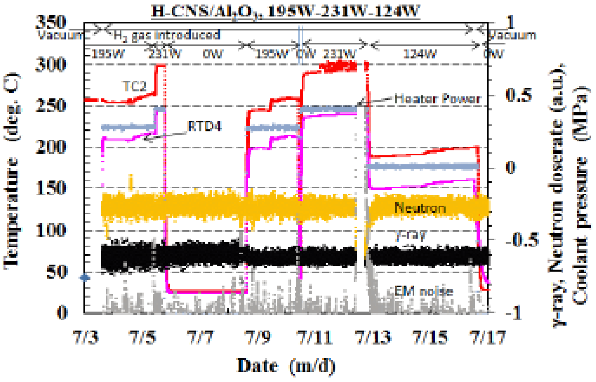

Figure 9. Neutron and γ-ray signals as well as heater power in the H–CNS/Al_2O_3 run, showing no relation between these and the temperature change.

(A2) Long-term stability, or fluctuation in terms of standard deviation, is better than 0.5°C.
(A3) Conversion coefficient, $\mathrm{d}W/\mathrm{d}T$ = (0.97 ±0.08) W/deg with an oil-flow rate of 20 cm^3/min.
(A4) Heat recovery efficiency is (0.88 ±0.03) with heat removal time constant of (30 ±1.2) min.

The first trial runs with a 50 g of the CNS sample (silica-included Cu·Ni nano-compound containing 4.1 g of Ni) mixed with 200 g of $\mathrm{Al_2O_3}$ are summarized with the following remarks:

(B1) Both TC2 at the oil outlet and RTD's inside the reaction chamber show higher temperatures than those for the blank sample, which could imply a long-lasting excess power of 20 W (i.e., 5 W/g-Ni).
(B2) The assumed excess heat appears to be on the same order as that of the CNZ (Cu·Ni/Zi2O3) sample yielding an excess power of 2 W/g-Ni.
(B3) Further measurements with increased amount of the sample and more precise comparison are necessary to confirm the excess power.

Acknowledgement

The authors thank Admatechs Co. Ltd. for providing the CNS sample and its TEM, EDS, ICP and XRD analyses.

References

[1] Akira Kitamura, Yu Sasaki, Yuki Miyoshi, Akira Taniike, Akito Takahashi, Reiko Seto and Yushi Fujita, *J. Condensed Matter Nucl. Sci.* **4** (2011) 56–68.
[2] Y. Miyoshi, H. Sakoh, A. Taniike, A. Kitamura, A. Takahashi, R. Seto and Y. Fujita, *J. Condensed Matter Nucl. Sci.* **10** (2013) 46–62.
[3] Y. Miyoshi, H. Sakoh, A. Taniike, A. Kitamura, A. Takahashi, R. Seto and Y. Fujita, *Proc. JCF12* (2012) 1–9.
[4] H. Sakoh, Y. Miyoshi, A. Taniike, Y. Furuyama, A. Kitamura, A. Takahashi, R. Seto, Y. Fujita, T. Murota, T. Tahara, to be published.
[5] H. Sakoh, Y. Miyoshi, A. Taniike, Y. Furuyama, A. Kitamura, A. Takahashi, R. Seto, Y. Fujita, T. Murota, T. Tahara, *Proc. JCF13*.
[6] A. Takahashi, A. Kitamura, R. Seto, Y. Fujita, H. Sakoh, Y. Miyoshi, A. Taniike, Y. Furuyama, T. Murota and T. Tahara, to be published.
[7] Technical info. J01400001F (Matsumura Oil Co. Ltd.).

J. Condensed Matter Nucl. Sci. 15 (2015) 240–245

Research Article

Hydrogen Absorption and Excess Heat in a Constantan Wire with Nanostructured Surface

U. Mastromatteo* and A. Bertelè

STMicroelectronics, via Tolomeo, 1 20010 Cornaredo Milano, Italy

F. Celani†

National Institute of Nuclear Physics, Frascati Nat. Lab.; Via E. Fermi 40, 00044 Frascati, Rome, Italy

Abstract

To go beyond the important and encouraging results obtained in Pd–D and Pd–H systems, overcoming the limitations related to the relative rareness of Pd, several tests were made using constantan wires with nanostructured surface in hydrogen atmosphere and temperatures up to 350°C.

Keywords: Constantan, LASER, LENR, Palladium, Transmutations

1. Introduction

Why Constantan: As per Celani's data presented at ICCF17 in 2012, Constantan has at least five times more catalytic power (related to H_2 dissociation) than palladium. Hence Constantan is not only much cheaper than Pd, but it is also more effective in supporting the Anomalous Heat Effect (AHE) process. Two different Constantan wires were used: with nanostructured layers (Celani) and bulk (Mastromatteo).

A Constantan wire (diameter 200 μm, length 25 cm, weight ∼50 mg), previously treated to induce the formation of two nanostructured layers on its surface, was used for AHE detection in hydrogen atmosphere at different temperatures. The reactor (Fig. 1) and wire main parameters were monitored (heater power, wire resistance and temperature, chamber temperature, hydrogen pressure, ambient temperature) from ambient up to the maximum temperature of 350°C.

After the temperature exceeded 150°C, we observed a substantial decrease in the wire resistance as already highlighted in previous experiments with a similar material [1]. Conversely, using a material without nanostructured surface treatment, the wire resistance change was negligible. A thermal reactor calibration was performed with several tests

---

*E-mail: ubaldo.mastromatteo@libero.it

†Also at: International Society for Condensed Matter Nuclear Science, Latium#1 Group, Via Cavour 26, 03013 Ferentino (FR), Italy.

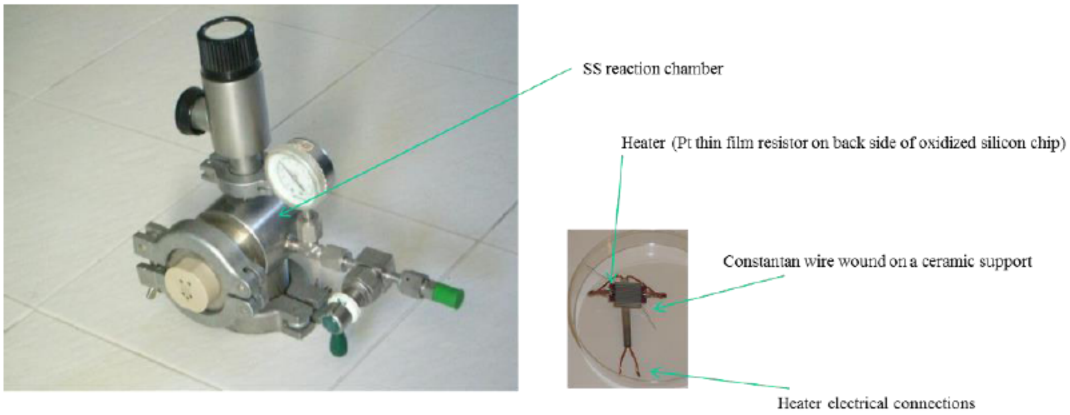

Figure 1. Reaction chamber and typical sample holder .

using inert materials. Then, using the surface-treated wire (after stabilization of the resistance value >170°C), we observed a decrease in the necessary heater power in comparison with the power used during reactor calibration. The highest deviation of 1.2 W (a 5% reduction in input power) was measured at 350°C.

After a "positive " test generating excess heat, an EDX analysis of the active wire in areas with surface morphological changes showed the presence of elements unrelated to the original composition of Constantan wire. The transmutation elements found are also the same highlighted by other researchers in similar test conditions, even though they were using different materials or alloys. Similar findings were also observed with thin films of palladium in deuterium or hydrogen gas at room temperature. It is interesting to note that in hydrogen, hot spots and transmutations occurred only with irradiation by means of low-power HeNe laser [3].

2. Material Characteristics and Preparation

As reported by Celani in ICCF17 [1,2], the material used in the experiments described here is commercial, low cost ISOTAN 44, with a nominal composition Cu55Ni44Mn. It was developed many years ago by Isabellenhutte Heusler, GmbH, KG-Germany. The ISOTAN 44 was selected for the following reasons:

(a) The possibility, at least in principle, of producing *nano-micro structures* at the surface, or even deeper into the bulk, using *selective oxidation of Cu in the alloy* at high temperatures (650–1050°C) and segregation of pure Ni by fast cooling.
(b) To obtain three-dimensional nano-structures, called *Skeleton type*. Such three-dimensional geometry has several intrinsic potentialities with respect to gas absorption.
(c) To use ONLY one material (Constantan alloy) and take advantage of its intrinsic, multi-element composition. This reduces the complexity of preparation and the cost. Our treatment process, in principle, is similar to what used for SELF-SUPPORTED catalyzer manufacturing; catalyzers often used in oil refining processes.

3. H_2 Absorption

While heating the wire from ambient temperature up to a maximum temperature of 350°C, the reactor and wire main parameters were continuously monitored (heater power, *wire resistance* and temperature, chamber temperature,

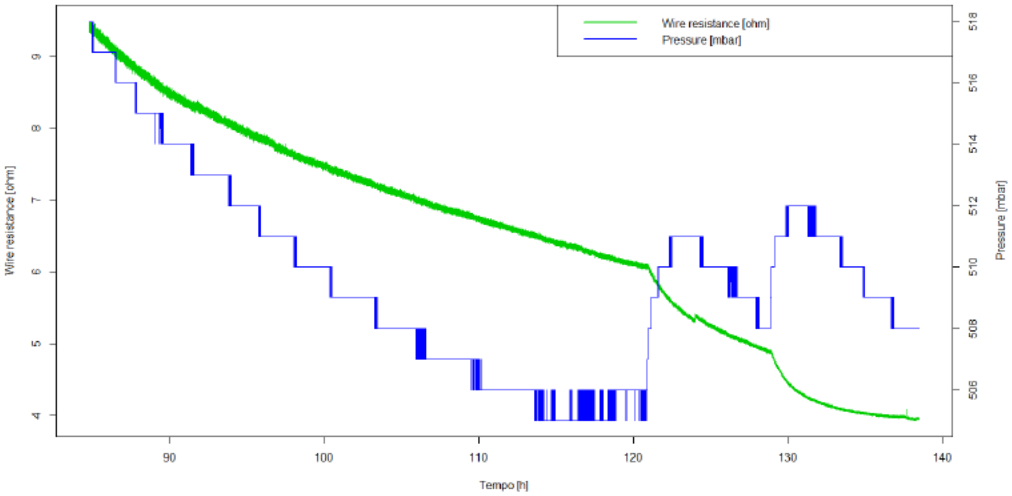

Figure 2. The graph shows the wire resistance and pressure decrease above a threshold temperature (temporary pressure increase is due to programmed temperature increase).

hydrogen pressure, ambient temperature).

As mentioned before, at temperatures above 150°C, we observed a substantial decrease in the wire resistance, together with a very clear pressure reduction in the chamber, indicating quite high hydrogen absorption (Fig. 2) [1]. An estimate of the H/Ni ratio can be done, based on the volume of the chamber (about 300 cm^3) and the initial pressure (500 mbar). The pressure change (in three steps) is about 3.5%, corresponding to 4.7×10^{-4} H_2 absorbed moles; 40% of Ni in the wire (120 mg) indicates 48 mg = 8.3×10^{-4}mol, and then 4.7 × 2 / 8.3 = 1.1 H/Ni ratio.

4. Excess Heat Production

Figure 3 shows a screen shot which summarizes the trend of excess power produced in several experiments. Reactor calibrations have been performed without "active" material on the heated wire. It was also observed that tests with the active material had a thermal trend similar to that of the calibration test or with very small excess power.

Several experiments instead showed a clear (up to about 2 W) decrease of the input power needed to reach the temperature of the chamber established with the calibration curve (X axis, T_{reactor}–T_{ambient}). This 2 W change is therefore attributable to extra heat production inside the reactor. All data shown were obtained with indirect heating of the wire; that is, using the platinum heater underneath the silicon chip. It can also be noted that until a wire temperature reaches 120°C, the excess power value for all of the test is under the estimated error (dotted line) while the higher deviation from the calibration curve is at 300°C (2.2 W).

Indeed, a strange trend was noted: direct heating of the wire tended to reduce the excess heat. So, to convince ourselves this was not an artifact, or behavior related to instability of the system, we produced a deliberate reduction of excess heat by moving part of the power to direct heating, and then returning to indirect heating.

In this way—as can be noted by the presence of points with the same color (meaning the same experiment) with different values of extra power but with the same value of delta T (X-axis at 280°C)—it is confirmed that the value of the excess heat measured was real within the limits of the estimated error (±250 mW).

Here is more detail: as described above, in the reaction chamber it is possible to split the input power between

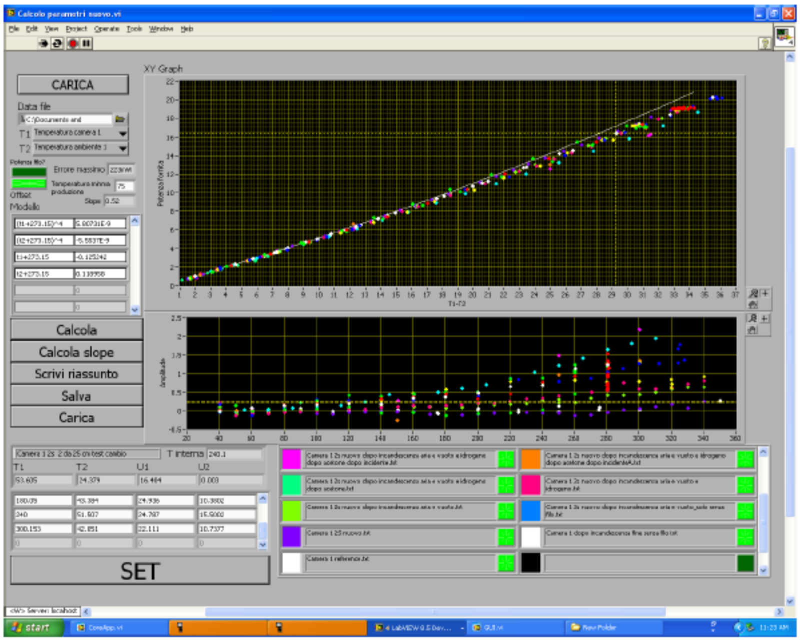

Data file: C:\Documents and
T1: Temperatura camera 1
T2: Temperatura ambiente 1
Errore massimo: 223mW
Temperatura minima produzione: 75
Slope: 0.52

Modello	
(t1+273.15)^4	5.00731E-9
(t2+273.15)^4	-5.5837E-9
t1+273.15	-0.125242
t2+273.15	0.119958
	0
	0

Camera 1 2s 2 da 25 cn test cambio
T interna: 240.1

T1	T2	U1	U2
53.605	24.379	16.404	0.003

180.09	43.384	24.936	10.3802
240	51.937	24.787	15.5002
300.153	42.851	22.111	10.7377
0	0	0	0

<W> Server: localhost

Figure 3. Excess power evaluation.

the oxidized silicon heater and the Constantan wire wound on the ceramic support (the wire and heater are in thermal contact), with the measurement of the temperature of the Constantan wire made through a miniaturized Pt 100 sensor in contact with the wire itself. So, the temperature of the wire can be determined by distributing power between the heater (indirect) and the wire (direct). As stated earlier, at the same temperature of the wire (obtained by setting the control system to maintain a constant temperature, which in this case was 280°C), it was observed that by fixing part of the direct power to a value different from zero, the total power supplied externally to maintain the set temperature (the sum of the power to the heater and the wire), was greater than in the case of zero direct power. In our opinion this means that at this temperature with only indirect heating power, some extra power was generated in the Constantan wire (Fig. 3 vertical column of red dots at 280°C).

5. Transmutations

EDX analysis of the active wire after a "positive" test (with excess heat) showed many hot spots with the presence of elements unrelated to the original composition of the Constantan wire. The elements found are the same ones found by other researchers in similar test conditions using different materials (Fig. 4).

In particular, the EDX spectra in Fig. 5 are from experiments done in a Siena laboratory under the direction of Prof. Piantelli. They are from a pure nickel rod of 0.5 mm diameter and about 10 cm length heated up to 350°C inside a stainless steel chamber filled with hydrogen at a pressure of less than 1 bar. The system produced long-lasting excess heat of several watts, and clear transmutation effects were found at the end of the experiment. Similar findings were also observed with thin films of palladium in deuterium or hydrogen gas at room temperature, with the very specific circumstance that in the case of hydrogen the hot spots and transmutations occurred only with irradiation with a

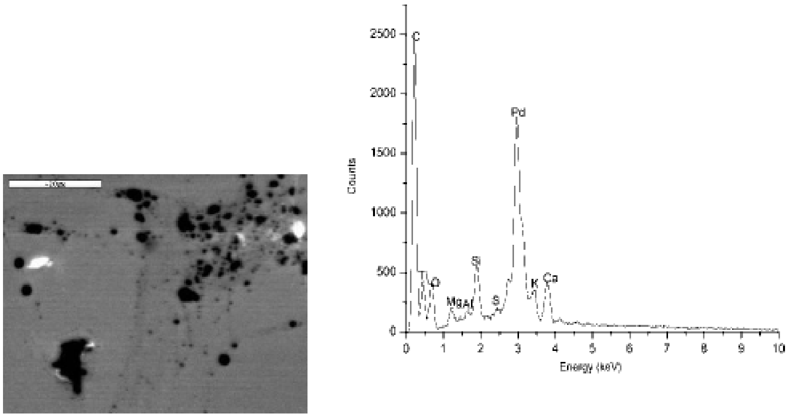

Figure 4. EDX Spectrum of a spot on Pd sample processed 76 days with 2mW/cm^2 He-Ne laser.

low-power He–Ne laser [3]. What is important to note is that in all the experiments, the atomic weights of the detected elements are all below nickel or palladium. In our opinion this important nuclear signature deserves more attention by researchers for the purpose of obtaining a better interpretation of these anomalies.

6. Conclusions

The concreteness of LENR anomalies appears to be confirmed in several experiments with different embodiments, even though the explanation of the phenomenon still seems far away. The random activation of the surface of the material under test indicates a low probability of the "ignition" conditions for the reactions, and raises the question of why the reaction only occurs at some points and not over the entire surface (Fig. 6). Some stimuli (LASER) on the material increase the probability of reaction on Pd, although apparently not on Ni or Constantan. A test through an optical

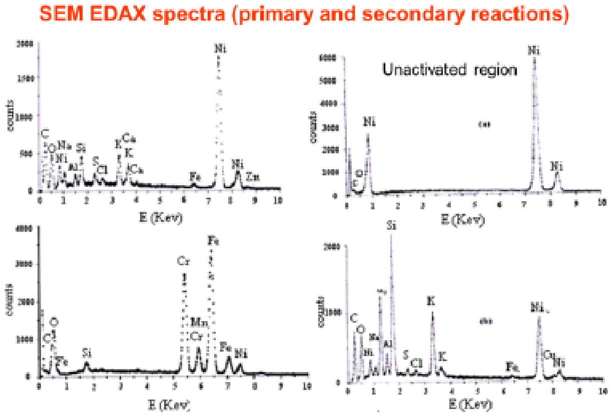

Figure 5. Ni–H experiments. Source: Poster presented at the 2005 Pontignano workshop by Prof. Piantelli and collaborators.

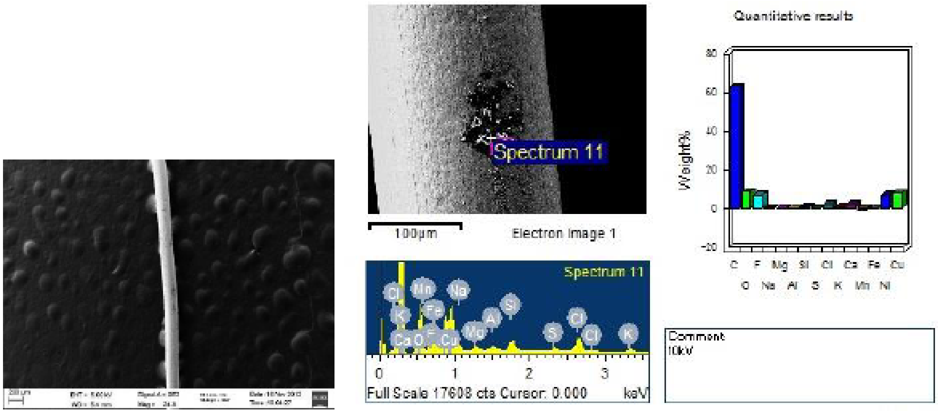

Figure 6. EDX Spectrum of a spot on constantan wire after an excess power experiment.

window on a Constantan wire at 300°C did not produced anomalous heat. The specific power output is estimated in the tens of kilowatts per kilogram.

References

[1] F. Celani et al., Cu–Ni–Mn alloy wires, with improved sub-micrometric surfaces, used as LENR device by new transparent, dissipation-type, calorimeter, *ICCF17,* 10–18 August 2012, Daejeon, South Korea.

[2] F. Celani et al., Experimental results on sub-micro structured Cu–Ni alloys, at X Inter, Workshop on Anomalies in Hydrogen–Metal Systems, Pontignano, Italy, April 10–14, 2012, publishing in (*J. Chem. Mat. Res.*, March 2013).

[3] V. Nassisi et al., Modification of Pd–H_2 and Pd–D_2 Thin Films Processed by He–Ne Laser, *J. Condensed Matter Nucl. Sci.* **5** (2011) 1–6

J. Condensed Matter Nucl. Sci. 15 (2015) 246–255

Research Article

Celani's Wire Excess Heat Effect Replication*

Mathieu Valat†

Martin Fleischmann Memorial Project, 7 rue de l'Eglise 30190 St Geniès de Malgoirès, France

Ryan Hunt

Hunt Utilities Group, 2331 Dancing Wind Rd. SW, Pine River, MN 56474, USA

Bob Greenyer

Hunters Moon, Reeds Lane, Sayers Common,Hassocks, W Sussex, BN6 9JG, UK

Abstract

This paper describes progress made by the Martin Fleischmann Memorial Project while attempting to replicate Celani's experiments. Celani claimed to see consistent and reproducible excess heat generation results coming from treated constantan wires using different protocols. The design of the cell is described in detail, with attention to the choice of materials, the design geometry and operating conditions. Differences between the original experiment and later replications that improved believability are explored. Results and interpretations are discussed.

Keywords: Constantan wire, Hydrogen, Nickel nano-powder

---

1. Introduction

During ICCF-17 in Daejeon, South Korea, Celani demonstrated an apparatus that used a treated constantan wire as the active material in a hydrogen atmosphere. This wire had been specially treated to enable activation for the sub-micrometric material. Before the end of the conference, the newly organized Martin Fleischmann Memorial Project (MFMP) decided as its first project to replicate the Celani experiment using wires provided by Celani.

Three different protocols similar to Celani's [1] have been used. The first one was identical to the one presented at ICCF-17 [2]. A second, slightly improved protocol similar to the one later used by Celani et al. [3] was then used. Finally, we compared the active cell to a dummy cell in order to make the results independent of the laboratory ambient temperature changes.

---

[*] This work is dedicated to the memory of the great Prof. Martin Fleischmann.

[†] E-mail: mathieu.valat@gmail.com

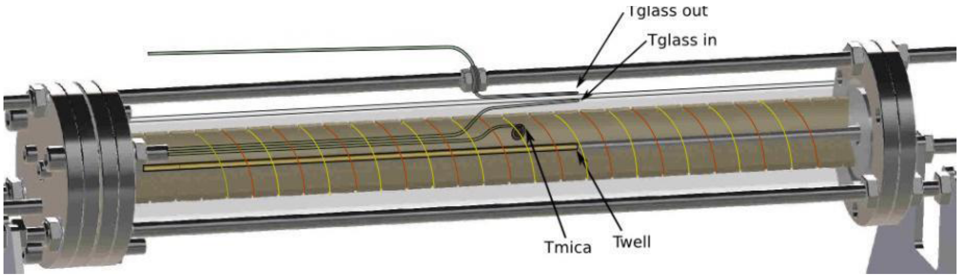

Figure 1. Design of the replica. In red the active wire wound in parallel with the heating wire in yellow.

2. Original Replication of the Experiment

The first experiments used a device similar to Celani's. The reaction chamber was a Schott Duran borosilicate tube 40 mm OD, 3.2 mm thick and 300 mm long equipped with Conflat flanges at each end. A third flange was used for thermocouples and power leads. The low transmittance at infrared wavelengths of this type of tube is important because it allowed Celani to assume that most of the heat loss was by radiation. Two wires were wound in parallel, the first one being the active wire prepared by Celani (200 μm), and the second one being a 150 μm nichrome wire (80% Ni, 20% Cr from Goodfellow). The wires were wound on mica supports. We used 0.5 mm thick mica whereas Celani used 3 mm ones. The mica was pre-baked in an oven for 30 min at 330°C prior to use in order to complete the polymerisation process of the silicone binder used during the mica manufacturing. The wires were not wound as closely together as Celani's device. One-meter long wires were wrapped on 28 cm length on the mica supports, whereas Celani wrapped 1 m of wire per 12 cm. This is the main difference from the original design. Another difference was related to the equipment used to monitor the experiment.

The system was placed 20 cm above an aluminum plate. Four thermocouples were used in this setup. The first one measured the ambient temperature 50 cm away from the experiment; the second one was placed on the mica support; the third one was positioned on the inner surface of the glass tube; and the last one was on the outer surface of the tube. An additional thermocouple was placed inside the central support, which is called the "well". Celani used Kapton tape to glue the thermocouple on the glass surface, but we did not, because the tape stores heat locally, and also because of the difficulty of reproducing this design correctly. We found that the elastic property of the stainless steel sheath was sufficient to allow an acceptable measurement of the glass tube in contact with the thermocouple. The end-tip of the thermocouple measuring the outer surface temperature of the tube was placed at half the height of the tube, half the length of the horizontal tube with a large length of its end sheath making an asymptotic curve meant to collect heat and prevent the sheath from playing the role of a heat sink. We operated in constant voltage mode. The acquisition system was based on a custom board made by Hunt Utilities Group with data acquisition at 50 samples/s and 16 bit resolution.

Experiments were performed in parallel in Europe and in the United States. In Europe the room temperature was regulated with a precision of ± 1.4°C. In the US the system was placed in a vent hood with continuous airflow having a stability of ± 1°C.

3. Method of Excess Energy Calculation Compared to the Celani's Experiment

The original experiment done by Celani used the Stefan–Boltzmann black body radiation law to calculate the heat loss of the system using the emissivity of the glass tube. The calculation of the heat loss using this law is only valid in a vacuum. In addition to the energy lost by radiation, it is necessary to take into account the heat loss by conduction and convection. In order to simplify the calculations, Celani calculated the effective emission coefficient of the cell that empirically includes the other sources of heat loss. This method is not accurate enough. It is much better to calibrate the cell with an inactive wire for comparison.

To evaluate the influence of the different parameters, we looked at the variation in the thermal response of the system when calibrated under different gas mixtures and pressures inside the tube. The wire temperature is difficult to measure because the closest thermocouple is placed on the mica, and not on the wire. Moreover, exposure to highly thermally conductive hydrogen gas makes comparisons of wire temperatures close to impossible. Therefore only the external temperature of the glass tube was used to calculate the thermal energy (Fig. 1). The calibration curve was obtained by increasing the input power from 25 to 100 W in 5 W steps.

4. Calibrations and Results of the Original Attempt

Altogether 13 calibrations were made in Europe with an untreated 200 μm constantan wire. Three typical gas mixtures composed of Ar, He, and H_2 were used: 75% H_2 with 25% Ar, 100% He or 100% H_2 at 1 bar, 2 bar and 3.5 bar. Figure 2 shows an example, three calibrations at 1 bar.

For calibration we used a 200 μm diameter constantan wire coated with MnO on the surface (manufactured by BLOCK). It was supposed to be a good candidate for cell calibrations because it is advertized as the most stable constantan on the market in any operating conditions. We discovered that the manufacturer should say it is stable in any condition other than in a hydrogen atmosphere! Almost 2.8% variation of resistance was observed in this wire during calibrations. This variation raised serious questions about the possible “activation” of the BLOCK constantan.

However, compared to Celani’s wire, this material showed good stability at high temperature, the MnO surface having an oxide surface similar to the active wire. It also had resistivity and structural behaviour identical to Celani’s wire.

The two blue lines shown in Fig. 2 are the very first calibrations done with the BLOCK wire (*dark blue*) and the Celani wire (*light blue*). For the latter, it was not necessary to extend the temperature range higher as it is assumed that it would not deviate from the linearity of the curve. This was also not done because Celani advised us not to expose the wire to helium, because it would take the place of mono-atomic hydrogen in the “skeleton” of the nanomaterial, obstructing that path during later exposure to hydrogen. The light red line is the highest calibration baseline, where the BLOCK constantan wire was used in hydrogen.

The thermal gap between these two calibrations is very large. In terms of timeline, the dark blue curve was generated first, then almost all the others calibrations were close to the light red line. (They are not shown in this figure for the sake of simplicity.)

It is possible that hydrogen changes the optical transmittance/opacity characteristics of the borosilicate tube, thus modifying the thermal response of the system. Changing the tube would have reset this effect. It has also been postulated by Langmuir [5] that glass may have better properties to recombine hydrogen than other materials.

A series of test was performed to evaluate the leakage rate, the effect of the mixture on the system and on calibrations. This information can be extracted from the logbook[a]. This was done to anticipate the behaviour of the wire after the first exposure to hydrogen, which is known to change it irreversibly.

A mistake made by the operator required to replace the tube, and clean the chamber and the mica before installing the active wire. Then power input was set to the previous value with an upper limitation of 45 W. In doing only the first range of power input that was used to generate the light blue calibration curve, we ensured the change of the tube and the modifications made on the cell did not impact the previous calibrations.

A final step was necessary before getting into the excess energy mode. This step is also known as the “loading phase”. It consists in exposing the wire to hydrogen for the first time, then increasing the electrical input power in

---

[a] http://goo.gl/1i9B2f

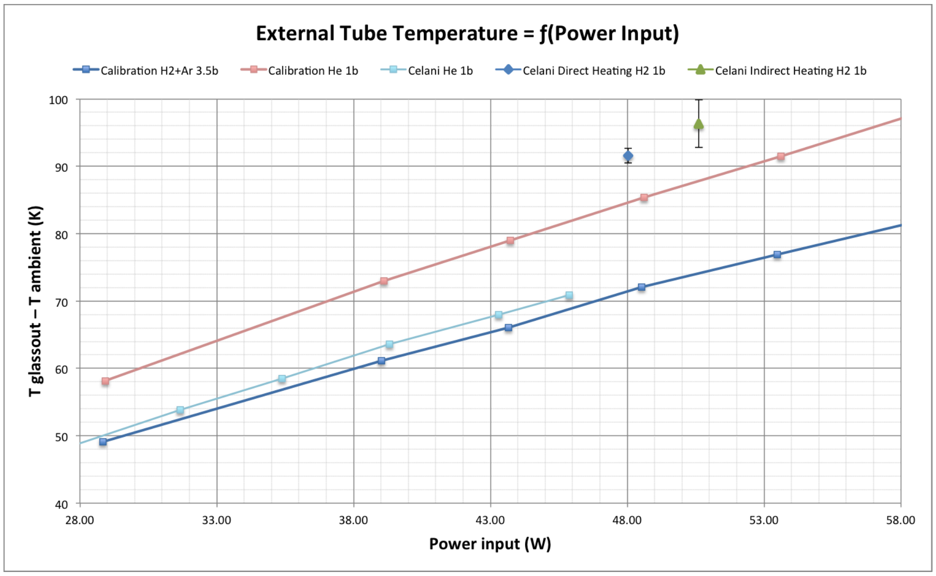

Figure 2. Results compared to the calibrations. The calibration in red reached the highest temperatures of all calibrations done.

order to achieve a dramatic reduction of the wire resistance. Further details are given in Section 7. The resistance was reduced by 16% of its original value from 19.4 Ω down to 16.3 Ω.

Soon after the resistance stopped dropping, the wire was set in the replication condition, with an input of 51 W of direct current in the nichrome wire (indirect heating), in an atmosphere of pure di-hydrogen. In Fig. 2, the measurement shows excess energy compared to the calibrated thermal response of 6 W in averaged value of the darker red plot, if we compare to the light red calibration line the graph shows an estimation of 20 W excess energy. This was run for 24 h before the power was switched to the Celani wire.

Whereas the input power is slightly less (48 W), the energy provided by the wire is similar. After this, power is generated in the same range as before, 6 W for two days. Then the cell was prepared for shipping to Switzerland where it produced similar results.

Due to many improper conditions, and a lack of confidence in doing this type of experiment for the first time, it was decided by the project members to move forward with a better protocol.

In this new experiment a “dummy” cell gave a permanent baseline to the active cell. Due to the unstable nature of this cell design, a permanent baseline is an asset to understanding the system. All the work done before remained archived in a comprehensive folder accessible by everyone[b] on the internet to verify the measurements.

While many people remember results reported during ICCF 17 and NI Week 2012 of 30% excess energy, we were surprised to be informed by Celani that results in this range were no longer attainable. These results were a mistake in the measurements, induced by the power supply, that underestimated power input, adding to the apparent excess energy.

---

[b] http://goo.gl/2VRb0k

5. Description of the New Protocol Done in Dynamic Vacuum

Celani did a test in December 2012 that involved a two-layer wire and a three-hundred-layer wire installed in the cell he used previously. The variations that characterised this test are related to the pressure induced within the chamber of the cell. Instead of having positive relative pressure, the chamber is put under constant vacuum in order to artificially insulate the wire within the reaction chamber and increase its thermal dissipation. With higher temperature involving less power input, the signal/noise ratio is increased. This technique also addresses some legitimate concerns about the validity of measurement made between H_2 and He, and the pressure variation of the gas, which would change the heat dissipation. It also improved the thermal stability. Finally, it enhanced infrared radiation over conduction and convection.

This protocol is available in two forms, as a table[c] or as a text[d]. To summarize briefly, two locations ran this protocol almost synchronously, in the USA and in Europe. The protocol is again split in two major steps, the calibrations and the experimental run.

Each set of two cells is run simultaneously with similar power input and conditions to create a valid baseline for comparison, in a calibration. This baseline is established under conditions identical to the live experimental run that follows. The only major distinction between the calibration and the live run is that the loading process is not done before the calibration. When the thermal response is established for each specific input power level, a third order polynomial approximation is made with a 95% confidence level as a minimum. Finally, this polynomial equation is inserted into the software in order to compare the current temperature reading with the baseline. By simple subtraction it gives the excess heat in real time for the Live Open Science broadcast.

This protocol allows us to set conditions for the wire to be loaded and unloaded back and forth. This is an interesting test because it tends to stress the material, induce a flux of protons, and speed up the aging process in comparison to the static pressure test.

6. Description of the Second Iteration Apparatus

The second apparatus is a modification of the first attempt with the aim to fix the wounding density and to be as close as possible to the original cell presented in ICCF-17. It uses a modified version of the first attempt, where the wrapping is more concentrated at the center using 12 cm of the central part of the tube instead of using almost the entire length of 30 cm. The mica supports are made of MACOR instead of steel. This is identical to Celani's apparatus, and it improves the insulation on the sides of the system.

The most noticeable change in this experiment is that two cells are mounted in the same place. One cell contains treated constantan wires made by Celani and the other one contains nichrome wires that are considered not reactive at such low temperatures with hydrogen.

The data acquisition as well as the power supply is duplicated to provide the additional means corresponding to the mirroring of the initial cell. The nichrome is re-designed to get as close as possible to the median value of the resistance reached by the wire during and after loading. A diameter of 0.3 mm is hence used in place of the 0.15 mm to fit this constraint.

Three thermocouples are used to measure the surface temperature of the tube on each cell. This was a good way to measure the value of the thermal gradient withstood by the tube. In Europe the end-tip of each thermocouple was warped in an SEM-type carbon sticky tape to allow better and stronger thermal coupling between the two parts. In America, a copper ring was added and wrapped on the surface of the tube to make the coupling.

---

[c] http://goo.gl/VY5MMB

[d] http://goo.gl/z42Eqv

The loading process however is done differently between the two cells. Because the “passive cell” has a non-activated wire, this cell is never exposed to hydrogen. Only the “active cell” is loaded with hydrogen until the resistance drop reaches a constant value. Then the vacuum is pulled again in both cells before starting electrical power input.

The vacuum level is identical in both cells during the experiment phase and constantly measured. We decided to use a vacuum of 2 mbar in both laboratories because that is the highest vacuum the European lab was able to achieve. We soon realized that this level of vacuum was high enough to deload the wires almost completely and quite quickly, even though it was not high enough to thermally insulate the wire from its environment.

Whereas the thermal stability of the room was improved in Europe, the US team decided to use insulating materials forming a box around the cells and flow constant temperature air over the cells to achieve a more stable environment.

7. Analysis of the Resistance Drop

The resistance drop is an effect that was assumed upfront by Celani to be related to the level of hydrogen the material stores in its metallurgical lattice [1]. This assumption is derived from the work done by McKubre et al. on how deuterium absorption relates to the increase of resistance. While McKubre presented his work on the H/Pd or the D/Pd system, with a description of a Baranovsky curve of the system studied [6]; no similar study has been done so far of the H/Ni system. Hence it is an assumption that must be taken with caution. However Ni was already a candidate for excess heat effect study, due to the close chemical properties of Pd and Ni.

Figure 3 is plot showing how the resistance of the wire changes over time. The temperature of the wire is unknown; only the temperature of the mica holding the wire is known, and it is equal to 200°C. The power was held constant for six hours, and then turned off for one hour. The aim was to monitor regularly how the resistance changes over time.

As we can see the resistance is reduced as time goes on. This might be due to reduction of the surface oxides present on the surface of the wire up to a point. However, resistance drops down to 30% of its original value cannot be explained with oxide reduction only, another phenomenon is taking place in the sample.

Because the value of resistance before and after the one-hour power down period is identical, the effect of the cooling is negligible. But one unexpected effect on the understanding of the resistance variation using this power input pattern was observed: the variation of resistance is a nonlinear effect. This is proved by the increase of the amplitude

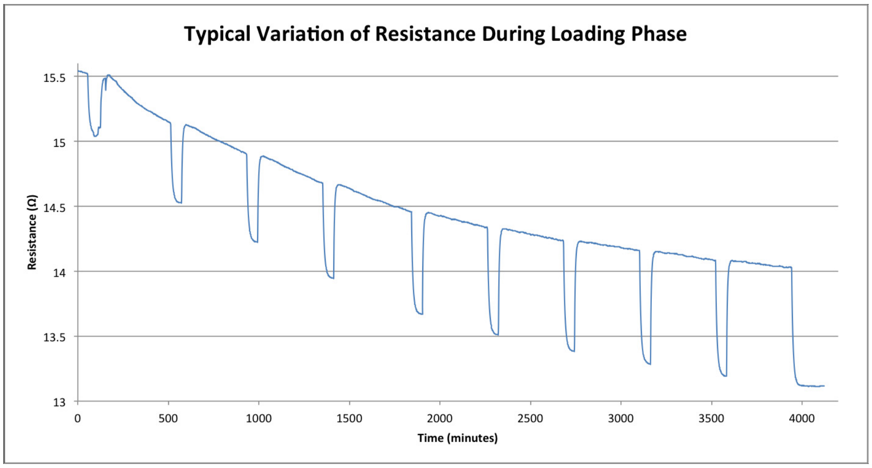

Figure 3. Example of resistance drop while the wire is set at proper temperature under hydrogenated atmosphere. Power is set on for 6 h then turned down for 1 h, 10 times.

of the drop each time it happens. We can then assume that if the resistance drop is related to hydrogen absorption, then the effect is tempering while the ratio Ni/H is still increasing.

The most compelling understanding MFMP has is that resistance drop requires a specific minimal temperature to start appearing. While temperature is increasing, the resistance is also increasing too. Once this value is passed, the resistance drops by 10% up to 30% and sometimes more.

8. Analysis of the Latest Results

Even though some limitations are induced by the setup, interesting results were obtained, demonstrating the capabilities of Celani's technology. While we compared the cells to one another, we carefully calibrated them under identical condition without any exposure to hydrogen. Helium or vacuum were used for calibrations. Vacuum was only used in the identical comparative configuration.

One other variation of temperature between the passive cell and the calibration is due to the nature of the gas used. Although He is a much smaller atom that the hydrogen molecule, the vibrational mode of this gas allows it to expel more heat than helium does, hence lowering the thermal response consequently. Calibration against Ar would have been a good option since the heat transfer is similar to di-hydrogen.

Figure 4 shows the comparison between calibrations and the run for each cell, in an identical environment. As explained above, helium creates a different thermal response of the cells. We expected to see the calibration show a hotter temperature than the hydrogen run. This is seen with the dummy apparatus. However, the cell using the active component from Celani runs significantly hotter than the dummy cell. A maximum of 5°C is seen for 25 W of power input as shown in Fig. 5.

The main issue with this protocol is that hydrogen exposure of the borosilicate tube is not even between the two cells. While the activated wire in one cell is loading, the second Celani wire – the one not yet activated – is still exposed

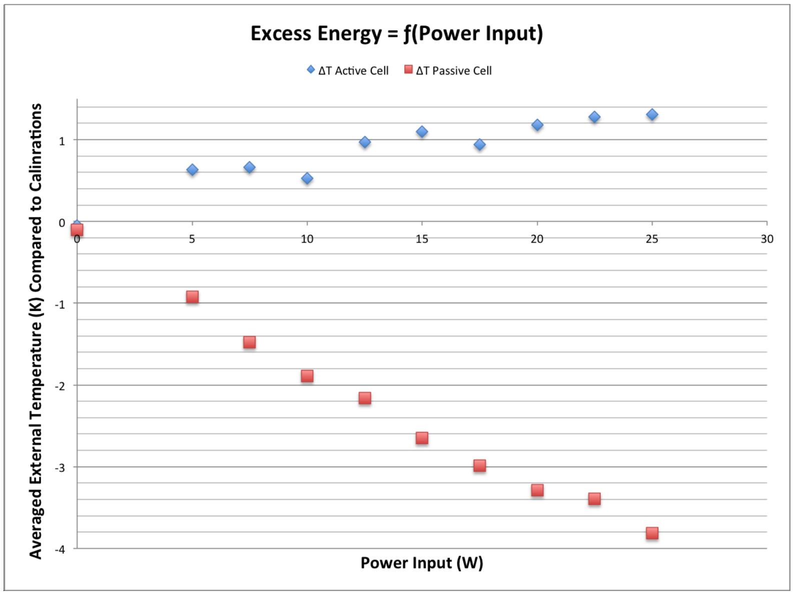

Figure 4. Results of the differential test subtracted to the helium calibrations. Active cell shows consistently higher temperature compared to calibration whereas passive cell is cooler.

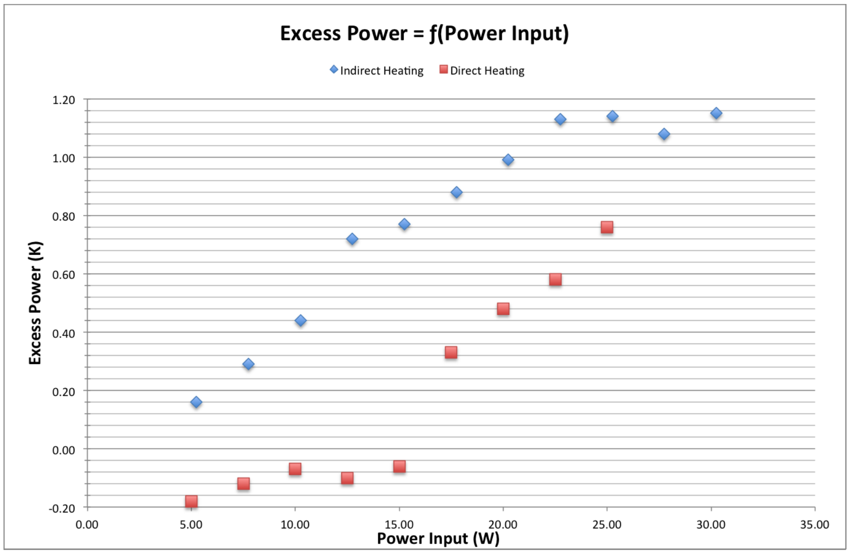

Figure 5. Excess power as a function of power input on a set of differential apparatus under dynamic vacuum condition.

to vacuum. Since we did not have the optical instruments to evaluate the changes of the glass characteristics, we cannot characterize this effect. This will eventually be the subject of further investigations.

Another effect that takes place on the surface of the wires is related to the cycling of loading and unloading. This

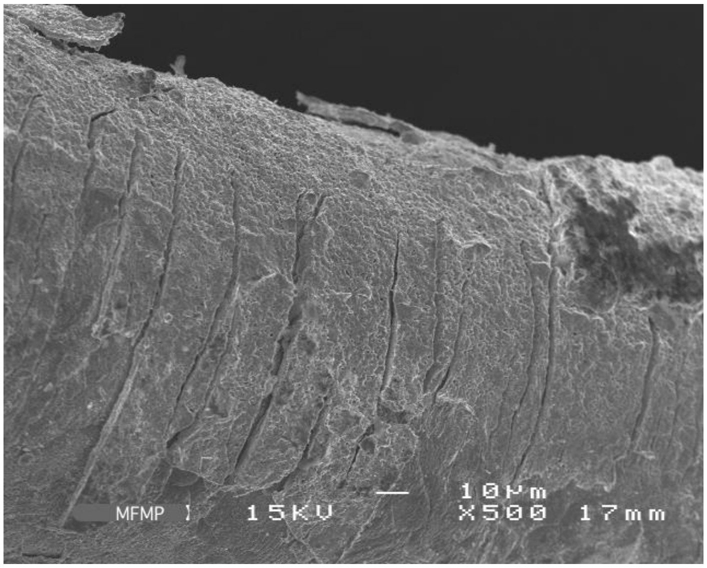

Figure 6. SEM image of the surface of the wire used under the repetitive dynamic vacuum protocol. Hydrogen embrittlement as well as vacuum conditions have forced the hydrogen to leave the wire, inducing cracks on the surface of the material.

is shown by the protocol used. As soon as the cells are put under active vacuum, the resistance of the wire rapidly increases. This releases hydrogen from the wire, which produces apparent excess heat.

The yield of energy released by the system is lower and lower over time and shows a fatigue effect. This is probably due to expansion of surface cracks that takes place. This would also be triggered by enlargement of cavities volumes in sub-surface microstructure. Finally, repetitive reduction and oxidation of the metal structure tends to disrupt the structure, as shown in Fig. 6.

9. Conclusions

The results produced by the original experiments done by the Martin Fleischmann Memorial Project show very similar orders of magnitude to what Celani has shown in his papers. Because Celani discarded his results during ICCF-17 and NI-Week 2012 due to an acquisition issue that under-estimated measurement of the input power, we also discard these results, and do not include them in our comparisons.

The range of coefficient of performance provides a solid answer to questions made regarding the level of excess energy showed by the apparatus built by Celani. With an optimum yield of excess heat measured for 15 W of power input, the system is very interesting. During the first test 12% excess heat was demonstrated, and 5% in the second test.

However, the calorimetric method used in that case is very much a concern and required a lot of effort to master, which should not be necessary. Two main criticisms are relevant to this colorimetric method. First, during the experiment, the infrared emission is changed a little because of the reduction of the oxide layer originally present on the surface of the tested treated wire during calibration. Secondly, the sensitivity of the system to environmental changes is pronounced, making it difficult to implement, measure, and achieve confidence in this method.

There is also a possibility that the tube changes its transparency while pressurized with hydrogen. This is one of the many possibilities that could change the measurements over time.

Finally, the experimental run under vacuum showed the same trend without replicating the amplitude of the results. Between a lack of confidence due the inexperienced operator in the first attempt, and the small signal during the last attempt, conclusions about the nature and the amplitude of the effect are still to be verified. Mass-flow calorimetry has been widely requested in crowd-sourced comments and by the scientific community. This will soon be implemented.

Acknowlegements

We are grateful to Professor Francesco Celani for supplying his wires, and for providing help and advice to members of the project. Amazing work has been done by the MFMP team across the globe. During the last months we were working tirelessly to build up this project from scratch. This work has been made possible with the invaluable help of Paul Hunt and the team in Hunt Utilities Group. Finally, all this work would not have been possible without the work, comments and generous donations made by our followers on our web site. Thank you very much to all.

References

[1] F. Celani, E.F. Marano, A. Spallone, A. Nuvoli, B. Ortenzi, S. Pella, E. Righi, G. Trenta, F. Micciulla, S. Bellucci, S. Bartalucci, M. Nakamura, E. Purchi, G. Zangari, S. Cupellini, A. Mancini, F. Maggiore and A. Ovidi, Experimental results on sub-micro structured Cu–Ni alloys under high temperatures hydrogen/deuterium interactions, *International Workshop on Anomalies in Hydrogen Loaded Metals*, Pontignano (Siena) - Italy (10-14 April 2012).

[2] Francesco Celani, E. F. Marano, A. Spallone, A. Nuvoli, E. Purchi, M. Nakamura, B. Ortenzi, S. Pella, E. Righi, G. Trenta, S. Bartalucci, A. Ovidi, G. L. Zangari, F. Micciulla and S. Bellucci, Cu—Ni–Mn alloy wires, with improved sub-micrometric surfaces, used as LENR device by new transparent, dissipation-type, calorimeter, *ICCF-17,* Daejeon, South Korea, 2012.

[3] Francesco Celani, E. Purchi, A. Nuvoli, A. Spallone, M. Nakamura, B. Ortenzi, S. Pella, A. Ovidi, G. Vassallo, S. Bartalucci, E. Righi and G. Trenta, Evidence of anomalous heat evolution, on surface modified Constantan wires, after prolonged H2 absorption and subsequent measurements under dynamic vacuum, Private communication.

[4] SCHOTT DURAN ® Tubing, Capillary and Rod of Borosilicate Glass 3.3.

[5] Irving. Langmuir, G.M.J. Mackay, The dissociation of hydrogen into atoms, Parts I–III, *J. Am. Chem. Soc.* **36**(8) (1914) 1708–1722.

[6] M. McKubre and F. Tanzella, Using resistivity to measure H/Pd and D/Pd loading: method and significance, ICCF-12, Yokohama, Japan, 2005.

J. Condensed Matter Nucl. Sci. 15 (2015) 256–267

Research Article

Water-free Replication of Pons–Fleischmann LENR

William H. McCarthy*

2156 Old Middlefield Way Mountain View CA 94043, USA

Abstract

Statistically significant heat is produced by a method similar to Pons and Fleischmann but not involving electrolysis or water. Instead of putting hydrogen into electrodes by operation for a few days, hydrogen solute is incorporated into electrode alloys by temperature and pressure, before the cell is assembled.

Keywords: Calorimetry, Copper, Hydrogen, Nuclear reaction

---

1. Introduction, Rationale

The Low Energy Nuclear Reaction (LENR) system described here is fundamentally similar to the Pons and Fleischmann (P&F) [1] innovation as developed by many scientists over two decades. A more simple method was sought to avoid some of the complications of the electrolytic method, but to retain the fundamental metallurgy of P&F, notably the heavy saturation of the metal with hydrogen. Practical advantages could be had by loading the metal with hydrogen before trying to produce a nuclear reaction, rather than doing so by electrolysis during the operation of the cell. These include eliminating the need for recombining the electrolytic oxygen and hydrogen gasses, with the concomitant safety advantage of avoiding failure of a catalyst to do that. Also, if a dry system could be found, temperatures in the realm of commercial steam generation should be much more easy to obtain than with electrolysis.

Absent electrolysis, palladium would not be a good choice because the hydrogen saturation would not be retained at ambient pressure when the electric current was switched off. Many other metals, when rapidly cooled from high temperatures and pressures, retain small concentrations of hydrogen that are well above ambient saturation levels,. Iron, copper and nickel are a few examples. Among that set, copper is the easiest to process. LENR has often been observed in nickel, which has some (metallurgical) similarity to copper. For instance, copper and nickel form a complete set of binary solid solutions with no intermetallic compounds (monel, cupronickel, etc.) Typically, light hydrogen works with nickel, which has practical advantages over deuterium used in most of the palladium cathodes.

Substantial effort was expended in quenching encapsulated copper and some of its alloys from high temperature and hydrogen pressure. Since electrolytic cells have occasionally continued to produce LENR after switching off the

---

*E-mail: santander@earthlink.net

electricity, it was thought that effect might be reproduced in this system by quickly installing the quenched copper or other alloys into a calorimeter. None of those tests produced anomalous heat and the experimental difficulties were formidable. Thinking about those results, it seemed that perhaps the Nuclear Active Environment (NAE) is not static as in the quenched copper case. That is, putting all the right materials together without any dynamic impulse to move charged particles, they may not encounter one another, no matter how unhappy they may be in the stress fields of the deformed metallic lattice. Where is the dynamism in P&F? Perhaps the hydrogen bubbles on the cathode surface locally obstruct electron flow out of the cathode to set up charge variations within the cathode just sufficient to get solute ions to move. Potentially, that could account for the infamous irreproducibility of the P&F effect. Those bubbles must change significantly depending on details of electrode geometry, suspended matter in the electrolyte, current density and other apparently minor variables.

Applying the scientific method (per the Conference title), a working hypothesis was conceived to assemble the above ideas and knowledge into a test program to clarify some of the uncertainties in LENR and to improve the generation of anomalous heat. It is expected that industrially significant products will eventually result. That working hypothesis includes the following elements:

(1) Near super-saturation of hydrogen into a metallic lattice is a necessary, but not sufficient, prerequisite to these reactions (either stable hydrogen isotope and a variety of metals can be used).
(2) The NAE is not static nor electromechanically uniform on a μmeter scale or smaller (variations of electric current in location and time along the surface of an electrode are important and may account somewhat for the

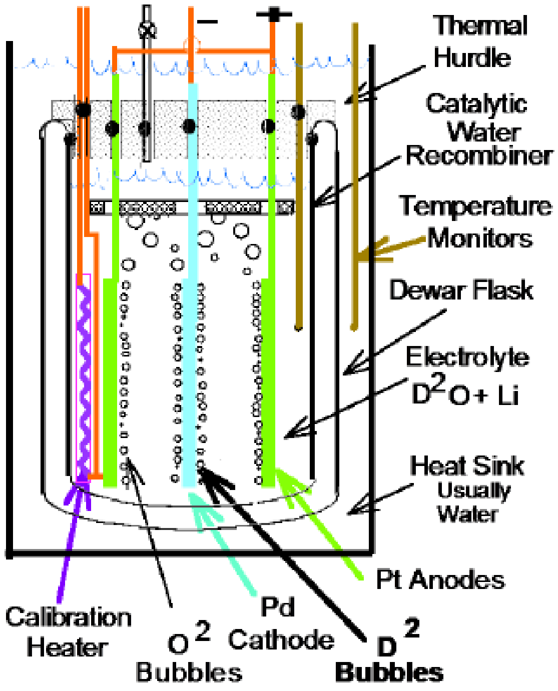

Figure 1. Pons and Fleischmann schematic arrangement.

lack of reproducibility typical of LENR.)

(3) Other light element solutes may be reactants (lithium and boron are of particular interest.)

Following that working hypothesis, cells were built, more like electronic capacitors than electrolytic cells, with copper alloy electrodes separated by a dielectric containing small electrically-conducting particles. Those particles inject electric current at discrete, separated, locations along the surfaces of the electrodes. That is the reverse of the electrolytic system where electrons depart the electrode, except where obstructed by a critically sized (dielectric) gas bubble. Fine graphite particles have been substituted for the hydrogen bubbles. The spacial separation of conduction is obvious in both cases. Also, some change over time (due to Brownian motion), functionally equivalent to bubble motion (due to gravity) might take place, provided that the graphite particles are small enough and their embedment is heavy and hot enough. In spite of pyrophoric considerations, metallic powders are expected to be studied in future.

Copper-based alloys and light hydrogen were chosen for practical reasons. Vacuum-pump oil and silicone grease have been used to suspend the graphite particles. Schematic diagrams, showing the features that are salient here, for a composite P&F electrolytic cell and for a typical dry, no electrolysis, cell are given in Figs. 1 and 2, respectively.

2. Experiments Described

2.1. The cell

In the present arrangement, shown in Fig. 2, the electric current is distributed over the electrode surface by an array of tiny graphite particles suspended in oil or grease. The electrodes are strips of copper alloy about 0.13 mm (0.005 inch) thick, 7 mm (0.28 inch) wide and 64 mm (2.5 inch) long. Hydrogenation of the electrodes is carried out in capsules pressurized to about 20 bar (300 psig) at 600–900°C. After 30 min or so, the capsule is water quenched. Dehydro-

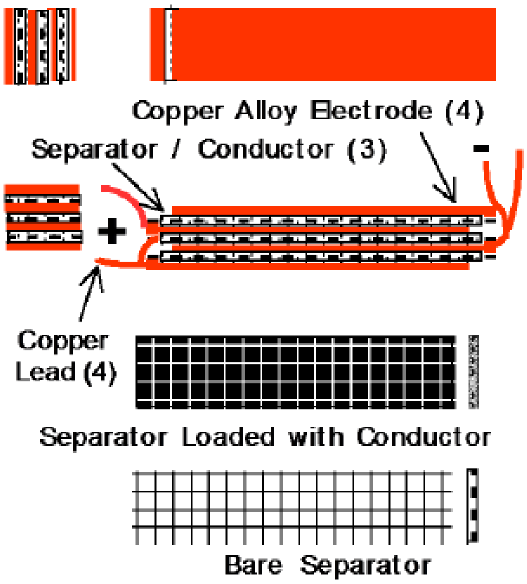

Figure 2. Schematic of the dry cell .

genation to prepare control electrodes is done by several vacuum (20 μm Hg) anneals at about 700°C alternated with argon pressurization (20 bar). Cells are prepared from alternating stacks of these electrodes separated by textile mesh saturated with a petroliferous suspension containing graphite particles. These cells are thus poor (low Q) capacitors of a few microfarads and 3–20 Ω.

2.2. Calorimetry

A typical seebeck calorimeter, as used here, is based on a thermopile consisting of a series string of eight to ten Type-E thermocouple junction pairs. For this spider structure, the warmer junctions are cemented at the edges and between two strips of polycarbonate that form the base of the specimen carrier. The alternate cold junctions are cemented to similar polycarbonate strips attached to the body of the calorimeter, which is maintained at ambient temperature. Thin copper channels are cemented to the carrier polycarbonate on both sides, to stiffen the assembly and disperse any temperature gradients. The specimen is clamped to one side of the carrier with small brass screws and nuts. Thin rubber pads are usually included to prevent short circuits, without seriously affecting the sensitivity of the calorimeter. A joule heater is attached to the opposite side of the carrier, in as symmetrical a fashion as its geometry and that of the specimen allows. That electrical resistance heater consists of nichrome wire wrapped around a strip of polycarbonate and covered with a thin layer of silicone adhesive.

The thermocouple wires have three functions in this arrangement: They mechanically support the specimen/heater carrier, they signal the voltage corresponding to the temperature difference between carrier and ambient to measure the thermal power deposited on the carrier and they provide most of the thermal hurdle that maintains that temperature difference. The sensitivity of the calorimeter can be adjusted by selecting the diameter and length of thermocouple wires.

A sketch of the power sensitive part of such a calorimeter is shown in Fig. 3. A complete assembly is diagrammed in Fig. 4.

2.3. Calorimeter

The spider is enclosed in a vacuum chamber as shown schematically in Fig. 4. That chamber has a clamshell design consisting principally of two copper half-cylinders, each brazed to steel quarter-spheres on the ends. The enclosure is mechanically pumped (about 20 μm Hg) to eliminate convection and greatly minimize gas-conduction heat transfer.

There is some radiation cooling of the spider assembly. At the power levels used here, however (less than 650 mW), radiation can account for no more than one-quarter of the heat passed from the spider to the enclosure shell. It was found in practice that that level of thermal radiation is insufficient to produce detectable nonlinearity in the test results.

2.4. Testing

Cells are activated by direct current provided by a lead-acid battery. Thus, power factor concerns are eliminated. Current is controlled by a single-transistor power supply of the author's design and construction. The same Hewlett Packard Model 3445A voltmeter is used for all current and voltage (hence power) data. Cheap DVMs are connected to aid in adjustment and error finding but such data are not included here. The HP 3445 instrument provides visual digital output with least count of one millivolt. The range of power levels used here is from about 50–600 mW. The corresponding HP3445 range is typically 0.8–5.0 V. A four-wire arrangement is used to connect the power supply to the specimen or joule heater. Current is supplied by one pair of the quad and voltage is measured with the other pair. Voltage drops in the leads are thereby not included in the results. Further, the HP 3445 voltmeter has very high input impedance.

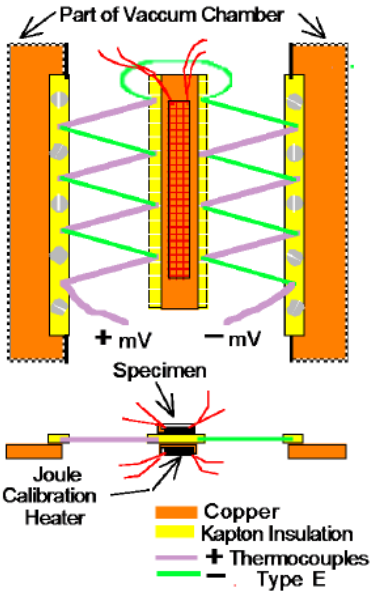

Figure 3. Seebeck calorimetry spider (heat sensor).

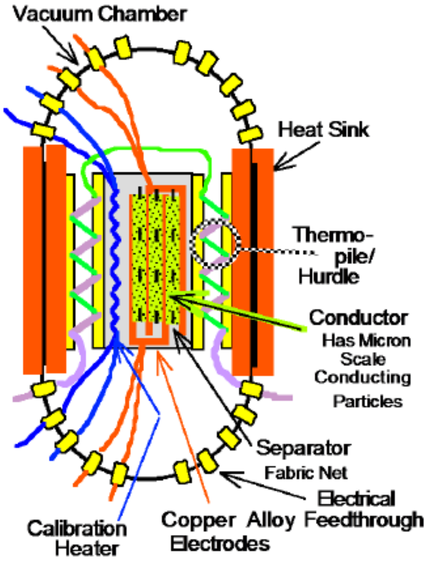

Figure 4. Calorimeter assembly.

A device is available to reverse automatically the specimen polarity. It is based on an electromechanical relay and Type 555 integrated timing circuit. In practice, with a reversal period of roughly ten minutes, any power factor concern is insignificant.

Voltage is measured directly. Current is measured by the voltage drop across a standardized string of 10 W resistors. For any test run, the same resistor(s) are used for both specimen and calibration heater. Joule heaters are designed to be fairly close in resistance to specimens. The standardized resistors are selected to be in the same range. Thereby, only one range of the HP 3445 is normally used for joule and specimen readings (both current and voltage) over a moderate range of input power – often those raw measurements are mutually within a factor of about three. Comparability among all four voltage, current, joule and specimen measurements is thus assured.

Thermopile output (dependent variable) is assessed using a Leeds & Northrup Model K-2 potentiometer. That 1960s era manually balanced wheatstone bridge uses a calomel standard cell. It has a least count of 1 μV. At a typical calibration minimum input of about 50 mW, the thermopile produces about 1 mV.

The procedure is to power the cell or heater to some fairly arbitrary power level and wait perhaps an hour for thermal equilibrium, as shown by near constancy in the K-2 readings. Then typically three readings, separated by 5–10 min, are recorded. Input power is then adjusted, and/or input is switched between specimen (or polarity) and joule heater. To get some semblance of randomness, power levels are changed arbitrarily (not in up or down series, nor in order of power level). For efficiency, however, specimen and calibration will usually be switched at roughly the same power level. A set of the order of 50–100 equilibrium calibration and specimen data points is thus acquired over several days

Readings are taken while power is stabilizing and the cell is coming to equilibrium. Those data are useful to assess calorimeter performance and to estimate total anomalous energy produced during a run. Only equilibrium data are reported here, however. So far, only manual data recording on paper has been employed, without automated data acquisition. The raw data are entered onto an Excel spreadsheet to calculate powers, provide least-squares equations for calibration and specimen performance and to compile ancillary results.

Data analysis and graphic displays are relied upon to define the performance of specimens and calibration heater, rather than trying to compare individual data points. Thus, the considerable trouble required for operation at precisely the same set of input levels for both heater and specimen measurements is avoided.

3. Experiment Results

3.1. Rough description of the experiment array

About two score of test runs have been performed, so far, to explore the effects of electrode alloy, separator and conductor composition, processing and testing technique. Electrodes have been prepared from three copper based, intentionally alloyed, compositions plus two types of unalloyed copper. Commercial materials were used: the presence of tramp elements is assumed. Intentional solid solutes were lithium and boron at total concentrations of less than one weight percent. Those alloys were cast and rolled to thin sheet or foil by the author. He added nominally two weight percent lithium or boron master alloys to commercial copper to get the desired compositions. Those copper base master alloys are normally used for copper deoxidization. Electrode materials were hydrogenated, dehydrogenated or prepared without hydrogen adjustment. Some electrodes were made of cold rolled material.

Eleven compositions of conductor have been tried. Particle content in those suspensions ranged from 2 to 19 vol.%. Cells that produced anomalous heat had typical resistance (it changes during testing) of about 3–20 Ω. Less resistance made specimens uncontrollable by the simple power supplies used. Input power was about 50–600 mW. Maximum anomalous power was 35 mW. One early cell at 100 Ω resistance produced 5 mW excess, which was within the upper half of the three-sigma band. Adjustment to 12 Ω resulted in 15 mW excess, then above the band.

3.2. An active cell

Some results from an active cell are given in Fig. 5. One electrode was a copper, 0.75 wt.% boron alloy hydrogenated at 820°C and 20 bar (300 psig) for 45 min, water quenched in capsule. The other electrode derived from a commercial copper tube. The separator was a layer of medical gauze about 25 μm (0.001 inch) thick. To make the conductor, it was saturated with a suspension containing nominally 3 μm (120 μinch) graphite particles in mechanical vacuum pump oil. Specimen resistance was about nine ohms to start.

Figure 5 is a plot of thermopile output versus input power for that example. Three-sigma statistical limits for the joule calibration data are defined by the band between the solid green lines in Fig. 5. That band is 3.2 mW wide and 0.4 mV tall ($\pm 3\sigma$). The 18 calibration data points are shown as green circles (in essentially isopower subsets of three). The green dashed line is the least-squares fit of the joule calibration data. Red triangles and blue squares indicate data points for the low-Q capacitor specimen. Corresponding dashed lines are the least-squares fits, direct and reverse polarity, respectively.

Both specimen lines and all data points are above (in output) and to the left (less input for given output) than he upper three-sigma limit of the calibration data. Above about 250 mW, that separation is roughly another three-sigma amount. Therefore, the probability (assuming normal distribution and other standard statistical criteria) that the specimen and heater outputs are the same is less than 0.3%. It appears, however, that polarities are indistinguishable from one another.

Even though the low-Q capacitor results are substantially significant statistically, the magnitude of anomalous power (excess of output power over input) is small, as illustrated by Fig. 6. Anomalous power is plotted against input, with red and triangles for direct polarity and blue and squares for reverse. Symbols are data points and lines are corresponding least-squares fits, of course.

The excess power is moderately scattered over the range of 10–30 mW for the input range of 100–310 mW. Each of the three black dashed vectors define a given locus of relative anomalous power: 6, 9 and 12% of input power. All of the data fall within the 6–12% anomalous band. They tend to cluster around the 9% vector.

3.3. A control cell

A cell using commercial copper electrode materials subjected to dummy hydrogenation was prepared. Instead of high temperature pressurization with hydrogen, alternating vacuum and argon pressurization was used. The conductor was similar in dimensions but moderately different in composition versus the active cell of Subsection B. Resistance was about 10 Ω. Results in the form of a plot of input power versus thermopile output are shown in Fig. 7.

As in the active example, the joule calibration data are shown as green circles for the individual measurements (three per power level). The three-sigma band is defined by solid green lines. A dashed green line shows the least-squares fit. The three-sigma band is 11.2 mW wide by 0.2 mV tall.

Specimen data are shown by black triangles. Least-squares fit for the capacitor is the dashed black line. In this case, there was no anomalous power because the dashed lines are indistinguishable, each from the other. There was no point in considering polarity, because the electrodes are identical. This specimen behaved thermally exactly as did the joule heater.

4. Plausibility of Nuclear and Chemical Energy

The active specimen of Figs. 5 and 6 produced a modest 406 J of anomalous energy during the testing described above. That amount is not quite enough to run one Christmas-tree light for 1 min (7.5 W times 60 s = 450 J). It was determined by averaging the beginning and ending excess power of each measurement step by the time elapsed during that step. The resulting step energies were added together over the whole set of 71 measurement steps recorded during

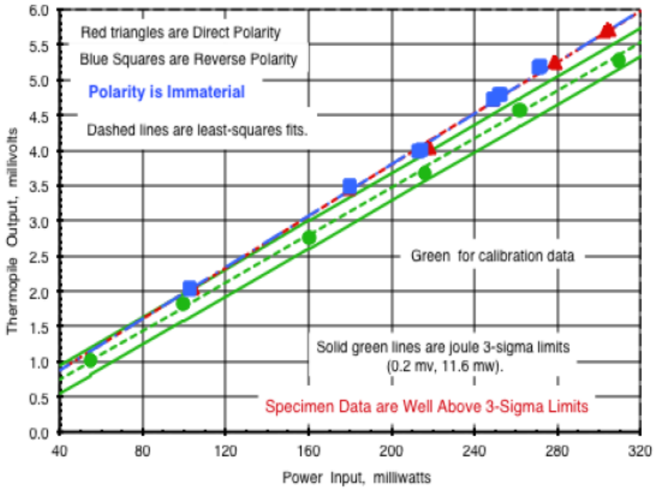

Figure 5. Test and calibration: copper, boron and hydrogen.

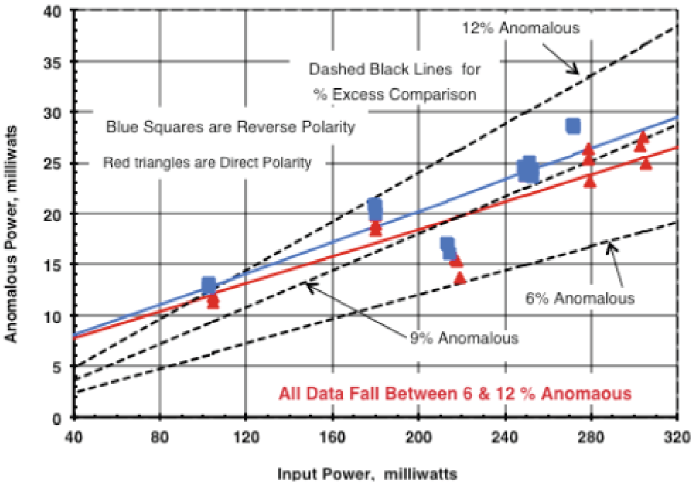

Figure 6. Anomalous vs. input power.

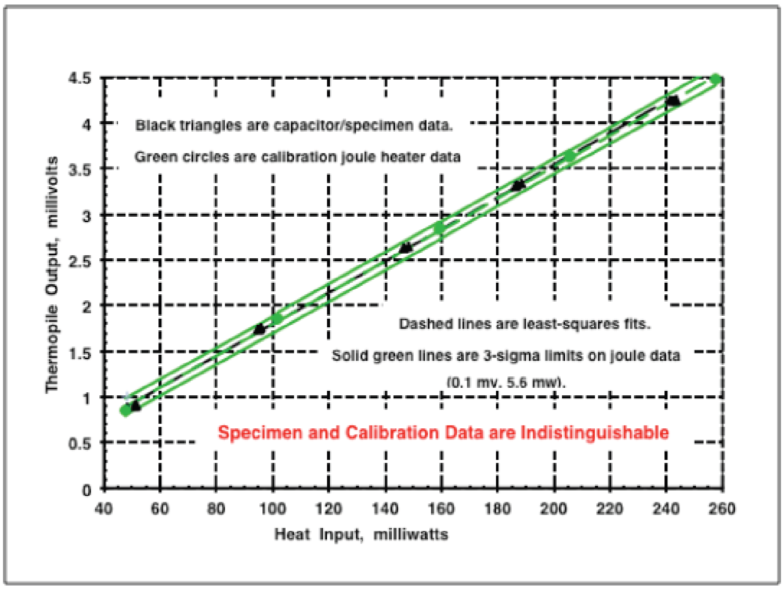

Figure 7. Test and calibration of dehydrogenated copper (control).

activation of the specimen. Step-time was usually 5 min and the total time over all steps was 6.32 h (6.8% more than if all steps were precisely 5 min). Excess energy is the difference between total energy measured and the input energy. Total power here is the millivolt output of the thermopile, as measured by the K-2 potentiometer, converted to power using the equation obtained from activating the joule heater at various calibration power levels interspersed among the specimen measurement steps. Input is, of course, the product of voltage and current at each measurement step.

To assess whether the observed 406 J produced in the active specimen described here could be nuclear and/or chemical in nature, we can compare it to the energy that would result from the amounts of the various constituents of the specimen were they to undergo selected chemical or nuclear reactions, the energetics of which have been published. The calculations and published thermochemical and nuclear values used will be made available upon request. Also, readers are encouraged to apply their own chemical, physical and nuclear coefficients to the materials and dimensions reported here, to perform their own analysis of whether chemical, nuclear, or effects unknown to the author may be at work here. The specimen of Figs. 5 and 6 conforms well geometrically with the diagram of Fig. 2, which may be used to more fully understand the array of materials involved.

4.1. Chemistry

The specimen electrodes described above consist of four strips total of copper alloy 0.13 mm (0.005 inch) thick. Each is 0.76 mm (0.30 inch) wide by 6.53 mm (2.5 inch) long. Were they to be completely oxidized to Cu_2O, the (ambient) enthalpy change would be 7.7 times the 406 J produced in testing. Assuming that only 25 μm (0.001 inch) of copper on the six layers touching conductor were oxidized to Cu_2O, there would still be about four times more chemical energy evolved than produced here. With one exception, no change in appearance of any electrode has been observed following testing but the oxidation described above would be obvious. Also, there is no source of oxygen, or similar material, in the calorimeter because it is evacuated during testing. The one exception involved sulfur in the conductor, erroneously thought to be in an inert form; after test, the black films on electrodes seemed typical of Cu_2S.

Consider oxidation of the separator/conductor. That is polyvinyl chloride (PVC, medical) gauze soaked with oil containing graphite particles, with sometimes a proprietary inert powder addition. To be conservative and avoid complexity, assume it made entirely of gasoline or similarly energetic alkane. The gauze was 25 μm (0.001 inch) thick and there were three layers of separator/conductor pressed against the electrodes. That volume of gasoline would yield about three times the 406 J produced, if completely burned to carbon dioxide and water. There was no oxygen available to do that and no such thing was observed.

Perhaps the oil of the conductor could polymerize, crack or react in some way with the PVC or graphite. It seems inconceivable that could be more energetic than the decomposition to elements (C and H_2)of an equal volume of alkane, say octane or dodecane, to produce their enthalpies of formation (250 and 352 kJ/mol, respectively). Accounting for their molecular weights and densities yields a volumetric enthalpy of 1.5 kJ/ml, for either alkane. The 406 J of anomalous heat works out to 700 times the alkane decomposition heat estimated in this way. Also, there was no evidence of any such reaction.

Suppose that only the hydrogen dissolved in the electrodes was oxidized to yield the excess energy observed. One published relationship between solubility of hydrogen in copper and temperature at ambient pressure is:

$$C = 0.102 \exp\left(-4,535/T\right),$$

where C is the hydrogen concentration in atomic percent and T is the temperature in K. Using that relationship and a square-root of pressure rule, one finds the hydrogen concentration in the present electrodes to be 0.00720 at.%, further assuming that concentration to be preserved following electrode processing at 820°C and 20 atm. Applying the mass of the electrodes and the enthalpy of formation of water results in the 406 J produced being about nineteen thousand times the heat possible from burning that dissolved hydrogen.

4.2. Nuclear reaction

Now consider the energy that might be produced by some nuclear reactions taking place in the 0.00720 at.% hydrogen dissolved in the electrodes as described in the previous subsection (about 9×10^{-8} hydrogen moles). Some potential nuclear reactions of light and heavy hydrogen with themselves and with lithium, beryllium, boron, nickel, copper or palladium are shown in Table 1.

Table 1 is based on simple arithmetic differences between the well known and published masses of the various reactant and product isotopes involved.

First, suppose boron 11 alloying-ingredient reacts with all of the light hydrogen in the electrodes to produce three helium 4 isotopes per boron 11 and 8.68 MeV, per Table I. That reaction would produce 185 times the 406 J measured, assuming the hydrogen content from processing the electrodes at 820°C and 20 atm. was retained. Should the retention correspond to only 600°C and 5 atm, the ratio of complete hydrogen burnup to energy produced would still be a factor of 33. If the reaction produced carbon and 15.95 MeV, per the table, it would be 340 times the 406 J with the nominal 820°C, 20 atm. processed electrodes or 60 times the observed output with degraded (600°C, 5 atm.) electrodes.

Second, consider that the light hydrogen reacted with the majority (69%) copper 63 content of the copper electrodes, producing zinc 64 and 7.7 MeV, per Table 1. That would be 164 times the observed anomalous power for nominal electrodes and 29 times for degraded ones.

Third, the very small heavy hydrogen content (0.0151 at.%) of the ordinary hydrogen mix used here could conceivably be responsible for the observed anomalous energy production. The maximum intrinsic output then would be 0.0036 MeV based on total hydrogen content (0.0151% abundance of D in H times the 23.8 MeV of the top line in Table 1). (The other two heavy hydrogen reactions listed produce only a fraction of the 23.8 MeV, and dangerous

Table 1. Potential nuclear reactions of light elements with hydrogen

Reactants		Products	Mass difference per reaction		Energy (kW-h/g) reacted	Value (US $ of energy/g)
			AMU	MeV		
H^2+ H^2	→	**He^4**	**0.02560**	**23.837**	**1,59,619**	**3192**
H^2+ H^2	→	**He^3 + H^1**	**0.00433**	**4.032**	**26,825**	**537**
H^2+ H^2	→	**He^3 +n^1**	**0.00351**	**3.268**	**21,745**	**435**
Li^6+ H^2	→	**2 He^4**	**0.02402**	**22.363**	**74,874**	**1497**
Li^7+ H^1	→	2 He^4	0.01862	17.340	58,056	1161
Be^9+ H^1	→	Li^6+ He^4	0.00228	2.125	5685	114
Be^9+ H^2	→	**Li^7+ He^4**	**0.00768**	**7.148**	**17,387**	**348**
B^{10}+ H^2	→	**3 He^4**	**0.01923**	**17.905**	**39,965**	**799**
B^{11}+ H^1	→	3 He^4	0.00932	8.679	19,372	387
B^{10}+ H^2	→	**C^{12}**	**0.02704**	**25.176**	**56,231**	**1125**
B^{11}+ H^1	→	C^{12}	0.01713	15.950	35,624	712
Ni^{62}+ H^1	→	Cu^{63}	0.00657	6.120	2607	52
Cu^{63}+ H^1	→	Zn^{64}	0.00828	7.709	3232	65
Pd^{106}+ H^1	→	Ag^{107}	0.00621	5.787	1451	29
Pd^{105}+ H^2	→	**Ag^{107}**	**0.01409**	**13.122**	**3290**	**66**
Fission Comparison (U^{235})			0.21050	196	5589	112
H_2+O_2	→	H_2O	Nil (3E-9)	2.5 eV	3.7 E-3	7.5 E-5
Coal+O_2	→	CO_2	Nil (1E-9)	1.1 eV	7.0 E-4	1.4 E-5

Value based on 0.10$ per electrical kWh delivered and 20% thermal to electric power conversion efficiency thermal to electric power.

radiation.) The 406 J observed here is, on this basis, a minimum of 13 times that which could result from complete burnup of the heavy hydrogen content of these electrodes.

In summary, it is apparent that the 820°C, 20 atm. processing of the electrodes discussed here could load them with sufficient light hydrogen to account for the 406 J of anomalous heat observed. Two reactions of light hydrogen with the boron alloying content and one with the copper were considered. Even if much of the hydrogen dissolved in the high temperature and pressure treatment is not retained (equivalent to only 600°C and 5 atm.) the remainder is still adequate. The heavy hydrogen content of the natural hydrogen used is, however, insufficient. If reacted chemically, the hydrogen in the electrodes is insufficient, by at least three orders of magnitude, to account for the anomalous energy observed. Chemical oxidation of the electrodes, or of the separator/conductor, might produce up to 10 times the anomalous energy shown if there could be any chemical reactant in the evacuated chamber that was used. Such a reaction would be obvious, but was not seen. Any chemical degradation of the separator/conductor, also unseen, would yield insufficient energy to account for these results. A chemical basis for these results is, therefore very unlikely but some, as yet undefined, nuclear reaction is probable. Table 1 lists a few, of many, possibilities. These low-Q capacitors need to be operated for months, at least, instead of the hours here, to produce sufficient nuclear reaction product necessary to elucidate what reaction(s) are responsible.

5. Conclusions

Pons–Fleischmann fundamentals are replicated, once again. This low-Q capacitor system, like several LENR methods, uses materials and processes foreign to electrolysis. Copper alloys containing light hydrogen replace deuterium-saturated palladium. Oil, containing tiny conducting particles, substitutes for lithium-bearing heavy water electrolyte. Tiny conductive solid particles replace the small deuterium bubbles deposited on P&F cathodes, for microscopic charge distribution across electrode surfaces.

The excess of output heat over input electrical energy is small (roughly 10% on good days) but statistically significant. It is barely possible that the small amount of anomalous energy shown here could have a chemical source. There are at least a few nuclear reactions, however, that do account for the energy observed, by margins of over 100 times. To uncover the reaction(s) responsible, it will be necessary to operate these cells for prolonged time and then to measure the reaction products.

No incubation period for anomalous heat was observed with low-Q capacitors. If excess heat appeared, it was there when the system stabilized (in less than an hour). This system seems consistent and reproducible but systematic repetition was not attempted. Exploring the large experiment space was desired rather than detailing it. Prospects for improvement are manifold. Development of commercial power generation appears to be feasible. In particular, the normal boiling temperature of water, as in electrolysis, is no limitation. The outlook for a supercritical steam source (say 400°C) is good.

Common, inexpensive materials and processes (e.g. Cu, light H, vacuum, thermocouples) are used instead of rare, expensive and exotic ones (Pd, D, mass-transfer calorimetry). Thus, LENR can now be advanced by a larger set of researchers and financial supporters than before. The resource limits and preliminary success of the present author attest to that fact.

There is much to be done.

Acknowledgements

The author acknowledges substantial help from the LENR community. In particular he wants to thank Drs. Robert A. Huggins, Thomas O. Passell and Roger Stringham for much beneficial discussion and cogent advice. Graphite powders were provided by Albert Tamashausky, Asbury Graphite Mills. Copper master alloys were supplied by Belmont Metals Inc.

References

[1] M. Fleischmann, S. Pons and M. Hawkins, *J. Electroanal.* **61** (1989) 301.

J. Condensed Matter Nucl. Sci. 15 (2015) 268–278

Research Article

Surface Preparation of Materials for LENR: Femtosecond Laser Processing

Scott A. Mathews*
The Catholic University of America, 620 Michigan Ave NE, Washington, DC 20064, USA

David J. Nagel and Brandon Minor
The George Washington University, 2121 I St NW, Washington, DC 20052, USA

Alberto Pique
Naval Research Laboratory, 4555 Overlook Ave SW, Washington, DC 20375, USA

Abstract

Because surfaces have been shown to be important for Low Energy Nuclear Reactions (LENR), their preparation for experiments or energy generators is naturally of interest. We demonstrate that irradiation of Pd with pulses from a femtosecond laser produces surface topography with features on both micro- and nano-meter size scales. Micrographs of these features were analyzed to obtain the spatial frequencies for later correlation with production of excess heat.

Keywords: Femtosecond lasers, LENR, Low energy nuclear reactions, Surface modification

---

1. Introduction

The experimentally proven ability to produce nuclear reactions with chemical energies is a vexing scientific problem with great practical promise. Because of data from many past experiments, it appears possible to produce clean power using small and cost-effective distributed generators. Much data, and some theories, indicate that LENR occur on or very near the surfaces of materials. Hence, the willful preparation of surfaces of materials for LENR experiments and power generators is an important topic. Oddly, it has received relatively little attention. Many techniques can be employed to modify the composition and structure of surfaces of materials for use as LENR substrates. We report here on the first use of laser structuring prior to experiments as a means to promote the functionality of cathodes for LENR electrochemical experiments. This work is not to be confused with studies in which laser light was shined onto LENR materials during experimental runs to trigger or increase production of excess power [1–3].

---

*E-mail: mathewss@cua.edu

Section 2 gives a brief summary of LENR, and reviews some past work on surfaces of cathodes for electrochemical loading and foils for gas permeation experiments. Then, we survey some of the methods that might prove beneficial for making the surfaces of diverse materials active for the occurrence of LENR. The effects of lasers of widely different pulse lengths on materials surfaces are summarized. In particular, femtosecond lasers have been found to produce surface structures with widely varied spatial frequencies. Next, we describe the laser and experimental setup employed for the work reported here. Samples of Pd were exposed to varying numbers of femtosecond pulses, with the energy per pulse being another variable. Scanning electron micrography was used to examine the samples after laser processing. The observed structures were generally in the micrometer range, but some features as small as 20 nm were seen. The micrographs were analyzed using MatLab to obtain the distribution of spatial frequencies. We will use the laser irradiated foils as cathodes in future calorimetric electrochemical experiments. We note possible additional physical and chemical processes than might be used to modify the structures and composition of laser-induced features.

2. LENR and Surface Studies

LENR, initially called “cold fusion”, are now well established experimentally [4]. These reactions were and remain contentious, mainly because there is no accepted theoretical explanation of how it is possible to employ chemical energies on the scale of an eV to trigger nuclear reactions with energies in the range of MeV.

The field of scientific research on LENR involves many ways to bring together isotopes of hydrogen with materials, and numerous techniques for measurements of the results of such interactions. Currently, there are two main approaches to producing LENR, electrochemical loading of deuterons into Pd and gas loading of protons onto Ni. The first of these is widely used in scientific studies. The second is expected to be the basis for practical energy generators. In both of these cases, the measurement of energy amplification (from electrical to thermal) is of great interest.

There is experimental evidence that, at least in several cases, LENR occur on the surfaces of materials. This is not to exclude the possibility that such reactions also occur within the bulk of materials. If LENR occur exclusively or preferentially on surfaces, practical energy generators based on them should be simpler in both construction and operation.

A significant database exists for the likelihood that LENR occur upon surfaces in electrochemical loading experiments. One of the clearer indications is an experiment done by Storms in which he reversed the electrode materials from the normal configuration of a Pd cathode and Pt anode. During the course of the run, Pd atoms dissolved from the Pd anode and were deposited on the Pt cathode. Only a thin film was produced, but excess heat was still measured [5]. It was found early in the field that the production of excess power in electrochemical experiments scaled linearly with the flux of deuterons through the surface of a Pd cathode. This is significant circumstantial evidence for the importance of surfaces for production of LENR.

There is relatively little published data on the locations where LENR occur in gas loading experiments. Possibly the best example is from experiments by Iwamura and his colleagues [6]. The experiments involved permeation of deuterons, which originated in the gas phase, through Pd foils containing multiple thin layers of CaO. A thin layer of Cs was deposited on the surface of the Pd foils prior to the runs. Sensitive surface analytical measurements during the course of the experiments indicated that Pr appeared in place of the Cs. Depth profiling of the foils showed that the Pr was confined within 10 nm of the surface [7].

3. Surface Modification and Characterization

We emphasize that two steps, (a) surface modification and (b) subsequent determination of the makeup and structures of surfaces, are mandatory for LENR as they are for numerous other processes in physics, chemistry, biology and engineering.

Techniques for tailoring the composition and structure of surfaces are numerous. Many of them are well developed commercially in the microelectronics and other industries. The three major types of processes for production of integrated circuits, MEMS and other microdevices are patterning, etching and deposition. The primary processes for production of nano-scale structures are the same three top-down techniques, and also the bottom-up physical or chemical growth of nanomaterials. All of the techniques in these categories, individually and in combinations, are available for modification of surfaces of materials that will go into LENR experiments and generators.

Many experimental tools are used to characterize commercial micro- and nano-materials and devices, that is, to determine their composition and structure. They involve irradiating the items of interest with photons, electrons or ions, and simultaneously measuring the photons, electron or ions that result from the bombardment. Optical and electron methods, and atomic force microscopes, are widely used for imaging of structures. We employed a Scanning Electron Microscope (SEM) in this work. Figure 1 is a flow diagram for our program. This paper deals with the first three aspects, the procurement, modification and characterization of the Pd cathodes for later LENR experiments.

It must be noted that our characterization work to date is informative, but well short of what is possible. There are many methods for obtaining the surface composition and structure of materials beyond scanning electron microscopy and analysis. They include a wide variety of means to measure the distribution of elements on a surface, notably Auger electron analysis and secondary ion mass spectroscopy. And, there are other methods for obtaining structure on atomic levels, notably x-ray diffraction and atomic force microscopy. Castagna and his colleagues [8] employed the last two tools to obtain the surface crystalline orientation and the scale of roughness of Pd cathodes they produced. Then, they ran those cathodes in electrochemical cells and measured the amount of excess heat produced. It was found that (100) surface crystal orientations and atomic-scale roughness in the range of 1–4 inverse microns gave the best excess heat production.

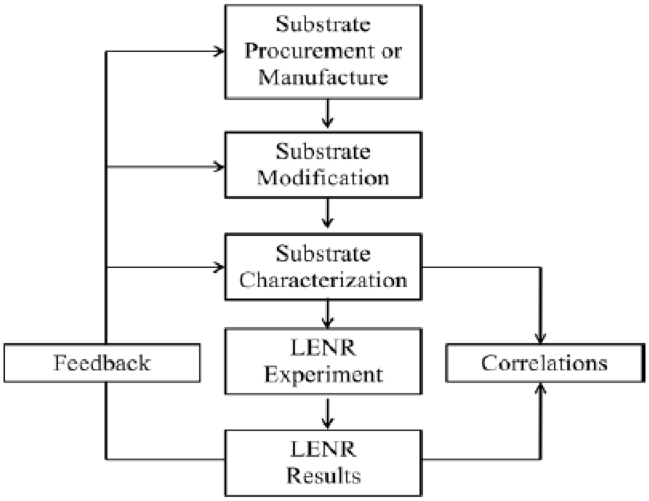

Figure 1. Sequences of steps in the current program.

4. Laser Effects on Surfaces

The ability to produce short pulses of laser light was demonstrated soon after the development of the laser in 1960 [9]. That technology enabled generation of pulses approaching gigawatts in optical power. When focused to spots 10 μm, and even smaller in diameter, irradiances on the order of or greater than 10^{15} W/cm^2 were achievable. It was found that such power densities produced plasmas on the surfaces of targets with extreme temperature gradients in space and time, sometimes on the order of a million degrees over distances of less than tens of micrometers and faster than tens of nanoseconds. The high temperatures and pressures in the plasmas caused significant, albeit localized effects on the targets beyond melting, vaporization and plasma formation. The field of laser processing of solid surfaces emerged from these observations [10], including a specialization to femtosecond laser processing [11].

When laser pulses on the order of picoseconds and shorter strike a solid, they interact with electrons at solid state densities, because there is insufficient time for establishment of a laser-photon-absorbent surface plasma. Such interactions can produce features on targets that are termed Laser Induced Periodic Surface Structures (LIPSS). They have been observed for decades [12]. But, they are not yet thoroughly predictable in behavior. For instance, in some transparent materials, periodic structures will form inside the material, rather than on the surface. As LIPSS have become a more popular topic of research, ways have been found to create structures with periodicities somewhat larger than, similar to and even smaller than the wavelength λ of the laser. These observations have prompted investigations into the origins of such vastly different spatial frequencies.

Structures with two different frequencies commonly appear on LIPSS: High Spatial Frequency LIPSS (HSFL) and Low Spatial Frequency LIPSS (LSFL). Their spatial frequencies are typically about 10 and 100% of the laser wavelength, respectively [13]. HSFL can be produced using the shorter wavelength second harmonic light from a particular laser. They normally appear at a lower fluence than LSFL. Increasing the number of pulses put on a given spot both makes the laser-affected area on the target larger and produces more LSFL.

We are investigating whether or not the LIPSS produced on a Pd target by a femtosecond laser might promote LENR. The following sections describe the laser and focal setup, the foils used, the features found on them and our analyses of the spatial frequency distributions of those features.

5. Experimental Setup and Parameters

Fifty-micron thick Palladium foils about 7 × 40 mm were purchased from Sigma-Aldrich. The foils were 99.9% pure on a trace metal basis. A Pharos SP laser (Light Conversion, Ltd., Vilnius Lithuania) operating at $\lambda = 1.03$ μm was used to irradiate the foils. The laser output was linearly polarized and orthogonal to the long dimension of the Pd foil. The laser pulse duration was measured at the laser output, using an optical correlator, and found to be between 190 and 210 fs. The delivered pulses were approximately 210–230 fs, due to dispersion in the optical system. The laser pulses were focused onto the Pd foils using a 10× microscope objective, model LMH-10X-YAG (OFR-Thorlabs, Newton NJ), with a numeric aperture of 0.25 and an effective focal length of 20 mm. The focused laser beam had a Gaussian profile with an estimated spot size of 10–15 μm (FWHM). The laser delivered individual pulses at a rate of 200 kHz. Hence, the maximum number of shots on a given spot was delivered in a time of only 0.5 ms. All laser exposures were performed in ambient air.

The Pd foils were translated using a precision XY translation stage (Aerotech Inc., Pittsburgh PA). In addition to translating the sample in a raster pattern, the program that drove the XY motion also controlled an electro-optic modulator in the laser. Hence, a preprogrammed number of shots could be fired on each location with a chosen laser power. A burst of laser pulses was fired every 25 μm. Five square regions were laser irradiated with 1, 3, 10, 30, and an unknown number exceeding 100 shots/spot. Within each square region, the laser power was adjusted to one of five power settings, ranging from 0.35 to 1.1 W. These laser powers corresponded to laser fluences varying from 0.96 to 3.1 J/cm^2. In this way, a single Pd foil was created that allowed us to investigate the laser induced surface texturing as

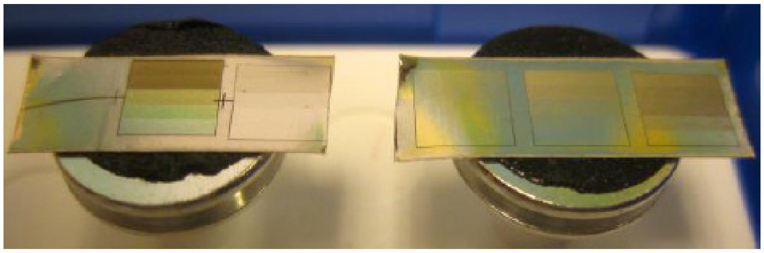

Figure 2. Visible light mages of the laser irradiated Pd foil cut into two pieces and mounted on 1 cm diameter SEM stubs. The squares are 5 mm on a side. The six regions are (left to right) not irradiated, heavy irradiation, and these numbers of shots per spot: 1, 3, 10 and 30. The total numbers of shots on the heavily irradiated square are not known, but exceeded 100. The focal spot laser fluences varied within each band inside of each square (bottom to top): 0.96, 1.1, 1.4, 2.4 and 3.1 in J/cm^2.

a function of both laser power and number of laser shots.

6. Optical Appearance

Visual examination of the irradiated Pd foils revealed colors that depended on the angle of observation. This indicated that those colors were due to diffraction. That observation immediately implied that there were structures on the surfaces of the foils with spatial wavelengths near the wavelengths of visible light, that is, fractions of a micrometer. Fig. 2 shows a photograph (taken under an ordinary fluorescent light) of the Pd foil, cut into two pieces and mounted on the stubs for the scanning electron microscope.

7. SEM Images

A Zeiss Sigma VP scanning electron microscope was employed to obtain micrographs of the laser processed Pd. A secondary electron signal was measured with an in-lens detector. We recorded SEM images of the unirradiated part and many of the irradiated areas on the Pd foil. Several of them are presented in this section to show the effects of the laser pulses on the target under various conditions.

Figure 3 is an image taken from the unirradiated part of the Pd foil. It contains significant structures. However, it will be seen that the features observed on the laser-processed parts of the foil are very different from those present in this figure. That is, the pre-shot structures seen in Fig. 3 seem to be irrelevant. We note that irradiation of a target with short pulse laser effectively cleans it, in addition to altering the surface topography.

One of the basic concerns in this study was the completeness of the coverage of the target surface with laser-effected regions. That coverage is determined by the spacing of the individual laser focal spots, the fluence per pulse and the number of shots placed onto the same spot. Figure 4 shows the coverage for fluence values between 0.96 and 2.4 J/cm^2 and for 3 and 30 shots on a given spot. It can be seen that a low fluence and smaller number of shots yields sparse coverage of the Pd surface. At the other extreme illustrated, the larger fluences and number of shots gives patterns over most of the surface. At this time, we do not know which, if any, of the achievable coverages is best for production of excess energy. The optimum structures for production of LENR are similarly unknown.

The next concern is the shapes of the structures within the focal spots, again as a function of the fluence and number of shots. Visual inspection of the images showed that there were two primary types of structures, roughly parallel lines and sponge-like regions, plus some small spherical features. Figure 5 shows three spots each subjected to over 100 laser shots at two magnifications. It is seen that the edges of these spots, which were subjected to lower fluencies, exhibit the

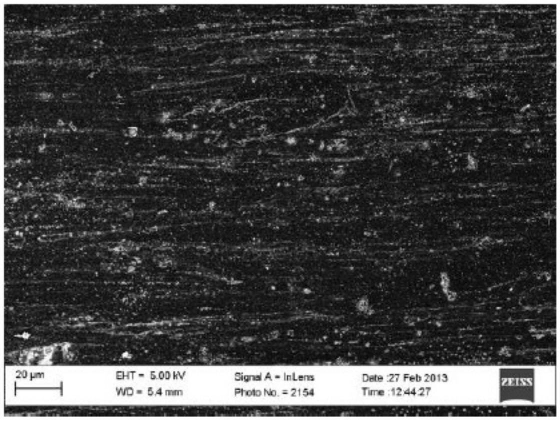

Figure 3. SEM image of a region of the Pd foil not subjected to the femtosecond laser pulses.

parallel structures, while their centers have the disordered and more equiaxed sponge-like features. The approximate periodicity of the parallel structures is evident, even though they are somewhat curved.

The pseudo-linear structures we produced vary in detail, depending on the number of shots. Figure 6 shows examples for two low-fluence (0.96 J/cm^2) cases, one with 30 shots and the other with over 100 shots. The first shows rows of singular features, while the latter has paired structures, both roughly periodic.

The final comparison of SEM images in Fig. 7 shows two high-magnification regions of the sponge-like structures on targets subjected to 3 shots at 1.1 J/cm^2 and greater than 100 shots at 2.4 J/cm^2. This mixture of fluences does not mask the trend for the disordered structures to grow somewhat with increasing shot number.

Small spherical objects appear in the bottom part of Fig. 6 and both parts of Fig. 7. These provide evidence that, at some point during the train of multiple pulses striking the target, the temperature of at least small parts of the Pd exceeded the melting point of 1554°C. It seems likely that the fine structures produced by the earlier shots were heated past the melting point by the later shots in a series of multiple shots.

Examination of higher magnification images than presented in Figs. 5–7 showed both irregular and spherical features on the scale of 20 nm, near the resolution limit of the microscope.

We emphasize that the images presented here and analyzed in the following section are only small samples for the large number of combinations of the parameters, namely the laser fluence and number of shots on each spot, plus all the potential laser and geometrical variables.

8. Image Analysis

Simple inspection of the SEM images shows the existence of LIPSS in some regions of the irradiated spots on the Pd foil. But, it was necessary to analyze the images to obtain quantitative information on spatial frequencies of the Pd structures. Such data might be of use for later correlations of surface structures with the performance of the laser-processed foils in LENR experiments. Those analyses and a sample result from them are described in this section.

Two steps were employed in order to obtain the spectrum of spatial frequencies. First, the varying brightness in the images was determined as a function of position along lines across the images. That brightness is dependent on the number of secondary electrons generated and intercepted by the detector when the SEM beam strikes a fine spot on the target being imaged. The geometry of the surface and the instrument both influence the electron signal and,

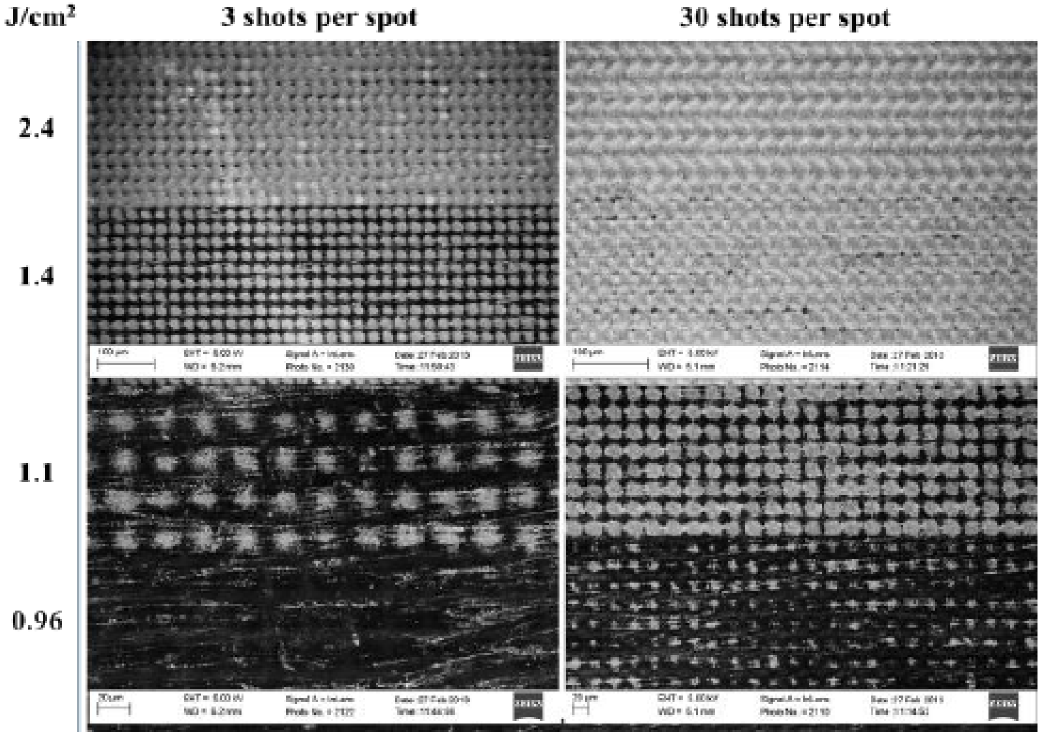

Figure 4. Micrographs for the noted fluences per shot and numbers of shots on individual locations on the Pd foil. The magnifications are indicated by the labeled bars in the lower left hand corner of each micrograph.

hence, the apparent brightness from each location on the target. Despite such limitations, the brightness vs distance plots do depend on the structures present on the Pd foil. All images contained 1024 × 768 pixels after digitization using MatLab. Hence, the brightness vs distance plots contained numbers of points depending on whether the lines were oriented horizontally or vertically relative to the images (and the long dimension of the Pd foil). We used the highest magnification available images. These typically had 100 pixels per micron on the Pd sample. The brightness values were normalized to the 0–1 range.

The second step in the analyses was to subject the brightness vs distance plots to a Fast Fourier Transform (FFT), again using MatLab. Because the plots were relatively noisy, the brightness vs distance curves were subjected to a smoothing function prior to use of the FFT. The resulting spectra contained peaks that quantified the spatial frequencies in the samples.

We focused on the images shown in the top of Fig. 6 and the bottom of Fig. 7 because they were good examples of both the linear and sponge-like features produced by the femtosecond laser. Fig. 8 is one example of the brightness variation taken along a vertical line in the image on the top of Fig. 7, about one third of the way from the left edge to the right edge. As indicated, the brightness vs distance plot was smoothed. The results of the FFT are shown in the bottom of Fig. 8. It is seen that there is one dominant spatial frequency at about 0.25 inverse micrometers. Analyses such as this will be made for many more lines in regions of targets irradiated with different fluences and numbers of

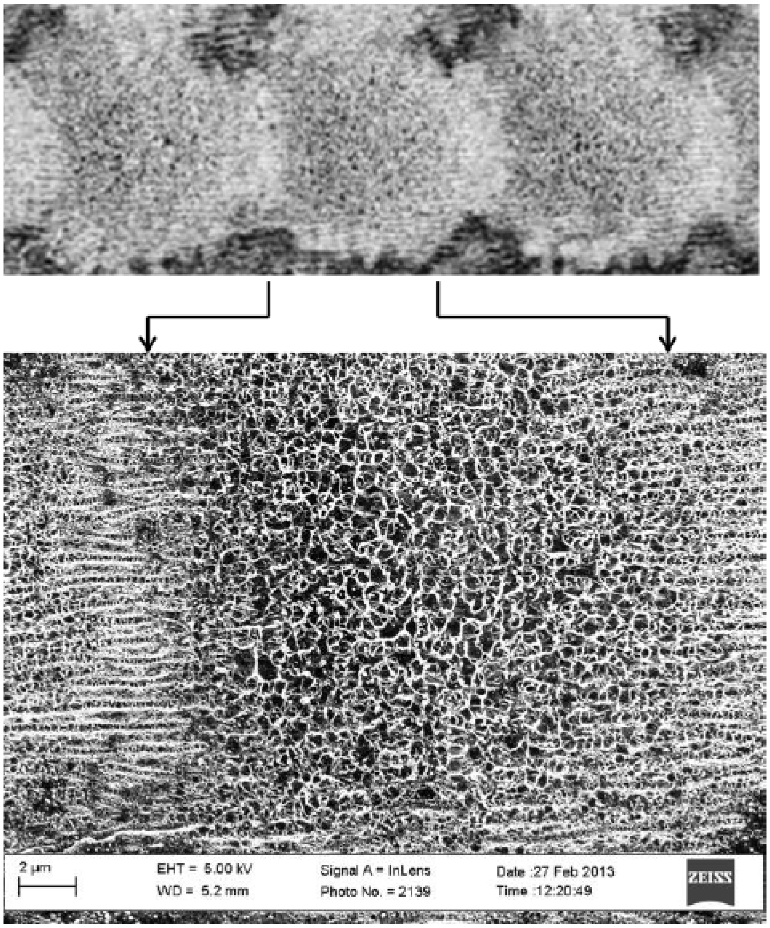

Figure 5. Top. Images of three spots irradiated with ovwe 100 shots at 3.1 J/cm^2. Bottom. Higher magnification of the central spot showing the two major types of structures observed in this work.

shots.

9. Discussion

The aim of this paper was to exploit LIPSS, but not necessarily advance their understanding. There are several possibilities for the influence of the produced and analyzed laser-induced structures on the ability to produce LENR. One is that the structures reported here will have no beneficial influence on generation of excess power. Another is that they will assist in the production of power, but the variety of structures will not matter. That is, LIPSS of different characters and scales will help with the production of LENR. And, it might be that those variations will prove significant, with some producing no or little excess power and others causing significant increases in the rate of LENR.

It might happen that laser processing of surfaces of materials for LENR, followed by a second and separate physical

Figure 6. Images showing roughly parallel and periodic structures for 30 shots (top) and over 100 shots.

or chemical process, will be beneficial. Deposition of thin films of other materials onto the laser targets is one option. Etching of the features seen above in order to remove the finest structures or sharpen the larger structures is also possible. The problem, of course, is the very large number and range of parameters, even with one step of surface preparation. Only some of them were exercised in this study. An additional step in surface preparation adds many possibilities. However, it might turn out that doubly processed cathode surfaces will prove to be the best for production of LENR.

10. Planned Work

The next phase of our program is to repeat the laser exposures shown in this paper in order to insure that they are reproducible, at least statistically. In the process, we will continue to perform parametric studies in order to insure that we can willfully produce structures with desired shapes and sizes within the limits of surface processing with a femtosecond laser.

Having a wide variety of structures on the surfaces of a single Pd foil enables combinatorial experiments. If cathodes with diverse structures in different locations of the cathode produce excess heat, then we will make new cathodes with

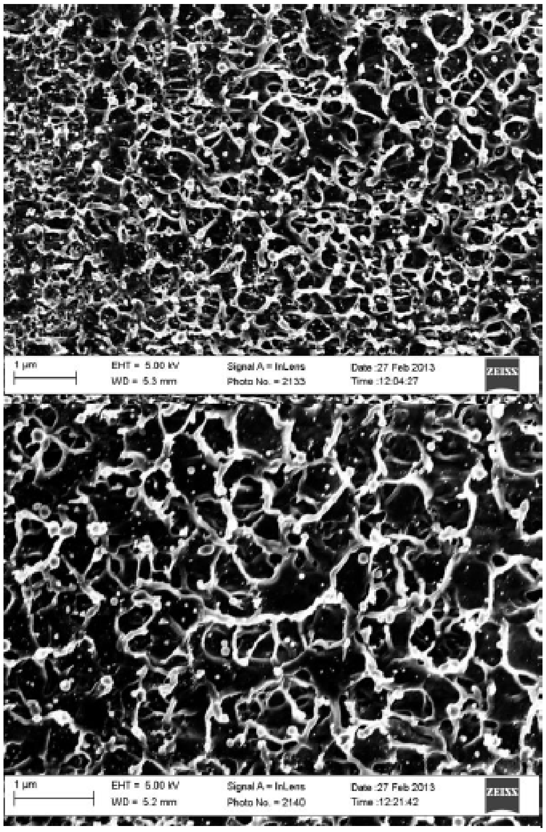

Figure 7. Comparison of central focal regions for spots with 3 shots (top) and over 100 shots.

larger areas of the surface topographies that were present on the initial sample. Sequential experiments will permit us to identify the structures, and the associated laser processing parameters, with the ability to produce the most excess power.

As noted earlier, the work reported here deals with the first three steps in a research program to produce excess power electrochemically and to correlate performance with the structures on the surfaces of Pd cathodes. Figure 1 shows all parts of the program. A Seebeck calorimeter has been constructed and calibrated, and will be used in the near future to run laser-processed cathodes.

References

[1] D.J. Cravens and D.G. Letts, Practical techniques in CF research: triggering methods, *Proc. ICCF-10, Condensed Matter Nuclear Science*, P.L. Hagelstein and S.R. Chubb (Eds.), World Scientific, Singapore, 2006, pp. 171–181.

[2] V. Violante et al., Material science on Pd–D system to study the occurrence of excess power, *Proc. ICCF-12, Condensed Matter Nuclear Science*, A. Takahashi et al. (Eds.), World Scientific, Singapore, 2006, pp. 55–64.

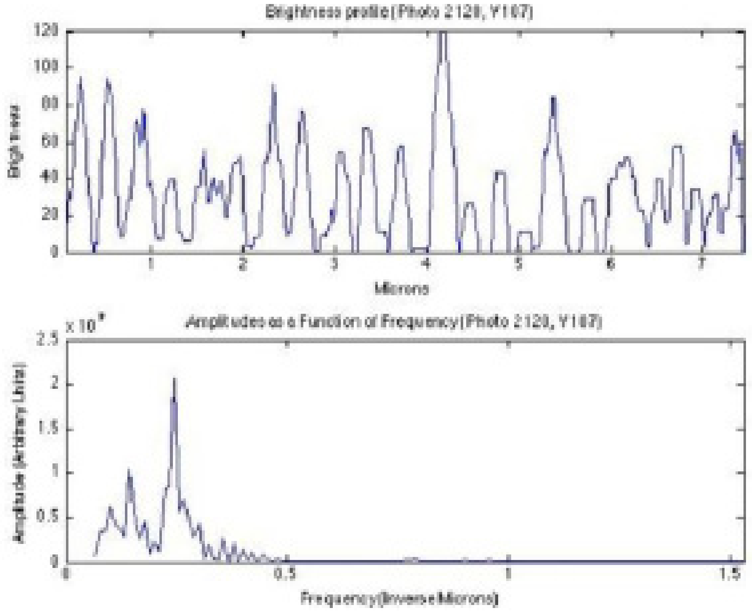

Figure 8. Top: brightness vs distance from Photo Number 2120 in Fig. 6. Bottom: the spectrum of spatial frequencies, where the horizontal scale is in inverse micrometers.

[3] V. Nassisi et al., Modification of PH_2 and Pd–D_2 thin films processed by a He–Ne laser, *J. Cond. Matter Nucl. Sci.* **5** (2011) 1–6.

[4] E. Storms, *The Science of Low Energy Nuclear Reactions*, World Scientific, New Jersey, 2007.

[5] E. Storms, Excess power production from platinum cathodes using the Pons–Fleischmann effect, *Proc. 8th Int. Conf. on Cold Fusion,* F. Scarammuzzi (Ed.), Italian Physical Society, 2000, pp. 55–61.

[6] Y. Iwamura, T. Itoh and S. Sakai, Observations of low energy nuclear reactions induced by D_2 gas permeation through Pd complexes*, Proc. of ICCF-9*, X. Z. Li (Ed.), Singhua Univ. Press, 2002, pp. 1412—146.

[7] Y. Iwamura et al., Low energy nuclear transmutation in condensed matter induced by D_2 gas permeation through Pd complexes: correlation between deuterium flux and nuclear products, *Proc. ICCF-10, Condensed Matter Nuclear Science*, P.L. Hagelstein and S.R. Chubb (Eds.), World Scientific, Singapore, 2006, pp. 435–446.

[8] E. Castagna et al., Metallurgical characterization of Pd electrodes employed in calorimetric experiments under electrochemical deuterium loading, *Proc. ICCF-14*, D. J Nagel et al. (Eds.), 2008, pp. 44450.

[9] http://en.wikipedia.org/wiki/Laser#History

[10] W.M. Steen and J. Mazumder, *Laser Material Processing*, Springer, London, 2010.

[11] Md. S. Ahasn and M.S. Lee, *Femtosecond Laser Processing of Materials: Fundamentals, Technologies, and Applications*, Lago Academic, Saarbaiicken (Germany) 2014.

[12] A.Y. Vorobyev, V.S. Makin and C. Guo, Periodic ordering of random surface nanostructures induced by femtosecond laser pulses on metals, *J. Appl. Phys.* **101** (2007) 34903.

[13] J. Bonse et al., Femtosecond laser-induced periodic surface structures, *J. Laser Applications* **24** (2012) 42006.

J. Condensed Matter Nucl. Sci. 15 (2015) 279–287

Research Article

LENR Excess Heat may not be Entirely from Nuclear Reactions

David J. Nagel*

NUCAT Energy LLC and The George Washington University, USA

Roy A. Swanson

University of Colorado, CO 80523, USA

Abstract

Some theories of the mechanisms active in producing Lattice Enabled (or Low Energy) Nuclear Reactions (LENR) predict the formation of compact objects with binding energies and sizes intermediate between those of atoms and nuclei. The existence of compact objects remains unproven. But, if such objects exist and are formed during what are now called LENR experiments, they might release substantial energy without any nuclear reactions. Because of the small size of hypothetical compact objects, it is thought that the protons or deuterons at their centers might subsequently participate in nuclear reactions, producing more energy, transmutation products or energetic quanta. Such a two-step sequence could explain the relatively low production rates of nuclear reaction products, and also difficulties in correlating excess heat with the amounts of such products.

Keywords: Energy, Low energy nuclear reactions, Mechanisms for LENR

1. Introduction

During heavy-water electrochemical experiments in the mid-1980s, Fleischmann and Pons found that more thermal energy came out of their experiments with Pd cathodes than was put in electrically. The excess heat was greater than could be explained by any chemical reactions. Hence, they postulated that the excess energy was due to unexpected nuclear reactions. It is now well established experimentally that the amount of excess heat measured in many experiments greatly exceeds what can be attributed to chemistry [1]. For this reason, and also because of numerous reports of nuclear reaction products and energetic radiations, it is widely believed that excess heat is due primarily, and maybe exclusively, to nuclear reactions. Hence, the field is now usually called Low Energy *Nuclear* Reactions (LENR). We prefer the more precise terminology Lattice Enabled Nuclear Reactions.

Given the envisioned simultaneous generation of heat and products from nuclear reactions, it is reasonable to expect them to be related quantitatively. The best linking of heat with nuclear products is the correlation of the

---

*E-mail: nagel@gwu.edu

produced excess energy with quantities of helium-4. That relationship was discovered by Miles in 1993 [2], reviewed by Bressani in 1998 [3] and Miles in 2003 [4], and well demonstrated in the work of McKubre and his colleagues in 2000 [5]. Fits to their measured amounts of heat and helium gave roughly 32 MeV per reaction, close to the gamma ray energy occasionally emitted during conventional fusion of two deuterons to form ^{4}He. Despite all the work, the heat–He relationship remains contentious. Other quantitative correlations between excess heat and nuclear products are desirable, but might be difficult to obtain for the reasons discussed below.

Our focus is the alternative scenario for production of excess heat and observation of low levels of nuclear reaction products and radiations. It is far from new, but has received relatively little attention. Several theorists have postulated the formation of “compact objects” with sizes and energies between those of atoms and nuclei. If such objects do form, they could account for some or all of the measured excess heat without the requirement that nuclear reactions occur.

Nuclear reactions might follow the formation of the compact objects because of their small sizes, similar to how nuclear reactions occur in muon-catalyzed fusion. The presence of a heavier muon in place of a lighter electron results in atoms and molecules with much smaller sizes than usual. This brings nuclei into closer-than-normal proximity and greatly increases conventional fusion probabilities. The process is summarized in the next section. The third section reviews the compact object theories of by Mills, Maly and Vavra, Dufour, Heffner, Mayer and Reitz, and Meulenberg and Sinha. Based on these theories, the possibility that not all of the excess heat in LENR experiments is due to nuclear processes is examined in the fourth section. The last section considers possibilities for experimental discovery of compact objects.

2. Muon-Catalyzed Fusion

This process provides a model for the formation and nuclear reactions of compact objects, which is experimentally and theoretically well established. The possibility of using negative muons to promote fusion of hydrogen isotopes was published first in 1950 [6]. The fundamental notion is due to the muon being 207 times heavier than the electron. Replacement of an electron with a muon in an atomic or molecular orbital will result in the new orbital being about 207 times smaller than originally. The radius of a hydrogen atom, with a muon in place of the normal electron, is 285 fm [7]. The small size is due to the inverse scaling of orbital radii with mass. This applies to atoms and binary molecular ions with nuclei of protons (P), deuterons (D) and tritons (T). In a D–e–T molecule, the two nuclei are separated by about 100 pm. In a muonated D–μ–T molecule, they approach each other more closely during even low-temperature molecular vibrations due to their initially smaller spacing. This increases the probability of their tunneling through the Coulomb barrier and fusing. That is, the tunneling probabilities and associated nuclear reaction rates are greatly increased (catalyzed). The fusion probability is highest if the two nuclei are a deuteron and triton, although D–D fusion can also be muon-catalyzed.

The sequence of steps during muon-catalyzed fusion is indicated in Fig. 1. The cycle starts with introduction of a muon into a mixture of heavy water (D_2O) and tritiated (generally TDO) water, which is often frozen for experimental convenience. The muons can displace electrons in D or T atoms, leading to formation of the D–μ–T molecule, the nuclei of which quickly fuse. The fusion produces 17.6 MeV of energy, which is carried off by the two particles that are produced, a fast neutron and an alpha particle. The muon can be liberated and start another cycle, or can stick to the outgoing alpha particle 1% of the time. If the latter happens, the muon and alpha particle will separate about one third of the time, freeing the muon for another cycle.

There are a few practical problems with muon-catalyzed fusion for production of energy. The first is that an accelerator is needed to produce the muons in the first place, usually by the production and decay of pions. That process is very energy consumptive due to the need to use a high-energy particle accelerator to make the pions. Second, the muon has a very short lifetime of 2.2 μs. And, some of the muons are lost by staying with the liberated alpha particles. As many as 150 fusion reactions have been observed, on average, from one muon, although theoretical estimates are

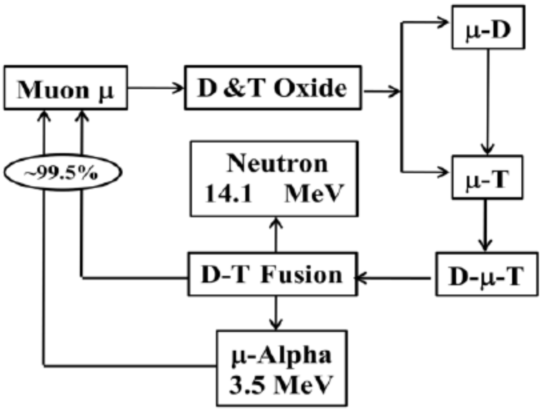

Figure 1. Simplified schematic of the cycle in which muons form compact molecules of D and T in heavy and tritiated water, and then fuse, liberating both energy and most of the muons.

almost twice that value [6,8]. Muon-catalyzed fusion is a factor of about five short of energetic breakeven. The cost of tritium is another factor.

The existence of compact atoms and molecules involving muons enhances interest in the possibility that other compact objects might play a role in LENR. Theories about the formation and characteristics of such new compact objects constitute the next section.

3. Compact Object Theories

Like smaller nuclei and larger atoms, the compact objects envisioned by different LENR theoreticians have characteristics that can be described and quantified. The most important characteristics deal with energies, sizes and lifetimes. The formation energies for compact objects are clearly of great interest in a field that hopes to produce energy generators. And, there is the open question about excitation energies in addition to the ground-state binding energy for any specific compact object.

The sizes of such objects will, like the sizes of nuclei and atoms, be only approximate due to the distributed character of wave functions. However, just as nuclei have overall sizes on the scale of femtometers, and atoms have sizes on the scale of tenths of nanometers, it is possible to define the size of various theoretical compact objects. Orbital diameters can suffice for that purpose.

It might be that, once formed, the compact objects are stable like atoms, and not subject to spontaneous or other decay processes, like many radioactive nuclei. However, it is also possible that these envisioned objects are not stable. The basic question of the stability of hypothetical compact objects is unresolved. Maybe, if they exist, they have escaped attention because they are not stable. No estimates of their lifetimes are available.

The reader of theories dealing with particular visions of compact objects might be incredulous that, after decades of increasingly sophisticated experimental research, such objects have remained undiscovered. However, the situation is not unprecedented. In astronomy and cosmology, the existence of two entities, dark matter and dark energy, has been invoked to rationalize the observed dynamics of the overall universe. However, neither dark matter nor dark energy has been directly detected to date.

In the rest of this section, we will provide brief overviews of the several theories of compact objects with references to the detailed papers and postings by their authors. The ideas vary widely in their development, with some having virtually no elaboration and others including specific values for binding energies and orbital radii. Their common characteristic is having binding energies greater than those known for H or D atoms or molecules, and sizes that are substantially smaller than those that are well known both experimentally and theoretically for atoms and molecules which contain H isotopes.

Late in the 1980s, Randell Mills postulated the existence of a deeply bound form of hydrogen, which he called the hydrino [9]. The least binding energy, and hence the energy that might be released during formation of the entity, was thought to be 41 eV. More tightly bound levels were postulated to have higher binding energies. If such tightly bound energy levels existed, they should be evidenced in spectra and, possibly, in electron scattering experiments. The spectral evidence for the hypothetical levels is not compelling [10]. And, the scattering experiments do not seem to have been done. Hence, the existence of Mills' envisioned deeply bound energy levels in hydrogen is still an open question.

There were two papers by Maly and Vavra on compact objects in the 1990s, stimulated by reports of cold fusion [11]. They dealt with "deep Dirac levels" in various atoms. Those levels are solutions of the Dirac equation, the relativistic analog of the Schrodinger equation in Quantum Mechanics. The papers give energies and charge distributions for compact objects. The binding energies fall in the range of 300–500 keV and the orbital radii are on the scale of femtometers. The authors of the papers considered experiments to test for the existence of these levels. They pointed to calorimetric evidence from LENR experiments as indirect evidence of the levels they computed.

In the mid-1990s, Dufour proposed the existence of bound states that result from equilibrium between the attractive electrostatic force and the repulsive electro-weak force [12]. He termed the entities Hydrex and Deutex, depending on whether a proton or deuteron was involved. The radii of various energy levels of the Hydrex were computed to be in the range of 1.78–3.47 fm. Their binding energies varied widely from about 393 keV for the lowest (n = 1) quantum level to 36 keV for n = 20 and beyond to small energies for higher quantum numbers. Dufour envisioned the Hydrex as a composite with oscillatory behavior between a proton with a very close electron and a neutron–neutrino pair.

Another theory on compact objects called "deflation fusion" was posted on the internet in 2007 and published during the next year by Heffner [13]. He considered oscillatory electron dynamics, where initially the electron wave functions are dispersed widely over atomic volumes (Bohr radius = 5.3 nm), causing nuclei to mutually repel. The electrons then return to regions closer to the nuclei, screening their repulsion during motion toward an (instantaneous) equilibrium state. For this brief state, it is possible that the nuclei approach close enough (<picometers?) so that the nuclear wave functions can overlap. This releases energy in the form of infrared and visible radiation from fusion-excited molecular electronic, vibrational or rotational states.

In the "deflation fusion" picture, a close-approach electron is envisioned to have a finite, but very short-lived (attosec) probability, to be "captured" in the neighborhood of, or actually within a nucleus at distance scales as short as fractional femtometers (fm or fermis). The electron capture amounts to wave function collapse and a charge neutral "compact object" formed may be viewed as a completely screening atom. Or, the situation may be thought of as "catalytic", because the deflated H atom may penetrate a nearby nuclear Coulomb barrier via short distance tunneling.

Heffner wrote of weakly bound pairs of electrons in the same state with opposed spins. In his concept, the existence of these electron pairs increases the probability of creation of a "deflated paired state". In that state, the two electrons have wavelengths sufficiently small to exist "in the nucleus." This was offered as the explanation of the occurrence of "cold fusion" [14].

In 2011, Mayer and Reitz published an article entitled "Electromagnetic Composites on the Compton Scale" [15]. They postulated a small three-body entity, called a tresino. Such particles would consist of a central proton or deuteron, plus two orbital electrons with anti-aligned spins. The compact size of the tresino makes the electron spin-spin interaction stronger than in the negative H ion, which is composed of the same three particles. Computations based on a simple Schrodinger equation gave 3.7 keV for the binding energy for a tresino and 386 fm for the orbital radius of the two electrons. Note that this is much smaller than both the Bohr radius in ordinary atoms (52.9 pm) and the 100 pm

D–T separation in ordinary D–e–T molecules. However, for D–μ–T, the nuclear separation is about 100/207 pm, or 483 fm, leading to muon-catalyzed fusion.

If tresinos do form, their subsequent reactions with nearby nuclei might have a relatively high probability. Mayer and Reitz hypothesized how tresinos can induce nuclear reactions due to their compact sizes, much as happens in muon-catalyzed fusion. More specifically, a negatively-charged deuteron tresino would be attracted electrostatically to another deuteron. The small size of tresinos could lead to the close approach of the two deuteron nuclei, resulting in a neutron transfer reaction and the production of tritium [16].

Assuming that tresinos can form, the Mayer and Reitz argued that they might explain two major current scientific riddles, the heating of the earth in geology [16] and dark matter in astronomy [17]. Finally, the two authors applied the concept of the composite particle to explain aspects of LENR. The heat observed in calorimetric experiments could be attributed to tresino formation. Note that the tresino formation mechanism does not require nuclear reactions for the production of energy. Tritium formation is reportedly due to tresino-caused neutron transfer reactions in highly loaded Pd, that is, Pd with a high ratio of the concentration of protons or deuterons to the Pd atom concentration.

Meulenberg and Sinha have also addressed the mechanism of LENR by consideration of compact objects. Their approach also involves a short term composite of two electrons and either a proton or deuteron, along with a bare proton or deuteron [18]. Their mechanism is the formation of such an object, followed by D–D fusion. That is, the approach necessarily involves nuclear reactions. They envision that the non-uniform lattices in heavily loaded Pd involve localized and high-frequency phonon modes. Those vibrations produce dynamic electrostatic fields that interact strongly with electrons in the materials. The resultant "potential inversion" causes the formation of "lochons", that is, local-charged-boson–electron pairs, giving deuterons compact screening and a net negative charge. That removes the coulomb barrier, leading to the D^{+}–D^{-} fusion.

In a recent paper [19], Meulenberg summarized the related work by Naudts [20], who arrived at a total orbital energy of the rest mass of the electron times the fine structure constant, specifically, 511 keV/137 = 3.7 keV and a radius of about 390 fm. These values are essentially identical to those for tresino formation. Meulenberg considered an interpretation of Naudt's results to be closer to those predicted by Maly and Vavre, who used the Dirac equations, since they are specific to fermions (such as electrons) [21].

Recently, in response to reports of high LENR powers from the Ni–H system, Dufour hypothesized the existence of a new composite system, which he terms the Hypole[22]. He envisions a Ni nucleus about 1.9 pm from a proton, with an electron orbiting the combination. Both the proton and electron are within the electron shells of the Ni atom. Dufour gives the Hypole formation energy as 10.5 keV. Because of the picometer separation of the Ni nucleus and proton, Dufour applies the new term "pico-chemistry" to LENR reactions that follow formation of Hypoles.

The compact object theories just surveyed are all essentially concepts with some supporting computations. It is natural to ask why such compact objects have not been observed previously. The answer might be that very special conditions are needed for their formation in observable numbers. For example, Mayer and Reitz envision spin alignment of the two electrons in a tresino. Having two spin-aligned electrons simultaneously near each other and either a proton or deuteron is required for tresino formation. That might be a very rare circumstance because of chemical and thermal effects. This is offered as a potential reason that such composite particles have not been observed before.

4. Implications

It is simple to compute the implications of the formation of compact objects, and possible, but not assured subsequent nuclear reactions. If formation of compact objects is indeed the initial step in the production of excess heat, the total amount of excess energy E_{T} depends on the number N_{C} of reactions that form compact objects, the energy E_{C} released per formation of a compact object, the fraction f_{N} of the compact object formation reactions that lead to subsequent nuclear reactions, and the energy E_{N} released per nuclear reaction:

$$E_{\mathrm{T}} = N_{\mathrm{C}}(E_{\mathrm{C}} + \Sigma f_{\mathrm{N}} E_{\mathrm{N}}). \tag{1}$$

The summation is over the number of subsequent distinct exothermic nuclear reactions. The values of f_{N} can range from zero (no secondary nuclear reactions) to unity (when a particular nuclear reaction follows each compact object formation event). Importantly, the energies E_{C} are thought to be mostly in the keV range, while the energies $\mathrm{E_N}$ are generally in the MeV range.

The fraction of the excess heat due to nuclear reactions, namely $(N_{\mathrm{C}} \sum f_{\mathrm{N}} E_{\mathrm{N}}/E_{\mathrm{T}})$, can be as low as zero or as high as nearly unity. The energy gain $(E_{\mathrm{T}}/E_{\mathrm{INPUT}})$ will be determined by the values of the parameters, almost all of which are currently unknown. Note that, if there were no secondary nuclear reactions, there would be no production of radioactive products.

Figure 2 is a conceptual plot of Eq. (1), divided through by E_{C}, for the case that there is only one possible subsequent nuclear reaction. N_{C} is large. And, some of the compact object theories, indicate that the ratio of $E_{\mathrm{N}}/E_{\mathrm{C}}$ is on the order of one thousand. Hence, a plot such as the one in Fig. 2 would be very steep. This shows the great sensitivity of the total excess energy to the probability f_N of nuclear reactions following the formation of a compact object.

The additional complexity just described makes the correlation of overall excess heat with the amount of nuclear products difficult to quantify and, possibly, much more widely variable. This is because excess energy from LENR experiments and generators might be initially, and maybe largely, due to formation of compact object without any or with only some nuclear reactions, as in Eq. (1). Any nuclear reactions that do occur, and their manifestations (reaction products or energetic particles) would depend on the lifetime of the compact objects, their diffusion rates and their probability of reacting with nearby substrate or impurity nuclei. Note that the availability and spatial distribution of impurity nuclei can vary widely, especially due to defects in the host material.

We defined f_N as the ratio of nuclear reactions to the formations of compact objects. Hence, the number of nuclear reactions is $N_{\mathrm{C}} f_{\mathrm{N}}$. If one transmuted element formed or energetic particle were emitted for each nuclear reaction, then the correlation between total excess heat and measures of elements or particles would be as follows:

$$(E_{\mathrm{T}}/N_{\mathrm{C}} f_{\mathrm{N}}) = (E_{\mathrm{C}}/f_{\mathrm{N}}) + E_{\mathrm{N}}. \tag{2}$$

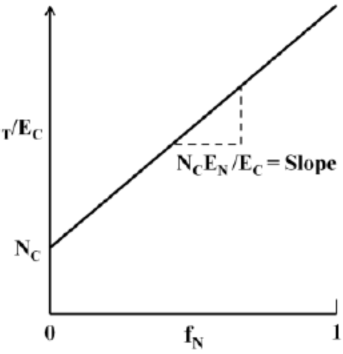

Figure 2. Schematic of Eq.(1) rearranged to exhibit the dependence on f_{N} of the excess energy normalized to the formation energy of a compact object.

Again, we assumed only one type of nuclear reactions for simplicity. This shows that the relationship between excess heat and the number of transmuted atoms depends inversely on the value of f_N. For low values of f_N, the amount of excess heat would be relatively low, but the ratio of heat to number of transmutations $(E_\mathrm{T}/N_\mathrm{C}f_\mathrm{N})$ could be relatively high. If $f_N$increased toward unity, the ratio of heat to transmutation products would be determined by the energy released by each nuclear reaction. This is the situation envisioned in the absence of the formation of compact objects, that is, if the only heat producing reactions were nuclear. Figure 3 addresses the correlation between the total excess energy and some manifestation of nuclear reactions, such as the concentration of transmutation products or the number of emitted energetic particles.

If compact objects did form and were followed by some nuclear reaction in each case, it would be difficult to know that the compact objects actually formed. This is due to the large ratio of $E_\mathrm{N}/E_\mathrm{C}$. Examination of the case of $f_\mathrm{N} = 1$ makes this point. For this situation, the energy given by Eq. (1) becomes the following for $f_\mathrm{N} = 1$ and $N_\mathrm{C} = N_\mathrm{N}$, the number of nuclear reactions:

$$E_\mathrm{T} = N_\mathrm{N}(E_\mathrm{C} + E_\mathrm{N}). \tag{3}$$

The large ratio of $E_\mathrm{N}/E_\mathrm{C}$ makes it possible to ignore E_C relative to E_N. Similarly, Eq. (2) collapses as follows:

$$(E_\mathrm{T}/N_\mathrm{N}) = E_\mathrm{N}. \tag{4}$$

Both Eqs. (3) and (4) are what would be expected if all the excess energy were due to nuclear reactions, that is, there were no formation of compact objects. But, the equations hold to a good approximation even with the formation of compact objects, if each is followed by a nuclear reaction, since $E_\mathrm{C}/E_\mathrm{N}$ is small.

Storms has postulated the existence of a “nuclear active environment” of still unknown composition and structure in which LENR occur [23]. If the initial reactions are not nuclear, but are instead the exothermic formation of a compact objects, a nuclear active environment is not a requirement. However, in that case, it is still undoubtedly necessary to have a particular combination of material (composition and structure) and ambient (sonic, magnetic or other fields) conditions favorable to the formation of compact objects.

5. Discussion

The theories about the formation and implications of compact objects may be significant to understanding LENR. Observations of large excess energies, not explicable by chemistry, might not require the occurrence of nuclear reactions. However, the numerous measurements of nuclear products and of emitted energetic particles certainly do require nuclear reactions for their explanation.

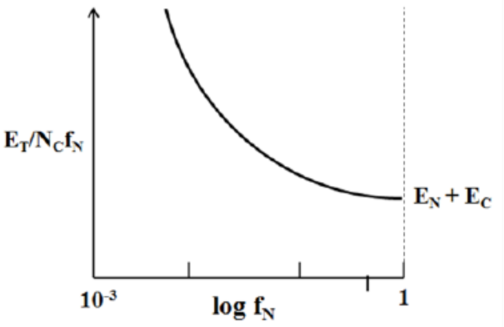

Figure 3. Schematic of the ratio of excess energy to the number of nuclear reactions as a function of the probability of secondary nuclear reactions.

It can be asked if there is any hope of inferring the formation of compact objects from total excess energies and some measures of nuclear reactions. Doing that would seem to require control of the values of f_N in order to plot graphs such as those shown schematically in Figs. 2 and 3. That might be possible if samples of alternating monolayers of different materials could be made, possibly by Atomic Layer Epitaxy. If compact objects formed in only one of the two types of layers, the probability of reactions with nuclei in the other very close layer of material would depend on the geometry and atomic makeup of the second layer. The production of samples, and the constraint of compact object formation to only one of the layers, would both be very challenging experimentally.

If it is either very difficult or impossible to use excess energy and nuclear reaction products to infer the existence of compact objects, there might be other, more direct means of proving their existence. It seems that spectroscopic searches for energy levels predicated by the compact object theories might be fruitful. Such experiments can be done in two ways. The first is the use of Electron Energy Loss Spectroscopy. That is done in transmission electron microscopes, where the beam can be limited to probing a very small volume. A sophisticated sample stage would be required for that approach. The second technique would be to use ultraviolet, X-ray or gamma ray absorption to search for spectral features at the predicated binding energies. Such experiments would best be done using synchrotron radiation, at least for the ultraviolet and X-ray spectral ranges. Success with either of these techniques would hinge on the number of compact objects in the volume of a sample being probed, that is, on their production rates and lifetimes integrated over the experiment duration.

Proving the existence of compact objects and assessing their relevance to LENR are two separate and important steps. If those two features are established, then further theoretical work will be required to quantitatively relate measured LENR rates to basic parameters. The overall rates of heat production and appearance of new elements or energetic particles would depend critically on the f_N parameters. It would be very desirable to obtain theoretical values for such fractions. Doing that would require tunneling calculations given initial separations and thermal vibration amplitudes for various combinations of compact objects and other nuclei. Those computations are possible with current tools.

If the fundamental mechanisms and probabilities for formation of compact objects were available, the overall dynamics for production of heat, nuclear reaction products and energetic particles could be computed. Such calculations would require three-dimensional and time-dependent simulations of the overall flow of matter and energy on or within the solids that support the formation of compact objects.

Before the advent of theories of compact object formation, only chemical and nuclear energies were considered during analysis of LENR experiments. If compact objects are proven to exist, and if they are involved in what are now called LENR experiments, then their characteristics must also be considered to understand the energetics and dynamics of "LENR" experiments.

Resolution of this question about the source of excess heat will probably not come from any clear yes-or-no experiments. It is conceivable that, under some conditions, all of the excess energy is indeed due to nuclear reactions and, under other conditions, little of it is nuclear. Intermediate situations could also exist. Much additional quantitative experimental and theoretical work will be necessary to determine what actually happens for various conditions.

Acknowledgements

Helpful correspondences with Frederick Mayer and Andrew Meulenberg are recalled with pleasure. Useful comments from the reviewer were welcome.

References

[1] E. Storms, *The Science of Low Energy Nuclear Reactions*, World Scientific, 2007, pp. 53–61.

[2] M. Miles, Correlation of excess power and helium production during D_2O and H_2O electrolysis using palladium cathodes, *J. Electroanalytical Chem.* **346** (1993) 99.

[3] T. Bressani, Nuclear physics aspects of cold fusion experiments: scientific summary after ICCF-7, *Proc. ICCF-7*, 1998, 32–38.

[4] M. Miles, Correlation of excess enthalpy and helium-4 production: a review, *Proc. of ICCF-10*, World Scientific, 2003, pp. 123–131.

[5] M.C.H. McKubre et al., The emergence of a coherent explanation for anomalies observed in D/Pd and H/Pd systems: evidence for ^{4}He and ^{3}He production, *Proc. ICCF-8*, 2000, pp. 3–10.

[6] http://en.wikipedia.org/wiki/Muon-catalyzed_fusion

[7] http://answers.yahoo.com/question/index?qid=20111127115120AAiFb2a

[8] S.E. Jones, Muon-catalysed fusion revisited, *Nature* **321**1 (1986) 127–133,

[9] R.L. Mills et al., Catalyst induced hydrino transition (CIHT) electrochemical cell, http://www.blacklightpower.com/publications/ (2013) and ttp://rvanspaa.freehostia.com/Hydrinos_explained.html

[10] R.L. Mills et al., Mechanism of soft X-ray continuum radiation from low-energy pinch discharges of hydrogen and ultra-low field ignition of solid fuels, http://www.blacklightpower.com/publications/ (2014).

[11] J.A. Maly and J. Vavra, Electron transitions on deep Dirac levels I, *Fusion Technol.* **24** (1993) 307–318. [http://www.ans.org/pubs/journals/fst/a_30206] and Electron transitions on deep Dirac levels II, *Fusion Technol.* **27** (1995) 59–70 [http://www.ans.org/pubs/journals/fst/a_30350].

[12] J. Dufour et al., From 'Cold Fusion' to 'Hydrex and 'Deutex States of Hydrogen', *Proc. ICCF-6*, M. Okamoto (Ed.), New Energy and Industrial Development Organization, 1996, pp. 482–495.

[13] H. Heffner, Deflation fusion: speculations regarding the nature of cold fusion, http://mtaonline.net/∼hheffner/ and www.mtaonline.net/∼hheffner/DeflationFusion2.pdf (2007) and *Infinite Energy*, Issue 80 (2008) 38–46.

[14] H. Heffner, http://mtaonline.net/∼hheffner/CFnuclearReactions.pdf

[15] F.J. Mayer and J.R. Reitz, Electromagnetic composites at the compton scale, *Int. J. Theoret. Phys.* **51** (2012) 322–330.

[16] F.J. Mayer and J.R. Reitz, Thermal energy generation in the earth, *Nonlinear Processes Geophys.* **21** (2014) 1–12.

[17] F.J. Mayer and J.R. Reitz, Compton composites late in the early universe, *Galaxies* **2** (2014) 382–409.

[18] K.P. Sinha and A. Meulenberg, Tunneling beneath the ^{4}He* fragmentation energy, *J. Condensed Matter Nucl. Sci.* **4** (2011) 241–255 and Lochon-mediated low-energy nuclear reactions, *J. Condensed Matter Nucl. Sci.* **6** (2012) 55–63.

[19] A. Meulenberg, From the naught orbit to the ^{4}He *Excited S*tate, *J. Condensed Matter Nucl. Sci.* **10** (2013) 15–29 and arXiv:physics/0507193_ (2013).

[20] J. Naudts, On the hydrino state of the relativistic hydrogen atom, http://arxiv.org/abs/physics/0507193 (2005).

[21] A. Meulenberg and K.P. Sinha, Deep electron orbits in cold fusion, *J. Condensed Matter Nucl. Sci.* **13** (2014) 368–377.

[22] J. Dufour, An introduction to the pico-chemistry hypothesis, *J. Condensed Matter Nucl. Sci.* 10 (2013) 40–45.

[23] E. Storms, The nature of the nuclear-active environment required for low-energy nuclear reactions, *Infinite Energy*, Issue 45 (2002) 32–37.

J. Condensed Matter Nucl. Sci. 15 (2015) 288–294

Research Article

The Case for Deuteron Stripping with Metal Nuclei as the Source of the Fleischmann–Pons Excess Heat Effect

Thomas O. Passell*

TOP Consulting, P.O. Box 336, Palo Alto, CA 94302-0336, USA

Abstract

Evidence is cited from the research literature on metals containing absorbed deuterium supporting the hypothesis that the excess heat episodes observed over the past 25 years are the result of exothermic deuteron stripping reactions with atomic nuclei of the absorbing metal. The deuteron stripping reaction is one in which the neutron half of the mass 2 deuteron is captured by an atomic nucleus while the proton half of the deuteron is ejected, repelled by the coulomb field of the positively charged metal nucleus. This hypothesis provides a plausible explanation why so little external radiation accompanies the episodes of excess heat first observed by Fleischmann and Pons [1]. The reaction products from stable isotopes of the host metal are a proton with energies up to 9.2 MeV energy and a recoiling nucleus with energies of $\sim$100–to 600 keV. These two reaction products are retained near their birthplace because their range in solids is less than $\sim$100 μm. The emitted proton is energetic enough to produce by (p,n), (p,α), (p,T), and (p,X-ray), reactions with host metal nuclei and their light-element impurities, the small number of neutrons, alpha particles, tritium atoms (T), and X-rays, occasionally observed associated with deuterated Ti and Pd. The PIXE process (proton induced X-ray emission) is expected in which numerous K, L, and M X-rays of the absorbing metal are produced. For metals with thicknesses of >1 mm the vast majority of such X-rays do not escape the metal. In experiments with foils of the host metal sufficiently thin, low levels of charged particles (mostly protons) have been observed. Some of the observed protons were at energies larger than 3.0 MeV, the largest possible energy of protons from the fusion of two deuterons. Widely observed He^4 and tritium are known products of the deuteron stripping reaction with Li^6, which is a major constituent of electrolytes and a minor impurity in most metals. In any case, researchers have observed small but definite indicators of nuclear reactions other than d+d fusion in deuterated metals at temperatures not significantly above ambient.

Keywords: Deuterium, Energy, Metals, Nuclear, Oppenheimer–Phillips

1. Introduction

One of the most robust sets of observations over the past 25 years following the initial claims of excess heat in March, 1989, have been many episodes of excess heat in palladium and titanium cathodes polarized in lithium deuteroxide or potassium carbonate electrolytes [1]. Yet the nature of the implied nuclear reaction source of that excess heat

---

*E-mail: top94302@gmail.com

has remained unresolved. The most persuasive reason behind the assertion that the heat source is of nuclear origin is its sheer amount, many times greater than any conceivable chemical or metallurgical process in so small a mass of materials. The most common reasons for doubting a nuclear source of the excess heat has been the absence of experimental proof of the predicted amount of the product(s) of any hypothesized nuclear reaction. If the deuteron stripping reaction turns out to be the primary source of the excess heat episodes then it will be understandable why expected levels of the nuclear reaction products have gone undetected all these years. Subtle metal isotope abundance shifts and protons are difficult to identify in such experiments.

This paper presents evidence for the deuteron stripping reaction as the possible primary source of the observed excess heat episodes. The evidence comes from a few of the hundreds of papers published in the proceedings of 18 international conferences on this subject since 1989. Most of the entire set of papers are available as downloadable items from the web site lenr-canr.org [1].

This reaction type was first studied by Oppenheimer and Phillips in 1935 [2]. In a series of deuteron bombardments in the Berkeley cyclotron their colleagues observed products of the (d,p) reaction with target metal nuclei significantly greater than products of all the other deuteron reactions with the same nuclei at the same energy. They theorized that the (d,p) reaction probability should be much larger than the other reactions at a given deuteron energy because the (d,p) reaction did not require the entire deuteron to enter the target nucleus. The neutron end of the cigar-shaped deuteron had no coulomb repulsion to overcome and might allow an interaction in which the neutron end of the deuteron was captured by the target nucleus while the proton was physically still outside the main portion of the target's repulsive coulomb field. Thus the proton can be stripped away by the strength of the repulsion by the positively charged metal nucleus – readily overcoming the proton's weak binding energy of 2.25 MeV to its neutron companion; hence the name, the deuteron stripping reaction.

If the preference for stripping relative to production of a compound nucleus is extrapolated from the heavy elements at $\sim$5-MeV deuteron bombarding energies down to near thermal (sub-eV) energies, the preference for stripping to compound nucleus formation is in the range of millions to one.

2. Logic of the Evidence for (d,p) Stripping Reactions in Deuterated Pd and Ti

The logic of the evidence is as follows: (A) An extensive study at the University of Rome showed evidence for the emission of gamma rays at an energy of $\sim$89 keV/photon from a deuterated palladium cathode during a 150-hour episode of credibly measured excess heat [3]; (B) Interpretation of the $\sim$89 keV gamma rays as plausible evidence for the production of the radioactive isotope Pd^{109}; (C) Assumption that the production of Pd^{109} is plausible evidence for the deuteron stripping reaction on stable isotope Pd^{108}; (D) Calculation of the total excess heat represented by the heat from the Pd^{108} deuteron stripping reaction (3.87 MeV/reaction) and the heat of the radioactive beta decay of Pd^{109} to Ag^{109}; (E) Finding the total energy represented by the above calculation to be a significant fraction of the total excess heat actually measured during 150 of the 1000 h experiment; (3) (F) finding evidence of small changes in isotopic abundance among three of the six isotopes in palladium that had produced excess heat and (G) reported observation of protons with energies greater than the maximum possible from d+d fusion (3.0 MeV) emitted from thin foils of deuterated titanium during changes in sample temperature. (see Kieth et al. ICCF10 proceedings within [1])

3. Isotopic Abundance Ratio Changes among three of the six Pd Isotopes from Cathodes That Had Produced Excess Heat

A significant indication of the direct involvement of the Pd metal atomic nuclei in reactions producing excess heat is the change in the ratio of the abundance of three of the six Pd isotopes relative to one another after excess heat episodes – compared to those same ratios measured in the virgin Pd material.

Due to the generosity of Professor Arata and his colleague Dr. Zhang, at the University of Osaka, four samples of palladium powder were obtained from their experiments which had produced excess heat [4]. Three were from the sealed interiors of hollow palladium cylindrical cathodes each of which had been observed to produce excess heat of $\sim$ 60 MJ during a six-month period of electrolysis. The fourth was virgin material from the same batch of powdered Pd. Passell and George reported the results of neutron activation analysis (NAA) on all four samples from which one can derive abundance ratio changes for Pd^{110}, Pd^{102}, and Pd^{108} [5]. These three Pd isotopes are the only ones that produce gamma-ray-emitting radioactive isotopes following neutron capture in NAA.

The result was the observation of an increase in the ratio of Pd^{110} to $\mathrm{Pd}^{102}$and Pd^{108}, respectively, relative to those of the virgin material. These isotopic ratio changes indicate that these Pd isotopes must have been differently affected by whatever nuclear reaction between deuterons and each of them caused the expression of excess heat. One such difference is the likelihood of different probabilities of the (d,p) reactions on each separate Pd isotope, the Q's of which vary from 2.88 MeV for Pd^{110}, 3.87 MeV for Pd^{108}, to 5.54 MeV for Pd^{102}. The amounts of the ratio changes ranged from +8(0.8)% for 110/108 to +24(11)% for 110/102. If the cause of the ratio changes were a heat-producing (d,p) reaction that differed among the Pd isotopes, the changes are of the right order of magnitude to explain the amount of excess heat reported by Arata and Zhang [4]. Of course all three isotopes could be sources of heat, not just 108 and 102 Also the remaining stable Pd isotopes with masses of 104, 105, and 106, not amenable to NAA ratio measurements, could also be producing heat by deuteron stripping reactions.

4. Appearance of Sc^{46} from Electrolysis of Titanium

Another piece of supporting evidence comes from the electrolysis of titanium metal cathodes by Mengoli and coworkers at the University of Padua [6]. After some twenty days of electrolysis at 95 Degrees C in which several hundred kilojoules of excess heat had been observed, they employed two high-resolution germanium gamma ray detectors in coincidence to discover the appearance of radioactive Sc^{46} in the cathodes. (The two gamma rays emitted by Sc^{46} in its decay to Ti^{46} are in coincidence.) The total number of Sc^{46} isotopes produced were only sufficient to account for an insignificant amount (1×10^{-7} J) of the observed excess heat. Two possible mechanisms for Sc^{46} production are: (1) $\mathrm{Ti}^{48}(\mathrm{d},\alpha)\mathrm{Sc}^{46}$ and (2) $\mathrm{Sc}^{45}(\mathrm{d,p})\mathrm{Sc}^{46}$ from possible scandium impurity in the titanium. Both reactions are very unlikely because the first one requires a compound nucleus with the deuteron and the second one the million-fold higher probability stripping reaction with a possible scandium impurity at the PPB to PPM level in titanium. Thus the more probable (d,p) stripping reaction in any or all of the five stable isotopes of titanium (46–50) might well have been present and responsible for the observed excess heat. In effect, the scandium isotope emissions can be considered as the barely measurable tip of an energy iceberg.

5. Discussion

Some highly unusual shielding effects are necessary to allow thermal energy deuterons in metal lattices to undergo stripping reactions. One can speculate that shielding by the electrons in the metal electron conduction band must make possible the close approach of deuterons in the deuterium ion conduction band [7] to the metal atoms' nuclei to allow the stripping reaction to occur. The relatively stringent deuterium flux levels apparently required in Pd and Ti must be necessary before such unexpected nuclear reactions occur. It has been known since 1929 that hydrogen in palladium existed interstitially as positive ions that could undergo electro-diffusion like electrons through a Pd wire, only in the opposite direction [7]. Thus one might plausibly imagine coherent behavior in both the electron and ion conduction bands to be operating to allow close enough deuteron approach to metal nuclei to allow stripping.

If a deuteron stripping reaction is possible for the nucleus of element 46 (palladium) and 22 (titanium), it follows that similar reactions might be found among the >20 other metal elements (and their trace interstitial elements such as boron and lithium) known to absorb hydrogen. If such should be the case, a very large matrix of experiments will be required to determine the extent of the generality of such reactions.

Thus stripping reactions on each of some 30% (∼80) of all 281 stable isotopes give many more possibilities of producing useful heat than the one d+d reaction. Their exothermic reaction heats range from 1.1 to 9.4 MeV (with Ti^{47}) vs 23.8 MeV for d+d→He^4; however this is not a significant disadvantage.

Reviewers of this paper have raised some obvious questions about my selection of key parts of the evidence cited above. First, why focus on the appearance of 89 keV photon radiation reported by the Gozzi group at the University of Rome (3).? Clearly there are many possible sources besides Pd^{109} decay of radiation in the energy band they reported (within 1 keV of 89 keV). Viewing the list of 210 known gamma rays from 87.0 to 91.0 keV we note only one of significant percentage in the decay of any Pd radioactive isotope –that of the 88.03 keV gamma from Pd^{109} decay. The same gamma transition is emitted in Cd^{109} decay. So, how do we know that Pd is more probable as the radiation source than Cd? First, the radiation images on the X-ray film are lined up parallel to the cathode of the cell. Second, the cathode of the cell is a bundle of 150 Pd wires, basically 100% Pd. Third, the film images are a series of 69 small spots apparently caused by radiation from deeper layers of the wire bundle that could only exit via gaps between outer layers of Pd wires. Fourth, through detailed analyses of the 69 spots on the film, the Rome researchers could assign a narrow range of energies to the gamma source, since each spot could be optically identified with one of the deeper layers of wires. Gamma rays from these deeper layers of wires were observed to be attenuated by varying thicknesses of Pd wires in the outer layers. Use of the known attenuation coefficients of Pd allowed derivation of the photon energy to the narrow range of 88–90 keV. Of course X-ray film is not the ideal detector of gamma rays so their paper states that the energy of the gamma rays could have energies as high as 150 keV. If one considers the details of Pd^{109} decay, some 3% of the gamma emissions lie at energies of several hundreds of keV

The Gozzi group suggested that Cd^{109} might be the source since it decays to the same Ag^{109m} level as does Pd^{109}. However their supposition of Cd^{109}production by the Pd^{105}+23.8 MeV alpha→Cd^{109} + gamma is clearly unlikely since no He^4 atoms were found inside the body of the Pd wires in this experiment.

Gozzi et al. also state that the total energy in the 89 keV photons is only ∼0.5% of the excess heat measured during the 150 h film exposure, which agrees with the criticism that those gamma rays are not, in themselves, a major source of the excess heat. However, IF they are from Pd^{109} decay, they become the tip of an energy iceberg. First, each of the 88.036 keV gammas in Ag^{109m} decays to the ground state of Ag^{109} accompanied by 25 parallel decays of soft conversion electrons and silver X-rays with the same 88.03 keV energy content. Taking this into account multiplies the 0.5% by 25 times to ∼12%. In addition, the beta decay energy of Pd^{109} to Ag^{109m} is about 1.1 MeV. The average energy of electrons in that beta spectrum is about 300 keV. Thus each gamma photon implies the existence of 26 times as many 300 keV beta decay electrons. Thus part of the rest of the energy iceberg brings the total energy into a significant fraction of the observed excess heat about 100 times the energy in the photon itself, i.e. ∼50%.

Once we accept the existence of Pd^{109}, we must deal with the energetics of its production. Assuming the production is by Pd^{108}(d,p)Pd^{109}, then each Pd^{109} indicates that the energy associated with each exothermic stripping reaction has occurred, adding its Q of 3.87 MeV per reaction .

In summary, we can associate an energy of 88 keV +25 times 88 keV + 26 times 300 keV + 26 times 3.87 MeV with each 88 keV photon observed. So the energy iceberg is about 118,000 keV relative to only 88 keV per photon or a multiplier of about 1340 times. Using this multiplier on the Gozzi et al estimate of 0.5% of the 2.4 megajoules of excess heat observed during the 150 h film exposure, leads to an impossibly high number of 673% of the excess heat observed. Thus the estimate of the 0.5% by the authors is probably high by about a factor of 10 or more. That estimate is attempting to use analysis of 69 spots on a film to quantify the source, a procedure highly dependent on particular assumptions of uncertain validity.

We can reasonably assume that this extrapolation is the likely reason for the large mismatch in estimated and observed excess heat. If the error is of the order of a factor of ten, then we are left with only 67% of the observed heat explained by deuteron stripping on Pd^{108} alone. How do we explain additional heat sources in this situation?

The most obvious answer is to assume that Pd^{108} was not the only Pd isotope active with the deuteron stripping process. The other likely suspects are those Pd isotopes similar in every way except their exothermic Q values. These would be Pd^{104}, Pd^{106} and Pd^{110}, (Pd^{102} with only 1% abundance is being ignored). Pd^{105} has a larger Q of 7.35 MeV but it exhibits a larger spin change in the stripping reaction than the three zero spin even-even (even numbers of both protons and neutrons) isotopes. Larger spin changes are associated with reduced probability of a given nuclear reaction. The sum of Pd^{104} and Pd^{110} abundances are only $\sim$82% of the abundance of Pd^{108}. Thus we might expect the sum of Pd^{104} and Pd^{110} would double the amount of heat produced by Pd^{108} alone. Adding the Pd^{106} contribution, with its abundance very nearly the same as Pd^{108}, triples the expected heat relative to that calculated from Pd^{108} reaction radiation.

Finally, we note a surprising result from the Univ. of Rome study [3]. Their Pd cathode differs from rod, wire, foil, and mesh shapes used by other researchers over the past 25 years. It is a tightly bound bundle of 150 Pd wires, each with a 250 μm diameter so that dips and gaps occur between the outermost (e.g. seventh, sixth, fifth, etc.) layers of wires; the radiation emitted to darken the X-ray film did not come from that seventh outermost layer of wires but from the sixth, fifth, fourth, etc. concentric layers instead.

The benefits of this cathode structure are two: First, the spots on the X-ray film are distinct and geometrically identifiable in a way to show beyond doubt that the radiation does indeed originate at the cathode; and second, it suggests that deuteron flux may be the significant factor in excess heat production – since interior layers emitting the radiation are more likely to exhale previously absorbed deuterium, covered as they are by gas bubbles at frequent intervals during electrolysis.

6. Conclusions

Evidence presented above is certainly not yet definitive –only suggestive. With so little evidence of nuclear reactions beyond the sheer amount of excess heat all theories have had a difficult time explaining the results of experiments. For example, Gozzi et al. made one of the most thoroughly and expertly executed searches for He^4 expected from a set of episodes of excess heat, yet found far less than predicted [3]. None were found buried in the metal cathode wires. This is evidence that some other process is at work besides the widely assumed reaction $d+d \rightarrow He^{4\cdot}$.

The protons emitted in the deuteron stripping reactions are energetic enough to excite the first few excited states of nuclei throughout the periodic table. This is a well-known process called coulomb excitation. While these reactions are produced with cross sections only in the range of a few barns, they would be readily observable in cases where excess heat at watt levels is occurring. The first few excited states of most nuclei are well known to high precision and should therefore be a good indicator of the presence of protons from deuteron stripping reactions. Positive identification of this process requires high resolution gamma ray detection.

In addition to coulomb excitation, fast protons can be expected to create neutrons by (p,n) reactions. However such (p,n) reactions with metal atom nuclei are inhibited by the coulomb barrier of the metal atom and secondly by the fact that the reactions with metal nuclei are mostly endothermic by several MeV. Thus most such reactions with metal nuclei are unlikely to be significant. However, such conditions are not so inhibiting for deuterons in the lattice. Protons can elastically collide with lattice deuterons, leading to subsequent d+d fusion reactions by recoiling deuterons. This two stage process drastically reduces the number of final fusion generated neutrons. Still under some assumptions this might lead to observable neutrons outside the experiment.

Since observations of neutrons outside previous experiments have failed to correlate neutron levels with excess heat measurements, more recent excess heat observations have almost never included neutron detection. It would be premature to conclude that the protons from deuteron stripping reactions are ruled out by previous failures to observe external neutrons, since so few first class neutron measurements have been made coupled with first class observations of excess heat.

Small amounts of tritium have been observed associated with both excess heat and pulsed glow discharges. In the cases showing excess heat the tritium levels are of the order of one million times lower than expected if tritium-producing reactions were a significant fraction of those producing excess heat. However, the significance of such observations far outweighs the amounts observed. The unambiguous nature of the detection of tritium shows that nuclear reactions can occur in deuterated palladium, a remarkable proof of the possibility of nuclear reactions in this system (see papers by F.Will et al. and T. Claytor et al. in [1]).

Confirmation of this hypothesis will require finding at least one unequivocal product of the deuteron stripping among elements that absorb deuterium. The search for gamma ray emitters may be more sensitive and less subject to question than the search for excess heat. Moving beyond Ti and Pd to mono-isotopic elements such as scandium, cobalt, terbium, thulium and tantalum might prove fruitful, as each one gives a well-characterized prolific gamma ray emitter of convenient half life (weeks to months) after experiencing a deuteron stripping reaction.

A 1953 thesis by W.B. Hillig gives evidence for hydrogen transport in titanium and tantalum metal in ways similar to such phenomena more thoroughly studied in palladium. Thus we may not be limited to stripping reactions in the expensive metal, palladium [8].

Pursuing the deuteron stripping hypothesis is a significant departure compared with current ones. A large advantage of the deuteron stripping hypothesis is the lack of ambiguity over the mechanism for conversion of energy from excited nuclei to heat. Heating by fast protons stopping in matter is a well established heating phenomena.

Acknowledgments

The late M. Fleischmann and S. Pons initiated interest in this subject in March 1989. Significant contributors to this research include: M. McKubre, F. Tanzella, S. Crouch-Baker, E. Storms, D. Gozzi, G. Mengoli, D. Cravens, D. Letts, X.Z. Li, F. Celani, V. Violante, A. de Ninno, F. Scaramuzzi, A. Takahashi, Y. Arata, Y.C. Zhang, J. Dash, A. El Boher, G. Miley, M. Miles, T. Claytor, G. Preparata, T. Tripodi, J. Warner, T. Mizuno, M. Srinivasan, J. Bockris, S. Szpak, P. Mosier-Boss, M. Swartz, D. Rolison, D. Nagel, R. Stringham, G. Lonchampt, J.P. Biberian and many of their colleagues. My particular thanks go to J. Rothwell , E. Mallove, and G. Miley for maintaining means of publication of results under difficult circumstances. R. George was helpful in obtaining key samples of heat-producing palladium for NAA and TOF-SIMS analysis. T. Benson and M. Cherin provided valuable services in laboratory work involving the search for He^4 and gamma rays. F. Iskander and D. O'Kelley facilitated NAA at the Research Reactor at the University of Texas. D. Kuttikad supported the PGNAA at the Research Reactor at the University of Missouri, Columbia. Supporting the effort on the theoretical side were P. Hagelstein, S. and T. Chubb, Y. Kim and J. Schwinger. Individuals within EPRI, in particular J. Santucci, J. Taylor, and K. Yeager and personnel at the U.S. Naval Research Laboratory are acknowledged for approving financial support crucial to the early years of this research. I thank M. Melich for supporting this effort in ways too numerous to mention. I also thank B. Raby, G. Egan, W. Loewenstein, M. Rabinowitz, F. Rahn, A. Machiels, M. Passell, J. Passell, C. Green, A. Passell, R. Nightingale, A. Miller, S. Crouch-Baker, J. Brennan, C. Brennan, S. Brennan, P. Cox, R. Williams, two anonymous reviewers, and many other colleagues for comments helpful in improving this manuscript.

References

[1] Papers by M. Fleischmann, S. Pons, M. McKubre, E. Storms, Y. Arata, Y. Zhang, D. Gozzi, A. De Ninno, V. Violante, A. El Boher, X.Z. Li, S. Szpak, M. Swartz, A. Takahashi, D. Cravens, J. Dash, M. Miles, D. Letts, P. Mossier-Boss, G. Miley and F. Celani, Downloadable from among $\sim$4000 papers at lenr-canr.org.

[2] J.R. Oppenheimer and M. Phillips, Note on the transmutation function for deuterons, *Phys. Rev.* **48** (1935) 500–502.

[3] D. Gozzi, F. Cellucci, P.L. Cignini, G. Gigli, M. Tomellini, E. Cisbani, S. Frullani and G.M. Urciuoli, X-ray, heat excess, and He-4 in the D/Pd system, *J. Electroanal. Chem.* **452** (1998) 251. (***) 2002-11-06 and 2002-11-07

[4] Y. Arata and Y.C. Zhang, Excess heat and mechanism of cold fusion reaction, *Proc. of ICCF-5*, 9–13 April 1995, Monte Carlo, Monaco, S. Pons (ED.), pp. 483–494, (***) 2005-12-08, 2003-12-11, 2005-06-29.

[5] T. Passell, Pd-110/Pd-108 ratios and trace element changes in particulate palladium exposed to deuterium gas, *Proc. of ICCF-10*, Cambridge, Mass., 24–29 August, 2003, P. Hagelstein and S. Chubb (Eds.), pp. 399–403, (***) 2003-10-14.

[6] M. Bernardini, G. Manducci, G. Mengoli and G. Zannoni, Anomalous effects induced by D_2O electrolysis at titanium, *Proc. of ICCF-8*, 21–26 May 2000, Lerici, Italy, F. Scaramuzzi (Ed.), pp. 39–45.

[7] C. Bartolomeo, M. Fleischmann, G. Larramona, S. Pons, J. Roulette, H. Sugiera and G. Preparata, Alfred Coehn and After: The alpha, beta, gamma of the palladium-hydrogen system, *Proc. of ICCF-4*, Vol. 1, Dec. 6–9, 1993, Lahaina, Maui, Hawaii, EPRI Report TR-104188, July, 1994, T.O. Passell and M.C.H. McKubre (Eds.), pp. 19-1 to 19-47.

[8] W.B. Hillig, Proton transfer, electrical resistivity, and magnetic susceptibility in the tantalum-hydrogen and titanium-hydrogen systems, A dissertation submitted in partial fulfillment of the requirements for the degree of Doctor of Philosophy at the Univ. of Michigan, 1953.

Note: (***) with numbers indicate papers so-labeled on lenr-canr.org

J. Condensed Matter Nucl. Sci. 15 (2015) 295–304

Research Article

Explaining Cold Fusion

Edmund Storms*
KivaLabs, Santa Fe, NM, USA

Abstract

Five assumptions are identified that apply to all theories. These assumptions and several others are used to create a new explanation of low energy nuclear reactions (cold fusion) based on formation of a novel active environment within a variety of materials. The method to form this environment and the nuclear consequences are described. The fusion process is proposed to occur when a form of metallic hydrogen is created in nano-cracks. Methods to test the model are provided. Engineering variables are identified and used to show how the process can be controlled and amplified. These assumptions can also be used to evaluate other proposed explanations.

Keywords: Cold fusion, Hydroton, LENR, Mechamism, Theory

---

1. Introduction

The phenomenon referred to as cold fusion (CF) in this paper is defined as a nuclear process initiated on specific occasions in apparently ordinary material without application of significant energy. The process produces unexpected heat and nuclear products without significant radiation when any isotope of hydrogen is present. This phenomenon, first discovered by Fleischmann and Pons [1], has now been demonstrated by many replications [2,3] and is on its way to commercial application [4]. Nevertheless, a satisfactory explanation has not been generally accepted, resulting in general rejection of the claims and inefficient investigation of behavior. This paper describes criteria useful in evaluating all proposed explanations and provides a new explanation consistent with these requirements. The assumptions on which this approach is based are justified and methods to test the resulting model are suggested. As required of a useful model, many new predictions are made and a path to improved reproducibility and control is suggested. The model has been expanded in a recently published book [5].

2. Assumptions

All the theories start with assumptions, which if incorrect will doom a model no matter now much argument and

---

*E-mail: storms2@ix.netcom.com

mathematical support are applied. Five basic assumptions are proposed here as a basis to judge all models, including the one described later in the paper.

Assumption 1. CF cannot occur in a "normal" material but requires formation of a unique condition called a nuclear-active-environment (NAE) [6].

Spontaneous nuclear reactions, other than radioactive decay, are not observed to occur in ordinary materials. Because spontaneous CF is observed, a unique condition in which the nuclear process can occur must be present. To fully appreciate this requirement, certain facts must be considered.

A chemical lattice consists of tightly coupled and interacting atoms having the lowest energy state for that configuration. Vacancy formation, such as is created by absence of an atom from the structure, is controlled by the same laws that control how the atoms themselves are arranged. These vacancies are considered by chemists to be part of the normal chemical structure and, therefore, not available to form the NAE.

These atoms and electrons rapidly interact and easily transfer excess local energy throughout the structure. Once local energy exceeds a few eV, chemical or structural changes will be produced. These processes will absorb energy before it can reach a level sufficient to affect a nuclear process. This well known behavior of a chemical system eliminates local concentration of energy in any form as a step in initiating the nuclear process.

In addition, if a novel quantum mechanical process were proposed, this process would have to be energetically favored in a chemical system and not cause chemical changes that would be noticed. In other words, not only must the nuclear behavior be explained but also the proposed process must not predict unobserved chemical behavior. This limitation can be avoided if the nuclear reaction occurs where these interactions with the chemical structure can be avoided, i.e. in a novel NAE. Identifying the NAE then becomes the challenge.

Assumption 2. The heat energy and nuclear products are produced by the same basic process operating in the same NAE.

An effect so rare and difficult to produce, as is cold fusion, would logically have only a single mechanism and condition for its operation. Nevertheless, the observations indicate several other kinds of nuclear processes might occur while the CF process is underway, which might cause confused interpretation. For example, hot fusion products can be generated as cracks form [7–10] (called fractofusion). In addition, energetic radiation might result from unusual energy states having no relationship to CF or energy might result on occasion from zero-point based processes [11]. As an example, claims for low-level energetic particle and neutron emission may have no relationship to the CF process [12,13], instead being caused by occasional hot fusion. Consequently, the observed effects need to be carefully assigned to the correct source and not used to confuse an explanation for CF by including behavior that might be in apparent violation of this assumption.

Assumption 3. Cold fusion is not hot fusion.

Hot fusion occurs when nuclei of deuterium are forced together by application of kinetic energy or by substituting a muon for the electron in D_2. The final nucleus then fragments and releases the excess mass energy as kinetic energy. Four products result with neutrons being the more easily detected. In contrast, cold fusion requires application of no additional kinetic energy and results in very few nuclear products, only weak radiation, and very few neutrons, if any. Ironically, CF was rejected because it failed to behave like hot fusion. Instead, the novel behavior of CF reveals operation of a new phenomenon having no direct relationship to how hot fusion operates. A visual comparison is made between the two effects in Fig. 1.

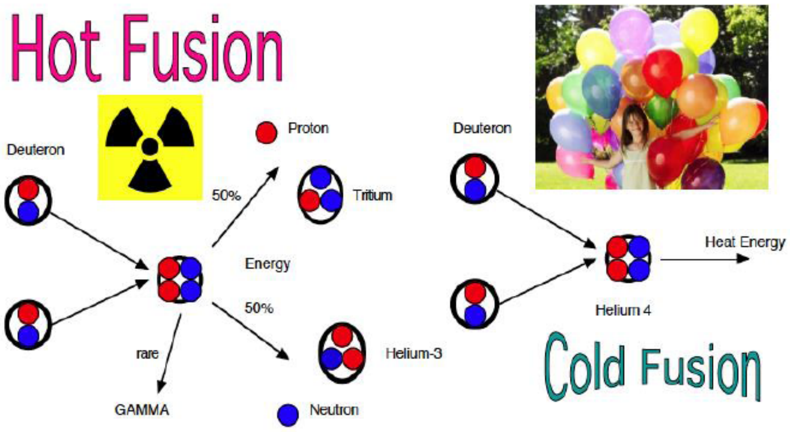

Figure 1. Comparison between hot fusion and cold fusion using deuterium.

Fusion can occur once two nuclei get close enough, either by forcing them together by applying kinetic energy or by forming a molecular structure using a muon [14]. Because the muon is about 200 times heavier than an electron, but has the same charge, it can act as a bonding electron and bring the two nuclei close enough to fuse. This process has been called cold fusion [15], an incorrect interpretation because although fusion occurs, the products known to result from cold fusion are not produced.

Ion bombardment of a material using low energy D^+ has been proposed to cause CF [16]. This is also an incorrect conclusion, because once again, the expected nuclear products produced by hot fusion result. Apparently, when two d are brought close enough for the strong force to operate, either by a muon or by applying kinetic energy, the products typical of hot fusion result, not those produced by cold fusion.

Cold fusion only occurs when a NAE is present that can support a unique fusion process. This process must first bring the two nuclei close enough to fuse and then dissipate the resulting energy without energetic particle emission. The process has no apparent relationship to hot fusion and needs to be viewed as a separate process, in the view of the author.

Assumption 4. The explanation must apply to each method for producing cold fusion and the resulting behavior.

CF can be initiated using at least five separate methods, each of which strives to inject hydrogen isotopes into a solid material. These methods involve different materials containing different impurities as well use of different levels of applied energy. A model must show how these different conditions can produce the same result by identifying an active feature common to all. This is an extension of Assumption #2.

Assumption 5. No Law of Nature is violated.

The important laws are:

The Laws of Thermodynamics apply to all processes within a chemical system. The laws state that energy is conserved, the energy cannot be spontaneously concentrated in local regions above a small limit, and all spontaneous changes require release of Gibbs energy. Any mechanism proposed to create a condition able to initiate a nuclear reaction in a chemical structure must take these laws into account.

Conservation of energy and momentum apply to all nuclear reactions when nuclear energy is released to the surroundings. Excess mass-energy is released by emission of particles that carry the energy as result of their velocity and mass, including photons. Release of significant mass-energy during conventional nuclear reactions by vibration of the nucleus to cause phonon generation is not observed. A relationship between CF and the Mössbauer Effect, which has been suggested, is tenuous at best because the Mössbauer Effect involves energy in the keV range while CF emits energy in the MeV range.

Laws of probability limit the reaction rate of a process when assembly of components is required before the process can start. Each member of the assembly requires time to accumulate in one location as they diffuse through the material by a random process. Because the cluster grows larger by addition of one nucleus at a time, assembly of a large cluster can be expected to be too slow to account for the observed amount of power.

No published model is consistent with all of these limiting assumptions and requirements. In addition, most models are either in conflict with one or more basic Laws of Nature or are in conflict with observed behavior when CF occurs. The theory proposed here attempts to avoid these deficiencies while maintaining logical consistency with known behavior.

3. Sequence of the CF Process

The process of initiating the CF reaction is proposed to involve four separated but connected parts, the first three of which involve normal chemical behavior. First, formation of the NAE must obey rules that apply to a chemical process (Assumption #1) because it forms in a chemical structure, and Gibbs energy (Assumption 5) must be released. Second, hydrogen ions must populate the lattice that surrounds the NAE, so as to be available once the fusion process starts. The resulting concentration is determined by the chemical property of the material and ambient conditions. Third, these ions must move and eventually find the NAE. This process involves diffusion and is influenced in part by temperature, concentration gradient, and applied voltages (electrodiffusion).

The forth and final stage in the process occurs when two or more hydrogen atoms come together within the NAE to create what is named a *Hydroton* for the purpose of this model. This structure is unique because it has the ability to reduce the Coulomb barrier while dissipating mass-energy in small quanta. The "magic" of the process is located in this molecular structure. Once this structure forms, rapid fusion takes place without further effort. Most theories only address this final aspect of the CF process while proposing an entirely different mechanism.

Nothing can happen until the NAE forms. Consequently, attention must first be directed to creating enough NAE to cause a detectable effect. Once the NAE forms, the reaction rate is determined by several variables, as described in section IV and not by anything done to directly influence the nuclear reaction process. In other words, once the Hydroton forms, no further external influence is believed possible, as would be expected for such an energetic reaction.

4. Basic Features of the Proposed Model

The NAE is a gap having a critically small size created by stress relief [17,18]. The gap size is limited by the physical size of the material in which it occurs and the morphology of the material in which the stress is generated. A source of such stress can be identified in all successful materials that have been studied [19–22].

The hydrogen nuclei assemble in the gap and form a covalent bonded molecule (Hydroton) with release of Gibbs energy, thereby stabilizing the gap to high temperatures. Each gap might host thousands of these molecular chains in various stages of formation and fusion.

The chain resonates along its axis, which allows two nuclei to periodically get close enough to start the fusion process, but not close enough for the strong force to operate. Excess mass–energy is lost by emission of a weak coherent photon from each nucleus in opposite directions. The resonance cycle briefly terminates this process before additional photons can be emitted. Another photon set is emitted at the next cycle when two nuclei briefly again get close enough. This periodic emission of photons takes place until all mass has been converted to energy (Table 1) and the two nuclei become a single nucleus without excess mass energy. The photons have a range of energies, with most of them being absorbed by the apparatus. A few of the most energetic photons escape and are detected.

Because the electrons have a high probability in the Hydroton structure of being located between the nuclei, the Coulomb barrier is reduced and the electron can be incorporated into the final nucleus when it forms after most excess mass-energy has been lost. An antineutrino is emitted at that time without significant energy because very little extra energy remains. Predicted nuclear reactions are summarized in Table 1.

Fusion of deuterium is proposed to produce ^{4}H, which decays by rapid emission of a weak beta and a neutrino. This reaction might be detected by a search for weak Bremsstrahlung. In the same manner, fusion of p and d creates tritium, which slowly decays by emitting a weak beta + neutrino, as is normally the case. Fusion of protium (light hydrogen) produces stable deuterium. This deuterium can then fuse with p to form tritium or with d to form helium. A few of the tritium nuclei can fuse with deuterium to produce helium and a neutron, which is the proposed source of the few neutrons observed when tritium is produced.

Figure 2 shows a cartoon of four stages in the fusion process. First, a small gap forms and the hydrogen ions located between the metal atoms diffuse into this gap. Once there, they react to form a chain of covalent bonded atoms. Normal chaotic vibration of this structure eventually becomes coherent and results in a resonance along the axis. As the resonance wave passes, each nucleus periodically gets close to its neighbor, whereupon a weak photon is emitted from each in opposite direction and with opposite spin. This process is proposed to be the great mystery of LENR. Photon emission continues until a sufficient number of photons have been emitted to convert all excess mass to energy, whereupon the two nuclei combine into a single nucleus along with the bonding electron. The frequency of the emitted photons is expected to increase as the structure collapses toward the final product. These photons are converted to heat by the usual process as they are absorbed well away from the NAE but before most photons can leave the apparatus.

The process satisfies all the requirements observed behavior has revealed by allowing mass energy to gradually leak out of the fusing nucleus. The resulting ^{4}H decays rapidly by weak beta emission. When tritium forms, it also decays by weak beta, but more slowly. The other possible product is deuterium, which is stable. The same mechanism operates regardless of which hydrogen isotope is present. Only the resulting products are different.

5. Scientific Predictions

The Hydroton is proposed to be metallic hydrogen (MH) [25–27]. Consequently, when attempts are made to form MH by subjecting H_2 to high pressure, a brief and intense nuclear reaction is predicted to produce heat and radiation once the MH forms, thereby causing observed damage to the diamond anvil used to apply huge pressure.

The heat claimed by Rossi [4] and others using Ni + H_2 does not result from transmutation, but is predicted to result from formation of deuterium, followed by tritium and helium formation.

Tritium is predicted to form at an increasing rate when H is used to initiate CF as a consequence of reaction with the deuterium that forms.

Table 1. Predicted nuclear reactions

d + e + d $\rightarrow$ ^{4}H (fast decay) $\rightarrow$ ^{4}He + e, $Q = \sim 23$ MeV
d + e + p $\rightarrow$ ^{3}H (slow decay) $\rightarrow$ ^{3}He + e, $Q = \sim 4.9$ MeV [23,24]
p + e + p $\rightarrow$ ^{2}H (stable), $Q = \sim 1.4$ MeV
t + e + p $\rightarrow$ ^{4}H $\rightarrow$ ^{4}He + e
t + e + d $\rightarrow$ ^{5}H $>^4$H + n $\rightarrow$ ^{4}He + e

The Q values give an estimated overall energy release.

Broad frequency RF radiation [22, 28] is predicted to result from resonance of the Hydroton structure, most of which is absorbed by the apparatus. This radiation is expected to carry away only a small fraction of the total energy.

6. Engineering Predictions

Engineering behavior is determined by variables over which a person hopefully has control. Knowing the mechanism, other than that hydrogen is the reactant, is not important. However, identifying the variables and showing their mathematical relationship to the overall process is important to achieve initiation and control. In the case of CF, power production is the behavior requiring control. Power production as heat is described by the following equation.

$$\text{Power generated} = K[XAC\,\exp(-B/RT)]. \tag{1}$$

X is a value determined by which hydrogen isotope is reacting. If mostly deuterium is present, this number will be large. If mostly protium is used, the number will be small and variable, with a gradual increase as deuterium forms and fuses with either p or other d. (See Table 1 on previous page,) A is the number of NAE. The greater the number of sites in which the fusion reaction can occur, the faster energy can be generated. C is the concentration of hydrogen isotope in the material surrounding the NAE. This value depends on the chemical characteristics of the surrounding material, temperature, applied hydrogen activity, and rate at which the hydrogen can enter the material through the surface. Use of surface activation, ion bombardment, and high pressure (activity) will increase the concentration. B is the energy required to move hydrogen within the material. Several different conditions can be used to move hydrogen ions. This equation is based on the movement being enhanced by temperature as a driver for diffusion. Concentration gradients or application of an electric field will increase the rate of movement, thereby increasing power production by making

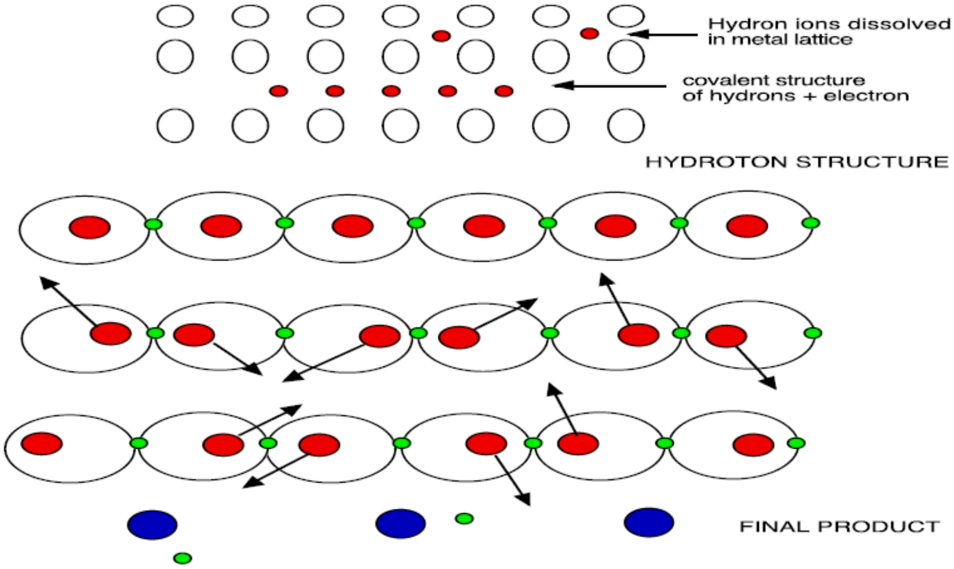

Figure 2. Cartoon of the sequence in the proposed fusion process. The green colored electrons are shown in their most probable location while traveling in the indicated path.

the hydrogen more available to the NAE [29,30]. T is the temperature (K) of the material surrounding the NAE. K is the constant used to resolve the measurement units for the different variables. R is the gas constant.

The temperature reached within the generator depends on how effectively power can be lost. Transfer of energy occurs several different ways, including by radiation, conduction, and convection. For this discussion, the controlling loss will be assumed to result from conduction through the material surrounding the NAE, as described by the following equation.

$$\text{Power Loss} = \Delta T * \lambda \tag{2}$$

where ΔT is the average temperature difference across the barrier having a thermal conductivity = λ. As long as the rate of energy loss is equal to the rate of energy creation by the CF process, temperature will remain stable.

Arbitrary but plausible values for the variables in Eqs. (1) and (2) are used to show the effect of temperature on power production and power loss in Fig. 3. The amount of power produced will be modified somewhat by changes in hydrogen content $[C]$ as temperature is changed, but this variable will not be considered right now. As can be seen in Fig. 3, at low temperatures, the effect of temperature is small, allowing the system to dissipate energy without runaway heating. However, once the rate of production exceeds the rate of loss, where the loss rate line crosses the production rate line, further increase in temperature cannot be stopped until hydrogen loss from the material or destruction of the NAE stops fusion.

These equations can be used to understand the behavior of all energy generators using CF including the E-Cat HT as designed by A. Rossi and tested by Levi et al. [31] The active core in this generator, consisting of Ni + H_2 with an unstated activator, does not produce significant energy at room temperature, as would be expected based on Eq. (1). Consequently, application of electric power to resistors surrounding the core is used to increase the temperature of the core. To start the process, the core is heated from room temperature until what they call a self-sustaining mode is observed. Based on Fig. 3, such a condition would seem to occur when temperature began to show a large effect

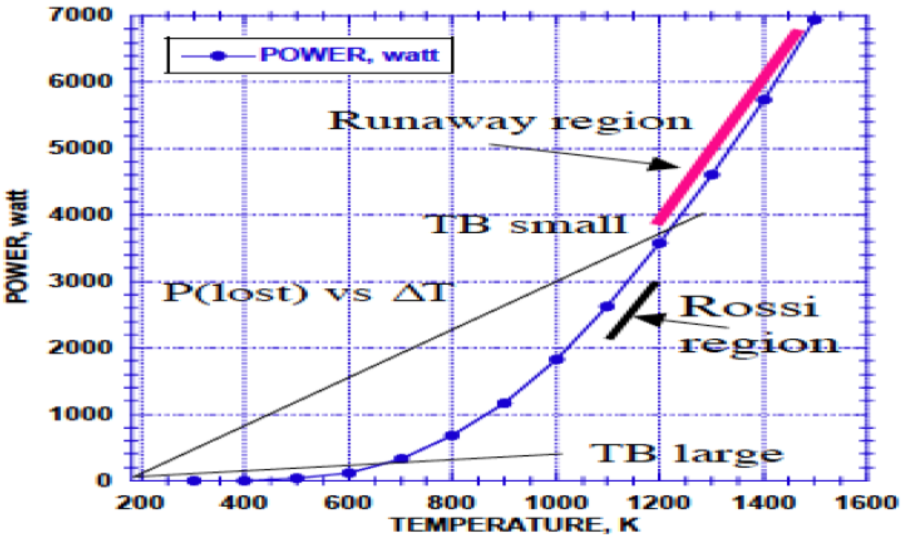

Figure 3. Effect of temperature on the amount of power. The straight lines show the relationship between power loss and ΔT for two different amounts of thermal resistance (TB). Runaway occurs when power produced exceeds power loss, as indicated by the red line. The “Rossi region” indicates where the E-Cat HT is operated below the runaway region.

on power production near 700 K. Temperature is increased further until significant power is generated, but without runaway. To insure runaway does not occur, applied power is then turned off briefly until temperature drops, after which power is again applied and temperature is allowed to reach the previous level before applied power is again stopped. Thus, control is achieved by periodically changing applied power to keep the temperature below the runaway region, but hot enough on average to produce significant power. This method avoids the challenge of exactly matching produced power with dissipated power so near the runaway temperature. The equations show how control can be achieved several other ways as well. For example, fusion at each temperature can be increased by increasing the concentration of hydrogen isotopes in the material several different ways, by using deuterium instead of light hydrogen, and by increasing the number of NAE sites in the generator. Local runaway might occur but this would be self-limiting as hydrogen concentration in the local region is reduced at the higher temperature.

"Ignition" of a large sample (1 cm cube) reported by Fleischmann and Pons [1] can also be explained. In this case, a cube of palladium had been electrolyzed in D_2O for many hours, allowing a large amount of deuterium to enter the metal. Apparently, the electrolyte boiled dry, thereby exposing the sample to gas, which is much less effective in removing heat compared to the liquid. As result, temperature of the cube rose rapidly as runaway started. The hot metal melted through the glass beaker, burned through the bench top, and dropped to the concrete floor before loss of deuterium allowed the metal to cool. Similar less-dramatic runaway events have been observed on other occasions and are called "life-after-death", a term applied when heat continues after electrolysis has stopped.

7. Proposed Test of the Model

The model can be tested as follows:

(1) The tritium production rate can be related to the D/H atom ratio in the material. When pure H is used, the rate will start at zero and increase with time as deuterium is made and fuses with the surrounding H. The concentration of deuterium and ^{4}He will also increase as energy is made. Of course, the NAE must be present for this reaction to start.
(2) Weak photon radiation can be detected when CF energy is made, which has a large range of energy, with most photons having too little energy to leave the apparatus. The radiation is expected to have coherent characteristics. Rapid beta decay of ^{4}H is also expected when helium is detected.
(3) The CF effect can be initiated as result of nano-sized crack formation, generally in the surface region as a result of stress relief. This stress can be created many different ways in many different materials.
(4) The rate of energy production can be described by Eq. (1).

8. Conclusions

Cold fusion is real, not related to hot fusion, and requires a significant change to take place in a material for it to occur.

Present lack of acceptance and progress is caused by lack of effective guidance by theory.

Behavior of all materials using all isotopes of hydrogen can be explained by a single basic mechanism operating in a single NAE.

The NAE is created as nano-gaps resulting from stress relief mainly in the surface region.

The nuclear-active structure, called *Hydroton,* is a form of metallic hydrogen that forms in the nano-gaps.

Heat is generated by formation of ^{4}He, tritium, or deuterium, depending on which hydrogen isotope is present, accompanied in each case by emission of weak photon radiation having a range of energy.

Transmutation results only as consequence of a fusion reaction, which provides the energy required to overcome the large Coulomb barrier.

9. Summary

A collection of five plausible assumptions can be used to evaluate proposed theories of cold fusion. When applied, no present theory is consistent with all of them. Consequently, a new model is created that is consistent with all the proposed assumptions, violates no Law of Nature, is consistent with all major observations, and can predict many new behaviors. The model can be applied to guide engineering development by creating more efficient devices, improving reproducibility, and achieving better control of energy production. Tests to determine if the model is correct are suggested. Mathematical descriptions will be undertaken once the concept is demonstrated to be correct.

Acknowledgement

I am grateful to Brian Scanlan for the many very productive discussions, insights into how the CF process might work, and for his financial support. I'm looking forward to his theory of how the Hydroton might form and function to be published.

References

[1] Fleischmann, M., S. Pons and M. Hawkins, Electrochemically induced nuclear fusion of deuterium, *J. Electroanal. Chem.* **261** (1989) 301–308 and errata in **263** (1989) 187–188.

[2] Storms, E.K., *The Science of Low Energy Nuclear Reaction,* World Scientific, Singapore, 2007, 312 pp.

[3] Storms, E.K., The status of cold fusion, *Naturwissenschaften* **97** (2010) 861.

[4] Rossi, A., Method and apparatus for carrying out nickel and hydrogen exothermal reaction, WO20110005506 (2011), USA.

[5] Storms, E., *The Explanation of Low Energy Nuclear Reaction*, Infinite Energy Press, Concord, NH, 2014, 365 pp.

[6] Storms, E.K., The nature of the energy-active state in Pd—D, *Infinite Energy*, Issues 5 and 6 (1995) 77.

[7] Lipson, A.G. et al., Generation of DD-reactions in a ferroelectric KD_2PO_4 single crystal during transition through Curie point (Tc = 220 K), in *Condensed Matter Nuclear Science, ICCF-12,* Yokohama, Japan: World Scientific, Singapore, 2005.

[8] Preparata, G. Fractofusion revisted. in Anomalous nuclear effects in deuterium/solid systems*, AIP Conference Proceedings 228,* Brigham Young Univ., Provo, UT, American Institute of Physics, New York, 1990.

[9] Takeda, T. and T. Takizuka, Fractofusion mechanism, *J. Phys. Soc. Japan* **58**(9) (1989) 3073.

[10] Lipson, A.G. et al., Neutron emission in monocrystals of KD_2PO_4, stimulated by ferroelectric phase transition*, Pis'ma Zh. Tekh. Fis.* **18**(16) (1992) 90 (in Russian).

[11] Jiang, X.-l., Y. Zhang and Z. Zhang. Nuclear transmutation in non- equilibrium systems by ultra-closed range casimir effect, in *15th Int. Conf. on Condensed Matter Nuclear Science,* Rome, Italy, ENEA, Italy, 2009.

[12] Mosier-Boss, P.A., A Review on nuclear products generated during low-energy nuclear reactions (LENR), *J. Cond. Matter Nucl. Sci.* **6** (2012) 135–148.

[13] Mosier-Boss, P.A. et al., Comparison of Pd/D co-deposition and DT neutron generated triple tracks observed in CR-39 detectors, *Eur. Phys. J. Appl. Phys.* **51**(2) (2010) 20901–20911.

[14] Balin, D.V. et al., Experimental investigation of the muon catalyzed d-d fusion, *Phys. Lett. B* **141**(3/4) (1984) 173.

[15] Rafelski, H.E. et al., *Cold fusion: muon-catalyzed fusion, J. Phys. B* **24** (1991) 1469.

[16] Tsyganov, E.N. et al., Registration of energy discharge in D + D = 4He* reaction in conducting crystals (simulation of experiment), *Nucl. Instr. and Meth. in Phys. Res. B* **309** (2013) 95–104.

[17] Storms, E.K., The role of voids as the location of LENR, *J. Cond. Matter Nucl. Sci.* **11** (2013) 123–141.

[18] Storms, E.K., Cold fusion from a chemist's point of view, *Infinite Energy* **18**(108) (2013) 13–18.

[19] Violante, V. et al., Metallurgical effects on the dynamic of hydrogen loading in Pd, in *The 9th Int. Conf. on Cold Fusion, Condensed Matter Nuclear Science*, Tsinghua Univ., Beijing, China, Tsinghua Univ. Press, 2002.

[20] Mazzolai, F.M., P.G. Bordoni and F.A. Lewis, Elastic energy dissipation effects in the palladium-hydrogen system, *J. Less-Common Met.* **74** (1980) 137.

[21] Huggins, R.A., Fundamental considerations relating to the insertion of hydrogen isotopes into mixed conductors at high activities, *Mater. Res. Soc. Symp. Proc.* **210** (1991) 317.

[22] Afonichev, D. and M. Murzinova, Indicator of the process of cold fusion, *Int. J. Hydrogen Energy* **28** (2003) 1005–1010.

[23] Romodanov, V.A., Tritium generation during the interaction of plasma glow discharge with metals and a magnetic field, in *Tenth Int. Conf. on Cold Fusion,* Cambridge, MA, World Scientific, NJ, 2003.

[24] Romodanov, V.A., Y.B. Skuratnik and A.K. Pokrovsky, Generation of tritium for deuterium interaction with metals, in *8th Int. Conf. on Cold Fusion*. 2000, Lerici (La Spezia), Italy, Italian Physical Society, Bologna, Italy.

[25] Wigner, E. and H.B. Huntington, On the possibility of a metallic modification of hydrogen, *J. Chem. Phys.* **3**(12) (1935) 764.

[26] Horowitz, C.J., Cold nuclear fusion in dense metallic hydrogen, *Astrophys. J.* **367** (1991) 288.

[27] Nellis, W.J., A.L. Ruoff and I.F. Silvera, Has Metallic Hydrogen Been Made in a Diamond Anvil Cell? arXiv:1201.0407 [cond-mat.other], 2012.

[28] Afonichev, D.D. High-frequency radiation and tritium channel, in *Tenth Int. Conf. on Cold Fusion*, Cambridge, MA, World Scientific, NJ, 2003.

[29] Mizuno, T. et al., Anomalous gamma peak evolution from SrCe solid state electrolyte charged in D_2 gas, *Int. J. Hydrogen Energy* **22** (1997) 23.

[30] Biberian, J.-P. et al., Electrolysis of $LaAlO_3$ single crystals and ceramics in a deuteriated atmosphere, in *The Seventh International Conference on Cold Fusion*, Vancouver, Canada, ENECO Inc., Salt Lake City, UT, 1998.

[31] Levi, G. et al., Indication of anomalous heat energy production in a reactor device. arXiv:1305.3913v3, 2013.

J. Condensed Matter Nucl. Sci. 15 (2015) 305–313

Research Article

Progress in Development of Diamond-based Radiation Sensor for Use in LENR Experiments

Charles Weaver*, Mark Prelas, Haruetai Kasiwattanawut, Joongmoo Shim,
Matthew Watermann, Cherian Joseph Mathai and Shubra Gangopadhyay
SKINR – University of Missouri, USA

Eric Lukosi
University of Tennessee, Knoxville, USA

Abstract

This work discusses the ongoing development of diamond-based radiation sensors for spectrometry within the environments found in low energy nuclear reaction (LENR) experiments. Specifically discussed are the efforts to demonstrate the robustness of palladium-electrode sensors. This includes fabrication methods, characterization and calibration techniques, and the results of deuterium gas loading trials which demonstrate performance throughout the entire test. The results are positive. One notable peak in the spectrometry results; additional trials are required to both determine the cause of this peak and determine which criteria.

Keywords: Charged particle spectroscopy, Diamond sensors, Radiation detection

---

1. Introduction

Efforts to perform spectroscopy on any neutrons or charged particles which may be produced by low energy nuclear reaction (LENR) phenomena have predominantly used CR-39 chips [1–4]. Although CR-39 has been demonstrated to be a useful spectroscopy method [5] with relatively low material costs, several of its attributes [6] have driven investigation into other detection methodologies. Most notably, the treatment and analysis of CR-39 is time-intensive and it is an integrating detector, which prohibits it from being used in real-time analysis. Conversely, conventional neutron spectroscopy methods which provide real-time analysis, such as scintillation detectors, are difficult to implement within the active LENR environment where they will have the highest detection efficiency. Therefore they cannot detect particles which may only transport over very short distances. The most popular neutron spectroscopy systems also require post processing techniques for n–γ discrimination due to their different sensitivities for different types of ionizing radiation.

---

*E-mail: weavercl@missouri.edu

The recent availability of large, electronic-grade, single-crystal diamonds (EGSCD) has generated a great amount of work in the creation of diamond-based radiation detectors. EGSCD-based detectors possess a number of advantages which makes them applicable to LENR systems. The mechanical robustness, inert chemistry, and radiation hardness of diamond allows its use within hostile environments. High charge-carrier mobility and charge collection efficiency near 100% allow diamond to be used in real-time spectroscopy while the 5.5 eV band gap of diamond provides an inherently low noise floor across a wide temperature range. Diamond also exhibits a linear response with increasing energy deposition and has demonstrated a resolution less than one percent for high energy particles [7]. What makes diamond particularly relevant for neutron spectroscopy is its low photon interaction cross-section, which removes the need for the n–γ discrimination techniques required by scintillator-based detectors.

In short, the use of a diamond-based neutron sensor, referred to as a diamond sensor (DS) throughout the rest of this paper, incorporates the advantages of traditional solid-state systems with the advantages of real-time signal analysis while avoiding the issues commonly associated with both. The most significant downside for diamond-based radiation sensors is cost; the number of manufacturers is currently small, but costs will come down as production methods improve and more vendors become available. The method of adapting a diamond sensor for LENR experiments was initially described at ICCF-17. It consists of tasks which can be divided into three categories: sensor fabrication, creating surface features, and achieving high deuterium gas loading.

Fabrication of a diamond-based detector which is sufficiently resistant to the deuterium environments in LENR experiments is the first step. Preliminary results presented at ICCF-17 [8] described attempts to produce ohmic contacts on a diamond plate using the reactive sputtering of diamond-like carbon (DLC). However these contacts did not survive exposure to deuterium, and additional attempts to produce in the interim continued to demonstrate poor adhesion. This required us to evaluate alternate materials and deposition methods. This paper presents the fabrication methods of additional diamond sensors and the results of evaluating those diamond sensors; the materials and deposition techniques used to create the contacts, $I - V$ characterization of the contacts, the calibration of the sensors, and the results of their exposure to deuterium.

Once the procedure for fabricating deuterium-resistant ohmic contacts is sufficiently reproducible we will then develop treatment methods to produce the surface structures believed to be necessary for the production of LENR phenomena. The theoretical basis of how these structures facilitate LENR phenomena has been explained in the literature [9]. After the requisite surface structures have been observed using SEM techniques, the final step is achieving high gas loading. The methods used to achieve high loading will be those which have previously claimed reproducible LENR phenomena [10].

2. Fabrication

The successful fabrication and operation of a diamond sensor depends on three components: the diamond substrate, the electrical contacts, and the associated electronics for signal analysis. Two electronic-grade diamond plates of dimension 3×3×0.5 mm diamond plate were purchased from Element Six for use as diamond substrates. The plates showed no signs of crystal defects or band gap impurities when previously characterized using Raman spectroscopy and spectrophotometry. Before metallization, any persistent organic compounds, oxide layers, and residual metallic ions were removed from the diamond plate using the RCA clean procedure listed in Table 1; after each step the diamonds were rinsed with deionized water and placed in a deionized water bath while the solution used in the next step was prepared.

Once cleaned, a diamond substrate was placed within a mask. The mask consisted of two plates: one which held the diamond in place by centering it within a hole 3 mm in diameter; the second used a hole 2 mm in diameter centered over the diamond plate to permit deposition on a small region of the substrate. The masked substrate was then attached within the deposition chamber for contact deposition. The previous efforts to fabricate diamond sensors reported at

Table 1. Diamond plate cleaning procedure.

Step	Solution	Temp. (°C)	Time (min)
1	Aqua Regia	150	20
2	NH_4OH:H_2O_2:H_2O (1 : 1 : 1)	150	20
3	Piranha	150	20
4	H_2SO_4:HNO_3:$HClO_4$ (1 : 1 : 1)	150	30

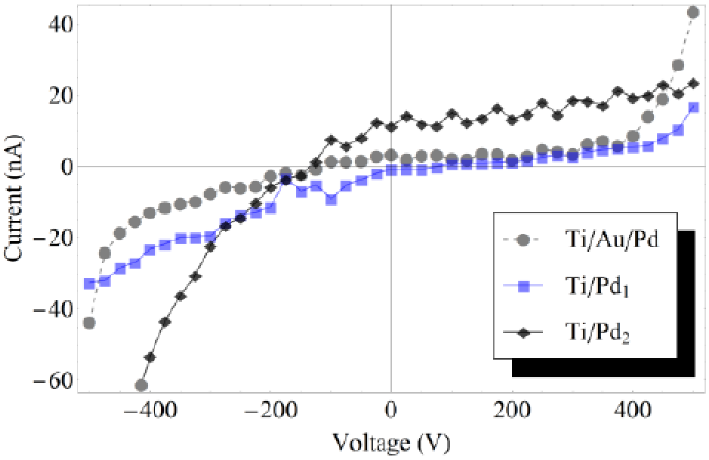

Figure 1. $I - V$ Characteristics of diamond sensors.

ICCF-17 used diamond-like carbon (DLC) films as the contact material; these contacts delaminated during deuterium loading and persistent difficulties with adhesion required the use of materials more commonly found in diamond contact formation: titanium, gold, and palladium. Titanium is one of the carbide-forming metals with a demonstrated history of producing ohmic contacts on diamond [11] but it requires oxygen and deuterium diffusion barriers. Without these barriers any titanium that exists in the contact, but is not bonded to the diamond, would react and damage the contacts. Palladium is used for two reasons: it is a lattice material metal which can achieve high loading and will therefore be treated to develop the microscale structures necessary for LENR to occur in future work; Pd is also an effective oxygen diffusion barrier. Gold was initially used as a deuterium diffusion barrier, but it was avoided in sensors 2 and 3 due to concerns regarding adhesion with the other materials. After one side of the diamond plate was metalized, the plate was removed from the mask, flipped over, replaced in the mask, and the same deposition process was performed on the other side.

Table 2. Diamond sensor film materials and thicknesses.

Sensor	Ti (nm)	Au (nm)	Pd (nm)
1	50	20	100
2	50	0	150
3	50	0	130

The film thicknesses deposited on the diamond plates are available in Table 2. The first of these diamond sensor fabrication attempts used three films which were all deposited by thermal evaporation: 50 nm base layer of titanium, 20 nm layer of gold, and 100 nm of palladium. During the Pu-239 calibration, discussed below, it became apparent that there was a problem with the contacts and the metalized plate was consequently inserted into an argon tube furnace for 20 min at 500˚C to promote the formation of TiC and improve contact quality. At some point during the annealing process the thin film delaminated from the diamond surface. These issues were avoided while constructing sensors 2 and 3 by replacing thermal evaporation with RF sputtering for titanium deposition. The gold layer was also removed and the palladium thickness was increased. The same film thicknesses were applied to both sides of a diamond plate; once one side had been metalized, the diamond was flipped over within the mask and the process was repeated.

3. Characterization and Calibration

Once both depositions were complete, a now-metalized diamond was mounted using silver paste onto a transistor package which featured two electrically isolated legs. After the silver paste dried, two wire bonds were made using aluminum wire 20 μm in diameter. One bond connected the package to the ground leg of the applied bias; the other bond connected the exposed palladium surface of the diamond sensor to the high voltage leg of the applied bias. The current–voltage characteristics of the assembled diamond sensor were then measured using a Keithley 6487 picoammeter. Each sensor exhibited the desired ohmic behavior between 150–250 V bias as shown in Fig. 1 which was previously determined to be the bias which achieved 100% charge collection efficiency for these sensors [8].

Each diamond sensor was then installed in a Canberra 7404 alpha spectrometer and energy-calibrated using a Pu-239 check source. The results of energy calibration are available in Fig. 2. The calibration curve of sensor 1, labeled TiAuPd, displays two peaks. The peak on the right corresponds to the expected full-energy peak of Pu-239 at 5156 keV. The peak below 2000 keV was the motivation for annealing and subsequent loss of the contact discussed above. The second sensor (TiPd$_1$) displays an unexpectedly high noise but was tested for deuterium resistance. The curve which corresponds to the third sensor, labeled TiPd$_2$, features the expected spectrum.

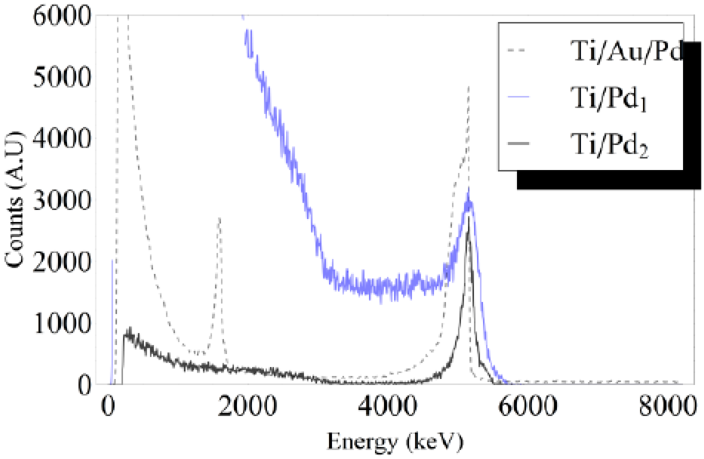

Figure 2. Pu-239 Diamond sensor energy calibration spectra.

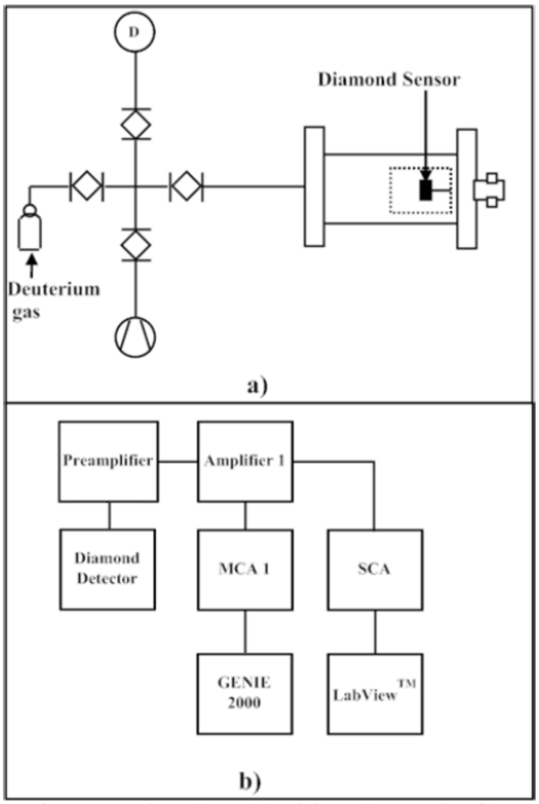

Figure 3. Experimental setup (a) and electronic connections (b).

4. Gas Loading Setup and Procedure

The diamond sensor under investigation was removed from the alpha spectrometer after calibration and connected within the chamber shown in Fig. 3a. The diamond sensor was then connected to the associated electronics shown in Fig. 3b by the BNC feedthrough on the chamber. The electronics for signal processing consisted of a preamplifier, two amplifiers, one single-channel analyzer, one card of a Canberra Multiport II USB Multichannel Analyzer array, and two independent computers which operated the Canberra Genie2000 spectroscopy and LabView edge-counting software programs.

Before initiating a gas trial, the chamber containing the diamond sensor was vacuumed using a roughing pump to a pressure below 13 Pa measured using an MKS 722 Baratron absolute capacitance manometer. After sufficient degassing of materials which had adhered to the inner surface of the chamber, a trial was initiated by closing the vacuum valve and opening the valve to the deuterium tank to fill the chamber with deuterium at a pressure of 690 kPa. A +200 V bias was then applied to the chip and both software programs were started simultaneously. To minimize the number of atmosphere changes for each sensor, trials were run as long as possible; the durations of the diamond sensor trials are shown in Table 3.

At the conclusion of each trial the chamber was opened and the diamond sensor was inspected using three methods.

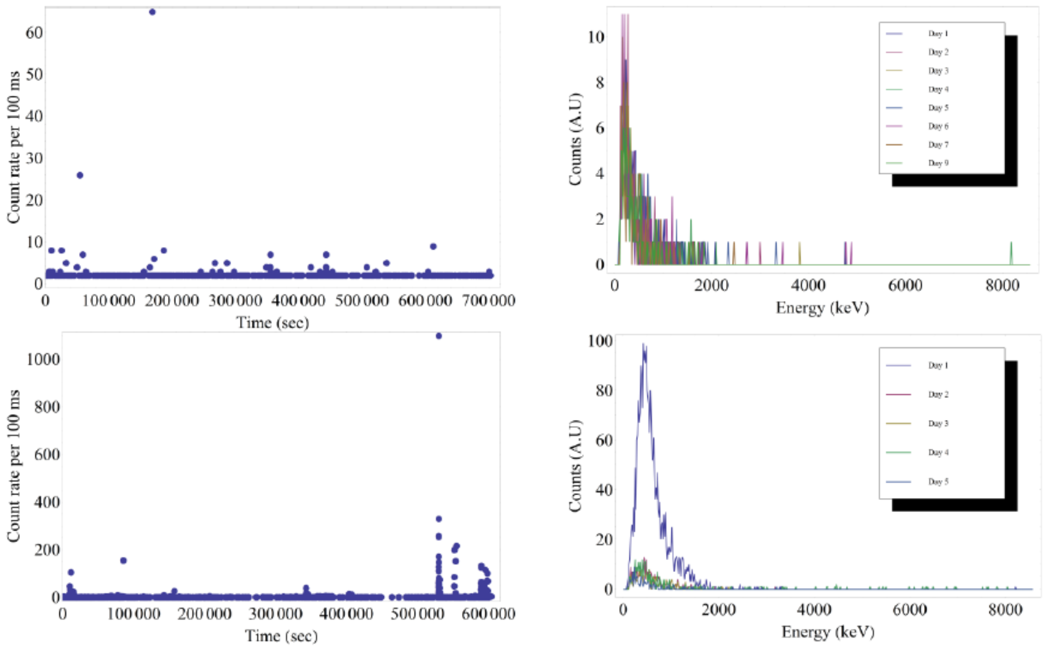

Figure 4. SCA (*left*) and spectroscopy (*right*) results for diamond sensor 2 – $TiPd_1$ trials 1 (*top*) and 2 (*bottom*).

Table 3. Diamond sensor trial durations.

Sensor	Trial	Duration (days)
2 – $TiPd_1$	2 – 1	9
2 – $TiPd_1$	2 – 2	5
3 – $TiPd_2$	3 – 1	7

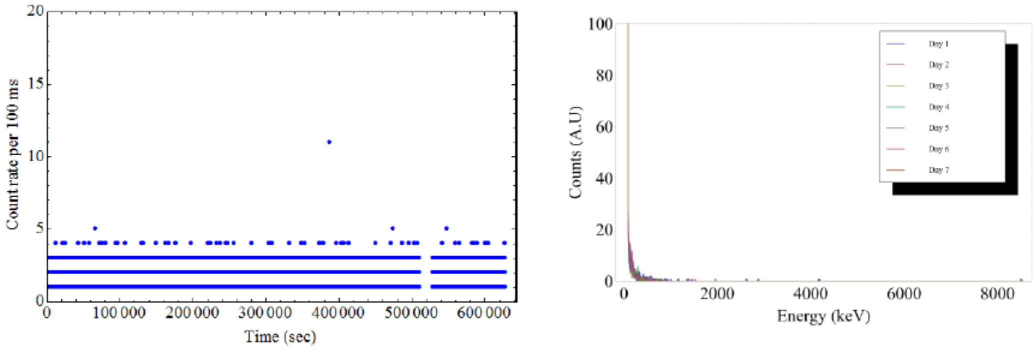

Figure 5. SCA (*left*) and spectroscopy (*right*) results for diamond sensor 3 – $TiPd_2$.

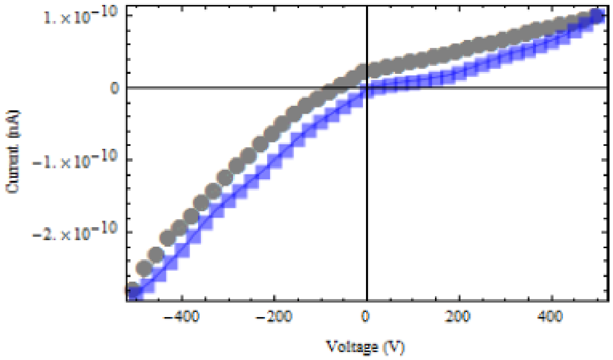

Figure 6. $I - V$ Characteristics of diamond sensor 2 after two deuterium loadings.

The energy calibration of the sensor was rechecked using the Pu-239 calibrated source. The detector $I - V$ behavior was rechecked to determine if any significant changes in the electrical behavior of the sensor took place during deuterium exposure. Scanning electron microscopy was used to locate any microscale defects which have been observed in the literature [12].

5. Results

The first diamond sensor (TiAuPd) failed during annealing. Diamond sensors 2 and 3 appear to have survived the deuterium exposure while producing some interesting results. The spectroscopy and counting results of deuterium exposure for diamond sensors 2 and 3 are available in Figs. 4 and 5, respectively. The spectroscopy results of trials 2 – 1 and 3 – 1 contain no peaks above the noise floor, although count rate data include rare occurrences of counts rates far above the background. Spectroscopy and count rate data also suggest that some reaction occurred with an average energy of 650 keV and FWHM of 400 keV on day five of trial 2-2.

SEM scans of the sensors which were taken after each sensor trial was finished contained one anomalous result shown in point of little evidence of the micro-ruptures or other irregular particle phenomena described in the literature

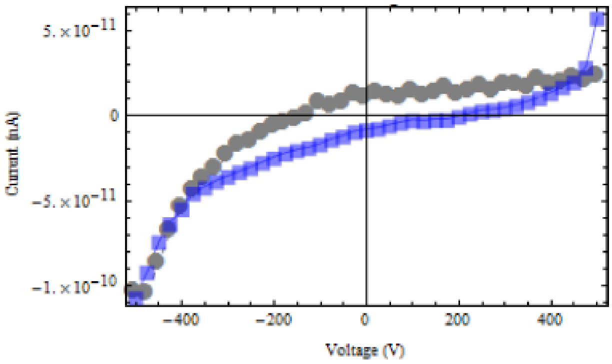

Figure 7. $I - V$ Characteristic of diamond sensor 3 after deuterium loading.

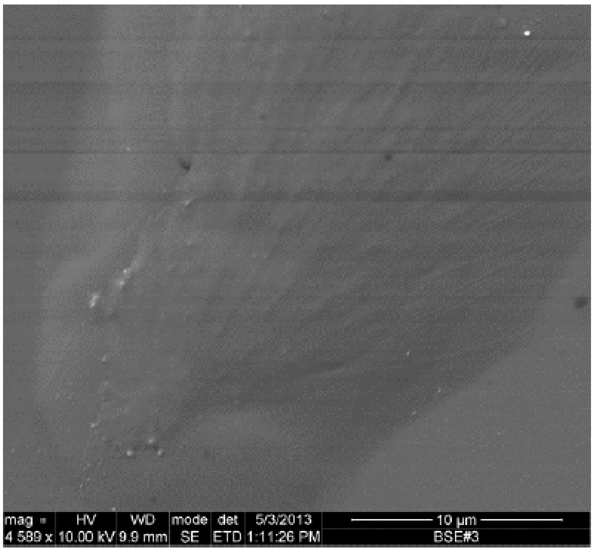

Figure 8. Anomalous spot found during SEM inspection of diamond sensor 2 after second deuterium loading.

[4]. The contact resistance of sensors 2 and 3 decreased during deuterium exposure which improved the $I - V$ curves shown in Figs. 6 and 7. Figure 6 shows $I - V$ Characteristics of diamond sensor 2 after two deuterium loadings and Fig. 7 shows $I - V$ Characteristic of diamond sensor 3 after deuterium loading.

6. Conclusions

The results of this work confirm progress in the development of diamond-based radiation sensors with the end goal of *in situ* incorporation for LENR experiments. It demonstrates diamond sensors which exhibit the same diagnostic responses before and after deuterium exposure which suggests that the sensor continue to function within the deuterium environment. Spectroscopy and counter data suggest that some reaction occurred within the cathode during deuterium pressure loading. However no conclusions can be made at this time regarding the source of these apparent energy peaks. They may have been the result of contact deformation as metallic titanium within the contacts absorbed deuterium which migrated through the outermost palladium film. Similarly, palladium is known to deform with deuterium loading and this may have also released the charge which was interpreted by the electronics to be an energetic particle.

This will be examined in the diamond sensors currently under development, which will reincorporate gold into the films as an intermediate to prohibit deuterium diffusion into the titanium. Once those sensors have demonstrated their resistance to deuterium, the exposed palladium electrode can be prepared using techniques in the literature to achieve the requisite microstructures. Once the surface preparation is sufficiently reproducible, the complete sensors can then be exposed to a high deuterium loading. Previously reported results can then be independently evaluated using real-time spectrometry which is effectively a part of the active nuclear environment.

Acknowledgements

The authors would like to thank the Sidney Kimmel Institute for Nuclear Renaissance at the University of Missouri for their scientific, administrative, and economic support personnel of this work.

References

[1] S. Mahadeva, Wide-ranging studies on the emission of neutrons and tritium by LENR configurations: an historical review of the early BARC results, *Low-Energy Nuclear Reactions and New Energy Technologies Sourcebook*, Volume 2, American Chemical Society, 2009, pp. 35–57.

[2] M.A. Prelas and E. Lukosi, Neutron emission from cryogenically cooled metals under thermal shock, *Proc. 17 th Int. Conf. on Cold Fusion*, Daejeon/Korea, 2012, pp. 13–17.

[3] S. Szpak, P. Mosier-Boss, F. Gordon, J. Dea, M. Miles, J. Khim and L. Forsley, LENR research using co-deposition, *Proc. ICCF14* (2008).

[4] P.A. Mosier-Boss, A review on nuclear products generated during low-energy nuclear reactions (LENR), *J. Condensed Matter Nucl. Sci.* **6** (2012) 135.

[5] J.A. Frenje, C.K. Li, F.H. Séguin, D.G. Hicks, S. Kurebayashi, R.D. Petrasso, S. Roberts, V.Y. Glebov, D.D. Meyerhofer, T.C. Sangster, J.M. Soures, C. Stoeckl, C. Chiritescu, G.J. Schmid and R.A. Lerche, Absolute measurements of neutron yields from DD and DT implosions at the OMEGA laser facility using CR-39 track detectors, *Rev. Sci. Instr.* **73** (2002) 2597.

[6] S.A. Durrani, Nuclear tracks today: Strengths, weaknesses, challenges, *Radiation Measurements* **43** (2008) S26–S33.

[7] C. Manfredotti, CVD diamond detectors for nuclear and dosimetric applications, *Diamond and Related Materials* **14** (2005) 531–540.

[8] E. Lukosi, M. Prelas, J. Shim, H. Kasiwattanawut, C. Weaver, C.J. Mathai and S. Gangopadhyay, Diamond-based radiation sensor for LENR experiments part 1: sensor development and characterization, *17th Int. Conf. Cold Fusion*, ICCF-17 Secretariat, Daejeon, Korea, 2012, p. 6.

[9] E. Storms, B. Scanlan, N. Santa Fe and C. Greenwich, Role of cluster formation in the LENR process, *15th Int. Conf. on Condensed Matter Nuclear Science*, 2009. Rome, Italy: ENEA. p, 2009.

[10] E. Storms, Status of cold fusion (2010), *Naturwissenschaften* **97** (2010) 861–881.

[11] T. Tachibana, B. Williams and J. Glass, Correlation of the electrical properties of metal contacts on diamond films with the chemical nature of the metal-diamond interface. II. Titanium contacts: A carbide-forming metal, *Phy. Rev. B* **45** (1992) 11975.

[12] M. Srinivasan, Neutron emission in bursts and hot spots: signature of micro-nuclear explosions? *J. Condensed Matter Nucl. Sci.* **4** (2011) 12.

J. Condensed Matter Nucl. Sci. 15 (2015) 314–320

Research Article

Investigation of Possible Neutron Production by D/Ti Systems under High Rates of Temperature Change

Charles Weaver*

SKINR – University of Missouri, USA

Mark Prelas, Joongmoo Shimn and Haruetai Kasiwattanawut

Nuclear Science and Engineering Institute, University of Missouri, USA

Shubhra Gangopadhyay and Cherian Mathai

Electrical and Computer Engineering Department, University of Missouri, USA

Abstract

This paper discusses recent attempts to reproduce thermal shock experiments from 1991 using additional diagnostics. This was motivated by an apparent series of neutron bursts which were observed during the deuterium loading of titanium powder at cryogenic temperatures. The neutron count rate and temperature measurements are presented for control and experimental trials. Some neutrons were observed during trials, but the magnitude of the burst which motivated this work could not be replicated. Control trials with inert gas, which should produce no reaction, also demonstrated neutron signal. Future experimental directions are also discussed.

Keywords: Gas loading, Neutron production, Temperature shock, Titanium

---

1. Introduction

Since the announcement by Fleischmann and Pons in 1989, a number of low energy nuclear reaction (LENR) experiments have been enacted; some claimed to observe neutrons [1–3] while a majority claimed a null result [4]. Of the experiments which recorded evidence of neutrons, significant inconsistency existed among energy and emission frequency [5]. One series of experiments were carried out at the University of Missouri in 1991 using titanium powder which had been saturated with deuterium at cryogenic temperatures; the recently published results indicated that in excess of two million neutrons were produced within a very short time when the system was rapidly heated [6]. There was also a simultaneous effort by the community to develop the theoretical mechanism for this neutron production and determine whether it was hot fusion, a variant of hot fusion called fractofusion [7], or an entirely new process.

---

*E-mail: weavercl@missouri.edu

It was decided in 2012 to perform gas loading experiments similar to those which were completed in 1991. Preliminary results of this recent series were obtained using functionally equivalent apparatus were presented at ICCF-17; they showed consistent results with the 1991 experiments and the literature, namely uncommon temporary increases in neutron production rate during a thermal shock event. Shortly after ICCF-17, the series of significant bursts shown in Fig. 1 were recorded by the helium-3 counter during the cryogenic loading of titanium with deuterium. These observed bursts were similar in duration and magnitude to those observed in 1991. The burst lasted for 10 min and produced 1.5 million total raw neutron counts. After this series of bursts, additional software-controlled diagnostic systems were incorporated to the setup and additional trials were performed. The primary systematic improvements which have been incorporated within the last year are: software-controlled data-logging which now allows for continuous observation of several system parameters of interest; the use of standardized titanium powders whose relatively high surface area should allow for improved deuterium absorption; and the inclusion of argon trials as a control to determine whether or not the apparent neutron signals recorded during experiment are gas-dependent. If the neutron signal only appears during deuterium trials, it would reinforce the claim that neutrons are actually being observed. If the experiment can demonstrate neutron production in a way which is reproducible, deuterium-dependent, and statistically-relevant, then neutron spectrometry will be added to the observation suite and pulse shape discrimination will be used to distinguish the signal from sporadic low-energy gamma rays in the background.

2. Theory

The theory which governs the behavior of these experiments relies on fractofusion, whereby large potential gradients are produced along grain boundaries and within cracks that form during the deuterium loading of the metal under investigation, in this case titanium [7,8]. Once the titanium sample is sufficiently loaded with deuterium at −196°C, both within individual grains and along the boundaries, a rapid temperature increase may drive a cluster of deuterons

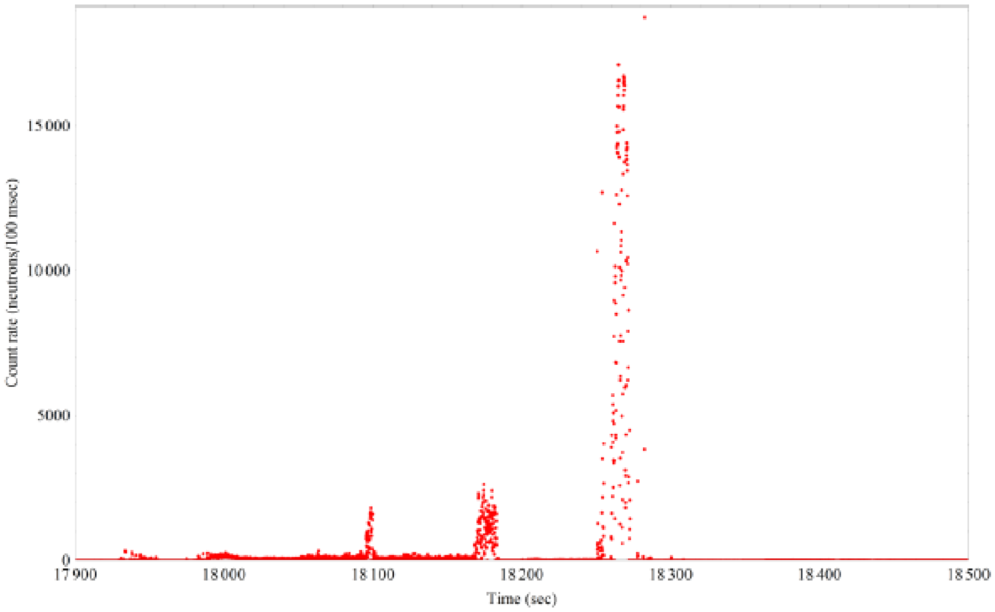

Figure 1. Anomalous neutron signal during cryogenic deuterium loading.

close enough together for some to overcome the Coulomb barrier and fuse [2,9]. In this case, the process reduces to very abrupt periods of hot fusion, which should consist of roughly even branching ratios for tritium and neutron emission seen below. In other types of LENR experiments, namely electrolysis and co-deposition experiments [10], this was not the case; neutrons were measured with an energy range spanning 3–10 MeV [11] instead of the monoenergetic 2.45 MeV neutrons which would be produced in (2).

$$ {}^{2}_{1}\mathrm{D} + {}^{2}_{1}\mathrm{D} \rightarrow \mathrm{T}\,(1.01\ \mathrm{MeV}) + \mathrm{p}^{+}(3.02\ \mathrm{MeV}), \tag{1} $$

$$ {}^{2}_{1}\mathrm{D} + {}^{2}_{1}\mathrm{D} \rightarrow {}^{3}_{2}\mathrm{He}(0.82\,\mathrm{MeV}) + {}^{1}_{0}\mathrm{n}(2.45\,\mathrm{MeV}), \tag{2} $$

$$ {}^{2}_{1}\mathrm{D} + {}^{2}_{1}\mathrm{D} \rightarrow {}^{4}_{2}\mathrm{He} + \gamma(23.84\ \mathrm{MeV}). \tag{3} $$

3. Experimental, Apparatus and Method

The apparatus used in these experiments is divided into two categories: sample preparation and thermal shock. Common to both categories was the u-tube; a 3/8" 316 L stainless steel tube bent to a 180° “U” shape which contained the titanium powder in use. One end of the u-tube terminated in a fitting; the other end terminated in a cap and was the loading port for titanium powder into the tube. As shown in Fig. 2, a 1/8" × 20" type K thermocouple was connected to one end of the tee and fed into the u-tube through a 1/8" adapter fitting. The thermocouple probe tip was placed in the middle of the bend so that it would be in contact with the titanium sample. The other tee connected to the rest of the experimental apparatus described below.

The materials used in the experiments were titanium and deuterium gas. The titanium consisted of 99.99% pure, −325 mesh, dehydrided, titanium powder purchased from Alfa Aesar. The powdered form of titanium provided the maximum surface area and highest potential loading of commercially available stock. The methods used to prohibit oxidation of the titanium powder are detailed below.

3.1. Sample preparation

The sample of titanium powder was prepared in an inert argon atmosphere to minimize the possibility for a reaction between the titanium and either oxygen or hydrogen in the air before deuterium loading. The apparatus used to accomplish was: the u-tube, a portable glove box, a diaphragm pump, a bottle containing the dehydrided titanium to be loaded into the u-tube, two wrenches, and a reducing fitting. The parts were first cleaned using alcohol and acetone (if appropriate) to minimize glove box contamination and tear hazards. They were then placed within a portable glove box (PGB) and the glove box was sealed shut. The air was then vacuumed out of the glove box using a diaphragm pump rated for 100 μTorr. The pump valve was then closed and a purge was conducted by partially filling the PGB with argon. Three purges were conducted. The PGB was then refilled with argon, leaving enough room to manipulate the tools and materials, and the argon tank valve closed. The cap was then removed from the u-tube and the ½–3/8” reducer fitting attached. The titanium bottle was then opened and approximately half of the dehydrided titanium was poured into the tube.

The titanium bottle was then closed and resealed, the valves on the u-tube were closed, and the PGB contents removed. The u-tube was reconnected to the experimental setup immediately after removal from the PGB. The rest of the experimental apparatus was then evacuated using a Pfeiffer HiCube 80 turbomolecular pump station. The rest of the apparatus was then purged using argon in the same manner as the portable glove box. Once the air removal procedure

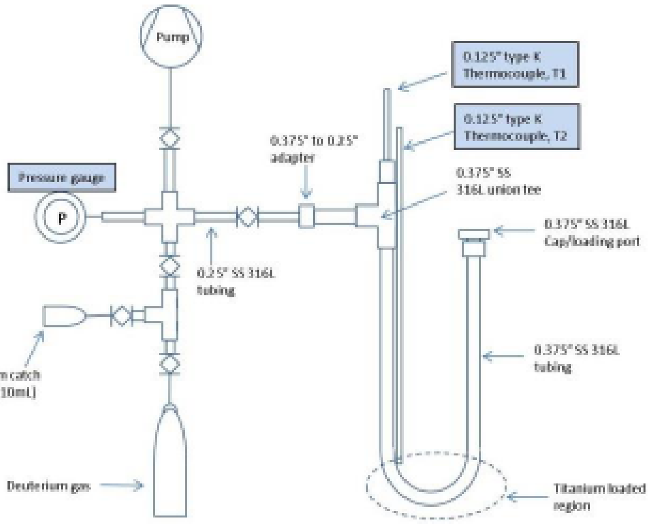

Figure 2. Experimental apparatus for thermal shock experiment.

was complete, the valve separating the u-tube was slowly opened and the entire assembly was then evacuated overnight so deuterium loading could proceed in the morning.

Before deuterium was introduced to the u-tube, the valve on the catch tank was closed to isolate the catch tank from the rest of the experimental system. The valve on the pump was then closed to isolate the vacuum from the rest of the system. The valve to the pressure regulator of the deuterium tank was then opened, allowing deuterium gas to flow into the u-tube up to a pressure of 100 Psi g. After several minutes the deuterium loading was complete, the valve was closed to the deuterium tank, the deuterium tank was disconnected, and the titanium-containing portion of the tube was lowered into a LN_2 bath. The thermal shock procedures were initiated after the bend of the u-tube, which contains the titanium, was exposed to LN_2 for several hours.

3.2. Thermal shock

The thermal shock apparatus used in these experiments consisted of: a cryogenic bath filled with liquid nitrogen (LN_2); a heated water bath; a polyethylene-moderated 252257 helium-3 counter from LND, Inc., which included a Tennelec Tc 952 high voltage power supply, Orten 142PC preamplifier**,** Ortec 673 amplifier and gated integrator, and Ortec 550 single channel analyzer; a computer capable of running the LabView data-logging program; a National Instruments SCB-68 Connector Block; and the experimental apparatus shown in Fig. 2. The instrumentation attached to the experimental apparatus consisted of a Druck DP104 pressure gauge capable of measuring 68.9 MPa (10,000 Psi g), a type K thermocouple mechanically bound to the u-tube exterior; and a catch tank to capture deuterium gas and other products produced during the experiment for future RGA analysis. Before thermal shock trials were enacted the helium-3 counter was allowed to run uninterrupted to observe any potential defects in device function.

The helium-3 counter output, pressure gauge output, and both thermocouples were connected to the SCB-68 for data logging before an experiment; data were monitored by LabView program developed for this experiment. The signal from the helium-3 counter was fed into an edge-counting virtual instrument. The potential difference produced by the thermocouple was converted into a temperature value using virtual instruments which had been previously verified to report accurate results. The pressure gauge was set to output a 0–5 V signal proportional to a pressure scale between 0 and 10,000 Psi g. The pressure results were proportional to the temperature results and are not presented due to space. All data were continuously recorded by the LabView program with a period of 10 Hz over a period of days.

After each reloading of the u-tube with new titanium, the experimental apparatus was placed in the insulated LN bath for a period of at least six hours to achieve maximum deuterium loading, with LN_2 replenished as necessary. Once sufficient time had passed and the LabView software was recording, the lid of the cryogenic bath was removed, and the u-tube end of the experimental apparatus was submerged up to the union tee within the heated water bath without touching the bottom. Once the thermal shock was complete, the heater was turned off and the system was allowed to return to room temperature. Once the apparatus had reached room temperature, it was reinserted in the LN bath and the process was restarted a number of times for each titanium powder trial.

Control trials were enacted using argon gas after the deuterium trials were completed. At that time a .01–20 Hz software bandpass filter was incorporated into the thermocouple input channels within the LabView program to reduce the effect of high-frequency noise.

4. Results

A summary of peak neutron count rate and trial duration is provided in Table 1. Characteristic results for the trials are available in Figs. 3–5. Count data from the helium-3 detector were converted into millisecond-interval count rates. The thermal shock of deuterium-loaded titanium appeared to produce a small numbers of neutrons; however no burst was as large as the one observed during the series of 1991 experiments. The largest single burst observed in this series of experimental trials appears to have occurred during the argon control trial; as this behavior is unexpected, it was assumed that all of the bursts may be the result of a false signal occurring within the measurement electronics. However the error could not be consistently reproduced in trials.

5. Conclusions

The neutron burst from run 4 was of similar duration and magnitude to the burst observed in 1991. Although the results from run 4 were much larger than subsequent runs, some neutrons appear to have been detected during these additional thermal shock trials. More trials will be performed to try to consistently reproduce the large magnitude bursts Once that is complete, neutron spectroscopy will be implemented.

Two future research avenues are available. The first is to continue the series of experiments detailed here using a higher rate of temperature increase, which will require a redesign of the heating mechanism. The second option is to conduct additional experimental trials on deuterium loading of dehydrided titanium powders at cryogenic temperatures in order to replicate the burst shown in Figs. 3–5. Once the cryogenic neutron phenomenon is sufficiently replicated, attention could then return to thermal shock experiments.

Table 1. Summary of results using second experimental setup.

Trial	${}_{0}^{1}\mathrm{n}_{\mathrm{max}}$ (cts/100 μs)	$\Delta t_{\mathrm{trial}}$ (days)
He-3 check	3	1.86
1	14	4.07
2	46	4.80
3	9	6.92
4	28	1.79
Argon check	427	6.074

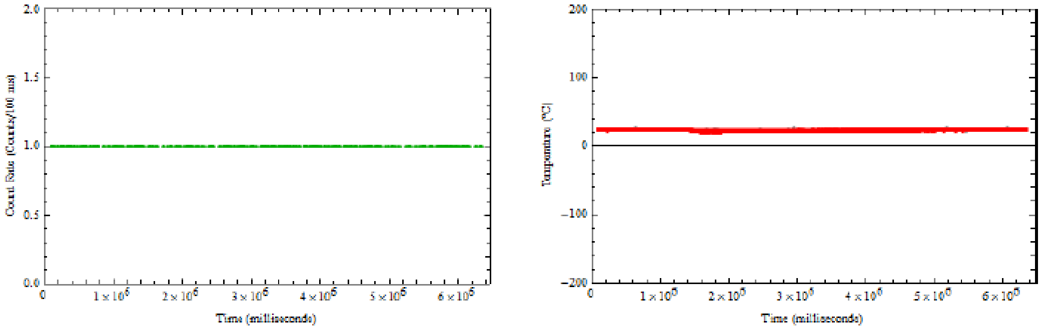

Figure 3. Typical background results from the helium-3 counter (*left*) and temperature gauge (*right*) during trials which show no count rates greater than one neutron per 100 mS when the system is at room temperature.

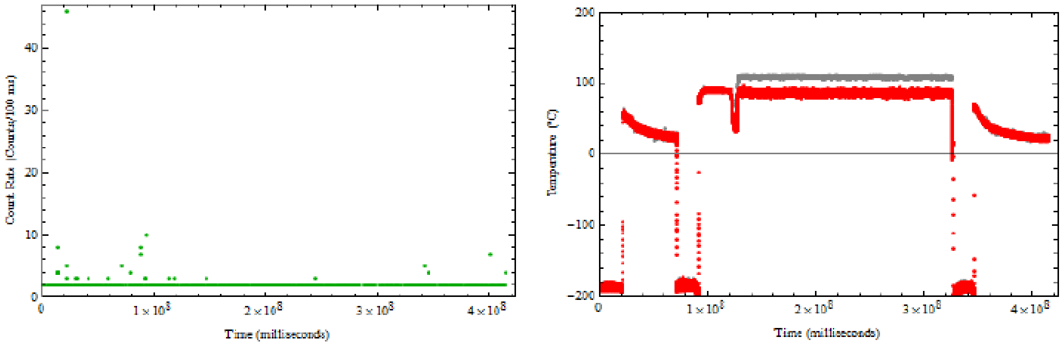

Figure 4. Data showing neutron count rate greater than 1 neutron per 100 ms (*left*) and temperature (*right*) during thermal shock trial 2. Interior u-tube temperature is in red, exterior temperature is in *gray*.

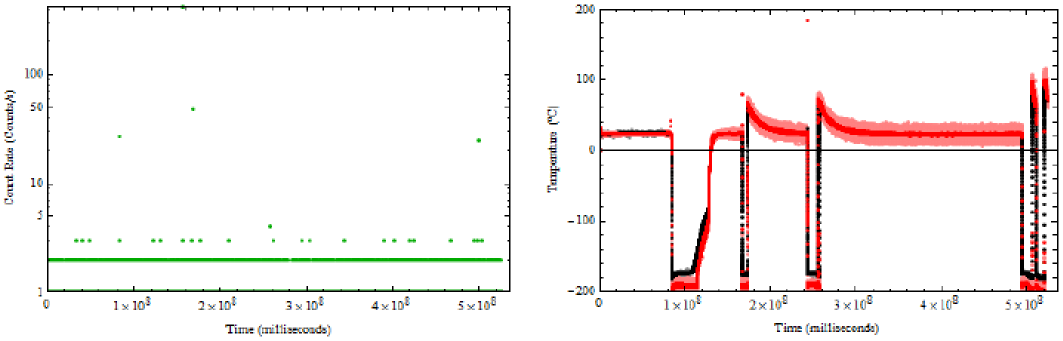

Figure 5. Count rate *(left)* and temperature (*right*) results of thermal shock control trials using argon gas which includes the following temperature data: u-tube exterior (*pink*), noise-filtered u-tube exterior (*red*), actual u-tube interior (*gray*), noise-filtered interior temperature (*black*). Actual interior temperature curve (*gray*) is obscured by noise in the external temperature channel (*pink*).

Acknowledgements

The authors would like to thank the research, administrative, and support personnel at Sidney Kimmel Institute for Nuclear Renaissance. We would also like to thank Dr. Jaewoo Kim of KAERI for his assistance and advice.

References

[1] T. Asami and N. Sano, Study on the phenomenon Reported "Neutron Generation at Room Temperature in a Cylinder Packed with Titanium Shavings and Pressurized Deuterium Gas", *J. Condensed Matter Nucl. Sci.* **5** (2011) 7.

[2] A.d. Ninno, A. Frattolillo, G. Lollobattista, L. Martinis, M. Martone, L. Mori, S. Podda and F. Scaramuzzi, Evidence of emission of neutrons from a titanium–deuterium system, *Europhys. Lett.* **9** (1989) 221.

[3] P.A. Mosier-Boss, A review on nuclear products generated during low-energy nuclear reactions (LENR), *J. Condensed Matter Nucl. Sci.* **6** (2012) 135.

[4] J. Huizenga and T. Harris, Cold fusion research, a report of the energy research advisory board to the United States Department of Energy, DOE/S-0073 DE90 005611. Washington, DC 20585, United States Department of Energy, 1989.

[5] M. Srinivasan, Neutron emission in bursts and hot spots: signature of micro-nuclear explosions? *J. Condensed Matter Nucl. Sci.* **4** (2011) 12.

[6] M.A. Prelas and E. Lukosi, Neutron emission from cryogenically cooled metals under thermal shock, *Proc. 17 th Int. Conf. Cold Fusion*, Daejeon/Korea, 2012, pp. 13–17.

[7] T. Takeda and T. Takizuka, Fractofusion mechanism, *J. Phys. Soc. Japan* **58** (1989) 3073.

[8] K. Yasui, Fractofusion mechanism, *Fusion Technol.* **22** (1992).

[9] E. Storms, Status of cold fusion (2010), *Naturwissenschaften* **97** (2010) 861–881.

[10] N. Kubota, A. Taniike and A. Kitamura, Production of high energy charged particles during deuteron implantation of titanium deuterides, *Conference Proceedings-Italian Physical Society*, Editrice Compositori; 1999, 2000, pp. 311–316.

[11] A. Roussetski, Application of CR-39 plastic track detector for detection of DD and DT-reaction products in cold fusion experiments, *Conference Proceedings-Italian Physical Society*, Editrice Compositori; 1999, 2000, pp. 253–258.

J. Condensed Matter Nucl. Sci. 15 (2015) 321–327

Research Article

Lessons from Cold Fusion Archives and from History

Jed Rothwell*
LENR-CANR.org, USA

Abstract

The field is somewhat chaotic. Results are inconsistent and seem contradictory. There is no widely accepted theoretical explanation. History shows that this kind of chaos is healthy in emergent science. In fields such as plasma fusion there is broad agreement and a solid theoretical basis, but not much progress. We should embrace chaos and celebrate intellectual ferment. Despite the confusion, the literature does prove the effect is real, and it teaches how to replicate. The literature includes many failed experiments. There are two kinds: amateur mistakes and noble failures. At Kamiokande they made amateur mistakes such as holding the palladium in their bare hands. To avoid such mistakes you should read textbooks, read the papers at LENR-CANR, and consult with an electrochemist. A noble failure would be Srinivasan spending six months at SRI trying to replicate the bulk nickel-hydrogen excess heat reported by Mills and replicated at BARC. Srinivasan concluded that he had no significant heat, and that the BARC results were in error. Success will only come thanks to failures such as this.

Keywords: Excess heat, History, Materials, Palladium

---

1. Introduction

There are about 2000 documents at LENR-CANR.org, ranging from the sublime to the ridiculous. What can we learn from all these papers? I have not read them all but I have read hundreds, and I think these are the most important lessons:

(1) Cold fusion is chaotic, and that is a good thing.
(2) The literature does prove the effect is real and it teaches how to replicate. I will point out specific papers that show how to replicate.
(3) This is a multidisciplinary subject. That means you better read the literature and consult with experts, or your experiment will fail.
(4) Finally, the worst error you can make is an unexamined assumption.

---

*E-mail: JedRothwell@gmail.com

2. Chaos

History shows that chaos, confusion and doubt are normal in emergent science. They are healthy. Here is wonderful description of Hahn and Meitner:

> *"Their early papers are a mixture of error and truth as complicated as the mixture of fission products resulting from the bombardments. Such confusion was to remain for long time a characteristic of much of the work on uranium." – E. Segré (Quoted by Mallove, p. 22)* [1]

We should embrace chaos and celebrate intellectual ferment. In plasma fusion there is broad agreement and a solid theoretical basis, but they have not made much progress. Cold fusion is still emerging. Yes, it has been 24 years by the calendar, but compared to plasma fusion this research is two months old. It has gotten roughly US $50 million since 1989, which is how much the DoE spends on plasma fusion every 2 months.[a]

History books sanitize the past. They hide the mistakes, the disputes and chaos that accompanied the birth of fission, and aviation, semiconductors, the laser, and many other breakthroughs. History books give you what I call the museum gallery illusion that the past was better than the present. When you spend an afternoon at the Metropolitan Museum of Art you may get the impression that all French painters in 1880 were consummate geniuses. For every Degas or Renoir there were dozens of third-rate artists. They never made it into the museums. If you want great art, you must settle for lots of schlock art. If you want great science, you must settle for a lot of second-rate science, and also many odd people.

You need many wannabe great artists because you never know who has talent. The early sketches by van Gogh were skilled but no more creative or memorable than the early work of many forgotten artists. A young person destined to do great work may not be aware of her own latent abilities. Martin Fleischmann, when you and I knew him, was hard-working. Long after he retired he would get up every morning and spend hours in his bathrobe puttering around writing papers and graphing data. He was not always so diligent. He told me once: "When I first arrived in England as a refugee I was the laziest boy you ever saw. The laziest boy in Europe. I found myself penniless and living in an abandoned chicken house. I said to myself, 'if you do not get to work, go to school and make something of yourself you will spend the rest of your life in a chicken house.'" I suppose if there had been no war, Martin might have been the indolent son of a rich family all of his life.

3. Cold Fusion is Real

The next lesson from the literature is that cold fusion is real. In September 1990, Fritz Will published a list of 92 researchers with positive results [2]. After people such as McKubre, Storms and Fritz Will himself published in 1990, the controversy should have ended. No other claim in the history of experimental science has been so widely replicated at such high signal to noise ratios yet still not believed.

Prof. Heinz Gerischer was a leading electrochemist and the Director of the Department of Physical Chemistry at the. He reviewed the evidence in 1991 and concluded "there [are] now undoubtedly overwhelming indications that nuclear processes take place in metal alloys [3]." For a distinguished professor this is emphatic. "Undoubtedly overwhelming" is shouting through a megaphone. Most qualified experts I know who have read the literature agree that the effect is real. Most so-called skeptics have not read the literature. I will grant, science is not a popularity contest, but informed opinion should carry weight.

---

[a] The plasma fusion FY 2012 budget was US $248 million. ITER is now expected to cost US $23 billion. http://articles.washingtonpost.com/2012-06-25/national/35461417_1_nuclear-fusion-iter-fusion-power

Graham Hubler recently said that we need: “either more reproducibility, proof positive that a nuclear process produces the heat, or a viable model, none of which we have at present.” I disagree. I think the literature shows that cold fusion is more reproducible than the transistor was in the early 1950s. The tritium; and the heat correlated with helium; together are proof-positive that the effect is nuclear. We have no viable model, but two out of three isn’t bad. I fear that Graham means to we must start over from scratch with every project to prove that cold fusion exists, like Sisyphus pushing the rock up the hill. If your funding agencies do not accept the proof already published by Mike McKubre, they will not accept your proof either. You will have to wait for Rossi.

4. How to Replicate Cold Fusion

Not only is cold fusion real, but the literature does teach how to replicate. And I am going to teach you how to replicate, in the next five minutes. There are many valuable papers about this. I like these three [4–6]:

(1) Miles, M. and K.B. Johnson, *Anomalous Effects in Deuterated Systems, Final Report*. Naval Air Warfare Center Weapons Division.
(2) Cravens, D. *Factors Affecting Success Rate of Heat Generation in CF Cells*, ICCF4.
(3) Storms, E., *How to produce the Pons–Fleischmann effect,* Fusion Technology.

The Miles paper is a masterpiece. It is famous because it shows the correlation between helium and heat. But, what got my attention is here:

This compares the performance of palladium from different sources. It shows that material is critical to success. The NRL material was pretty good, Johnson Matthey was the best, and palladium from miscellaneous sources at the bottom did not work. In the Johnson Matthey section, the three worked spectacularly well, producing 3–15 W/cm^3, which is about 10 times better than the others:

The notation JM (F/P) means “Johnson Matthey palladium provided by Fleischmann and Pons.” Fleischmann himself handed over these two cathodes to Miles. Johnson Matthey gave Miles the other one from the same stock. Miles told me this was the best palladium he ever used. So, I asked Martin about it. Here is our conversation as I recall it many years later:

JR: “Mel says you gave him the cathodes that work so well.”

MF: “Yes, I handed out many samples, to Mel and to others. Here’s the thing. When Uncle Martin gives you palladium, it works! When other people give you palladium, it doesn’t work. What does that tell you?! Hmmmm?”

JR: “It tells me the secret is in the material. So how did you know what material to use?”

MF: “I didn’t know! I asked my friends at Johnson Matthey.”

Martin told Johnson Matthey he wanted to load palladium with hydrogen to high levels, and they recommended the palladium that they had developed in the 1930s for hydrogen filters. The people at BARC and NASA later used that material as is, inside of Milton Roy hydrogen purifiers. They reported it worked well.

Okay, you start with the recommended palladium. Then you prepare it by various methods such as polishing the surface and doing electrolysis at low power to condition the metal. When Fleischmann and Pons went to France with Toyota, they improved their methods of preparation. The methods were hush-hush, but we know what they are. Because, at ICCF4, Dennis Cravens described his methods. Fleischmann said: “That’s my favorite paper. Dennis revealed our secrets! That’s just what we do!” So, to learn how to prepare the palladium, read Cravens.

This brings us to the third paper, by Edmund Storms. This teaches how to recognize good material. That is, how to winnow it out. This study began when the Tanaka Precious Metals Company sent Storms 90 foil cathodes. Storms devised a series of tests to separate the good ones from the bad ones, and methods to coax them into working better.

These methods include some of the one Cravens recommended" Polish to a mirror finish; wash with acetone; after washing "do not touch with fingers or tissue paper," Load slowly. Storms also described several ways to test a cathode as he prepared it, to predict how well it will work. For example, he wants to know if the palladium is weak, so he looks for cracks, and he uses a handheld micrometer to measure how much the palladium swells up during initial loading. He rejects palladium that swells more than 2%. Storms tested the 90 cathodes and he found 4 that passed all tests. These four produced robust heat. They worked repeatedly. It took Storms about a year to test all 90 samples.

So, this is how you replicate: Ask Johnson Matthey for 90 pieces of hydrogen filter palladium. Master the techniques described by Cravens. Then, spend a year testing them. With luck you will find a few that work. If you don't, get another 90 pieces of palladium and start over.

Fleischmann and Pons' work in France—using Johnson Matthey palladium and the techniques described by Cravens—culminated in spectacular results. In experiment 3 they got 294 MJ of excess energy at 101 W. In experiment 4 they got 250% excess. [7] These results might have been the making of cold fusion. They might have convinced the world that the effect is real. Alas, the opportunity was squandered. This project collapsed, I was told, because of greed and politics.

After Martin retired, he and I tried to buy some of the hydrogen filter palladium. Johnson Matthey told us they had changed the method of manufacturing it.[b] They offered to make us a kilogram with the old formula for US $50,000. Martin and I did not have that kind of money. We asked several researchers if they would like to go in with us, but no one expressed interest. By that time Violante was learning how to make reliable cathodes. I suppose he is gradually rediscovering secrets that Johnson Matthey has known for 80 years. Another rock, another hill. Uncle Martin did not get a chance to hand out more palladium, and we never found out whether other people could replicate those spectacular results from France.

The work by Mel Miles also ended badly. When the Navy found out what he was up to, they demoted him from Distinguished Fellow of the Institute to a menial job as a stock room clerk. So he retired [8].

5. Failed Experiments

Continuing our tour of the dark side, let us look at some failed experiments. There are hundreds in the literature. It is not pleasant reading about them, but you should try to understand what went wrong. Let us look at two examples: Srinivasan, and Kamiokande. The people at BARC did many fine experiments. They produced definitive results, especially with palladium. Their results with nickel light water cells are a puzzling mix of success and failure. Srinivasan led three tests:

Here is what else they found in Series 3:

Series 1. BARC (1992). Produced excess heat and tritium

Series 2. SRI (1994). Srinivasan visited SRI and tried to replicate Series 1. After 6 months of effort, he concluded that the excess heat was caused by recombination. He admitted it was a mistake. This is a noble failure.

Series 3. BARC (1996). Back in India, in these tests they made no attempt to measure heat, only tritium. Tritium was again detected, but not at levels as high as the first series.

Here is what else they found in Series 3: The tritium kept vanishing in a "sawtooth fashion." The authors wrote: "A close scrutiny of our sampling, distilling, and counting techniques confirms that the decrease in tritium level is genuine and not attributable to any artifact. We are strongly tempted to suggest that there is an as yet unidentified mechanism periodically 'cleansing' the electrolyte of tritium." [9] These results are as confusing as Hahn and Meitner's were in the 1930s.

---

[b] They no longer melted the metal under cracked ammonia. Fleischmann and Miles felt that the ammonia might be important. The newer hydrogen filter palladium might work. It has not been tested as far as I know.

The literature is full of weird results like this one. They cannot all be right, but unless you have a magic touchstone, you can not tell which is right and which is not. Theory is no guide. This is frustrating. But I think it is wonderful. You probably do not see things like this at plasma fusion conferences.

Kamiokande. In these studies, the particle detection was superb. Unfortunately, electrochemistry was treated as an afterthought. In 1991 and 1992, they did two sets of tests. They used a total of 50 cells, including gas loaded and electrochemical ones, plus Portland cement made with heavy water. The graduate thesis by Ishida devotes 120 pages to particle detection but only a few pages to the cells [10]. It says "the whole preparation of electrolytic cells was entrusted to groups from BYU and Texas A&M." I have not found a description of the electrochemistry in the published papers. Years after the tests, I spoke with American and Japanese electrochemists who heard about the project. This is what they told me:

- Texas A&M sent instructions along with the cells; i.e. what voltage to use, how to prepare the cathodes. The researchers at Kamiokande apparently ignored these instructions.
- All cells were run on the same circuit, even though the anodes and cathodes were of different sizes and shapes. The cells were wired electrically in series at first, until one cell failed. Then they were rewired in parallel.
- The cells were run at high voltage from the start, because the researchers wanted to get on with the experiment quickly. You are supposed to gradually ramp up, as Cravens and Storms said.
- The researchers were shown on national TV pulling out a cathode with their bare fingers, waving it at the camera, and then putting it back. This contaminates the cathode. The Japanese electrochemists watching this were aghast [11]. Again, Cravens, Storms or any electrochemist would have warned them not to do this.
- They employed no diagnostics other than neutrons; they did not attempt to measure excess heat or loading.
- They did not ask Mizuno or any other electrochemist to assist.

From an electrochemist's point of view, these people were trying to tune a piano with a sledgehammer. McKubre described this experiment as "a profligate squandering of resource and opportunity." He said: "With a little more thought and care, a little less hubris, and the inclusion of just one electrochemist, this could have been a crucial one-off experiment." Ikegami described this as "fishing in a dry hole." It is unlikely any of these cells produced a cold fusion effect.

The key lesson is: read the textbooks, read the literature, consult with experts. Most of the failed experiments went off the tracks because the researchers did not do their homework. It really is that simple.

As I mentioned, Fleischmann asked Johnson Matthey to recommend palladium. John Bockris once said to me: "I am not an expert in calorimetry, so I scouted out the best expert in Texas and asked him visit our lab. He came, looked at the apparatus and the data, and then he laughed and said: 'You do not need me; anyone can measure that much heat!'" If Fleischmann and Bockris felt comfortable asking others for help, you should too.

6. Unfounded Assumptions

Finally, let us look at the unfounded assumption. The most egregious error is not doing your homework. The most pernicious error is the unfounded assumption. That is, an assumption so widely held and taken for granted that no one notices it. Here is a fascinating example from the history of biology: the half-century struggle to determine where the genetic code is stored.

By 1900, people knew the laws of genetics. They learned them from observations of fruit flies and other species. Quoting a textbook from 1916: "we may reasonably suppose" that "in the chromosomes is found the material basis of every inherited character." Elsewhere it says "we assume" that a particular characteristic is governed by two different genes which may be in different chromosomes[c] [12]. They knew a lot, and they also knew the limits of their knowledge. Textbooks emphasized that they did not know the physical nature of the gene, and they were speculating about it.

The first question was: Are genes stored in proteins, carbohydrates, or the nucleic acid? Most experts concluded it must be in proteins. Why? Because protein is complex and varied. The acid was ruled out because it seemed, quote: "too simple" [13],[d] and too "boring"[e].

To put it in modern terms: people thought that complex information has to be stored in a complex data storage medium. From our point of view, the notion that the acid is "too simple" sounds comical, because we are used to binary data storage in simple repetitive structures. We live in sea of information. Our computers store more bytes of data than there are grains of sand on all of the beaches of the earth [14].

There was some mechanical data storage back then, such as IBM punch-cards. Most people never encountered such things and had no feel for them. I doubt it would have occurred to a biologist in 1930 to consult with IBM engineers. Wide ranging cross-disciplinary collaboration is a great thing, but you have to have some idea who you want to collaborate with, and why. I do not think we know that either. Other people know the answers to our questions, but we do not know who they are, and they have never heard of us.

This "complicated storage" hypothesis had no basis in biology. It just drifted in through a window and settled in people's minds. Are there phantom unfounded notions holding back the development of cold fusion? John Bockris said: "The Coulomb barrier is a shibboleth! A myth!" The reader can be the judge of that. Many skeptics believe that all cold fusion reactions must produce a huge flux of neutrons. This belief is well-grounded in plasma fusion theory, unlike the "complicated storage" idea. Well-grounded or not, once the experiments proved there is no giant flux of neutrons, everyone should have put that belief aside. It has become an unquestioned assumption. A shibboleth. Are we making similar dogmatic mistakes? I can't tell; I would be as blind to them as you are. I can only caution you to be careful.

Let me close with the history of biology. By the mid-1940s they concluded that the gene is in nucleic acid. They were still floundering around trying to figure out the structure of DNA when along came James Watson, another lazy young man like Martin Fleischmann in the chicken house. By his own account, Watson was always ready to cut corners and goof off. He described a conference in Italy in 1951, a year before he discovered DNA. This is a picture of emergent science and the many odd people it attracts. It may make you feel better about our conferences:

> *"Much of the talk about the three-dimensional structure of proteins and nucleic acids was hot air. Though this work had been going on for over 15 years, most if not all of the facts were soft. Ideas put forward with conviction were likely to be the products of wild crystalographers who delighted in being in a field where their ideas could not be easily disproved. Thus, though virtually all biochemists . . . were unable to understand the arguments of the X-ray people, there was little uneasiness. It made no sense to learn complicated mathematical methods in order to follow baloney."* [15]

---

[c] Castle: "One mechanism will now suffice for all kinds of inheritance, this mechanism being found in the chromosomes. In them, we may reasonably suppose, is found the material basis of every inherited character. When the inheritance is of the simplest kind, involving presence or absence of color or some similar character, we assume that a genetic change has occurred in a single, definite locus in a particular chromosome, and that this single change is responsible for the observed inherited variation. Other characters depend on two or more genes, which may lie at different loci in the same chromosome, or even in different chromosomes. . . ."

[d] "Too simple" Asimov, I., A Short History of Biology. 1964: Natural History Press. ". . . it was taken for granted that the nucleic acid was subsidiary and that the protein was the thing itself. . . . Not only was faith in the protein molecule unshakable but, through the 1930s, all evidence seemed to point to the fact that nucleic acids were quite small molecules (made up of only four nucleotides each) and therefore far too simple to carry genetic instructions. The turning point came in 1944 . . ."

[e] "Boring" http://pablosorigins.blogspot.com/2009/11/history-of-dna-part-ii-proteins-vs-dna.html

References

[1] E. Mallove, *Fire From Ice,* Wiley, New York, 1991.

[2] F.G. Will, *Groups Reporting Cold Fusion Evidence,* National Cold Fusion Institute, Salt Lake City, UT, 1990.

[3] H. Gerischer, Memorandum on the present state of knowledge on cold fusion, Fritz Harber Institute der Max Planke, Berlin, 1991.

[4] M. Miles and K.B. Johnson, Anomalous effects in deuterated systems, Final Report, Naval Air Warfare Center Weapons Division, 1996.

[5] D. Cravens, Factors affecting success rate of heat generation in CF cells. in *Fourth Int. Conf. on Cold Fusion*, Lahaina, Maui: Electric Power Research Institute 3412 Hillview Ave., Palo Alto, CA 94304, 1993. .

[6] E. Storms, How to produce the Pons–Fleischmann effect, *Fusion Technol.* **29** (1996) 261.

[7] T. Roulette, J. Roulette and S. Pons, Results of ICARUS 9 experiments run at IMRA Europe, in *Sixth Int. Conf. on Cold Fusion, Progress in New Hydrogen Energy,* Lake Toya, Hokkaido, Japan, 1996, New Energy and Industrial Technology Development Organization, Tokyo Institute of Technology, Tokyo, Japan.

[8] B. Daviss, Reasonable doubt, in *New Scientist,* 2003, p. 36.

[9] T.K. Sankaranarayanan et al., Investigation of low-level tritium generation in Ni–H_2O electrolytic cells, *Fusion Technol.* **30** (1996) 349.

[10] T. Ishida, Study of the anomalous nuclear effects in solid deuterium systems, Tokyo University, 1992, p. 131.

[11] F. Nakano, Mohaya hitei dekinai jyouonkakuyuugou [The reality of cold fusion can no longer be denied], in Bungei Shunju, 1991.

[12] W.E. Castle, *Genetics and Eugenics,* Harvard University Press, 1916.

[13] I. Asimov, *A Short History of Biology,* Natural History Press, 1964.

[14] H. Kuniya, Shakai wo kaeru “biggu deeta” kakumei [The revolution in “big data” that is changing society], in Close-up Gendai. 2012, NHK.

[15] J. Watson, *The Double Helix,* Norton Critical Edition, 1980, p. 23.